frontiers | Research Topics

Hallmark of cancer: Avoiding immune suppression

Edited by
Benedetta Apollonio, Liusheng Peng, Michal Sheffer, Elias Joseph Sayour and Faris Q. B. Alenzi

Published in
Frontiers in Immunology
Frontiers in Oncology

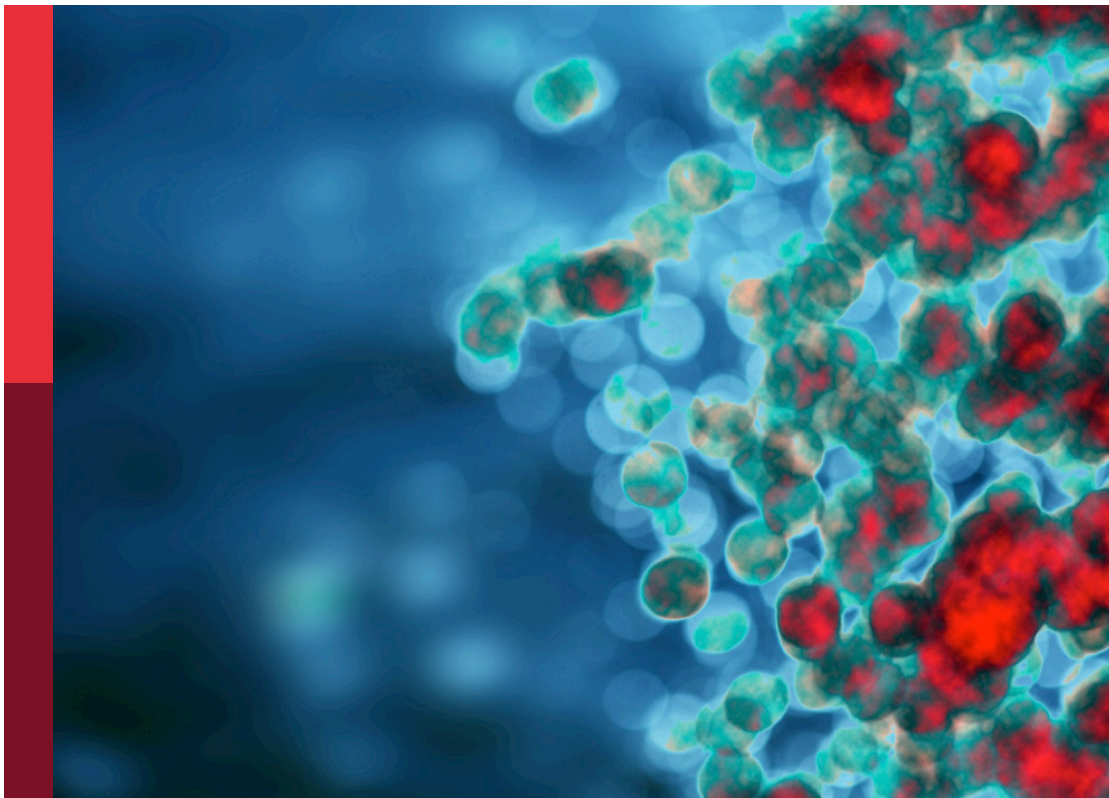

ISSN 1664-8714
ISBN 978-2-8325-2879-2
DOI 10.3389/978-2-8325-2879-2

About Frontiers

Frontiers is more than just an open access publisher of scholarly articles: it is a pioneering approach to the world of academia, radically improving the way scholarly research is managed. The grand vision of Frontiers is a world where all people have an equal opportunity to seek, share and generate knowledge. Frontiers provides immediate and permanent online open access to all its publications, but this alone is not enough to realize our grand goals.

Frontiers journal series

The Frontiers journal series is a multi-tier and interdisciplinary set of open-access, online journals, promising a paradigm shift from the current review, selection and dissemination processes in academic publishing. All Frontiers journals are driven by researchers for researchers; therefore, they constitute a service to the scholarly community. At the same time, the *Frontiers journal series* operates on a revolutionary invention, the tiered publishing system, initially addressing specific communities of scholars, and gradually climbing up to broader public understanding, thus serving the interests of the lay society, too.

Dedication to quality

Each Frontiers article is a landmark of the highest quality, thanks to genuinely collaborative interactions between authors and review editors, who include some of the world's best academicians. Research must be certified by peers before entering a stream of knowledge that may eventually reach the public - and shape society; therefore, Frontiers only applies the most rigorous and unbiased reviews. Frontiers revolutionizes research publishing by freely delivering the most outstanding research, evaluated with no bias from both the academic and social point of view. By applying the most advanced information technologies, Frontiers is catapulting scholarly publishing into a new generation.

What are Frontiers Research Topics?

Frontiers Research Topics are very popular trademarks of the *Frontiers journals series*: they are collections of at least ten articles, all centered on a particular subject. With their unique mix of varied contributions from Original Research to Review Articles, Frontiers Research Topics unify the most influential researchers, the latest key findings and historical advances in a hot research area.

Find out more on how to host your own Frontiers Research Topic or contribute to one as an author by contacting the Frontiers editorial office: frontiersin.org/about/contact

Hallmark of cancer: Avoiding immune suppression

Topic editors

Benedetta Apollonio — Istituto Tumori Bari Giovanni Paolo II, Italy
Liusheng Peng — Third Military Medical University, China
Michal Sheffer — Dana–Farber Cancer Institute, United States
Elias Joseph Sayour — University of Florida, United States
Faris Q.B. Alenzi — Prince Sattam Bin Abdulaziz University, Saudi Arabia

Citation

Apollonio, B., Peng, L., Sheffer, M., Sayour, E. J., Alenzi, F. Q. B., eds. (2023). *Hallmark of cancer: Avoiding immune suppression*. Lausanne: Frontiers Media SA. doi: 10.3389/978-2-8325-2879-2

Table of contents

frontiers | Frontiers in Oncology

TYPE Editorial
PUBLISHED 16 June 2023
DOI 10.3389/fonc.2023.1211456

OPEN ACCESS

EDITED AND REVIEWED BY
Sergei Kusmartsev,
Department of Urology, University of Florida, United States

*CORRESPONDENCE
Elias J. Sayour
elias.sayour@neurosurgery.ufl.edu

RECEIVED 24 April 2023
ACCEPTED 22 May 2023
PUBLISHED 16 June 2023

CITATION
Alenzi FQB, Apollonio B, Peng L, Sayour EJ and Sheffer M (2023) Editorial: Hallmark of cancer: avoiding immune suppression. *Front. Oncol.* 13:1211456. doi: 10.3389/fonc.2023.1211456

Editorial: Hallmark of cancer: avoiding immune suppression

Faris Q. B. Alenzi[1], Benedetta Apollonio[2], Liusheng Peng[3], Elias J. Sayour[4]* and Michal Sheffer[5]

[1]Prince Sattam Bin Abdulaziz University, Al-Kharj, Saudi Arabia, [2]S.S.D. Rare Tumors and Melanoma, IRCCS Istituto Tumori "Giovanni Paolo II", Bari, Italy, [3]Department of Microbiology and Biochemical Pharmacy, College of Pharmacy, Third Military Medical University, Chongqing, China, [4]Department of Neurosurgery, University of Florida, Gainesville, FL, United States, [5]Dana–Farber Cancer Institute, Boston, MA, United States

KEYWORDS

immunosuppression, metabolomics, tumor microenvironment, cancer immunotherapy, prediction

Editorial on the Research Topic
Hallmark of cancer: avoiding immune suppression

Immunosuppression remains a dominating force in the refractory nature of most malignancies. Unlocking immunotherapeutic efficacy requires a more detailed understanding of the cancer ecosystem, including neovascularization, hypoxia patterns, tumor metabolomics, stromal architecture and immunobiology. This understanding is critical to making more informed decisions regarding evolutionary biology, cancer cell senescence, and the tumor immune microenvironment and may be used to predict treatment strategies. In this Research Topic, papers are collated that focus on cancer-mediated immunosuppression as a hallmark. The review by Santiago-Sanchez et al. highlights the myriad of mechanisms and pathways implicated in cancer-mediated immunosuppression. The scope of work in the collection ranges from imaging and radiogenomics in ovarian cancer, to long-noncoding RNA prediction in hepatocellular carcinoma, and glucose metabolism and response to anti-PD-1 therapy in papillary thyroid cancer. Additional articles for this hallmark pertain to hypoxia and machine learning in lung adenocarcinoma, alternative splicing in bladder cancer while others focus on specific molecules of interest including SIGLEC15 in thyroid cancer, TIGIT expression in solid tumors, pyroptosis gene TP63 in osteosarcoma and HSP90 expression in lymphoma to inform immunotherapeutic application. As newer immunotherapy approaches continue to be developed, so must our understanding of the immune landscape across malignancies to inform rationale predictions and treatment modalities. The papers herein reflect a breadth of tools that could be used to make informed decisions in distinct cancer subsets. With the boom of artificial intelligence and public repositories harboring genomic and transcriptome data sets, it is conceivable that more accurate predictions regarding individual cancer biology will be made to inform treatment. The degree, scope and cell types involved in immunosuppression must be better delineated for cancer immunotherapy to meet its promise. The work herein helps add to the growing chorus of tools that will allow for more informed decisions regarding individual cancer

immunobiology and provide renewed hope that immunotherapy may be leveraged as an adaptable tool for patients based on their biology for more personalized intervention.

Author contributions

All authors listed have made a substantial, direct, and intellectual contribution to the work and approved it for publication.

Conflict of interest

ES discloses having patent applications on immunotherapeutic technologies many of which are optioned to commercial license.

The remaining authors declare that the research was conducted in the absence of any commercial or financial relationships that could be construed as a potential conflict of interest.

The handling editor SK declared a shared affiliation with the author ES at the time of review.

Publisher's note

frontiers in Immunology

ORIGINAL RESEARCH
published: 28 March 2022
doi: 10.3389/fimmu.2022.868067

Computed Tomography Imaging-Based Radiogenomics Analysis Reveals Hypoxia Patterns and Immunological Characteristics in Ovarian Cancer

Songwei Feng[1†], *Tianyi Xia*[2†], *Yu Ge*[1], *Ke Zhang*[1], *Xuan Ji*[1], *Shanhui Luo*[3] *and Yang Shen*[1*]

[1] Department of Obstetrics and Gynaecology, Zhongda Hospital, School of Medicine, Southeast University, Nanjing, China, [2] Department of Radiology, Zhongda Hospital, School of Medicine, Southeast University, Nanjing, China, [3] Department of Gynaecology, The Second Affiliated Hospital of Soochow University, Soochow University, Suzhou, China

OPEN ACCESS

Edited by:
Liusheng Peng,
Third Military Medical University, China

Reviewed by:
Tao Huang,
Shanghai Institute of Nutrition and Health (CAS), China
Fangdie Ye,
Fudan University, China

***Correspondence:**
Yang Shen
shenyang@seu.edu.cn

[†]These authors have contributed equally to this work

Specialty section:
This article was submitted to Cancer Immunity and Immunotherapy, a section of the journal Frontiers in Immunology

Received: 02 February 2022
Accepted: 28 February 2022
Published: 28 March 2022

Citation:
Feng S, Xia T, Ge Y, Zhang K, Ji X, Luo S and Shen Y (2022) Computed Tomography Imaging-Based Radiogenomics Analysis Reveals Hypoxia Patterns and Immunological Characteristics in Ovarian Cancer. Front. Immunol. 13:868067. doi: 10.3389/fimmu.2022.868067

Purpose: The hypoxic microenvironment is involved in the tumorigenesis of ovarian cancer (OC). Therefore, we aim to develop a non-invasive radiogenomics approach to identify a hypoxia pattern with potential application in patient prognostication.

Methods: Specific hypoxia-related genes (sHRGs) were identified based on RNA-seq of OC cell lines cultured with different oxygen conditions. Meanwhile, multiple hypoxia-related subtypes were identified by unsupervised consensus analysis and LASSO–Cox regression analysis. Subsequently, diversified bioinformatics algorithms were used to explore the immune microenvironment, prognosis, biological pathway alteration, and drug sensitivity among different subtypes. Finally, optimal radiogenomics biomarkers for predicting the risk status of patients were developed by machine learning algorithms.

Results: One hundred forty sHRGs and three types of hypoxia-related subtypes were identified. Among them, hypoxia-cluster-B, gene-cluster-B, and high-risk subtypes had poor survival outcomes. The subtypes were closely related to each other, and hypoxia-cluster-B and gene-cluster-B had higher hypoxia risk scores. Notably, the low-risk subtype had an active immune microenvironment and may benefit from immunotherapy. Finally, a four-feature radiogenomics model was constructed to reveal hypoxia risk status, and the model achieved area under the curve (AUC) values of 0.900 and 0.703 for the training and testing cohorts, respectively.

Conclusion: As a non-invasive approach, computed tomography-based radiogenomics biomarkers may enable the pretreatment prediction of the hypoxia pattern, prognosis, therapeutic effect, and immune microenvironment in patients with OC.

Keywords: radiogenomics, computed tomography, ovarian cancer, prognosis, molecular subtypes

INTRODUCTION

Ovarian cancer (OC) has the highest mortality rate among gynecologic cancers. Surgery and platinum-based chemotherapy are the mainstays of care for individuals with OC (1). Meanwhile, immunotherapy is a promising treatment option for various cancers, and it has improved the quality of life of certain OC patients (2). However, immunotherapy in OC still faces challenges, such as drug resistance and the lack of preoperative non-invasive predictive tools (3).

Hypoxia impacts the tumor microenvironment (TME) (4), angiogenesis, immunosuppression, and immune evasion (5). The hypoxic microenvironment regulates carcinogenesis, radiotherapy, and chemotherapy resistance (6). Based on the above evidence, a positive response to immunotherapy may depend on immune regulation within the TME. In recent years, this theory has been proven by a series of fundamental research. For example, intratumor tissue-resident memory T cells (T_{RM}) were found to express PD-1 and LAG-3, and the triggering of inhibitory receptors may lead to dysfunction that may limit the effectiveness of T_{RM} in inhibiting tumor growth (7). The attenuation of NRF1 degradation in hypoxic circumstances may impede tumor-associated macrophage polarization (8). Therefore, a comprehensive analysis of immunological characteristics due to hypoxia is a priority to improve treatment with immune checkpoint inhibitors (ICIs).

At present, a large number of studies have revealed the genesis of cancer through omics analysis. In lung cancer, key genes for disease progression were identified by various bioinformatics methods (9). Interestingly, cancer cell lines can also be identified by the incremental feature selection method (10). For OC, the ceRNA network was constructed, and novel insights of the regulatory mechanisms among mRNAs, lncRNAs, and miRNAs were provided (11). However, in most omics analyses, these studies did not focus on the combination of imaging data and sequencing data. Computed tomography (CT) is part of the standard of treatment and is used as a "road map" to guide debulking surgery and assess chemotherapy response in patients with OC (12). CT imaging-based radiomics allows for the translation of images into thousands of features followed by subsequent model building to improve prognostic prediction (13). Radiogenomics is a new cross-disciplinary research combining radiomics with genomics (14). In kidney cancer, it was shown that VHL mutations are significantly associated with well-defined tumor margins and nodular tumor enhancement (15). T2-derived texture metrics from the whole-tumor are used to assess response in therapy (16). Interestingly, radiogenomics can identify the landscape of m6A methylation modification in bladder cancer (17). Because of the intratumor heterogeneity in advanced ovarian cancer with peritoneal carcinomatosis, methods for assessing tumor heterogeneity using radiogenomics are needed to analyze whole-tumor heterogeneity rather than single biopsy sampling (18).

Hence, there have been many studies focusing on radiogenomics in ovarian cancer in recent years, but they mainly focused on the prediction of Classification of Ovarian Cancer (CLOVAR) (19) and BRCA mutations (20). Thus, we aimed to develop a radiogenomics approach to reveal the hypoxia pattern and immunological characteristics of patients with OC.

In this research, we collected the genomic data of 630 OC patients and then constructed three types of subtypes using hypoxia-related genes or hypoxia pattern regulator expression. We assessed the predictive value of the hypoxia subtypes and correlated it with TME. In addition, we developed a nine-gene next-generation sequencing panel for clinical application, and it may represent different hypoxic statuses. As for radiomics, a CT imaging signature based on the nine-gene panel classification was obtained using the radiomics algorithm. In a word, our findings revealed the critical role of hypoxia in TME and immunotherapy for OC patients. Most importantly, the CT imaging-based radiogenomics signature can make non-invasive predictions prior to treatment.

METHODS

Datasets and Data Preprocessing

The workflow of the study is depicted in **Figure 1**. We downloaded six samples from the GSE66894 dataset (21), namely, normoxia-cultured SKOV3 cell line samples (GSM1633848, GSM1633849, and GSM1633850) and hypoxia-cultured cell line samples (GSM1633857, GSM1633858, and GSM1633859). For hypoxia treatment, SKOV3 cells were exposed to 0.5% oxygen for 16 h. Subsequently, we used the limma package (22) for the analysis of differentially expressed genes (DEGs), and |log fold change| >1 and adj. p-value <0.05 were set as the thresholds (23). Meanwhile, 1,694 genes identified in previous literature were used as HRGs from the Molecular Signatures Database (MsigDB) (24). Specific hypoxia-related genes in OC were screened by the overlap of the HRGs and the DEGs. In addition, RNA sequencing profiles and clinical data of patients with OC are available from The Cancer Genome Atlas (TCGA) (25) and Gene Expression Omnibus (GEO) databases (26), and mutational data of patients with OC were obtained only from the TCGA database. We excluded samples with no survival information and those sequenced repeatedly for the same patient. Finally, 374 patients in the TCGA-OV cohort and 260 patients in GSE32062 were retained for subsequent analysis. It is worth noting that FPKM data were converted to transcripts per kilobase million (TPM) data. Batch effects between these cohorts were removed using the sva package. In addition, The mRNA stemness score (RNAss) of OC cases in TCGA was acquired from previous studies (27).

Unsupervised Clustering Analysis

ConsensusClusterPlus package (28) was used to perform unsupervised clustering analysis for the classification of patients with OC. As for the clustering of hypoxia-related subtypes and gene-related subtypes, the parameters were set to

Abbreviations: OC, ovarian cancer; sHRGs, specific hypoxia-related genes; AUC, area under the curve; TME, tumor microenvironment; ICIs, immune checkpoint inhibitors; CT, computed tomography; CLOVAR, Classification of Ovarian Cancer; DEGs, differentially expressed genes; MsigDB, Molecular Signatures Database; TCGA, The Cancer Genome Atlas; PCA, principal component analysis; TIDE, tumor immune dysfunction and exclusion; TCIA, The Cancer Imaging Archive; ROI, region of interest.

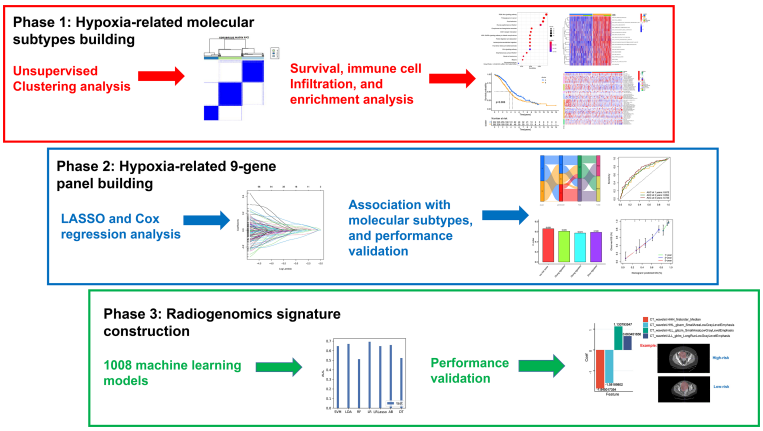

FIGURE 1 | The workflow of the study.

reps = 1,000 and pitem = 0.8 based on related gene expression (29). Principal component analysis (PCA) (30) and Kaplan–Meier analysis (log-rank test) were performed to identify whether different subtypes were relatively independent in prognosis and heterogeneity.

Immune Cell Infiltration Analysis

We simultaneously used diversified algorithms (TIMER (31), CIBERSORT (32), quanTIseq (33), MCP-counter (34), xCell (35), EPIC (36), and ssGSEA (37)] to estimate the abundances of immune cells or score of immune function in each OC sample. The ESTIMATE algorithm (38) was utilized to assess the overall state of the TME (immune score, stromal score, and tumor purity). Immune checkpoint-related gene and human leukocyte antigen (HLA) gene expressions were compared in different risk groups. In addition, the tumor immune dysfunction and exclusion (TIDE) algorithm (39) was used to assess the immunotherapy response of different patients.

Construction and Validation of the Nine-Gene Panel

Firstly, prognostic genes (p-value < 0.05) were screened using univariate Cox regression analysis in all hypoxia pattern-related regulators. Next, least absolute shrinkage and selection operator (LASSO) regression analysis and multivariate Cox regression analysis (stepwise method) were used to identify genes involved in a panel. We used the appropriate λ and Akaike information criterion (AIC) to control robustness in the model. All the above modeling processes were carried out in the TCGA-OV cohort. The hypoxia risk score was calculated as follows:

$$\sum_{i=1}^{n} \text{coefficient}_i * \text{expression}_i$$

where coefficient is the regression coefficient in multivariate Cox regression analysis, and expression is the RNA expression of each selected gene. Considering that we used the TCGA-OV cohort as the training cohort, we calculated hypoxia risk scores in the validation cohort (GSE32062) with the same formula. Subsequently, we divided all patients into high- and low-risk groups with the median score in the TCGA cohort. Finally, PCA, ROC, Kaplan–Meier, and Cox regression analyses were used to validate the prognostic value of the nine-gene panel in each cohort.

Comparison Between the Nine-Gene Panel and Other Signatures

Zhang et al. identified a glycolysis-related gene signature for OC patients (40). Zhou et al. identified a DNA methylation-driven gene signature (41). Moreover, Zheng et al. developed a risk stratification system based on glycolysis-related lncRNAs (42). Each signature's risk score was determined using normalized expression values and coefficients from references. On the basis of the TCGA-OV cohort in our study (374 patients), the C-indexes of the models were estimated and compared.

Functional Enrichment Analysis

Specific hypoxia-related genes were enriched in ClueGO of the Cytoscape software (43). The thresholds were set by default in the software. Meanwhile, we used gene set (c2.cp.kegg.v6.2.symbols) for running GSVA analysis in different hypoxia-related clusters (33). An adjusted p-value <0.05 was regarded as statistically significant. As for the hypoxia pattern regulators, Gene Ontology (GO) (44) and Kyoto Encyclopedia of Genes and Genomes (KEGG) (45) functional enrichment analyses were conducted. The thresholds were p-value <0.05 and q-value <0.05.

Drug Sensitivity Analysis

The pRRophetic package worked by utilizing gene expression and drug sensitivity data in cancer cell lines, and then the models were applied to the gene expression data from primary tumor biopsies (46). We used the above method to calculate the IC50 values of different samples.

Mutation Analysis

We used the MutSigCV package (47) to select oncogenes with higher mutation frequencies than the background and

subsequently used the maftools package (48) to display the mutation waterfall figure in different groups. In addition, we used this formula (total mutation frequency/38) to estimate the tumor mutational burden (TMB) score of each sample.

Radiomics Analysis in Computed Tomography Imaging

A total of 97 contrast-enhanced CT images of the abdomen and pelvis were selected from the Cancer Imaging Archive (TCIA) (49), which were matched with the TCGA-OV samples. The study eventually included 59 samples (inadequate image quality was excluded).

Considering the characteristics of the pelvic masses, we used arterial phase data from enhanced CT for the study. Manual segmentation was performed using ITK-SNAP in the cross-sectional layer of the largest tumor region. All patients were selected for repeat region of interest (ROI) segmentation 30 days after the initial segmentation, which was performed by different radiologists. The diversity in voxel sizes leads to variations in feature values, so for reconstruction with different voxel sizes, we used a voxel size resampling strategy to select reproducible image features: spline interpolation resamples all images to the same 1×1 mm pixel size. In addition, the voxel intensities within the ROI are discretized into a limited intensity range of 64 bins. Ultimately, we extracted 806 radiomics features from the ROI of each OC patient using PyRadiomics (V 2.0.0) (50). Original texture features were extracted from the texture features, shape-based features, gray-level co-occurrence matrix features, gray-level run-length matrix features, gray-level size zone matrix features, and gray-level difference matrix features. The repeatability of the retrieved characteristics from the two radiologists was validated using the intraclass correlation coefficient (ICC). In the succeeding studies, only characteristics with an interreader ICC >0.75 were included. Using nine-gene panel as a classifier, we established radiogenomics prediction models based on radiomics features from the ROI. We randomly selected 40 cases as the training dataset, and the remaining 19 cases were used as the testing dataset. The best AUC value in the testing dataset was utilized as the selection criterion to identify the best technique to develop the final model after we employed different dimensionality reductions and machine learning approaches for imaging genomics model construction. The above modeling processes were implemented using FeAture Explorer Pro (V 0.4.4) (51).

Statistical Analysis

All statistical analyses were performed using the R software (v.4.0.1) and Python (v.3.7.6). Detailed statistical methods for transcriptome data processing are covered in the above section. p <0.05 was considered statistically significant.

RESULTS

Specific Hypoxia-Related Genes in OC

Five hundred and ten DEGs were identified in the normoxia- and hypoxia-cultured OC cell lines (**Figures 2A, B** and **Supplementary File 1**). Subsequently, we overlapped the hallmark gene sets and the DEGs, and a Venn diagram showed 140 shared genes as sHRGs (**Figure 2C**). We performed ClueGO analysis in Cytoscape software to verify whether 140 sHRGs were associated with hypoxia-related metabolic processes. Not surprisingly, the results showed that sHRGs were mainly enriched in the proteasome and classical HIF-1 signaling pathways (**Figures 2D, E**).

Our data showed that 140 sHRGs were identified in cell lines and associated with hypoxia-related metabolic processes.

Characteristics of sHRG-Mediated Hypoxia Patterns

Based on the expression of 140 sHRGs, patients with OC were classified into two hypoxia patterns using unsupervised clustering analysis, namely, hypoxia-cluster-A (352 patients) and hypoxia-cluster-B (282 patients) (**Figure 3A**). PCA analysis revealed that the above two patterns were relatively independent (**Figure 3B**). Survival analysis showed that hypoxia-cluster-B had the worst prognosis (**Figure 3C**). Moreover, we also plotted heat maps to show the distribution of clinicopathological characteristics and hypoxia patterns (**Figure 3D**). Subsequently, GSVA and ssGSEA algorithms focused on biological processes and immune microenvironment between the different hypoxia patterns. The results showed that hypoxia-cluster-B was significantly upregulated in most pathways and showed immune activation characteristics, including the MAPK signaling pathway, Wnt signaling pathway, ECM–receptor interaction, MDSC, and NK cells (**Figures 4A, B**). Therefore, it is reasonable to assume that hypoxia-cluster-B showed an immune-inflamed tumor phenotype, and they may be the most responsive to immunotherapy. If immunotherapy is applied routinely, it will prolong the survival time in hypoxia-cluster-B. Although the hypoxia patterns could differentiate clinical outcomes in patients, the underlying regulators in these patterns are unknown. Hence, we identified DEGs in different hypoxia patterns (**Supplementary File 2**). The enrichment analysis of 770 regulators in different hypoxia patterns was carried out in GO and KEGG analyses (**Figures 4C, D**). Interestingly, the PI3K–Akt signaling pathway was significantly activated, which may suggest that it may play a key role in hypoxia-related metabolic processes in OC.

Our data showed that two hypoxia patterns were identified in the meta cohort, and hypoxia patterns suggested different immune phenotypes.

Identification of Hypoxia Pattern-Related Regulator Subtypes

In the above section, we screened out 770 differential expression genes in different hypoxia patterns to focus on their potential OC mechanisms. Based on the expression of 770 regulators, patients were classified into three subtypes using unsupervised clustering analysis, namely, gene-cluster-A (248 patients), gene-cluster-B (152 patients), and gene-cluster-C (234 patients) (**Figure 5A**). PCA analysis revealed that the above three subtypes were relatively independent (**Figure 5B**). Survival analysis showed that gene-cluster-B had the worst prognosis (**Figure 5C**).

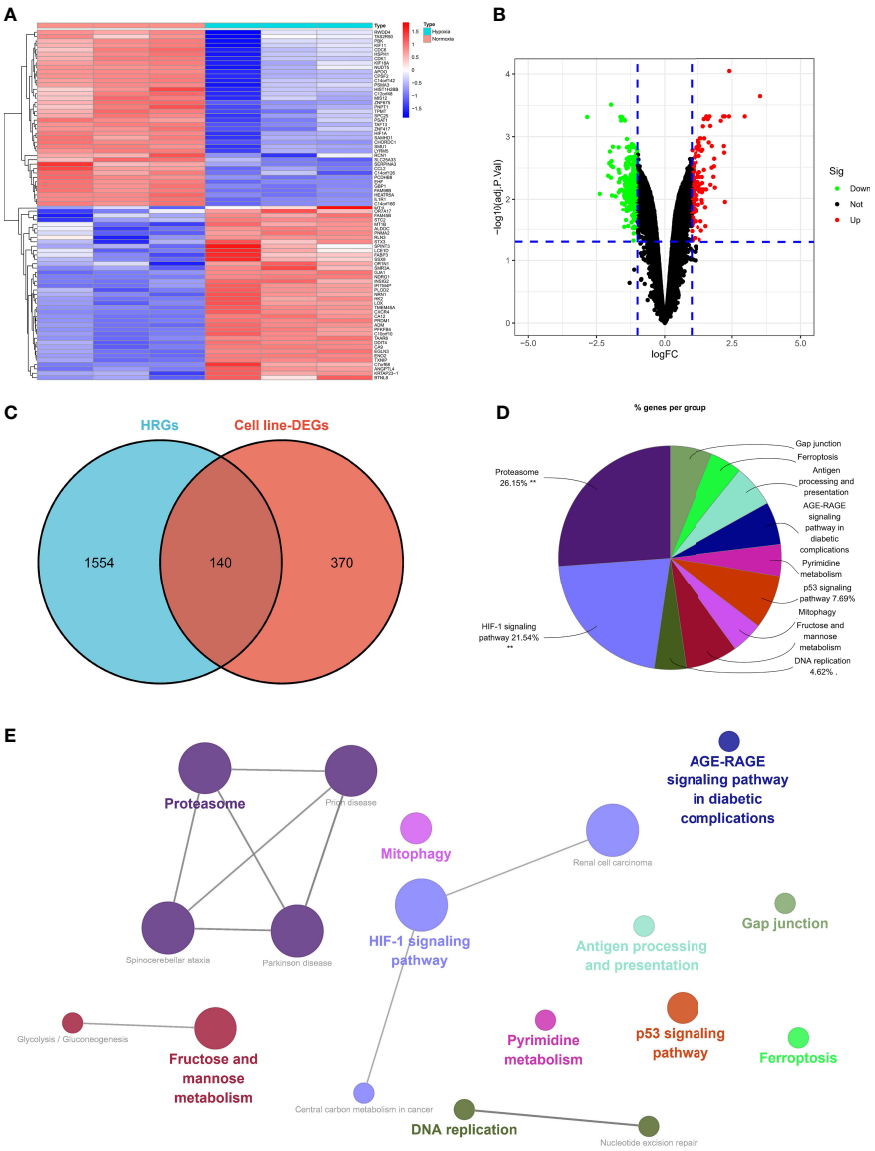

FIGURE 2 | Identification of sHRGs in ovarian cancer (OC). Heat map **(A)** and volcano plot **(B)** of differentially expressed genes (DEGs) in SKOV3 cell lines. **(C)** Venn diagram of hallmark gene sets from the MSigDB and DEGs. **(D)** Pie chart of ClueGO analysis. **(E)** Network diagram of ClueGO analysis.

Interestingly, the heat map showed that most regulators were significantly upregulated in gene-cluster-B than in the other subtypes (**Figure 5D**). In addition, we also compared the differential expression of 140 sHRGs in the three subtypes, and excitingly, all sHRGs were significantly different (**Figure 5E**).

Our data showed that hypoxia pattern-related regulator subtypes suggested another perspective on their critical regulating role on the hypoxic microenvironment.

Identification of the Hypoxia Risk Score for Each Patient With OC

Although the hypoxia patterns or regulator subtypes can predict differences in survival and immune characteristics, molecular subtypes were studied based on patient populations. The above method cannot accurately predict the hypoxia risk status of each patient, so we evaluated individual patients based on the RNA expression of the above regulators for clinical application with the risk score. Firstly, regulators with p <0.05 from the univariate Cox regression analysis (TCGA-OV cohort) were included in the LASSO regression analysis (**Supplementary File 3**). Subsequently, redundant regulators were removed by LASSO regression (**Figures 6A, B**), and correlation coefficients were determined by multivariate Cox regression analysis (stepwise method) (**Figure 6C**). Finally, we developed a nine-gene panel calculating risk scores, namely, TGFBI, GAS1, HRASLS2, ENHO, AHNAK2, MMP1, C2orf88, FOXA2, and CXCL9. The formula for calculating the

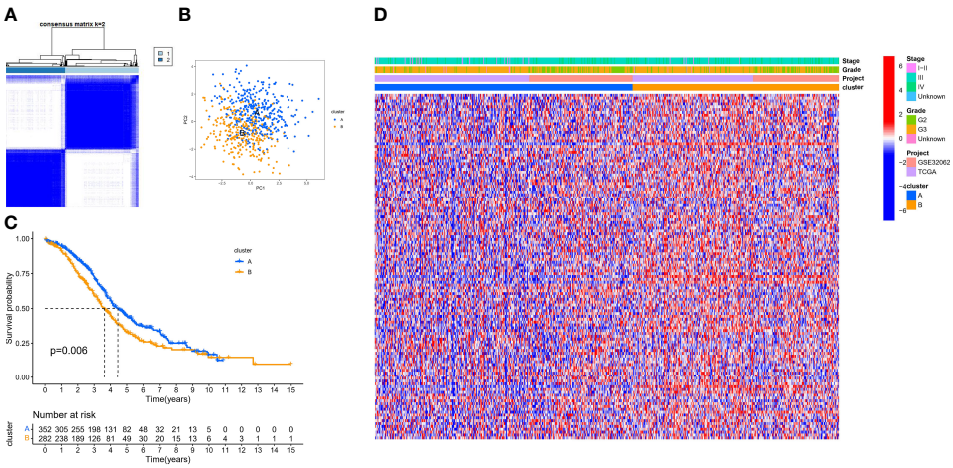

FIGURE 3 | The different hypoxia patterns in patients with OC. **(A)** Heat map of unsupervised clustering analysis. **(B)** Principal component analysis (PCA) analysis of different hypoxia patterns. **(C)** Kaplan–Meier analysis of overall survival time in different hypoxia patterns. **(D)** Heat map of the distribution of clinicopathological characteristics and two hypoxia patterns.

hypoxia risk score is as follows: hypoxia risk score = (0.132009353 × expression level of TGFBI) + (0.131635755 × expression level of GAS1) + (−0.106191762 × expression level of HRASLS2) + (−0.163100133 × expression level of ENHO) + (0.145369988 × expression level of AHNAK2) + (−0.053663201 × expression level of MMP1) + (−0.089183891 × expression level of C2orf88) + (−0.055649255 × expression level of FOXA2) + (−0.194630892 × expression level of CXCL9).

Considering that we used the TCGA-OV cohort as the training cohort, we also calculated patients' risk scores in the validation cohort (GSE32062) with the same formula. Subsequently, we divided all patients with OC into high- and low-risk groups with the median score in the training cohort. To explore the relationship between the three subtypes, namely, hypoxia patterns, pattern-related regulator subtypes, and hypoxia risk group, we visualized the relationship using the Sankey diagram (**Figure 6D**). The results

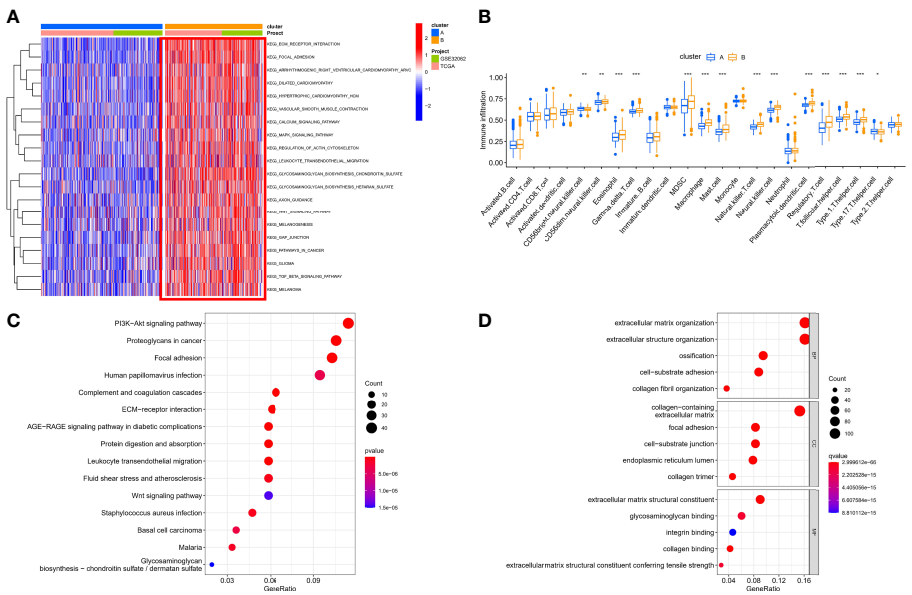

FIGURE 4 | The immunological and biological characteristics in different hypoxia patterns. **(A)** GSVA analysis in different hypoxia patterns using kegg.v7.4 gene sets. **(B)** Box plot of immune cells in different hypoxia patterns. **(C)** Bubble plot of KEGG enrichment analysis. **(D)** Bubble plot of GO enrichment analysis. *p < 0.05, **p < 0.01, ***p < 0.001.

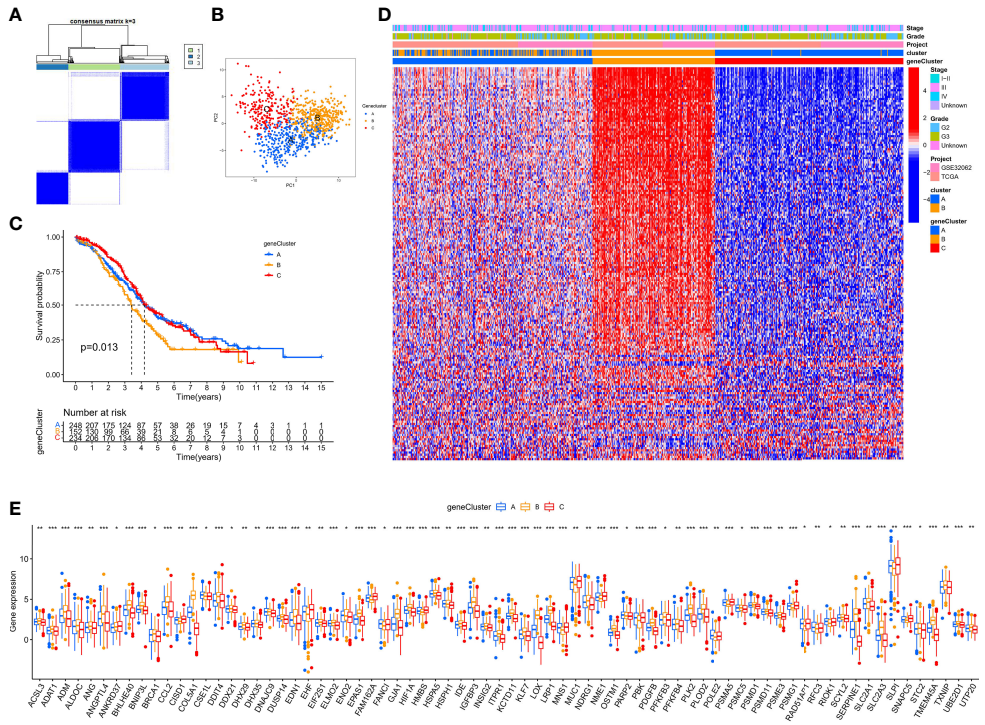

FIGURE 5 | Hypoxia pattern-related regulator subtypes. **(A)** Heat map of unsupervised clustering analysis. **(B)** PCA analysis of different gene subtypes. **(C)** Kaplan–Meier analysis of overall survival time in different gene subtypes. **(D)** Heat map of distribution of clinicopathological characteristics and three gene subtypes. **(E)** Box plot of 140 sHRGs in three subtypes. *p < 0.05, **p < 0.01, ***p < 0.001.

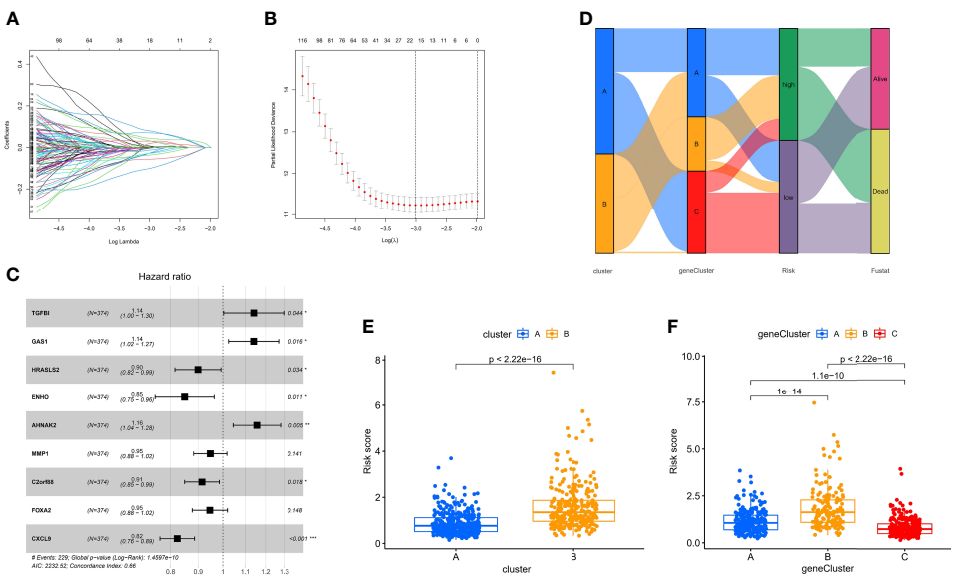

FIGURE 6 | Identification of the nine-gene next-generation sequencing panel. **(A, B)** Determination of the number of regulators using LASSO analysis. **(C)** Forest plot of multivariate Cox regression analysis. **(D)** Sankey diagram of the three types of subtypes. **(E)** Analysis of differences in hypoxia risk score of different hypoxia patterns. **(F)** Analysis of differences in hypoxia risk score of different hypoxia pattern-related regulator subtypes.

showed that most patients with poor prognosis in molecular subtypes were closely related to patients in the high-risk group. In addition, the box plot confirmed our results that hypoxia-cluster-B and gene-cluster-B had higher hypoxia risk scores (**Figures 6E, F**).

Our data showed that the nine-gene next-generation sequencing panel may represent different hypoxic statuses and be more convenient for clinical application.

Prognostic Value of Hypoxia Risk Score

Although a small portion of the sample was mixed, PCA analysis demonstrated that hypoxic risk scores had a potential classification ability for the TCGA cohort (**Figure 7A**) and the GEO cohort (**Figure 7D**). Kaplan–Meier analysis showed that survival time was significantly shorter in the high-risk group than in the low-risk group (**Figures 7B, E**), which indicated that hypoxia risk score has an excellent predictive value. Meanwhile, the AUC values of the TCGA cohort (**Figure 7C**) and the GEO cohort (**Figure 7F**) at 1, 3, and 5 years reached 0.672, 0.694, and 0.733 and 0.643, 0.693, and 0.717, respectively. To highlight the predictive value of the hypoxia score, we compared another risk score from references, such as glycolysis genes, DNA methylation-driven genes, and glycolysis-related lncRNAs. In 374 patients from the TCGA cohort, the C-index value showed that hypoxia risk score had the most robust predictive performance (**Figure 7G**). In addition, we performed univariate and multivariate Cox regression analyses of the hypoxia risk score and clinical characteristics in different cohorts. The results showed that hypoxia risk score is an independent prognostic factor in the TCGA cohort (**Supplementary Figures 1A, B**) and the GEO cohort (**Supplementary Figures 1C, D**). Finally, we plotted a nomogram based on risk group and another significant factor in multivariate Cox regression analysis (**Supplementary Figure 1E**). The calibration curve showed that the prediction curves are close to the standard curve in the TCGA cohort (**Supplementary Figure 1F**) and the GEO cohort (**Supplementary Figure 1G**).

Our data showed that hypoxia risk score had an excellent survival prediction ability.

Immunological Characteristics of Hypoxia Risk Score

To comprehensively explore the relationship between different risk groups and immune cell infiltration, we explored immune cell infiltration based on the six algorithms. The heat map showed immune cells with differential distribution in different algorithms (**Supplementary Figure 2**). Interestingly, the low-risk group had more abundant levels of antitumor immune cell infiltration, such as NK cells, $CD4^+$ T cells, $CD8^+$ T cells, macrophages, and mast cells. Not all patients in the TCGA-OV cohort received immunotherapy; hence, we evaluated the ability of hypoxia risk score to predict immunotherapy response and survival in the cohort treated with anti-PD-L1 [IMvigor (52)]. As with the TCGA-OV cohort, patients with high hypoxia risk score had worse OS in the IMvigor cohort (**Supplementary Figure 3A**). Excitingly, in the complete remission (CR) or partial response (PR) subgroup, patients typically had a lower hypoxia risk score (**Supplementary Figure 3B**). We used the ssGSEA algorithm to explore changes in immune function and the ESTIMATE algorithm to explore changes in the immune microenvironment (**Figure 8A**). We found immune function in a more active state, higher immune score, and lower stromal score in the low-risk group (**Figures 8B, C**). In addition, we also explored immune checkpoint and HLA mRNA expression in different risk groups. Most of the HLA and immune checkpoints were upregulated in the low-risk group, such as PDCD1, CTLA4, CD274, HLA-A, and HLA-F (**Figures 8D, E**).

Given that TMB and immunotherapy are strongly associated in a study (53), we explored somatic mutation characteristics and TMB status in different risk groups. Among the different risk groups, TP53, TTN, and MUC16 were shared mutated genes (**Figures 9A, B**). In the low-risk group, the samples had a higher rate of mutation (94.85% vs. 90.51%). Notably, the box plot showed that the low-risk group had

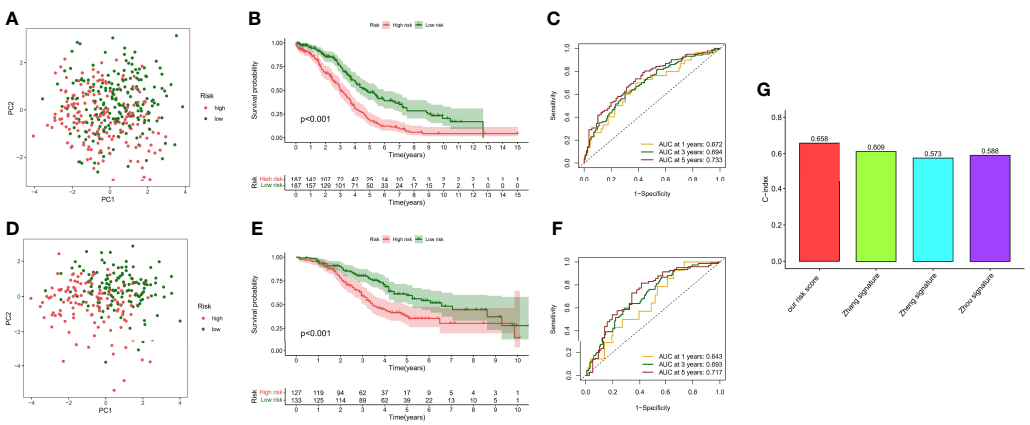

FIGURE 7 | Survival analysis and model comparison of the hypoxia risk score. **(A)** PCA analysis in the TCGA cohort. **(B)** Kaplan–Meier analysis of different risk groups in the TCGA cohort. **(C)** ROC curve of the 1-, 3-, and 5-year survival prediction in the TCGA cohort. **(D)** PCA analysis in the GEO cohort. **(E)** Kaplan–Meier analysis of different risk groups in the GEO cohort. **(F)** ROC curve of the 1-, 3-, and 5-year survival prediction in the GEO cohort. **(G)** C-index of different risk scores.

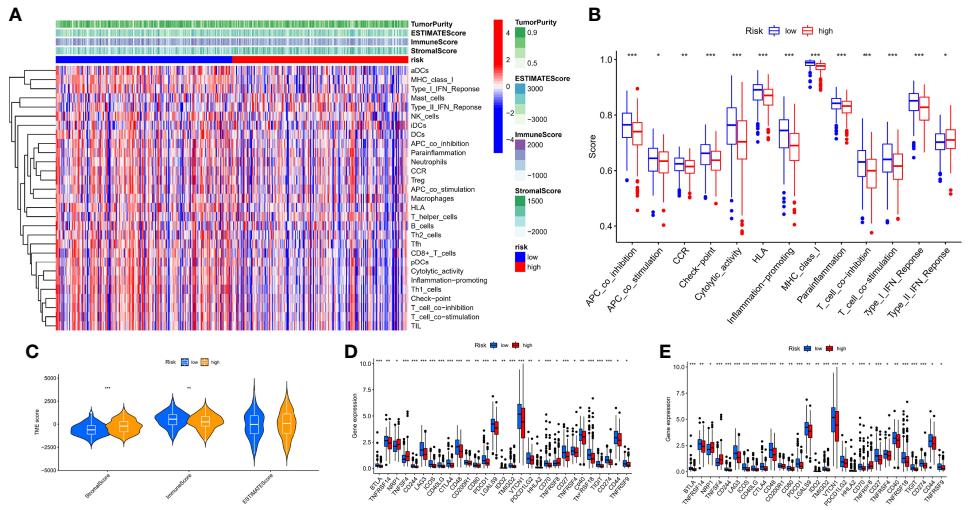

FIGURE 8 | Characteristics of the immune microenvironment in different risk groups. **(A)** Heat map of the result of ssGSEA and ESTIMATE algorithm. **(B)** Analysis of differences in the immune function of different risk groups. **(C)** Analysis of differences in TME score of different risk groups. **(D)** Analysis of differences in immune checkpoint mRNA expression of different risk groups. **(E)** Analysis of differences in HLA mRNA expression of different risk groups. *$p < 0.05$, **$p < 0.01$, ***$p < 0.001$.

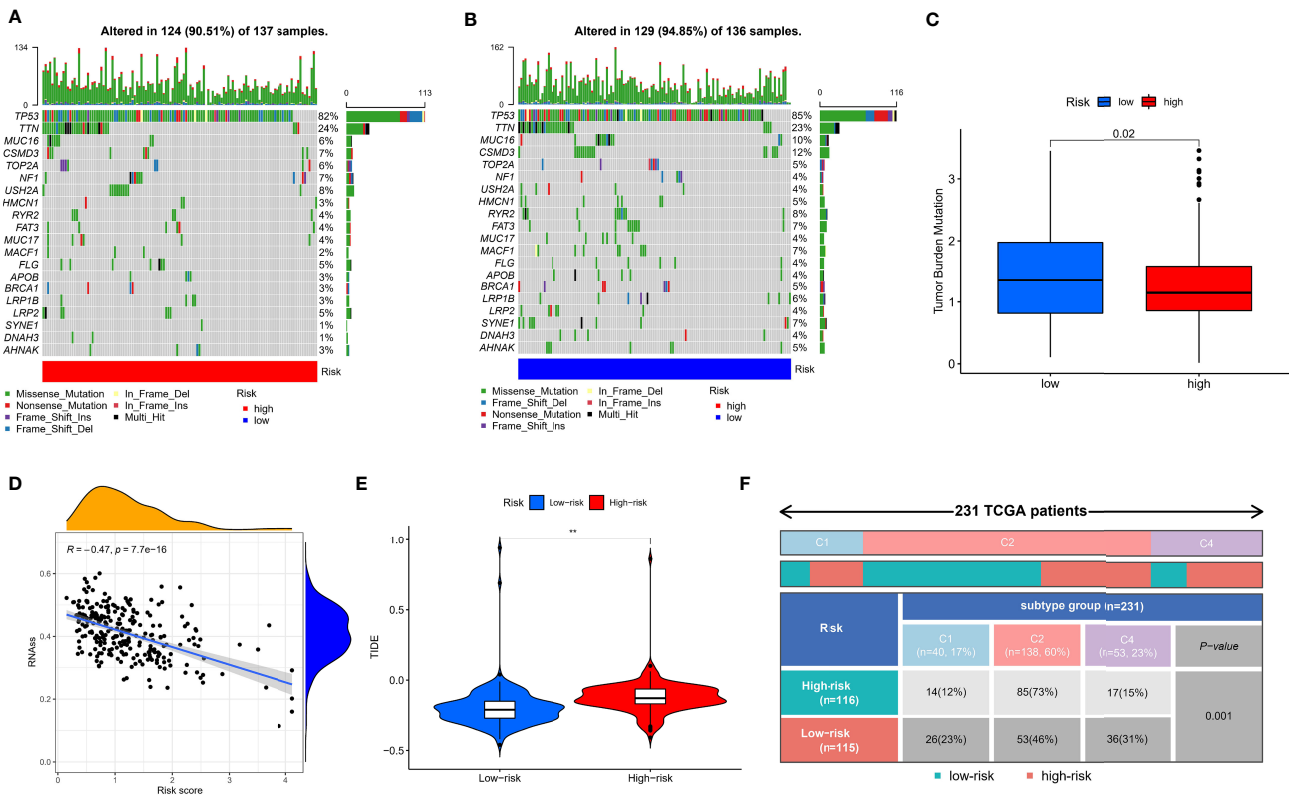

FIGURE 9 | Mutation, TIDE, and stemness characteristics in different risk groups. **(A)** Frequency of somatic mutations in the high-risk group. **(B)** Frequency of somatic mutations in the low-risk group. **(C)** Analysis of differences in TMB score of different risk groups. **(D)** Correlation analysis of hypoxia risk score with stemness score. **(E)** Analysis of differences in TIDE score of different risk groups. **(F)** The distribution of immunological subtypes in different risk groups. **p < 0.001.

a higher TMB score (**Figure 9C**). The cancer stemness theory posits that stemness scores are a response factor in immunotherapy (54). We found that as the hypoxia risk score increased, the stemness score decreased (**Figure 9D**). Moreover, the TIDE algorithm was used to evaluate the response to immunotherapy. The results showed that the low-risk group had a lower TIDE score, as we predicted in the IMvigor cohort, representing the possibility that the low-risk group had a better response to immunotherapy (**Figure 9E**). Thorsson et al. developed six immune subtypes across more than 10,000 tumor samples comprising 33 diverse cancer types (55). Of these, three immune subtypes can be annotated in the TCGA-OV cohort (231 patients), namely, Immune C1, Immune C2, and Immune C4. There is no doubt that our risk groupings were distributed differently among the different immunophenotypes (**Figure 9F**).

Our data showed new insights into the mechanisms underlying tumor hypoxia risk score and immunotherapy.

The Role of Hypoxia Risk Score in Chemotherapy

The IC50 values of six common chemotherapeutic medicines were quantified in OC patients, namely, bleomycin (**Supplementary Figure 4A**), cisplatin (**Supplementary Figure 4B**), paclitaxel (**Supplementary Figure 4C**), docetaxel (**Supplementary Figure 4D**), etoposide (**Supplementary Figure 4E**), and gemcitabine (**Supplementary Figure 4F**). In detail, the IC50 levels of bleomycin and docetaxel were significantly higher in the low-risk group. In contrast, the IC50 levels of paclitaxel were significantly higher in the high-risk group.

Our data indicated that the low-risk group was more sensitive to paclitaxel, while the high-risk group was more sensitive to bleomycin and docetaxel.

Construction of Optimal Radiomics Signatures

Based on the above results, the hypoxia risk score based on the nine-gene next-generation sequencing panel had a possibility for clinical application, but the method is still invasive. Hence, we used the radiomics approach to match with different risk groups. We selected 40 cases as the training set and another 19 cases as the independent testing set. Using the constructed different risk groups (high-risk and low-risk) as a classifier, we extracted the radiomics features from these CT images for the established radiogenomics signature. A total of 1,008 models were constructed by combining different methods (**Supplementary File 4**). We found that the combination of the following methods had better AUC values: the *Z*-score method for normalization (**Figure 10A**), the PCC method for feature preprocessing (**Figure 10B**), the RFE method for dimensionality reduction (**Figure 10C**), and the logistic regression method for calculating coefficient (**Figure 10D**). Finally, we obtained the following four features and coefficients for constructing the optimal radiomics signatures (**Figure 10E**): radiomics score = (−1.845017354 × CT_wavelet-HHH_firstorder_Median) + (−1.58189802 × CT_wavelet-HHL_glszm_SmallAreaLowGrayLevelEmphasis) + (1.130793547 × CT_wavelet-HLL_glszm_SmallAreaLowGrayLevelEmphasis) + (0.663451656 × CT_wavelet-LLL_glrlm_LongRunLowGrayLevelEmphasis). Using the above radiomics

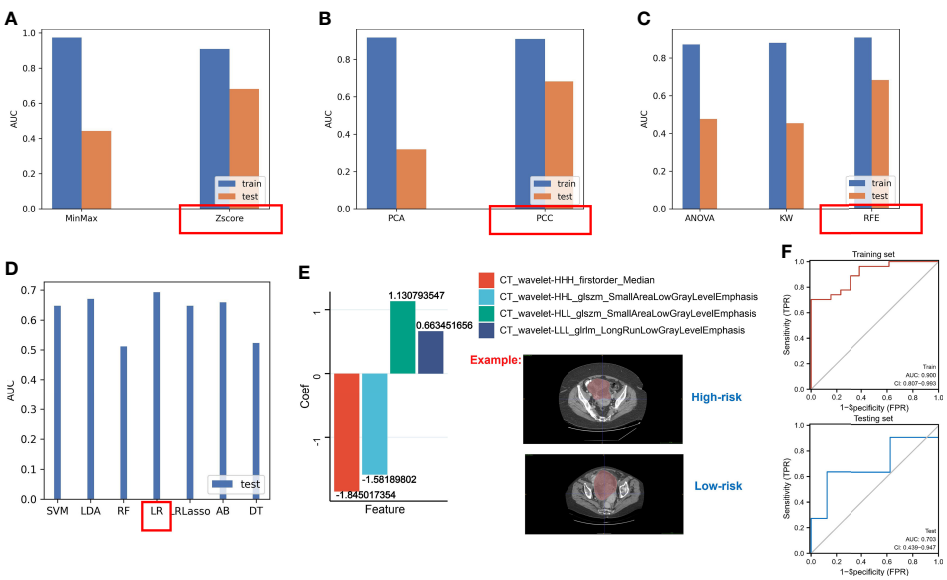

FIGURE 10 | The AUC values of different methods. **(A)** The AUC values of methods for normalization. **(B)** The AUC values of methods for feature preprocessing. **(C)** The AUC values of methods for dimensionality reduction. **(D)** The AUC values of methods for generating the final signature. **(E)** LR regression coefficients and features. **(F)** The AUC values of the testing set and the training set based on the optimal radiomics signature.

signature, the AUC values of the training set and the test set were 0.900 and 703, respectively (**Figure 10F**).

Our data showed that a novel non-invasive approach based on CT biomarkers may enable the pretreatment prediction of hypoxia risk in patients with OC.

DISCUSSION

There is growing evidence that the hypoxia microenvironment plays a key role in immune response and tumorigenesis on the basis of dysregulated expression of hypoxia-related genes. Most previous studies focused on single regulators about hypoxia in OC. For example, hypoxia-inducible factor-1α (HIF-1α) has been proven to play an important role in promoting OC chemoresistance, tumor metastasis, and immunosuppression (56). The high expression of maspin induced by hypoxia might be associated with a poor prognosis of ovarian clear cell carcinoma (57). More importantly, although some researchers have identified hypoxia-related genetic signatures to improve the prognosis of patients with ovarian cancer (58, 59), they neglected that specific hypoxia-related genes in OC should be analyzed to construct a risk signature. Hence, we performed the identification of specific hypoxia regulators in OC based on cell lines treated with different oxygen conditions. Subsequently, we established different hypoxia patterns (hypoxia-cluster-A and hypoxia-cluster-B) and identified regulators that may influence different hypoxia patterns. Moreover, we also established different gene subtypes (gene-cluster-A and gene-cluster-B) based on the expression of regulators. In immune analysis, we revealed that hypoxia-cluster-B and gene-cluster-B correspond to the immune-inflamed phenotype, which contains many antigen-presenting cells that activate an adaptive immune response. However, hypoxia-cluster-A and gene-cluster-A correspond to the immune-excluded phenotype (60). To date, immunotherapy outcomes in OC have been disappointing, likely due to the highly immunosuppressive TME, low TMB, and low checkpoint expression in patients with OC (61). Therefore, our study provides a novel understanding of the OC microenvironment based on hypoxia. If immunotherapy is applied routinely, it will prolong the survival time in hypoxia-cluster-B and gene-cluster-B. Hence, these findings will improve the future application of precise personalized therapy for OC.

Although hypoxia patterns could differentiate clinical outcomes and immune perturbations in OC patients, the underlying regulators in different patterns are unknown. We found significantly altered pathways in the enrichment analysis, including the MAPK signaling pathway, Wnt signaling pathway, ECM–receptor interaction, and PI3K–Akt signaling pathway. As a classic cancer pathway, these pathways have been widely reported in ovarian cancer (62, 63). However, our findings gave researchers a new direction in the future: how does hypoxia interfere with TME in OC through the classic cancer pathways?

Although the hypoxia patterns can predict differences in survival and immune characteristics, molecular subtypes were studied based on populations. The above method cannot accurately predict the hypoxia risk status of each patient, so we used the RNA expression of nine hypoxia pattern-associated regulators for clinical application with hypoxia risk score. Most patients with poor prognosis in molecular subtypes were closely related to patients in the high-risk group, and hypoxia-cluster-B and gene-cluster-B had higher hypoxia risk score. Of the nine genes, some of them were shown to be involved in the regulation of biological functions in ovarian cancer, such as TGFBI which is involved in polyploid cell formation and in response to paclitaxel (64); extracellular vesicles carrying the MMP1 mRNA promoted peritoneal metastasis of ovarian cancer (65). The FOXA2 protein was mainly positively expressed in the nucleoplasm of OC cells and was associated with FIGO staging and lymph node metastasis (66). Further analysis revealed that hypoxia risk score could be used not only to predict the prognosis of patients with OC but also to accurately distinguish different immunological characteristics. In addition, HLA mRNA expression, immune checkpoint mRNA expression, TMB, and stemness score were significantly correlated with hypoxia risk score, indicating the ability of the risk score to assess the effectiveness of immunotherapy. We found that the low-risk group was more sensitive to paclitaxel, while the high-risk group was more sensitive to bleomycin and docetaxel. It follows that the quantitative model can define the hypoxia status of each sample. Thus, these results validate that the hypoxia-related model can be conveniently used for clinical assessment.

>However, genomic models are invasive; therefore, we developed a convenient method to predict hypoxic subtypes based on CT imaging in our study. Although the sample size of OC in the TCIA database is limited, we found the following combinations of methods with better AUC values: the *Z*-score method for normalization, the PCC method for feature preprocessing, the RFE method for dimensionality reduction, and the logistic regression method for calculating coefficient. Using the above radiomics signature, the AUC values of the training set and the test set were 0.900 and 703, respectively. There is extensive heterogeneity at the genomic level in primary OC and peritoneal implants, and single-site biopsy sequencing clearly does not meet our requirements (67), at which point a radiogenomics approach can provide a comprehensive assessment (68).

In brief, the current studies of radiogenomics in OC are minimal and mainly plagued by time-consuming manual segmentation. However, based on current artificial intelligence (AI) research on other tumors (69), we speculate that radiogenomics in OC could be used as novel biomarkers for drug selection and assessment of immunological characterization in the future.

DATA AVAILABILITY STATEMENT

The datasets presented in this study can be found in online repositories. The names of the repository/repositories and accession number(s) can be found in the article/**Supplementary Material**.

AUTHOR CONTRIBUTIONS

SF and TX conceived and designed the study. YS was responsible for the materials. SF drafted the article. YS, SL, YG, XJ, and KZ revised the article critically. All authors provided their final approval of the submitted version.

FUNDING

This study was supported by the National Natural Science Foundation of China (No. 82072078), Jiangsu Province Key Research and Development Project (SBE2020741118), and Postgraduate Research & Practice Innovation Program of Jiangsu Province.

SUPPLEMENTARY MATERIAL

The Supplementary Material for this article can be found online at: https://www.frontiersin.org/articles/10.3389/fimmu.2022.868067/full#supplementary-material

Supplementary Figure 1 | Identification of independent prognostic value and Nomogram. **(A)** Forest plot of univariate Cox regression analysis in the TCGA cohort. **(B)** Forest plot of multivariate Cox regression analysis in the TCGA cohort. **(C)** Forest plot of univariate Cox regression analysis in the GEO cohort. **(D)** Forest plot of multivariate Cox regression analysis in the GEO cohort. **(E)** Nomogram. **(F)** Calibration curve of nomogram for OS prediction at 1 year, 3 years, and 5-years in the TCGA cohort. **(G)** Calibration curve of nomogram for OS prediction at 1 year, 3 years, and 5-years in the GEO cohort.

Supplementary Figure 2 | Heat map of different types of immune cells based on 6 algorithms.

Supplementary Figure 3 | Predictive value of hypoxia risk score in the immunotherapy cohort. **(A)** Kaplan-Meier analysis of IMvigor cohort. **(B)** Analysis of differences in hypoxia risk score of different response.

Supplementary Figure 4 | Drug sensitivity analysis in different risk groups. **(A)** IC50 levels of Bleomycin. **(B)** IC50 levels of Cisplatin. **(C)** IC50 levels of Paclitaxel. **(D)** IC50 levels of Docetaxel. **(E)** IC50 levels of Etoposide. **(F)** IC50 levels of Gemcitabine.

Supplementary File 1 | DEGs in normoxia and hypoxia cultured cell lines.

Supplementary File 2 | DEGs in different hypoxia patterns.

Supplementary File 3 | The results of univariate Cox regression analysis in 770 reguators.

Supplementary File 4 | The results of 1008 radiomics signatures in training and testing sets.

REFERENCES

1. Torre LA, Trabert B, DeSantis CE, Miller KD, Samimi G, Runowicz CD, et al. Ovarian Cancer Statistics, 2018. *CA Cancer J Clin* (2018) 68(4):284–96. doi: 10.3322/caac.21456
2. Ghisoni E, Imbimbo M, Zimmermann S, Valabrega G. Ovarian Cancer Immunotherapy: Turning Up the Heat. *Int J Mol Sci* (2019) 20(12):2927. doi: 10.3390/ijms20122927
3. Odunsi K. Immunotherapy in Ovarian Cancer. *Ann Oncol* (2017) 28 (suppl_8):viii1–7. doi: 10.1093/annonc/mdx444
4. Mathieu J, Zhang Z, Zhou W, Wang AJ, Heddleston JM, Pinna CM, et al. HIF Induces Human Embryonic Stem Cell Markers in Cancer Cells. *Cancer Res* (2011) 71(13):4640–52. doi: 10.1158/0008-5472.CAN-10-3320
5. Semenza GL. HIF-1: Upstream and Downstream of Cancer Metabolism. *Curr Opin Genet Dev* (2010) 20(1):51–6. doi: 10.1016/j.gde.2009.10.009
6. Gilkes DM, Semenza GL, Wirtz D. Hypoxia and the Extracellular Matrix: Drivers of Tumour Metastasis. *Nat Rev Cancer* (2014) 14(6):430–9. doi: 10.1038/nrc3726
7. Beumer-Chuwonpad A, Taggenbrock RLRE, Ngo TA, van Gisbergen KPJM. The Potential of Tissue-Resident Memory T Cells for Adoptive Immunotherapy Against Cancer. *Cells* (2021) 10(9):2234. doi: 10.3390/cells10092234
8. Ma B, Cheng H, Mu C, Geng G, Zhao T, Luo Q, et al. The SIAH2-NRF1 Axis Spatially Regulates Tumor Microenvironment Remodeling for Tumor Progression. *Nat Commun* (2019) 10(1):1034. doi: 10.1038/s41467-019-08618-y
9. Zhou Y, Xu B, Zhou Y, Geng G, Zhao T, Luo Q, et al. Identification of Key Genes With Differential Correlations in Lung Adenocarcinoma. *Front Cell Dev Biol* (2021) 9:675438. doi: 10.3389/fcell.2021.675438
10. Ding S, Li H, Zhang YH, Zhou X, Feng K, Li Z, et al. Identification of Pan-Cancer Biomarkers Based on the Gene Expression Profiles of Cancer Cell Lines. *Front Cell Dev Biol* (2021) 9:781285. doi: 10.3389/fcell.2021.781285
11. Zhou Y, Zheng X, Xu B, Hu W, Huang T, Jiang J. The Identification and Analysis of mRNA-lncRNA-miRNA Cliques From the Integrative Network of Ovarian Cancer. *Front Genet* (2019) 10:751. doi: 10.3389/fgene.2019.00751
12. Vargas HA, Huang EP, Lakhman Y, Ippolito JE, Bhosale P, Mellnick V, et al. Radiogenomics of High-Grade Serous Ovarian Cancer: Multireader Multi-Institutional Study From the Cancer Genome Atlas Ovarian Cancer Imaging Research Group. *Radiology* (2017) 285(2):482–92. doi: 10.1148/radiol.2017161870
13. Gillies RJ, Kinahan PE, Hricak H. Radiomics: Images Are More Than Pictures, They Are Data. *Radiology* (2016) 278(2):563–77. doi: 10.1148/radiol.2015151169
14. Lubner MG. Reflections on Radiogenomics and Oncologic Radiomics. *Abdom Radiol (NY)* (2019) 44(6):1959. doi: 10.1007/s00261-019-02047-7
15. Karlo CA, Di Paolo PL, Chaim J, Hakimi AA, Ostrovnaya I, Russo P, et al. Radiogenomics of Clear Cell Renal Cell Carcinoma: Associations Between CT Imaging Features and Mutations. *Radiology* (2014) 270(2):464–71. doi: 10.1148/radiol.13130663
16. Horvat N, Veeraraghavan H, Khan M, Blazic I, Zheng J, Capanu M, et al. MR Imaging of Rectal Cancer: Radiomics Analysis to Assess Treatment Response After Neoadjuvant Therapy. *Radiology* (2018) 287(3):833–43. doi: 10.1148/radiol.2018172300
17. Ye F, Hu Y, Gao J, Liang Y, Liu Y, Ou Y, et al. Radiogenomics Map Reveals the Landscape of M6a Methylation Modification Pattern in Bladder Cancer. *Front Immunol* (2021) 12:722642. doi: 10.3389/fimmu.2021.722642
18. Garziera M, Roncato R, Montico M, De Mattia E, Gagno S, Poletto E, et al. New Challenges in Tumor Mutation Heterogeneity in Advanced Ovarian Cancer by a Targeted Next-Generation Sequencing (NGS) Approach. *Cells* (2019) 8(6):584. doi: 10.3390/cells8060584
19. Vargas HA, Wassberg C, Fox JJ, Wibmer A, Goldman DA, Kuk D, et al. Response. *Radiology* (2015) 274(2):625. doi: 10.1148/radiol.13130625
20. Meier A, Veeraraghavan H, Nougaret S, Lakhman Y, Sosa R, Soslow RA, et al. Association Between CT-Texture-Derived Tumor Heterogeneity, Outcomes, and BRCA Mutation Status in Patients With High-Grade Serous Ovarian Cancer. *Abdom Radiol (NY)* (2019) 44(6):2040–7. doi: 10.1007/s00261-018-1840-5
21. Wilson C, Qiu L, Hong Y, Karnik T, Tadros G, Mau B, et al. The Histone Demethylase KDM4B Regulates Peritoneal Seeding of Ovarian Cancer. *Oncogene* (2017) 36(18):2565–76. doi: 10.1038/onc.2016.412
22. Ritchie ME, Phipson B, Wu D, Hu Y, Law CW, Shi W, et al. Limma Powers Differential Expression Analyses for RNA-Sequencing and Microarray Studies. *Nucleic Acids Res* (2015) 43(7):e47. doi: 10.1093/nar/gkv007
23. Liu J, Chen C, Wang Y, Qian C, Wei J, Xing Y, et al. Comprehensive of N1-Methyladenosine Modifications Patterns and Immunological Characteristics in Ovarian Cancer. *Front Immunol* (2021) 12:746647. doi: 10.3389/fimmu.2021.746647
24. Sun X, Luo H, Han C, Zhang Y, Yan C. Identification of a Hypoxia-Related Molecular Classification and Hypoxic Tumor Microenvironment Signature for Predicting the Prognosis of Patients With Triple-Negative Breast Cancer. *Front Oncol* (2021) 11:700062. doi: 10.3389/fonc.2021.700062

25. Wang Z, Jensen MA, Zenklusen JC. A Practical Guide to The Cancer Genome Atlas (TCGA). *Methods Mol Biol* (2016) 1418:111–41. doi: 10.1007/978-1-4939-3578-9_6
26. Clough E, Barrett T. The Gene Expression Omnibus Database. *Methods Mol Biol* (2016) 1418:93–110. doi: 10.1007/978-1-4939-3578-9_5
27. Malta TM, Sokolov A, Gentles AJ, Burzykowski T, Poisson L, Weinstein JN, et al. Machine Learning Identifies Stemness Features Associated With Oncogenic Dedifferentiation. *Cell* (2018) 173(2):338–54.e15. doi: 10.1016/j.cell.2018.03.034
28. Seiler M, Huang CC, Szalma S, Bhanot G. ConsensusCluster: A Software Tool for Unsupervised Cluster Discovery in Numerical Data. *OMICS* (2010) 14 (1):109–13. doi: 10.1089/omi.2009.0083
29. Wang L, Zhang W, Yang T, He L, Liao Y, Lu J. Construction and Comprehensive Analysis of a Stratification System Based on AGTRAP in Patients With Hepatocellular Carcinoma. *Dis Markers* (2021) 2021:6144476. doi: 10.1155/2021/6144476
30. David CC, Jacobs DJ. Principal Component Analysis: A Method for Determining the Essential Dynamics of Proteins. *Methods Mol Biol* (2014) 1084:193–226. doi: 10.1007/978-1-62703-658-0_11
31. Li T, Fan J, Wang B, Traugh N, Chen Q, Liu JS, et al. TIMER: A Web Server for Comprehensive Analysis of Tumor-Infiltrating Immune Cells. *Cancer Res* (2017) 77(21):e108–10. doi: 10.1158/0008-5472.CAN-17-0307
32. Chen B, Khodadoust MS, Liu CL, Newman AM, Alizadeh AA. Profiling Tumor Infiltrating Immune Cells With CIBERSORT. *Methods Mol Biol* (2018) 1711:243–59. doi: 10.1007/978-1-4939-7493-1_12
33. Plattner C, Finotello F, Rieder D. Deconvoluting Tumor-Infiltrating Immune Cells From RNA-Seq Data Using Quantiseq. *Methods Enzymol* (2020) 636:261–85. doi: 10.1016/bs.mie.2019.05.056
34. Becht E, Giraldo NA, Lacroix L, Buttard B, Elarouci N, Petitprez F, et al. Estimating the Population Abundance of Tissue-Infiltrating Immune and Stromal Cell Populations Using Gene Expression. *Genome Biol* (2016) 17 (1):218. doi: 10.1186/s13059-016-1070-5. [Published Correction Appears in Genome Biol. 2016 Dec 1;17 (1):249].
35. Aran D, Hu Z, Butte AJ. Xcell: Digitally Portraying the Tissue Cellular Heterogeneity Landscape. *Genome Biol* (2017) 18(1):220. doi: 10.1186/s13059-017-1349-1
36. Racle J, Gfeller D. EPIC: A Tool to Estimate the Proportions of Different Cell Types From Bulk Gene Expression Data. *Methods Mol Biol* (2020) 2120:233–48. doi: 10.1007/978-1-0716-0327-7_17
37. Hänzelmann S, Castelo R, Guinney J. GSVA: Gene Set Variation Analysis for Microarray and RNA-Seq Data. *BMC Bioinform* (2013) 14:7. doi: 10.1186/1471-2105-14-7
38. Yoshihara K, Shahmoradgoli M, Martínez E, Vegesna R, Kim H, Torres-Garcia W, et al. Inferring Tumour Purity and Stromal and Immune Cell Admixture From Expression Data. *Nat Commun* (2013) 4:2612. doi: 10.1038/ncomms3612
39. Jiang P, Gu S, Pan D, Fu J, Sahu A, Hu X, et al. Signatures of T Cell Dysfunction and Exclusion Predict Cancer Immunotherapy Response. *Nat Med* (2018) 24(10):1550–8. doi: 10.1038/s41591-018-0136-1
40. Zhang D, Li Y, Yang S, Wang M, Yao J, Zheng Y, et al. Identification of a Glycolysis-Related Gene Signature for Survival Prediction of Ovarian Cancer Patients. *Cancer Med* (2021) 10(22):8222–37. doi: 10.1002/cam4.4317
41. Zhou M, Hong S, Li B, Liu C, Hu M, Min J, et al. Development and Validation of a Prognostic Nomogram Based on DNA Methylation-Driven Genes for Patients With Ovarian Cancer. *Front Genet* (2021) 12:675197. doi: 10.3389/fgene.2021.675197
42. Zheng J, Guo J, Zhu L, Zhou Y, Tong J. Comprehensive Analyses of Glycolysis-Related lncRNAs for Ovarian Cancer Patients. *J Ovarian Res* (2021) 14(1):124. doi: 10.1186/s13048-021-00881-2
43. Shannon P, Markiel A, Ozier O, Baliga NS, Wang JT, Ramage D, et al. Cytoscape: A Software Environment for Integrated Models of Biomolecular Interaction Networks. *Genome Res* (2003) 13(11):2498–504. doi: 10.1101/gr.1239303
44. Gene Ontology Consortium. Gene Ontology Consortium: Going Forward. *Nucleic Acids Res* (2015) 43(Database issue):D1049–56. doi: 10.1093/nar/gku1179
45. Kanehisa M, Goto S. KEGG: Kyoto Encyclopedia of Genes and Genomes. *Nucleic Acids Res* (2000) 28(1):27–30. doi: 10.1093/nar/28.1.27
46. Geeleher P, Cox N, Huang RS. Prrophetic: An R Package for Prediction of Clinical Chemotherapeutic Response From Tumor Gene Expression Levels. *PLoS One* (2014) 9(9):e107468. doi: 10.1371/journal.pone.0107468
47. Lawrence MS, Stojanov P, Polak P, Kryukov GV, Cibulskis K, Sivachenko A, et al. Mutational Heterogeneity in Cancer and the Search for New Cancer-Associated Genes. *Nature* (2013) 499(7457):214–8. doi: 10.1038/nature12213
48. Mayakonda A, Lin DC, Assenov Y, Plass C, Koeffler HP. Maftools: Efficient and Comprehensive Analysis of Somatic Variants in Cancer. *Genome Res* (2018) 28(11):1747–56. doi: 10.1101/gr.239244.118
49. Prior F, Smith K, Sharma A, Kirby J, Tarbox L, Clark K, et al. The Public Cancer Radiology Imaging Collections of The Cancer Imaging Archive. *Sci Data* (2017) 4:170124. doi: 10.1038/sdata.2017.124
50. van Griethuysen JJM, Fedorov A, Parmar C, Hosny A, Aucoin N, Narayan V, et al. Computational Radiomics System to Decode the Radiographic Phenotype. *Cancer Res* (2017) 77(21):e104–7. doi: 10.1158/0008-5472.CAN-17-0339
51. Song Y, Zhang J, Zhang YD, Hou Y, Yan X, Wang Y, et al. FeAture Explorer (FAE): A Tool for Developing and Comparing Radiomics Models. *PLoS One* (2020) 15(8):e0237587. doi: 10.1371/journal.pone.0237587
52. Snyder A, Nathanson T, Funt SA, Ahuja A, Buros Novik J, Hellmann MD, et al. Contribution of Systemic and Somatic Factors to Clinical Response and Resistance to PD-L1 Blockade in Urothelial Cancer: An Exploratory Multi-Omic Analysis. *PLoS Med* (2017) 14(5):e1002309. doi: 10.1371/journal.pmed.1002309
53. Chan TA, Yarchoan M, Jaffee E, Swanton C, Quezada SA, Stenzinger A, et al. Development of Tumor Mutation Burden as an Immunotherapy Biomarker: Utility for the Oncology Clinic. *Ann Oncol* (2019) 30(1):44–56. doi: 10.1093/annonc/mdy495
54. Walcher L, Kistenmacher AK, Suo H, Kitte R, Dluczek S, Strauß A, et al. Cancer Stem Cells-Origins and Biomarkers: Perspectives for Targeted Personalized Therapies. *Front Immunol* (2020) 11:1280. doi: 10.3389/fimmu.2020.01280
55. Thorsson V, Gibbs DL, Brown SD, Wolf D, Bortone DS, Ou Yang TH, et al. The Immune Landscape of Cancer. *Immunity* (2018) 48(4):812–30.e14. doi: 10.1016/j.immuni.2018.03.023. [Published Correction Appears in Immunity. 2019 Aug 20;51(2):411-412].
56. Wang X, Du ZW, Xu TM, Wang XJ, Li W, Gao JL, et al. HIF-1α Is a Rational Target for Future Ovarian Cancer Therapies. *Front Oncol* (2021) 11:785111. doi: 10.3389/fonc.2021.785111
57. Lee EJ, Park SJ, Lee C, Yim GW, Kim JW, Kim HS. Hypoxia-Induced Maspin Expression Affects the Prognosis of Ovarian Clear Cell Carcinoma. *In Vivo* (2022) 36(1):212–20. doi: 10.21873/invivo.12693
58. Wei C, Liu X, Wang Q, Li Q, Xie M. Identification of Hypoxia Signature to Assess the Tumor Immune Microenvironment and Predict Prognosis in Patients With Ovarian Cancer. *Int J Endocrinol* (2021) 2021:4156187. doi: 10.1155/2021/4156187
59. Chen X, Lan H, He D, Xu R, Zhang Y, Cheng Y, et al. Multi-Omics Profiling Identifies Risk Hypoxia-Related Signatures for Ovarian Cancer Prognosis. *Front Immunol* (2021) 12:645839. doi: 10.3389/fimmu.2021.645839
60. Chen DS, Mellman I. Elements of Cancer Immunity and the Cancer-Immune Set Point. *Nature* (2017) 541(7637):321–30. doi: 10.1038/nature21349
61. Chardin L, Leary A. Immunotherapy in Ovarian Cancer: Thinking Beyond PD-1/PD-L1. *Front Oncol* (2021) 11:795547. doi: 10.3389/fonc.2021.795547
62. Zhang W, Wu Q, Liu Y, Wang X, Ma C, Zhu W. LncRNA HOTAIR Promotes Chemoresistance by Facilitating Epithelial to Mesenchymal Transition Through miR-29b/PTEN/PI3K Signaling in Cervical Cancer. *Cells Tissues Organs* (2022) 211(1):16–29. doi: 10.1159/000519844
63. Li F, Zhu W, Wang Z. Long Noncoding RNA LINC00460 Promotes the Progression of Cervical Cancer *via* Regulation of the miR-361-3p/Gli1 Axis. *Hum Cell* (2021) 34(1):229–37. doi: 10.1007/s13577-020-00447-2
64. Shang X, Yuan B, Li J, Xi F, Mao J, Zhang C, et al. TGFBI Is Involved in the Formation of Polyploid Cancer Cells and the Response to Paclitaxel. *Ann Transl Med* (2021) 9(8):693. doi: 10.21037/atm-21-1698
65. Yokoi A, Yoshioka Y, Yamamoto Y, Ishikawa M, Ikeda SI, Kato T, et al. Malignant Extracellular Vesicles Carrying MMP1 mRNA Facilitate Peritoneal Dissemination in Ovarian Cancer. *Nat Commun* (2017) 8:14470. doi: 10.1038/ncomms14470

66. Shang H, Shi L, Jiang X, Zhou P, Wei Y. Correlation Between High Expression of FOXA2 and Improved Overall Survival in Ovarian Cancer Patients. *Med Sci Monit* (2021) 27:e928763. doi: 10.12659/MSM.928763
67. Bashashati A, Ha G, Tone A, Ding J, Prentice LM, Roth A, et al. Distinct Evolutionary Trajectories of Primary High-Grade Serous Ovarian Cancers Revealed Through Spatial Mutational Profiling. *J Pathol* (2013) 231(1):21–34. doi: 10.1002/path.4230
68. Nougaret S, Tardieu M, Vargas HA, Reinhold C, Vande Perre S, Bonanno N, et al. Ovarian Cancer: An Update on Imaging in the Era of Radiomics. *Diagn Interv Imaging* (2019) 100(10):647–55. doi: 10.1016/j.diii.2018.11.007
69. van Heeswijk MM, Lambregts DM, van Griethuysen JJ, Oei S, Rao SX, de Graaff CA, et al. Automated and Semiautomated Segmentation of Rectal Tumor Volumes on Diffusion-Weighted MRI: Can It Replace Manual Volumetry? *Int J Radiat Oncol Biol Phys* (2016) 94(4):824–31. doi: 10.1016/j.ijrobp.2015.12.017

Conflict of Interest: The authors declare that the research was conducted in the absence of any commercial or financial relationships that could be construed as a potential conflict of interest.

Publisher's Note: All claims expressed in this article are solely those of the authors and do not necessarily represent those of their affiliated organizations, or those of the publisher, the editors and the reviewers. Any product that may be evaluated in this article, or claim that may be made by its manufacturer, is not guaranteed or endorsed by the publisher.

frontiers | Frontiers in Immunology

ORIGINAL RESEARCH
published: 28 April 2022
doi: 10.3389/fimmu.2022.893137

Aberrant HSP90 Expression in Lymphocytes and HSP90 Response to Anti-PD-1 Therapy in Lymphoma Patients

Zarema Albakova[1], Yana Mangasarova[2], Akhmet Albakov[3], Elena Nikulina[2], Sergey Kravchenko[2] and Alexander Sapozhnikov[1,4]*

[1] Department of Immunology, Lomonosov Moscow State University, Moscow, Russia, [2] National Medical Research Center for Hematology, Moscow, Russia, [3] Department of Innovation, Chokan, Almaty, Kazakhstan, [4] Department of Immunology, Shemyakin and Ovchinnikov Institute of Bioorganic Chemistry Russian Academy of Sciences (RAS), Moscow, Russia

HSP90 family of molecular chaperones has been shown to be implicated in various stages of tumor growth and development. Recent studies have highlighted the role of extracellular HSP90 in tumor immunology, however, the role that HSP90 plays in the regulation of immune responses and the impact of cancer immunotherapy, including immune checkpoint blockade, on HSP90 is still unclear. Here we assessed the surface and intracellular expression of constitutive cytosolic HSP90β isoform, mitochondrial HSP90 homolog TRAP1 and co-chaperone STIP1/HOP in T, NK, B and NKT cells derived from peripheral blood and bone marrow samples of patients with Hodgkin and B-cell Non-Hodgkin lymphomas. HSP90β and STIP1 were overexpressed in B lymphocytes, while TRAP1 expression was decreased in T, B, NK and NKT cells of lymphoma patients. HSP90 overexpression in B cells was not associated with malignant B cell clones, since no clonotypic B cells were detected by immunoglobulin heavy chain (IgH) gene rearrangements. PD-1 blockade was found to differently affect the intracellular and surface HSP90 in T, B, NK and NKT cells in patients with relapsed or refractory classical Hodgkin lymphoma. Modulating HSP90 was found to affect the NK cell degranulation response and IFNγ production in lymphoma patients. These findings provide the rationale to further explore HSP90 homologs for improving patient response to cancer immunotherapy.

Keywords: HSP90, lymphocytes, cancer immunotherapy, extracellular HSP90, PD-1 blockade, Hodgkin lymphoma, Non-Hodgkin lymphoma

OPEN ACCESS

Edited by:
Liusheng Peng,
Third Military Medical University, China

Reviewed by:
Wenwei Yin,
Chongqing Medical University, China
Jinsong Hu,
Xi'an Jiaotong University, China

****Correspondence:***
Zarema Albakova
zarema.albakova14@gmail.com

Specialty section:
This article was submitted to Cancer Immunity and Immunotherapy, a section of the journal Frontiers in Immunology

Received: *10 March 2022*
Accepted: *06 April 2022*
Published: *28 April 2022*

Citation:
Albakova Z, Mangasarova Y, Albakov A, Nikulina E, Kravchenko S and Sapozhnikov A (2022) Aberrant HSP90 Expression in Lymphocytes and HSP90 Response to Anti-PD-1 Therapy in Lymphoma Patients. Front. Immunol. 13:893137. doi: 10.3389/fimmu.2022.893137

INTRODUCTION

HSP90 family of molecular chaperones plays crucial in protein folding, degradation and maturation of client proteins (1, 2). HSP90 family is composed of four homologs, such as stress-inducible HSP90α, constitutive HSP90β, tumor necrosis factor receptor-associated protein 1 (TRAP1) and glucose-regulated protein 94 (GRP94) (1, 3, 4). HSP90α and HSP90β isoforms primarily reside in cytosol, TRAP1 in mitochondria and GRP94 in endoplasmic reticulum (ER), where HSP90 isoforms

act in a variety of cellular processes, including unfolded protein response, mitochondrial metabolism, lipid metabolism, autophagy and apoptosis (4). Cytosolic HSP90s work in collaboration with co-chaperones, including HSP70-HSP90 organizing protein (HOP/STIP1), protein phosphatase 5, cyclophilin 40, FK506-binding protein, activator of HSP90 ATPase homolog 1 (Aha1), p23 and cell division cycle 37 (Cdc37) (5–7). Under various stress conditions, HSP90 homologs may translocate from their primary location and can be released into the extracellular milieu (8–10). In the context of cancer, HSP90 homologs have been shown to be implicated in the regulation of epithelial-mesenchymal transition, metastasis, cancer cell stemness, invasion, apoptosis resistance and tumor immunity [reviewed in (4)].

Lymphoma is a heterogeneous group of tumors divided into two main types, such as Hodgkin lymphoma (HL) and Non-Hodgkin Lymphoma (NHL) (11, 12). Classical HL (cHL) is the most common subtype of HL, which is characterized by the presence of malignant Hodgkin and Reed-Sternberg (HRS) cells (13, 14). Even though HRS cells are germinal cell –derived B cells, they rarely express classical B cell markers (11). NHL lymphoma primarily consists of B-cell lymphomas (BCL) while other NHL subtypes include T- and NK- cell lymphomas (15). HL patients are usually treated with chemotherapy and radiotherapy while NHL patients are treated with chemotherapy combined with anti-CD20 (11, 12, 16). Even though the response rate is high, relapses occur in substantial number of lymphoma patients. Relapsed or refractory (r/r) cHL patients are treated with high-dose chemotherapy followed by an autologous hematopoetic stem cell transplantation (ASCT) (11). r/r cHL can also be treated with Nivolumab, an inhibitor of immune checkpoint programmed death-1 (PD-1) (11, 17). Even though cancer immunotherapy showed encouraging results in r/r patients, still some patients do not benefit from it, suggesting that it is critical to identify patients who will likely respond to the therapy.

In our previous study, we have used machine learning to show that HSP90β and TRAP1 are aberrantly expressed in the urine of cancer patients and that the HSP90β, TRAP1 and co-chaperones can be used to identify cancer patients (18). Since lymphoma originates from lymphocytes we sought to analyze the expression of HSP90β, TRAP1 and STIP1 co-chaperone in peripheral blood and bone marrow lymphocytes of patients with Hodgkin and Non-Hodgkin lymphomas. We show that B lymphocytes have the highest expression of HSP90β and STIP1 in lymphoma patients. We also show that PD-1 blockade differentially affects intracellular and surface HSP90s content in lymphocytes of r/r cHL patients. Since HSP90s may modulate immune responses, altering HSP90 expression and localization may further affect functional activity of immune cells. In this regard, we found that HSP90 downregulation impairs NK cell degranulation response and IFNγ production. To the best of our knowledge, this is the first study to assess the expression of HSP90β, TRAP1 and STIP1 in peripheral blood and bone marrow lymphocytes and the role of anti-PD-1 immunotherapy on HSP90 expression in cancer patients.

MATERIALS AND METHODS

Patient Samples

Peripheral blood (PB) and bone marrow (BM) samples were collected from B-NHL (n=5) and cHL (n=3) patients and healthy individuals (n=4). B-NHL group consisted of patients with diffuse large B-cell lymphoma (DLBCL, n=3) and primary mediastinal large B-cell lymphoma (PMBCL, n=2) while cHL group consisted of patients with nodular sclerosis HL (NSHL, n=3). HL and B-NHL patients included in the study were newly diagnosed patients with no previous history of treatment, unless otherwise specified. Samples were also obtained from relapsed or refractory cHL patients (n=3) receiving Nivolumab (Opdivo, Bristol-Myers Squibb) prior to the therapy and after 24 hours post-Nivolumab treatment. All patients were Epstein-Barr virus (EBV)- negative to exclude EBV-associated lymphomas. The median age of patients was 42 years old. Peripheral blood mononuclear cells (PBMCs) and bone marrow mononuclear cells (BM MNCs) were isolated using Ficoll-Paque density gradient centrifugation. The study was approved by the Research Ethics Committee of the Federal State Budgetary Institution 'National Medical Research Center for Hematology' of the Ministry of Health of the Russian Federation. All subjects had provided written informed consent in accordance with the Declaration of Helsinki.

Antibodies and Flow Cytometry

Cells were stained with fluorescently conjugated anti-human antibodies: APC/Cy7 anti-CD3 (HIT3a), APC anti-CD19 (HIB19), Pacific Blue anti-CD3 (HIT3a), FITC anti-human IFNγ (4S.B3) (all Sony Biotechnology), PE-Vio 770 anti-CD56 (REA196), FITC anti-Granzyme B (REA226), APC/Cy7 anti-CD107a (LAMP-1) (H4A3) (all Miltenyi Biotec).

HSP90β, TRAP1 and STIP1 Surface and Intracellular Staining

Cells were stained with anti-human TRAP1-RPE (3H4-2H6, Sigma-Aldrich), primary antibody against HSP90β (EPR16621), STIP1 (EPR6605) and the secondary antibody goat anti-rabbit IgG H&L PE preadsorbed (all Abcam). Mouse IgG1-PE (Invitrogen) and PE-rabbit IgG (Abcam) were used as isotype controls. FcR blocking reagent (Miltenyi Biotec) was used to block non-specific binding. For intracellular staining, cells were fixed and permeabilized with Cytofix/Cytoperm (BD Biosciences) and stained with antibodies for intracellular proteins. For surface and intracellular staining, dead cells were excluded from gating with the use of Sytox Blue dead stain and Fixable Viability Dye eFluor 506 (Invitrogen), respectively.

IgH Gene Rearrangement Detection

B-cell clonality (IgH gene rearrangements) was assessed using fragment analysis for V-D-J rearrangements of IgH (FR1, FR2, FR3), as previously described (19). The reaction mixture included 100–200 ng of DNA. PCR conditions: initial denaturation at 95°C (5 min), 35 cycles of PCR at 92°C (35s), 60°C (35s) and 72°C (35s) and final elongation at 72°C (10 min).

PCR was performed on an automatic thermal cycler DNA Engine (BioRad, Hercules, USA). The ABI PRISM 3130 Genetic Analyzer (Applied Biosystems, USA) was used for fragment analysis of PCR products. Results were visualized using the GeneMapper v. 4.0 (Applied Biosystems, USA).

NK Cell Stimulation, HSP90 Inhibition, CD107a/Granzyme B and IFNγ Analysis

NK cells were stimulated as previously described (20). Briefly, PBMCs and BM MNCs were incubated in RPMI 1640 with L-glutamine (Capricorn Scientific), supplemented with 10% Fetal Bovine Serum (FBS, Capricorn Scientific) and penicillin/streptomycin (Capricorn Scientific) with HSP90 inhibitor - geldanamycin (GA, 0.1μM) (Abcam) or DMSO in the presence or absence of the recombinant human (rh) IL-2 (100 IU/ml) (Miltenyi Biotec) and rhIL-15 (10 ng/ml) (Miltenyi Biotec) overnight at 37°C 5% CO_2 prior to the addition of APC-Cy7 anti-CD107a (Miltenyi Biotec). Cells then were stimulated with anti-NKp46/anti-CD2 (human NK cell activation/expansion kit, Miltenyi Biotec) for 5 hours at 37°C, according to the manufacturer instruction. The incubation was done in complete RPMI medium, supplemented with Brefeldin A (Sony Biotechnology) at a final dilution of 1/1000. Cells were then stained for surface markers and intracellular Granzyme B (Miltenyi Biotec) or IFNγ (Sony Biotechnology) and analyzed by flow cytometry.

Statistics

All statistical analyses were performed using GraphPad Prism 9. Results are expressed as mean ± standard error of the mean (SEM). In accordance with the data distribution, parametric tests including two-sample t-test and ANOVA and non-parametric methods including Mann Whitney test were employed for the data analysis. P values < 0.05 were considered to be statistically significant.

RESULTS

Immune Subpopulations in PBMCs and BM MNCs in HL and NHL Patients

Patients with newly diagnosed HL and B-NHL lymphoma had abnormal frequency of lymphocytes in peripheral blood compared to healthy controls (**Figure 1A**). HL and NHL patients differed by the frequency of immune population in PBMCs and BM MNCs (**Figure 1**). HL patients had higher frequency of T cells ($CD3^+CD56^-$) and NKT ($CD3^+CD56^+$) cells in peripheral blood and bone marrow compared to NHL patients. NHL patients had higher frequency of peripheral blood NK cells compared to HL patients, however, the difference was not statistically significant ($p>0.05$) (**Figure 1A**). Increased frequency of B cells ($CD19^+CD3^-$) and decreased frequency of NK cells ($CD56^+CD3^-$) were observed in bone marrow compared to peripheral blood in HL and NHL lymphoma (**Figure 1**).

Intracellular and Surface HSP90β, TRAP1 and STIP1 Expression in PB- and BM-Derived Lymphocytes in Lymphoma Patients

The intracellular expression of HSP90β (iHSP90β), iTRAP1 and iSTIP1 varied in peripheral blood lymphocytes of NHL and HL

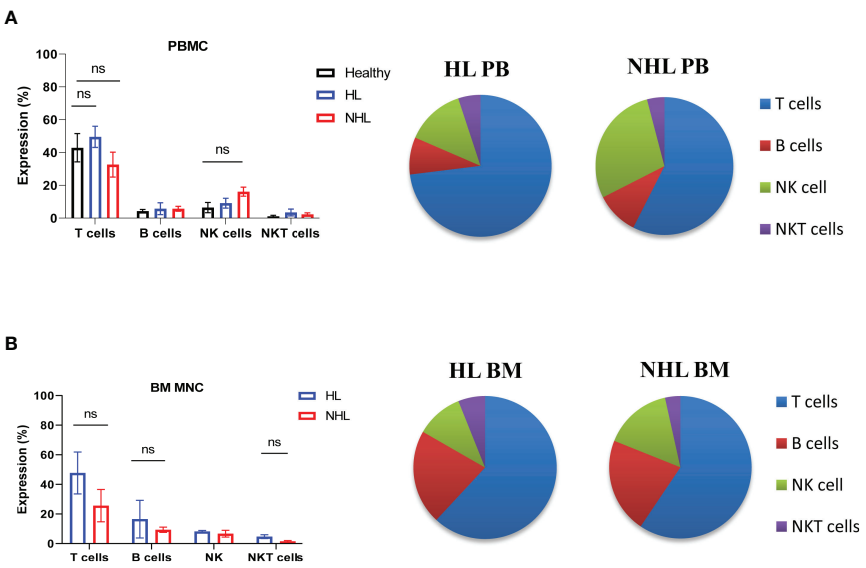

FIGURE 1 | Frequency of lymphocytes in peripheral blood and bone marrow samples derived from patients with HL and NHL patients. The percentage of T cells ($CD3^+$ $CD56^-$), B cells ($CD3^-CD19+$), NK cells ($CD3^-$, $CD56^+$) and NKT cells ($CD3^+CD56^+$) in peripheral blood **(A)** derived from HL, NHL patients and healthy controls and bone marrow samples **(B)** derived from HL and NHL patients. Graphs show mean ± SEM. ns, not significant. PB, peripheral blood; BM, bone marrow.

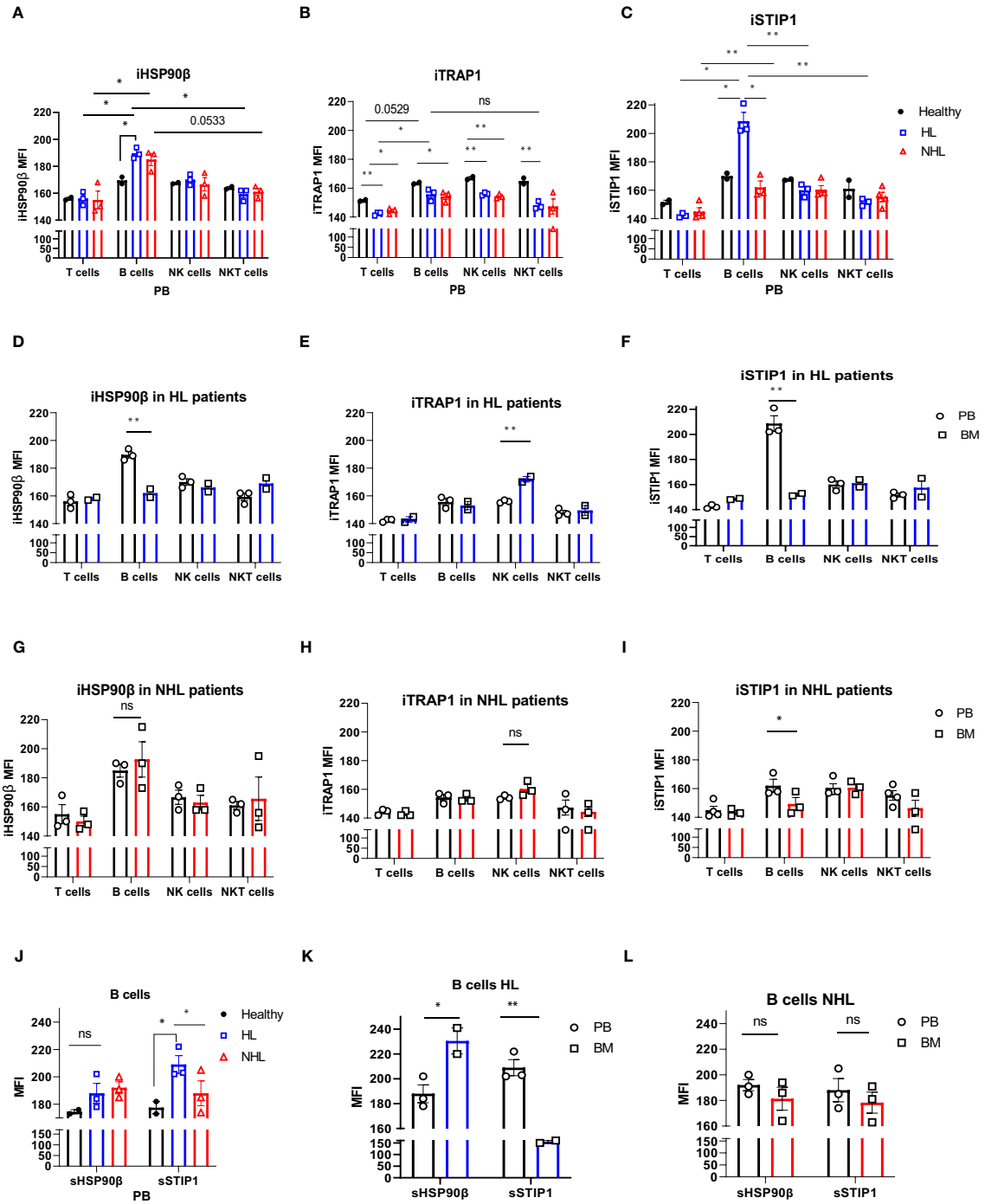

FIGURE 2 | Intracellular and surface HSP90β, TRAP1 and STIP1 expression in PB- and BM- derived lymphocytes of lymphoma patients. The mean level of intracellular expression of HSP90β (iHSP90β) **(A)**, iTRAP1 **(B)** and iSTIP1 **(C)** (as mean fluorescence intensity; MFI) in lymphocytes derived from PB of HL (n=3), NHL (n=3) patients and healthy controls (n=2). The expression of iHSP90β **(D)**, iTRAP1 **(E)** and iSTIP1 **(F)** in lymphocytes derived from BM of HL (n=2) and iHSP90β **(G)**, iTRAP1 **(H)** and iSTIP1 **(I)** in NHL (n= 3) patients. **(J–L)** Surface HSP90β and STIP1 expression in B lymphocytes derived from PB and BM samples of lymphoma patients. **(J)** The expression of sHSP90β and sSTIP1 in B cells derived from PB of HL (n=3), NHL patients (n=3) and healthy controls (n=2). **(K)** The expression of sHSP90β and sSTIP1 in B cells derived from PB and BM of HL (n=2). **(L)** The expression of sHSP90β and sSTIP1 in B cells derived from PB and BM of NHL (n=3) patients. Graphs show mean ± SEM. ns, not significant, *p<0.05, **p< 0.01.

patients. B cells showed significantly higher iHSP90β expression compared to other peripheral blood lymphocytes (T, NK and NKT cells) in lymphoma patients (**Figure 2A**). iHSP90β and iSTIP1 were significantly overexpressed in peripheral B cells of HL patients compared to healthy controls (**Figures 2A, C**). Bone marrow B lymphocytes showed significantly lower iHSP90β and iSTIP1 expression compared to peripheral B cells in HL patients (**Figures 2D, F**). By contrast, iHSP90β and iTRAP1 expression was comparable in BM- and PB- derived B cells of NHL patients (**Figures 2G, H**). Similar to HL patients, PB-derived B cells showed increased expression of iSTIP1 in NHL patients (**Figure 2I**). iTRAP1 was significantly decreased in peripheral blood lymphocytes in lymphoma patients compared to healthy controls (**Figure 2B**). Notably, HL patients showed higher iTRAP1 expression in bone marrow NK cells compared to peripheral blood NK cells (**Figure 2E**). sSTIP1 was significantly increased on the surface of B cells in peripheral blood of patients with HL lymphoma compared to healthy controls and NHL patients (**Figure 2J**). sHSP90β was significantly increased in bone marrow-derived B cells compared to the peripheral blood B cells of HL patients while sSTIP1 was significantly increased in peripheral blood B cells compared to bone marrow B cells in HL patients (**Figure 2K**). By contrast, sHSP90β and sSTIP1 were decreased in BM-derived B cells compared to peripheral blood B cells in NHL patients, however the difference was not statistically significant ($p>0.05$) (**Figure 2L**). These data suggest that surface and intracellular expression of HSP90β vary between peripheral blood and bone – marrow B cells and that the HL and NHL lymphomas differ by the expression of intracellular and surface HSP90β and STIP1 in B lymphocytes.

B-Cell Clonality Analysis in HL and NHL Patients

To determine whether high HSP90 expression in B cells is associated with malignant B cell clones, we performed B-cell clonality analysis (IgH gene rearrangements) using PB and BM samples from HL and NHL patients (**Figure 3** and **Supplementary Figure 3**). No malignant B cell clones were detected in PB and BM of HL and NHL patients (**Figures 3A–D** and **Supplementary Figure 3**), suggesting that high HSP90 expression in B cells may not be associated with malignant B cell phenotype.

Anti-PD-1 Treatment Affects HSP90s Expression in Lymphocytes of r/r cHL Patients

Patients with refractory or relapsed cHL undergoing Nivolumab treatment were presented with conglomerate lymph node masses at diagnosis (**Figure 4**). We assessed the effect of anti-PD-1 therapy on the frequency of immune cells and the expression of HSP90β, TRAP1 and STIP1 in T, B, NK and NKT cells prior to and 24 hours after the treatment of patients with r/r cHL. Blocking PD-1 affected the frequency of immune cell population in the peripheral blood at 24 hours of the treatment (**Figure 5A**). The median percentage of T cells was decreased after 24 hours of anti-PD-1 treatment (**Figure 5A**). One patient showed increased frequency of peripheral blood NK cells (**Figure 5B**). Increased frequency of NK cells after anti-PD-1 therapy has been also shown previously in cancer patients (21).

iHSP90β decreased in T, B, NK and NKT cells. Two patients showed increased HSP90β expression on the surface of peripheral blood B cells (**Figures 5C, D**). PD-1 blockade did not affect iTRAP1 expression, but increased sTRAP1 (**Figures 5E, F**). PD-1 blockade did not affect iSTIP1 in lymphocytes, although 1 patient showed increased iSTIP1 in NK cells (**Figures 5G, H**). sSTIP1 was decreased in lymphocytes following anti-PD-1 treatment (**Figures 5G,H**). Since PD-1 blockade altered HSP90 expression in peripheral blood, we sought to determine whether similar changes occur in bone marrow lymphocytes. Consequently, we examined intracellular and extracellular HSP90β, TRAP1 and STIP1 in bone marrow lymphocytes from Patient 1 before and after the anti-PD-1 treatment and compared it to the HSP90 expression in peripheral blood of this patient (**Figure 6**). PD-1 blockade upregulated intracellular and downregulated surface HSP90β in BM-derived B cells (**Figures 6A, B**). By contrast, anti-PD-1 blockade downregulated intracellular and upregulated STIP1 expression in bone marrow B cells (**Figures 6E, F**). PD-1 blockade also downregulated intracellular and surface HSP90β and STIP1 expression in BM-derived NKT cells (**Figures 6A, B, E, F**). sHSP90β was decreased in peripheral blood and bone marrow B cells following anti-PD-1 therapy (**Figure 6B**). Interestingly, anti-PD-1 therapy resulted in decreased expression of iTRAP1 in BM-derived NK cells (**Figure 6C**). It is also interesting to note that PB- and BM- derived B cells differentially expressed iHSP90β after 24 hours of treatment with anti-PD-1 (**Figure 6A**). These findings suggest that anti-PD-1 treatment affects the frequency of lymphocytes and their intracellular and surface HSP90 expression in r/r cHL lymphoma patients, however, further studies are required to assess the effect of anti-PD-1 treatment on HSP90 expression and localization in bone marrow and peripheral blood lymphocytes.

HSP90 Downregulation Affects NK Cell Degranulation Response and IFNγ Production in Healthy Donors and Lymphoma Patients

Since anti-PD-1 treatment may alter HSP90 expression, we sought to determine whether modulating HSP90 level would affect the functional activity of NK cells. IL-2/IL-15-preactivated NK cells from healthy controls were more responsive to anti-NKp46/anti-CD2 stimulation, resulting in higher frequency of $CD107a^+$ Granzyme B^+ NK cells, as compared to NK cells from BCL patients (**Figure 7A**). By contrast, IL-2/IL-15/anti-NKp46/anti-CD2 stimulation resulted in increased frequency of $CD107a^+IFN\gamma^+$ NK cells in BCL patients, as compared to healthy controls (**Figure 7D**). HSP90 inhibition decreased the frequency of CD107a +/Granzyme B+ in healthy controls, bone marrow and peripheral blood NK cells of BCL patients (**Figures 7A, B**). HSP90 inhibition downregulated the expression of CD107a on

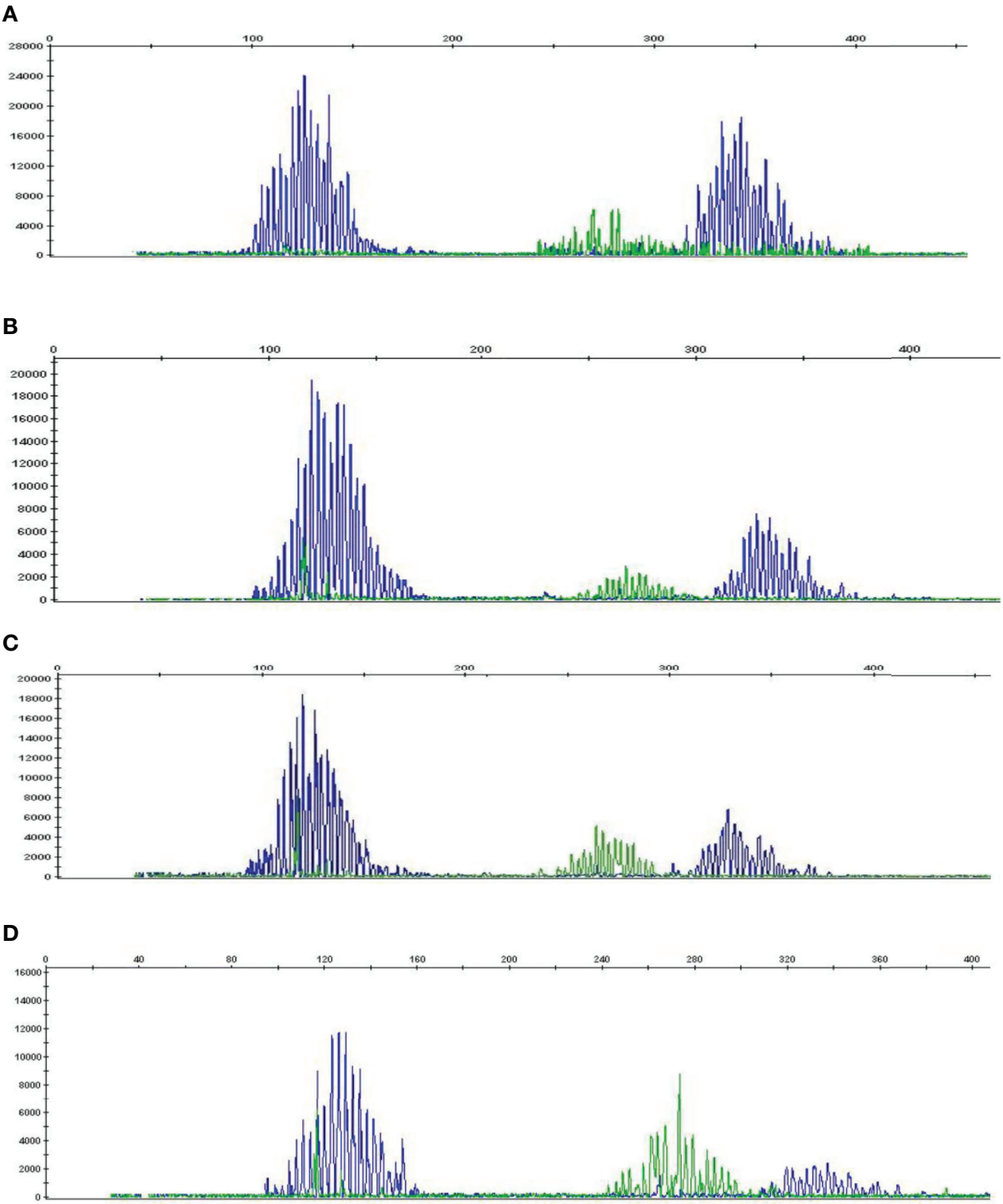

FIGURE 3 | B-cell clonality analysis (IgH gene rearrangements) in PB and BM of HL and NHL patients. Representative graphs showing a Gaussian distribution of multiple peaks in **(A)** peripheral blood and **(B)** bone marrow in NHL patient and **(C)** peripheral blood and **(D)** bone marrow in HL patient.

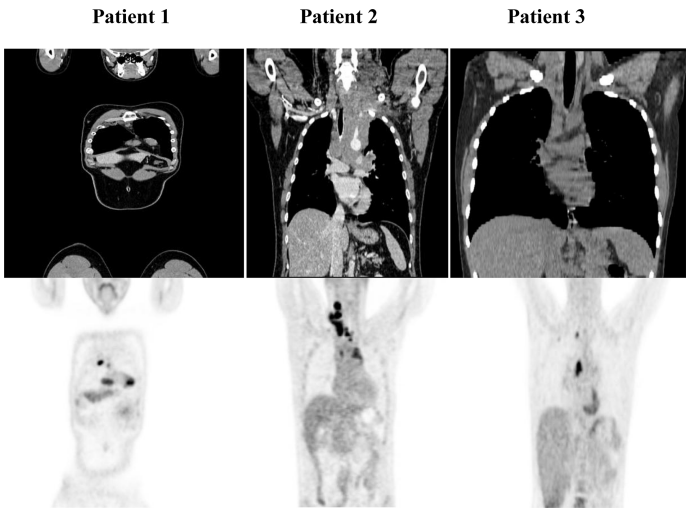

FIGURE 4 | PET/CT of r/r cHL patients prior to the initiation of anti-PD-1 treatment. Patient 1 presented with conglomerate lymph node masses at the anterosuperior mediastinum with the size of 37x21 mm, SUV 6.4 and the paragastric conglomerate with the size of 45x42 mm, SUV 7.4. Patient 2 presented with cervical lymph nodes with the size of 6.6mm, SUV 4.7 and with conglomerate lymph node mass at the anterosuperior mediastinum with the size of 74x42 mm, SUV 7.7. Patient 3 presented with conglomerate lymph node mass at the anterosuperior mediastinum with the size of 43x32 mm, SUV 8.2. SUV, standardized uptake value.

the surface of bone marrow and peripheral blood NK cells, leading to double positive CD107a+ Granzyme B+ NK cells lose their CD107a+ expression and become single positive Granzyme B^+ NK cells upon stimulation (**Figure 7C**). HSP90 inhibition also decreased the percentage of $CD107^+IFN\gamma^+$ NK cells in response to IL-2/IL-15 and anti-NKp46/anti-CD2 stimulation (**Figure 7D**). These data suggest that downregulating HSP90 may impair NK cell degranulation response and IFNγ production in lymphoma patients.

DISCUSSION

We have assessed the expression of constitutive and mitochondrial HSP90 and HSP90 co-chaperone STIP1/HOP in two major types of lymphoma- Hodgkin lymphoma and Non-Hodgkin lymphoma. We showed that two lymphomas differ by the expression of intracellular and surface content of HSP90β and STIP1 in peripheral blood and bone marrow lymphocytes. Intriguingly, peripheral blood B cells showed to be the major type of lymphocytes with abnormal expression of HSP90s inside and on their surface in lymphoma patients. HSP90β and STIP1 were also aberrantly expressed on the surface of bone marrow B cells in lymphoma patients. Since HSP90 overexpression may potentially be associated with circulating malignant B cell clones, we have performed B-cell clonality analysis. No malignant B cell clones were found in the blood and bone marrow of HL and NHL patients, suggesting that high HSP90 expression in B cells may not be associated with malignant phenotype. Several studies reported that extracellular HSPs associate with B regulatory phenotype (22, 23). In a recent study, Wang and colleagues reported that regulatory B cells have high expression of HSP70 (24). Along this line, Tang et al. demonstrated that extracellular BiP/GRP78 induces regulatory B cell phenotype (22). Extracellular HSP60 stimulates B cells to produce IL-10 and IL-6 while HSP60-stimulated B cells induce the proliferation and IFNγ and IL-10 production in T cells (23). These data suggest that altered expression of HSP90 in B cells may affect B cell responses in bone marrow and peripheral blood of lymphoma patients.

Recently, Zavareh and colleagues demonstrated that HSP90 inhibitors downregulate surface PD-L1 expression in mouse models *via* the regulation of HSP90 clients (c-Myc and STAT3) (25). HSP90 inhibition also showed to potentiate anti-tumor activity of PD-1 and CTLA-4 blockade *in vivo* (26, 27). Here, we showed that treatment with anti-PD-1 altered the expression and localization of HSP90β, TRAP1 and STIP1 in peripheral blood lymphocytes in refractory HL patients. PD-1 blockade also affected HSP90 content and localization in bone marrow lymphocytes. Notably, PD-1 blockade resulted in increased surface HSP90 expression in lymphocytes. Previous studies demonstrated that HSPs can be upregulated on the surface of immune cells following ER stress (28, 29). These studies suggest that there is interplay between immune checkpoints and HSP90s and that lymphocytes may upregulate surface HSP90 expression in response to anti-PD-1 immunotherapy, however, further studies are required to understand the role of cancer immunotherapy on the HSP90 expression.

Several studies reported high expression of PD-1 on NK cells in cancer patients (30, 31). Furthermore, Vari and colleagues highlighted an important role of PD-1/PD-L1 axis in the functional activity of NK cells in lymphoma patients (30). Taking into account that anti-PD-1 immunotherapy may affect HSP90 expression in NK cells, we assessed the effect of HSP90

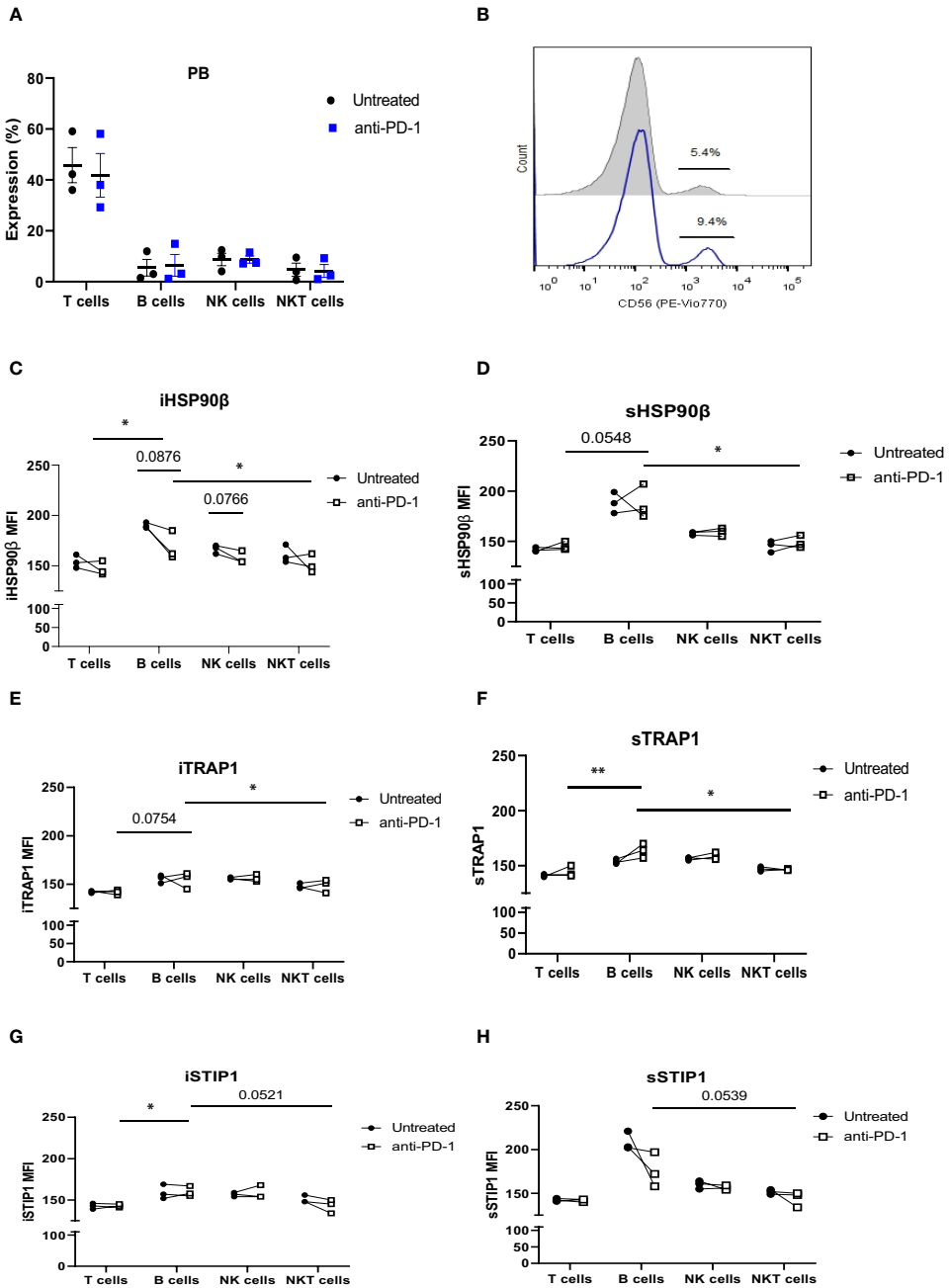

FIGURE 5 | The effect of anti-PD-1 treatment on HSP90 expression in peripheral blood lymphocytes in r/r cHL patients. **(A)** Frequencies of T, B, NK and NKT cells following 24hr treatment with Nivolumab in r/r cHL patients (n=3). **(B)** Representative histogram showing increase in NK cell frequency after 24hr treatment with Nivolumab. iHSP90β expression **(C)** and sHSP90β **(D)**, iTRAP1 **(E)** and sTRAP1 **(F)**, iSTIP1 **(G)** and sSTIP1 **(H)** in peripheral blood lymphocytes of r/r cHL patients at 24 hrs treatment with Nivolumab (n=3). ns, not significant, *p<0.05, **p< 0.01.

downregulation on the degranulation response, granzyme B and IFNγ production in NK cells of lymphoma patients. We found that HSP90 inhibition downregulates CD107a expression and IFNγ production in NK cells upon stimulation. These results are consistent with previous findings showing that HSP90 inhibitors downregulate IFNγ secretion by NK cells (32). It is important to note that geldanamycin blocks HSP90 ATPase activity and thus, inhibits all four HSP90 isoforms, including HSP90α, HSP90β, TRAP1 and GRP94 in NK cells, suggesting that it is critical to identify specific HSP90 homolog responsible for the regulation of

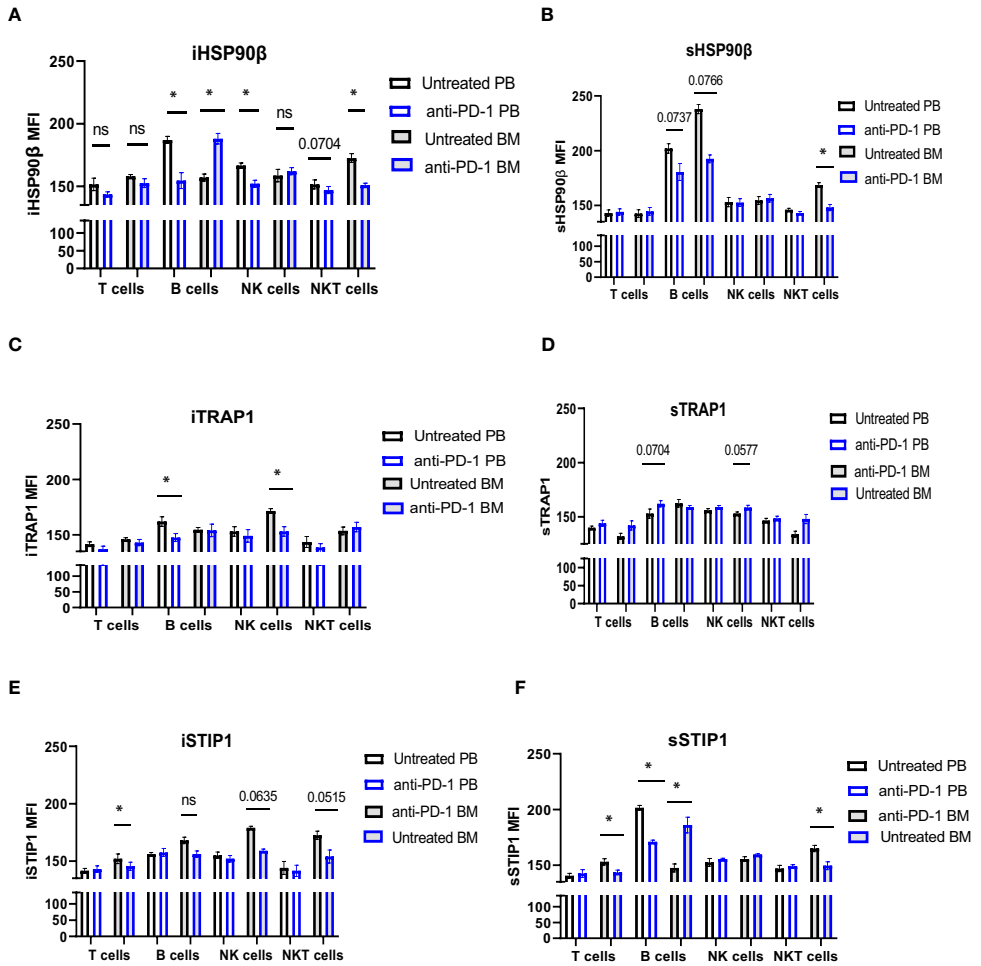

FIGURE 6 | The effect of anti-PD-1 on the HSP90 expression in PB and BM lymphocytes in r/r cHL patient. Intracellular **(A, C, E)** and surface **(B, D, F)** expression of HSP90β **(A, B)**, TRAP1 **(C, D)** and STIP1 **(E, F)** in PB and BM lymphocytes in r/r cHL patient (n=1). Graphs show mean ± SD. ns, not significant, *p<0.05. PB, peripheral blood; BM, bone marrow.

CD107a+ expression and IFNγ production in NK cells. Recent studies have demonstrated that cell metabolism plays a critical role in NK cell functional activity (33). Wang and colleagues reported that inhibition of glycolysis downregulates NK cell IFNγ production and CD107a expression (34). Authors also showed that glycolysis inhibition abrogated Granzyme B production while inhibition of oxidative phosphorylation (OXPHOS) did not affect Granzyme B production by NK cells (34). In our study we showed that geldanamycin inhibited CD107a expression and IFNγ production while Granzyme B production was not affected, suggesting that HSP90 inhibitor may affect both, i.e. glycolysis and OXPHOS. In this regard, mitochondrial HSP90 homolog TRAP1 showed to be a critical regulator of OXPHOS and glycolysis, suggesting that TRAP1 may be a potential isoform responsible for the downregulation of CD107a expression and IFNγ production in NK cells, however, this warrants further investigation (35, 36).

In summary, we showed that lymphoma patients have abnormal expression of HSP90s in bone marrow and peripheral blood B cells. PD-1 blockade altered the intracellular and surface HSP90 expression in immune population in r/r HL patients. Altering the level of HSP90 may inhibit cytotoxic activity of peripheral blood and bone marrow NK cells. Further understanding the effect of cancer immunotherapy on intracellular and extracellular HSP90 may help in identification of patients who will likely benefit from the treatment.

CONCLUSION

HSP90 molecular chaperones play critical role in proteome homeostasis and showed to be implicated in various hallmarks of cancer. We show that constitutive, mitochondrial HSP90s and HSP90 co-chaperone STIP1/HOP are aberrantly expressed in B cells of lymphoma patients. Since approved and emerging cancer immunotherapeutics include immune checkpoint inhibitors, we

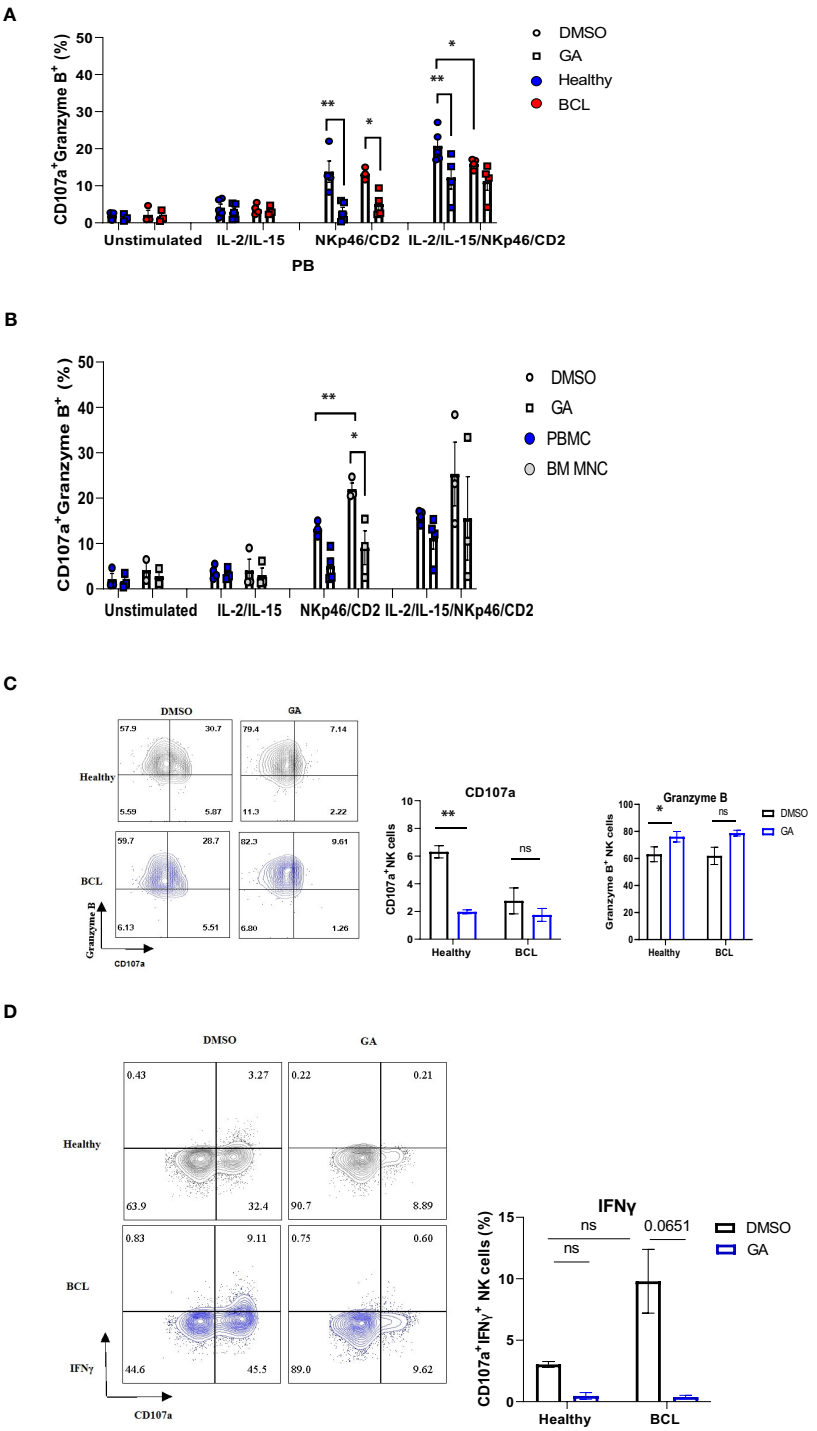

FIGURE 7 | The effect of HSP90 inhibition on the NK cell degranulation response, granzyme B and IFNγ production in lymphoma patients. NK cell degranulation, as measured by CD107a surface expression, and granzyme B/IFNγ production in PB (n=4) of lymphoma patients and healthy controls (n=5) and BM (n=3) of lymphoma patients. PBMC **(A)** and BM MNC **(B)** were pre-treated with geldanamycin (0.1μM) or DMSO in the presence of IL-2 (100IU/ml) and IL-15 (10 ng/ml) and stimulated with anti-NKp46/anti-CD2. **(C)** Representative flow cytometry plots of $CD107a^+$/Granzyme B^+ double positive NK cells on the left and the frequency of CD107a single positive (SP) and Granzyme B SP NK cells in response to IL-2/IL-15 and anti-NKp46/anti-CD2 stimulation. **(D)** Representative flow cytometry plots of $CD107a^+$ $IFNγ^+$ NK cells on the left and the frequency of $CD107a^+IFNγ^+$ NK cells in response to IL-2/IL-15 and anti-NKp46/anti-CD2 stimulation. Graphs show mean ± SEM. ns, not significant, *p<0.05, **p< 0.01. GA, Geldanamycin; BCL, B-cell lymphoma.

have assessed the effect of anti-PD-1 treatment on HSP90 expression in refractory/relapsed lymphoma patients. We showed that anti-PD-1 affects HSP90 level and localization in immune cells of lymphoma patients. Additionally, we found that modulating HSP90 level may impair functional activity of NK cells. Further understanding of the effect of immunotherapies on HSP90 may improve treatment response in lymphoma patients.

DATA AVAILABILITY STATEMENT

The original contributions presented in the study are included in the article/**Supplementary Material**. Further inquiries can be directed to the corresponding author.

ETHICS STATEMENT

The studies involving human participants were reviewed and approved by Research Ethics Committee of the Federal State Budgetary Institution 'National Medical Research Center for Hematology' of the Ministry of Health of the Russian Federation. The patients/participants provided their written informed consent to participate in this study.

AUTHOR CONTRIBUTIONS

ZA, conceived, designed and conducted experiments, analyzed the data, and wrote the manuscript. YM, provided clinical expertise and supervised clinical part of the project. AA, contributed to editing of the manuscript and funding acquisition. EN, contributed to the gene rearrangement analysis. SK, contributed to the clinical part of the project. AS, provided administrational support. All authors contributed to the article and approved the submitted version.

FUNDING

This work was funded by RFBR, project number 20-315-90081. YM was supported by the RAKFOND grant 2020-02.

ACKNOWLEDGMENTS

Authors are grateful to the patients and volunteers for supporting our study. We thank Professor Sergei Nedospasov and Professor Nina Drize for their help with samples. We thank Dr Yury Rubtsov for consulting and helping us with reagents. The authors are grateful to the staff of the National Medical Research Center for Hematology (Moscow, Russia). We also thank the Laboratory of Cell Interations of the Shemyakin and Ovchinnikov Institute of Bioorganic Chemistry RAS (Head – Alexander Sapozhnikov, Moscow, Russia) for using their laboratory equipment. We are grateful to the Chokan (Almaty, Kazakhstan) for fully sponsoring and supporting our project.

SUPPLEMENTARY MATERIAL

The Supplementary Material for this article can be found online at: https://www.frontiersin.org/articles/10.3389/fimmu.2022.893137/full#supplementary-material

REFERENCES

1. Johnson JL. Evolution and Function of Diverse Hsp90 Homologs and Cochaperone Proteins. *Biochim Biophys Acta (BBA) - Mol Cell Res* (2012) 1823(3):607–13. doi: 10.1016/j.bbamcr.2011.09.020
2. Schopf FH, Biebl MM, Buchner J. The HSP90 Chaperone Machinery. *Nat Rev Mol Cell Biol* (2017) 18(6):345–60. doi: 10.1038/nrm.2017.20
3. Kampinga HH, Hageman J, Vos MJ, Kubota H, Tanguay RM, Bruford EA, et al. Guidelines for the Nomenclature of the Human Heat Shock Proteins. *Cell Stress Chaperones* (2009) 14(1):105–11. doi: 10.1007/s12192-008-0068-7
4. Albakova Z, Mangasarova Y, Albakov A, Gorenkova L. HSP70 and HSP90 in Cancer: Cytosolic, Endoplasmic Reticulum and Mitochondrial Chaperones of Tumorigenesis. *Front Oncol* (2022) 12. doi: 10.3389/fonc.2022.829520
5. Zuehlke A, Johnson JL. Hsp90 and Co-Chaperones Twist the Functions of Diverse Client Proteins. *Biopolymers* (2010) 93(3):211–7. doi: 10.1002/bip.21292
6. Barrott JJ, Haystead TAJ. Hsp90, an Unlikely Ally in the War on Cancer. *FEBS J* (2013) 280(6):1381–96. doi: 10.1111/febs.12147
7. Albakova Z, Armeev GA, Kanevskiy LM, Kovalenko EI, Sapozhnikov AM. HSP70 Multi-Functionality in Cancer. *Cells* (2020) 9:(3). doi: 10.3390/cells9030587
8. Shin BK, Wang H, Yim AM, Le Naour F, Brichory F, Jang JH, et al. Global Profiling of the Cell Surface Proteome of Cancer Cells Uncovers an Abundance of Proteins With Chaperone Function. *J Biol Chem* (2003) 278 (9):7607–16. doi: 10.1074/jbc.M210455200
9. Cid C, Regidor I, Poveda PD, Alcazar A. Expression of Heat Shock Protein 90 at the Cell Surface in Human Neuroblastoma Cells. *Cell Stress Chaperones* (2009) 14(3):321–7. doi: 10.1007/s12192-008-0076-7
10. Albakova Z, Siam MKS, Sacitharan PK, Ziganshin RH, Ryazantsev DY, Sapozhnikov AM. Extracellular Heat Shock Proteins and Cancer: New Perspectives. *Trans Oncol* (2021) 14(2):100995. doi: 10.1016/j.tranon.2020.100995
11. Connors JM, Cozen W, Steidl C, Carbone A, Hoppe RT, Flechtner H-H, et al. Hodgkin Lymphoma. *Nat Rev Dis Primers* (2020) 6(1):61. doi: 10.1038/s41572-020-0189-6
12. Andrew DZ, Leo IG, Jeremy SA, Ranjana HA, Nancy LB, Paolo FC, et al. NCCN Guidelines Insights: B-Cell Lymphomas, Version 3.2019. *J Natl Compr Cancer Network J Natl Compr Canc Netw* (2019) 17(6):650–61. doi: 10.6004/jnccn.2019.0029
13. Steidl C. The Ecosystem of Classical Hodgkin Lymphoma. *Blood* (2017) 130 (22):2360–1. doi: 10.1182/blood-2017-10-807172
14. Albakova Z, Mangasarova Y, Sapozhnikov A. Heat Shock Proteins in Lymphoma Immunotherapy. *Front Immunol* (2021) 12:660085. doi: 10.3389/fimmu.2021.660085
15. Wang L, Qin W, Huo Y-J, Li X, Shi Q, Rasko JEJ, et al. Advances in Targeted Therapy for Malignant Lymphoma. *Signal Transduction Targeted Ther* (2020) 5(1):15. doi: 10.1038/s41392-020-0113-2
16. Susanibar-Adaniya S, Barta SK. 2021 Update on Diffuse Large B Cell Lymphoma: A Review of Current Data and Potential Applications on Risk Stratification and Management. *Am J Hematol* (2021) 96(5):617–29. doi: 10.1002/ajh.26151
17. Ramchandren R, Domingo-Domènech E, Rueda A, Trněný M, Feldman TA, Lee HJ, et al. Nivolumab for Newly Diagnosed Advanced-Stage Classic Hodgkin Lymphoma: Safety and Efficacy in the Phase II CheckMate 205 Study. *J Clin Oncol* (2019) 37(23):1997–2007. doi: 10.1200/JCO.19.00315

18. Albakova Z, Norinho DD, Mangasarova Y, Sapozhnikov A. Heat Shock Proteins in Urine as Cancer Biomarkers. *Front Med (Lausanne)* (2021) 8:743476. doi: 10.3389/fmed.2021.743476
19. van Dongen JJM, Langerak AW, Brüggemann M, Evans PAS, Hummel M, Lavender FL, et al. Design and Standardization of PCR Primers and Protocols for Detection of Clonal Immunoglobulin and T-Cell Receptor Gene Recombinations in Suspect Lymphoproliferations: Report of the BIOMED-2 Concerted Action BMH4-CT98-3936. *Leukemia* (2003) 17(12):2257–317. doi: 10.1038/sj.leu.2403202
20. Al-Hubeshy ZB, Coleman A, Nelson M, Goodier MR. A Rapid Method for Assessment of Natural Killer Cell Function After Multiple Receptor Crosslinking. *J Immunol Methods* (2011) 366(1):52–9. doi: 10.1016/j.jim.2011.01.007
21. Youn J-I, Park S-M, Park S, Kim G, Lee H-J, Son J, et al. Peripheral Natural Killer Cells and Myeloid-Derived Suppressor Cells Correlate With Anti-PD-1 Responses in non-Small Cell Lung Cancer. *Sci Rep* (2020) 10(1):9050. doi: 10.1038/s41598-020-65666-x
22. Tang Y, Jiang Q, Ou Y, Zhang F, Qing K, Sun Y, et al. BIP Induces Mice CD19hi Regulatory B Cells Producing IL-10 and Highly Expressing PD-L1, FasL. *Mol Immunol* (2016) 69:44–51. doi: 10.1016/j.molimm.2015.10.017
23. Cohen-Sfady M, Nussbaum G, Pevsner-Fischer M, Mor F, Carmi P, Zanin-Zhorov A, et al. Heat Shock Protein 60 Activates B Cells *via* the TLR4-MyD88 Pathway. *J Immunol* (2005) 175(6):3594. doi: 10.4049/jimmunol.175.6.3594
24. Wang L, Fu Y, Yu B, Jiang X, Liu H, Liu J, et al. HSP70, a Novel Regulatory Molecule in B Cell-Mediated Suppression of Autoimmune Diseases. *J Mol Biol* (2021) 433(1):166634. doi: 10.1016/j.jmb.2020.08.019
25. Zavareh RB, Spangenberg SH, Woods A, Martínez-Peña F, Lairson LL. HSP90 Inhibition Enhances Cancer Immunotherapy by Modulating the Surface Expression of Multiple Immune Checkpoint Proteins. *Cell Chem Biol* (2021) 28(2):158–168.e155. doi: 10.1016/j.chembiol.2020.10.005
26. Song K-H, Oh SJ, Kim S, Cho H, Lee H-J, Song JS, et al. HSP90A Inhibition Promotes Anti-Tumor Immunity by Reversing Multi-Modal Resistance and Stem-Like Property of Immune-Refractory Tumors. *Nat Commun* (2020) 11 (1):562. doi: 10.1038/s41467-019-14259-y
27. Mbofung RM, McKenzie JA, Malu S, Zhang M, Peng W, Liu C, et al. HSP90 Inhibition Enhances Cancer Immunotherapy by Upregulating Interferon Response Genes. *Nat Commun* (2017) 8(1):451. doi: 10.1038/s41467-017-00449-z
28. Raiter A, Lipovetzki J, Lubin I, Yerushalmi R. GRP78 Expression in Peripheral Blood Mononuclear Cells is a New Predictive Marker for the Benefit of Taxanes in Breast Cancer Neoadjuvant Treatment. *BMC Cancer* (2020) 20 (1):333. doi: 10.1186/s12885-020-06835-z
29. Chaumonnot K, Masson S, Sikner H, Bouchard A, Baverel V, Bellaye P-S, et al. The HSP GRP94 Interacts With Macrophage Intracellular Complement C3 and Impacts M2 Profile During ER Stress. *Cell Death Dis* (2021) 12(1):114. doi: 10.1038/s41419-020-03288-x
30. Vari F, Arpon D, Keane C, Hertzberg MS, Talaulikar D, Jain S, et al. Immune Evasion *via* PD-1/PD-L1 on NK Cells and Monocyte/Macrophages is More Prominent in Hodgkin Lymphoma Than DLBCL. *Blood* (2018) 131(16):1809–19. doi: 10.1182/blood-2017-07-796342
31. Benson DM Jr, Bakan CE, Mishra A, Hofmeister CC, Efebera Y, Becknell B, et al. The PD-1/PD-L1 Axis Modulates the Natural Killer Cell Versus Multiple Myeloma Effect: A Therapeutic Target for CT-011, a Novel Monoclonal Anti-PD-1 Antibody. *Blood* (2010) 116(13):2286–94. doi: 10.1182/blood-2010-02-271874
32. Huyan T, Li Q, Dong D-D, Yang H, Zhang J, Huang Q-S, et al. Heat Shock Protein 90 Inhibitors Induce Functional Inhibition of Human Natural Killer Cells in a Dose-Dependent Manner. *Immunopharmacol Immunotoxicology* (2016) 38(2):77–86. doi: 10.3109/08923973.2015.1119159
33. Mah AY, Cooper MA. Metabolic Regulation of Natural Killer Cell IFN-γ Production. *Crit Rev Immunol* (2016) 36(2):131–47. doi: 10.1615/CritRevImmunol.2016017387
34. Wang Z, Guan D, Wang S, Chai LYA, Xu S, Lam K-P. Glycolysis and Oxidative Phosphorylation Play Critical Roles in Natural Killer Cell Receptor-Mediated Natural Killer Cell Functions. *Front Immunol* (2020) 11. doi: 10.3389/fimmu.2020.00202
35. Sciacovelli M, Guzzo G, Morello V, Frezza C, Zheng L, Nannini N, et al. The Mitochondrial Chaperone TRAP1 Promotes Neoplastic Growth by Inhibiting Succinate Dehydrogenase. *Cell Metab* (2013) 17(6):988–99. doi: 10.1016/j.cmet.2013.04.019
36. Yoshida S, Tsutsumi S, Muhlebach G, Sourbier C, Lee M-J, Lee S, et al. Molecular Chaperone TRAP1 Regulates a Metabolic Switch Between Mitochondrial Respiration and Aerobic Glycolysis. *Proc Natl Acad Sci USA* (2013) 110(17):E1604–12. doi: 10.1073/pnas.1220659110

Conflict of Interest: The authors declare that the research was conducted in the absence of any commercial or financial relationships that could be construed as a potential conflict of interest.

Publisher's Note: All claims expressed in this article are solely those of the authors and do not necessarily represent those of their affiliated organizations, or those of the publisher, the editors and the reviewers. Any product that may be evaluated in this article, or claim that may be made by its manufacturer, is not guaranteed or endorsed by the publisher.

frontiers | Frontiers in Immunology

ORIGINAL RESEARCH
published: 28 April 2022
doi: 10.3389/fimmu.2022.880288

Establishment of a lncRNA-Based Prognostic Gene Signature Associated With Altered Immune Responses in HCC

Xiawei Li[1,2], *Zhiqian Zhang*[2], *Mingcheng Liu*[2], *Xing Fu*[2], *Jun A*[2], *Guoan Chen*[2], *Shian Wu*[1] *and Jin-Tang Dong*[2*]

[1] Department of Genetics and Cell Biology, College of Life Sciences, Nankai University, Tianjin, China, [2] Laboratory Department of Human Cell Biology and Genetics, School of Medicine, Southern University of Science and Technology, Shenzhen, China

OPEN ACCESS

Edited by:
Elias Joseph Sayour, University of Florida, United States

Reviewed by:
John Ligon, University of Florida, United States
Paul Castillo, University of Florida, United States

***Correspondence:**
Jin-Tang Dong
dongjt@sustech.edu.cn

Specialty section:
This article was submitted to Cancer Immunity and Immunotherapy, a section of the journal Frontiers in Immunology

Received: *21 February 2022*
Accepted: *05 April 2022*
Published: *28 April 2022*

Citation:
Li X, Zhang Z, Liu M, Fu X, A J, Chen G, Wu S and Dong J-T (2022) Establishment of a lncRNA-Based Prognostic Gene Signature Associated With Altered Immune Responses in HCC. Front. Immunol. 13:880288. doi: 10.3389/fimmu.2022.880288

Hepatocellular carcinoma (HCC) is a common malignancy with higher mortality, and means are urgently needed to improve the prognosis. T cell exclusion (TCE) plays a pivotal role in immune evasion, and lncRNAs represent a large group of tumor development and progression modulators. Using the TCGA HCC dataset (n=374), we identified 2752 differentially expressed and 702 TCE-associated lncRNAs, of which 336 were in both groups. As identified using the univariate Cox regression analysis, those associated with overall survival (OS) were subjected to the LASSO-COX regression analysis to develop a prognosis signature. The model, which consisted of 11 lncRNAs and was named 11LNCPS for 11-lncRNA prognosis signature, was validated and performed better than two previous models. In addition to OS and TCE, higher 11LNCPS scores had a significant correlation with reduced infiltrations of CD8+ T cells and dendritic cells (DCs) and decreased infiltrations of Th1, Th2, and pro B cells. As expected, these infiltration alterations were significantly associated with worse OS in HCC. Analysis of published data indicates that HCCs with higher 11LNCPS scores were transcriptomically similar to those that responded better to PDL1 inhibitor. Of the 11LNCPS lncRNAs, *LINC01134* and *AC116025.2* seem more crucial, as their upregulations affected more immune cell types' infiltrations and were significantly associated with TCE, worse OS, and compromised immune responses in HCC. LncRNAs in the 11LNCPS impacted many cancer-associated biological processes and signaling pathways, particularly those involved in immune function and metabolism. The 11LNCPS should be useful for predicting prognosis and immune responses in HCC.

Keywords: hepatocellular carcinoma (HCC), T cell exclusion, lncRNA, prognosis, *LINC01134*, *AC116025.2*

INTRODUCTION

Hepatocellular carcinoma (HCC) is one of the most common human malignancies and the third leading cause of cancer-associated deaths worldwide (1, 2). Several therapies such as surgical resection, liver transplantation, radiotherapy, and chemotherapy are available for HCC treatment. However, the survival of patients with advanced or metastatic HCC is quite limited, and the lack of timely diagnosis, prognosis evaluation, and effective treatments are some of the reasons (3, 4). It is thus imperative to develop prognostic models that can help decision making in HCC treatment.

Accumulating evidence indicates that immunotherapy is a promising strategy for cancer treatment, which largely relies on the successful application of immune-checkpoint inhibitors (ICIs) at present (1, 5–7). The combination of ICIs and conventional therapies are also under development as additional therapeutic strategies for HCC treatment (8). For instance, combined administration of the PDL1 inhibitor atezolizumab and the VEGF inhibitor bevacizumab has become a first-line therapeutic strategy for advanced HCC (9). Although immunotherapy has shown remarkable outcomes, only one-third of patients benefit from it (10). One of the main factors affecting the effectiveness of immunotherapy is tumor immune evasion (11, 12). Cancer cells evade the immune system to avoid antitumor immunity and enhance tumor malignancy (1, 13, 14), and T cell exclusion (TCE) is one of the primary mechanisms for tumor immune escape (15). Some immunosuppressive factors exclude T cells, especially cytotoxic CD8+ T cells, from infiltration tumors, making a tumor "cold". Hence, it is crucial to construct accurate prognostic models for TCE in HCC, which could help predict patient response to immunotherapy.

Long noncoding RNAs (lncRNAs) are a common type of noncoding RNAs with more than 200 nucleotides in length and play essential roles in cancer development and progression (1, 16–18). For example, lncRNAs regulate cancer progression by changing the transcriptome and proteome of cancer cells and influencing the infiltration of immune cells to alter the immune microenvironment (19–21). LncRNAs could thus act as immune regulators in tumor immune evasion. Therefore, gaining more insights into T cell exclusion-related lncRNAs could potentially improve understanding the roles of TCE and lncRNAs in immunotherapy.

Currently, there are hardly any studies examining TCE-related lncRNAs in HCC, yet such lncRNAs could be potential therapeutic targets and prognostic markers. In this study, we identified differentially expressed and TCE-associated lncRNAs and used them to develop a prognosis signature to predict immune responses to HCC. The model consisted of 11 lncRNAs and was named 11LNCPS for 11-lncRNA prognosis signature. In addition to OS and TCE, higher 11LNCPS scores had a significant correlation with reduced infiltrations of CD8+ T cells and dendritic cells (DCs) and decreased infiltrations of Th1, Th2, and pro B cells. These infiltration alterations were significantly associated with worse OS in HCC. HCC patients with higher 11LNCPS scores were transcriptomically similar to those who responded better to PDL1 inhibitor. Two of the 11LNCPS lncRNAs, *LINC01134* and *AC116025.2*, were more crucial because their upregulations affected more immune cell types' infiltrations and were significantly associated with worse OS, TCE, and compromised immune function in HCC. LncRNAs in the 11LNCPS impacted many cancer-associated biological processes and signaling pathways, particularly those involved in immune function and metabolism.

MATERIALS AND METHODS

Data Sources and Processing

Gene expression data and clinicopathological characteristics of HCCs used in this study were generated by the Cancer Genome Atlas (TCGA) and are available at https://www.cancer.gov/about-nci/organization/ccg/research/structural-genomics/tcga. Downloaded data included FPKM (fragments per kilobase of transcript per million) reads-based gene expression data and the raw read count values. The R package "TCGAbiolinks" was used for downloading (22). After screening for data quality, 374 HCC samples were retained in this study. Of the 374 cases, one lacked prognostic information, so 373 were used for model construction and survival analyses (**Figure 1**). In addition, the tumor immune dysfunction and exclusion (TIDE) algorithm, as described in a previous study (15), was used to determine both the T cell exclusion (TCE) level and the T cell dysfunction level using the FPKM expression matrix.

To explore what chemokines/cytokines and immune checkpoint ligands mediate the communications between HCC cells and CD8+ T cells, we analyzed a single-cell RNA-sequencing (scRNS-seq) data of HCC (GSE146115) available in the Gene Expression Omnibus (GEO) (23). After performing imputation on the dropouts by the "scImpute" algorithm (24), the R package "Seurat" (25) was used for dimensional reduction, clustering analysis, and cell type annotation. Finally, the CellChat Explorer (26) program was used to infer the biologically significant interactions between chemokines, cytokines, and immune checkpoint (ICP) ligands and their receptors in the interactions between HCC cells and CD8+ T cells.

Identification of HCC- and TCE-Associated lncRNAs

To identify lncRNAs that are differentially expressed between HCC and adjacent morphologically normal liver tissues, we used the R packages "edgeR" (27, 28) and "limma" (29) to analyze the 374 HCC tissues and 50 adjacent normal liver tissues. The thresholds of $P \leq 0.05$ and $|\log2FC|$ (FC: Fold change) > 0.5 were used. The GENCODE database (30) was used to identify lncRNAs.

After HCC tissues were divided into TCE-higher (n = 187) and TCE-lower (n = 187) groups by the median TCE level following the TIDE analysis, the edgeR-limma procedure was also used to identify differentially expressed lncRNAs between the two TCE groups.

LncRNAs differential expression between HCC and normal tissues and between TCE-higher and TCE-lower groups were identified as HCC- and TCE-associated lncRNAs.

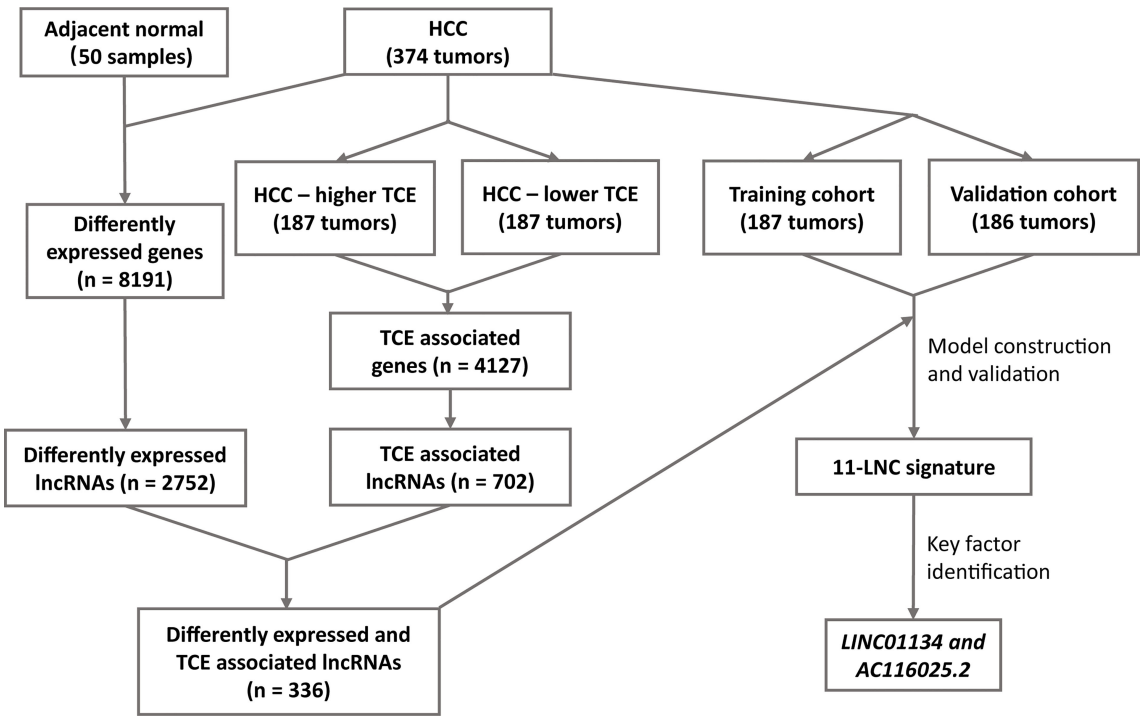

FIGURE 1 | The workflow of the study. Expression data of hepatocellular carcinoma (HCC) and adjacent normal liver tissues were compared to identify differentially expressed lncRNAs in HCC. All HCC with expression data were divided into higher and lower T cell exclusion (TCE) levels using the TIDE analysis. Higher- and lower-TCE groups were compared to identify TCE-associated lncRNAs. Differentially expressed and TCE-associated lncRNAs were then merged to identify differently expressed and TCE-associated lncRNAs, which were then subjected to LASSO and multivariate Cox analyses to construct the 11LNCPS predictive of patient survival. *LINC01134* and *AC116025.2* were then identified as the critical members of the signature.

Construction and Validation of a TCE-Associated lncRNA Prognostic Model: 11LNCPS

The 373 HCCs with prognostic information were randomly assigned to the training cohort (n = 187) and validation cohort (n = 186) at a 1:1 ratio using the R package "caret". Univariate Cox regression analysis was performed to assess the association of each differentially expressed and TCE-associated lncRNA with the overall survival (OS) in the training cohort. LncRNAs significantly correlated with OS ($P \leq 0.001$) were subjected to the LASSO-COX regression analysis (31) to develop the prognostic model (i.e., 11LNCPS). Based on the model, a risk score (RS) for OS was built based on a linear combination of the regression coefficient derived from the multivariate Cox regression model and the expression level of the optimized lncRNAs.

The 11LNCPS score (risk score) was computed as follows: Risk score = $\sum_{i=1}^{N}(C_i \times Factor_i)$, where N represents the number of prognostic factors, $Factor_i$ represents the expression of lncRNAs, and C_i represents the regression coefficient of the multivariate Cox regression model (1, 32, 33).

HCCs in the training cohort were then divided into two groups using the median, one with higher 11LNCPS scores and the other with lower scores, for model evaluation. Kaplan-Meier analysis was used for overall survival, with the log-rank test to evaluate statistical significance.

The time-dependent receiver-operating characteristic (ROC) analysis was performed to evaluate the accuracy of the 11LNCPS classifier in survival prediction at 1, 2, and 3 years in the training cohort. The calibration curves, Harrell's concordance index (C-index) curves, and ROC Areas under the curves (AUCs) were calculated for model evaluation. Calibration curves were calculated by calibrating the function implemented in the "rms" package to assess the predictive ability. The 11LNCPS was also validated in the validation and entire cohorts. In addition, the 11LNCPS model was compared with two previously reported effective HCC prognostic models for ROC, C-index, and prediction error curves in the validation cohort using the packages of "MASS", "timeROC", "survival", and "survminer". One was the 8-gene model containing *H2AFX*, *SQSTM1*, *ITM2A*, *PFKP*, *TPD52L1*, *ACSL4*, *STRN3*, and *CPEB3* (34); and the other was the 4-gene model containing *CENPA*, *SPP1*, *MAGEB6*, and *HOXD9* (35).

Analysis of the Association of 11LNCPS Scores With Immune Responses in HCC

Considering that TCE is primarily related to the immune escape (15), we applied the xCell computational method (36–38) to estimate the enrichment scores (xCell scores) of different immune cell types in HCCs with higher and lower 11LNCPS scores.

A total of 374 HCC samples with normalized gene expression FPKM data and standard annotation were used to analyze the distribution of 34 types of immune cells using the xCell pipeline. The 34 types of immune cells included CD4+ naive T-cells, CD4+ T-cells, CD4+ memory T-cells, CD4+ Tcm (central memory T cell), CD4+ Tem (effective memory T cell), CD8+ naive T-cells, CD8+ T-cells, CD8+ Tcm, CD8+ Tcm, Treg cells, gamma delta T cells (Tgd cells), Th1 cells, Th2 cells, natural killer T cell (NKT), natural killer cell (NK), pro B-cells (B cell progenitors), naive B-cells, B-cells, memory B-cells, class-switched memory B-cells, plasma cells, monocytes, macrophages, macrophages M1, macrophages M2, dendritic cell (DC), activated dendritic cell (aDC), conventional dendritic cell (cDC), plasmacytoid dendritic cell (pDC), immature dendritic cell (iDC), neutrophils, eosinophils, mast cells, and basophils.

The Kaplan-Meier (K-M) analysis was performed to assess whether the infiltrating status of different immune cell types affects patient survival in HCC. Survival outcomes were calculated and visualized using the R packages "survival" and "survminer". The correlation between an xCell score and an immune cell type was analyzed with $P \leq 0.05$ and $|\log2\ (FC)| > 0.25$ following the procedure described previously (36), and the outcome was visualized using the R packages "pheatmap", "EnhancedVolcano" and "ggpubr".

TIDE algorithm was then applied to evaluate the association of 11LNCPS scores with TCE and T cell dysfunction. HCCs were divided into higher and lower 11LNCPS scores using the median, and the TIDE algorithm (15) was then applied to each group. The outcome was visualized using "ggpubr".

To determine whether the 11LNCPS score is associated with therapeutic responses to ICIs, the 373 HCCs were divided into two groups, one with higher and one with lower 11LNCPS scores, using the median. The Subclass Mapping (SubMap) algorithm (39) was then applied to measure the correspondence between the two 11LNCPS groups and groups of malignancies with and without responses to anti-CTAL-4, anti-PD-1, and anti-PD-L1 therapies from previous studies (40, 41). The outcome was visualized using the R packages of "pheatmap" and "ggpubr".

Gene Ontology (GO) Enrichment, Kyoto Encyclopedia of Genes and Genomes (KEGG) Pathway Analysis, and Gene Set Enrichment Analysis (GSEA)

To determine the critical biological pathways and characteristics of HCC determined by 11LNCPS score, the GO, KEGG pathway analysis, and GSEA (42, 43) were applied to HCCs with higher and lower 11LNCPS scores using the R packages "GSEABase", "clusterProfiler" (44), "enrichplot", and "org.Hs.eg.db". Briefly, the edgeR-limma procedure was used to find differentially expressed genes (DEGs) between HCCs with higher-RS and those with lower RS in TCGA. DEGs with thresholds of $P \leq 0.05$ and $|\log2FC|$ (FC: Fold change) > 0.5, were subjected to GO and KEGG analysis. Go analysis included BP (biological process), CC (cellular component), and MF (molecular function). For GSEA, all DEGs were subjected to the "GSVA" package (45) after ranking from high to low based on their FC values. A P value smaller than 0.05 was considered significant in the GSEA. The hallmark gene set "h.all.v7.1.symbols.gmt" was downloaded from https://www.gsea-msigdb.org/and subjected to "GSVA" in a similar fashion.

Identification of Critical Members of the 11LNCPS lncRNAs

For each of the 11 lncRNAs in the 11LNCPS, a series of analyses were performed to identify the core one. The Kaplan-Meier survival analysis was performed to assess whether a lncRNA's expression level is associated with the overall survival (OS) in the 373 HCC patients.

Correlation of each lncRNA's expression level with T cell exclusion (TCE) was ranked based on the Spearman correlation coefficient value, with those greater than 0.2 with $P \leq 0.05$ considered significant. Infiltration levels of prognosis-associated immune cells were also compared between HCCs with higher and lower 11LNCPS scores and HCCs with higher and lower expression levels of the 11LNCPS lncRNAs. Those with a lower level. LncRNAs whose higher expression levels significantly correlated with worse patient OS, whose Spearman correlation coefficient values were greater than 0.2 ($P \leq 0.05$), and that affected infiltrations of more immune cell types were considered crucial members of the 11LNCPS, including *LINC01134* and *AC116025.2*. The outcome was visualized by the R packages "pheatmap", "ggpubr", "corrplot" and "ggplot2".

Test of Whether *LINC01134* and *AC116025.2* Affect TCE and T Cell Dysfunction

The relationship between *LINC01134* and *AC116025.2* expression and TCE or T cell dysfunction was tested using the TIDE algorithm, and the outcome was visualized using the "ggpubr" R package.

Enrichment Analysis for Biological Functions Affected by the Critical 11LNCPS lncRNAs

To explore the biological functions of *LINC01134* and *AC116025.2* in HCC, we performed GO, KEGG, and GSEA analysis in HCCs as described in the previous enrichment analysis.

Cell Lines and Cell Culture

Normal liver cells QSG-7701 and LO2 were kindly provided by Dr. Liang Yang of the Southern University of Science and Technology. HCC cell lines HepG2 and Huh-7 were purchased from the BeNa Culture Collection (Beijing, China). The Jurkat cell line was kindly provided by Dr. Lili Ren of Shenzhen People's Hospital. The DMEM medium (Gibco, USA) supplemented with antibiotics (Biological Industries, Israel) and 10% FBS (Gibco) was used for liver cell culture. The RPMI 1640 medium (Gibco) supplemented with antibiotics and 10% FBS were used for Jurkat cells. All cells were cultured at 37 °C in a humidified atmosphere containing 5% CO_2.

Cell Transfection and Conditioned Medium (CM) Preparation

Both the negative control siRNAs (si-NC) and the *LINC01134* siRNAs were provided by GenePharma (Shanghai, China). Sequences of siRNAs against *LINC01134* were 5′-GACAGGTTTGAGCTAGAAAC-3′ (si-*LINC01134*-1) and 5′-GCAAAUGCACAGCGAGGAAAG-3′ (si-*LINC01134*-5). At confluency of 30–50%, HepG2 or Huh-7 cells were transfected with siRNAs using the Lipofectamine RNAiMAX reagent (Invitrogen, USA). After 48 hours, transfected cells were split into two portions. One was used for RNA isolation and gene expression analysis, and the other was grown in a 6-well plate for 48 hours to collect the conditioned medium (CM). Each experiment was repeated twice unless otherwise stated.

Quantitative Real-Time Polymerase Chain Reaction (qRT-PCR)

Total RNA was extracted from cultured cells using the Eastep Super Total RNA Extraction Kit (Promega, USA) and reverse transcribed into cDNA using the HiScript III All-in-one RT SuperMix Perfect for qPCR Kit (Vazyme, China). PCR was performed with the KT SYBR qPCR Mix (Ktsm-life, China) using the qTOWER 3.0 PCR system (Jena Industries, Germany). Primers and their sequences are as follow: *LINC01134*, 5′-ATGAACAGCAAATGCACAGCG-3′ (forward) and 5′- ATAGGTCTTGGCTGGTTCTCG-3′ (reverse); *AC116025.2*, 5′-TGGAGCAGAAAGAGCTGTCTCAAG-3′ (forward) and 5′-TGTCAGGAAACTGTGTGGACG-3′ (reverse); *CXCL1*, 5′-CTGGCTTAGAACAAAGGGGCT-3′ (forward) and 5′-TAAAGGTAGCCCTTGTTTCCCC-3′ (reverse); *CXCL2*, 5′-CCCATGGTTAAGAAAATCATCG-3′ (forward) and 5′-CTTCAGGAACAGCCACCAAT-3′ (reverse); *CXCL3*, 5′-CGCCCAAACCGAAGTCATAG-3′ (forward) and 5′-ACCTTGCCTTCTTTGTCTTTGTTGGA-3′ (reverse); and β-actin, 5′-TCCCTGGAGAAGAGCTACGA-3′ (forward) and 5′-GCTCCCCTTGTTCAGTATCTTTT-3′ (reverse). In the PCR, β-actin served as the endogenous control. The relative expression of genes was calculated using the $-2\Delta\Delta$Ct method.

T Cell Migration Analysis

T cell migration was analyzed using the transwell assay as previously described (46–48). Briefly, Jurkat cells (10^6 cells/ml) were washed with PBS and serum-starved for 3 hours, 10^5 cells in 0.1 ml were then seeded onto an 8.0-μm pore size insert (Corning, USA), and 400 μl complete medium or CM were then added to the lower chambers of a 24-well plate (Corning). After incubation at 37°C for 16 hours in an incubator, migrated cells in the lower chambers were collected and counted using an automated cell counter (Invitrogen). The numbers of migrated cells in different groups were normalized by the number of cells from the complete medium group.

Statistical Analysis

The R software (version 4.1.1) was used for all statistical analyses and plot drawings except as specifically stated. Patients were randomly grouped using the "caret" R package. The univariate and multivariate Cox proportional hazards regression analyses were performed using the "survival" package. Kaplan-Meier analysis was used for overall survival, with the log-rank test to evaluate statistical significance. Statistical differences between the two groups were assessed using the Wilcoxon test. The grouping basis (the cutoff point) was the median value of each corresponding index.One-way ANOVA with Bonferroni's multiple-comparisons test was performed for qPCR and T cell migration analysis using the GraphPad Prism (GraphPad Prism 8). $P < 0.05$ was considered statistically significant unless otherwise stated.

RESULTS

Identification of Differentially Expressed and TCE-Associated lncRNAs in HCC

The workflow of the entire study is summarized in **Figure 1**. In total, the TCGA database contained 374 HCC cases with gene expression data. All the 374 cases were used for the identification of differentially expressed and TCE-associated lncRNAs. One of the 374 cases lacked prognostic information and thus was excluded for model construction and survival analysis. Using the 374 HCCs and 50 cases of noncancerous liver tissues with expression profiling and other information, two groups of differentially expressed genes (DEGs) were identified from a total of 56493 human genes, including lncRNA, other noncoding RNA, and protein coding genes. One group contained 8191 genes that were differentially expressed between HCCs and normal liver tissues, with 6438 upregulated and 1753 downregulated in HCC (**Figure 1** and **Figure S1A**). Among these 8191 DEGs, 2752 were lncRNAs (**Figure 1**). The other group contained 4127 TCE-associated genes that were differentially expressed between HCCs with higher TCE scores and those with lower TCE scores, including 2914 upregulated and 1213 downregulated in the TCE-higher group (**Figure 1** and **Figure S1B**). Of the 4127 TCE-associated genes, 702 were lncRNAs (**Figure 1**). In total, 336 lncRNAs were both differentially expressed and TCE-associated in HCC (**Figure 2A** and **Table S1**).

Construction of the TCE-Associated 11 lncRNA Prognostic Signature (11LNCPS) in HCC

Of the 374 HCC cases, one lacked prognostic information and thus was excluded for model construction and survival analysis. The 373 HCCs with survival data were divided into the training (n = 187) and validation (n = 186) cohorts. Each differentially expressed TCE-associated lncRNA in the training cohort was subjected to the univariate Cox regression analysis to evaluate its association with patients' overall survival (OS). Fifty-four lncRNAs were significantly associated with prognosis ($P < 0.001$) (**Table S1**). The LASSO-Cox regression analysis was then performed, in which tenfold cross-validation was applied to overcome overfitting with an optimal λ value of 0.028393 selected (**Figure 2B**). A combination of 11 lncRNAs had non-zero LASSO coefficients and thus was the most robust prognostic value (**Figure 2C**). This combination of 11 lncRNAs was named 11 lncRNA prognostic signature (11LNCPS). The 11 lncRNAs included *LINC01134*, *C2orf27A*,

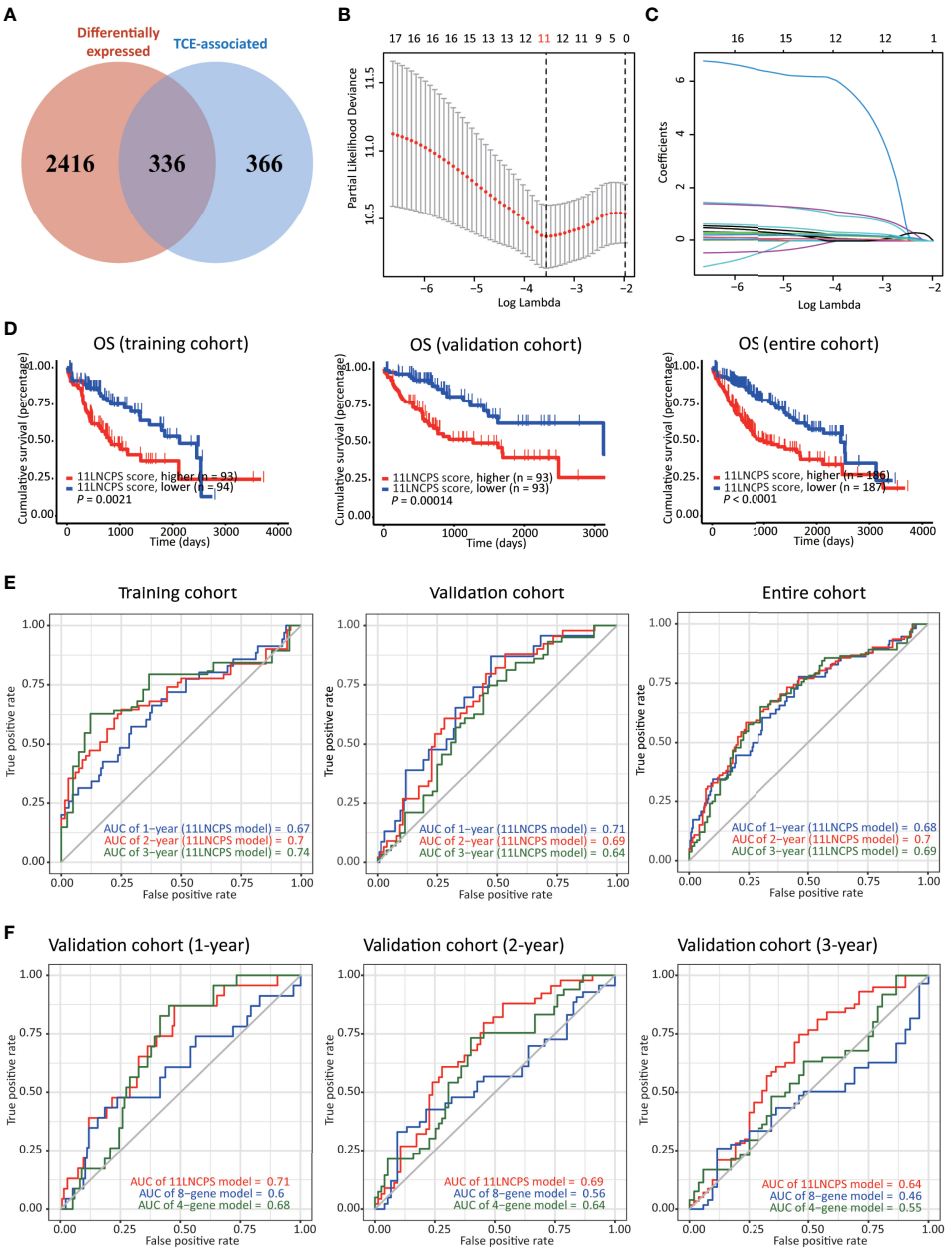

FIGURE 2 | Construction, validation, and evaluation of an 11-lncRNA signature predictive of prognosis (11LNCPS) in HCC patients. **(A)** Venn diagram showing the overlapping lncRNAs (n = 336) between lncRNAs differentially expressed in HCC (n = 2752, red) and those associated with T cell exclusion (TCE, n = 702, blue). **(B)** Partial likelihood deviance of varying numbers of prognostic lncRNAs revealed by the LASSO regression model. The grey lines represent the partial likelihood deviance ± standard error (SE). The two vertical lines represent optimal values based on the minimum criteria and 1-SE criteria. The proper log (Lambda) value was chosen *via* the minimum criteria. **(C)** Identification of 11 lncRNAs by the LASSO logistic regression model with non-zero coefficients. **(D)** The Kaplan–Meier analysis of overall survival (OS) in the training cohort (left), validation cohort (center), and entire cohort (right) cohort of TCGA HCC patients with higher and lower 11LNCPS scores based on the median. The cutoff value of group dividing was the median RS score. **(E)** Receiver operating characteristic (ROC) curves of the 11LNCPS model for evaluating the predictability of OS in 1, 2, and 3 years in the training cohort (left), validation cohort (center), and entire cohort (right) cohort. **(F)** Comparison of ROC curves between the 11LNCPS model (red) and the previously established 8-gene model (blue) and 4-gene model (green) for 1, 2, and 3 years OS in the validation cohort.

LINC00501, *AC104066.3*, *AC034229.4*, *CASC8*, *FAM225B*, *AL451069.3*, *AL161669.3*, *AC116025.2* and *LINC00632*.

To determine the 11LNCPS score, the Cox multivariate regression analysis was used to evaluate each of the 11 lncRNA's contribution to the 11LNCPS (**Table 1**), which resulted in the following formular for calculating the risk score (i.e., 11LNCPS score) in an HCC: 11LNCPS score = 0.214579 × expression of *LINC01134* + 0.019508 × expression of *C2orf27A* + 1.045738 ×

TABLE 1 | Univariate and multivariate Cox regression analysis for overall survival in the training cohort of HCCs from TCGA (n = 187).

Variables	Univariate analysis				Multivariate analysis			
	HR	*P* value	HR.95L	HR.95H	HR	*P* value	HR.95L	HR.95H
LINC01134	2.957099	**0.001928**	1.490262	5.867717	1.23934	0.667749	1.49026198	5.8677175
C2orf27A	1.713252	**0.000121**	1.301973	2.254449	1.0197	0.932463	1.30197261	2.25444941
LINC00501	5.639399	**3.96E-05**	2.47158	12.8674	2.845499	0.124401	2.47158045	12.8674025
AC104066.3	7.467815	**0.003104**	1.969993	28.30886	3.471175	0.139087	1.96999337	28.3088586
AC034229.4	1.903967	**0.003121**	1.242232	2.918208	1.151052	0.67269	1.24223153	2.91820769
CASC8	1.554184	**0.00019**	1.232892	1.959205	1.353236	**0.043159**	1.23289183	1.95920478
FAM225B	7935.61	**0.008989**	9.418916	6685897	1382.301	0.108321	9.41891643	6685896.61
AL451069.3	1.115362	**0.009697**	1.026798	1.211566	1.093651	0.101831	1.02679797	1.21156582
AL161669.3	1.250841	**0.000155**	1.113895	1.404623	1.254475	**0.001296**	1.1138952	1.40462346
AC116025.2	2.414076	**0.000745**	1.446456	4.028994	1.251545	0.526933	1.44645621	4.02899437
LINC00632	1.833973	**0.005234**	1.198149	2.807209	1.450143	0.153236	1.19814937	2.80720913

HR, hazard ratio; HR.95L, low 95% confidence interval of HR; HR.95H, high 95% confidence interval of HR. Significant P values (≤ 0.05) are in bold.

expression of *LINC00501* + 1.244493 × expression of *AC104066.3* + 0.140677 × expression of *AC034229.4* + 0.302498 × expression of *CASC8* + 7.231505 × expression of *FAM225B* + 0.089521 × expression of *AL451069.3* + 0.226717 × expression of *AL161669.3* + 0.224378 × expression of *AC116025.2* + 0.371662 × expression of *LINC00632*.

Construction of the TCE-Associated 11 lncRNA Prognostic Signature (11LNCPS) in HCC

To test the validity and effectiveness of the 11LNCPS in HCC, we calculated the 11LNCPS risk score for each case in the training, validation, and entire cohorts; divided HCCs in each cohort into the higher- and lower-risk groups using the median 11LNCPS score; and performed a series of analyses (**Figures 2D–F** and **Figures S2A–D**). The Kaplan-Meier analysis demonstrated that the OS rate was better in patients with lower 11LNCPS scores than those with higher scores in each cohort ($P \leq 0.05$, **Figure 2D**).

The area under ROC curve (AUC) for 1, 2, and 3 years reached 0.67, 0.7, and 0.74, respectively, in the training cohort; 0.71, 0.69, and 0.64, respectively, in the validation cohort; and 0.68, 0.7, and 0.69, respectively, in the entire cohort (**Figure 2E**). These AUC curves indicate a reasonable discrimination power of the 11LNCPS in HCC. Additionally, the 11LNCPS's C-index was greater than 0.60 for 1, 2, and 3 years in each cohort, showing an excellent predictive accuracy of the 11LNCPS (**Figure S2A**). Furthermore, the calibration curve demonstrated good consistency for 1, 2, and 3 years in each cohort (**Figure S2B**).

We also compared our 11LNCPS model with two reported models, i.e., the 8-gene model (34) and the 4-gene model (35) in the validation cohort. For each of the 3 time points (1, 2, and 3 years), 11LNCPS showed a higher AUC value (**Figure 2F**) and a higher C-index (**Figure S2C**). Each model's predicted error line overlapped well with the reference line (**Figure S2D**), demonstrating a lower predicted error rate for each of the 3 models.

The 11LNCPS Scores Nicely Correlate With Immune Responses to HCC

We applied the xCell algorithm to the RNA-seq datasets of the 374 HCCs to determine the infiltration levels of 34 types of immune cells (**Figure S3**). The correlation between an immune cell infiltration and patient OS was evaluated using the Kaplan-Meier analysis (**Figure 3A** and **Figure S4**). Altered infiltrations of 7 types of immune cells were significantly associated with OS (**Figure 3**). Increased infiltrations of CD8+ naive, CD8+ Tcm, CD8+ T, and pDC cells were associated with better OS, while increased infiltrations of Th1, Th2, and pro B cells were associated with a worse OS in HCC (**Figure 3A**).

To evaluate the relationship between the 11LNCPS and immune responses to HCC, we divided all HCCs into higher and lower 11LNCPS scores using the median and compared the distribution of different immune cell types between the two groups (**Figure 3B** and **Figure S5**). HCCs with higher 11LNCPS scores had decreased infiltrations of CD8+ Tcm, macrophages, macrophages M2, aDCs, and cDCs immune cells and increased infiltrations of Th1, Th2, pro B, B, and basophils cells (**Figure 3B**). In the Kaplan-Meier analysis, alterations in 4 of the 10 immune cell types were significantly associatged with OS (**Figure 3A**). The 4 alterations included decreased filtration of CD8+ Tcm cells and increased filtrations of Th1, Th2, and pro B cells (**Figures 3A, B**).

TIDE is a computer program that models the induction of T cell dysfunction in tumors with higher infiltration of cytotoxic T cells and the prevention of T cell infiltration in tumors with lower levels of such cells (15). To further explore the impact of 11LNCPS lncRNAs on immune responses in HCC, we compared HCCs with higher and lower 11LNCPS scores for TCE and T cell dysfunction levels which were analyzed using the TIDE program. HCCs with higher 11LNCPS scores had significantly higher TCE scores and lower T cell dysfunction levels than those with lower 11LNCPS scores ($P \leq 0.05$) (**Figures 3C, D**).

Using the SubMap analysis, we compared HCCs with higher and lower 11LNCPS scores to malignancies with and without responses to immunotherapies from previous studies (41, 49). HCCs with higher 11LNCPS scores were significantly associated with malignancies that respond to a PDL1 inhibitor (**Figure 3E**, $P < 0.05$).

Functional Impact of the 11LNCPS on HCC Cells

Differentially expressed genes were identified in HCCs with higher and lower 11LNCPS scores (**Figure S6**). Such genes

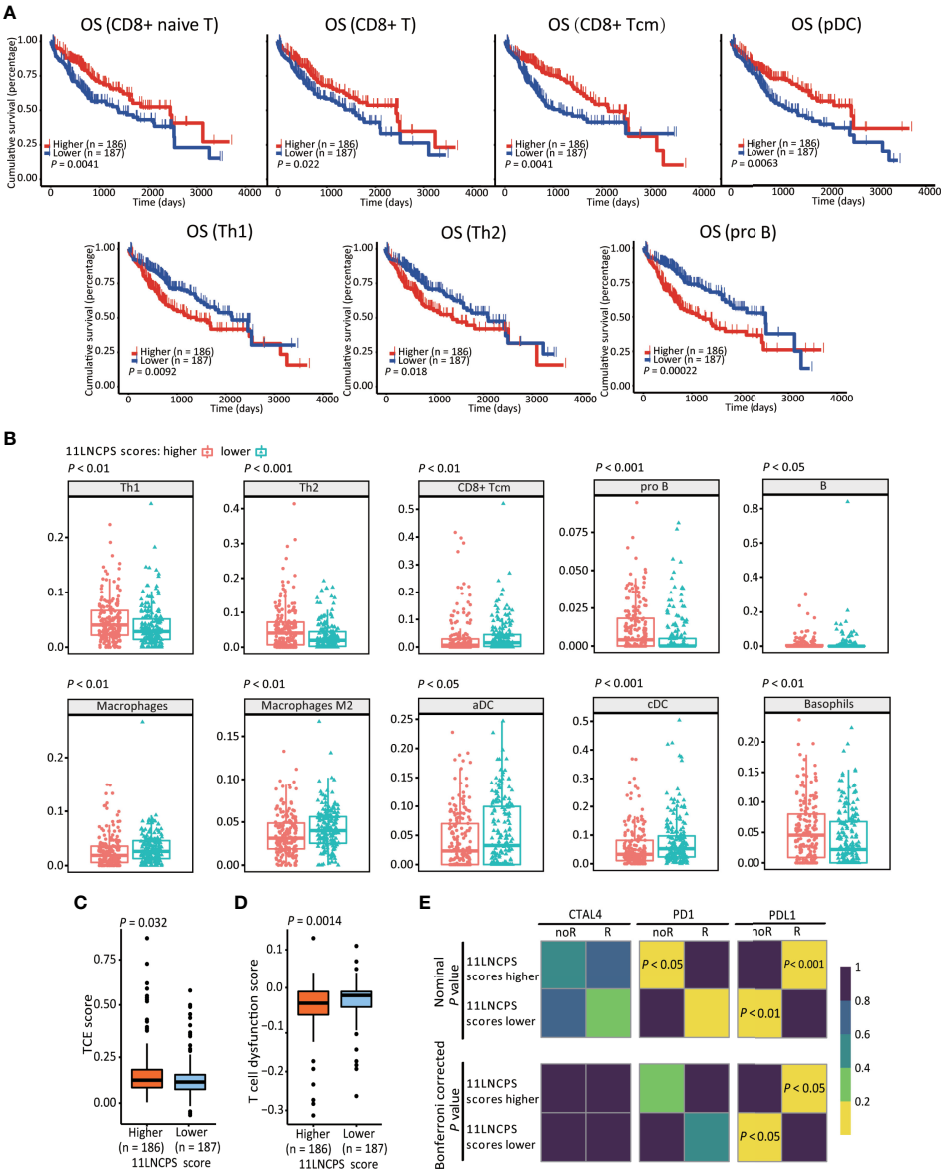

FIGURE 3 | The 11LNCPS scores predict immune responses in HCC. **(A)** Increased infiltrations of Th1, Th2, and pro B cells are associated with worse OS, while that of CD8+ Tcm, CD8+ T, and pDC cells with better OS in HCC, as determined by the Kaplan-Meier analysis. **(B)** The infiltration level is different ($P < 0.05$) between HCCs with higher 11LNCPS scores (red) and lower scores (blue) for 10 types of immune cells. **(C, D)** HCCs with higher 11LNCPS scores have higher TCE scores **(C)** and lower T cell dysfunction scores **(D)**. **(E)** Higher 11LNCPS scores are associated with better therapeutic responses to immune checkpoint inhibitors (ICIs) in HCC patients. Nominal and Bonferroni corrected *P* values are shown for the correlation between 11LNCPS scores and ICI responses (CTAL4, PD1, and PD-L1). noR, non-responder; R, responder. Grid colors indicate the correlation *P* values.

were analyzed to evaluate the effect of 11LNCPS lncRNAs on different biological processes and signaling pathways using the GO, KEGG pathway, and GSEA analyses (**Figure 4**).

Many biological processes identified in the GO analysis are involved in the cell cycle and DNA replication. These processes included organelle fission, nuclear division, DNA-dependent DNA replication, cell cycle checkpoint, chromosomal region, DNA replication preinitiation complex, single-stranded DNA helicase activity, ATPase activity, and DNA replication origin binding.

In the KEGG pathway analysis, the top-ranked pathways were involved in cell cycle and ligand-receptor interactions, including cytokine and cytokine receptor-related signaling and the viral proteins' interactions with cytokines and cytokine receptors (**Figure 4B**). They also included metabolism-associated pathways such as retinol, drug, and xenobiotics (**Figure 4B**).

The GSEA analysis resulted in similar findings (**Figure 4C**). Specifically, signaling pathways related to cell cycle and DNA replication were significantly enriched in HCCs with higher

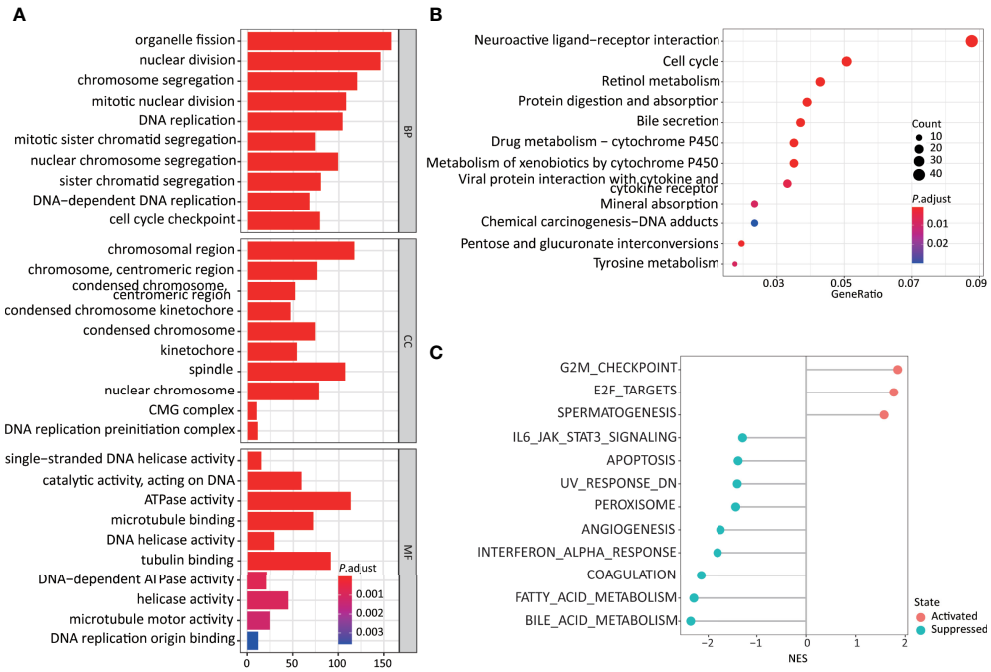

FIGURE 4 | Higher 11LNCPS scores are associated with several cancer hallmarks and immunological characteristics of HCC. **(A, B)** GO enrichment **(A)** and KEGG pathway **(B)** analysis of differentially expressed genes (DEGs) between HCCs with higher and lower 11LNCPS scores. The heights of bars and sizes of dots represent the count of genes, while the colors represent the adjusted *P*-value. **(C)** Significantly enriched cancer hallmarks in HCCs with higher 11LNCPS scores, as analyzed by the GSEA. Red and blue dots indicate a pathway's activation and suppression, respectively. The x-axis shows normalized enrichment scores (NES). All pathways with *P* values smaller than 0.05 are shown.

11LNCPS scores, including G2M checkpoint, E2F targets, cell cycle, and UV response containing DNA replication genes. Signaling pathways related to metabolism, immune function, and cell death were significantly suppressed in HCCs with higher 11LNCPS scores, including fatty acid metabolism, bile acid metabolism, IL6-JAK-STAT3 signaling, IFNα response, and apoptosis.

Therefore, the 11LNCPS appears to affect cell cycle signaling pathways, DNA replication, immune function, and cell death.

LINC01134 and *AC116025.2* Are Most Crucial Than Other lncRNAs in the 11LNCPS

To rank the 11LNCPS's 11 lncRNAs for their contributions to the signature, we analyzed them for the association of expression change with OS and immune responses in HCC. In the Kaplan-Meier analysis, the increased expression in 5 of the 11 lncRNAs was significantly associated with worse OS, including *LINC01134*, *AC104066.3*, *AC034229.4*, *AC116025.2*, and *LINC00632* (**Figure 5A** and **Figure S7**).

Based on the TCE scores revealed by the Spearman analysis, increased expression in 8 of the 11 lncRNAs was significantly associated with TCE ($P < 0.05$). These 8 lncRNAs and their Spearman coefficient values were *C2orf27A*, 0.41; *LINC01134*, 0.33; *AC104066.3*, 0.33; *LINC00632*, 0.31; *AC034229.4*, 0.29; *AC116025.2*, 0.26; *FAM225B*, 0.24; and *LINC00501*, 0.13, respectively (**Figure 5B**).

We further evaluate their effects on immune cell infiltration for the 5 lncRNAs whose expression increase was significantly associated with a worse OS.

While expression change in *LINC01134* or *AC116025.2* significantly affected the infiltrations of 5 immune cell types, expression change in other 11LNCPS lncRNAs altered 3 or 4 types (**Figure 5C** and **Figure S8**). Specifically, *LINC01134* and *AC116025.2* upregulation was significantly associated with increased infiltrations of Th1, Th2, and pro B immune cells but decreased infiltrations of CD8+ naive T and CD8+ Tcm cells (**Figure 5C** and **Figures S8A, D**). For the other 3 11LNCPS lncRNAs associated with OS, *AC034229.4* upregulation was associated with increased infiltrations of Th1, Th2, and pro B cells (**Figure S8C**); and higher levels of *AC104066.3* and *LINC00632* were associated with increased infiltrations of Th2 and pro B cells and decreasing infiltration of CD8+ naive T cells (**Figures S8B, E**).

Additionally, HCCs with higher *LINC01134* or *AC116025.2* expression had higher TCE scores and reduced T cell dysfunction levels (**Figures 5D, E**).

Upregulation of *LINC01134* and *AC116025.2* Could Impact Immune Responses and Other Biological Processes in HCC

Similar to the analyses of 11LNCPS for its potential impact on biological processes and signaling pathways, we divided HCCs with higher and lower expression levels of *LINC01134* or *AC116025.2*, identified differentially expressed genes, and performed GO, KEGG pathway, and GSEA analyses (**Figure S9**).

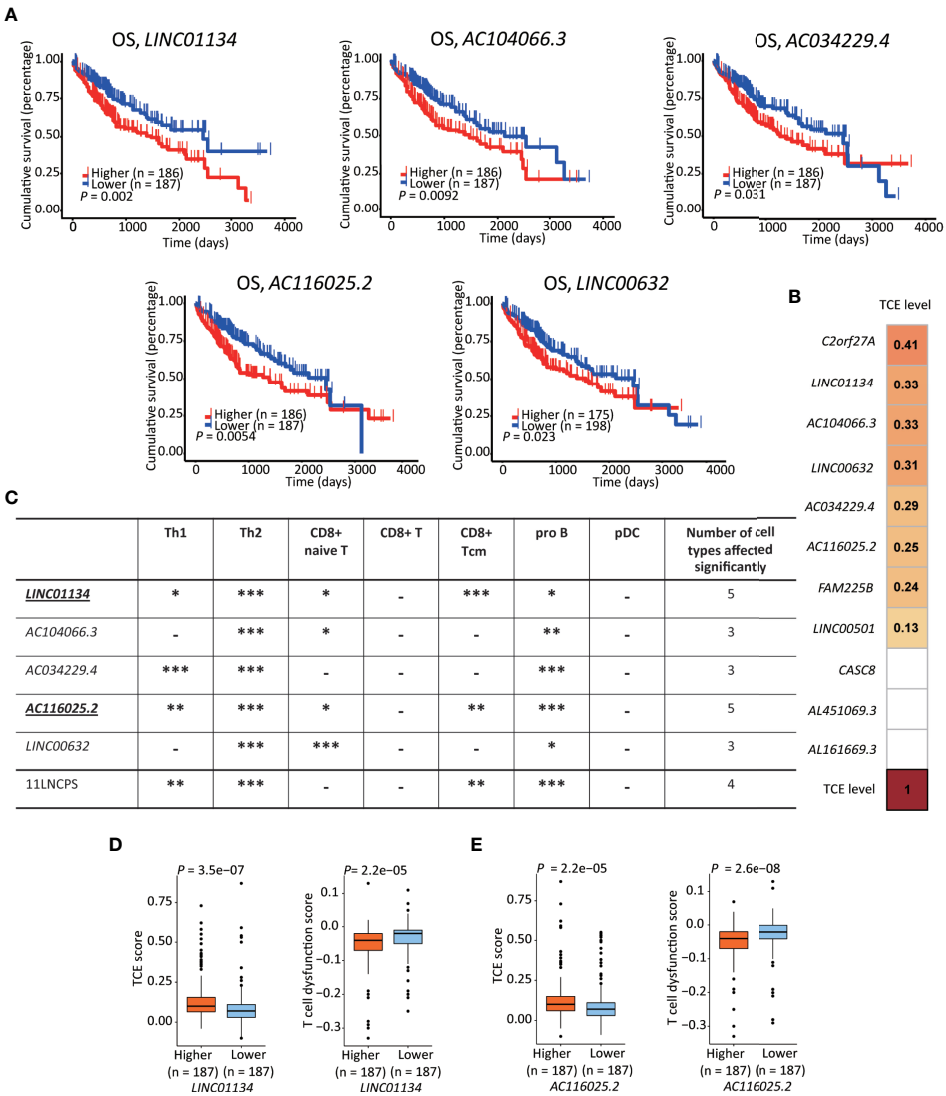

FIGURE 5 | *LINC01134* and *AC116025.2* are the most crucial lncRNAs of the 11LNSPS. **(A)** An association of higher expression level with worse OS in HCC patients was detected for 5 of the 11LNCPS lncRNAs, including *LINC01134*, *AC104066.3*, *AC034229.4*, *AC116025.2*, and *LINC00632*, as determined by the Kaplan-Meier survival analysis. **(B)** Coefficient values for each lncRNA in the 11LNCPS, as indicated in colored grids and determined by the Spearman analysis. Colored grids indicate those whole expression alterations were statistically significant. **(C)** Statistical evaluation of the correlation between the infiltration (indicated by an xCell score) of a prognosis-associated immune cell type and expression levels of prognosis-associated lncRNAs in HCC. HCCs were divided into higher and lower groups using its median expression level for each lncRNA, and xCell scores for each immune cell type were compared between the two groups by the Wilcoxon test. The 11LNCPS was used as a control. -$P > 0.05$; *$P \leq 0.05$; **$P \leq 0.01$; ***$P \leq 0.001$. **(D, E)** Higher *LINC01134* **(D)** and *AC116025.2* **(E)** levels are associated with higher TCE scores and reduced T cell dysfunction levels in HCC, as analyzed by the TIDE algorithm.

The most enriched processes for *LINC01134* in the GO enrichment analysis included cell chemotaxis and chemokine response related biological processes, chromosome related molecular function, receptor-ligand activity, and chemokine binding cellular component (**Figure 6A**, left).

In the KEGG pathway analysis, *LINC01134* upregulation was significantly associated with diverse immune-related signaling pathways, including chemokines/cytokines and their receptors and T and B cell receptors. Some cancer-associated pathways were identified, including PI3K-Akt, Rap1, cell cycle, glioma, and p53 (**Figure 6B**, left).

In the GSEA analysis, *LINC01134* upregulation was associated with the active cell cycle (e.g., E2F targets and G2M checkpoint). It was also associated with cancer pathways (e.g., MYC targets) (**Figure 6C**, left). On the other hand, *LINC01134* upregulation was inversely related to pathways of immune (IFNγ response, IFNα response, IL6-JAK-STAT3, IL2-STAT5), metabolism (bile acid metabolism, fatty acid metabolism),

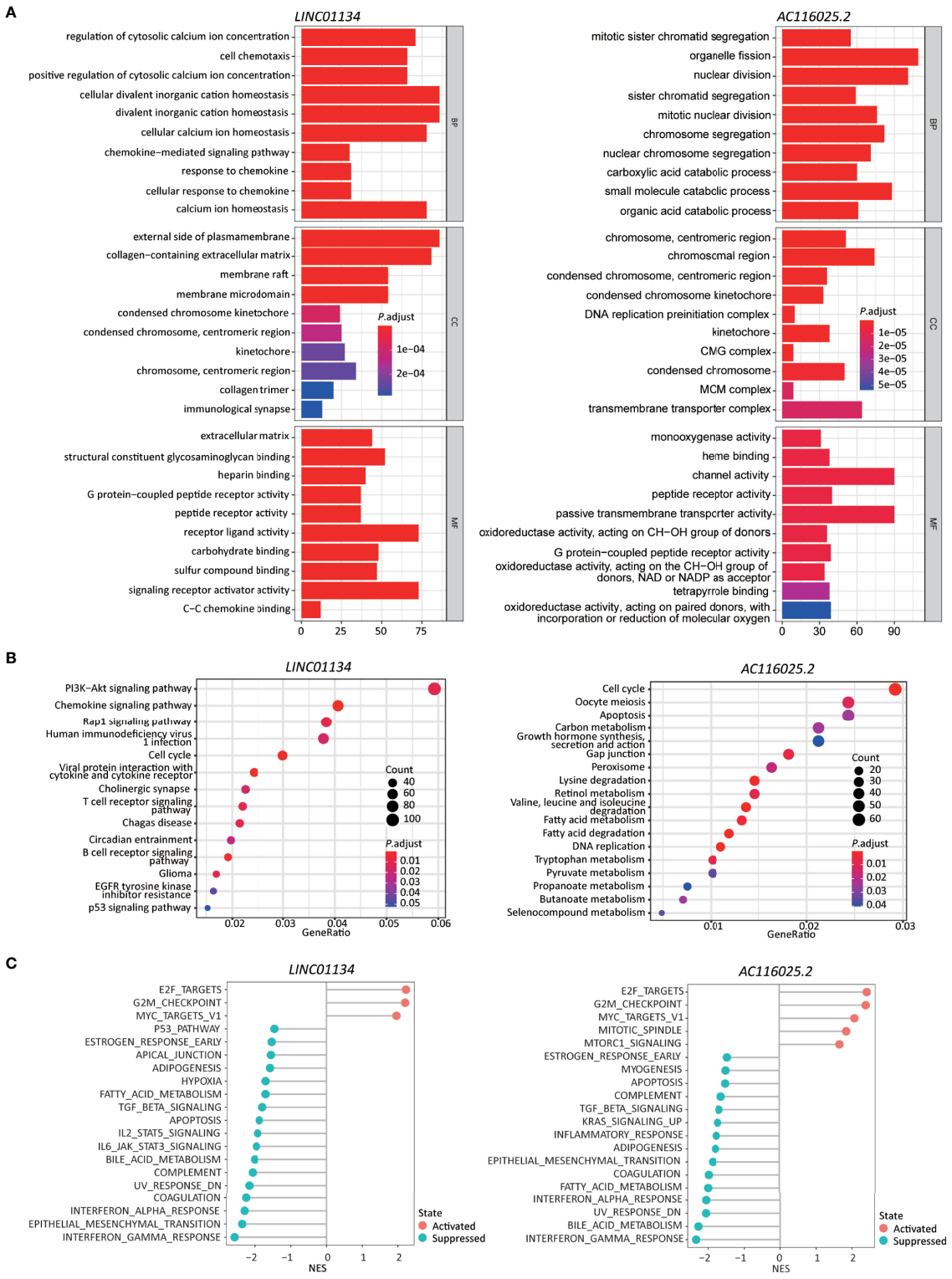

FIGURE 6 | Higher expression levels of *LINC01134* and *AC116025.2* are associated with several cancer hallmarks and immunological characteristics of HCC. **(A, B)** GO enrichment **(A)** and KEGG pathway **(B)** analyses between HCCs with higher- and lower-levels of *LINC01134* (left in each panel) and *AC116025.2* (right in each panel). The heights of bars and sizes of dots represent the count of genes, while the colors represent the adjusted *P*-value. **(C)** Significantly enriched cancer hallmarks in HCCs with higher expression levels of *LINC01134* (left) and *AC116025.2* (right), as analyzed by the GSEA. The red and blue colors of dots indicate a pathway's activation and suppression, respectively. The x-axis shows normalized enrichment scores (NES). All pathways with *P* values smaller than 0.05 are shown.

apoptosis, epithelial-mesenchymal transition, UV response, TGFβ, hypoxia, and p53 (**Figure 6C**, left).

These results support the role of *LINC01134* in the cell cycle, cell death, immunity, chemokine expression, and chemotaxis in HCC.

In the GO analysis, *AC116025.2*-associated genes were primarily enriched in cell division, catabolic metabolism, chromosome and transporter complex, receptor and channel activities, and oxidoreductase activity (**Figure 6A**, right).

In the KEGG analysis, *AC116025.2*-associated genes were enriched for pathways in the cell cycle, DNA replication, metabolism, and apoptosis (**Figure 6B**, right). Multiple metabolic pathways were enriched, including carbon metabolism, retinol metabolism, fatty acid metabolism, tryptophan metabolism, and propanoate metabolism (**Figure 6B**, right).

In the GSEA, *AC116025.2* upregulation was associated with cell cycle activities and cancer-related pathways such as E2F targets, G2M checkpoint, MYC targets, MTORC1 signaling, and mitotic spindle (**Figure 6C**, right). On the other hand, *AC116025.2* upregulation was associated with reduced activities of signaling pathways related to immune, metabolism, and cell death, including IFNγ response, IFNα response, inflammatory response, bile acid metabolism, fatty acid metabolism, apoptosis, UV response, epithelial-mesenchymal transition, KRAS signaling, TGFβ signaling, and estrogen response (**Figure 6C**, right).

LINC01134 and *AC116025.2* Upregulation Correlates With the Expression of Some Chemokines, Cytokines, and ICP Ligands

Immune responses often involve cytokines, chemokines, and their receptors. Therefore, we investigated whether expression changes in *LINC01134* and *AC116025.2* are associated with chemokines, cytokines, and ICP ligands in HCC. In the scRNA-seq data, CD8+ cells could be annotated (**Figure S10A**). We thus identified the chemokines, cytokines, and ICP ligands synthesized by HCC cells and could mediate CD8+ T cells' recruitment using the CellChat algorithm (26).

In total, 22 cytokines and chemokines were identified, including *CXCL12*, *CCL5*, *CXCL16*, *CCL16*, *CXCL10*, *CCL20*, *IL7*, *CCL15*, *CXCL2*, *IL15*, *CCL3*, *CCL4*, *CXCL8*, *CXCL9*, *CXCL11*, *CXCL1*, *CCL28*, *CCL2*, *CXCL13*, *CXCL3*, *CXCL6*, and *CCL22* (**Figure 7A**, left). We also identified 26 ICP ligands that could bind to their ICPs, including *HLA-A*, *HLA-B*, *HLA-C*, *HLA-E*, *CD70*, *PVR*, *HLA-F*, *LGALS9*, *CEACAM1*, *HLA-DRA*, *ICOSLG*, *HLA-DMA*, *HLA-DPB1*, *HLA-DOA*, *HLA-DRB1*, *CD86*, *TNFSF15*, *HLA-DQB1*, *HLA-DPA1*, *HLA-DMB*, *TNFSF4*, *HLA-DQA1*, *CD48*, *HLA-DOB*, *RAET1E*, and *RAET1G* (**Figure 7A**, right). Using the Spearman correlation analysis, we found that *LINC01134* upregulation in HCC was negatively correlated with the following genes ($R_S > 0$, $P \leq 0.05$): *CXCL1*, *CXCL2*, *CXCL3*, *HLA-C*, and *HLA-E* and was positively correlated with *LGALS9* ($R_S < 0$, $P \leq 0.05$) (**Figure 7B**). For *AC116025.2*, its upregulation was positively associated with *CXCL1*, *CXCL8*, *CXCL20*, and *TNFSF4* ($R_S > 0$, $P \leq 0.05$) (**Figure 7C**).

Upregulation of *LINC01134* and *AC116025.2* in HCC Cell Lines and the Impact of *LINC01134* on *CXCL2* and *CXCL3* Expression and T Cell Migration

To test the impact of *LINC01134* and *AC116025.2* on HCC, we measured their expression in two HCC cell lines using qRT-PCR and found that both *LINC01134* and *AC116025.2* were significantly upregulated in HepG2 and Huh-7 HCC cell lines compared to normal liver cell lines QSG-7701 and LO2 (**Figure 8A**). We also knocked down *LINC01134* expression in the two HCC cell lines and measured the expression of three cytokines whose expression correlated with *LINC01134* in HCC samples. *LINC01134* knockdown significantly increased the expression of *CXCL2* and *CXCL3* (**Figure 8B**). Consistent with the upregulation of *CXCL2* and *CXCL3* by *LINC01134* knockdown, conditioned medium from HCC cells with *LINC01134* knockdown significantly increased the migration of Jurkat T cells (**Figure 8C**). These findings support the role of *LINC01134* in HCC.

DISCUSSION

It is increasingly apparent that lncRNAs play crucial roles in the development and progression of cancers, including HCC, and TCE is a common mechanism for cancer cells to evade immune surveillance. In this study, we applied the recently developed TIDE program to available sequencing datasets of HCC to identify TCE-associated lncRNAs in HCC. Combing such lncRNAs with those differentially expressed in HCCs and subjecting them to additional statistical analyses, we developed an expression-based gene signature that predicts patient prognosis in HCC (**Figures 1**, **2**; **Table 1**). This signature consisted of 11 lncRNAs and was thus named 11 lncRNA prognostic signature (11LNCPS).

The 11LNCPS model appears to be robust. For example, the 11LNCPS score predicted patient OS in the training cohort of HCC and the validation and entire cohorts (**Figure 2D**). In addition, the discrimination power of the 11LNCPS was evident as the values of the area under ROC curves (AUC) for 1, 2, and 3 years were quite good in the training, validation, and entire cohorts of HCC (**Figure 2E**). Furthermore, the model's C-index, which reflects predictive accuracy, was excellent, as indicated by values greater than 0.60 for 1, 2, and 3 years in each cohort (**Figure S1C**). The calibration curve demonstrated a good consistency for 1, 2, and 3 years in each cohort (**Figure S1D**).

The 11LNCPS model also appears to be more robust than two previously developed mRNA models, including the 8-gene model (34) and the 4-gene model (35). The 11LNCPS's AUC values were equal or higher than those for the other two models in the validation cohort (**Figure 2F**), and so were the C-index values (**Figure S1E**).

Significantly, the 11LNCPS scores appear to predict the status of immune responses to HCC cells. Specifically, higher 11LNCPS scores were significantly associated with increased infiltrations of Th1, Th2, pro B, B, and basophils immune cells and decreased

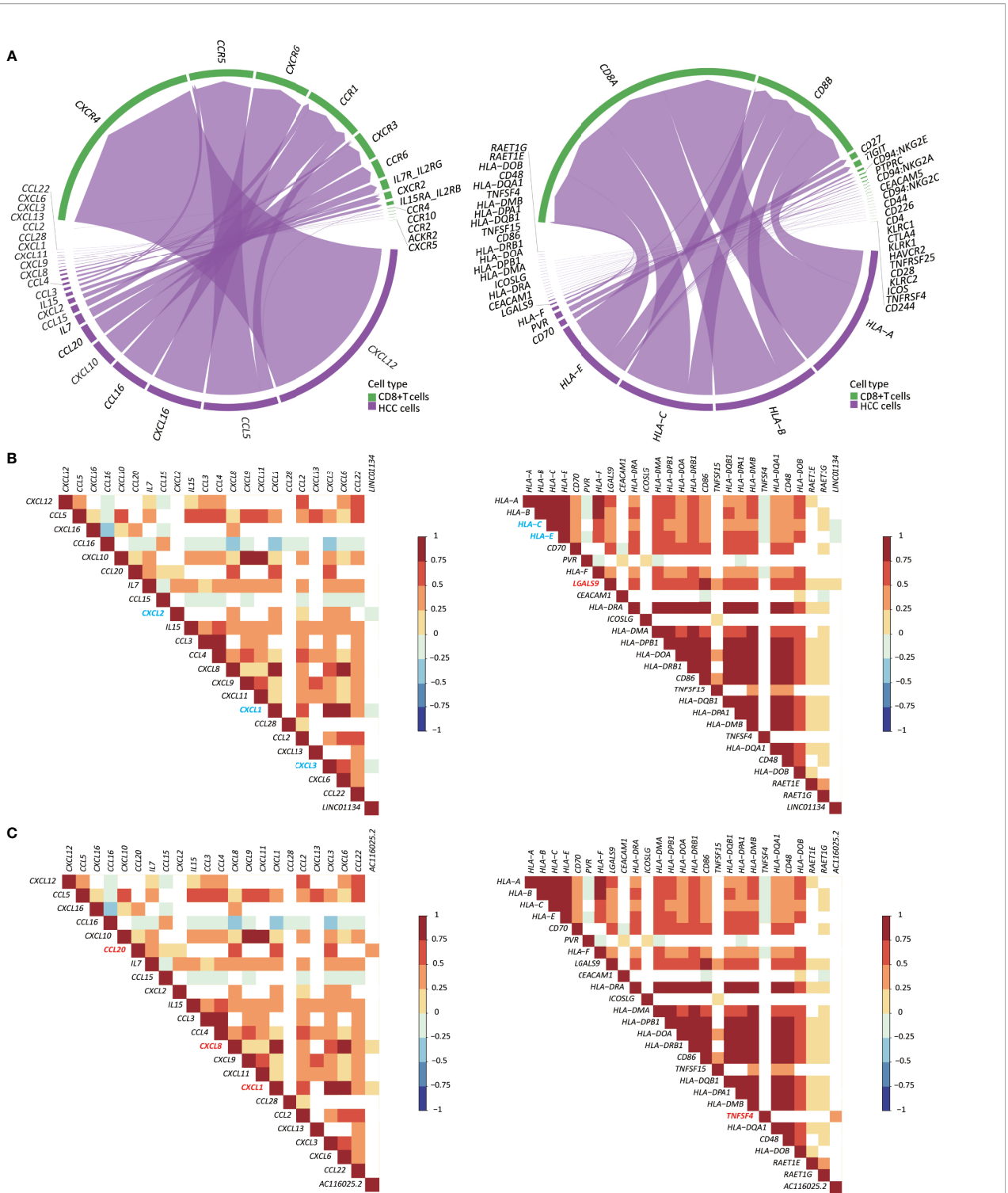

FIGURE 7 | Expression of *LINC01134* and *AC116025.2* is associated with the expression of some cytokines, chemokines, and immune checkpoint (ICP) ligands in HCC. **(A)** The chord diagram shows heterotypic signal transduction between HCC cells (purple) and CD8+ T cells (green), with purple arrows pointing from cytokines and chemokines (left) or ICP ligands (right) in HCC cells to their respective receptors in CD8+ T cells. **(B, C)** Expression of *LINC01134* **(B)** and *AC116025.2* **(C)** is associated with the expression of some cytokines and chemokines (left) or ICP ligands (right), as determined by the Spearman analysis. Grid colors and gradient color bars indicate Spearman coefficient values, with white color indicating a lack of statistical significance. Cytokines, chemokines, and ICP ligands with a positive association with *LINC01134* or *AC116025.2* expression are marked by red, while those with a negative correlation are marked by blue.

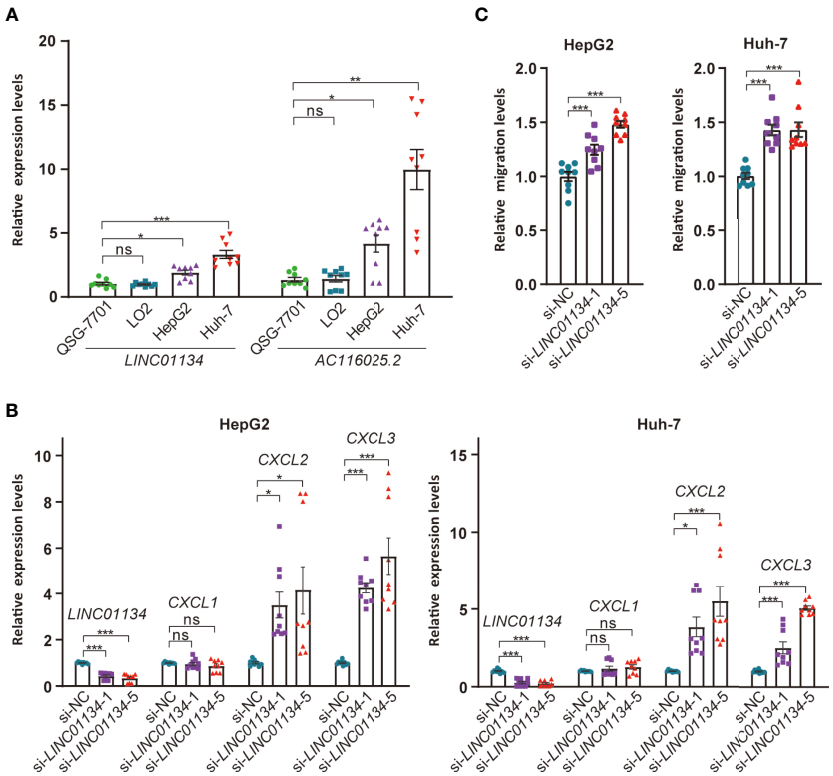

FIGURE 8 | Expression and functional tests of key member lncRNAs of the 11LNCPS in HCC cell lines. **(A)** Expression of *LINC01134* and *AC116025.2* in normal liver cell lines QSG-7701 and LO2 and HCC cell lines HepG2 and Huh-7, as detected by qRT-PCR. Data were normalized by β-actin mRNA levels and standardized by the control group levels. **(B)** Knockdown of *LINC01134* in HepG2 (left) and Huh-7 (right) HCC cells increased the expression of *CXCL2* and *CXCL3*, as detected by qRT-PCR. **(C)** Knockdown of *LINC01134* in HepG2 (left) and Huh-7 (right) HCC cells increased the migration of Jurkat T cells, as detected by the transwell assay. ns, $P > 0.05$; *$P \leq 0.05$; **$P \leq 0.01$; ***$P \leq 0.001$.

infiltrations of CD8+ Tcm, macrophages, M2 macrophage, aDCs, and cDCs immune cells in HCC (**Figure 3B** and **Figure S4**). Of them, decreased infiltration of CD8+ Tcm and increased infiltrations of Th1, Th2, and pro B cells were significantly correlated with worse patient OS in the same cohort of HCCs (**Figure 3A**). Additionally, higher 11LNCPS scores were associated with increased TCE (**Figure 3C**) and reduced T cell dysfunction (**Figure 3D**). Furthermore, HCCs with higher 11LNCPS scores significantly corresponded to malignancies that respond to PDL1 inhibition in immunotherapeutic studies, as analyzed by the SubMap program (**Figure 3E**). It is thus likely that HCCs with higher 11LNCPS scores respond better to immunotherapies than those with lower scores.

The 11LNCPS model was developed from differentially expressed and TCE-associated lncRNAs in HCC, so the impact of 11LNCPS scores on immune response and patient survival could be due to TCE to a greater extent. Many publications have reported the association of TCE with patient prognosis, tumor immune microenvironment, and treatment resistance (1, 11–15).

Immune cell infiltration to the tumor microenvironment determines the sensitivity of cancer cells to immunotherapy (50–53). In this regard, the 11LNCPS could predict the infiltration of cancer-related immune cells, as 11LNCPS scores were significantly associated with infiltration levels of 10 types of immune cells, and infiltration alterations in 7 of the 10 were associated with patient survival in HCC (**Figures 3A, B**). One major type is CD8+ T cells, whose infiltration was reduced in HCCs with higher 11LNCPS scores (**Figure 3B**). Reduced infiltration of CD8+ cells also occurred more frequently in HCCs with the upregulation of *LINC01134* or *AC116025.2* (**Figure 5C**). More importantly, reduced infiltration of CD8+ T cells, including naïve T and Tcm cells, negatively impacted patient survival in HCC (**Figure 3A**). Such an inverse correlation between the 11LNCPS score and the infiltration of CD8+ T cells further indicates the relevance of the 11LNCPS in HCC because CD8+ T cells play important roles in the killing of cancer cells. For example, CD8+ cytotoxic T lymphocytes (CTLs) kill cancer cells (54, 55); and CD8+ T cells, in total or in the form of naïve or memory cells, also play critically important roles in host defenses against tumor cells (38, 56). An inverse correlation between reduced CD8+ T cells and worse patient survival has been reported, although naïve T and Tcm cells were not distinguished in these studies (51, 54, 57–62).

Similar to CD8+ T cells, decreased infiltration of plasmacytoid dendritic cells (pDCs) was significantly associated with worse patient survival in HCC (**Figure 3A**), and a decrease in the

infiltration of conventional DCs (cDCs) and activated DCs (aDCs) was more frequent in HCCs with higher 11LNCPS scores (**Figure 3B**). DCs play important roles in immune responses and tumor development. As antigen-presenting cells, pDCs function in adaptive immune responses to different antigens, including tumor antigens, and thus impact tumor development (63–65). Upon TRAIL-dependent mechanism and stimulation from other immune cells, activated pDCs indeed exert an anti-tumor function (57, 58, 66–68).

Opposing to the infiltrations of CD8+ cells and DCs, increased infiltration of CD4+ T helper cells, including Th1 and Th2 cells, and B cell progenitors (pro B) were significantly associated with worse patient survival and higher 11LNCPS scores in HCC (**Figures 3A, B**). Th1 and Th2 cells play important immunoregulatory roles in adaptive immunity, including the activation of B cells and cytotoxic T cells (69, 70). but their role in HCC development is not well understood (71). It is reported that a global Th1/Th2-like cytokine shift, i.e., an increase in Th2 cytokines but a decrease in Th1 cytokines, is associated with HCC metastasis (72), implicating Th1 and Th2 cells in HCC progression. We noticed that the association of Th1 cells with HCC prognosis is inconsistent between different studies (73). The role of pro B cells in HCC is not well understood either.

Immune cells' infiltration into a tumor involves heterotypic signaling between tumor cells and immune cells. Such signaling is often mediated by chemokines, cytokines, and ICP ligands. Several such molecules could play roles in the 11LNCPS-associated modulation of the immune microenvironment in HCC. Taking advantage of the recently developed CellChat algorithm (26) and the availability of single-cell RNA sequencing (scRNA-seq) data of HCC (23), we were able to annotate CD8+ T cells. Subsequently, we identified the chemokines, cytokines, and ICP ligands that could mediate the recruitment of CD8+ T cells (**Figures S8A**, **B**). They included 22 chemokines and cytokines (**Figure 7A**, left) and 26 ICP ligands (**Figure 7A**, right). The expression of *LINC01134* was negatively correlated with that of *CXCL1*, *CXCL2*, *CXCL3*, *HLA-C*, and *HLA-E* but positively correlated with that of *LGALS9* (**Figure 7B**). Meanwhile, *AC116025.2* expression was positively correlated with *CXCL1*, *CXCL8*, *CXCL20*, and *TNFSF4* (**Figure 7C**). We could not annotate other types of 11LNCPS associated immune cells (e.g., Th1, Th2, etc.).

The 11 lncRNAs could impact multiple biological processes and signaling pathways in HCC. When HCCs with higher 11LNCPS scores were compared to those with lower scores, many processes and pathways were significantly enriched, particularly those of DNA replication, cell cycle, metabolism, signaling between cytokines and their receptors, and other ligand-receptor signaling pathways (**Figure 4**). Signaling pathways related to immune function and apoptosis were also significantly suppressed in HCCs with higher 11LNCPS scores, including the IL6-JAK-STAT3 signaling and IFNα response (**Figure 4C**).

Of the 11 lncRNAs in the 11LNCPS, *LINC01134* and *AC116025.2* appear more crucial than the others. For example, *LINC01134* and *AC116025.2* were among the 5 11LNCPS lncRNAs whose upregulation was significantly associated with worse patient OS in HCC (**Figure 5A**). In addition, the association of an upregulation with infiltration alteration was detected in more types of immune cells for *LINC01134* or *AC116025.2* than other lncRNAs (**Figures 5B, C**). Furthermore, HCCs with higher *LINC01134* or *AC116025.2* levels had significantly higher levels of TCE and lower scores of T cell dysfunction (**Figures 5D, E**). Increased TCE levels and reduced T cell dysfunction scores are associated with patient prognosis (37). LncRNA *LINC01134* has been well implicated in HCC, as it undergoes upregulation, promotes cell proliferation and invasion, suppresses apoptosis, and induces oxaliplatin resistance in HCC (74–77). Therefore, whereas *LINC01134* is more crucial in the 11LNCPS, there are hardly any published studies on *AC116025.2* in any types of cancers. The upregulation of both *LINC01134* and *AC116025.2* also occurs in HCC cell lines, as detected by qRT-PCR in HepG2 and Huh-7 HCC cells (**Figure 7D**).

LINC01134 upregulation in HCC modulates multiple biological processes and signaling pathways (**Figure 6**). Of particular interest is that many of which are involved in immune functions, as *LINC01134* upregulation altered receptor-ligand activities, chemokine binding cellular component, chemokine signaling, cytokine and cytokine receptor, T and B cell receptor signaling, etc. (**Figure 6**). *LINC01134* upregulation also affects other cancer-related processes and pathways, including chromosome related molecular function, cell cycle and related pathways (E2F targets, G2M checkpoint, etc.), cancer-related pathways (PI3K-Akt, Rap1, MYC, etc.), cell death and related pathways (IFNγ response, IFNα response, etc.), IL6-JAK-STAT3 signaling, IL2- STAT5 signaling, epithelial-mesenchymal transition, UV response, TGFβ signaling, hypoxia, and P53 pathway (**Figure 6**). These findings further indicate that *LINC01134* impacts HCC *via* complicated signaling pathways, particularly those involved in immune functions. Consistent with these findings, *LINC01134* knockdown in HCC cell lines significantly increased the expression of chemokines *CXCL2* and *CXCL3* (**Figure 8B**), and conditioned medium from HCC cells with *LINC01134* knockdown increased the migration of T cells (**Figure 8C**).

Many *AC116025*-associated processes and pathways overlap with those of *LINC01134*, including receptor activity, cell cycle, metabolism, and cell death and related signaling pathways, E2F targets, G2M checkpoint, MYC, UV response, epithelial-mesenchymal transition, IFNγ response, IFNα response, UV response, epithelial-mesenchymal transition, bile acid metabolism, fatty acid metabolism, TGF-β signaling, etc. *AC116025.2* upregulation is less potent than *LINC01134* upregulation in its effects on immune-related processes and pathways. It did not significantly affect chemokine binding cellular component, chemokine signaling, cytokine and cytokine receptor, T and B cell receptor signaling, etc. (**Figure 6**).

Of note is that *AC116025.2* upregulation affects more metabolism-related pathways than *LNC001134* upregulation. In the KEGG pathway analysis, while 7 of the top 18 pathways affected by *AC116025.2* upregulation were metabolism-related,

none of the top 14 affected by *LNC001134* were (**Figures 6B, D**), even though they both affected bile acid metabolism and fatty acid metabolism in the GSEA enrichment assay (**Figures 6C, F**). Tumor cell metabolism reprograms immune cell infiltration (78, 79), so the association of *AC116025.2* with alterations in multiple metabolic pathways could suggest how *AC116025.2* might modulate T cell exclusion.

In summary, after identifying differentially expressed and TCE-associated lncRNAs in HCC, we developed and validated a robust lncRNA-based gene signature named 11LNCPS for 11-lncRNA prognosis signature. The 11LNCPS predicts not only prognosis but also immune cells' responses to tumor cells, including decreased infiltrations of CD8+ T cells, macrophages, and DCs, as well as increased infiltrations of Th1, Th2, pro B cells. Of the 11 lncRNAs in the 11LNCPS, *LINC01134* and *AC116025.2* appear more crucial than the others. Expression alterations in the 11LNCPS lncRNAs, particularly the upregulation of *LINC01134* and *AC116025.2*, modulate multiple signaling pathways, including immune responses and cell metabolism. The 11LNCPS could help predict immune responses in HCC and provide candidate therapeutic targets for the treatment of HCC.

DATA AVAILABILITY STATEMENT

Publicly available datasets were analyzed in this study. This data can be found in TCGA (https://www.cancer.gov/about-nci/organization/ccg/research/structural-genomics/tcga/) and GEO (https://www.ncbi.nlm.nih.gov/geo/) database.

AUTHOR CONTRIBUTIONS

JD, XL, ZZ, and ML contributed to conception and design of the study. XL and XF curated the data. XL performed the statistical analysis. XL wrote the first draft of the manuscript. JD, JA, ZZ, GC, and SW edited and wrote sections of the manuscript. JD supervised the study. All authors contributed to manuscript revision, read, and approved the submitted version.

FUNDING

This study is supported in part by grant JCYJ20200109141229255 from the Science, Technology and Innovation Commission of Shenzhen Municipality.

ACKNOWLEDGMENTS

We thank Dr. Jianming Zeng (University of Macau) and his bioinformatics team for generously sharing their experience and codes. We also thank Mr. Bingbiao Lin, Ms. Qingqing Huang and Dr. Xiafei Zeng, for their advice and help during the study.

SUPPLEMENTARY MATERIAL

The Supplementary Material for this article can be found online at: https://www.frontiersin.org/articles/10.3389/fimmu.2022.880288/full#supplementary-material

REFERENCES

1. Zhang Y, Zhang L, Xu Y, Wu X, Zhou Y, Mo J. Immune-Related Long Noncoding RNA Signature for Predicting Survival and Immune Checkpoint Blockade in Hepatocellular Carcinoma. *J Cell Physiol* (2020) 235(12):9304–16. doi: 10.1002/jcp.29730
2. Sung H, Ferlay J, Siegel RL, Laversanne M, Soerjomataram I, Jemal A, et al. Global Cancer Statistics 2020: GLOBOCAN Estimates of Incidence and Mortality Worldwide for 36 Cancers in 185 Countries. *CA Cancer J Clin* (2021) 71(3):209–49. doi: 10.3322/caac.21660
3. Fu Y, Liu S, Zeng S, Shen H. From Bench to Bed: The Tumor Immune Microenvironment and Current Immunotherapeutic Strategies for Hepatocellular Carcinoma. *J Exp Clin Cancer Res* (2019) 38(1):396. doi: 10.1186/s13046-019-1396-4
4. Yang JD, Heimbach JK. New Advances in the Diagnosis and Management of Hepatocellular Carcinoma. *BMJ* (2020) 371:m3544. doi: 10.1136/bmj.m3544
5. Olson B, Li Y, Lin Y, Liu ET, Patnaik A. Mouse Models for Cancer Immunotherapy Research. *Cancer Discov* (2018) 8(11):1358–65. doi: 10.1158/2159-8290.CD-18-0044
6. Hilmi M, Vienot A, Rousseau B, Neuzillet C. Immune Therapy for Liver Cancers. *Cancers (Basel)* (2019) 12(1):77. doi: 10.3390/cancers12010077
7. Rizvi S, Wang J, El-Khoueiry AB. Liver Cancer Immunity. *Hepatology* (2021) 73 Suppl 1:86–103. doi: 10.1002/hep.31416
8. Ho DW, Tsui YM, Chan LK, Sze KM, Zhang X, Cheu JW, et al. Single-Cell RNA Sequencing Shows the Immunosuppressive Landscape and Tumor Heterogeneity of HBV-Associated Hepatocellular Carcinoma. *Nat Commun* (2021) 12(1):3684. doi: 10.1038/s41467-021-24010-1
9. Ruf B, Heinrich B, Greten TF. Immunobiology and Immunotherapy of HCC: Spotlight on Innate and Innate-Like Immune Cells. *Cell Mol Immunol* (2021) 18(1):112–27. doi: 10.1038/s41423-020-00572-w
10. Lim H, He D, Qiu Y, Krawczuk P, Sun X, Xie L. Rational Discovery of Dual-Indication Multi-Target PDE/Kinase Inhibitor for Precision Anti-Cancer Therapy Using Structural Systems Pharmacology. *PloS Comput Biol* (2019) 15(6):e1006619. doi: 10.1371/journal.pcbi.1006619
11. Wu SZ, Roden DL, Wang C, Holliday H, Harvey K, Cazet AS, et al. Stromal Cell Diversity Associated With Immune Evasion in Human Triple-Negative Breast Cancer. *EMBO J* (2020) 39(19):e1040. doi: 10.15252/embj.2019104063
12. Wang Q, Li M, Yang M, Yang Y, Song F, Zhang W, et al. Analysis of Immune-Related Signatures of Lung Adenocarcinoma Identified Two Distinct Subtypes: Implications for Immune Checkpoint Blockade Therapy. *Aging (Albany NY)* (2020) 12(4):3312–39. doi: 10.18632/aging.102814
13. Hato T, Goyal L, Greten TF, Duda DG, Zhu AX. Immune Checkpoint Blockade in Hepatocellular Carcinoma: Current Progress and Future Directions. *Hepatology* (2014) 60(5):1776–82. doi: 10.1002/hep.27246
14. Zhang HH, Mei MH, Fei R, Liu F, Wang JH, Liao WJ, et al. Regulatory T Cells in Chronic Hepatitis B Patients Affect the Immunopathogenesis of Hepatocellular Carcinoma by Suppressing the Anti-Tumour Immune Responses. *J Viral Hepat* (2010) 17 Suppl 1:34–43. doi: 10.1111/j.1365-2893.2010.01269.x
15. Jiang P, Gu S, Pan D, Fu J, Sahu A, Hu X, et al. Signatures of T Cell Dysfunction and Exclusion Predict Cancer Immunotherapy Response. *Nat Med* (2018) 24(10):1550–8. doi: 10.1038/s41591-018-0136-1
16. Yu WD, Wang H, He QF, Xu Y, Wang XC. Long Noncoding RNAs in Cancer-Immunity Cycle. *J Cell Physiol* (2018) 233(9):6518–23. doi: 10.1002/jcp.26568
17. Sanchez Calle A, Kawamura Y, Yamamoto Y, Takeshita F, Ochiya T. Emerging Roles of Long Non-Coding RNA in Cancer. *Cancer Sci* (2018) 109(7):2093–100. doi: 10.1111/cas.13642
18. Xu M, Xu X, Pan B, Chen X, Lin K, Zeng K, et al. LncRNA SATB2-AS1 Inhibits Tumor Metastasis and Affects the Tumor Immune Cell

Microenvironment in Colorectal Cancer by Regulating Satb2. *Mol Cancer* (2019) 18(1):135. doi: 10.1186/s12943-019-1063-6
19. Carpenter S, Fitzgerald KA. Cytokines and Long Noncoding RNAs. *Cold Spring Harb Perspect Biol* (2018) 10(6):a028589. doi: 10.1101/cshperspect.a028589
20. Wang CJ, Zhu CC, Xu J, Wang M, Zhao WY, Liu Q, et al. The lncRNA UCA1 Promotes Proliferation, Migration, Immune Escape and Inhibits Apoptosis in Gastric Cancer by Sponging Anti-Tumor miRNAs. *Mol Cancer* (2019) 18 (1):115. doi: 10.1186/s12943-019-1032-0
21. Hong W, Liang L, Gu Y, Qi Z, Qiu H, Yang X, et al. Immune-Related lncRNA to Construct Novel Signature and Predict the Immune Landscape of Human Hepatocellular Carcinoma. *Mol Ther Nucleic Acids* (2020) 22:937–47. doi: 10.1016/j.omtn.2020.10.002
22. Colaprico A, Silva TC, Olsen C, Garofano L, Cava C, Garolini D, et al. TCGAbiolinks: An R/Bioconductor Package for Integrative Analysis of TCGA Data. *Nucleic Acids Res* (2016) 44(8):e71. doi: 10.1093/nar/gkv1507
23. Su X, Zhao L, Shi Y, Zhang R, Long Q, Bai S, et al. Clonal Evolution in Liver Cancer at Single-Cell and Single-Variant Resolution. *J Hematol Oncol* (2021) 14(1):22. doi: 10.1186/s13045-021-01036-y
24. Li WV, Li JJ. An Accurate and Robust Imputation Method Scimpute for Single-Cell RNA-Seq Data. *Nat Commun* (2018) 9(1):997. doi: 10.1038/s41467-018-03405-7
25. Butler A, Hoffman P, Smibert P, Papalexi E, Satija R. Integrating Single-Cell Transcriptomic Data Across Different Conditions, Technologies, and Species. *Nat Biotechnol* (2018) 36(5):411–20. doi: 10.1038/nbt.4096
26. Jin S, Guerrero-Juarez CF, Zhang L, Chang I, Ramos R, Kuan CH, et al. Inference and Analysis of Cell-Cell Communication Using CellChat. *Nat Commun* (2021) 12(1):1088. doi: 10.1038/s41467-021-21246-9
27. Robinson MD, McCarthy DJ, Smyth GK. Edger: A Bioconductor Package for Differential Expression Analysis of Digital Gene Expression Data. *Bioinformatics* (2010) 26(1):139–40. doi: 10.1093/bioinformatics/btp616
28. McCarthy DJ, Chen Y, Smyth GK. Differential Expression Analysis of Multifactor RNA-Seq Experiments With Respect to Biological Variation. *Nucleic Acids Res* (2012) 40(10):4288–97. doi: 10.1093/nar/gks042
29. Ritchie ME, Phipson B, Wu D, Hu Y, Law CW, Shi W, et al. Limma Powers Differential Expression Analyses for RNA-Sequencing and Microarray Studies. *Nucleic Acids Res* (2015) 43(7):e47. doi: 10.1093/nar/gkv007
30. Frankish A, Diekhans M, Ferreira AM, Johnson R, Jungreis I, Loveland J, et al. GENCODE Reference Annotation for the Human and Mouse Genomes. *Nucleic Acids Res* (2019) 47(D1):D766–73. doi: 10.1093/nar/gky955
31. Tibshirani R. Regression Shrinkage and Selection *via* the LASSO. *J R Stat Soc B* (1996) 58:267–88. doi: 10.2307/2346178
32. Xu F, Lin H, He P, He L, Chen J, Lin L, et al. A TP53-Associated Gene Signature for Prediction of Prognosis and Therapeutic Responses in Lung Squamous Cell Carcinoma. *Oncoimmunology* (2020) 9(1):1731943. doi: 10.1080/2162402x.2020.1731943
33. Gao WZ, Guo LM, Xu TQ, Yin YH, Jia F. Identification of a Multidimensional Transcriptome Signature for Survival Prediction of Postoperative Glioblastoma Multiforme Patients. *J Trans Med* (2018) 16(1):368. doi: 10.1186/s12967-018-1744-8
34. Zhang Z, Li J, He T, Ouyang Y, Huang Y, Liu Q, et al. The Competitive Endogenous RNA Regulatory Network Reveals Potential Prognostic Biomarkers for Overall Survival in Hepatocellular Carcinoma. *Cancer Sci* (2019) 110(9):2905–23. doi: 10.1111/cas.14138
35. Long J, Zhang L, Wan X, Lin J, Bai Y, Xu W, et al. A Four-Gene-Based Prognostic Model Predicts Overall Survival in Patients With Hepatocellular Carcinoma. *J Cell Mol Med* (2018) 22(12):5928–38. doi: 10.1111/jcmm.13863
36. Aran D. Cell-Type Enrichment Analysis of Bulk Transcriptomes Using Xcell. *Methods Mol Biol* (2020) 2120:263–76. doi: 10.1007/978-1-0716-0327-7_19
37. Aran D, Hu Z, Butte AJ. Xcell: Digitally Portraying the Tissue Cellular Heterogeneity Landscape. *Genome Biol* (2017) 18(1):220. doi: 10.1186/s13059-017-1349-1
38. Deng L, Lu DH, Bai YN, Wang YP, Bu H, Zheng H. Immune Profiles of Tumor Microenvironment and Clinical Prognosis Among Women With Triple-Negative Breast Cancer. *Cancer Epidem Biomar* (2019) 28(12):1977–85. doi: 10.1158/1055-9965.Epi-19-0469
39. Hoshida Y, Brunet JP, Tamayo P, Golub TR, Mesirov JP. Subclass Mapping: Identifying Common Subtypes in Independent Disease Data Sets. *PloS One* (2007) 2(11):e1195. doi: 10.1371/journal.pone.0001195
40. Roh W, Chen PL, Reuben A, Spencer CN, Prieto PA, Miller JP, et al. Integrated Molecular Analysis of Tumor Biopsies on Sequential CTLA-4 and PD-1 Blockade Reveals Markers of Response and Resistance. *Sci Transl Med* (2017) 9(379):eaah3560. doi: 10.1126/scitranslmed.aah3560
41. Mariathasan S, Turley SJ, Nickles D, Castiglioni A, Yuen K, Wang Y, et al. TGFbeta Attenuates Tumour Response to PD-L1 Blockade by Contributing to Exclusion of T Cells. *Nature* (2018) 554(7693):544–8. doi: 10.1038/nature25501
42. Mootha VK, Lindgren CM, Eriksson KF, Subramanian A, Sihag S, Lehar J, et al. PGC-1alpha-Responsive Genes Involved in Oxidative Phosphorylation are Coordinately Downregulated in Human Diabetes. *Nat Genet* (2003) 34 (3):267–73. doi: 10.1038/ng1180
43. Subramanian A, Tamayo P, Mootha VK, Mukherjee S, Ebert BL, Gillette MA, et al. Gene Set Enrichment Analysis: A Knowledge-Based Approach for Interpreting Genome-Wide Expression Profiles. *Proc Natl Acad Sci U.S.A.* (2005) 102(43):15545–50. doi: 10.1073/pnas.0506580102
44. Yu G, Wang LG, Han Y, He QY. Clusterprofiler: An R Package for Comparing Biological Themes Among Gene Clusters. *OMICS* (2012) 16(5):284–7. doi: 10.1089/omi.2011.0118
45. Hanzelmann S, Castelo R, Guinney J. GSVA: Gene Set Variation Analysis for Microarray and RNA-Seq Data. *BMC Bioinf* (2013) 14:7. doi: 10.1186/1471-2105-14-7
46. Sanz-Ortega L, Rojas JM, Marcos A, Portilla Y, Stein JV, Barber DF. T Cells Loaded With Magnetic Nanoparticles are Retained in Peripheral Lymph Nodes by the Application of a Magnetic Field. *J Nanobiotech* (2019) 17 (1):14. doi: 10.1186/s12951-019-0440-z
47. Messmer D, Fecteau JF, O'Hayre M, Bharati IS, Handel TM, Kipps TJ. Chronic Lymphocytic Leukemia Cells Receive RAF-Dependent Survival Signals in Response to CXCL12 That are Sensitive to Inhibition by Sorafenib. *Blood* (2011) 117(3):882–9. doi: 10.1182/blood-2010-04-282400
48. Yu Y, Liao L, Shao B, Su X, Shuai Y, Wang H, et al. Knockdown of MicroRNA Let-7a Improves the Functionality of Bone Marrow-Derived Mesenchymal Stem Cells in Immunotherapy. *Mol Ther* (2017) 25(2):480–93. doi: 10.1016/j.ymthe.2016.11.015
49. Riaz N, Havel JJ, Makarov V, Desrichard A, Urba WJ, Sims JS, et al. Tumor and Microenvironment Evolution During Immunotherapy With Nivolumab. *Cell* (2017) 171(4):934–49.e16. doi: 10.1016/j.cell.2017.09.028
50. Horton B, Spranger S. A Tumor Cell-Intrinsic Yin-Yang Determining Immune Evasion. *Immunity* (2018) 49(1):11–3. doi: 10.1016/j.immuni.2018.07.001
51. Li J, Byrne KT, Yan F, Yamazoe T, Chen Z, Baslan T, et al. Tumor Cell-Intrinsic Factors Underlie Heterogeneity of Immune Cell Infiltration and Response to Immunotherapy. *Immunity* (2018) 49(1):178–93.e7. doi: 10.1016/j.immuni.2018.06.006
52. Muraoka D, Seo N, Hayashi T, Tahara Y, Fujii K, Tawara I, et al. Antigen Delivery Targeted to Tumor-Associated Macrophages Overcomes Tumor Immune Resistance. *J Clin Invest* (2019) 129(3):1278–94. doi: 10.1172/JCI97642
53. Mantovani A, Marchesi F, Malesci A, Laghi L, Allavena P. Tumour-Associated Macrophages as Treatment Targets in Oncology. *Nat Rev Clin Oncol* (2017) 14(7):399–416. doi: 10.1038/nrclinonc.2016.217
54. Farhood B, Najafi M, Mortezaee K. CD8(+) Cytotoxic T Lymphocytes in Cancer Immunotherapy: A Review. *J Cell Physiol* (2019) 234(6):8509–21. doi: 10.1002/jcp.27782
55. Gattinoni L, Klebanoff CA, Restifo NP. Paths to Stemness: Building the Ultimate Antitumour T Cell. *Nat Rev Cancer* (2012) 12(10):671–84. doi: 10.1038/nrc3322
56. Fann M, Godlove JM, Catalfamo M, Wood WH3rd, Chrest FJ, Chun N, et al. Histone Acetylation is Associated With Differential Gene Expression in the Rapid and Robust Memory CD8(+) T-Cell Response. *Blood* (2006) 108 (10):3363–70. doi: 10.1182/blood-2006-02-005520
57. Speiser DE, Liénard D, Rufer N, Rubio-Godoy V, Rimoldi D, Lejeune F, et al. Rapid and Strong Human CD8+ T Cell Responses to Vaccination With Peptide, IFA, and CpG Oligodeoxynucleotide 7909. *J Clin Invest* (2005) 115 (3):739–46. doi: 10.1172/jci23373

58. Molenkamp BG, Sluijter BJ, van Leeuwen PA, Santegoets SJ, Meijer S, Wijnands PG, et al. Local Administration of PF-3512676 CpG-B Instigates Tumor-Specific CD8+ T-Cell Reactivity in Melanoma Patients. *Clin Cancer Res* (2008) 14(14):4532–42. doi: 10.1158/1078-0432.Ccr-07-4711
59. Gordon-Alonso M, Hirsch T, Wildmann C, van der Bruggen P. Galectin-3 Captures Interferon-Gamma in the Tumor Matrix Reducing Chemokine Gradient Production and T-Cell Tumor Infiltration. *Nat Commun* (2017) 8 (1):793. doi: 10.1038/s41467-017-00925-6
60. Brewitz A, Eickhoff S, Dähling S, Quast T, Bedoui S, Kroczek RA, et al. CD8(+) T Cells Orchestrate pDC-XCR1(+) Dendritic Cell Spatial and Functional Cooperativity to Optimize Priming. *Immunity* (2017) 46(2):205–19. doi: 10.1016/j.immuni.2017.01.003
61. Han Q, Wang Y, Pang M, Zhang J. STAT3-Blocked Whole-Cell Hepatoma Vaccine Induces Cellular and Humoral Immune Response Against HCC. *J Exp Clin Cancer Res* (2017) 36(1):156. doi: 10.1186/s13046-017-0623-0
62. Dangaj D, Bruand M, Grimm AJ, Ronet C, Barras D, Duttagupta PA, et al. Cooperation Between Constitutive and Inducible Chemokines Enables T Cell Engraftment and Immune Attack in Solid Tumors. *Cancer Cell* (2019) 35 (6):885–900.e10. doi: 10.1016/j.ccell.2019.05.004
63. Liu C, Lou Y, Lizée G, Qin H, Liu S, Rabinovich B, et al. Plasmacytoid Dendritic Cells Induce NK Cell-Dependent, Tumor Antigen-Specific T Cell Cross-Priming and Tumor Regression in Mice. *J Clin Invest* (2008) 118 (3):1165–75. doi: 10.1172/jci33583
64. Schuster P, Lindner G, Thomann S, Haferkamp S, Schmidt B. Prospect of Plasmacytoid Dendritic Cells in Enhancing Anti-Tumor Immunity of Oncolytic Herpes Viruses. *Cancers (Basel)* (2019) 11(5):651. doi: 10.3390/cancers11050651
65. Reizis B, Bunin A, Ghosh HS, Lewis KL, Sisirak V. Plasmacytoid Dendritic Cells: Recent Progress and Open Questions. *Annu Rev Immunol* (2011) 29:163–83. doi: 10.1146/annurev-immunol-031210-101345
66. Matsui T, Connolly JE, Michnevitz M, Chaussabel D, Yu CI, Glaser C, et al. CD2 Distinguishes Two Subsets of Human Plasmacytoid Dendritic Cells With Distinct Phenotype and Functions. *J Immunol (Baltim Md 1950)* (2009) 182 (11):6815–23. doi: 10.4049/jimmunol.0802008
67. Lou Y, Liu C, Kim GJ, Liu YJ, Hwu P, Wang G. Plasmacytoid Dendritic Cells Synergize With Myeloid Dendritic Cells in the Induction of Antigen-Specific Antitumor Immune Responses. *J Immunol (Baltim Md 1950)* (2007) 178 (3):1534–41. doi: 10.4049/jimmunol.178.3.1534
68. Böttcher JP, Bonavita E, Chakravarty P, Blees H, Cabeza-Cabrerizo M, Sammicheli S, et al. NK Cells Stimulate Recruitment of Cdc1 Into the Tumor Microenvironment Promoting Cancer Immune Control. *Cell* (2018) 172(5):1022–37.e14. doi: 10.1016/j.cell.2018.01.004
69. Okoye IS, Wilson MS. CD4+ T Helper 2 Cells–Microbial Triggers, Differentiation Requirements and Effector Functions. *Immunology* (2011) 134(4):368–77. doi: 10.1111/j.1365-2567.2011.03497.x
70. Subbannayya Y, Haug M, Pinto SM, Mohanty V, Meas HZ, Flo TH, et al. The Proteomic Landscape of Resting and Activated CD4+ T Cells Reveal Insights Into Cell Differentiation and Function. *Int J Mol Sci* (2020) 22(1):275. doi: 10.3390/ijms22010275
71. Basu A, Ramamoorthi G, Albert G, Gallen C, Beyer A, Snyder C, et al. Differentiation and Regulation of TH Cells: A Balancing Act for Cancer Immunotherapy. *Front Immunol* (2021) 12:669474. doi: 10.3389/fimmu.2021.669474
72. Zhu Y, Yang J, Xu D, Gao XM, Zhang Z, Hsu JL, et al. Disruption of Tumour-Associated Macrophage Trafficking by the Osteopontin-Induced Colony-Stimulating Factor-1 Signalling Sensitises Hepatocellular Carcinoma to Anti-PD-L1 Blockade. *Gut* (2019) 68(9):1653–66. doi: 10.1136/gutjnl-2019-318419
73. Yan J, Liu XL, Xiao G, Li NL, Deng YN, Han LZ, et al. Prevalence and Clinical Relevance of T-Helper Cells, Th17 and Th1, in Hepatitis B Virus-Related Hepatocellular Carcinoma. *PloS One* (2014) 9(5):e96080. doi: 10.1371/journal.pone.0096080
74. Zheng S, Guo Y, Dai L, Liang Z, Yang Q, Yi S. Long Intergenic Noncoding RNA01134 Accelerates Hepatocellular Carcinoma Progression by Sponging microRNA-4784 and Downregulating Structure Specific Recognition Protein 1. *Bioengineered* (2020) 11(1):1016–26. doi: 10.1080/21655979.2020.1818508
75. Rong Z, Wang Z, Wang X, Qin C, Geng W. Molecular Interplay Between Linc01134 and YY1 Dictates Hepatocellular Carcinoma Progression. *J Exp Clin Cancer Res* (2020) 39(1):61. doi: 10.1186/s13046-020-01551-9
76. Wang C, Chen Y, Chen K, Zhang L. Long Noncoding RNA LINC01134 Promotes Hepatocellular Carcinoma Metastasis *via* Activating AKT1S1 and NF-kappaB Signaling. *Front Cell Dev Biol* (2020) 8:429. doi: 10.3389/fcell.2020.00429
77. Ma L, Xu A, Kang L, Cong R, Fan Z, Zhu X, et al. LSD1-Demethylated LINC01134 Confers Oxaliplatin Resistance *via* SP1-Induced P62 Transcription in Hepatocellular Carcinoma. *Hepatology* (2021) 74(6):3213–34. doi: 10.1002/hep.32079
78. Joseph A, Juncheng P, Mondini M, Labaied N, Loi M, Adam J, et al. Metabolic Features of Cancer Cells Impact Immunosurveillance. *J Immunother Cancer* (2021) 9(6):e002362. doi: 10.1136/jitc-2021-002362
79. Vazquez Rodriguez G, Abrahamsson A, Turkina MV, Dabrosin C. Lysine in Combination With Estradiol Promote Dissemination of Estrogen Receptor Positive Breast Cancer *via* Upregulation of U2AF1 and RPN2 Proteins. *Front Oncol* (2020) 10:598684. doi: 10.3389/fonc.2020.598684

Conflict of Interest: The authors declare that the research was conducted in the absence of any commercial or financial relationships that could be construed as a potential conflict of interest.

frontiers | Frontiers in Immunology

ORIGINAL RESEARCH
published: 10 June 2022
doi: 10.3389/fimmu.2022.906889

Comprehensive Analysis and Reinforcement Learning of Hypoxic Genes Based on Four Machine Learning Algorithms for Estimating the Immune Landscape, Clinical Outcomes, and Therapeutic Implications in Patients With Lung Adenocarcinoma

Zhaoyang Sun[1†], Yu Zeng[2†], Ting Yuan[1†], Xiaoying Chen[1], Hua Wang[1] and Xiaowei Ma[1,3*]*

[1] Department of Laboratory Medicine, Ren Ji Hospital, Shanghai Jiao Tong University School of Medicine, Shanghai, China, [2] Department of Thyroid and Neck Tumor, Tianjin Medical University Cancer Institute and Hospital, National Clinical Research Center for Cancer, Key Laboratory of Cancer Prevention and Therapy, Tianjin's Clinical Research Center for Cancer, Tianjin, China, [3] Institute of Molecular Medicine, Department of Laboratory Medicine, Shanghai Key Laboratory for Nucleic Acid Chemistry and Nanomedicine, State Key Laboratory of Oncogene and Related Genes, Ren Ji Hospital, Shanghai Jiao Tong University School of Medicine, Shanghai, China

OPEN ACCESS

Edited by:
Liusheng Peng,
Third Military Medical University, China

Reviewed by:
Dan Wang,
Hubei University of Science and Technology, China
BL Gan,
Guangxi Medical University, China

***Correspondence:**
Hua Wang
fdeduwh@126.com
Xiaowei Ma
m138902y@hotmail.com

[†]These authors have contributed equally to this work and share first authorship

Specialty section:
This article was submitted to Cancer Immunity and Immunotherapy, a section of the journal Frontiers in Immunology

Received: *29 March 2022*
Accepted: *11 May 2022*
Published: *10 June 2022*

Citation:
Sun Z, Zeng Y, Yuan T, Chen X, Wang H and Ma X (2022) Comprehensive Analysis and Reinforcement Learning of Hypoxic Genes Based on Four Machine Learning Algorithms for Estimating the Immune Landscape, Clinical Outcomes, and Therapeutic Implications in Patients With Lung Adenocarcinoma. Front. Immunol. 13:906889. doi: 10.3389/fimmu.2022.906889

Background: Patients with lung adenocarcinoma (LUAD) exhibit significant heterogeneity in therapeutic responses and overall survival (OS). In recent years, accumulating research has uncovered the critical roles of hypoxia in a variety of solid tumors, but its role in LUAD is not currently fully elucidated. This study aims to discover novel insights into the mechanistic and therapeutic implications of the hypoxia genes in LUAD cancers by exploring the potential association between hypoxia and LUAD.

Methods: Four machine learning approaches were implemented to screen out potential hypoxia-related genes for the prognosis of LUAD based on gene expression profile of LUAD samples obtained from The Cancer Genome Atlas (TCGA), then validated by six cohorts of validation datasets. The risk score derived from the hypoxia-related genes was proven to be an independent factor by using the univariate and multivariate Cox regression analyses and Kaplan–Meier survival analyses. Hypoxia-related mechanisms based on tumor mutational burden (TMB), the immune activity, and therapeutic value were also performed to adequately dig deeper into the clinical value of hypoxia-related genes. Finally, the expression level of hypoxia genes was validated at protein level and clinical samples from LUAD patients at transcript levels.

Results: All patients in TCGA and GEO-LUAD group were distinctly stratified into low- and high-risk groups based on the risk score. Survival analyses demonstrated that our risk

score could serve as a powerful and independent risk factor for OS, and the nomogram also exhibited high accuracy. LUAD patients in high-risk group presented worse OS, lower TMB, and lower immune activity. We found that the model is highly sensitive to immune features. Moreover, we revealed that the hypoxia-related genes had potential therapeutic value for LUAD patients based on the drug sensitivity and chemotherapeutic response prediction. The protein and gene expression levels of 10 selected hypoxia gene also showed significant difference between LUAD tumors tissues and normal tissues. The validation experiment showed that the gene transcript levels of most of their genes were consistent with the levels of their translated proteins.

Conclusions: Our study might contribute to the optimization of risk stratification for survival and personalized management of LUAD patients by using the hypoxia genes, which will provide a valuable resource that will guide both mechanistic and therapeutic implications of the hypoxia genes in LUAD cancers.

Keywords: lung adenocarcinoma, hypoxia gene, immune landscape, overall survival, prognosis, therapeutic implications

INTRODUCTION

Lung cancer histology is determined according to the WHO classification based primarily on the light microscopic appearance of the malignant cells (adenocarcinoma, squamous carcinoma, large cell carcinomas, and small cell carcinoma) (1). Among lung cancers, lung adenocarcinoma (LUAD) is the most commonly diagnosed subtype, accounts for 40% of all diagnosed lung cancers, and has an average 5-year survival rate of only 15% (2, 3). The incidence of LUAD has increased significantly over the past two decades, especially among women (4). As a highly aggressive disease with significant heterogeneous prognosis across individuals, the molecular mechanisms underlying LUAD progression remain elusive (5). The International Union Against Cancer (UICC) tumor–node–metastasis (TNM) staging system was widely used for LUAD prognosis assessment (6). However, TNM-based clinical assessment method has so far proved inadequate in predicting clinical outcomes and treatment decision. Therefore, it has become one of the hot spots in clinical research to find more valuable prognosis indexes of LUAD.

Hypoxia, or lack of oxygen, is a feature of most solid tumors (7). Studies have shown that hypoxia-inducible factors (HIFs) are highly expressed in osteosarcoma stem cells (OSCs), and a significant decrease in stem cell proliferation and migratory activity was found after selective inhibition of HIF-1α or HIF-2α (8). During tumor progression, hypoxia develops when tumor growth exceeds the ability of available vasculature to supply tumor cells with oxygen and nutrients (9). Tumor hypoxia is one of the worst prognosis factors for survival (10). Multiple studies have demonstrated that hypoxia condition is an important cause of promoting the proliferation and angiogenesis, chemoradiotherapy resistance of cancer cells, migration, invasion, and metastatic growth at distant sites, which are significant obstacles to treatment and cause significant adverse prognostic ramifications (11–13). In LUAD, the upregulation of multiple hypoxic-related genes has been reported to have a significant prognostic value, such as *HIF-1α* (14), *NLUCAT1* (15), *TRB3* (16), *GBE*1 (17), and *CCL28* (18), highlighting the potential therapeutic value of targeting hypoxic-related genes, and the prognostic assessment and treatment decision. In view of the crucial role of hypoxic in the LUAD, hypoxic-related genes may be an effective way to predict the prognosis and therapeutic benefit for LUAD patients, individually.

In the present study, a range of machine learning and bioinformatic approaches were combined and used to excavate and screen robust candidate genes to explore in depth the potential correlation between hypoxia and LUAD, followed by the establishment and verification of an individualized hypoxia-derived signatures (**Figure 1**). Our findings provide further insight into the role of hypoxic-related genes in LUAD and provide a comprehensive demonstration that they are promising prognostic markers and therapeutic targets for LUAD.

METHODS

Patient Samples

In March 2022, three LUAD tissues and their paired non-tumorous lung tissues were collected for quantitative real-time PCR (qRT-PCR) detection from the Ren Ji Hospital. All specimens were evaluated for histological features by pathologists according to criteria. The investigators obtained approval from the Ethics Committee of the Ren Ji Hospital, affiliated Shanghai Jiao Tong University School of Medicine to conduct the study (Ethics Approval Number KY2021-220-B). All procedures were carried out in accordance with the Declaration of Helsinki and relevant Chinese policies.

RNA Isolation and Quantitative Real-Time PCR

Trizol reagent (Spark Jade, Qingdao China) was used to extract the nucleic acids from three pairs of LUAD tissues and their paired normal tissues according to the manufacturer's

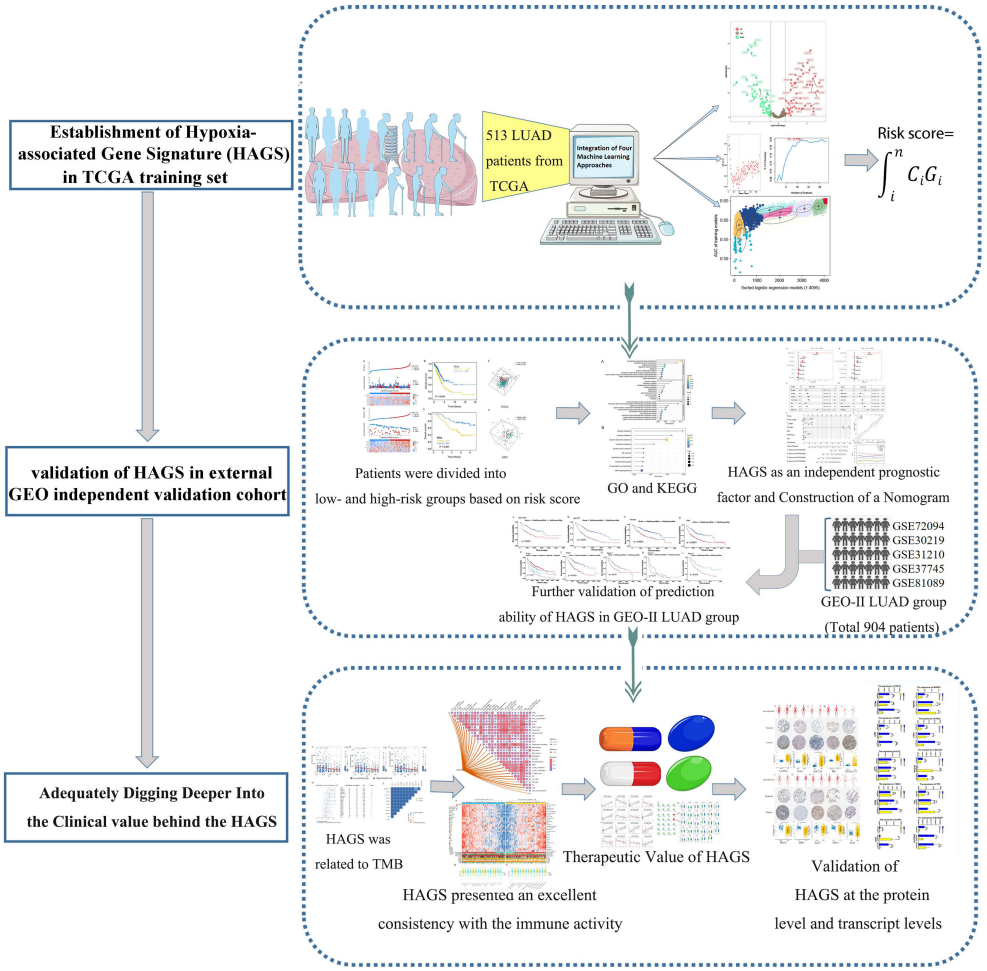

FIGURE 1 | Flowchart for developing an individualized hypoxia-associated gene-based prognostic signature for LUAD.

instructions. Then, qRT-PCR reactions were performed with 2xHQ SYBR qPCR mix (ZOMANBIO, Beijing, China) by using the 7500 fast real-time PCR system ((Applied Biosystems, USA). The primers of 10 selected hypoxia genes in this study are outlined in **Table 1**.

Date of Acquisition

Gene expression profiles (fragments per kilobase million, FPKM normalized) and the corresponding clinical parameters of 572 primary LUAD patients and healthy people were downloaded from The Cancer Genome Atlas–Lung Adenocarcinoma (TCGA-LUAD) (https://portal.gdc.cancer.gov/) and were used as the training set. Datasets GSE13213 from the microarray datasets generated by Agilent-014850 Whole Human Genome Microarray 4x44K G4112F (Probe Name version) were downloaded from Gene Expression Omnibus (https://www.ncbi.nlm.nih.gov/geo/query/acc.cgi?acc) and was used as external independent validation set, including 117 LUAD patients. In addition, five datasets, namely, GSE72094, GSE30219, GSE31210, GSE37745, and GSE81089 from the same chip platform (Affymetrix Human Genome U133 Plus 2.0 Array) were integrated into a new cohort and were used as the other validation set, namely, GEO-II LUAD group, which contained a total of 904 I–IV LUAD patients (I, 557; II, 178; III, 99; IV, 70) meeting the criterion. Batch effects from the five independent datasets above were corrected by using the ComBat function (sva R package).

Construction of Gene Signature by Integrating Four Machine Learning Algorithms

A total of 572 transcriptome data from TCGA were divided into 513 LUAD tumors group and 59 normal tissues group. The R package DESeq2 was applied to perform the differential expression analysis of hypoxia-related gene between tumors group and normal tissues group, followed by plotting the volcano plots for differentially expressed hypoxia-related gene using R package ggplot2. The hypoxia-related differentially expressed genes (DEGs) were defined as $|\log2 \text{ fold change}| > 0.05$, $p < 0.05$. Then, dimensionality reduction was further

TABLE 1 | The primers of 10 selected hypoxia genes.

Gene name	Primer sequences	
	Forward Primer	Reverse Primer
GAPDH	GGAGCGAGATCCCTCCAAAAT	GGCTGTTGTCATACTTCTCATGG
PGK1	TGGACGTTAAAGGGAAGCGG	GCTCATAAGGACTACCGACTTGG
SLC2A5	GAGGCTGACGCTTGTGCTT	CCACGTTGTACCCATACTGGA
TPI1	CTCATCGGCACTCTGAACG	GCGAAGTCGATATAGGCAGTAGG
B4GALNT2	CACTGAACACCCTTGCTGATG	CAGCTTCCGGTCACTGGTAG
TPST2	AGTCCTCGGTCTACCTGTCG	GGCGTACATCACCTCGATGG
FBP1	CGCGCACCTCTATGGCATT	TTCTTCTGACACGAGAACACAC
KLF7	AGACATGCCTTGAATTGGAACG	GGGGTCTAAGCGACGGAAG
SDC4	GGACCTCCTAGAAGGCCGATA	AGGGCCGATCATGGAGTCTT
PKP1	TTTGCCGTCGGACCAAAAGAT	GAACCTCGATTGGAGTGGCTC

performed on differentially expressed hypoxia-related gene in LUAD tumors based on survival data by using the weighted random forest and sliding windows sequential forward feature selection (SWSFS) method, which was realized by R package ranger, a weighted version of random forest. The SWSFS method was used to identify the top important hypoxia-related DEGs by increasing DEGs one by one to the random forest model by the order of variable importance score (VIS). In the RF model, the ordinate (left) represents the out of bagging (OOB)' error rate, which measured the performance of different gene combinations consisting of a specific number of hypoxia-related DEGs. In the RF model having the lowest error rate, the current hypoxia-related DEGs combination was screened out for further analysis.

To enhance the accuracy and reliability of the established HAGS, we make further screening of hypoxia-related DEGs by training the XGBoost model using the xgboost package in R language. The XGBoost model was used to analyze the contribution of each hypoxia-related DEGs to survival state in 513 LUAD tumors group; the top-ranked hypoxia-related DEGs with the VIS value of 0.01above were screened out for further analysis. After screening by two methods mentioned above, we used the intersection of RF model and the XGBoost model to identify candidate genes, followed by employing the support vector machine–recursive feature elimination (SVM–RFE) algorithms (19). SVM–RFE has been widely used to rank features and select the most significant features subset for classification. In this study, the hypoxia-related DEGs subset with the best accuracy for classifying survival status was chosen to be the HAGS by the mean of fivefold cross-validation in the SVM predictive model.

Finally, the HAGS subset screened by three models above was determined by Gaussian mixture model (GMM), which is a very feasible approach and has a good hierarchical agglomerative clustering performance (20). Logistic regression analysis was used to construct combined models of different gene sets combinations to predict survival status in LUAD patients. The area under the curves (AUCs) were calculated by constructing the receiver operating characteristic (ROC) curves to assess the predictive value of all logistic regression models. Then, the GMM was used to cluster gene sets according to the AUC values of all different gene sets combinations. The gene sets combinations with the highest AUC will be selected and determined as the final HAGS subset to establish HAGS. Ultimately, the risk score of HAGS was determined through the optimal parameter of logistic regression analysis and was calculated by the formula: risk score $= \int_i^n C_i G_i$, where C_i represents the coefficient of gene i, and G_i is the normalized expression value of gene i.

Validation of the HAGS

The risk score formula above was used to calculate risk scores for each LUAD patient. Then, the median score of the LUAD individuals in the training and external validation groups was used as a risk cutoff value to classify all LUAD individuals into the high- and low-risk groups. The survival status, hypoxia-associated gene expression, and overall survival (OS) time was compared between the two subgroups *via* Kaplan–Meier analysis, respectively. The gene expression levels were normalized by log transformation for each gene. Principal component analysis (PCA) was performed to observe the clustering conditions of LUAD individuals in different risk levels, visualized by the "scatterplot3d" R package.

Gene Ontology and Kyoto Encyclopedia of Genes and Genomes Pathway Enrichment Analyses

Next, the co-expression genes of differential hypoxia-associated gene between high- and low-risk LUAD patients were chosen to perform Gene Ontology (GO) and Kyoto Encyclopedia of Genes and Genomes (KEGG) analyses, which was conducted by using the clusterProfiler package. Enrichment significance thresholds were set at $p < 0.05$ and false discovery rate (FDR) <0.05. GO analysis was used to map all DEGs to GO terms in the GO database (http://www.geneontology.org/) to analyze the main functions of the DEGs. The KEGG pathway database (www.genome.jp/kegg/) is a synthetic database, which was used to analyze the biochemical pathways of the DEGs of interest.

Independent Prognostic Factors Analysis of Risk Score and Construction of a Nomogram Prediction Model

After the extraction of clinical information (age, grade, and stage) of LUAD patients in the TCGA and GSE 13213 cohort, univariate and multivariate prognostic analyses were used to

demonstrate whether the risk score could be an independent prognostic factor. Based on the multivariate Cox regression analysis for risk score and other clinicopathological factors by the rms R package, a clinically adaptable nomogram prediction model was established to predict the survival probability of 513 LUAD individuals in 1, 3, 5, and 8 years from the TCGA group. Then, the calibration analysis and time-dependent ROC (tROC) curve were used to evaluate the prognostic value of nomogram for LUAD patients.

Correlation Analyses Between HAGS and the Immune Activity

The single-sample gene set enrichment analysis (ssGSEA), an application and extension of Gene Set Enrichment Analysis (GSEA) algorithm, calculates separate enrichment scores for each pairing of a sample and gene set. To explore the relationship between the HAGS and the immune activity, we uploaded the gene expression matrix data of LUAD patients from TCGA. For 513 LUAD patients, the infiltration levels of 16 types of immune cells and the activity of 13 immune-related pathways were quantified using enrichment scores calculated by ssGSEA algorithm in R package gsva. Then, the Spearman correlation analyses were performed to evaluate the correlation between the levels of risk score and the infiltration levels of immune cells and immune-related pathways by R packages, "ggcor." Similarly, the Spearman correlation of infiltration levels for different immune cells and immune-related pathways were also performed to analysis possible relationships between them.

In addition, based on expression profiling data retrieved from the TCGA database, the ssGSEA was used to quantify the 29 infiltrating immune cells types and immune-related pathways of 513 LUAD in the training set, which was divided into 256 high-risk score groups and 257 low-risk score groups based on the risk score. Then, statistical difference between the two groups was compared by the Wilcoxon test. The mutation status of TP53, KRAS, and epidermal growth factor receptor (EGFR), which was calculated by package "maftools," was also displayed to gain insights into the tumor mutation burden between low- and high-risk groups stratified by the risk score. The clinical features (gender and survival) and TNM stage of patients between the two groups were also illustrated as an annotation.

Analysis of the Tumor Mutation Status in the Low and High HAGS Risk Score Groups

The tumor mutational burden (TMB) is defined as the total number of somatic/acquired mutations per coding area of a tumor genome (Mut/Mb) (21) and calculated as the number of non-synonymous protein coding variants divided by the total sequenced genome length. To inquire about the association between the TMB and HAGS risk, we next compared the tumor mutation status between the low and high HAGS risk score groups. First, the RNA-seq data of 513 LUAD samples in the TCGA group was annotated by the annotation files (gencode.v22.annotation.gene.probeMap). Then, the mutational data of TCGA samples was identified and matched against the somatic point mutation database (Genomic Data Commons Data Portal, https://portal.gdc.cancer.gov/), which was used to check for the presence of mutation in large populations of control individuals. Significantly mutated genes ($p < 0.05$) between the low and high HAGS risk groups and the interaction effect of gene mutations were analyzed by maftools; only genes mutating more than 50 times in at least one group will be considered. The statistical significance test for the proportion of mutation was evaluated by one-sided z-test and two-sided Chi-square, and $p < 0.05$ was considered as significant.

Correlation Analysis Between Hypoxia-Associated Gene Expression and Drug Sensitivity

The drug sensitivity data used in our study were downloaded from the CellMiner database (https://discover.nci.nih.gov/cellminer/home.do). The CellMiner database includes rapid access to and comparison of gene expression levels of 360 microRNAs, 22,379 genes, and 20,503 compounds incorporating 102 Food and Drug Administration (FDA)-approved drugs (22, 23). First, the gene expression and drug sensitivity data from the same sample were downloaded. Then, the drug sensitivity data were filtered after clinical trials verification and FDA standard certification. Eventually, we combined the 10 hypoxia-associated gene expressions with the retained drug sensitivity data to perform the Spearman correlation analysis. Higher Spearman Cor value indicates a stronger correlation.

Chemotherapeutic Response Prediction

Based on the largest publicly available pharmacogenomics database [the Genomics of Drug Sensitivity in Cancer (GDSC), https://www.cancerrxgene.org/], we further predicted the chemotherapeutic response for each patient with high and low risk in the TCGA group to evaluate the value of hypoxia-derived signatures for LUAD treatment in the clinic. The half-maximal inhibitory concentration (IC50) of 28 antitumor drugs recommended by The American Joint Committee on Cancer (AJCC) guidelines for cancer treatment were calculated using the R package "pRRophetic," which could simultaneously construct prediction models using transcriptome and drug sensitivity data derived from GDSC and apply it to the transcriptome information of 513 LUAD samples to generate predicted drug IC50s for each sample. Finally, the difference in the IC50s of 30 common antitumor drugs between the high- and low-risk groups was compared using the Wilcoxon signed-rank test. The prediction process was implemented by R package "pRRophetic" where the samples' half-maximal inhibitory concentration (IC50) was estimated by ridge regression, and the prediction accuracy was evaluated by 10-fold cross-validation based on the GDSC training set (24).

External Validation of Proteins and Transcription Levels of the HAGS

Human Protein Atlas antibody-based protein expression data are freely available online from the Human Protein Atlas (HPA)

(www.proteinatlas.org) (25), a comprehensive database that provides the information on the tissue and cell distribution of 26,000 human proteins. The protein expressions of 10 hypoxia-associated genes (*TPST2*, *SDC4*, *KLF7*, *SLC2A5*, *TPI1*, *FBP1*, *B4GALNT2*, *PGK1*, *PKP1*, and *GAPDH*) in normal and LUAD tumor tissues were investigated based on the results of specific antibodies obtained from HPA. The human model diagrams illustrating the organ biodistribution of 10 genes in the human body were generated using gganatogram, an R package for modular visualization of anatograms and tissues based on ggplot2.

RESULTS

Construction and Validation of HAGS by Integrating Four Machine Learning Algorithms

To improve the reliability, validity, and accuracy of HAGS, we integrated four different machine learning algorithms to select the most reliable hypoxia-associated genes set. First, the hypoxia-related DEGs between tumors group and normal tissues group were illustrated with a volcano plot (**Figure 2A**), which was derived from "DESeq"-based differential gene expression analysis. Second, supervised random forest (RF) models were used to identify the top important hypoxia-related DEGs from the selected hypoxia-related DEGs (**Figure 2B**). Using RF–OOB algorithm, the subset of DEGs with the minimal value of OOB error was selected to be the optimal feature. Meanwhile, the top-ranked hypoxia-related DEGs were also generated by using the XGBoost algorithm based on the contribution (gain) of each hypoxia-related DEG to survival state (**Figure 2C**). Third, the intersection of the random forest model and the XGBoost model were analyzed by SVM–RFE algorithms to further screen gene set with the best accuracy for classifying survival status of LUAD patients (**Figures 2D, E**). Finally, from all different gene sets combinations selected through models above, the GMM was used to determine the final hypoxia-associated genes signature subset (**Figure 2F**), including *TPST2*, *SDC4*, *KLF7*, *SLC2A5*, *TPI1*, *FBP1*, *B4GALNT2*, *PGK1*, *PKP1*, and *GAPDH*. Based on the expression of these candidate genes, the risk score of HAGS for each patient in TCGA and GEO groups was calculated by the formula: $\text{Risk score} = \int_{i}^{n} C_i G_i$, where Ci represents the coefficient of gene i, and Gi is the normalized expression value of gene i.

After each patient received a risk score according to the personalized formula of HAGS above, we divided patients in the TCGA training group into low-risk (n = 257) and high-risk groups (n = 256) by using the median risk score as the threshold value. As show in **Figure 3A**, according to the median, all patients in the TCGA-LUAD group were distinctly stratified into low- and high-risk groups with the increasing risk score. By displaying the risk scores, survival status, and the expression of 10 hypoxia-associated genes in a dot plot or heat map, we found that patients with high-risk scores had higher expression of *PKP1*, *B4GALNT2*, *KLF7*, *GAPDH*, *TPI1*, and *PKP1*. Kaplan–

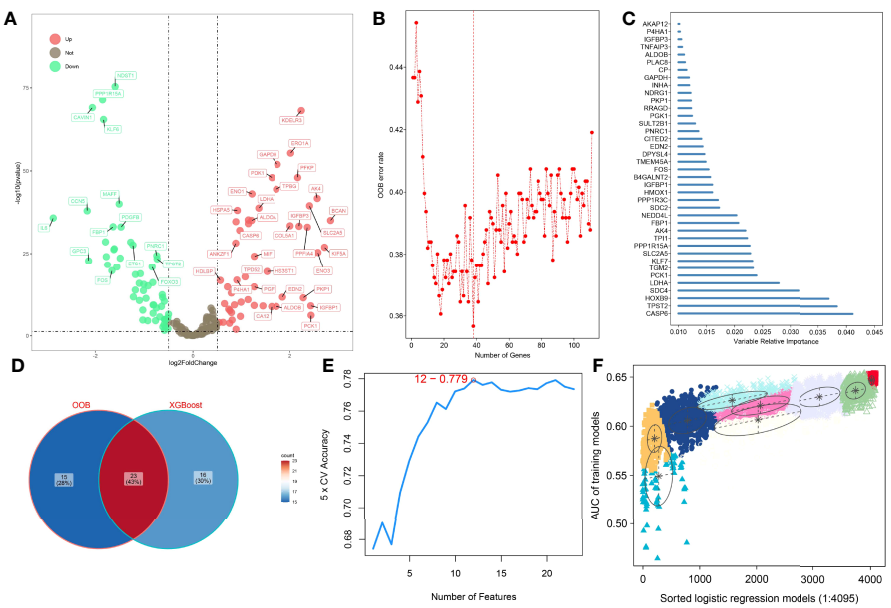

FIGURE 2 | Four machine learning algorithms were integrated to establish the HAGS. **(A)** The DEGs between the tumors group and normal tissues group were illustrated with a volcano plot. **(B)** Supervised random forest models were used to identify the top important hypoxia-related DEGs. **(C)** Top 39 features selected using XGBoost and the corresponding variable importance score. x-Axis indicates the importance score, which is the relative number of a variable that is used to distribute the data; y-axis indicates the top 39 weighted variables. **(D)** The intersection of the random forest model and the XGBoost model. **(E)** The SVM–RFE algorithms were used to further screen gene set. **(F)** The GMM was used to determine the final HAGS.

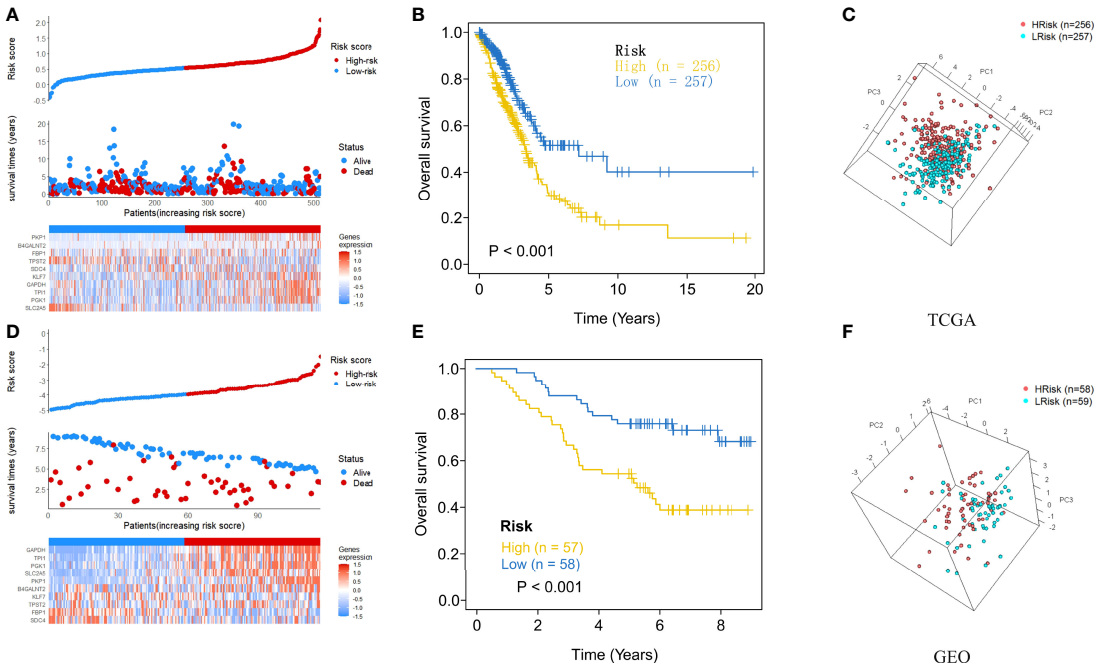

FIGURE 3 | The risk score plots, OS status plots, and heatmaps of these 10 hypoxia-associated genes in the TCGA and GEO groups. **(A)** Risk score distribution, OS status, and the expression of 10 hypoxia-associated genes of LUAD patients in TCGA group. Red means high risk, blue means low risk. **(B)** Kaplan–Meier plot found that the HAGS divided patients into high- and low-risk groups with significant difference in OS. **(C)** Based on PCA analysis, the 513 LUAD patients in TCGA were distributed into two sections according to the risk score. **(D–F)** Similar results were also found in the GEO group. OS, overall survival; PCA, principal component analysis.

Meier survival curves presented a significantly higher number of deaths in the high-risk group than in the low-risk group ($p < 0.0001$, **Figure 3B**), suggesting that the newly developed HAGS was able to effectively predict survival. Moreover, PCA analysis revealed that the individuals in different risk levels could be distinctly distributed into two sections based on the risk score (**Figure 3C**). Similarly, patients in GEO were also divided into low-risk (n = 59) and high-risk groups (n = 58), and the results of Kaplan–Meier analysis and PCA were consistent with the results of the TCGA-LUAD group mentioned above (**Figures 3D–F**).

Enrichment Analyses of GO and KEGG Pathways

To evaluate the functional and biological implications of differentially expressed genes (DEGs) and further recognize important functional phenotypes of these genes between high- and low-risk LUAD patients, GO and KEGG pathways enrichment analyses of DEGs were performed, respectively. GO described DEGs in terms of their related biological processes, cellular components, and molecular function. Result from GO enrichment analyses illustrated that the DEGs were enriched in 30 GO terms, including 10 terms in biological processes, 10 terms in cellular component, and 10 terms in molecular function (**Figure 4A**). Additionally, 10 significant KEGG pathways were identified (**Figure 4B**), including one most significant types of pathways, namely, arginine and proline metabolism, proved to be an important metabolism pathway for lung cancer (26).

Evaluation of Risk Score as an Independent Prognostic Factor for LUAD and Construction of a Nomogram for OS Prediction in LUAD Patients

After the extraction of clinical information (age, grade, and stage) of LUAD patients in the TCGA and GEO cohort, univariate and multivariate Cox regression analyses were performed to demonstrate whether the risk score derived from the HAGS model could serve as an independent prognostic factor for OS in LUAD patients. In the univariate Cox, the risk score was significantly associated with OS in both the training cohort from TCGA group and external validation dataset from GEO ($p < 0.001$, **Figures 5A, B**). The multivariate Cox regression analyses also indicated that the risk score was also proven to be an independent factor predicting OS in both TCGA and GEO cohorts ($p < 0.001$, **Figures 5C, D**).

Next, in order to acquire a more accurate quantitative method for disease progression and survival probability of LUAD patient, we constructed a nomogram to estimate the 1-, 3-, 5-, and 8-year survival probabilities of 513 patients with LUAD by integrating the risk score and different clinicopathological factors, including sex, age, risk score, tumor stage, T stage (tumor size), and N stage (lymph node metastasis) (**Figure 5E**). The calibration plots of the

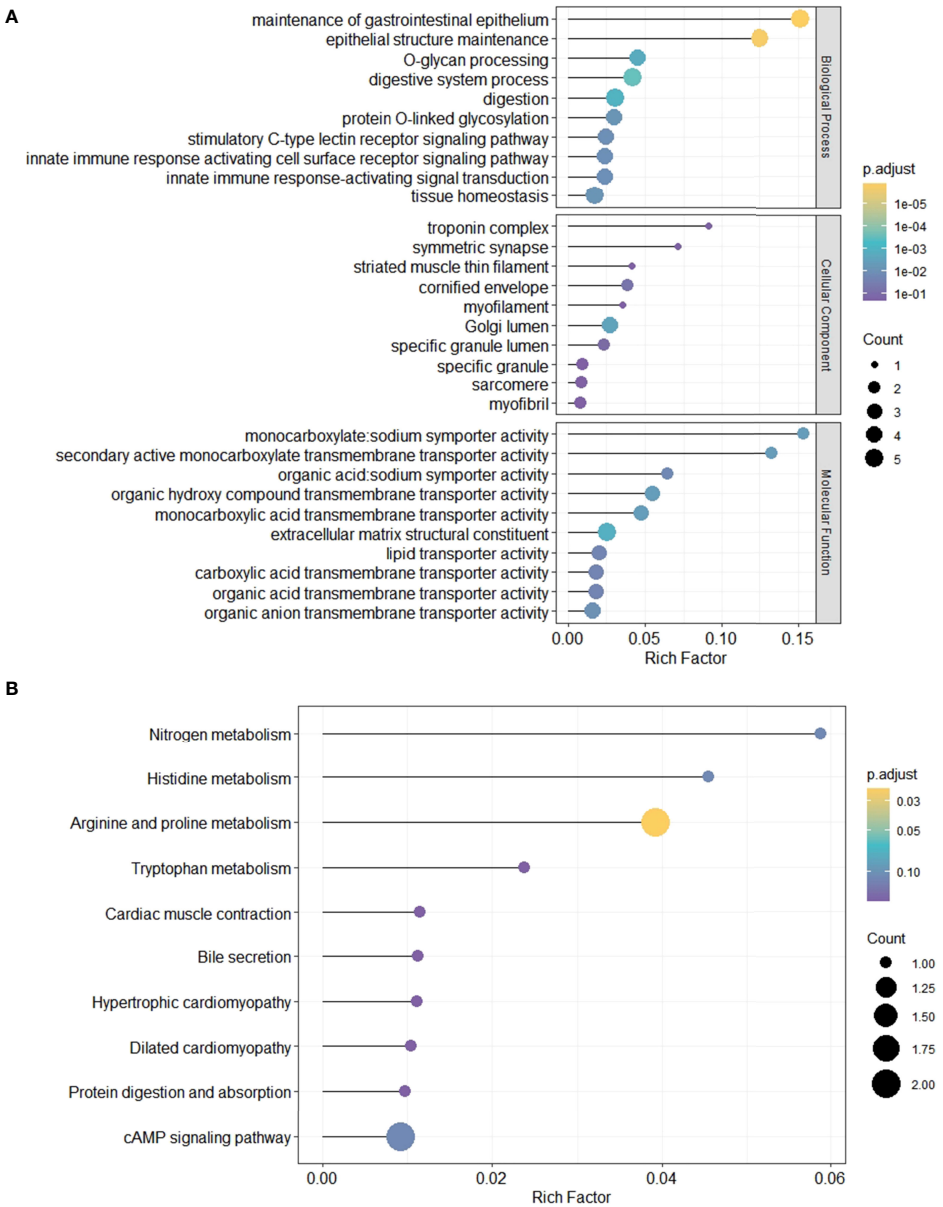

FIGURE 4 | GO and KEGG pathway enrichment analyses of DEGs between high- and low-risk LUAD patients. *p*-value: purple, high (bottom); yellow, low (top). The size of the dots represents the number of DEGs. **(A)** GO analysis results. **(B)** KEGG pathway enrichment analyses results. *p*.adjust, adjusted *p*-value.

nomogram for 1-, 3-, 5-, and 8-year survival (**Figure 5F**) indicated that the OS estimated by the nomogram was extremely closely to the actual OS. Time-dependent ROC (tROC) curves of 5-year OS showed that the nomogram exhibited the most stable and powerful ability for predicting survival, with an average AUC above 0.7, much better than other clinicopathological factors (**Figure 5G**). These results further support the powerful discriminative ability of the HAGS in conjunction with clinicopathological factors for predicting survival in LUAD.

Association Between HAGS Risk Score and the Clinical Characteristics of LUAD

Given the diversity and complexity of different LUAD cases in clinical samples, we further investigated the distribution of the HAGS risk score in LUAD patients with different gender, age, survival status, and TNM stage. We found that there is no difference in LUAD patients with different TNM stage and gender in TCGA group (**Figures 6A–E**), only a significant difference was detected between patients with different survival status ($p < 0.05$, **Figure 6F**). In the GEO-II LUAD group, the

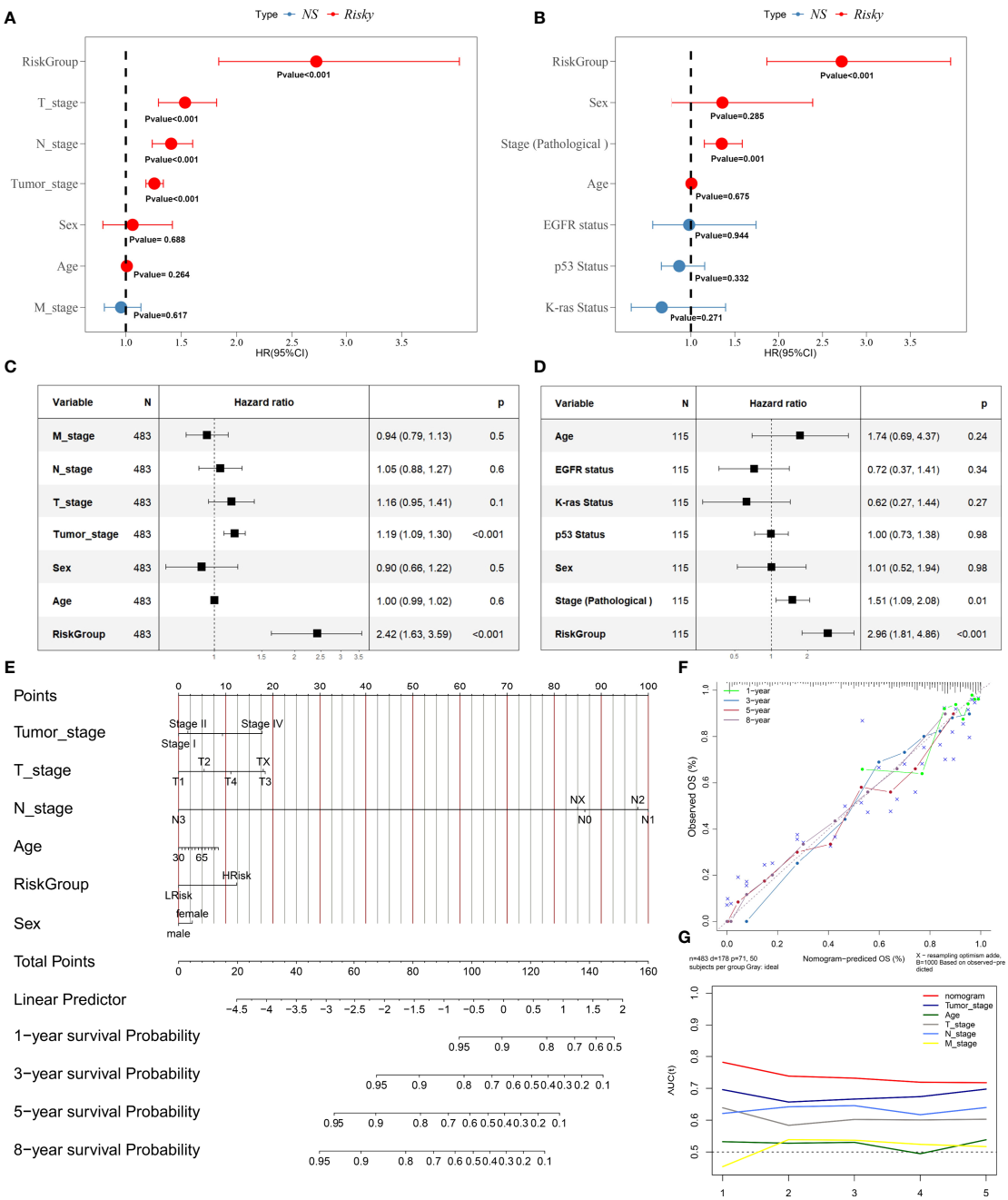

FIGURE 5 | Evaluation of risk score as an independent prognostic factor and construction of nomogram for predicting overall survival in LUAD patients. **(A–D)** Results of the univariate and multivariate Cox regression analyses regarding OS in the TCGA and GEO. **(E)** Construction of the nomogram was based on sex, age, risk score, tumor stage, T stage, and N stage in the TCGA cohort. **(F)** Calibration plot analysis indicated that the nomogram showed a high accuracy of survival prediction. **(G)** tROC analysis demonstrated that the nomogram had the most powerful capacity for survival prediction by comparing with other clinicopathological factors.

elderly (>60), male, and dead populations all had significantly higher risk score than those in the younger (≤60), female, and alive populations, respectively ($p < 0.05$, **Figures 6G–I**).

Then, in order to explore whether the 10-gene signature could be widely and accurately used to determine the survival conditions in different clinical characteristics, the Kaplan–Meier curves analysis was conducted in different subgroups with different age (≤60 and >60), gender (male and female), and stage (I–IV) from the GEO-II LUAD group. The results indicated that individuals in the low HAGS risk group had significantly better OS than individuals in the high HAGS risk group for all subgroups ($p < 0.001$, **Figures 7A–H**). These results

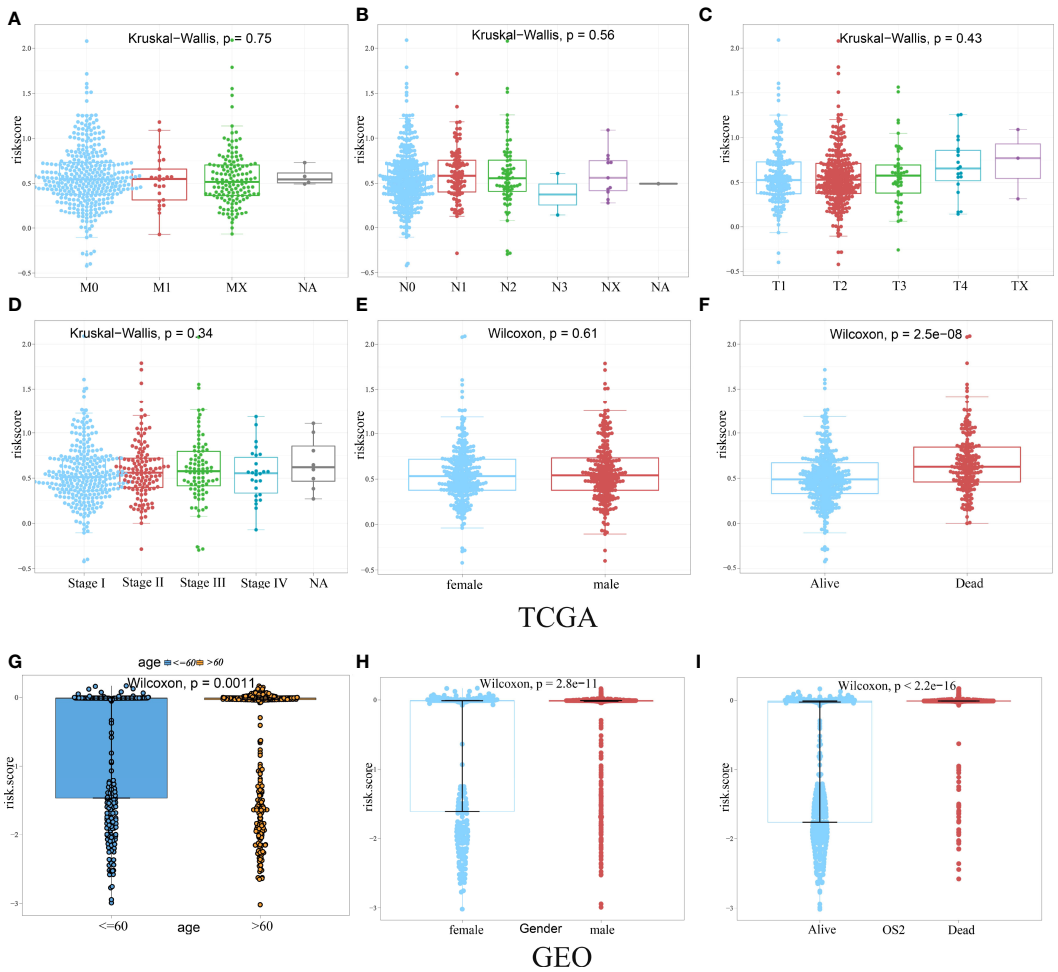

FIGURE 6 | Difference analysis of the distribution of HAGS risk score in different TNM stage **(A–D)**, age **(G)**, gender **(E, H)**, and survival status **(F, I)**. Statistical difference of three or more groups was compared by the Kruskal–Wallis test and that of two groups was compared by the Wilcoxon test.

also demonstrated that the hypoxia-associated signatures had reliable ability for predicting the OS of different subgroups, regardless of the difference in age, gender, and stage.

Correlation of TMB With Hypoxia-Associated Signatures in LUAD

We also checked for the somatic mutation in the Genomic Data Commons (GDC) data portal of the National Cancer Institute (https://portal.gdc.cancer.gov/) to investigate HAGS risk-related mechanisms based on TMB in LUAD. A comparison of cumulative mutant frequency between samples of the low- and the high-HAGS risk groups showed that less somatic mutations were observed in the high-HAGS risk group, including non-synonymous and synonymous mutations (**Figures 8A–C**). Concurrently, maftools analysis results showed that 22 mutated more frequently in LUAD patients in the low HAGS-risk group, including *RYR2*, *KEAP1*, *PCDH11X*, *CSMD3*, *ADAMTS12*, *SI*, *CACNA1E*, *ASTN1*, *LRP1B*, *RYR3*, *APOB*, *XIRP2*, *TNR*, *ZFHX4*, *PCLO*, *TP53*, *SPTA1*, *FAT3*, *CDH10*, *DNAH9*, *TTN*, and *FLG* (**Figure 8D**). Moreover, significant co-occurrences were observed among these mutated genes (**Figure 8E**).

Relationship Between HAGS and the Immune Activity

Correlation analyses between HAGS and the immune activity revealed that the risk scores in 513 LUAD patients were positively correlated with the levels of the APC co-inhibition, APC co-stimulation, B cells, CCR, $CD8^+$ T cells, checkpoint, cytolytic activity, DCs, HLA, inflammation promotion, macrophages, major histocompatibility complex (MHC) class I, neutrophils, parainflammation, pDCs, T-cell co-inhibition, T-cell co-stimulation, T-helper cells, Tfh, Th1 cells, tumor-infiltrated lymphocyte (TIL), and Treg ($p < 0.01$, **Figure 9**). The Spearman correlation of different immune cells revealed that the expression levels of checkpoint was positively correlated with the levels of infiltrating CCR, T-cell co-inhibition, and TIL, respectively; the expression levels of inflammation

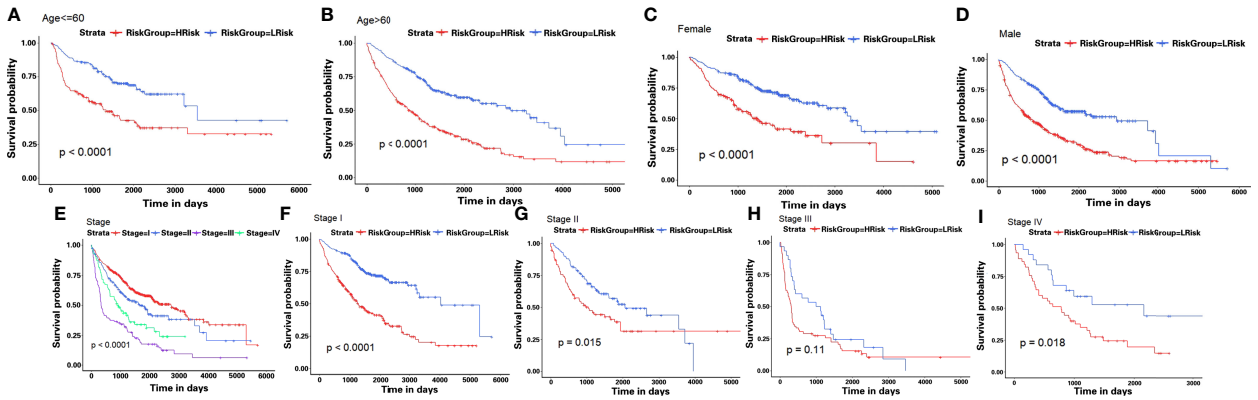

FIGURE 7 | Kaplan–Meier survival analyses of the HAGS risk score in different subgroups. **(A–I)** LUAD patients in the low-risk group showed a more promising OS than the high-risk group in all subgroups ($p < 0.001$).

promotion was positively correlated with the levels of $CD8^+$ T cells; TIL was positively correlated with the T-cell co-stimulation ($r \geq 0.90$). Those genes with strong correlations may also be functionally correlated, and future studies about hypoxia could incorporate them into existing knowledge.

Based on the ssGSEA, we further compared the enrichment scores of 16 types of immune cells and the activity of 13 immune-related pathways between the low- and high-risk groups in the TCGA cohorts. The comparison of the immune activity level between high- and low-risk groups in the TCGA dataset revealed that the high-risk subgroup generally showed lower activity of immune-related pathways and had lower levels of infiltration of immune cells, such as type I interferon (IFN) response, Th2 cells, cytolytic activity, MHC class I, T-cell co-stimulation, Th1 cells, CD8 T cells, parainflammation, Treg, checkpoint, inflammation promotion, and APC co-inhibition, than those in the low-risk group (**Figure 10**, $p < 0.05$), whereas only the levels

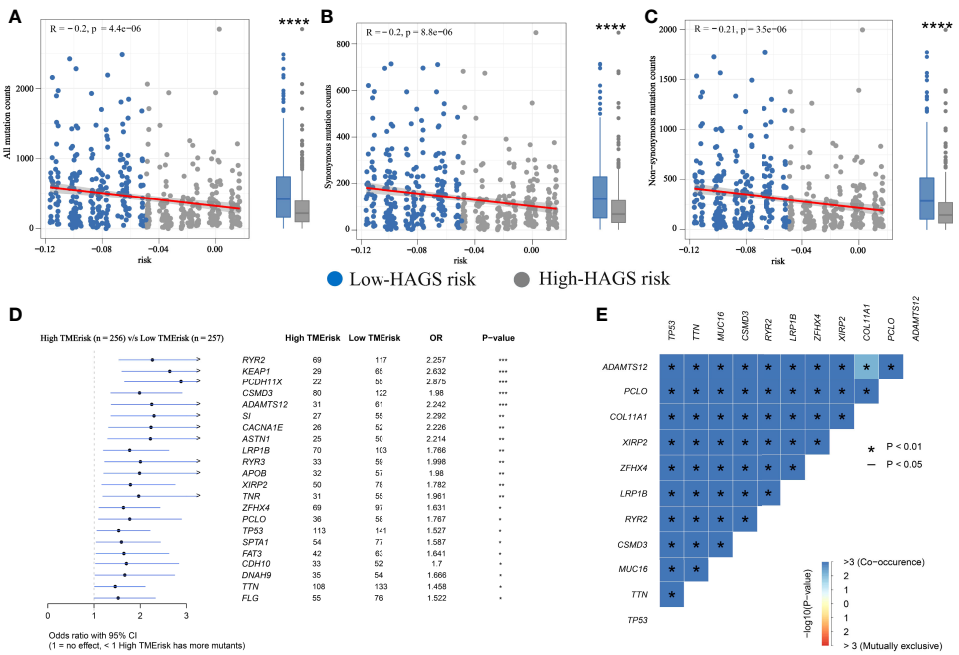

FIGURE 8 | Hypoxia-associated signatures were related to TMB. **(A–C)** Association between all mutation counts, synonymous mutation counts, non-synonymous mutation counts, and HAGS risk score and their distribution in the low and the high HAGS risk groups. **(D)** Forest plot of genes mutating differentially between the low and the high HAGS risk groups. **(E)** Interaction effect of genes mutating differentially between the low and the high HAGS risk groups. *p < 0.05; **p < 0.01; ***p < 0.001; ****p < 0.0001.

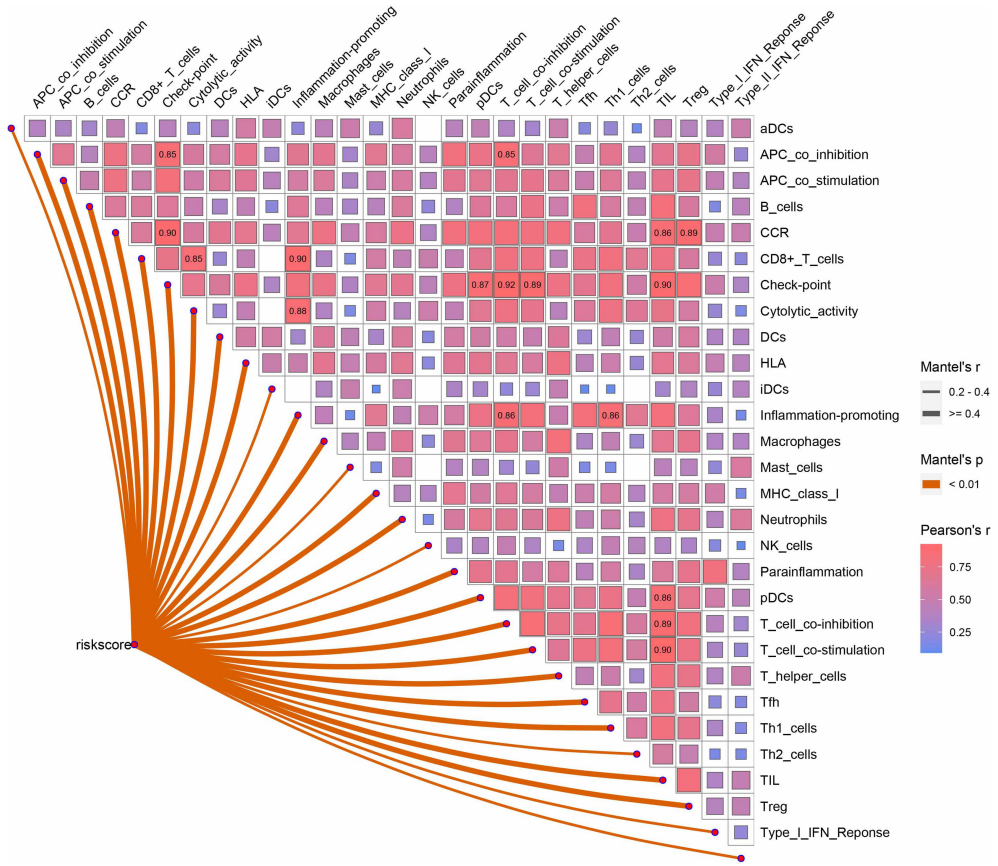

FIGURE 9 | Correlation between HAGS and immune cells infiltration. The correlation between risk score and specific immune cells is shown with solid lines; the line color is related to the *p*-value. The square colors represent Pearson correlation coefficients between different immune cells; only the Pearson r ≥0.85 is displayed.

of type II IFN response, B cells, macrophages, and mast cells in the high-risk group were significantly higher than those in the low-risk group, suggesting that the HAGS presented an excellent consistency with the immune activity.

Drug Sensitivity Analysis of Hypoxia-Associated Gene

Based on the analysis of the correlation between 10 hypoxia-associated genes and drug sensitivity, significant correlation was found between the expression levels of the 10 genes and drug sensitivity ($p < 0.001$, **Figure 11**). The higher the expression of FBP1, the stronger the drug sensitivity of fulvestrant, raloxifene, and LEE-011 ($p < 0.001$). The higher the expression of SDC4, the weaker the drug sensitivity of oxaliplatin, ifosfamide, carmustine, estramustine, etoposide, epirubicin, and nilotinib ($p < 0.001$). SLC2A5 expression had a significant positive relationship with the drug sensitivity of megestrol acetate and nandrolone phenpropio ($p < 0.001$). The higher the expression of PKP1 and TPST2, the stronger the drug sensitivity of calusterone and abiraterone, respectively ($p < 0.001$). The expression of KLF7 had a significant positive relationship with the sensitivity of bleomycin and lenvatinib ($p < 0.001$).

Comparison of the Sensitivity to Anticancer Drugs Between LUAD Patients With Different Hypoxia-Associated Risk Scores

To further explore the value of hypoxia-associated gene sets for therapy in LUAD patient, we estimate the IC50s of the 28 common anticancer drugs for each sample through the expression matrix of hypoxia-associated gene in each LUAD sample from TCGA group. A comparison between the high- and low-risk groups found that the IC50s of docetaxel and camptothecin (Campt), two FDA-approved chemotherapeutics for cancer treatment, were higher in patients with lower HAGS risk score, which suggests that increased HAGS risk was accompanied by increased sensitivity to docetaxel and Campt (**Figure 12**). In other words, these two drugs may have the therapeutic potential to treat LUAD patient with HAGS high risk.

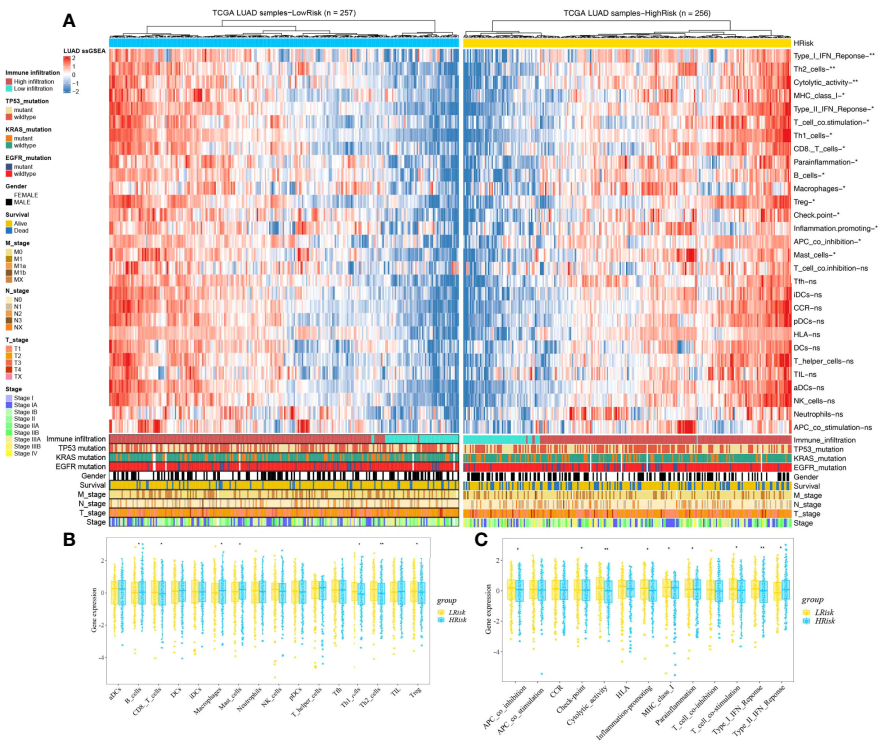

FIGURE 10 | Landscape of immune cell infiltrations in the low and high TME risk groups. **(A)** The heatmap shows the normalized scores of immune cell infiltrations. Blue represents cells with lower infiltration, and red represents cells with higher infiltration. **(B, C)** The statistical difference between the two groups was compared by the Wilcoxon test. *$p < 0.05$; **$p < 0.01$; ns, not significant. In the lower panel, mutation status of TP53, KRAS, and EGFR; gender, survival; TNM stage; and stage were annotated.

Validation of the Expression of the HAGS

To evaluate differences in hypoxia-associated gene expression at the protein level, images of immunohistochemistry (IHC) staining of protein expression in normal tissues and LUAD tumors tissues were downloaded from the HPA and analyzed. As showcased in **Figure 13**, the protein expression level of five of these genes (*GAPDH*, *PGK1*, *SLC2A5*, *TPI1*, and *B4GALNT2*) was prominently higher in LUAD cancers when compared to the normal tissue (*$p < 0.05$, **Figure 13**). Otherwise, four of these genes (*TPST2*, *FBP1*, *KLF7*, and *SDC4*) were expressed at a low level, and no difference in expression levels of PKP1were noted between normal tissues and LUAD tumors tissues.

Validation Experiment of Clinical Samples From LUAD Patients at the Gene Transcript Levels

Eventually, the expression level of 10 hypoxia-associated genes was verified at transcript levels. It is heartening to note that the expression level of all 10 hypoxia genes showed significant differences at least two paired samples of three LUAD tissues and the paired non-tumorous lung tissues (**Figure 14**).

DISCUSSION

As the most commonly diagnosed histological type of lung cancer, LUAD severely affects human health and possesses both extremely high morbidity and mortality in clinic (27). LUAD is the leading cause of cancer death worldwide, and its incidence is increasing worldwide (28). Notably, even at an early stage, LUAD patients also hold a high metastasis rate and present different prognosis (29). Studies investigating LUAD-associated genes may improve the prognosis, diagnosis, treatment, and prognosis assessment of LUAD patients. In the last few decades, a multitude of genes related to hypoxia have been identified and studied in various cancers (30–32). However, although numerous studies have explored the relationship between hypoxia and tumor formation, the deep-seated relationship between hypoxia-associated genes set and prognosis of LUAD patients remains quite limited.

In the present study, we developed a new HAGS (HAGS) by integrating four machine learning algorithms to predict clinical outcomes and therapeutic responses in LUAD patients, followed by performing internal and external validation for its performance in TCGA and GEO groups, respectively. Our results demonstrate that HAGS, as an independent prognostic

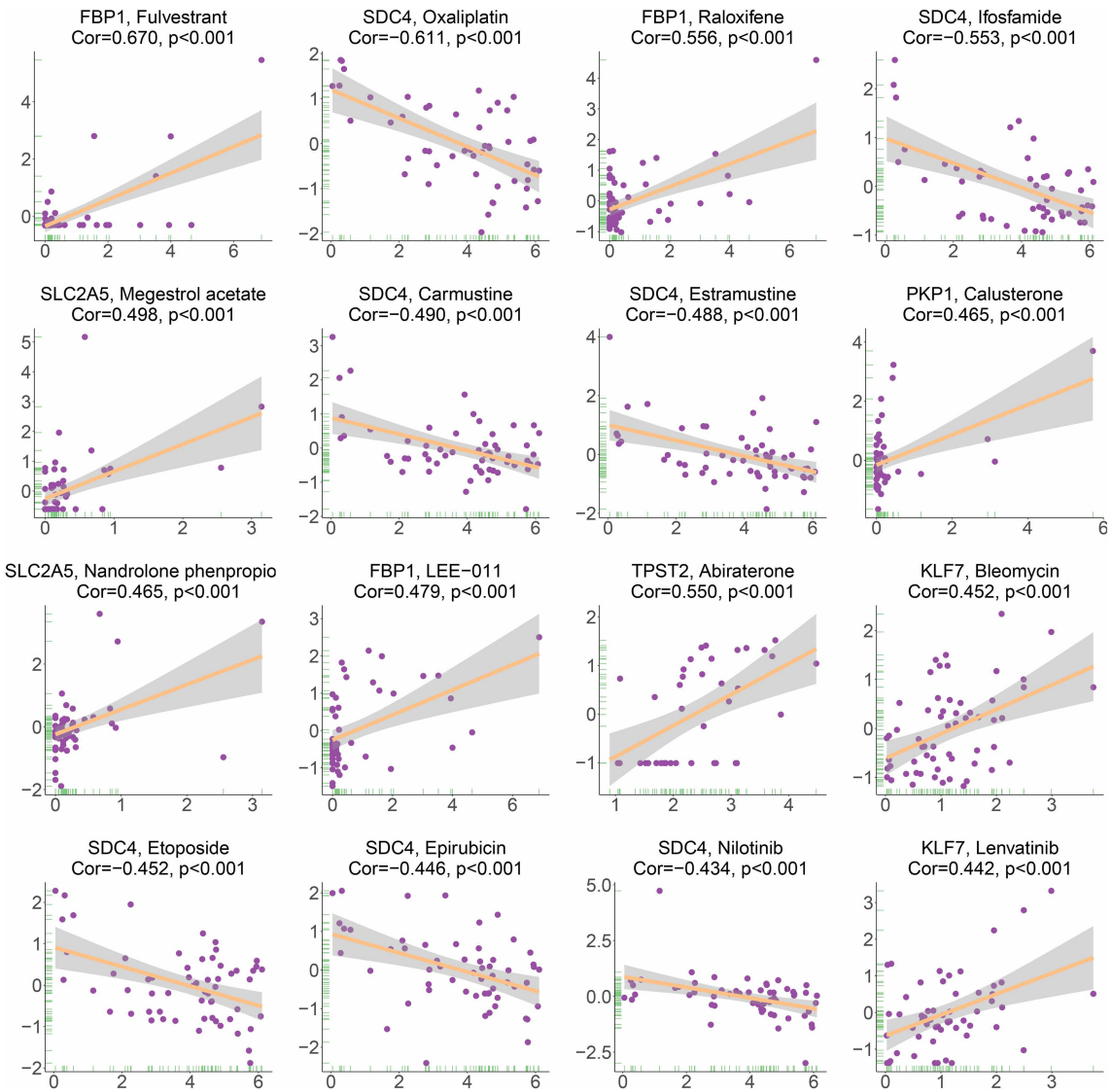

FIGURE 11 | Correlation between HAGS and drug sensitivity analysis.

factor, had a considerable effect on predicting the OS of LUAD patients. LUAD patients in the high HAGS risk group presented worse OS, lower TMB, and lower immune activity. Moreover, we revealed that the hypoxia-associated gene had a strong statistical association with the drug sensitivity of multiple FDA-approved drugs and had potential therapeutic value for LUAD patients based on the chemotherapeutic response prediction. Finally, validation studies on the expression levels of 10 hypoxia-associated genes were further analyzed to comprehensively confirm the reliability of selected gene set.

Unlike most previous studies that only use one single machine learning approach, our study established HAGS by integrating four different machine learning approaches to maximally improve the accuracy of our model. Finally, 10 hypoxia-associated genes (*TPST2*, *SDC4*, *KLF7*, *SLC2A5*, *TPI1*, *FBP1*, *B4GALNT2*, *PGK1*, *PKP1*, and *GAPDH*) were identified and combined as HAGS. Among these 10 hypoxia-associated genes, only *PGK1* and *GAPDH* are well-known hypoxia-regulated genes; the hypoxia-based function of *PGK1* and *GAPDH* have been adequately validated in lots of studies (33–36). Tyrosylprotein sulfotransferase 1 and 2 (*TPST-1* and *TPST-2*) are both responsible for the catalysis of tyrosine sulfation of chemokine receptors, such as *CXCR4* (Refs 93, 95, 96, 97, 98, 99) (37), it has previously been demonstrated that the *TPST 1* expression was significantly associated with lymph node metastasis and the TNM stage in patients with lung cancer and may be a negative prognostic biomarker of lung cancer (38, 39). However, the studies depicting the function of *TPST2* in cancer are extremely rare, so that the screen of this gene in our study indicates that its in-depth investigation in LUAD or other cancers should be performed to elucidate its underlying mechanisms. Sulfate proteoglycan syndecan-4 (*SDC4*)

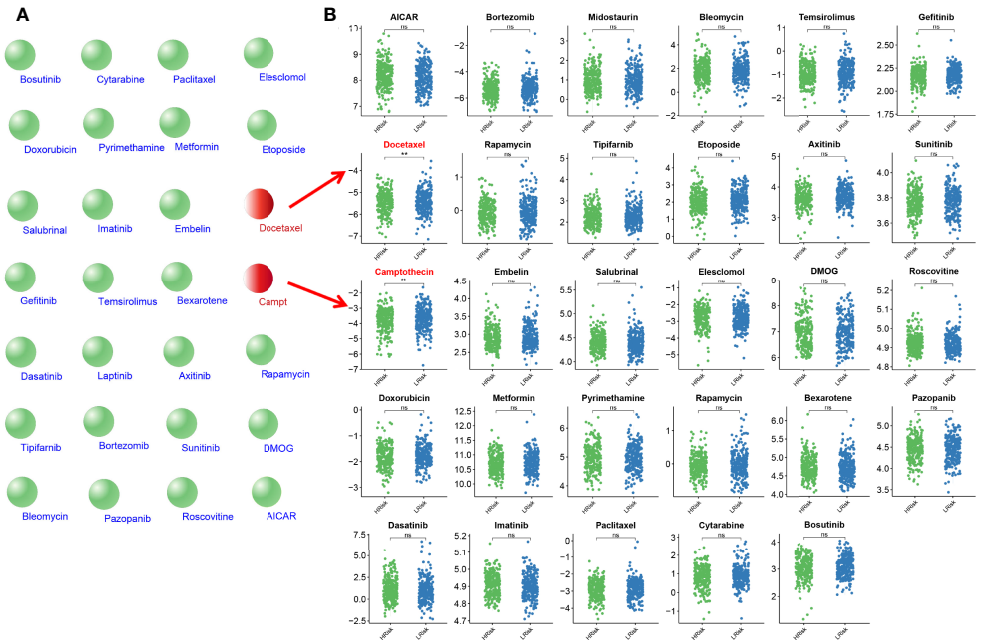

FIGURE 12 | Estimated drug sensitivity in LUAD patients with high and low HAGS risk. **(A)** The 28 common anticancer drugs may have therapeutic potential for LUAD patient. **(B)** The difference in the IC50s of 30 common antitumor drugs between the high- and low-risk groups was compared by using the Wilcoxon signed-rank test. $^{**}p < 0.01$; ns, not significant.

is an important member of Syndecans (SDCs) family, which is a family of transmembrane heparan sulfate proteoglycans (HSPGs) ubiquitously expressed on cell surfaces in mammals and plays a critical role in cell adhesion, migration, proliferation, differentiation, and angiogenesis through independent and growth factor mediated signaling (40). It has already been demonstrated that the *SDC4* exhibited multiple functions in tumor pathogenesis and progression (41), but the in-depth knowledge about *SDC4* is still very limited. For example, recently, Yang et al. for the first time identified *SDC4* as a direct anti-hepatocellular carcinoma (HCC) cellular target of bufalin in inhibiting cell proliferation, invasion, and angiogenesis (42). These indicated that the functional importance of *SDC4* in tumors, especially its roles in hypoxia, still needs more studies. Krüppel-like factor 7 (*KLF7*) is a member of the *KLF* family of zinc finger transcription factors and has antioncogenic functions in multiple cancer, such as human oral squamous cell carcinoma (OSCC) (43), glioma (44), gastric cancer (45), endometrial cancer (46), ovarian cancer (47), and non–small cell lung cancer (48). There is evidence that *KLF7* and hypoxia work together to influence cell apoptosis, but it is not yet fully understood how they will act together to affect tumor development and progression (49). *SLC2A5*, which promotes lung adenocarcinoma cell growth and metastasis by enhancing fructose utilization, was proven to be overexpressed in LUAD, and the expression was associated with prognosis (50). The result of IHC staining from the HPA also demonstrated that the protein expression of SLC2A5 was significantly overexpressed in LUAD tumors tissues compared to the normal tissues (**Figure 13C**). However, the regulation of *SLC2A5* in lung cancer has not been fully elucidated, especially when hypoxia is involved (50). *TPI1* (triosephosphate isomerase 1) was overexpressed in various types of cancers and might be induced by hypoxia in pan-cancer (51). *FBP1* (fructose-1,6-bisphosphatase) is known as a rate-limiting enzyme in gluconeogenesis, which is an important process in cell energy metabolism. The association between *FBP1* expression status and hypoxia had just been found in recent years, and relevant research is very limited (52). Tumor-hypoxia-related studies that are directly relevant to *B4GALNT2* and *PKP1* in hypoxia are few and far between.

Previous studies did not investigate these 10 hypoxia-related genes as a signature to predict the clinical outcomes of LUAD patients. A majority of these 10 hypoxia-related genes are involved in the complex regulation of progression in LUAD or other cancers. Considering the complexity of the genetic network, tumor progression is more likely to depend on the systematical interaction network based on a group of critical hypoxia-related genes rather than a single one. Therefore, the HAGS, that is, a comprehensive gene set combining 10 hypoxia-related genes, exhibited a powerful predictive prognostic capacity for LUAD patients. Univariate and multivariate Cox regression analyses both indicated that the HAGS was an independent prognostic factor in LUAD patients, more importantly, independently of age, gender, and stage (**Figure 7**). In addition, the independent and robust prognostic performance of HAGS was also confirmed by integrating the risk score and clinicopathological factors to construct a nomogram, which could be used to monitor the clinical outcomes of LUAD patients (**Figure 5**).

Recently, TMB is an emerging biomarker and has proved to be a potential and effective biomarker for independently predicting

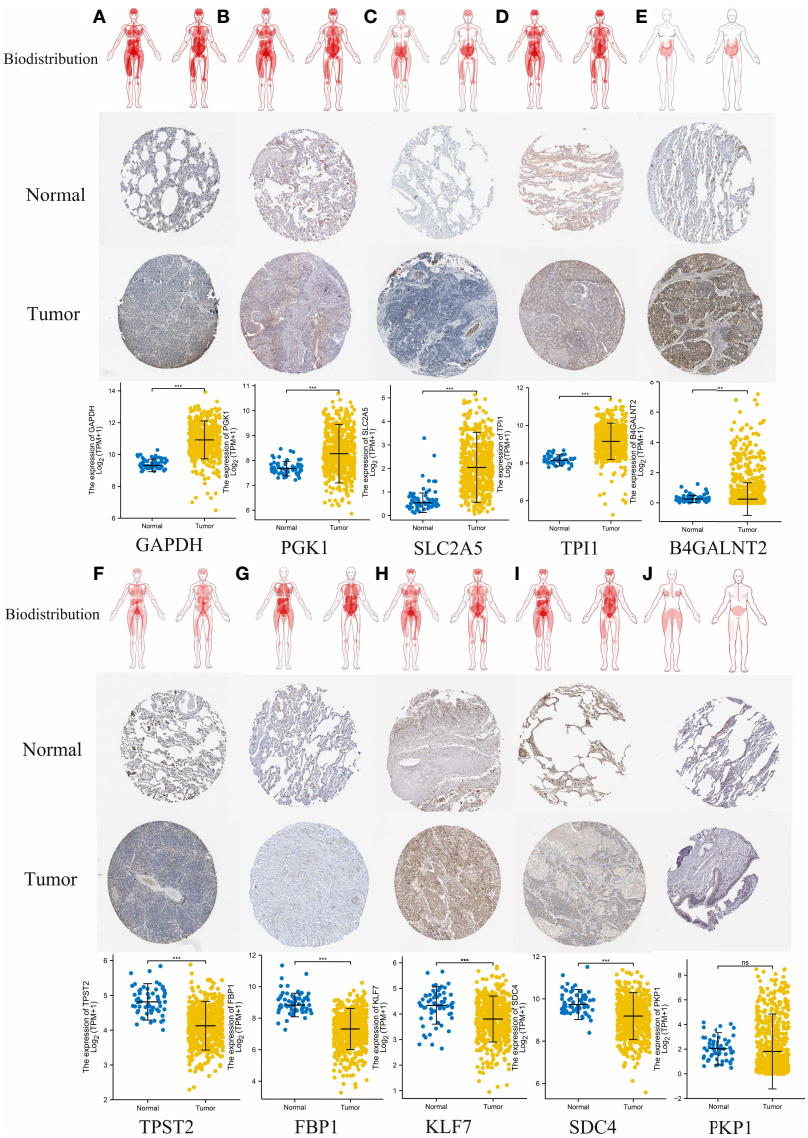

FIGURE 13 | Comparison of hypoxia-associated gene expression at the protein level. From top to bottom, panels **(A–J)** represent biodistribution, IHC staining of protein expression in normal tissues and LUAD tumors tissues, and comparison of expression levels between normal tissues and LUAD tumors tissues for each gene, respectively. **(A)** GAPDH. **(B)** PGK1. **(C)** SLC2A5. **(D)** TPI1. **(E)** B4GALNT2. **(F)** TPST2. **(G)** FBP1, **(H)** KLF7, **(I)** SDC4. **(J)** PKP1. ***p < 0.001; ns, not significant, $p > 0.05$.

response to immunotherapy (53), but the effect and the prognostic role of the TMB on outcomes varied dramatically across cancer types (54, 55). Emerging pieces of evidence showed that higher TMB tends to form more new antigens, making tumors more immunogenic, improving clinical response to immunotherapy and prolonging the overall survival (56–58). This is in perfect agreement with our result that patients in the low-HAGS risk group showed more somatic mutations (**Figures 8A–C**), strong immune activity (**Figure 10**), and better OS (**Figures 3B, E**). However, there were also studies showing the opposite, finding that high TMB was associated with worse prognosis (55, 59).

Recently, it was found that the drug responses and effect were influenced by hypoxia (60). Consistently, we found that the expression of certain hypoxia-associated genes had a significant positive relationship with the sensitivity of multiple drugs (**Figure 11**). In addition, we found a significant difference in IC50s of two anticancer drugs (docetaxel and camptothecin) between the high- and low-risk groups (**Figure 12**) by taking an integrative approach to analyzing the expression matrix of hypoxia-associated gene and the IC50s of the 28 common anticancer drugs in each LUAD sample. These signs suggested that hypoxia may exert a

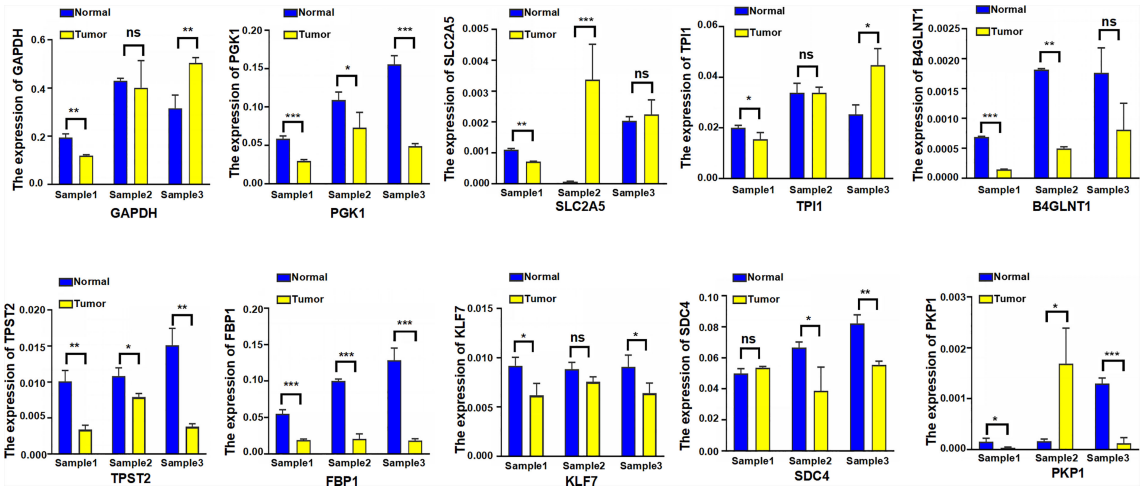

FIGURE 14 | The expression level of 10 hypoxia-associated genes were verified at transcript levels by using three paired samples of LUAD tissues and the paired non-tumorous lung tissues. Sample1, Sample2, and Sample3 were collected from three different LUAD patients; each sample was used to detect 10 hypoxia-associated genes simultaneously. *p < 0.05; **p < 0.01; ***p < 0.001; ns, not significant.

significant influence on drug sensitivity through the modulation of hypoxia-related pathways or genes, and more attention is require to study the effects of hypoxia on drug therapies.

CONCLUSION

In summary, we developed a new hypoxia-associated gene signature (HAGS) by integrating four machine learning algorithms to predict clinical outcomes and therapeutic responses in LUAD patients, followed by performing internal and external validation for its performance in the TCGA and GEO groups, respectively. Our results demonstrate that HAGS, as an independent prognostic factor, had a considerable effect on predicting the OS of LUAD patients. LUAD patients in the high HAGS risk group presented worse OS, lower TMB, and lower immune activity. Moreover, we revealed that the hypoxia-associated gene had a strong statistical association with the drug sensitivity of multiple FDA-approved drugs and had potential therapeutic value for LUAD patients based on the chemotherapeutic response prediction. Finally, to comprehensively confirm the reliability of selected genes, validation studies on the expression levels of 10 hypoxia-associated genes were further analyzed at protein level and transcript levels.

DATA AVAILABILITY STATEMENT

The datasets presented in this study can be found in online repositories. The names of the repository/repositories and accession number(s) can be found in the article/supplementary material.

ETHICS STATEMENT

The studies involving human participants were reviewed and approved by the Ethics Committee of the Ren Ji Hospital,affiliated Shanghai Jiao Tong University School of Medicine.

AUTHOR CONTRIBUTIONS

All authors listed have made a substantial, direct, and intellectual contribution to the work and approved it for publication.

FUNDING

This work was supported by the innovative research team of high-level local universities in Shanghai, the National Natural Science Foundation of China (grant numbers 82102479, 81873957, and 81861138043), and the Shanghai Committee of Science and Technology, China (grant number 19JC1413005).

REFERENCES

1. Bunn PA, Franklin W, Doebele RC. The Evolution of Tumor Classification: A Role for Genomics? *Cancer Cell* (2013) 24(6):693–4. doi: 10.1016/j.ccr.2013.11.019
2. Wang S, Du M, Zhang J, Xu W, Yuan Q, Li M, et al. Tumor Evolutionary Trajectories During the Acquisition of Invasiveness in Early Stage Lung Adenocarcinoma. *Nat Commun* (2020) 11(1):6083. doi: 10.1038/s41467-020-19855-x
3. Chen H, Carrot-Zhang J, Zhao Y, Hu H, Freeman SS, Yu S, et al. Genomic and Immune Profiling of Pre-Invasive Lung Adenocarcinoma. *Nat Commun* (2019) 10(1):5472. doi: 10.1038/s41467-019-13460-3
4. Bray FFJ, Soerjomataram I, Siegel RL, Torre LA, Jemal A. Erratum: Global Cancer Statistics 2018: GLOBOCAN Estimates of Incidence and Mortality Worldwide for 36 Cancers in 185 Countries. *CA.: Cancer J Clin* (2018) 68:394. doi: 10.3322/caac.21609
5. Liu L, Bi N, Wu L, Ding X, Men Y, Zhou W, et al. MicroRNA-29c Functions as a Tumor Suppressor by Targeting VEGFA in Lung Adenocarcinoma. *Mol Cancer* (2017) 16(1):50. doi: 10.1186/s12943-017-0620-0
6. Kerdidani D, Chouvardas P, Arjo AR, Giopanou I, Ntaliarda G, Guo YA, et al. Wnt1 Silences Chemokine Genes in Dendritic Cells and Induces Adaptive Immune Resistance in Lung Adenocarcinoma. *Nat Commun* (2019) 10(1):1405. doi: 10.1038/s41467-019-09370-z
7. Thienpont B, Steinbacher J, Zhao H, D Anna F, Kuchnio A, Ploumakis A, et al. Tumour Hypoxia Causes DNA Hypermethylation by Reducing TET Activity. *Nature* (2016) 537(7618):63–8. doi: 10.1038/nature19081
8. Peng G, Liu Y. Hypoxia-Inducible Factors in Cancer Stem Cells and Inflammation. *Trends Pharmacol Sci* (2015) 36(6):374–83. doi: 10.1016/j.tips.2015.03.003
9. Ye J, Fan J, Venneti S, Wan Y, Pawel BR, Zhang J, et al. Serine Catabolism Regulates Mitochondrial Redox Control During Hypoxia. *Cancer Discov* (2014) 4(12):1406–17. doi: 10.1158/2159-8290.CD-14-0250
10. Jain IH, Calvo SE, Markhard AL, Skinner OS, To T, Ast T, et al. Genetic Screen for Cell Fitness in High or Low Oxygen Highlights Mitochondrial and Lipid Metabolism. *Cell* (2020) 181(3):716–27. doi: 10.1016/j.cell.2020.03.029
11. Xie C, Ji N, Tang Z, Li J, Chen Q. The Role of Extracellular Vesicles From Different Origin in the Microenvironment of Head and Neck Cancers. *Mol Canc* (2019) 18(1):83. doi: 10.1186/s12943-019-0985-3
12. Keith B, Simon MC. Hypoxia Inducible Factors, Stem Cells and Cancer. *Cell* (2007) 129(3):465–72. doi: 10.1016/j.cell.2007.04.019
13. Sørensen BS, Horsman MR. Tumor Hypoxia: Impact on Radiation Therapy and Molecular Pathways. *Front Oncol* (2020) 10:562. doi: 10.3389/fonc.2020.00562
14. Fu R, Du W, Ding Z, Wang Y, Li Y, Zhu J, et al. HIF-1α Promoted Vasculogenic Mimicry Formation in Lung Adenocarcinoma Through NRP1 Upregulation in the Hypoxic Tumor Microenvironment. *Cell Death Dis* (2021) 12(4):394. doi: 10.1038/s41419-021-03682-z
15. Moreno Leon L, Gautier M, Allan R, Ilié M, Nottet N, Pons N, et al. The Nuclear Hypoxia-Regulated NLUCAT1 Long non-Coding RNA Contributes to an Aggressive Phenotype in Lung Adenocarcinoma Through Regulation of Oxidative Stress. *Oncogene* (2019) 38(46):7146–65. doi: 10.1038/s41388-019-0935-y
16. Cao X, Fang X, Malik WS, He Y, Li X, Xie M, et al. TRB3 Interacts With ERK and JNK and Contributes to the Proliferation, Apoptosis, and Migration of Lung Adenocarcinoma Cells. *J Cell Physiol* (2020) 235(1):538–47. doi: 10.1002/jcp.28993
17. Li L, Yang L, Fan Z, Xue W, Shen Z, Yuan Y, et al. Hypoxia-Induced GBE1 Expression Promotes Tumor Progression Through Metabolic Reprogramming in Lung Adenocarcinoma. *Signal Transduct. Target. Ther* (2020) 5(1):54. doi: 10.1038/s41392-020-0152-8
18. Huang G, Tao L, Shen S, Chen L. Hypoxia Induced CCL28 Promotes Angiogenesis in Lung Adenocarcinoma by Targeting CCR3 on Endothelial Cells. *Sci Rep-Uk.* (2016) 6(1):27152. doi: 10.1038/srep27152
19. Sanz H, Valim C, Vegas E, Oller JM, Reverter F. SVM-RFE: Selection and Visualization of the Most Relevant Features Through non-Linear Kernels. *BMC Bioinf* (2018) 19(1):432. doi: 10.1186/s12859-018-2451-4
20. Liu Z, Song Y, Xie C, Tang Z. A New Clustering Method of Gene Expression Data Based on Multivariate Gaussian Mixture Models. *Signal. Imag. Video. Process.* (2016) 10(2):359–68. doi: 10.1007/s11760-015-0749-5
21. Bravaccini S, Bronte G, Ulivi P. TMB in NSCLC: A Broken Dream? *Int J Mol Sci* (2021) 22(12):6536. doi: 10.3390/ijms22126536
22. Shankavaram UT, Varma S, Kane D, Sunshine M, Chary KK, Reinhold WC, et al. CellMiner: A Relational Database and Query Tool for the NCI-60 Cancer Cell Lines. *BMC Genomics* (2009) 10(1):277. doi: 10.1186/1471-2164-10-277
23. Li R, Yin Y, Ji X, Liu X, Li J, Qu Y. Pan-Cancer Prognostic, Immunity, Stemness, and Anticancer Drug Sensitivity Characterization of N6-Methyladenosine RNA Modification Regulators in Human Cancers. *Front Mol Biosci* (2021) 8:644620. doi: 10.3389/fmolb.2021.644620
24. Geeleher P, Cox N, Huang RS, Barbour JD. Prrophetic: An R Package for Prediction of Clinical Chemotherapeutic Response From Tumor Gene Expression Levels. *PLoS One* (2014) 9(9):e107468. doi: 10.1371/journal.pone.0107468
25. Asplund A, Edqvist PD, Schwenk JM, Pontén F. Antibodies for Profiling the Human Proteome-The Human Protein Atlas as a Resource for Cancer Research. *Proteomics* (2012) 12(13):2067–77. doi: 10.1002/pmic.201100504
26. Chen Y, Ma Z, Min L, Li H, Wang B, Zhong J, et al. Biomarker Identification and Pathway Analysis by Serum Metabolomics of Lung Cancer. *BioMed Res Int* (2015) 2015:1–9. doi: 10.1155/2015/183624
27. Cheng Y, Hou K, Wang Y, Chen Y, Zheng X, Qi J, et al. Identification of Prognostic Signature and Gliclazide as Candidate Drugs in Lung Adenocarcinoma. *Front Oncol* (2021) 11:665276. doi: 10.3389/fonc.2021.665276
28. Aschwanden A. The Worst is Yet to Come for the Greenland Ice Sheet. *Nature* (2020) 586(1):29–30. doi: 10.1038/d41586-020-02700-y
29. Shim WS, Yim K, Kim T, Sung YE, Lee G, Hong JH, et al. DeepRePath: Identifying the Prognostic Features of Early-Stage Lung Adenocarcinoma Using Multi-Scale Pathology Images and Deep Convolutional Neural Networks. *Cancers* (2021) 13(13):3308. doi: 10.3390/cancers13133308
30. Ma L, Hernandez MO, Zhao Y, Mehta M, Tran B. Tumor Cell Biodiversity Drives Microenvironmental Reprogramming in Liver Cancer. *Cancer Cell* (2019) 36(4):418–30. doi: 10.1016/j.ccell.2019.08.007
31. Ono Y, Bono H. Multi-Omic Meta-Analysis of Transcriptomes and the Bibliome Uncovers Novel Hypoxia-Inducible Genes. *Biomedicines* (2021) 9(5):582. doi: 10.3390/biomedicines9050582
32. Shimokawa H, Sunamura S, Satoh K. RhoA/Rho-Kinase in the Cardiovascular System. *Circ Res* (2016) 118(2):352–66. doi: 10.1161/CIRCRESAHA.115.306532
33. Liu X, Sun C, Zou K, Li C, Chen X, Gu H, et al. Novel PGK1 Determines SKP2-Dependent AR Stability and Reprograms Granular Cell Glucose Metabolism Facilitating Ovulation Dysfunction. *Ebiomedicine* (2020) 61:103058. doi: 10.1016/j.ebiom.2020.103058
34. Nakatsu Y, Yamamotoya T, Ueda K, Ono H, Inoue M. Prolyl Isomerase Pin1 in Metabolic Reprogramming of Cancer Cells. *Cancer Lett* (2020) 470:106–14. doi: 10.1016/j.canlet.2019.10.043
35. Zhang Y, Cai H, Liao Y, Zhu Y, Wang F, Hou J. Activation of PGK1 Under Hypoxic Conditions Promotes Glycolysis and Increases Stem Cell–Like Properties and the Epithelial–Mesenchymal Transition in Oral Squamous Cell Carcinoma Cells *via* the AKT Signalling Pathway. *Int J Oncol* (2020) 57(3):743–55. doi: 10.3892/ijo.2020.5083
36. Berkmann JC, Herrera Martin AX, Ellinghaus A, Schlundt C, Schell H, Lippens E, et al. Early pH Changes in Musculoskeletal Tissues Upon Injury—Aerobic Catabolic Pathway Activity Linked to Inter-Individual Differences in Local Ph. *Int J Mol Sci* (2020) 21(7):2513. doi: 10.3390/ijms21072513
37. Tao Y, Shi Y, Jia J, Jiang Y, Yang L, Cao Y. Novel Roles and Therapeutic Targets of Epstein–Barr Virus-Encoded Latent Membrane Protein 1-Induced Oncogenesis in Nasopharyngeal Carcinoma. *Expert Rev Mol Med* (2015) 17:e15. doi: 10.1017/erm.2015.13
38. Jiang Z, Zhu J, Ma Y, Hong C, Xiao S, Jin L. Tyrosylprotein Sulfotransferase 1 Expression is Negatively Correlated With C-Met and Lymph Node Metastasis in Human Lung Cancer. *Mol Med Rep* (2015) 12(4):5217–22. doi: 10.3892/mmr.2015.4096
39. Liu D, Zhou B, Liu R. An RNA-Sequencing-Based Transcriptome for a Significantly Prognostic Novel Driver Signature Identification in Bladder Urothelial Carcinoma. *Peerj* (2020) 8:e9422. doi: 10.7717/peerj.9422

40. Agere SA, Kim EY, Akhtar N, Ahmed S. Syndecans in Chronic Inflammatory and Autoimmune Diseases: Pathological Insights and Therapeutic Opportunities. *J Cell Physiol* (2018) 233(9):6346–58. doi: 10.1002/jcp.26388
41. Keller-Pinter A, Gyulai-Nagy S, Becsky D, Dux L, Rovo L. Syndecan-4 in Tumor Cell Motility. *Cancers* (2021) 13(13):3322. doi: 10.3390/cancers13133322
42. Yang H, Liu Y, Zhao M, Guo Q, Zheng X, Liu D, et al. Therapeutic Potential of Targeting Membrane-Spanning Proteoglycan SDC4 in Hepatocellular Carcinoma. *Cell Death Dis* (2021) 12(5):492. doi: 10.1038/s41419-021-03780-y
43. Ding X, Wang X, Gong Y, Ruan H, Sun Y, Yu Y. KLF7 Overexpression in Human Oral Squamous Cell Carcinoma Promotes Migration and Epithelial-Mesenchymal Transition. *Oncol Lett* (2017) 13(4):2281–9. doi: 10.3892/ol.2017.5734
44. Guan F, Kang Z, Zhang J, Xue N, Yin H, Wang L, et al. KLF7 Promotes Polyamine Biosynthesis and Glioma Development Through Transcriptionally Activating ASL. *Biochem Bioph. Res Co.* (2019) 514(1):51–7. doi: 10.1016/j.bbrc.2019.04.120
45. Li Y, Wang Q, Wang D, Fu W. KLF7 Promotes Gastric Carcinogenesis Through Regulation of ANTXR1. *Cancer Manag. Res* (2021) 13:5547–57. doi: 10.2147/CMAR.S308071
46. Wang J, Teng F, Chai H, Zhang C, Liang X. GNA14 Stimulation of KLF7 Promotes Malignant Growth of Endometrial Cancer Through Upregulation of HAS2. *BMC Canc.* (2021) 21:456. doi: 10.1186/s12885-021-08202-y
47. De Donato M, Babini G, Mozzetti S, Buttarelli M. KLF7: A New Candidate Biomarker and Therapeutic Target for High-Grade Serous Ovarian Cancer. *J Exp Clin Canc. Res* (2020) 39:265. doi: 10.1186/s13046-020-01775-9
48. Li K, Yuan C. MicroRNA103 Modulates Tumor Progression by Targeting KLF7 in Nonsmall Cell Lung Cancer. *Int J Mol Med* (2020) 46(3):1013–28. doi: 10.3892/ijmm.2020.4649
49. Lv J, Zhou J, Tong R, Wang B, Chen X, Zhuang Y, et al. Hypoxia−induced Mir −210 Contributes to Apoptosis of Mouse Spermatocyte GC−2 Cells by Targeting Kruppel−like Factor 7. *Mol Med Rep* (2019) 19(1):271–9. doi: 10.3892/mmr.2018.9644
50. Weng Y, Fan X, Bai Y, Wang S, Huang H, Yang H, et al. SLC2A5 Promotes Lung Adenocarcinoma Cell Growth and Metastasis by Enhancing Fructose Utilization. *Cell Death Discover.* (2018) 4(1):38. doi: 10.1038/s41420-018-0038-5
51. Zhang Q, Huang R, Hu H, Yu L, Tang Q, Tao Y, et al. Integrative Analysis of Hypoxia-Associated Signature in Pan-Cancer. *iScience* (2020) 23(9):101460. doi: 10.1016/j.isci.2020.101460
52. Ning XH, Li T, Gong YQ, He Q, Shen QI, Peng SH, et al. Association Between FBP1 and Hypoxia-Related Gene Expression in Clear Cell Renal Cell Carcinoma. *Oncol Lett* (2016) 11(6):4095–8. doi: 10.3892/ol.2016.4504
53. Hellmann MD, Ciuleanu T, Pluzanski A, Lee JS, Otterson GA, Audigier-Valette C, et al. Nivolumab Plus Ipilimumab in Lung Cancer With a High Tumor Mutational Burden. *New Engl J Med* (2018) 378(22):2093–104. doi: 10.1056/NEJMoa1801946
54. Jia P, Hu R, Pei G, Dai Y, Wang Y, Zhao Z. Deep Generative Neural Network for Accurate Drug Response Imputation. *Nat Commun* (2021) 12(1):1740. doi: 10.1038/s41467-021-21997-5
55. Wang ZM, Xu QR, Kaul D, Ismail M, Badakhshi H. Significance of Tumor Mutation Burden and Immune Infiltration in Thymic Epithelial Tumors. *Thorac Canc.* (2021) 12(13):1995–2006. doi: 10.1111/1759-7714.14002
56. Zhang W, Li C, Wu F, Li N, Wang Y, Hu Y, et al. Analyzing and Validating the Prognostic Value of a TNF-Related Signature in Kidney Renal Clear Cell Carcinoma. *Front Mol Biosci* (2021) 8:689037. doi: 10.3389/fmolb.2021.689037
57. Wu Z, Wang M, Liu Q, Liu Y, Zhu K, Chen L, et al. Identification of Gene Expression Profiles and Immune Cell Infiltration Signatures Between Low and High Tumor Mutation Burden Groups in Bladder Cancer. *Int J Med Sci* (2020) 17(1):89–96. doi: 10.7150/ijms.39056
58. Lv J, Zhu Y, Ji A, Zhang Q, Liao G. Mining TCGA Database for Tumor Mutation Burden and Their Clinical Significance in Bladder Cancer. *Biosci. Rep* (2020) 40(4):BSR20194337. doi: 10.1042/BSR20194337
59. Gao Y, Chen S, Vafaei S, Zhong X. Tumor-Infiltrating Immune Cell Signature Predicts the Prognosis and Chemosensitivity of Patients With Pancreatic Ductal Adenocarcinoma. *Front Oncol* (2020) 10:557638. doi: 10.3389/fonc.2020.557638
60. Iida Y, Aoki K, Asakura T, Ueda K, Yanaihara N, Takakura S, et al. Hypoxia Promotes Glycogen Synthesis and Accumulation in Human Ovarian Clear Cell Carcinoma. *Int J Oncol* (2012) 40(6):2122–30. doi: 10.3892/ijo.2012.1406

Conflict of Interest: The authors declare that the research was conducted in the absence of any commercial or financial relationships that could be construed as a potential conflict of interest.

frontiers | Frontiers in Immunology

ORIGINAL RESEARCH
published: 13 June 2022
doi: 10.3389/fimmu.2022.911902

Immunological Characteristics of Alternative Splicing Profiles Related to Prognosis in Bladder Cancer

Fangdie Ye[1,2†], Yingchun Liang[1,2†], Zhang Cheng[1,2†], Yufei Liu[1,2], Jimeng Hu[1,2], Weijian Li[1,2], Xinan Chen[1,2], Jiahao Gao[3] and Haowen Jiang[1,2,4]*

[1] Department of Urology, Huashan Hospital, Fudan University, Shanghai, China, [2] Fudan Institute of Urology, Huashan Hospital, Fudan University, Shanghai, China, [3] Department of Radiology, Huashan Hospital, Fudan University, Shanghai, China, [4] National Clinical Research Center for Aging and Medicine, Huashan Hospital, Fudan University, Shanghai, China

Several studies have found that pathological imbalance of alterative splicing (AS) events is associated with cancer susceptibility. carcinogenicity. Nevertheless, the relationship between heritable variation in AS events and carcinogenicity has not been extensively explored. Here, we downloaded AS event signatures, transcriptome profiles, and matched clinical information from The Cancer Genome Atlas (TCGA) database, identified the prognostic AS-related events *via* conducting the univariate Cox regression algorism. Subsequently, the prognostic AS-related events were further reduced by the least absolute shrinkage and selection operator (LASSO) logistic regression model, and employed for constructing the risk model. Single-sample (ssGSEA), ESTIMATE, and the CIBERSORT algorithms were conducted to evaluate tumor microenvironment status. CCK8, cell culture scratch, transwell invasion assays and flow cytometry were conducted to confirm the reliability of the model. We found 2751 prognostic-related AS events, and constructed a risk model with seven prognostic-related AS events. Compared with high-risk score patients, the overall survival rate of the patients with low-risk score was remarkably longer. Besides, we further found that risk score was also closely related to alterations in immune cell infiltration and immunotherapeutic molecules, indicating its potential as an observation of immune infiltration and clinical response to immunotherapy. In addition, the downstream target gene (DYM) could be a promising prognostic factor for bladder cancer. Our investigation provided an indispensable reference for ulteriorly exploring the role of AS events in the tumor microenvironment and immunotherapy efficiency, and rendered personalized prognosis monitoring for bladder cancer.

Keywords: tumor microenvironment, immunotherapy targets, prognostic, bladder cancer; alternative splicing

OPEN ACCESS

Edited by:
Liusheng Peng,
Third Military Medical University, China

Reviewed by:
Huaiyuan Xu,
Sun Yat-sen University Cancer Center (SYSUCC), China
Lili Li,
Wuhan University, China
Dongjie Chen,
Central South University, China

****Correspondence:***
Haowen Jiang
urology_hs@163.com

[†]These authors have contributed equally to this work

Specialty section:
This article was submitted to Cancer Immunity and Immunotherapy, a section of the journal Frontiers in Immunology

Received: *03 April 2022*
Accepted: *20 May 2022*
Published: *13 June 2022*

Citation:
Ye F, Liang Y, Cheng Z, Liu Y, Hu J, Li W, Chen X, Gao J and Jiang H (2022) Immunological Characteristics of Alternative Splicing Profiles Related to Prognosis in Bladder Cancer. Front. Immunol. 13:911902. doi: 10.3389/fimmu.2022.911902

INTRODUCTION

Bladder carcinoma is a common type of genitourinary system tumor worldwide, and carries a significant burden, responsible for an estimated 570000 new cases and 210 000 deaths annually (1). As a heterogeneous tumor, bladder carcinoma mainly progresses along two "trajectories", and each "trajectory" has distinct effects on its for prognosis. The one "trajectories" was non-muscle invasive

bladder cancer which was recurrent noninvasive tumors managed chronically, while muscle-invasive bladder cancers are progressive-stage or aggressive diseases that require multi-strategy treatment (2). Although remarkable breakthroughs in investigating the underlying biological mechanisms of bladder cancer have basically improved the diagnosis and treatment of this disease, the histology of bladder cancer is highly variable, potentially representing different molecular subtypes, which adds to the complexity of management (2, 3). Increasing number of articles have elaborated that genetic subtype may associated with distinct clinical responses to biotherapies, chemotherapies, and survival outcomes, confirming their clinical relevance (4–6). However, owing to high levels of inter-observer variability, judging these subtypes may be subjective, leading the human-bias for diagnosis, therapeutic benefits, and prognosis. Thus, there is imperative to understand the underlying mechanisms of genetic subtypes from multi-aspects and identify predictable biomarkers.

The tumor immune microenvironment (TIME) includes an array of immunocytes, including macrophages, T cells, neutrophiles, DC cells and NK cells. Increasing research demonstrated that the immunocytes in the tumor microenvironment interact with therapeutic drug, thereby affecting the clinical response of patients to treatment. These immunocytes could therefore act as targets to promote the overall survival of patients with bladder cancer (7–9). Recently, immunotherapy has yielded encouraging results in numerous malignancies and has received extensive attention (10). Bladder cancer has also been successfully treated by several immunotherapeutic strategies, such as Bacillus Calmette–Guerin (BCG) intravesical instillation or PD-L1antibody treatment. Nevertheless, the mechanisms of BCG-induced tumor-specific immunity remain obscure, and only 25% of progressive bladder cancers have remarkable clinical respond to immunotherapy treatment (11, 12). Therefore, the most effective strategy for accurately predicting the response of bladder cancer to immunotherapy or cancer progression may be based on the strategy of molecular risk distribution, which can help identify bladder cancer patients online through specific molecular characteristics, improve the prognosis accuracy, and optimize the benefit of immunotherapy.

Exact gene is incised *via* Alternative splicing (AS) to yield a quantity of special messenger RNA (mRNA) (13). It is known that AS includes seven types: mutually exclusive exons (ME), exon skip (ES), alternate terminator (AT), alternate promoter (AP), retained intron (RI), alternate donor site (AD), and alternate acceptor site (AA) (14). During tumor development, AS process changes abnormally, and alterations in critical tumor genes can play a pivotal role in oncogenesis, tumor progression, metastasis, and therapeutic response (15–18). Besides, some splicing factors have been confirmed to play a crucial role in the regulation of AS events (19). Notably, anomalous alternation of pivotal splicing factors can lead to the formation of carcinogenic splicing isoforms (20–22). heretofore, several studies have focused on exploring the function of AS-related mutation in bladder cancer (23–25).Recently, some articles have focused on the AS-based prognostic model of bladder cancer (26, 27). However, the correlation between prognostic-related AS events and immunotherapy/TIME is still unclear. Therefore, we conduct in-depth investigation of aberrant AS events to demonstrate the profiles of tumor microenvironment and the potential biological mechanisms of oncogenesis, further optimizing diagnosis, prognosis, and clinical strategies.

In our research, we outlined the AS-pattern and ascertain that AS events were closely related to the TIME and clinical outcome *via* comprehensive bioinformatic analysis based the TCGA-BLCA cohort. Next, we revealed downstream target genes (DYM) for prognostic-related AS events. The latent role of DYM in bladder cancer has also been explored. At the same time, we confirmed that DYM is associated with alteration of TIME, and silencing DYM can inhibit the cell proliferation, migration, invasion ability, and promote cell apoptosis.

MATERIAL AND METHODS

Acquisition of Multi-Omics Data Related to Bladder Cancer

In the and identify Cancer Genome Atlas (TCGA) SpliceSeq database, the alternative splicing events, including ME, ES, AT, AP, RI, AD, AA, were analyzed and summarized using the R package "Upset." The characteristics of AS events were interpreted using the percent spliced in (PSI), which is an index that can qualify variable splicing. AS event annotation: gene symbol, splicing type and splicing ID number. The transcriptome FPKM information and adjusted clinical data were acquired from the TCGA database. Patients' selection criteria: pathological result was transitional cell papilloma and carcinoma. Exclusion criteria: 1. Patients with less than 10 days of survival. 2. Patients without corresponding alternative splicing data. A total of 409 patients diagnosed with transitional cell papilloma and carcinoma, 13 patients were excluded by exclusion criteria, 396 patients were left. Deleting patients with missing clinical features when performing correlation analysis among risk score and clinicopathological profiles. The clinical data on patient's immunotherapy were collected from TCIA (https://www.tcia.at/home).

Construction and Validation of AS Events-Related Prognostic Signatures

The clinical information and corresponding AS events of the samples were matched according to the splicing ID number. Then, the prognostic-related AS events were identified *via* conducting univariate Cox regression algorism, which are displayed as a volcano map and Upset diagram. In addition, the top 20 AS events are presented in the quadrangle plot.

To construct a valuable prognostic model, LASSO regression analysis was employed to lessen the dimension of prognostic-related AS events and to select candidate features with prominent prognostic value. On this basis, multivariate Cox model was conducted to determine the final prognostic-related AS events, which were utilized to propose the prognostic model in this study. The formula was calculated as follows:

$$\text{Risk score} = \text{coefficient 1} \times \text{PSI AS event 1} + \text{coefficient 2} \times \text{PSI AS event 2} + \cdots + \text{coefficient n} \times \text{PSI AS event n}.$$

The patients were divided into high- and low-risk subgroups by determining the median risk score. Then the K-M survival curve was portrayed to estimate the difference of clinical outcome between two subgroups. Besides, the receiver operating characteristic (ROC) model depicts the clinical predictive performance of two subgroups. The forest was plotted to determine whether the risk score can independently predict the clinical outcome of patients.

To comprehensively assess the prognosis of each patient with bladder cancer, nomogram model which included the risk score, tumor stage, age, gender, and WHO grade was constructed. Subsequently, the calibration curve was calculated to evaluate the 1-, 3-, 5- year overall survival probabilities.

Characteristic of the Immune Microenvironment

To investigate the infiltration situation of immunocytes in the tumor microenvironment, three classical analyses were performed in this study. (1) The single sample gene-set enrichment analysis (ssGSEA) was conducted to explore the proportion of 29 immunocyte types in two distinct risk subgroups according to the previous publication (the gene-set was show in **Table S1**) (28). (2) The R package "ESTIMATE" was executed to evaluate the immune/stromal cell infiltration, which could indict the difference of TME between two distinct risky subgroups. (3) R package "CIBERSORT" was conducted to examine the proportion of 22 immunocyte types for each sample (the gene-set was show in **Table S2**) (29).

Effect of AS Events on ICB Treatment

Recent studies have indicated that the transcriptome of ICB-related genes may be closely related to clinical response of patients to immunotherapy. In this study, 47 ICB-related genes were extracted, such as programmed death 1 (*PD-1, also named PDCD1*), programmed death ligand 1 (*PD-L1*/*CD274*), the more information ICB-related genes were seen in **Table S3** (30). The Spearman correlation algorism was conducted to calculated the association between ICB-related genes and risk score to speculate the effect of immunotherapy.

Cell Culture and Infection

T24 and J82 bladder cancer cells were gained from the Type Culture Collection of the Chinese Academy of Sciences (Shanghai, China). The cells were maintained in DMEM medium with 10% fetal bovine serum at 37°C in cell incubator with 5% CO_2. 3×10^5 bladder cancer cells line were seeded into 6-well dishes, cultured for 24h, then transfected by using Lipofectamine 3000. biological experiments were carried out according to the appropriate transfection time. DYM transfection was identified using quantitative real-time PCR (qRT-PCR). The si-RNA sequences were listed as following: si-DYM-1: 5′-GGGUCCUGGAAAUCAUUAATT-3′, si-DYM-2: 5′-GGAGGAAGCAACCAUUUCATT -3′, si-con: 5′-UUCUGGCAACGUATCAGCUTT-3′.

Macrophage Polarization

THP-1 cells were donated by Dr. Cai from Shanghai Jiaotong University. THP-1 cells were induced to differentiate into M0 macrophages by 100 ng/ml PMA. In order to simulate the formation of tumor-associated macrophages(TAMs), the Falcon® Cell Culture Inserts (Corning, Corning, NY) was employed to construct the co-culture environment, the bladder cancer cells (T24/J82) were inoculated in the upper chamber, and M0 macrophages were inoculated in the lower chamber to achieve the effect of co-culture. After 48 hours, co-cultured macrophages were collected to obtain TAMs. CD206 and CD163 were used as markers of M2-type macrophages, and CD86 as markers of M1-type macrophages

ELISA

ELISA kit (R & D Systems) was used to detect the levels of IL6, IL-10, CCL2 and CCL3 in supernatant. The average values of the three independent experiments were shown by the histogram.

RNA Isolation and qRT-PCR

In order to verify knockdown efficiency, we extracted the purity RNA from cell lines *via* TRIzol Reagent (Invitrogen), and then SuperScript II Reverse Transcriptase (Invitrogen) was employed to transcribed mRNA into. The qRT-PCR reaction was conducted using an AB7300 thermocycler (Applied Biosystems). The relative expression of cDNA was normalized to that of *GAPDH*, and each reaction contained at least three separate biological replicates. The primers used are listed in **Table S4**.

Cell Proliferation Assay

For the cell counting kit-8 (CCK-8) assay, each experimental group was inoculated with a density of 2000/well in 96-well plates. After 1, 2, and 3 d, 110 μL mixed solution (CCK-8 + DMEM) was added to each 96-well plates and the cells were cultured for another 2 h. OD_{450} was measured to assess cell proliferation status.

Cell Migration and Invasive Ability

Cell migration and invasive ability were evaluated by cell scratch assay and transwell invasion assay, respectively. For the cell culture scratch assay, 2×10^5 BCa cells were seeded into six-well plates. After covering the whole plates, the cells were scratched with 1 mL pipette tips. The gap area was recorded at 0, 24, and 48 h, and assessed using Image J software. For the transwell invasive assay, 150 μL DMEM medium with 10% FBS was added into the lower chamber and 2×10^4 cells were seeded into the upper chambers. After 24 h, removed the cells which located on the upper surface of the chamber, and stained the invading cells on the lower chamber *via* crystal violet. The invaded cells were photographed and calculated in three random fields.

Flow-Cytometric Analysis

T24 and J82 cells were seeded into six-well plates, The cells were transfected with Si-con and Si-DYM for 24 hours in each well, then digested with trypsin and processed with cold PBS (4° C). We collected the suspension cells in the flow tube according to the manufacturer' s protocol. Finally, apoptosis was measured by using BD FACS caliber. All experiments were conducted in triplicate.

Statistical analysis

All data analyses were conducted *via* using the R software (version 4.0.2). The Wilcoxon test was carried out for comparative analysis of the two group characteristics, and the Kruskal-Wallis test was conducted for comparative analysis more than two group characteristics. Correlations between risk score, clinical characteristics, and other variables were calculated using the Pearson correlation test. The experiments were repeated at least three times.

RESULTS

Identification of Prognostic-Related AS Events

A summary of AS events is shown in **Figure 1**. 409 patients with bladder cancer were collected from the TCGA dataset, and thirteen patients with inadequate clinical information were excluded from this research. The clinical profiles of these patients were displayed in **Table 1**. The UpSet diagram comprehensively displays the AS event characteristics (**Figure S1A**). The results demonstrated that exon skip was the prevailing splicing type in bladder cancer, while the mutually exclusive exons had the lowest frequency. Then, a total of 2751 AS events were collected as potential prognostic biomarkers *via* performing univariate Cox regression analysis ($p < 0.05$). A comprehensive description of the 2751 AS events is shown in **Table S5**. The prognosis-related AS events were delineated using the UpSet diagram (**Figure S1B**). The volcano diagram was plotted to describe the AS events, and the quadrangle map summarizes the first 20 remarkable prognostic-related AS events (**Figure 2**). According to the λ value, the thirteen candidates AS events were selected by performing LASSO regression analysis, including C19orf57|47943|ES, ANK3|11845|AP, ANK3|11842|AP, MARCH6|71561|AP, ACTG1|44120|RI, AK9|77203|AT, DYM|45472|ES, PCSK5|86634|AT, MTFR1L|1212|AA, APBB3|73673|RI, TARBP2|22073|AA, MARS|22600|RI, MICALL2|78572|AA. (**Figure S3**). These independent prognostic-related AS events were chosen to construct AS-based risk models by performing multivariate Cox regression algorism, the risk model is calculated as follows:

$$\begin{aligned}\text{Risk score} = {} & 0.93 \times \text{PSI ANK3|11845|AP} - 1.51 \\ & \times \text{PSI C19orf57|47943|ES} - 1.07 \\ & \times \text{ACTG1|44120|RI} + 1.83 \\ & \times \text{AK9|77203|AT} - 0.5 \times \text{DYM|45472|ES} \\ & + 0.90 \times \text{PCSK5|86634|AT} + 3.09 \\ & \times \text{MICALL2|78572|AA}.\end{aligned}$$

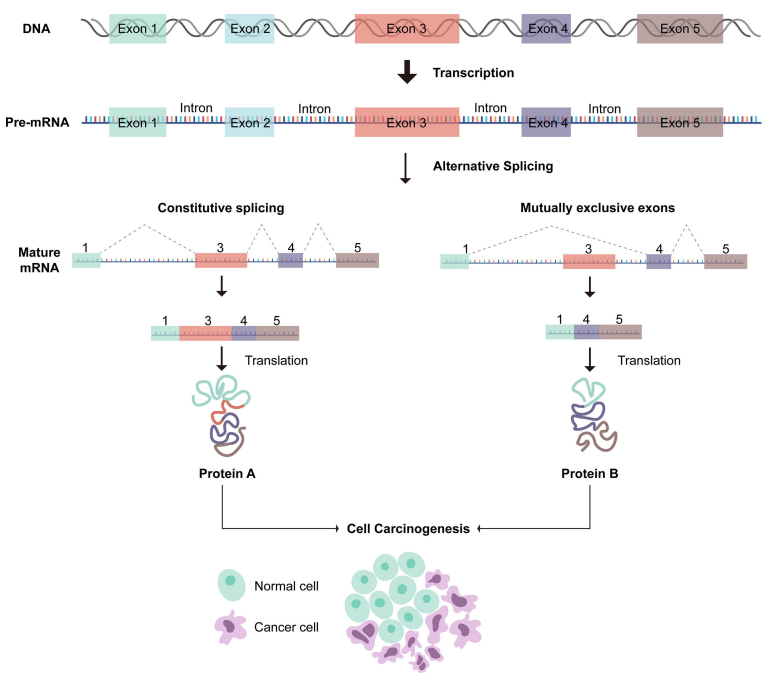

FIGURE 1 | A summary of alterative splicing events.

TABLE 1 | Baseline data of all bladder cancer patients.

Characteristics	Type	n	proportion (%)
Age	<=65	161	39.4
	>65	248	60.6
Gender	Female	106	25.9
	Male	303	74.1
Grade	High Grade	385	94.1
	Low Grade	21	5.1
	unkown	3	0.8
Stage	Stage I	2	0.5
	Stage II	130	31.8
	Stage III	139	34
	Stage IV	136	33.2
	unkown	2	0.5
T Stage	TO Stage	1	0.2
	T1Stage	3	0.8
	T2 Stage	120	29.4
	T3 Stage	194	47.4
	T4 stage	59	14.4
	unkown	32	7.8
M Stage	MO Stage	194	47.4
	M1Stage	11	2.7
	unkown	204	49.9
N Stage	NO Stage	237	57.9
	N1Stage	47	11.5
	N2 Stage	76	18.6
	N3 Stage	8	2
	unkown	41	10

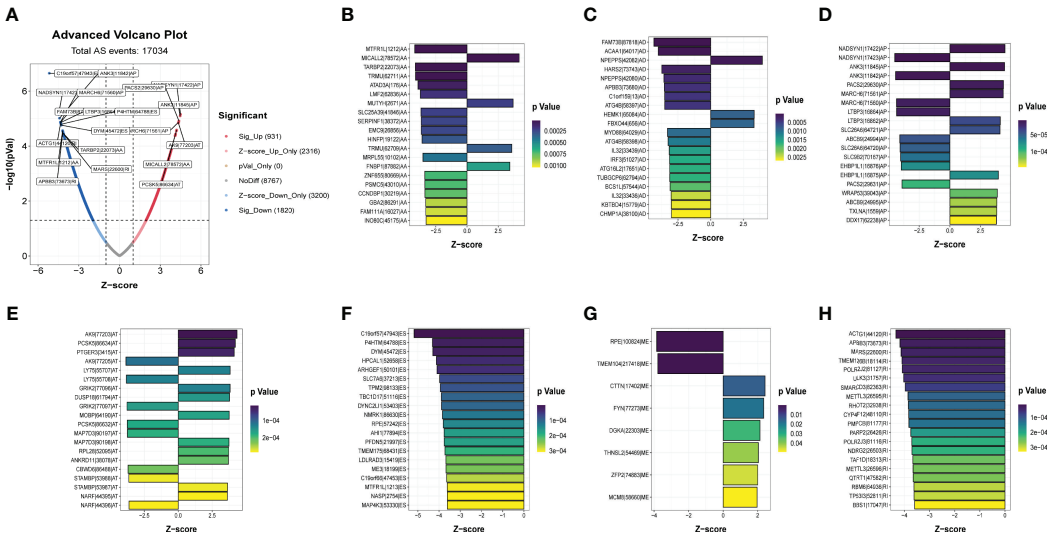

FIGURE 2 | Identification of the prognostic related AS events. **(A)**Volcano plots of prognostic related AS events. **(B-H)** The most significant prognostic related APs, MEs, RIs, AAs, ADs, ATs and ESs in TCGA-BLCA cohort.

Confirmation of Prognostic Model

Patients were classified into high- and low-risk subgroups for further analysis according to the cut-off value of the median risk score. The level of AS event PSI values in different subgroups is displayed in **Figure 3A**, and the dot plot displays the distribution of patient clinical outcomes (**Figures 3B, C**). In addition, the K-M analysis indicated that patients with high-risk scores exhibited poor clinical outcomes (**Figure 3D**). The ROC curve was then calculated to evaluate the prognostic value of risk models in bladder cancer patients. The area under curve (AUC) of our risk model at 1, 3- and 5-years was 0.713, 0.751, and 0.781, respectively (**Figure 3E**). The clinical variables and AS-related

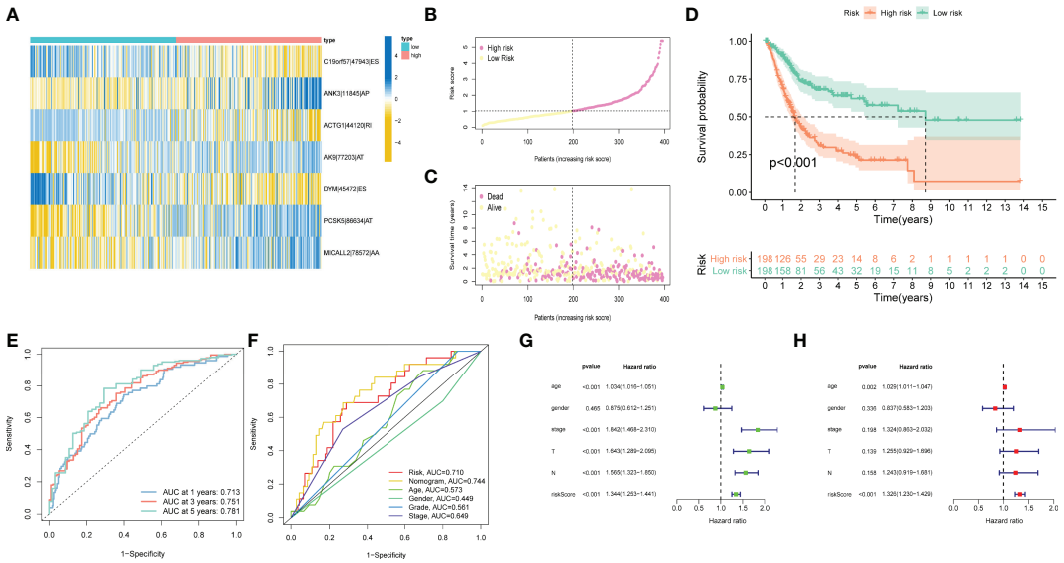

FIGURE 3 | Confirmation of prognostic model. **(A)** Heatmap of the AS events PSI values in bladder cancer. The color from red to green shows a trend from high to low expression. **(B)** The risk score curve exhibits the distribution of prognostic signature risk score. **(C)** The scatter plot exhibits survival times and survival status of bladder cancer patients. **(D)** K–M curve for high- and low-risk groups. **(E)** ROC curves of risk models for overall survival prediction at 1, 3 and 5 years. **(F)** ROC curves for predicting survival with different clinical variables. **(G)** The results of univariate Cox regression analyses. **(H)** The results of multivariate Cox regression analyses.

risk score were consolidated as nomogram model to perform the AUC analysis, we observed that this model gained the highest AUC value (**Figure 3F**), which indicated that the constructed nomogram model had higher sensitivity and specificity for predicting clinical outcomes. In addition, the results of univariate and multivariate Cox regression analyses demonstrated that the risk score can serve as an independent index for bladder cancer (**Figures 3G, H**). In addition, we observed remarkable differences in the risk scores between different clinical variables. The risk score increased with the advancement in clinical pathological stage ($p < 0.001$, **Figure 4B**) and high-grade tumor subtypes ($p < 0.001$, **Figure 4A**), which revealed that the risk score was positively related to tumor progression.

To comprehensively assess the prognosis of each patient with bladder cancer, the nomogram model which included the risk score, tumor stage, age, gender, and WHO grade was constructed to evaluate the 1-, 3-, and 5-year overall survival probabilities (**Figure 4C**). DCA analysis also demonstrated that the nomogram model showed the best prediction performance for 1-year OS in bladder cancer (**Figure 4D**). The calibration curve was close to 45°, indicating that the predicted values are close to the predicted values (**Figure 4E**).

Regulation of AS Events in TIME Alteration

To further validate whether AS events act as a factor that participates in the formation of the immune microenvironment, "ESTIMATE" R package was employed to calculate the immune score of samples, which displayed those patients with high risk score exhibited higher immune score, stromal score, and ESTIMATE score than those with low risk score (**Figure 4F**). Likewise, the ssGSEA results showed the distinction of the immune-related profiles between the two risk models. The results in **Figures 5A, B** presented the corresponding immune scores of immune-related profiles in high- and low-risk groups. The results showed that the infiltration of immunocytes such as Th1 immunocytes, NK cells, macrophages, aDCs, CD8+ T cells, and neutrophils was remarkably increased in the high-risk group. Immune signatures such as APC co-stimulation, HLA, MHC-class I, and T cell co-stimulation were also increased in the high-risk group. In addition, the CIBERSORT algorithm results revealed that the proportion of T cell regulators, plasma cells, CD8+ T cells, and B cells was negatively correlated with the risk score, and the abundance of resting dendritic cells, macrophages M0, and macrophages M2 were positively associated with the risk score (**Figures 5C–H**). The above results revealed that AS events may play an indispensable role in altering the TIME, and also demonstrated that the constructed risk model may act as a novel biomarker to elaborate the characteristics of immune regulation in bladder cancer.

Correlation of AS Events With ICB Key Molecules

The emergence of immunotherapy has altered the therapeutic landscape of bladder cancer, and the development of immune checkpoint inhibitors broaden the options for clinical decision-making in cancer treatment. First, six ICB key molecules were collected from published articles, including PD-L1, PD-1, PD-L2, TIM-3, IDO1, and CTLA-4. Then, correlations between the constructed risk score and ICB key molecules were determined to identify the potential prediction performance of AS events in the immunotherapy of bladder cancer (**Figure 6A**).

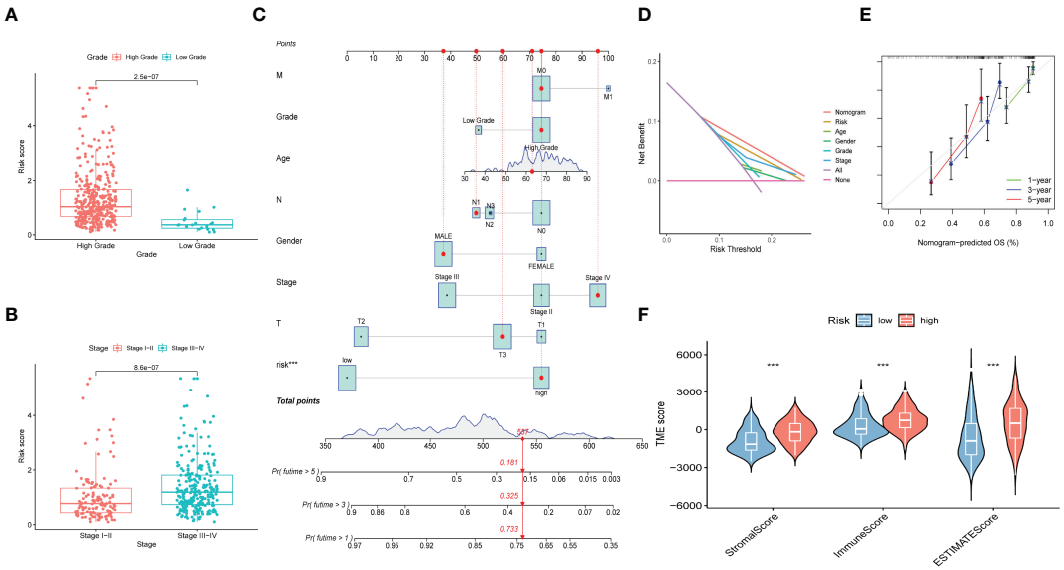

FIGURE 4 | Construction of prognostic nomogram and correlation of immune microenvironment features with different risk scores. **(A)** Risk scores of high and low tumor grades. **(B)** Risk scores of different tumor stages. **(C)** Nomogram established by risk score, age, gender, tumor grade, tumor stage and TNM clinical stage for predicting overall survival probability of bladder cancer patients. **(D)** DCA analysis displayed the prediction performance of selected model. **(E)** Calibration curve of 1-, 2-, 3-year nomogram, the predicted performances of the model are represented by the 45° gray lines. The green/blue/red line represents 1/3/5 years prediction ability. **(F)** ImmuneScore, StromalScore and ESTIMATE scores of high- and low-risk groups.

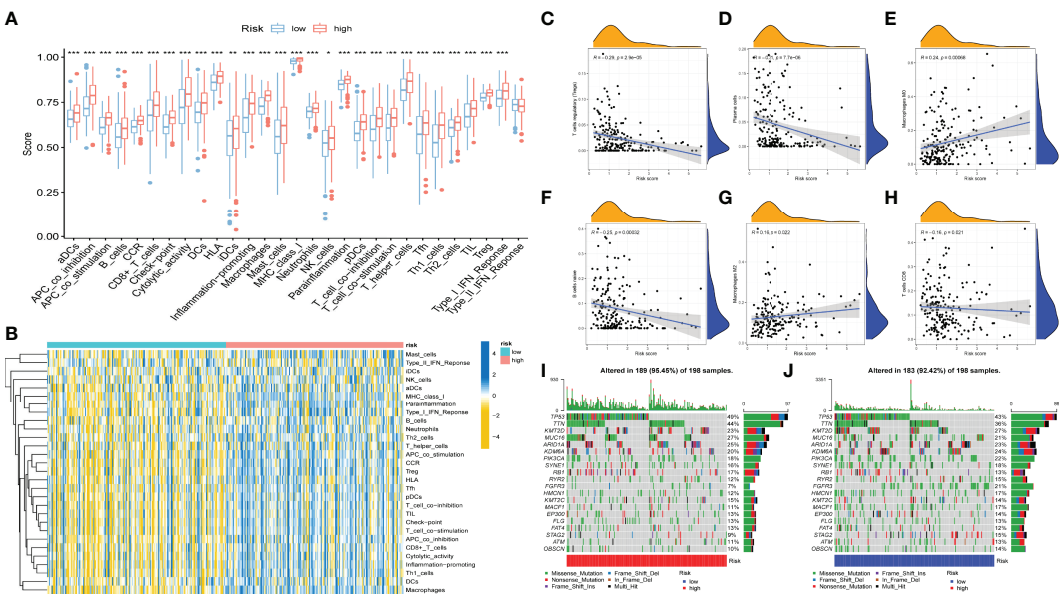

FIGURE 5 | Correlation between AS events and tumor immune microenvironment features. **(A)** Distinction of the immune related profiles between high- and low-risk score groups. The asterisks represented the statistical p value (*P < 0.05; **P < 0.01; ***P < 0.001). **(B)** Heatmap of immune scores and several immune characteristics of two risk score groups. Red indicates high expression and blue indicates low expression. **(C–H)** Correlation analyses of risk score with different immune cells. **(I–J)** The landscape of TMB of bladder cancer with high **(I)** and low risk score.

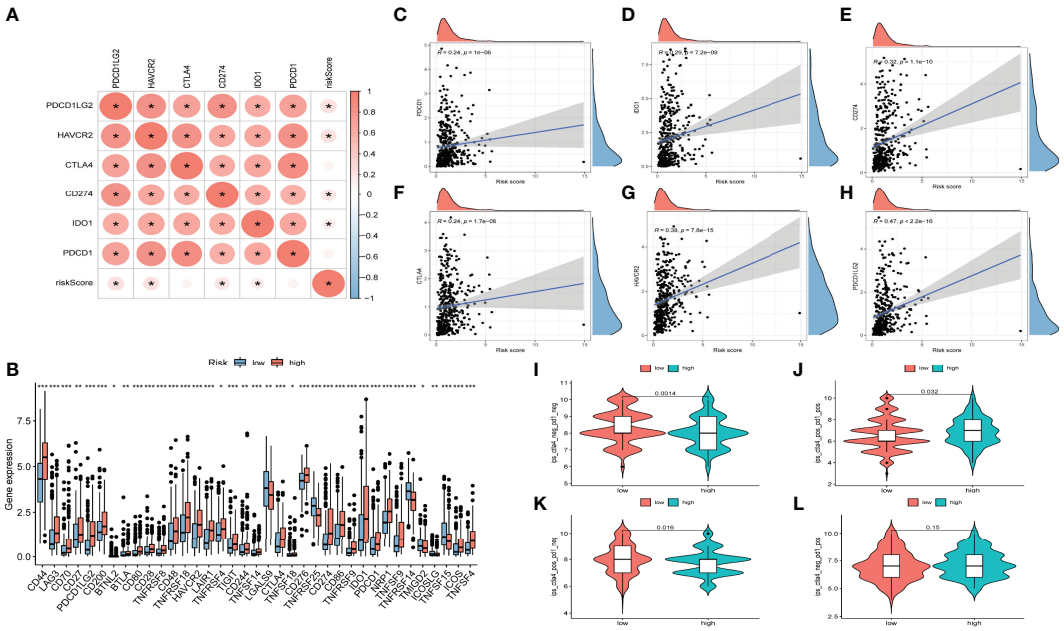

FIGURE 6 | Relationships between AS-based signatures and immune checkpoint blockage key molecules. **(A)** Correlation analyses among six immune checkpoint inhibitors and risk score. **(B)** Difference in expression levels of immune checkpoint blockade-related genes between high- and low-risk groups (*P < 0.05; **P < 0.01; ***P < 0.001). **(C–H)** The positive correlations of CTLA-4, IDO1, PD-L1(CD274), TIM-3(HAVCR2), PD-L2(PDCD1LG2) and PD-1(PDCD1) with risk score. **(I–L)** Efficacy score of immunotherapy.

Figures 6C–H shows that the risk score was remarkably positively related to CD274 (R=0.32, *P* =1.1e-10), PDCD1 (R=0.24, *P* =1e-06), CTLA4 (R=0.24, *P* =1.7e-06), HAVCR2 (R=0.38, *P* =7.8e-15), PDCD1LG2 (R=0.47, *P* <2.2e-16), and IDO1 (R=0.29, *P* =7, 2e-09). In addition, we further analysis the association among ICB-related genes and risk score. The results showed that these genes were significantly associated with risk score; LGALS9, TNFRSF25, TNFRSF14, TMIGD2, ICOSLG, and TNFRSF15 were remarkably reduced in patients with high risk scores, while the other genes were significantly up-regulated (**Figure 6B**), suggesting that AS events might serve as a considerable factor in immunotherapy. In addition, we examined the tumor mutation burden between the high (**Figure 5I**) and low risk groups (**Figure 5J**) and found no difference between the two groups. The **Figures 6I-L** displayed the exhibited the effect of immunotherapy between two groups that the effect of immunotherapy in patients with low risk group is more obvious.

Identification of AS Event-Related Genes

There was a total of seven target genes in the constructed risk model. We found that only DYM and MICALL2 genes affected the clinical outcome of bladder cancer. Therefore, the roles of DYM and MICALL2 in bladder cancer were investigated in further analyses. As we found that MICALL2 could not effectively distinguish different clinical pathologies and had little effect on TIME alterations (the results of the MICALL2-related analysis are presented in **Figure S2**), we mainly focused on the *DYM* gene. By investigating the expression level of DYM in bladder cancer tissues with different clinical stages and grades, we observed that DYM was upregulated in bladder cancer tissues with high grade as well as stage III and IV (**Figures 7A, B**). K-M analysis also demonstrated that upregulated DYM was related to poor clinical outcomes in bladder cancer in TCGA database(*P* value <0.001, **Figure 7C**), which was confirmed in GSE31684 (*P* value =0.021, **Figure 7D**). In addition, 32 of the 47 ICB-related gene expression levels were remarkable different between the high and low DYM expression subgroups, and the ICB key molecules (CD274, PDCD1, CTLA4, HAVCR2, PDCD1LG2, IDO1) were upregulated in patients with high DYM expression, suggesting that high expression of DYM might play an important role in mediating immune evasion (**Figure 7F**).

To further demonstrate the relationship between DYM and the immune environment characteristics in bladder cancer, a systematic analysis was conducted as described above. By separating the median DYM expression level, the samples were divided into two subgroups. Outcomes of the "ESTIMATE" analysis revealed that patients with higher DYM expression had a remarkably higher stromal score, immune score, and ESTIMATE score relative to patients with lower DYM expression (**Figures 7G–I**). ssGSEA results showed that the content of infiltration of immunocytes, including Th1 cells, Th2 cells, macrophages, aDCs, CD8+ T cells, NK cells, and neutrophils, and immune signatures such as APC co-stimulation, HLA, MHC-class I, and T cell co-stimulation were remarkably increased in patients with high DYM expression (**Figure 7E**). The above results indicate that the *DYM* gene might be involved in the alteration of the TIME.

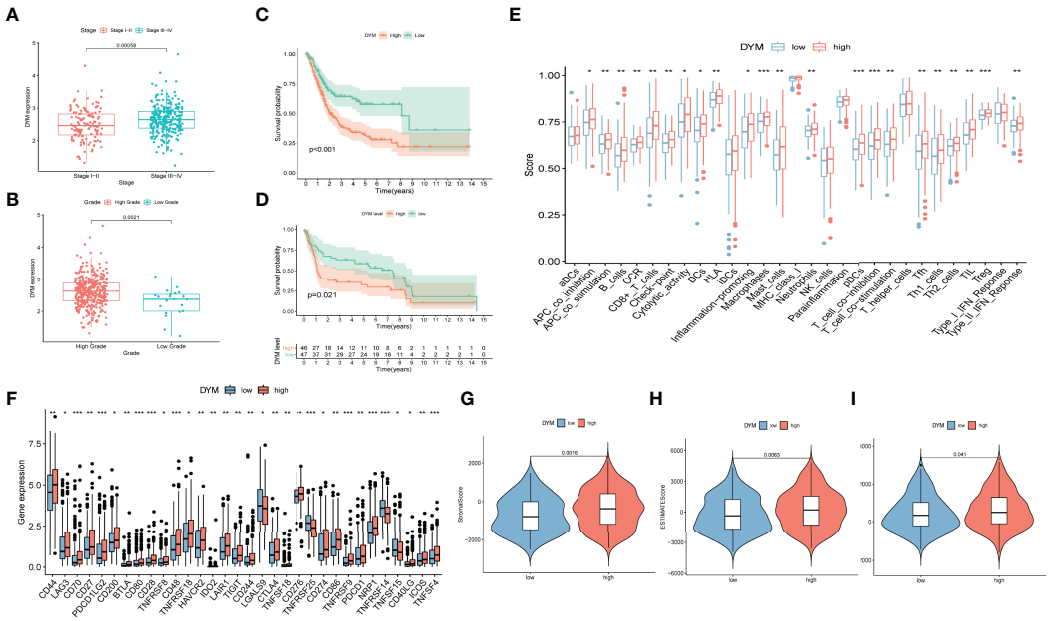

FIGURE 7 | The prognostic significance of DYM in bladder cancer and correlation of DYM with immune checkpoint blockage key genes and tumor immune microenvironment features. **(A)**Significant difference in DYM expression between distinct tumor stages. **(B)** Significant difference in DYM expression between high- and low-grade. **(C, D)** Higher expression level of DYM predicts lower survival probability in TCGA cohort **(C)** and GSE31684 **(D)**. **(E)** Distinction of the immune-related profiles between high- and low-DYM groups (*P < 0.05; **P < 0.01; ***P < 0.001). **(F)** Difference in expression levels of ICB-related genes between high- and low-DYM groups (*P < 0.05; **P < 0.01; ***P < 0.001). **(G-I)** Comparison of ESTIMATE analysis results between high- and low-DYM groups.

In order to verify the relationship between DYM gene and tumor immune microenvironment, the THP-1 cells were induced to differentiate into M0 macrophages by 100 ng/ml PMA, the **Figure 8B** displayed the THP-1 cell photograph and the **Figure 8C** displayed the M0 macrophages photograph. we co-cultured Si-con or Si-DYM bladder cancer cell lines with M0 macrophages to detect tumor markers of CD206, CD163 and CD86 macrophages (**Figure 8A**). Secondly, we investigated whether DYM gene affected the production of pro-inflammatory factors, immunosuppressive cytokines and chemokines, detected IL-1B, IL-6, IL-10, TNF, IL-8, CCL2, CCL3, CCL20, CXCL1, CXCL2 respectively, and the secretion level was detected with ELISA assay. The results displayed that the levels of CD206 and CD163 were reduced in both two bladder cancer cell lines, while the level of CD86 had no significant difference in T24, and increased in J82 cell line (**Figures 8D, E**). The levels of IL-6, IL-10, CCL2 were significantly decreased in both two bladder cancer cell lines, and Other transcription factors are uncertain in cell lines (**Figures 8F–I**). The ELISA assay exhibited that IL-6, CCL2 were significantly reduced in the supernatant (**Figures 8J, K**).

Knockdown of DYM Suppressed BCa Cell Proliferation, Invasion, Migration and Promoted Apoptosis *in vitro*

We further examined the biological function of *DYM gene* in the progression of bladder cancer. We designed siRNA targeting DYM, and the knockdown effect of DYM expression level is shown in the **Figure 9A**. The CCK8 assays confirmed that knockdown of DYM remarkably inhibited the proliferation ability of T24 and J82 cells (**Figures 9C, D**). In addition, the flow cytometry analysis displayed the effect of knockdown of DYM genes on cell apoptosis (**Figure 9B**). As shown in **Figures 9E–H**, both early apoptosis and late apoptosis of T24 and J82 cells were increased when transfected with Si-DYM compared with Si-con. Finally, Knockdown of DYM in T24 and J82 cells caused a remarkable reduction in cell invasion and migration ability (**Figures 10A–G**). In summary, our results demonstrated that the *DYM* gene not only plays an immune-related role in bladder cancer, but also promotes the proliferation, migration, metastasis and suppresses cell apoptosis of bladder cancer cells.

DISCUSSION

Owing to sophisticated molecular mechanisms such as genomic complexity, protein modification diversity, and epigenetics, bladder cancer is highly heterogeneous from a clinical perspective, making it difficult to predict its clinical outcomes accurately (6, 31, 32). Thus, stratifying patients and adopting treatment strategies only *via* pathological anatomy and TNM staging is relatively limited for clinical applications. It is regrettable that the majority of patients with bladder cancer cannot benefit from immunotherapy because of the occurrence of immune escape, mediated by multiple factors (33, 34).

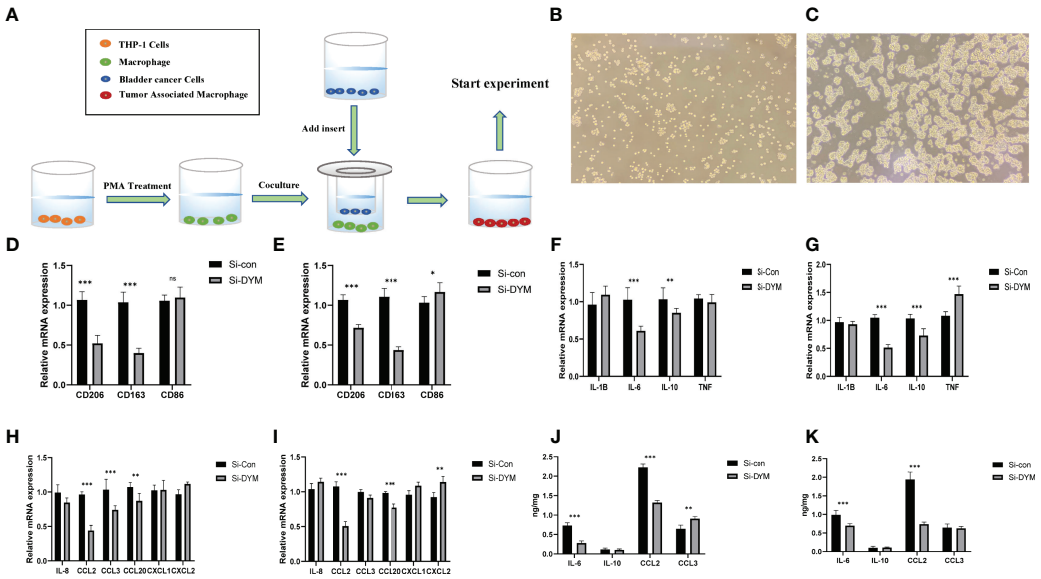

FIGURE 8 | Effects of DYM on tumor immune microenvironment. **(A)** Cell co-culture mechanism diagram. **(B–C)** THP-1 cell **(B)**, M0 macrophage **(C)** photos under microscope. **(D–I)** The expression of macrophage markers **(D, E)**, cytokines **(F–G)** and chemokines **(H, I)** of T24/J82 were detected by QRT-PCR. **(J, K)** ELISA was used to detect the expression of cytokines and chemokine of T24/J82. *P < 0.05, **P < 0.01, ***P < 0.001. ns P > 0.05.

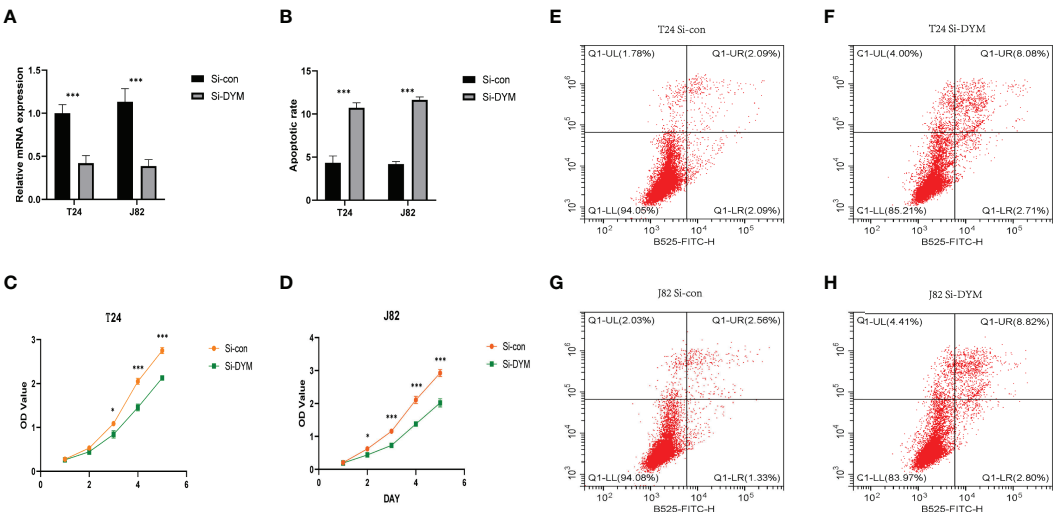

FIGURE 9 | Effects of DYM knockdown on bladder cancer cells proliferation and apoptosis *in vitro*. **(A)** qRT-PCR was used to detect the expression of DYM after T24/J82 cells transfected with DYM siRNA plasmids. **(B, E–H)** Cell apoptosis was detected by flow cytometry after transfection of Si-con or Si-DYM in T24/J82 cells. **(C, D)** The proliferation of T24 **(C)** and J82 cells **(D)** was examined by CCK-8 assay, which exhibited that DYM knockdown group had lower OD value. The representative images are presented. Black lines indicate the wound edge. *P < 0.05, **P < 0.01, ***P < 0.001.

Moreover, there are distinct inconsistencies among the responses of patients to both BCG and PD-1/PD-L1 immunotherapy (35, 36). Therefore, the design and development of more reliable prognostic tools for clinical outcome prediction are urgently necessitated, especially for immunotherapeutic prognosis, toward individualized and precise treatment of bladder cancer.

Increasing evidence has elucidated the significance of AS events in physiological or pathological processes, making AS events a novel perspective for understanding intricate pathological processes such as cancer (37, 38). Compared with transcriptome analysis, the investigation based on the alternative splicing level is conducive to the in-depth analysis of the causes,

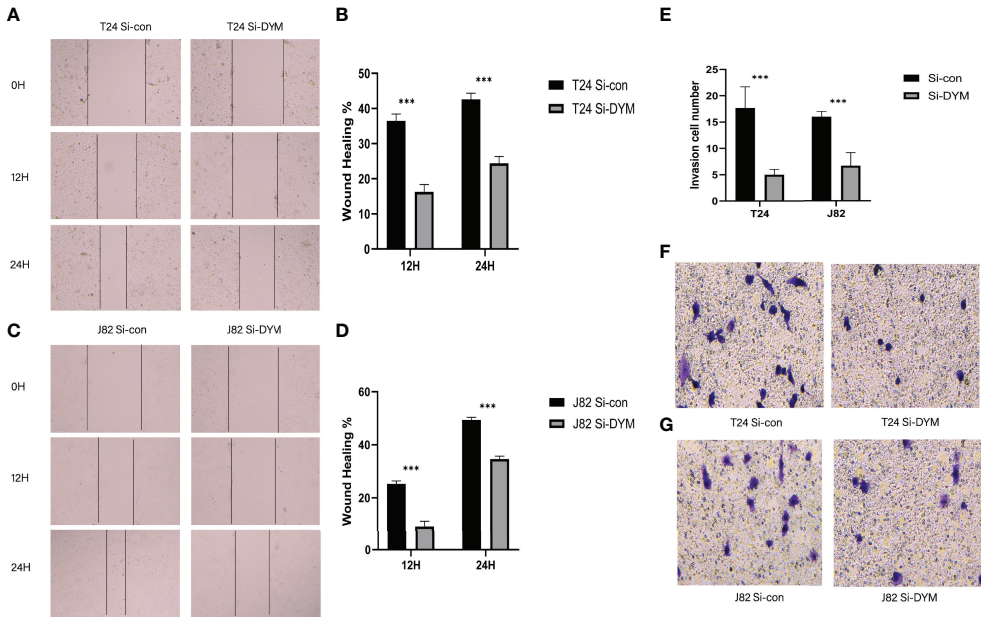

FIGURE 10 | Effects of DYM knockdown on bladder cancer cells invasion and migration *in vitro*. **(A–D)** The wound healing assay was performed to assess the effect of DYM knockdown on the migration of T24 and J82 cells. **(E–G)** Transwell assay was applied to detect the invasion ability of T24 and J82 cells. The representative images are presented. Black lines indicate the wound edge. *P < 0.05, **P < 0.01, ***P < 0.001.

progression and clinical results of diseases. If the up-regulation or down-regulation of genes is caused by alternative splicing alteration, what is the upstream regulatory mechanism and what substances lead to its alteration. Furthermore, the relationship between the alternative splicing modification characteristics of this gene and histone, DNA methylation can be explored. Encouragingly, with the progress in high-throughput sequencing technology, enormous achievements have been made in the study of the latent association between AS patterns and tumors. More importantly, the prognostic ability of AS events has also been widely tested in multiple cancers (14, 39, 40). In bladder cancer, specific AS events have been associated with worse prognosis (41, 42). However, current studies have mainly focused on specific AS events, and systematic analyses of the prognostic value of AS events are minor (43). Fan Z et al. depicted the prognostic signatures of bladder cancer based on AS events *via* comprehensive analysis at the genome-wide level, which revealed that prognostic-related AS events tended to affect the clinical outcome of bladder cancer patients and sensitivity to chemotherapy drugs (44). Nevertheless, a correlation analysis between AS events with TIME and immunotherapeutic outcomes in bladder cancer is still lacking.

In our study, we investigated the AS events in bladder cancer by multiple perspective analysis, selected the most correlative prognostic profiles, constructed a high-preciseness model, and predicted the individual overall survival rates of patients with bladder cancer accurately. Interestingly, the results showed that prognostic predictive signatures established according to the all AS patterns (AD, AA, AP, AT, ES, RI, ME) displayed an appreciable performance for predicting the clinical outcome of bladder cancer patients. Notably, grouped according to clinicopathological factors, these signatures were shown to have excellent prognostic capability. To create an effective and practical tool for clinical practice in bladder cancer, nomogram model contains prognostic characteristics and clinicopathological stages was established, and the predicted results were consistent with the actual results.

With continuous advancement of research into this area, increasing attention has been focused on the crucial role of AS events in TIME (45, 46). Indeed, identifying AS events in TIME might contribute significantly to the bladder cancer treatment. Taking advantage of the ESTIMATE, CIBERSORT, and ssGSEA enrichment analyses, we unveiled the role of AS events in the context of TIME in bladder cancer. The ESTIMATE and ssGSEA results indicated that the group with high-risk scores presented a greater activation of immune and stromal cells. The composition of stromal cells limits the entry of immune cells into the TME to play an anti-tumor role, which explains the poor clinical outcome in the high-risk group with active immune infiltration. The CIBERSORT results agreed with our hypothesis, and found that the risk score was positively correlated with M0 macrophages and M2 macrophages, which favors tumor progression in bladder cancer. Of note, six pivotal ICB targets and 33 ICB-related gene expression levels exhibited a distinct correlation with risk score. In addition, we found the patients with low risk score had superior immunotherapy outcomes, which suggests that risk score might be conducive to developing individual immunotherapeutic strategies and

predicting the outcomes (36). Patients with a low risk score may be better candidates for immunotherapy, while patients with a high risk score may prefer chemotherapy or targeted therapy strategies.

DYM encodes a protein that regulates Golgi-associated secretory pathways, which play an indispensable role in the early brain development and endochondral bone formation (47). To date, little is known about the effects of DYM in tumors, especially bladder cancer. This study showed that the high expression of DYM was significantly related to advanced clinicopathology and poor prognosis of bladder cancer. DYM expression was also correlated with TIME alteration and key genes of ICB immunotherapy (e.g., CD274, CTLA4, HAVCR2 and PDCD1). We found that after the knockdown of DYM gene, IL-6, CCL2 cytokines in the supernatant were down-regulated in the co-culture system of bladder cancer cells and macrophages, thereby reducing the recruitment of macrophages(CCL2 effection) and the transformation of macrophages into M2 macrophages(IL-6 effection). There may be a DYM-IL-6 signaling pathway axis. Subsequently, we confirmed that knockdown of DYM genes inhibited the cell proliferation, migration, invasion and promote apoptosis ability of bladder cancer cells.

Overall, subjects with higher DYM expression levels or higher risk scores presented more immune cells in the tumor microenvironment, indicating an enhanced immunophenotype but shorter OS. Consistent with our speculate hypothesize, previous researches have also displayed a correlation between low tumor purity, poor prognosis, and an activated immune phenotype (48, 49). Since the risk scores are related to the expression of ICB-related genes, it can be speculated that the effects of immune cells on tumors may be influenced by ICB pathways. Pan et al. found that bladder cancer with high immune infiltration exhibited a low response rate to ICB therapy, which might support our conjecture (50). These findings suggest that the evaluation of AS events in bladder cancer is conducive to immunotherapeutic choice and prognosis prediction, which has great clinical significance. Presumably, valuable insights into potential therapeutic targets may be revealed by elucidating the mechanisms underlying these events.

Owing to the lack of an ICB treatment dataset related to alternative splicing in the bladder cancer cohort, it was difficult to further explore the association between ICB therapeutic response and risk score. In addition, this study is based on public data sets for bioinformatics analysis, which need be confirmed by our dataset. In the future, we will attempt to collect clinical specimens from bladder cancer patients in Huashan Hospital, obtain alternative splicing event, transcriptome data and clinical information, and conduct prospective validation of this risk model, so as to make this topic more valuable for research. If the effect of DYM gene on tumor immune microenvironment can be verified in immunocompetent mouse model, the topic research in this paper will be further verified. Unfortunately, our laboratory lacks the corresponding experimental technology at present, which is expected to be further improved and optimized in the future.

CONCLUSION

Our study provided an indispensable reference for further investigation of the role of AS events in the tumor microenvironment and immunotherapy efficiency, and rendered personalized prognosis monitoring and potential biological treatment targets for bladder cancer.

DATA AVAILABILITY STATEMENT

All datasets generated for this study are included in the article material, including TCGA database (https://portal.gdc.cancer.gov/), and GEO dataset (https://www.ncbi.nlm.nih.gov/gds/): GSE31684.

AUTHOR CONTRIBUTIONS

FY: Conceptualization, Methodology, Writing – review & editing, Investigation. YLia and ZC: Investigation, Project administration. HJ: Conceptualization, Methodology, Writing – review & editing, Supervision. other authors contributed toward data collection and analysis. All authors contributed to the article and approved the submitted version.

FUNDING

This study was supported by the National Natural Science Foundation of China (Grant Numbers: 81872102).

ACKNOWLEDGMENTS

We sincerely appreciate all members who participated in data collection and analysis.

SUPPLEMENTARY MATERIAL

The Supplementary Material for this article can be found online at: https://www.frontiersin.org/articles/10.3389/fimmu.2022.911902/full#supplementary-material

Supplementary Figure 1 | (A) Intersections among the seven types of AS events in TCGA BLCA cohort by UpSet diagram. **(B)** Intersections among the seven types of prognostic related AS events by UpSet diagram.

Supplementary Figure 2 | (A) Tuning parameters (λ/lambda) selected in the LASSO model.

Supplementary Figure 3 | (A) Kaplan–Meier curve presenting suvival in high and low MICALL2 levels. **(B)** Comparison of MICALL2 expression between high- and low-grade. **(C)** Comparison of MICALL2 expression between major tumor stages. **(D–F)** Comparison of stromal score, immune score and ESTIMATE score between patients with high- and low-MICALL2 groups. **(G)** Distinction of the immune-related profiles between high- and low-MICALL2 groups. **(H)** Difference in expression levels of ICB-related genes between high- and low-MICALL2 groups.

REFERENCES

1. Siegel RL, Miller KD, Fuchs HE, Jemal A. Cancer Statistics, 2021. *CA Cancer J Clin* (2021) 71:7–33. doi: 10.3322/caac.21654
2. Lenis AT, Lec PM, Chamie K, Mshs MD. Bladder Cancer: A Review. *Jama* (2020) 324:1980–91. doi: 10.1001/jama.2020.17598
3. Lobo N, Shariat SF, Guo CC, Fernandez MI, Kassouf W, Choudhury A, et al. What Is the Significance of Variant Histology in Urothelial Carcinoma? *Eur Urol Focus* (2020) 6(4):653–63. doi: 10.1016/j.euf.2019.09.003
4. Choi W, Ochoa A, McConkey DJ, Aine M, Höglund M, Kim WY, et al. Genetic Alterations in the Molecular Subtypes of Bladder Cancer: Illustration in the Cancer Genome Atlas Dataset. *Eur Urol* (2017) 72(3):354–65. doi: 10.1016/j.eururo.2017.03.010
5. Seiler R, Ashab HAD, Erho N, van Rhijn BWG, Winters B, Douglas J, et al. Impact of Molecular Subtypes in Muscle-Invasive Bladder Cancer on Predicting Response and Survival After Neoadjuvant Chemotherapy. *Eur Urol* (2017) 72(4):544–54. doi: 10.1016/j.eururo.2017.03.030
6. McConkey DJ, Choi W. Molecular Subtypes of Bladder Cancer. *Curr Oncol Rep* (2018) 20:77. doi: 10.1007/s11912-018-0727-5
7. Efstathiou JA, Mouw KW, Gibb EA, Liu Y, Wu CL, Drumm MR, et al. Impact of Immune and Stromal Infiltration on Outcomes Following Bladder-Sparing Trimodality Therapy for Muscle-Invasive Bladder Cancer. *Eur Urol* (2019) 76 (1):59–68. doi: 10.1016/j.eururo.2019.01.011
8. Chen S, Zhang N, Shao J, Wang T, Wang X. Multi-Omics Perspective on the Tumor Microenvironment Based on PD-L1 and CD8 T-Cell Infiltration in Urothelial Cancer. *J Canc* (2019) 10:697–707. doi: 10.7150/jca.28494
9. Wang Y, Chen L, Yu M, Fang Y, Qian K, Wang G, et al. Immune-Related Signature Predicts the Prognosis and Immunotherapy Benefit in Bladder Cancer. *Cancer Med* (2020) 9(20):7729–41. doi: 10.1002/cam4.3400
10. Grosser R, Cherkassky L, Chintala N, Adusumilli PS. Combination Immunotherapy With CAR T Cells and Checkpoint Blockade for the Treatment of Solid Tumors. *Cancer Cell* (2019) 36:471–82. doi: 10.1016/j.ccell.2019.09.006
11. Pettenati C, Ingersoll MA. Mechanisms of BCG Immunotherapy and its Outlook for Bladder Cancer. *Nat Rev Urol* (2018) 15:615–25. doi: 10.1038/s41585-018-0055-4
12. Gopalakrishnan D, Koshkin VS, Ornstein MC, Papatsoris A, Grivas P. Immune Checkpoint Inhibitors in Urothelial Cancer: Recent Updates and Future Outlook. *Ther Clin Risk Manag* (2018) 14:1019–40. doi: 10.2147/TCRM.S158753
13. Baralle FE, Giudice J. Alternative Splicing as a Regulator of Development and Tissue Identity. *Nat Rev Mol Cell Biol* (2017) 18:437–51. doi: 10.1038/nrm.2017.27
14. Li Y, Sun N, Lu Z, Sun S, Huang J, Chen Z, et al. Prognostic Alternative mRNA Splicing Signature in non-Small Cell Lung Cancer. *Cancer Lett* (2017) 393:40–51. doi: 10.1016/j.canlet.2017.02.016
15. Sveen A, Kilpinen S, Ruusulehto A, Lothe RA, Skotheim RI. Aberrant RNA Splicing in Cancer; Expression Changes and Driver Mutations of Splicing Factor Genes. *Oncogene* (2016) 35:2413–27. doi: 10.1038/onc.2015.318
16. Climente-González H, Porta-Pardo E, Godzik A, Eyras E. The Functional Impact of Alternative Splicing in Cancer. *Cell Rep* (2017) 20:2215–26. doi: 10.1016/j.celrep.2017.08.012
17. Lee SC, Abdel-Wahab O. Therapeutic Targeting of Splicing in Cancer. *Nat Med* (2016) 22:976–86. doi: 10.1038/nm.4165
18. Calabrese C, Davidson NR, Demircioğlu D, Fonseca NA, He Y, Kahles A, et al. Genomic Basis for RNA Alterations in Cancer. *Nature* (2020) 578(7793):129–36. doi: 10.1038/s41586-020-1970-0
19. Tripathi V, Ellis JD, Shen Z, Song DY, Pan Q, Watt AT, et al. The Nuclear-Retained Noncoding RNA MALAT1 Regulates Alternative Splicing by Modulating SR Splicing Factor Phosphorylation. *Mol Cell* (2010) 39(6):925–38. doi: 10.1016/j.molcel.2010.08.011
20. Kędzierska H, Piekiełko-Witkowska A. Splicing Factors of SR and hnRNP Families as Regulators of Apoptosis in Cancer. *Cancer Lett* (2017) 396:53–65. doi: 10.1016/j.canlet.2017.03.013
21. Du JX, Zhu GQ, Cai JL, Wang B, Luo YH, Chen C, et al. Splicing Factors: Insights Into Their Regulatory Network in Alternative Splicing in Cancer. *Cancer Lett* (2021) 501:83–104. doi: 10.1016/j.canlet.2020.11.043
22. Takeiwa T, Mitobe Y, Ikeda K, Horie-Inoue K, Inoue S. Roles of Splicing Factors in Hormone-Related Cancer Progression. *Int J Mol Sci* (2020) 21 (5):1551. doi: 10.3390/ijms21051551
23. Guo Z, Zhu H, Xu W, Wang X, Liu H, Wu Y, et al. Alternative Splicing Related Genetic Variants Contribute to Bladder Cancer Risk. *Mol Carcinogen* (2020) 59(8):923–9. doi: 10.1002/mc.23207
24. Xie R, Chen X, Cheng L, Huang M, Zhou Q, Zhang J, et al. NONO Inhibits Lymphatic Metastasis of Bladder Cancer *via* Alternative Splicing of SETMAR. *Mol Ther* (2021) 29(1):291–307. doi: 10.1016/j.ymthe.2020.08.018
25. Xie R, Chen X, Chen Z, Huang M, Dong W, Gu P, et al. Polypyrimidine Tract Binding Protein 1 Promotes Lymphatic Metastasis and Proliferation of Bladder Cancer *via* Alternative Splicing of MEIS2 and PKM. *Cancer Lett* (2019) 449:31–44. doi: 10.1016/j.canlet.2019.01.041
26. Bielli P, Panzeri V, Lattanzio R, Mutascio S, Pieraccioli M, Volpe E, et al. The Splicing Factor PTBP1 Promotes Expression of Oncogenic Splice Variants and Predicts Poor Prognosis in Patients With Non-Muscle-Invasive Bladder Cancer. *Clin Cancer Res* (2018) 24(21):5422–32. doi: 10.1158/1078-0432.CCR-17-3850
27. Huang R, Zheng Z, Xian S, Zhang J, Jia J, Song D, et al. Identification of Prognostic and Bone Metastatic Alternative Splicing Signatures in Bladder Cancer. *Bioengineered* (2021) 12(1):5289–304. doi: 10.1080/21655979.2021.1964252
28. Bindea G, Mlecnik B, Tosolini M, Kirilovsky A, Waldner M, Obenauf AC, et al. Spatiotemporal Dynamics of Intratumoral Immune Cells Reveal the Immune Landscape in Human Cancer. *Immunity* (2013) 39(4):782–95. doi: 10.1016/j.immuni.2013.10.003
29. Newman AM, Liu CL, Green MR, Gentles AJ, Feng W, Xu Y, et al. Robust Enumeration of Cell Subsets From Tissue Expression Profiles. *Nat Methods* (2015) 12(5):453–7. doi: 10.1038/nmeth.3337
30. Zhang X, Wang Y AG, Qu C, Chen J. Pan-Cancer Analysis of PARP1 Alterations as Biomarkers in the Prediction of Immunotherapeutic Effects and the Association of Its Expression Levels and Immunotherapy Signatures. *Front Immunol* (2021) 12:721030. doi: 10.3389/fimmu.2021.721030
31. Kamoun A, de Reyniés A, Allory Y, Sjödahl G, Robertson AG, Seiler R, et al. A Consensus Molecular Classification of Muscle-Invasive Bladder Cancer. *Eur Urol* (2020) 77(4):420–33. doi: 10.1016/j.eururo.2019.09.006
32. Alifrangis C, McGovern U, Freeman A, Powles T, Linch M. Molecular and Histopathology Directed Therapy for Advanced Bladder Cancer. *Nat Rev Urol* (2019) 16:465–83. doi: 10.1038/s41585-019-0208-0
33. Butt SU, Malik L. Role of Immunotherapy in Bladder Cancer: Past, Present and Future. *Cancer Chemother Pharmacol* (2018) 81:629–45. doi: 10.1007/s00280-018-3518-7
34. Song D, Powles T, Shi L, Zhang L, Ingersoll MA, Lu YJ. Bladder Cancer, a Unique Model to Understand Cancer Immunity and Develop Immunotherapy Approaches. *J Pathol* (2019) 249:151–65. doi: 10.1002/path.5306
35. Larsen ES, Joensen UN, Poulsen AM, Goletti D, Johansen IS. Bacillus Calmette-Guérin Immunotherapy for Bladder Cancer: A Review of Immunological Aspects, Clinical Effects and BCG Infections. *APMIS Acta Patholo Microbiol Immuno Scandin* (2020) 128:92–103. doi: 10.1111/apm.13011
36. Bellmunt J, Powles T, Vogelzang NJ. A Review on the Evolution of PD-1/PD-L1 Immunotherapy for Bladder Cancer: The Future is Now. *Cancer Treat Rev* (2017) 54:58–67. doi: 10.1016/j.ctrv.2017.01.007
37. Nilsen TW, Graveley BR. Expansion of the Eukaryotic Proteome by Alternative Splicing. *Nature* (2010) 463:457–63. doi: 10.1038/nature08909
38. Ule J, Blencowe BJ. Alternative Splicing Regulatory Networks: Functions, Mechanisms, and Evolution. *Mol Cell* (2019) 76:329–45. doi: 10.1016/j.molcel.2019.09.017
39. Xie ZC, Wu HY, Dang YW, Chen G. Role of Alternative Splicing Signatures in the Prognosis of Glioblastoma. *Cancer Med* (2019) 8:7623–36. doi: 10.1002/cam4.2666
40. Lin P, He RQ, Huang ZG, Zhang R, Wu HY, Shi L, et al. Role of Global Aberrant Alternative Splicing Events in Papillary Thyroid Cancer Prognosis. *Aging* (2019) 11(7):2082–97. doi: 10.18632/aging.101902
41. Koch A, Hatina J, Rieder H, Seifert HH, Huckenbeck W, Jankowiak F, et al. Discovery of TP53 Splice Variants in Two Novel Papillary Urothelial Cancer

Cell Lines. *Cell Oncol (Dordrecht)* (2012) 35(1):243–57. doi: 10.1007/s13402-012-0082-8
42. Dueñas M, Pérez-Figueroa A, Oliveira C, Suárez-Cabrera C, Sousa A, Oliveira P, et al. Gene Expression Analyses in Non Muscle Invasive Bladder Cancer Reveals a Role for Alternative Splicing and Tp53 Status. *Sci Rep* (2019) 9 (1):10362. doi: 10.1038/s41598-019-46652-4
43. Arnold SA, Loomans HA, Ketova T, Andl CD, Clark PE, Zijlstra A. Urinary Oncofetal ED-A Fibronectin Correlates With Poor Prognosis in Patients With Bladder Cancer. *Clin Exp Metasta* (2016) 33:29–44. doi: 10.1007/s10585-015-9754-x
44. Fan Z, Zhang Z, Piao C, Liu Z, Wang Z, Kong C. Genome-Wide Analyses of Prognostic and Therapeutic Alternative Splicing Signatures in Bladder Urothelial Carcinoma. *Front Oncol* (2021) 11:626858. doi: 10.3389/fonc.2021.626858
45. Silva AL, Faria M, Matos P. Inflammatory Microenvironment Modulation of Alternative Splicing in Cancer: A Way to Adapt. *Adv Exp Med Biol* (2020) 1219:243–58. doi: 10.1007/978-3-030-34025-4_13
46. Li ZX, Zheng ZQ, Wei ZH, Zhang LL, Li F, Lin L, et al. Comprehensive Characterization of the Alternative Splicing Landscape in Head and Neck Squamous Cell Carcinoma Reveals Novel Events Associated With Tumorigenesis and the Immune Microenvironment. *Theranostics* (2019) 9 (25):7648–65. doi: 10.7150/thno.36585
47. Denais C, Dent CL, Southgate L, Hoyle J, Dafou D, Trembath RC, et al. Dymeclin, the Gene Underlying Dyggve-Melchior-Clausen Syndrome, Encodes a Protein Integral to Extracellular Matrix and Golgi Organization and is Associated With Protein Secretion Pathways Critical in Bone Development. *Hum Mutat* (2011) 32(2):231–9. doi: 10.1002/humu.21413
48. Zhang C, Cheng W, Ren X, Wang Z, Liu X, Li G, et al. Tumor Purity as an Underlying Key Factor in Glioma. *Clin Cancer Res* (2017) 23(20):6279–91. doi: 10.1158/1078-0432.CCR-16-2598
49. Rhee JK, Jung YC, Kim KR, Yoo J, Kim J, Lee YJ, et al. Impact of Tumor Purity on Immune Gene Expression and Clustering Analyses Across Multiple Cancer Types. *Cancer Immunol Res* (2018) 6(1):87–97. doi: 10.1158/2326-6066.CIR-17-0201
50. Pan S, Zhan Y, Chen X, Wu B, Liu B. Bladder Cancer Exhibiting High Immune Infiltration Shows the Lowest Response Rate to Immune Checkpoint Inhibitors. *Front Oncol* (2019) 9:1101. doi: 10.3389/fonc.2019.01101

Conflict of Interest: The authors declare that the research was conducted in the absence of any commercial or financial relationships that could be construed as a potential conflict of interest.

Publisher's Note: All claims expressed in this article are solely those of the authors and do not necessarily represent those of their affiliated organizations, or those of the publisher, the editors and the reviewers. Any product that may be evaluated in this article, or claim that may be made by its manufacturer, is not guaranteed or endorsed by the publisher.

frontiers | Frontiers in Immunology

TYPE Original Research
PUBLISHED 08 September 2022
DOI 10.3389/fimmu.2022.991656

OPEN ACCESS

EDITED BY
Liusheng Peng,
Third Military Medical University, China

REVIEWED BY
JinKu Zhang,
Hebei University, China
Jia Shi,
Wuxi Maternity and Child Health Care Hospital, China

*CORRESPONDENCE
Xinwei Yun
yunspider@126.com
Qiang Lin
linqiang1962@163.com
Huashui Li
wuxingli83@163.com

†These authors have contributed equally to this work

SPECIALTY SECTION
This article was submitted to Autoimmune and Autoinflammatory Disorders: Autoinflammatory Disorders, a section of the journal Frontiers in Immunology

RECEIVED 11 July 2022
ACCEPTED 19 August 2022
PUBLISHED 08 September 2022

CITATION
Xie W, Zeng Y, Hu L, Hao J, Chen Y, Yun X, Lin Q and Li H (2022) Based on different immune responses under the glucose metabolizing type of papillary thyroid cancer and the response to anti-PD-1 therapy.
Front. Immunol. 13:991656.
doi: 10.3389/fimmu.2022.991656

Based on different immune responses under the glucose metabolizing type of papillary thyroid cancer and the response to anti-PD-1 therapy

Wenjun Xie[1,2,3†], Yu Zeng[3†], Linfei Hu[3†], Jiaru Hao[4†], Yuzheng Chen[2,5], Xinwei Yun[3*], Qiang Lin[1,2*] and Huashui Li[1,2*]

[1]Department of General Surgery, Shengli Clinical Medical College, Fujian Provincial Hospital, Fuzhou, China, [2]Shengli Clinical Medical College, Fujian Medical University, Fuzhou, China, [3]Department of Thyroid and Neck Tumor, Tianjin Medical University Cancer Institute and Hospital, National Clinical Research Center for Cancer, Key Laboratory of Cancer Prevention and Therapy, Tianjin's Clinical Research Center for Cancer, Tianjin, China, [4]Department of Gastrointestinal Cancer Biology, Tianjin Medical University Cancer Institute and Hospital, National Clinical Research Center for Cancer, Key Laboratory of Cancer Immunology and Biotherapy, Tianjin, China, [5]Department of Endocrinology, Fujian Provincial Hospital, Shengli Clinical Medical College of Fujian Medical University, Fuzhou, China

Glucose metabolism-related genes play an important role in the development and immunotherapy of many tumours, but their role in thyroid cancer is ambiguous. To investigate the role of glucose metabolism-related genes in the development of papillary thyroid cancer (PTC) and their correlation with the clinical outcome of PTC, we collected transcriptomic data from 501 PTC patients in the Cancer Genome Atlas (TCGA). We performed nonnegative matrix decomposition clustering of 2752 glucose metabolism-related genes from transcriptome data and classified PTC patients into three subgroups (C1 for high activation of glucose metabolism, C2 for low activation of glucose metabolism and C3 for moderate activation of glucose metabolism) based on the activation of different glucose metabolism-related genes in 10 glucose metabolism-related pathways. We found a positive correlation between the activation level of glucose metabolism and the tumour mutation burden (TMB), neoantigen number, mRNA stemness index (mRNAsi), age, and tumour stage in PTC patients. Next, we constructed a prognostic prediction model for PTC using six glucose metabolism-related genes (PGBD5, TPO, IGFBPL1, TMEM171, SOD3, TDRD9) and constructed a nomogram based on the risk score and clinical parameters of PTC patients. Both the prognostic risk prediction model and nomogram had high stability and accuracy for predicting the progression-free interval (PFI) in PTC patients. Patients were then divided into high-risk and low-risk groups by risk score. The high-risk group was sensitive to paclitaxel and anti-PD-1 treatment, and the low-risk group was sensitive to sorafenib treatment. We found that the high-risk group was enriched in inflammatory response pathways and associated with high level of immune cell infiltration. To verify the accuracy of the prognostic prediction model, we knocked down PGBD5 in PTC cells and found that the proliferation ability of PTC cells was

10.3389/fimmu.2022.991656

significantly reduced. This suggests that PGBD5 may be a relatively important oncogene in PTC. Our study constructed a prognostic prediction model and classification of PTC by glucose metabolism-related genes, which provides a new perspective on the role of glucose metabolism in the development and immune microenvironment of PTC and in guiding chemotherapy, targeted therapy and immune checkpoint blockade therapy of PTC.

KEYWORDS

metabolic genes, papillary thyroid cancer classification, immune signatures, prognosis, PD-1, PGBD5

Introduction

The incidence of thyroid cancer (TC) has been increasing worldwide in recent decades. The most common histologic subtype of TC is papillary thyroid carcinoma (PTC), which is the only histologic subtype of TC that is systematically increasing in all countries (1). The incidence of PTC is almost always higher in women than in men (2). PTC is less malignant than other subtypes of TC, but many patients are still at risk of recurrence and metastasis, at which point the survival rate decreases significantly (3). The construction of prognostic prediction models by abnormally expressed genes as well as nomograms to assess the prognosis of tumour patients and the classification of tumour patients into high-risk and low-risk groups to guide treatment have been developed and applied in several tumourtypes (4, 5). However, reasonable and accurate prognostic prediction models are still lacking in PTC. The current study found that glucose metabolism plays an important role in the development and treatment of PTC (6, 7), and it is unknown whether a reasonable prognostic prediction model can be constructed to predict PTC prognosis and guide PTC treatment by glucose metabolism-related genes in PTC.

Various metabolic pathways have been suggested to play an important role in the development of cancer, such as aerobic glycolysis, glutamine catabolism, and fatty acid metabolism, which produce various nutrients that promote cell growth and proliferation (8–10). Compared to normal tissue, *in vitro* cancer tissue can use large amounts of glucose to produce lactate even in the presence of oxygen, a phenomenon known as aerobic glycolysis or the Warburg effect. Lactate dehydrogenase (LDHA), which is involved in glycolysis, is a transcriptional target of the oncogene MYC and is required for increased glycolysis and tumorigenesis in tumour cells, which provides the molecular basis for the Warburg effect (8). BRAF mutations, which are closely associated with the development of PTC, have also been found to be closely associated with overexpression of several competence metabolism-related genes (11, 12), and inhibition of metabolism-related gene expression has a significant inhibitory effect on PTC progression (13).

The importance of immunotherapy in tumour treatment is constantly being studied, and it forms the basis of cancer treatment together with surgical treatment, radiotherapy and targeted therapy (14). Current studies have found that the metabolism of energy in a variety of tumour cells can affect immune cell function and immunotherapeutic efficacy either by acting directly or influencing the tumour microenvironment (TME). Tumour depletion of glucose metabolically limits T-cell function, leading to their diminished antitumor capacity and thus tumour progression (15). Tumour cells produce large amounts of lactate through aerobic glycolysis and release excess lactate into the TME *via* monocarboxylate transporter protein 4 (16). Lactate in the TME inhibits the therapeutic efficacy of ipilimumab in melanoma (17). Increasing the pH in tumour tissue improves cytotoxic T lymphocyte infiltration and enhances anti-CTLA-4, anti-PD-1 and chimeric antigen receptor (CAR) T-cell therapy (18). However, the effect of glucose metabolism on immune cell infiltration and immunotherapy in PTC has rarely been reported. Therefore, predicting the sensitivity to immunotherapy before administering it to patients with advanced PTC is challenging, but necessary, for individualizing patient treatment and optimizing health care costs.

In this study, we hypothesized that glucose metabolism plays an important role in the development of PTC and modifies the immune microenvironment. Therefore, we clustered information from clinical samples of 501 patients in the TCGA-THCA cohort and 10 glucose metabolism-related pathways. Three subgroups of PTC were identified by unsupervised transcriptome analysis, namely, C1, C2, and C3. Next, we analysed the proportion of PTC subgroups by different clinical stage, mutation type, and frequency of each mutation type. We also compared the tumour mutation burden (TMB), neoantigen number, and mRNA stemness index (mRNAsi) occurring in each of the three subgroups. Then, we further generated the prognostic genes that contributed most to the progression-free interval (PFI) of PTC by Lasso Cox analysis, constructed a prognostic prediction model for

PTC based on six prognostic genes (PGBD5, TPO, IGFBPL1, TMEM171, SOD3, TDRD9), constructed a nomogram based on risk score and clinical parameters, divided patients into high risk (HRisk) and low risk (LRisk) groups based on risk score, and then analysed the prognostic differences, immune infiltration, clinical characteristics and sensitivity to drug treatment between the HRisk and LRisk groups. Finally, we evaluated the reliability of the scoring model by observing PGBD5 knock down in PTC. These studies will help to discover the mechanisms of PTC development and guide chemotherapy, targeted therapy and immunotherapy for PTC.

Materials and methods

Papillary thyroid cancer patient cohorts

We obtained TCGA-THCA cohort data from the TCGA data portal (https://www.cancer.gov/tcga/), which contains the gene expression profiles of 512 PTC patients. After eliminating the samples with no follow-up time, the gene expression information of 501 patients was finally retained for subsequent analysis. Gene mutation information was also downloaded through the TCGA data portal, and after matching clinical data, gene mutation information was collected for 401 patients. We divided the data of 501 patients into a training set (n=334) and a test set (n=167) based on a 2:1 ratio.

Gene set variation analysis

We downloaded 10 gene sets related to glucose metabolism from the GO terms and KEGG and REACTOME gene annotation collections from MSigDB (http://www.gsea-msigdb.org/gsea/msigdb/collections.jsp). Then, we used the gene set variation analysis (GSVA) package to calculate the enrichment scores of 10 glucose metabolism-related pathways, used the pheatmap package for clustering analysis, used the limma package in R software for differential analysis of 113 metabolic scores, and defined a signature with an absolute log2-fold change (FC) > 0.2 (adjusted P<0.05) as the differential expression signature. Finally, three subgroups of high, low and medium glucose metabolism activation (C1, C2 and C3) were obtained. Next, we evaluated the different genetic types between the different subgroups, including TMB, neoantigen number, mRNAsi, as well as the mutation types and mutation frequencies in the different subgroups.

Characterization of PTC subgroups

We identified differentially expressed genes (DEGs) among PTC subgroups using the limma package in R and defined genes with absolute log2FC>1 (adjusted P < 0.01) as DEGs. c2.cp.kegg.v7.2. symbols and h.all.v7.2. symbols downloaded from the Molecular Signature Database (https://www.gsea-msigdb.org/gsea/msigdb) were then used. The symbols gene set files, functional and pathway enrichment analysis was performed using the Cluster Analyser R package, setting the significance threshold to an adjusted P<0.05.

Screening of prognostic genes and construction of prognostic signatures

The genes associated with PFI of PTC were obtained from TCGA (unicox P < 0.05) and analysed with the DEGs by Venn analysis. Finally, 18 genes associated with the PFI of PTC were obtained. Then, the prognostic genes that contributed most to the PFI of PTC were further generated by Lasso Cox analysis to obtain six glucose metabolism-related genes associated with the prognosis of PTC, and the prognostic profile of glucose metabolism-related genes was constructed using the following formula: risk score = (0.540425503*PGBD5) + (-0.078740238 *TDRD9) + (- 0.281307051 *TMEM171)+(-0.008488446 *IGFBPL1)+(-0.171726033 *TPO)+(-0.001972683*SOD3). Then, the PTC group was divided into the HRisk and LRisk groups according to the expression of six prognostic genes. The prognostic differences, immune infiltration, clinical characteristics and differences in sensitivity to drug treatment were compared between the two groups. And functional and pathway enrichment analysis were performed for both groups by gene set enrichment analysis (GSEA) (19), and GSVA analysis (20).

Prognostic statistical analysis

The Kaplan-Meier(K-M) analysis was used to calculate the difference in PFI between the HRisk and LRisk groups in the different data sets.The time-dependent receiver operating characteristic (ROC) analysis was used to predict the area under the curve of risk scores for PFI at 1, 3, and 5 years for different data sets. The risk score and clinicopathological features (age, gender, disease stage, and signature) were evaluated by multivariate Cox regression analysis to screen independent risk factors for PFI.

Construction and evaluation of the nomogram

Using clinical data from all patients, we used the bootstrap self-sampling method to validate the predictive effect of the model using the model itself and then constructed nomogram by the regplot package. We divided the patients into high- and

low-scoring groups according to their total points to predict the prognostic differences. The ROC curves, calibration curves, clinical impact curve (CIC) and decision curve (DCA) were applied to evaluate the nomogram's prediction accuracy and stability.

Estimation of immune infiltration

The method used to estimate immune infiltration in this study was single-sample GSEA (ssGSEA) and quantified by the R package GSVA using the ssGSEA method. Using a predefined set of genes (usually from functional annotations or results of previous experiments), genes were sorted according to the degree of differential expression in the two types of samples, and then it was tested whether the predefined set of genes was enriched at the top or bottom of this sorting table.

Prediction of the benefit of each subgroup from chemotherapy, targeted therapy and immune checkpoint blockade therapy

The MD Anderson melanoma cohort that received anti-CTLA-4 or anti-PD-1 therapy was considered for the prediction of immunotherapy response (21). In addition, we performed SubMap (21) analysis of data obtained from the Genomics of Drug Sensitivity in Cancer (GDSC) database (https://www.cancerrxgene.org) to investigate the difference in sensitivity between the HRisk and LRisk groups after treatment with sorafenib or paclitaxel.

Cell culture and cell transfection

The TPC-1 and KTC-1cell lines were purchased from American Type Culture. All cell lines were identified by short tandem repeat analysis. TPC-1 and KTC-1 cells were cultured in RPMI-1640 medium (Gibco, USA) supplemented with 10% foetal bovine serum (FBS, Biological Industries, Israel), 2 mM L-glutamine (Gibco, USA), penicillin and streptomycin (Gibco, USA). Cells were maintained in a humidified incubator at 37°C and 5% CO2. To study the function of PGBD5, we synthesized a siRNA against PGBD5 (GenePharma, China). The sequence of the synthesized siRNA is shown in Supplementary Table 1. TPC-1 and KTC-1 cells were transfected using Lipofectamine 2000 (Invitrogen, USA) according to the manufacturer's protocol (serum-free medium was used for transfection) and replaced with complete medium containing 10% FBS after 6 h. Cells were harvested for subsequent experiments after continued incubation for 24 h.

RNA extraction and RT–qPCR

Total RNA was extracted from cells using TRIzol reagent (Spark Jade, AC0101-B) according to the manufacturer's instructions. For RT-qPCR, RNA was reverse transcribed to cDNA by using a Reverse Transcription Kit (Takara, Dalian, China). For RT-qPCR, PCRs were set up with 2xHQ SYBR qPCR Mix (ZOMANBIO, ZF501) on a 7500 Fast Real-Time PCR System (Applied Biological Systems), and PCRs were performed according to the manufacturer's description. All samples were normalized to β-actin. The primers used in RT-qPCR are listed in Supplementary Table 2.

Cell growth and proliferation assays

For cell proliferation assays, an EdU Kit (US EVERBRIGHT, C6015 M) was used according to the manufacturer's instructions. For the EdU assay, 5×104 cells were plated into 24-well plates and cultured in complete culture medium. After 24 hours, the cells were stained and photographed according to the instructions of the EdU kit.

Statistical analysis

For normally distributed continuous data, comparisons were made using the t-test, while non-normally distributed data were tested by the Wilcoxon rank sum test. Comparisons between more than two groups of factors were performed using the Kruskal-Wallis test. Differences in survival rates between groups were analyzed by K-M plots and log-rank tests. P values less than 0.05 were considered statistically significant differences. All analyses were performed using R version 4.0.2 (http://www.r-project.org). Statistical analysis of mRNA expression levels and EdU staining levels in PTC cells were performed using the software SPSS 22.0 (SPSS Inc., Armonk, NY, USA). All values are presented as the mean ± standard deviation (SD) of 3 independent replicates. Student's t test was performed to compare differences. Significant differences were indicated by $P<0.05$, $P<0.01$, $P<0.001$, and $P<0.0001$.

Results

Correlation of PTC subgroups with classical metabolic pathways and clinical features

We first quantified 10 glucose metabolism-related processes using the GSVA R package and then performed differential analysis to find subgroup-specific metabolic profiles. The results

of analysis showed that PTC patients could be divided into three subgroups (C1 for high activation, C2 for low activation, and C3 for moderate activation) based on the activation of glucose metabolism-related genes in different metabolic pathways. In addition, the correlation between the different subgroups and the clinicopathological information (age, gender, and clinical stage) of the patients were analysed. In the C1 subgroup and C3 subgroup, the proportion of patients aged >40 was higher, while those aged < 40 were mostly found in the C2 subgroup (Figure 1A). This suggested that in patients with PTC, there may be a significant positive correlation between the patient's age and the level of glucose metabolism in the organism. As shown in Figure 1B, the proportions of Stage II, Stage III, and Stage IV were higher in the C1 subgroup than in the C2 and C3 subgroups, suggesting that the higher the level of glucose metabolism activation in their bodies, the higher the patient's clinicopathological stage. We also observed that NRAS and HRAS mutations were mainly present in the C1 subgroup, while the more classical BRAF mutations occurred mostly in the C2 and C3 subgroups (Figure 1C). This illustrated the different responses of these two genomic subtypes when glucose metabolic stresses are different in PTC patients. NRAS and HRAS mutations may be more stimulated in patients when induced with higher glucose metabolic stress, while BRAF mutations are upregulated in the low glucose metabolic activation group.

Next, we also analysed whether there were differences in TMB (Figure 1D), tumour neoantigen number (Figure 1E), and mRNAsi (Figure 1F) in different subgroups. The results showed that TMB, neoantigen number, and mRNAsi were higher in C1 subgroup than in C2 and C3 subgroups, and the differences were statistically significant (all $P < 0.05$). This suggested that the high glucose metabolic level in PTC patients may be able to promote the production of TMB, neoantigen, and the expression of tumour stemness.

Finally, we performed differential analysis of metabolism-related genes in the C1 and C2 subgroups, setting log2-fold change (FC) >0.5 and P<0.05, and finally screened 152 DEGs (Figure 1G). Subsequently, we selected the 20 most significantly upregulated genes (ALDH2, MT3, ALDH4A1. ACAT1, MDH2, ENPP1, CHCHD10, NDUFB2, PPIF, COX8A, CYC1, SLC4A4, ENO3, PFKFB2, HKDC1, PPARGC1A, GPD1, OGDHl, NUPR1 and ALDOA) from 152 DEGs for enrichment analysis and found that these 20 differentially expressed genes were mainly enriched in the generation of ATP from ADP, ATP metabolic processes, glycolytic processes, and the production of precursor metabolites and energy (Figure 1H).

Screening of glucose metabolism-related genes associated with the PFI of PTC

Next, we obtained the genes associated with PFI of PTC (unicox $P < 0.05$), and performed Venn analysis with 152 previously obtained glucose metabolism DEGs, and finally obtained 18 genes associated with PFI in glucose metabolism DEGs (ALDOA,NDUFB2,PGBD5,RRAGD,ST3GAL4, CLCNKA, TDRD9,TMEM171,IGFBPL1,SELENOV,MT1F, MT1H,TPO,SOD3,TFCP2L1,CDH16,CARTPT,TFF3) (Figure 2A). The prognostic genes that contributed most to the PFI of PTC were then further generated by Lasso Cox analysis, and the formula was constructed as follows: Risk score = (0. 540425503*PGBD5) + (-0.078740238*TDRD9) + (-0.281307051*TMEM171) + (-0.008488446* IGFBPL1) + (-0.171726033*TPO) + (-0.001972683*SOD3) (Figure 2B, C). To confirm the strong predictive potential of the prognostic features constructed from the above analysis in different datasets, we used the caret package to divide the TCGA-THCA cohort into training and test sets uniformly and randomly. Next, in the training set, test set and entire set as a whole, we divided the patients into the high risk (HRisk) and low risk (LRisk) groups according to the expression of six glucose metabolism-related genes. We also ranked the patients in each dataset according to the risk score from low to high, and displayed the PFI according to the ranking and the event occurrence of the patients. The PFI of the HRisk group was significantly shorter than that of the LRisk group. Among the six glucose metabolism-related genes screened for prognostic relevance, the expression of five genes (TPO, IGFBPL1, TMEM171, SOD3, TDRD9) was higher in the LRisk group than in the HRisk group, except for PGBD5, which was significantly more highly expressed in the HRisk group than in the LRisk group (Figure 2D, E, F).

Analysis of prognostic differences between different risk groups and the accuracy of ROC curve prediction

Since we evenly randomized the PTC cohort into training and test sets by the caret software package, we next divided the patients between the training cohort, test cohort, and entire cohort groups into the HRisk and LRisk groups based on the median risk score of each group and compared the prognosis of PFI between the two groups. The results showed that the prognosis of patients in the HRisk group was worse than that in the LRisk group in all three datasets (all $P < 0.05$) (Figures 3A–C), and to further elucidate the accuracy of prognostic features in predicting patients' PFI, we also performed ROC curve prediction over time. In the training set, the area under the curve (AUC) of the prognostic features reached 0.824, 0.704, and 0.709 at 1, 3, and 5 years, respectively. Similarly, in the test set, the AUC results were 0.613, 0.603, and 0.716 at 1, 3, and 5 years, respectively, and in the entire set, the AUC results were 0.738, 0.668 and 0.700. Overall, our results suggested that the prognostic characteristics of genes related to glucose metabolism can predict the development of PTC with relatively high accuracy (Figures 3D–F). Finally, a multifactorial

10.3389/fimmu.2022.991656

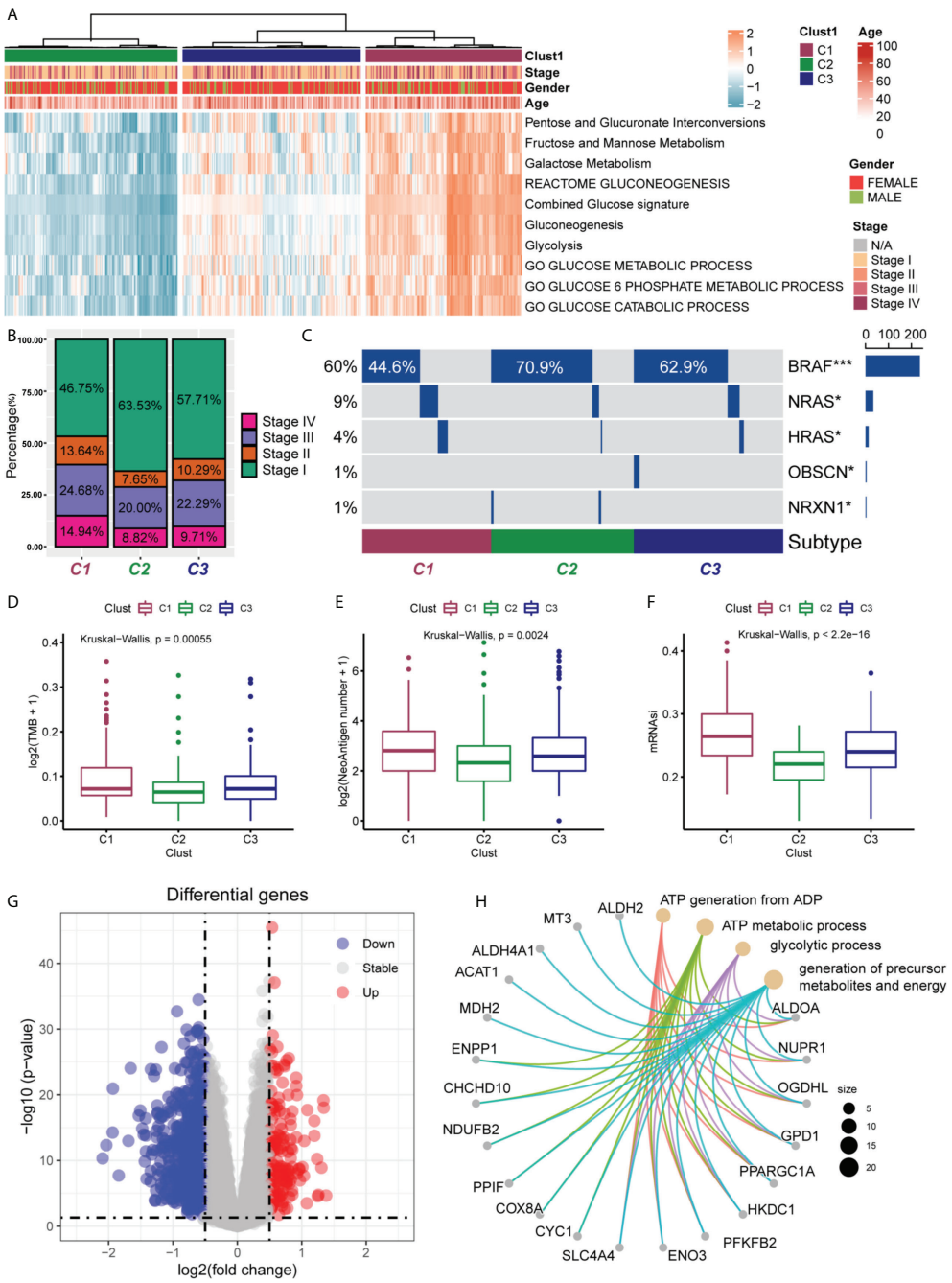

FIGURE 1
Clinical characteristics of PTC subgroups in TCGA. **(A)** Correlation of the subgroups of PTC patients (C1, C2 and C3) in the TCGA cohort with the 10 glucose metabolism-related pathways and the clinical characteristics of the patients. **(B)** Proportional distribution of the different pathological stages (stage I, II, III and IV) of PTC patients in the three subgroups. **(C)** Oncoprint of the mutational status of the three PTC subgroups. The frequency of NRAS and HRAS mutations were significantly higher in C1 subgroup than in C2 and C3 subgroups. The frequency of classical BRAF mutations was significantly higher in C2 and C3 subgroups than in C1 subgroup. *P < 0.05, ***P < 0.001. Differences in tumour mutation burden (TMB) **(D)**, number of neoantigens **(E)** and mRNA stemness index (mRNAsi) **(F)** among the three PTC subgroups. TMB, neoantigens and mRNAsi were all higher in C1 subgroup than in C2 and C3 subgroups. Statistical differences were compared by the Wilcoxon rank sum test. **(G)** Volcano plot of differentially expressed genes (DEGs) between the C1 and C2 subgroups. A total of 152 DEGs were screened (log2-fold change > 0.5, P < 0.05). **(H)** Enrichment analysis of the 20 most significantly upregulated DEGs.

10.3389/fimmu.2022.991656

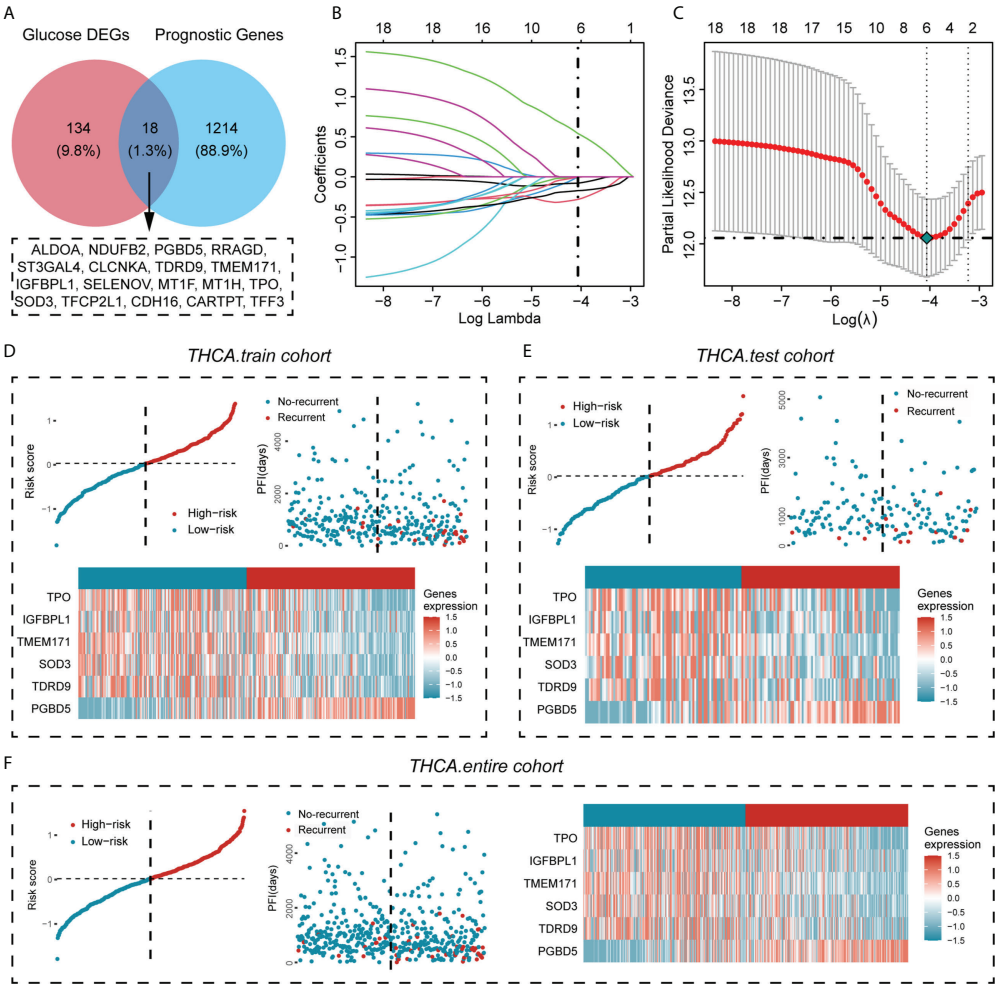

FIGURE 2
Screening for glucose metabolism-related genes highly associated with PFI and construction of a prognostic prediction model for PTC. **(A)** The genes associated with the PFI of PTC were obtained from the TCGA cohort (unicox P < 0.05) and overlapped with glucose metabolism DEGs, resulting in 18 genes associated with the PFI of PTC. **(B)** LASSO coefficient profiles of the prognostic value. **(C)** Partial likelihood distribution with the corresponding λ-logarithm value. **(D–F)** The distribution of risk scores for the three data cohorts (training cohort, test cohort and entire cohort), the recurrence and nonrecurrence PFIs of the three data cohorts and the heatmap of the expression of six prognostically relevant genes related to glucose metabolism in the High- risk and Low-risk groups.

Cox regression analysis confirmed the signature of the high risk score as an independent prognostic factor (Figures 3G–I). The above analysis showed that the risk score constructed by six glucose metabolism-related genes (PGBD5, TPO, IGFBPL1, TMEM171, SOD3, TDRD9) could well predict PFI in PTC patients.

Construction of the nomogram and evaluation of prediction accuracy

We constructed a nomogram based on the regplot package of clinicopathological information of all patients (Figure 4A) and classified patients into high- and low-scoring groups according to their total points to compare the prognostic differences and found that patients in the high-scoring group had a worse prognosis than those in the low-scoring group (Figure 4B). To further assess the accuracy of the total score in predicting the prognosis of PFI, we also plotted the ROC prediction curves over time. The AUC of the nomogram was 0.915, 0.868 and 0.941 at 1, 3 and 5 years, respectively (Figure 4C). Compared with the prognostic prediction model, the AUC of the nomogram was higher at 1, 3 and 5 years, indicating that the nomogram we constructed is highly reliable. The Hosmer-Lemeshow test also demonstrated that the predicted values of nomogram are highly consistent with the true values (p=0.96) (Figure 4D). This reflected that the predicted probability of the nomgram is close to the actual probability and the nomogram has an

10.3389/fimmu.2022.991656

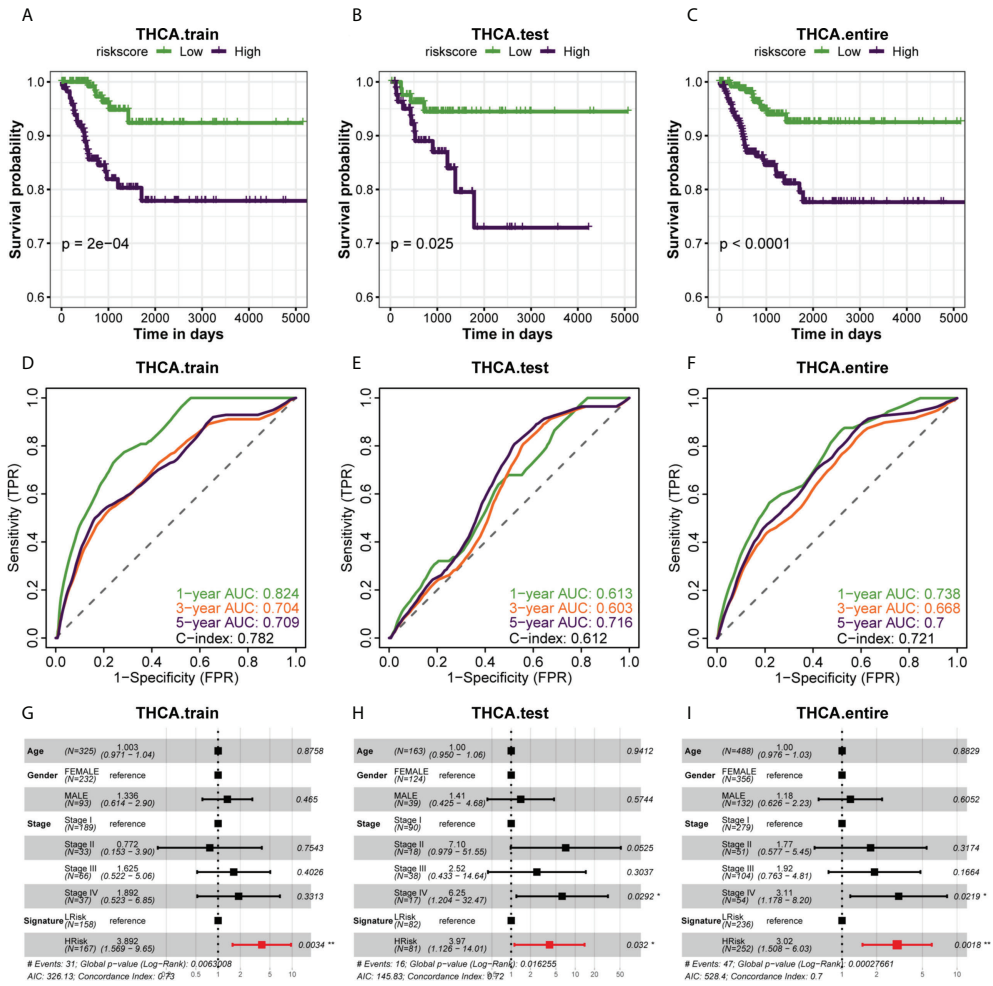

FIGURE 3
The association of different risk groups with the PFI of PTC. **(A–C)** The Kaplan-Meier survival curve of PFI for the three datasets (training set, test set, and entire set) in the TCGA cohort. Statistical significance of differences was developed by the log-rank test (P < 0.05 for all). **(D–F)** Time-dependent ROC analysis of the three datasets (training set, test set, and entire set) predicted the area under the curve of the risk score for the PFI at 1, 3, and 5 years, respectively. **(G–I)** Multivariate (age, gender, stage, signature) Cox regression analysis of three datasets (training set, test set, entire set).

acceptable calibration. In addition, the clinical impact curve (CIC) confirmed that the nomogram accurately predicted the event at risk thresholds from 0-0.3 (Figure 4E), and the decision curve analysis (DCA) confirmed that nomogram's predictive ability was better than clinical indicators (Figure 4F).

Pathway enrichment analysis of HRisk and LRisk and drug sensitivity prediction

By analysing the differences in enrichment pathways between the overall HRisk and LRisk groups, we found that in the HRisk group, there was activation of different cellular pathways, such as positive regulation of cell-cell adhesion, adaptive mediated immunity, granulocyte neutrophil chemotaxis migration, and extracellular encapsulating structure organization. In the LRisk group, there was also transport across the homeostasis barrier; in addition, endothelial signalling factor pathway, thyroid hormone biosynthetic generation, and skeletal muscle cell development were also activated in the LRisk group (Figure 5A). Then, we further evaluated the activation difference of the HALLMARK pathway between the HRisk and LRisk groups in the training and test set and found that IL6-JAK-STAT3, interferon-alpha response, apical junction and G2M checkpoint were activated in the HRisk group, while myogenesis and hypoxia were activated in the LRisk group (Figure 5B). The above enrichment analysis revealed that the level of inflammatory infiltration was higher in

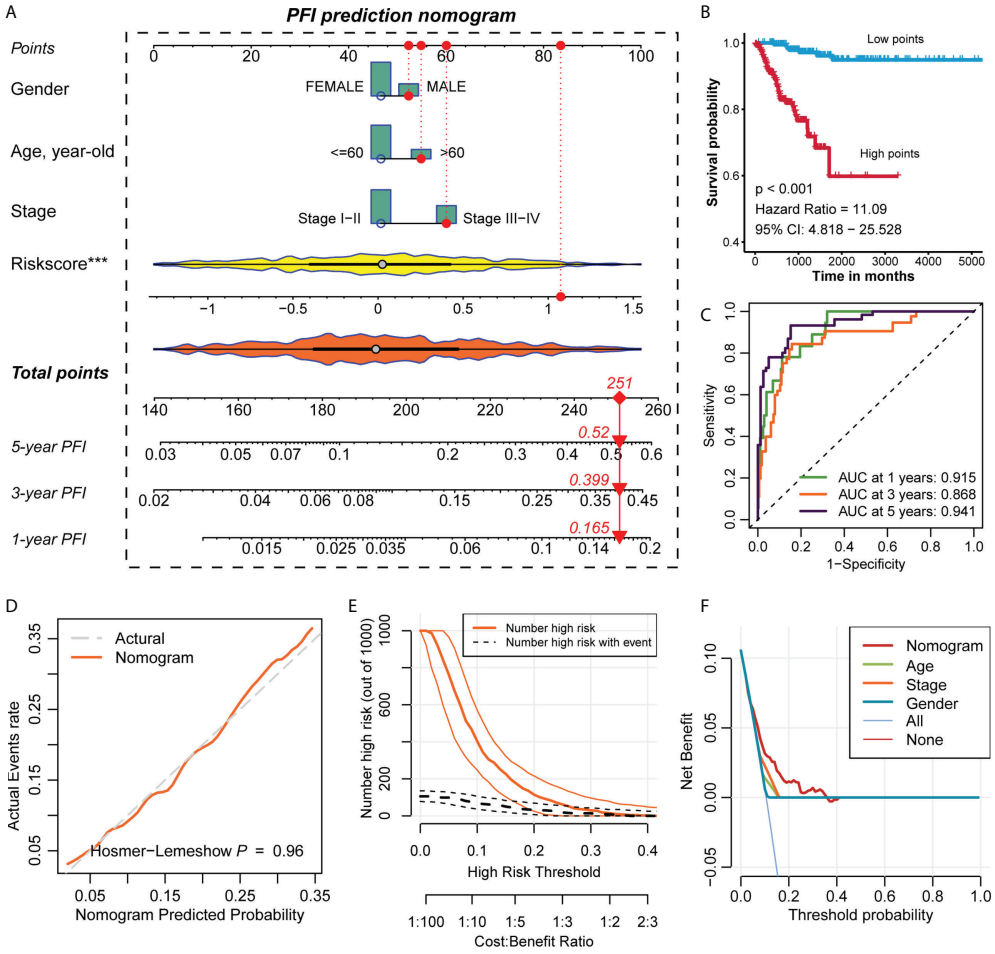

FIGURE 4
Construction of the nomogram and evaluation of prediction accuracy. **(A)** Construction of the nomogram based on the regplot package for the clinical data of all PTC patients. **(B)** The Kaplan-Meier survival curve of PFI of the high- and low-points groups in PTC. Statistical significance of differences was developed by the log-rank test (P < 0.05). **(C)** Time-dependent ROC analysis predicted the area under the curve of the nomogram for the PFI at 1, 3, and 5 years, respectively. **(D)** The calibration curves of the nomogram. **(E)** The clinical impact curves of the nomogram. **(F)** The decision curve analysis of the nomogram.

the HRisk group. This suggested that PTC patients in the HRisk group may develop metabolic inflammation, and the long-term presence of this inflammation can cause morphological and functional damage to the relevant organs and adversely affect the prognosis of tumour patients.

Paclitaxel is currently used as a first-line chemotherapeutic agent for PTC, while sorafenib is also being used in clinical trials for PTC. Here, we evaluated the response of different risk groups to these two drugs after their use. The results showed that the half maximal inhibitory concentration (IC50) of paclitaxel in the HRisk group was significantly lower than that of the LRisk group, both in the training cohort and the test cohort, while the IC50 of sorafenib in the HRisk group was significantly higher than that of the LRisk group, suggesting that patients in the HRisk group are more suitable for paclitaxel treatment, while patients in the LRisk group may be more suitable for sorafenib treatment (Figure 5C).

Analysis of immune checkpoint differences between HRisk and LRisk

By analysing the overall immune checkpoint expression differences between the HRisk and LRisk groups, we found that the expression levels of PD-L1, PD-L2, CTLA4, CD163, IFNG, TIGIT, GZMA, and GZMB were all higher in the HRisk group than in the LRisk group, and only VEGFA was higher in the LRisk group (Figure 6A). Patients in the HRisk group had

10.3389/fimmu.2022.991656

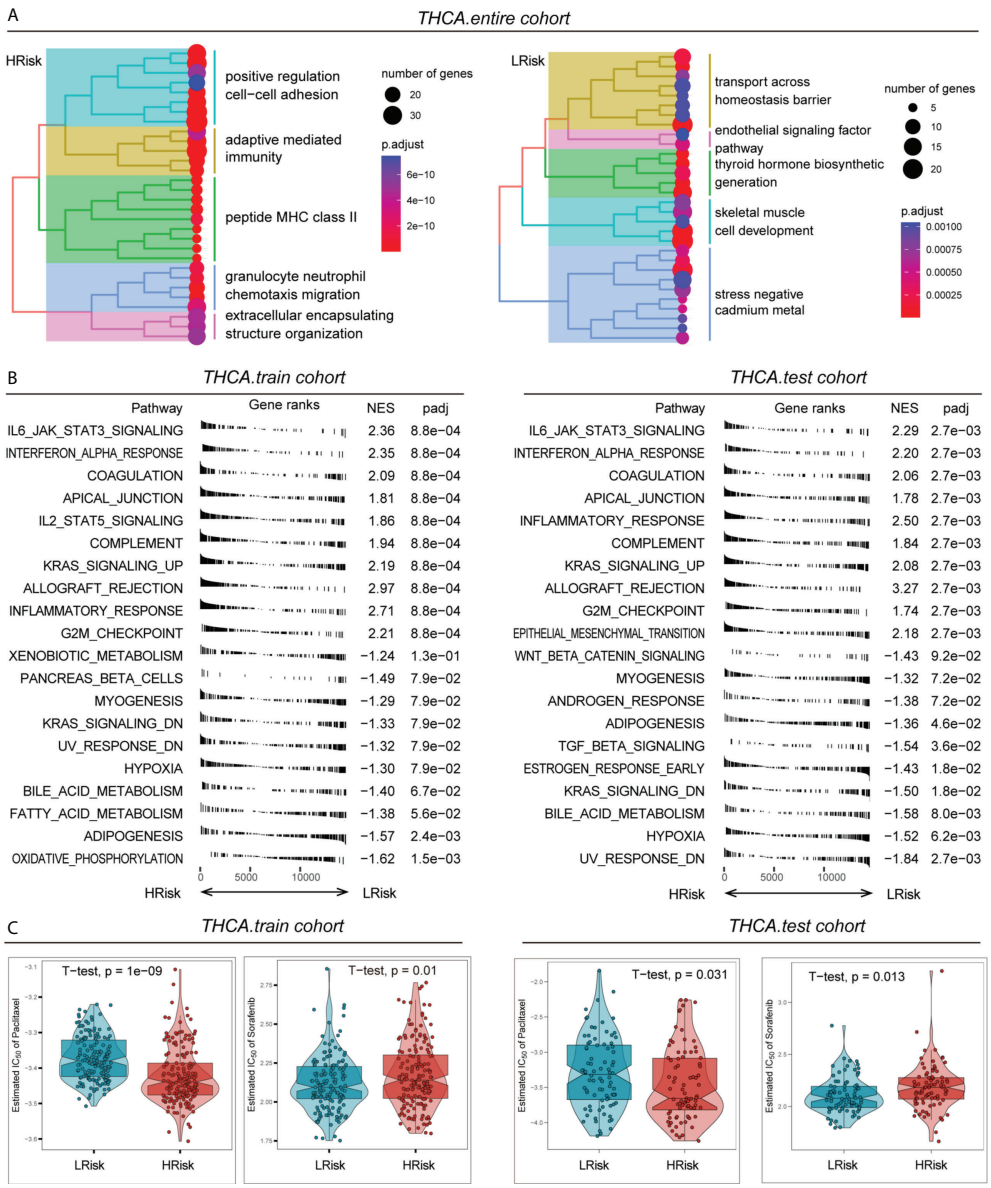

FIGURE 5
Pathway enrichment and drug sensitivity prediction of different risk groups. **(A)** Differences in the activation of different pathways of the HRisk and LRisk groups in the entire cohort. **(B)** Activation of different HALLMARK pathways in the HRisk and LRisk groups in the training cohort and test cohort. **(C)** Assessment of IC50 values for different drugs (paclitaxel or sorafenib) in the HRisk and LRisk groups in the training cohort and test cohort.

tumour cells that expressed a large number of immune checkpoints on their surface. When inhibitory receptors such as PD-L1 and CTLA-4 on the surface of tumour cells are expressed in large numbers, they can deprive T cells of their tumour cell-killing activity, thus enabling immune escape of tumour cells. Enrichment analysis of 28 immune-related gene sets by ssGSEA in the training cohort and test cohort revealed a higher infiltration of immune cells in the HRisk group (Figure 6B). The immune checkpoint blockade therapy with anti-PD-1 in the HRisk group of PTC patients may have a better therapeutic effect ($P < 0.01$) (Figure 6C).

PGBD5 regulates proliferation of papillary thyroid cancer cells

To verify the accuracy of the above study, we selected PGBD5, which is highly expressed in tumour tissues, for experimental

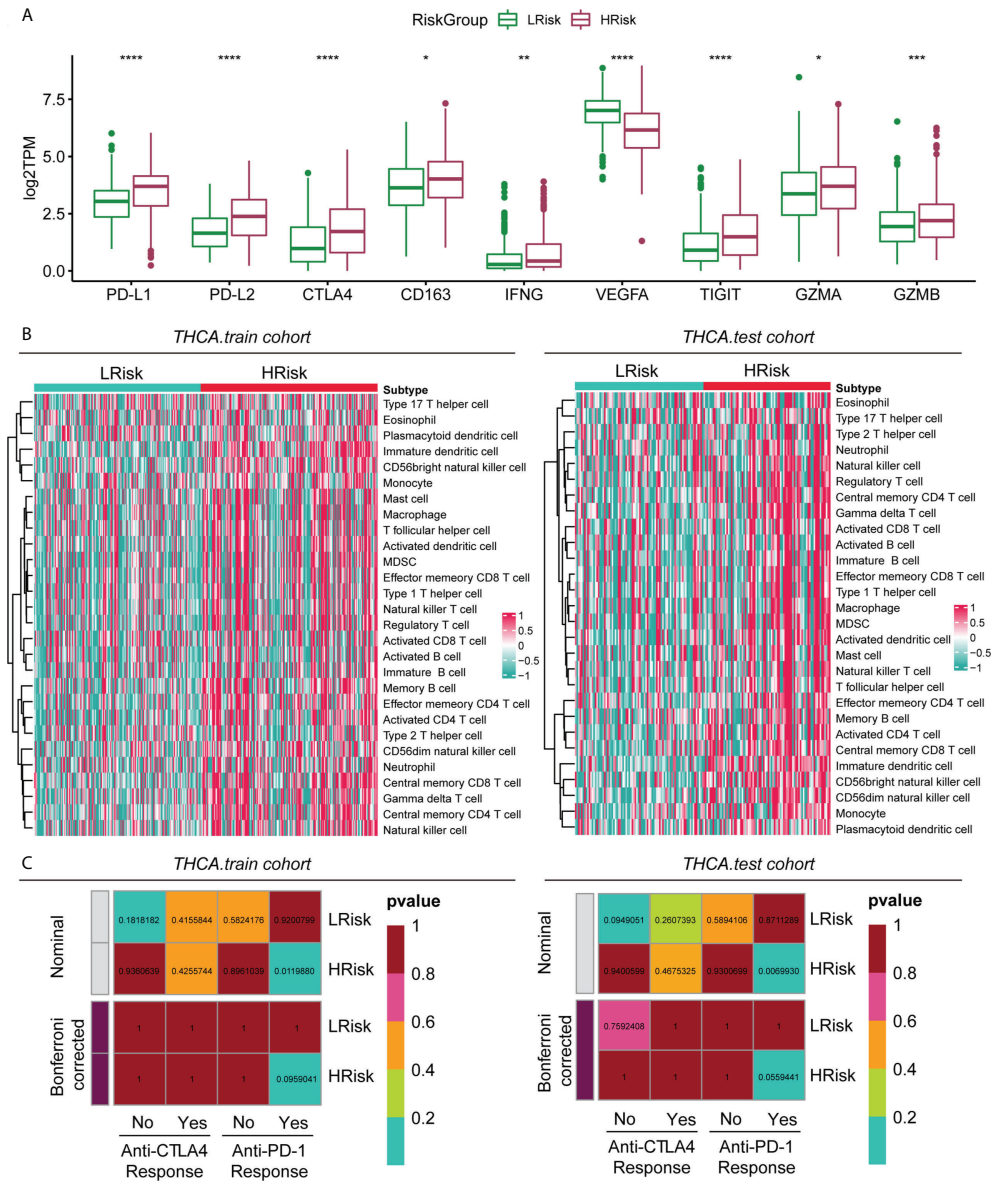

FIGURE 6
Immune characteristics of different groups in the metadataset. **(A)** Expression level (normalized count) of 9 immune checkpoint genes in the HRisk and LRisk groups. The significant difference was compared through the Kruskal–Wallis test, and the P values are labelled above each boxplot with asterisks (ns represents no significance, *P < 0.05, **P < 0.01, ***P < 0.001, ****P < 0.0001). **(B)** Heatmap describing the abundance of immune and stromal cell populations in the HRisk and LRisk groups. **(C)** Prediction results of the response to anti-CTLA-4 and anti-PD-1 therapy in the HRisk and LRisk groups by subclass mapping analysis.

validation. To explore the role of PGBD5 in PTC, we sought to characterize the altered cellular phenotype in PTC cells in the presence of PGBD5 deletion. In both TPC-1 and KTC-1 cell lines, PGBD5 was effectively knocked down by two siRNAs (si-PGBD5-1 and si-PGBD5-2) (Figure 7A). The proliferation of PTC cells was significantly reduced after PGBD5 was kncked down, as shown by EdU staining (Figure 7B). This demonstrated that PGBD5 was able to promote the proliferation of PTC cells, and when PGBD5 was knocked down, the proliferation ability of the cells was significantly diminished.

Discussion

PTC is a common malignant tumour. Since PTC is an inert tumour, its prognosis is often better (22). However, most

medical treatments are less effective in some patients when distant metastasis occur in PTC (23–25), so accurate prediction of the clinicopathological characteristics and responsiveness to treatments in each PTC patient is the focus of PTC research. Current studies have found that glucose metabolism-related genes play an important role in tumour development and various therapeutic modalities, including immunotherapy (26). To date, no comprehensive analysis has been performed using glucose metabolism-related genes as a prognostic model for PTC. In this study, we first verified that abnormal expression of glucose metabolism-related genes was closely associated with the clinicopathological features of PTC. We then constructed a prognostic prediction model of PTC using glucose metabolism-related genes. Patients were divided into the HRisk and LRisk groups by risk score, and immune cell infiltration and sensitivity to chemotherapy, targeted therapy and immune checkpoint blockade therapy were evaluated in different groups. Meanwhile, we accurately predicted the PFI of PTC patients by prognostic prediction model and nomogram.

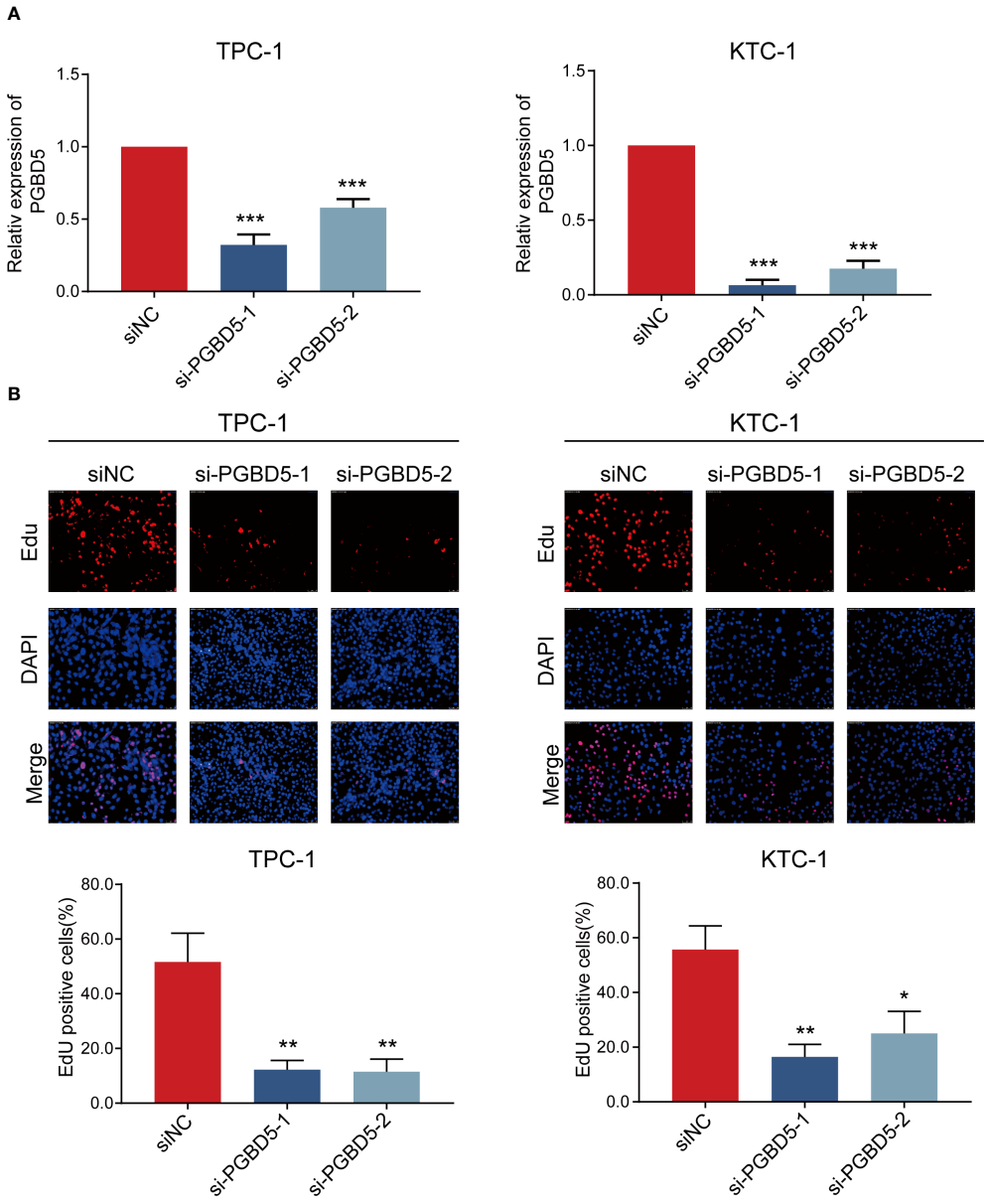

FIGURE 7
PGBD5 promotes PTC cell proliferation. **(A)** Confirmation of PGBD5 knockdown in TPC-1 and KTC-1 cells by RT-qPCR. **(B)** EdU analysis of TPC-1 and KTC-1cells after the inhibition of PGBD5. *P < 0.05, **P < 0.01, ***P < 0.001.

Different metabolic pathways are closely associated with the development and prognosis of a variety of tumours (8–10). To determine the clinicopathological characteristics of PTC subgroups that are closely related to glucose metabolic processes, in this study we identified three subgroups of PTC (C1, C2 and C3) by nonnegative matrix decomposition clustering using RNA sequencing data of 2752 genes associated with glucose metabolism. We found that glucose metabolism levels were positively associated with an older age and higher tumour stage in PTC, and both factors predicted a worse prognosis for the C1 subgroup with high glucose metabolism levels. We found that C1 subgroup were associated with higher TMB and higher neoantigens. TMB has a very important prognostic value in immunotherapy as a biomarker of immune checkpoint blockade response (27). Numerous studies have found that high TMB is positively correlated with better treatment outcomes after immunotherapy (28, 29). Neoantigens are abnormal peptides present on the surface of malignant tumour cells that are specifically expressed. Most neoantigens are the products of accumulated mutations in normal cells. Neoantigens have the potential to be recognized by T cells in the context of major histocompatibility complex class (30) and thus exert anticancer effects. Neoantigens have been used in cancer immunotherapy for CAR-T-cell therapy and the design and production of customized vaccines against tumour cells (31). C1 subgroup with higher TMB and more neoantigens may respond better to CAR-T-cell therapy and immune checkpoint inhibitors. C1 subgroup has a higher mRNAsi, which predicts that high glucose metabolism levels are associated with higher levels of PTC stemness, and tumour stemness is closely associated with survival, recurrence, metastasis, and drug resistance in many tumours (32–34). PTC development can be significantly inhibited by suppressing PTC stemness (35), therefore, for the C1 subgroup with high glucose metabolism levels, targeted stemness therapy may achieve good therapeutic results.

Because of the favourable prognosis of PTC, it is difficult to establish a good prognostic prediction model for PTC (36). In this study, we developed a prognostic model containing six glucose metabolism genes (PGBD5, TPO, IGFBPL1, TMEM171, SOD3, TDRD9) to predict the prognosis of PTC. This model has good predictive performance not only in the training cohort but also in the test cohort, indicating the high stability of this prognostic model. This model is an independent prognostic factor for PTC. This model and nomogram performed well in predicting the 1-year, 3-year and 5-year PFIs in PTC patients. Based on the results of the ROC curve analysis, we found that the nomogram outperformed the prognostic prediction model in predicting the PFI of PTC. We verified the reliability of these results by intervening in the transcript levels of glucose metabolism-related genes in PTC in the model.

Among the six glucose metabolism-related genes we screened (PGBD5, TPO, IGFBPL1, TMEM171, SOD3, TDRD9), only PGBD5 had significantly higher expression in the HRisk group. This finding suggests that PGBD5 overexpression may play an important role in the development of PTC. PGBD5 is an active DNA transposase expressed in most paediatric solid tumours and is an important oncogene (37, 38). It has been reported that in rhabdomyosarcoma cells PGBD5 is physically linked to genome-specific signal sequences that promote the induction of DNA rearrangements (39). In addition, a multiomics analysis showed that PGBD5 amplification was associated with poorer overall survival in lobular ductal types of invasive breast cancer (40). We observed a significant inhibition of PTC cell proliferation by siRNA inhibition of PGBD5 expression. This is consistent with the findings of PGBD5 in other tumours. Our present study is the first time to demonstrate that PGBD5 promotes the development of PTC. PGBD5 may be an important target to inhibit the development of PTC in the HRisk group.

The current TNM staging and pathological staging of PTC cannot guide chemotherapy, targeted therapy and immunotherapy for PTC. In this study, PTC was divided into the HRisk and LRisk groups, and we found that the HRisk group was sensitive to paclitaxel and anti-PD-1 therapy. Paclitaxel causes polymerization and stabilization of microtubules mainly by binding microtubule proteins and subsequently inhibits their dynamic properties at the mitotic spindle, which leads to tumour cell block in the G2/M cycle and induces apoptosis (41). We found that genes in the HRisk group are enriched in the G2M checkpoint signalling pathway, which may be the key factor for cell proliferation in the HRisk group. Therefore, paclitaxel may significantly inhibit tumour proliferation by affecting the G2/M phase process in the HRisk group. In the analysis of immune checkpoint gene expression in the HRisk and LRisk groups, we found that PDL-1 was highly expressed in the HRisk group, and that highly expressed PDL-1 could inhibit the migration and proliferation of T cells by binding to PD-1 of T cells, thus inducing tumour tolerance and T-cell failure. Anti-PD-1 could significantly reverse this process to restore the anticancer function of T cells (42); therefore, the HRisk group was more sensitive to anti-PD-1 treatment. The above results suggest that treatment with paclitaxel combined with anti-PD-1 in the HRisk group may lead to better therapeutic outcomes. We found that higher VEGFA expression in the LRisk group and high VEGFA expression were associated with higher lymph node metastasis and more advanced pathological stage in PTC and may promote the transformation of PTC to undifferentiated cancer (43, 44). The VEGF/VEGFR signalling pathway is an important target for the action of sorafenib (45), which could explain the more favourable treatment effect of sorafenib in the LRisk group. Dividing progressive PTC into the HRisk and LRisk groups according to the prognostic prediction model may be advantageous for the selection of appropriate therapeutic agents and more effective individualized treatment.

We must acknowledge the flaws and limitations of our experimental design, which may affect the overall relevance and credibility of our findings. First, as this work was mainly investigated by bioinformatic methods, there may be differences between different algorithms, and more basic and clinical experimental validation is needed to confirm this. Our study suggests that glucose metabolism-related genes are associated with RAS and BRAF mutations, but the mechanisms remain unclear and need to be further explored. In addition, we found that the HRisk group could benefit from paclitaxel and anti-PD-1 treatment, and the LRisk group could benefit from sorafenib treatment, which requires further confirmation of accuracy in clinical trials. Finally, based on our findings, we propose for the first time that PGBD5 could be a therapeutic target to inhibit the progression of PTC, which requires additional studies to further explore its accuracy.

Conclusion

Our study constructs a PTC prognostic prediction model and proposes a new approach for PTC classification through comprehensive analysis of glucose metabolism-related genes in PTC, providing a new perspective on the role of glucose metabolism in the development and immune microenvironment of PTC and new ideas for guiding chemotherapy, targeted therapy and immune checkpoint blockade therapy in PTC. In addition, we propose for the first time that PGBD5 can be used as a therapeutic target to inhibit PTC progression.

Data availability statement

The original contributions presented in the study are included in the article/Supplementary Material. Further inquiries can be directed to the corresponding authors.

Author contributions

Conceptualization: WX, HL, QL, LH, JH and YZ. Data curation: WX, JH, QL, and YZ. Formal analysis: WX, HL, YZ, XY, and LH. Funding acquisition: WX. Investigation: WX, XY, QL, and YZ. Methodology: WX, XY, and YZ. Project administration: LH, QL, and HL. Resources: YZ, QL, and JH. Software: WX, YZ, JH, XY, and HL. Supervision: LH and HL. Validation: WX, HL, JH, XY, and YZ. Visualization: HL, JH and WX. Writing – original draft: YC, WX, HL, and JH. Writing – review & editing: all authors. All authors contributed to the article and approved the submitted version.

Funding

This study was funded by Fujian provincial health technology project (No. 2020QNA007).

Acknowledgments

Sincerely thank the TCGA database, the Molecular Signature database and the Genomics of Drug Sensitivity in Cancer database and the authors who uploaded the original data. In addition. Thanks to all the authors who contributed to this article, and to the publisher for supporting this article.

Conflict of interest

The authors declare that the research was conducted in the absence of any commercial or financial relationships that could be construed as a potential conflict of interest.

Supplementary material

The Supplementary Material for this article can be found online at: https://www.frontiersin.org/articles/10.3389/fimmu.2022.991656/full#supplementary-material

References

1. Miranda-Filho A, Lortet-Tieulent J, Bray F, Cao B, Franceschi S, Vaccarella S, et al. Thyroid cancer incidence trends by histology in 25 countries: a population-based study. *Lancet Diabetes Endocrinol* (2021) 9(4):225–34. doi: 10.1016/S2213-8587(21)00027-9

2. Vaccarella S, Lortet-Tieulent J, Colombet M, Davies L, Stiller CA, Schüz J, et al. Global patterns and trends in incidence and mortality of thyroid cancer in children and adolescents: a population-based study. *Lancet Diabetes Endocrinol* (2021) 9(3):144–52. doi: 10.1016/S2213-8587(20)30401-0

3. Kim H, Kwon H, Moon BI. Association of multifocality with prognosis of papillary thyroid carcinoma: A systematic review and meta-analysis. *JAMA Otolaryngol Head Neck Surg* (2021) 147(10):847–54. doi: 10.1001/jamaoto.2021.1976

4. Zhao Y, Zhang Y, Dai C, Hong K, Guo Y. A signature constructed with mitophagy-related genes to predict the prognosis and therapy response for breast cancer. *Aging (Albany NY)* (2022) 14(15):6169–86. doi: 10.18632/aging.204209

5. Liu Y, Wang T, Li R. A prognostic risk score model for oral squamous cell carcinoma constructed by 6 glycolysis-immune-related genes. *BMC Oral Health* (2022) 22(1):324. doi: 10.1186/s12903-022-02358-0

6. Jeon MJ, You MH, Han JM, Sim S, Yoo HJ, Lee WK, et al. High phosphoglycerate dehydrogenase expression induces stemness and aggressiveness in thyroid cancer. *Thyroid* (2020) 30(11):1625–38. doi: 10.1089/thy.2020.0105

7. Suh HY, Choi H, Paeng JC, Cheon GJ, Chung JK, Kang KW. Comprehensive gene expression analysis for exploring the association between glucose metabolism

and differentiation of thyroid cancer. *BMC Cancer* (2019) 19(1):1260. doi: 10.1186/s12885-019-6482-7

8. Strickaert A, Corbet C, Spinette SA, Craciun L, Dom G, Andry G, et al. Reprogramming of energy metabolism: Increased expression and roles of pyruvate carboxylase in papillary thyroid cancer. *Thyroid* (2019) 29(6):845–57. doi: 10.1089/thy.2018.0435

9. Boroughs LK, DeBerardinis RJ. Metabolic pathways promoting cancer cell survival and growth. *Nat Cell Biol* (2015) 17(4):351–9. doi: 10.1038/ncb3124

10. Fiehn O, Showalter MR, Schaner-Tooley CE. Registered report: The common feature of leukemia-associated IDH1 and IDH2 mutations is a neomorphic enzyme activity converting alpha-ketoglutarate to 2-hydroxyglutarate. *Elife* (2016) 5:e12626. doi: 10.7554/eLife.12626

11. Feng C, Gao Y, Wang C, Yu X, Zhang W, Guan H, et al. Aberrant overexpression of pyruvate kinase M2 is associated with aggressive tumor features and the BRAF mutation in papillary thyroid cancer. *J Clin Endocrinol Metab* (2013) 98(9):E1524–33. doi: 10.1210/jc.2012-4258

12. Yoon M, Jung SJ, Kim TH, Ha TK, Urm SH, Park JS, et al. Relationships between transporter expression and the status of BRAF V600E mutation and f-18 FDG uptake in papillary thyroid carcinomas. *Endocr Res* (2016) 41(1):64–9. doi: 10.3109/07435800.2015.1066803

13. Wang SY, Wei YH, Shieh DB, Lin LL, Cheng SP, Wang PW, et al. 2-Deoxy-d-Glucose can complement doxorubicin and sorafenib to suppress the growth of papillary thyroid carcinoma cells. *PLoS One* (2015) 10(7):e0130959. doi: 10.1371/journal.pone.0130959

14. Kruger S, Ilmer M, Kobold S, Cadilha BL, Endres S, Ormanns S, et al. Advances in cancer immunotherapy 2019 - latest trends. *J Exp Clin Cancer Res* (2019) 38(1):268. doi: 10.1186/s13046-019-1266-0

15. Chang CH, Qiu J, O'Sullivan D, Buck MD, Noguchi T, Curtis JD, et al. Metabolic competition in the tumor microenvironment is a driver of cancer progression. *Cell* (2015) 162(6):1229–41. doi: 10.1016/j.cell.2015.08.016

16. Pouyss gur J, Marchiq Parks 1 SK, Durivault J, dralevi M, Vucetic M. 'Warburg effect 'controls tumor growth, bacterial, viral infections and immunity - genetic deconstruction and therapeutic perspectives. *Semin Cancer Biol* (2022). S1044-579X(22):00175-4. doi: 10.1016/j.semcancer.2022.07.004.

17. KeldermanS , HeemskerkB , van Tinteren H, van denBrom RR, Hospers GA, van den Eertwegh AJ, et al. Lactate dehydrogenase as a selection criterion for ipilimumab treatment in metastatic melanoma. *Cancer Immunol Immunother* (2014) 63(5):449–58. doi: 10.1007/s00262-014-1528-9

18. Pilon-Thomas S, Kodumudi KN, El-Kenawi AE, Russell S, Weber AM, Luddy K, et al. Neutralization of tumor acidity improves antitumor responses to immunotherapy. *Cancer Res* (2016) 76(6):1381–90. doi: 10.1158/0008-5472.CAN-15-1743

19. Subramanian A, Tamayo P, Mootha VK, Mukherjee S, Ebert BL, Gillette MA, et al. Gene set enrichment analysis: A knowledge-based approach for interpreting genome-wide expression profiles. *Proc Natl Acad Sci USA*. (2005) 102(43):15545–50. doi: 10.1073/pnas.0506580102

20. Hänzelmann S, Castelo R, Guinney J. GSVA: gene set variation analysis for microarray and RNA-seq data. *BMC Bioinf* (2013) 14:7. doi: 10.1186/1471-2105-14-7

21. Roh W, Chen PL, Reuben A, Spencer CN, Prieto PA, Miller JP, et al. Integrated molecular analysis of tumor biopsies on sequential CTLA-4 and PD-1 blockade reveals markers of response and resistance. *Sci Transl Med* (2017) 9(379): eaah3560. doi: 10.1126/scitranslmed.aah3560

22. Ho AS, Luu M, Zalt C, Morris LGT, Chen I, Melany M, et al. Mortality risk of nonoperative papillary thyroid carcinoma: A corollary for active surveillance. *Thyroid* (2019) 29(10):1409–17. doi: 10.1089/thy.2019.0060

23. Zelinskaya A. Immunocytochemical characteristics of thyrocytes in radioiodine refractory metastases of papillary thyroid cancer. *Exp Oncol* (2019) 41(4):342–5. doi: 10.32471/exp-oncology.2312-8852.vol-41-no-4.13705

24. Giuffrida R, Adamo L, Iannolo G, Vicari L, Giuffrida D, Eramo A, et al. Resistance of papillary thyroid cancer stem cells to chemotherapy. *Oncol Lett* (2016) 12(1):687–91. doi: 10.3892/ol.2016.4666

25. Lamartina L, Godbert Y, Nascimento C, Do Cao C, Hescot S, Borget I, et al. Locally unresectable differentiated thyroid cancer: outcomes and perspectives. *Endocrine* (2020) 69(1):133–41. doi: 10.1007/s12020-020-02245-0

26. Liu X, Zhao Y, Wu X, Liu Z, Liu X. A novel strategy to fuel cancer immunotherapy: targeting glucose metabolism to remodel the tumor microenvironment. *Front Oncol* (2022) 12:931104. doi: 10.3389/fonc.2022.931104

27. Hellmann MD, Ciuleanu TE, Pluzanski A, Lee JS, Otterson GA, Audigier-Valette C, et al. Nivolumab plus ipilimumab in lung cancer with a high tumor mutational burden. *N Engl J Med* (2018) 378(22):2093–104. doi: 10.1056/NEJMoa1801946

28. Domingo E, Camps C, Kaisaki PJ, Parsons MJ, Mouradov D, Pentony MM, et al. Mutation burden and other molecular markers of prognosis in colorectal cancer treated with curative intent: Results from the QUASAR 2 clinical trial and an Australian community-based series. *Lancet Gastroenterol Hepatol* (2018) 3 (9):635–43. doi: 10.1016/S2468-1253(18)30117-1

29. Sharabi A, Kim SS, Kato S, Sanders PD, Patel SP, Sanghvi P, et al. Exceptional response to nivolumab and stereotactic body radiation therapy (SBRT) in neuroendocrine cervical carcinoma with high tumor mutational burden: Management considerations from the center for personalized cancer therapy at UC San Diego moores cancer center. *Oncologist* (2017) 22(6):631–7. doi: 10.1634/theoncologist.2016-0517

30. Schumacher TN, Schreiber RD. Neoantigens in cancer immunotherapy. *Science* (2015) 348(6230):69–74. doi: 10.1126/science.aaa4971

31. Lv D, Khawar MB, Liang Z, Gao Y, Sun H. Neoantigens and NK cells: "Trick or treat" the cancers. *Front Immunol* (2022) 13:931862. doi: 10.3389/fimmu.2022.931862

32. Parizadeh SM, Jafarzadeh-Esfehani R, Hassanian SM, Parizadeh SMR, Vojdani S, Ghandehari M, et al. Targeting cancer stem cells as therapeutic approach in the treatment of colorectal cancer. *Int J Biochem Cell Biol* (2019) 110:75–83. doi: 10.1016/j.biocel.2019.02.010

33. Visvader JE, Lindeman GJ. Cancer stem cells: current status and evolving complexities. *Cell Stem Cell* (2012) 10(6):717–28. doi: 10.1016/j.stem.2012.05.007

34. Lei ZJ, Wang J, Xiao HL, Guo Y, Wang T, Li Q, et al. Lysine-specific demethylase 1 promotes the stemness and chemoresistance of Lgr5(+) liver cancer initiating cells by suppressing negative regulators of β-catenin signaling. *Oncogene* (2015) 34(24):3188–98. doi: 10.1038/onc.2015.129

35. Zhang W, Ruan X, Li Y, Zhi J, Hu L, Hou X, et al. KDM1A promotes thyroid cancer progression and maintains stemness through the wnt/β-catenin signaling pathway. *Theranostics* (2022) 12(4):1500–17. doi: 10.7150/thno.66142

36. Wang C, Qu Z, Chen L, Pan Y, Tang Y, Hu G, et al. Characterization of lactate metabolism score in breast and thyroid cancers to assist immunotherapy *via* Large-scale transcriptomic data analysis. *Front Pharmacol* (2022) 13:928419. doi: 10.3389/fphar.2022.928419

37. Henssen AG, Koche R, Zhuang J, Jiang E, Reed C, Eisenberg A, et al. PGBD5 promotes site-specific oncogenic mutations in human tumors. *Nat Genet* (2017) 49 (7):1005–14. doi: 10.1038/ng.3866

38. Henssen AG, Kentsis A. Emerging functions of DNA transposases and oncogenic mutators in childhood cancer development. *JCI Insight* (2018) 3(20): e123172. doi: 10.1172/jci.insight.123172

39. Henssen AG, Reed C, Jiang E, Garcia HD, von Stebut J, MacArthur IC, et al. Therapeutic targeting of PGBD5-induced DNA repair dependency in pediatric solid tumors. *Sci Transl Med* (2017) 9(414):eaam9078. doi: 10.1126/scitranslmed.aam9078

40. Sivadas A, Kok VC, Ng KL. Multi-omics analyses provide novel biological insights to distinguish lobular ductal types of invasive breast cancers. *Breast Cancer Res Treat* (2022) 193(2):361–79. doi: 10.1007/s10549-022-06567-7

41. Barbuti AM, Chen ZS. Paclitaxel through the ages of anticancer therapy: Exploring its role in chemoresistance and radiation therapy. *Cancers (Basel)* (2015) 7(4):2360–71. doi: 10.3390/cancers7040897

42. Shiravand Y, Khodadadi F, Kashani SMA, Hosseini-Fard SR, Hosseini S, Sadeghirad H, et al. Immune checkpoint inhibitors in cancer therapy. *Curr Oncol* (2022) 29(5):3044–60. doi: 10.3390/curroncol29050247

43. Salajegheh A, Pakneshan S, Rahman A, Dolan-Evans E, Zhang S, Kwong E, et al. Co-Regulatory potential of vascular endothelial growth factor-a and vascular endothelial growth factor-c in thyroid carcinoma. *Hum Pathol* (2013) 44(10):2204–12. doi: 10.1016/j.humpath.2013.04.014

44. Stuchi LP, Castanhole-Nunes MMU, Maniezzo-Stuchi N, Biselli- Chicote PM, Henrique T, Padovani Neto JA, et al. VEGFA and NFE2L2 gene expression and regulation by MicroRNAs in thyroid papillary cancer and colloid goiter. *Genes (Basel)* (2020) 11(9):954. doi: 10.3390/genes11090954

45. Jayson GC, Kerbel R, Ellis LM, Harris AL. Antiangiogenic therapy in oncology: current status and future directions. *Lancet* (2016) 388(10043):518–29. doi: 10.1016/S0140-6736(15)01088-0

frontiers | Frontiers in Immunology

TYPE Review
PUBLISHED 08 September 2022
DOI 10.3389/fimmu.2022.993624

OPEN ACCESS

EDITED BY
Elias Joseph Sayour,
University of Florida, United States

REVIEWED BY
Weinan Guo,
Fourth Military Medical University, China
Natalie Silver,
Cleveland Clinic, United States

*CORRESPONDENCE
James W. Hodge
jh241d@nih.gov

SPECIALTY SECTION
This article was submitted to Cancer Immunity and Immunotherapy, a section of the journal Frontiers in Immunology

RECEIVED 13 July 2022
ACCEPTED 17 August 2022
PUBLISHED 08 September 2022

CITATION
Santiago-Sánchez GS, Hodge JW and Fabian KP (2022) Tipping the scales: Immunotherapeutic strategies that disrupt immunosuppression and promote immune activation. *Front. Immunol.* 13:993624. doi: 10.3389/fimmu.2022.993624

Tipping the scales: Immunotherapeutic strategies that disrupt immunosuppression and promote immune activation

Ginette S. Santiago-Sánchez, James W. Hodge* and Kellsye P. Fabian

Center for Immuno-Oncology, Center for Cancer Research, National Cancer Institute, National Institutes of Health, Bethesda, MD, United States

Immunotherapy has emerged as an effective therapeutic approach for several cancer types. However, only a subset of patients exhibits a durable response due in part to immunosuppressive mechanisms that allow tumor cells to evade destruction by immune cells. One of the hallmarks of immune suppression is the paucity of tumor-infiltrating lymphocytes (TILs), characterized by low numbers of effector CD4+ and CD8+ T cells in the tumor microenvironment (TME). Additionally, the proper activation and function of lymphocytes that successfully infiltrate the tumor are hampered by the lack of co-stimulatory molecules and the increase in inhibitory factors. These contribute to the imbalance of effector functions by natural killer (NK) and T cells and the immunosuppressive functions by myeloid-derived suppressor cells (MDSCs) and regulatory T cells (Tregs) in the TME, resulting in a dysfunctional anti-tumor immune response. Therefore, therapeutic regimens that elicit immune responses and reverse immune dysfunction are required to counter immune suppression in the TME and allow for the re-establishment of proper immune surveillance. Immuno-oncology (IO) agents, such as immune checkpoint blockade and TGF-β trapping molecules, have been developed to decrease or block suppressive factors to enable the activity of effector cells in the TME. Therapeutic agents that target immunosuppressive cells, either by direct lysis or altering their functions, have also been demonstrated to decrease the barrier to effective immune response. Other therapies, such as tumor antigen-specific vaccines and immunocytokines, have been shown to activate and improve the recruitment of CD4+ and CD8+ T cells to the tumor, resulting in improved T effector to Treg ratio. The preclinical data on these diverse IO agents have led to the development of ongoing phase I and II clinical trials. This review aims to provide an overview of select therapeutic strategies that tip the balance from immunosuppression to immune activity in the TME.

KEYWORDS

immunosuppression, checkpoint blockade, immunocytokine, bintrafusp alfa, NC410, costimulatory receptors, vaccines

Introduction

Cancer immunoediting, which is defined by its three phases, namely, elimination, equilibrium, and escape, can determine the fate of a tumor cell (1, 2). Through the *elimination phase* tumor cells are destroyed by the innate and adaptive immune system (1, 2). During the *equilibrium phase* an immune-mediated tumor dormancy can occur through several poorly understood molecular mechanisms. Lastly, tumor cells that evade the *equilibrium phase* enter the *escape phase*, by losing their immunogenicity through the effect of several immunosuppressive cell types and dysregulated signaling molecules (2). Specifically, immune-edited tumor cells going through the *escape phase* may comprise modulation in PD-L1 expression, loss of antigen presentation or decrease in several proinflammatory cytokines (2).

Hence, the main goal of cancer immunotherapy is to harness the immune system to restore immune surveillance and achieve an antitumor response. The development of immune checkpoint blockade (ICB) therapies has revolutionized the oncology field in the past two decades by providing durable clinical response in several malignant tumors (3–5). To date, the U.S. Food and Drug Administration (FDA) has approved six immune checkpoint inhibitors (ICIs): ipilimumab, which targets cytotoxic T lymphocyte antigen-4 (CTLA-4); pembrolizumab, nivolumab, and cemiplimab, which target programmed cell death-1 (PD-1); and atezolizumab, durvalumab, and avelumab, which target programmed cell death-ligand 1 (PD-L1) (4, 6, 7).

Although the percentage of patients eligible for ICI therapy has increased from 1.54% in 2011 to 43.63% in 2018 (4), the portion of patients that benefits from these therapies remains limited (8–11). For example, in metastatic colorectal cancer (mCRC) in which the 5-year survival is 15%, only 3.5%-6.5% of mCRC patients respond to ICB (9–11). In advanced cancers, such as head and neck squamous cell carcinoma (HNSCC) and advanced melanoma, only 15%-20% and 33%-44% of the patients, respectively, benefit with pembrolizumab or nivolumab (anti-PD-1) treatment (4, 8, 12–15). Patients who do not benefit from immunotherapy are known to present primary resistance, while some of the responders will relapse after a period, presenting acquired resistance (16, 17).

Several mechanisms associated with primary resistance are: 1) lack of tumor-associated proteins (i.e., low mutational burden), 2) absence of antigen presentation (i.e., deletion in beta-2-microglobulin (b2M), silenced HLA), 3) genetic T cell alterations (i.e., high oncogenic PD-L1 expression), 4) T cell desensitization (i.e., mutations in the interferon-gamma (IFN-γ) pathway signaling), 5) lack of T cells (i.e., lack of antigen-specific T cell receptors (TCRs)), 6) inhibitory immune checkpoints (i.e., VISTA, LAG-3, TIGIT, TIM-3), and 7) overpopulation of immunosuppressive cells (i.e., tumor-associated macrophages (TAMs)), and regulatory T cells (Tregs) (16). On other hand, mechanisms associated with acquired resistance include the 1) loss of T cell function (i.e., mutations in IFN-γ pathway signaling), 2) lack of T cell recognition (i.e., defects on antigen presentation), 3) escape of mutation variants (i.e., loss of tumor immunogenicity), and 4) inhibitory immune checkpoints (i.e., VISTA, LAG-3, TIM-3) (16, 18). Melanoma and Hodgkin's lymphoma are among the cancers with an overall high response rate to anti-CTL4, and anti-PD-L1 ICIs, but with a high percentage rate of acquired resistance (18, 19).

These immunosuppressive mechanisms affect tumor-infiltrating lymphocytes (TILs), including helper $CD4^+$ T cells, cytotoxic $CD8^+$ T cells, B cells and natural killer (NK) cells (20–22), and ultimately the effectiveness of immunomodulatory strategies. Tumors with low or absent TILs, as in the case of 'cold' tumors, fail to respond to ICIs and are associated with poor prognosis (9, 10). Therefore, new approaches are emerging to overcome immune suppression in the TME, including ICIs in combination with costimulatory agents, metabolic modulators, and cancer vaccines, among others (16). This review discusses some of the most recent immune-oncology (IO) agents used in preclinical and clinical studies to overcome immune suppression (see Figure 1).

Non-specific targeting of the TME

Immunotherapies targeting CTLA-4 and the PD-1/PD-L1 axis

CTLA-4 and PD-1 are both checkpoint molecules expressed on T cells that upon ligand recognition hamper the cytotoxic function of effector T cells (Teff). Tumors exploit these inhibitory pathways by upregulating cognate ligands to avoid immune surveillance, thus allowing cancer cells to spread during the immunoediting *escape phase* (2, 23). Hence, the development of monoclonal antibodies (mAbs) targeting the so-called immune checkpoints has changed the landscape for patients who do not respond to conventional cancer treatments. Indeed, to date several ICIs represent the standard-of-care (SOC) for patients with advance melanoma, Merkel cell carcinoma, non-small cell lung carcinoma (NSCLC), HNSCC, MSI-CRC, and refractory Hodgkin's lymphoma (24–27).

Ipilimumab, which targets CTLA-4, is the first-in-class FDA-approved ICI for the treatment of melanoma that does not respond to chemotherapy (6, 28). Induction of CTLA-4 signaling inhibits Teff cell activation, proliferation, and cytokine secretion. Ipilimumab and other anti-CTLA-4 mAbs block the binding of CTLA-4 on activated T cells to its ligand, B7-1 (CD80) or B7-2 (CD86), on antigen presenting cells (9), thereby impeding this inhibitory pathway (29, 30). Moreover, there is evidence that anti-CTLA-4 therapy in combination with vaccine can block immunosuppression by shifting the Teff/Treg ratio. In a poorly immunogenic melanoma mouse tumor model,

10.3389/fimmu.2022.993624

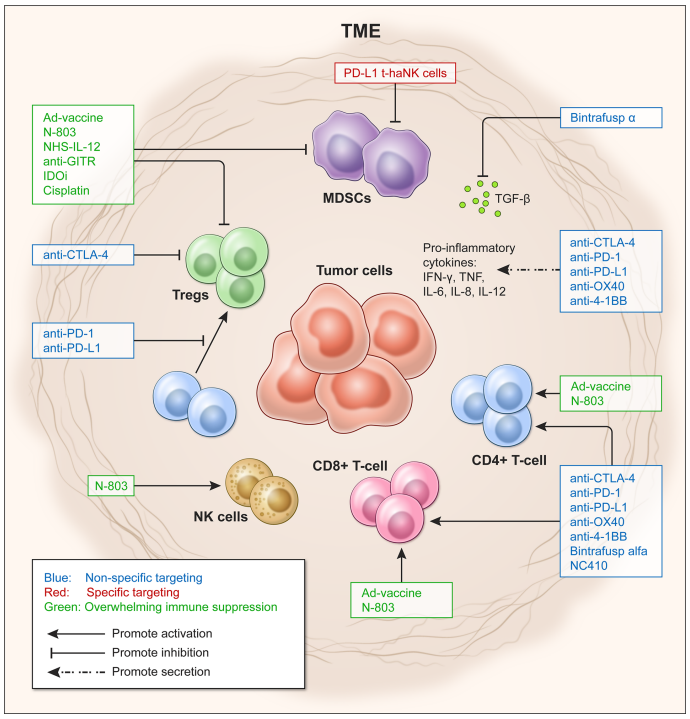

FIGURE 1
Targeting approaches to overcome immune suppression in the tumor microenvironment (TME). Effects of targeting the TME in a non-specific (blue) and specific manner (red), and by shifting Teff/Treg ratio to overcome immunosuppression (green).

combinatorial treatment with granulocyte-macrophage colony stimulating factor (GM-CSF)–transduced tumor cell vaccine and anti-CTLA-4 resulted in tumor rejection that was directly correlated with increased Teff/Treg ratio (31). In a follow-up study, it was elucidated that the activity of anti-CTLA-4 is mediated *via* selective Treg depletion within the tumor site (32). Although anti-CTLA-4 therapy has brought benefits in clinical trials of melanoma, refractory mCRC, hepatocellular carcinoma, and malignant mesothelioma, no improvement was observed in terms of overall survival (OS) in patients with metastatic castration-resistant prostate cancer (30). The mechanisms underlying the resistance to current anti-CTLA-4 therapy are poorly understood. One possible mechanism is the constitutive expression of CTLA-4 on Tregs, which can sequester the mAb from the Teff cells (24, 33). Therefore, combination therapies of anti-CTLA-4 with anti-PDL-1 and other treatment modalities represent current alternatives to circumvent immunosuppressive mechanisms present in many cancer malignancies.

Another ICI that has changed the landscape of immunotherapy in several advanced cancers are mAbs blocking the PD-1/PD-L1 axis. PD-1 (CD279), a transmembrane receptor expressed on T cells, B cells, NKs, and myeloid-derived suppressor cells (MDSCs) (34), exerts its inhibitory signaling upon binding to its cognate ligands PD-L1 (B7-H1) or PD-L2 (B7-H2), leading to a cascade of immunosuppressive mechanisms halting the cytotoxic Teff function (35–37). PD-L1 also has an essential role in converting $CD4^+$ T cells into Tregs, enhancing and sustaining the expression of the transcription factor FoxP3, and maintaining the suppressive function of Tregs. Therefore, suppressing the activation of the PD-1/PD-L1 axis can partially abrogate some of these immunosuppressive mechanisms. Nivolumab and pembrolizumab, both FDA-approved anti-PD-1 mAbs, are indicated for unresectable/metastatic melanoma, and NSCLC, among other cancers well-described by Vaddepally et al. (34). Avelumab, a fully human anti-PD-L1 mAb, is approved to treat metastatic Merkel cell carcinoma, locally advanced/metastatic urothelial carcinoma and advanced renal cell carcinoma if combined with axitinib, a tyrosine kinase inhibitor (34).

In contrast to nivolumab or pembrolizumab, which are IgG4 isotype antibodies, avelumab is an IgG1 isotype mAb that can mediate antibody-dependent cell-mediated cytotoxicity (ADCC) (38). Preclinical work from Boyerinas and colleagues showed the ability of avelumab to induce ADCC on several human cancer cells including lung, breast, and bladder cancer cell lines, in the presence of peripheral blood mononuclear cells (PBMCs) or NK cells (38). Notably, the lung cancer cell line, H460, which

expresses low-level MHC class and is resistant to cytotoxic T lymphocytes (CTL) lysis, was effectively lysed by purified NK cells in combination with avelumab (38). Additional work in chordoma, a rare bone cancer in the spine or skull, showed that avelumab significantly improved NK cell lysis of chordoma cells *via* ADCC *in vitro* (39). Hence, these findings demonstrate that, in addition to inhibiting the PD-1/PD-L1 axis, ADCC-mediated lysis may be another mechanism through which avelumab exerts its anti-tumor effect.

A substantial portion of patients derive limited benefit from ICI-based monotherapies. Therefore, ICIs are currently being evaluated in combination with chemotherapeutic agents, radiation, vaccines, or costimulatory molecules for those patients presenting primary or acquire resistance to ICIs (16, 23). Thus, identifying other molecules and pathways that can be targetable alone or in combination with current FDA-approved ICIs seems a feasible alternative to treat some advanced cancers.

Landscape of immune checkpoint blockade beyond targeting CTLA-4 and the PD-1/PD-L1 axis

Additional potential targets identified for immunotherapy are the costimulatory receptors 4-1BB (also known as TNFRSF9 or CD137), OX40 (TNFRSF4, ACT35, or CD134), and glucocorticoid-induced TNFR-related protein (GITR) (TNFRS18, AITR or CD357). These molecules belong to the tumor necrosis factor receptor superfamily (TNFRSF) and have been shown to boost antitumor immune response by regulating survival, proliferation, differentiation, and effector functions of immune cells (23, 40, 41). 4-1BB receptor is expressed in activated T and B cells, monocytes, macrophages, dendritic cells (DCs), Tregs, NK, neutrophils, eosinophils, and mast cells (42). The interaction of 4-1BB with its known ligands, TNFR-associated factor (TRAF) 1 and TRAF2, on APCs triggers signals that can stimulate cell division by downregulating proapoptotic molecules, such as Bim (43). Additionally, 4-1BB receptor/ligand interaction induces the proliferation of cytotoxic T cells, the expansion of effector and memory T cells (Tm), and triggers proinflammatory T helper (Th)1 cytokine production such as interleukin (IL)-6, IL-8, IL-12, tumor necrosis factor (TNF), and INF-γ, while suppressing Th2 cytokines (IL-4, IL-5, IL-13) (44, 45).

Similarly, costimulatory receptor OX40 is expressed in activated $CD4^+$ and $CD8^+$ T cells, Tregs, Th cells, NK, and neutrophils (23). Immunomodulatory functions associated with OX40 interaction with its ligand, OX40L, express on APCs; these include enhancing cytokine secretion, accumulation of antigen-reactive T cells and Tm cells during the peak of the primary immune response, as well as promoting T cell proliferation by T cell receptor (TCR) antigen stimuli (46, 47). Furthermore, OX40 signaling regulates the number of $CD4^+$ T cells generated during a primary clonal expansion and controls the size of the Tm pool (47, 48). Thus, OX40 is of utmost importance since quality and number of T cells are crucial to determine immunotherapy response (47). Lastly, OX40 interaction with OX40L in DCs has been shown to exert a role in DC activation, maturation (47) and promoting antitumor immunity (49).

The stimulatory checkpoint GITR is expressed in Tregs, activated NK cells, activated macrophages and DCs (50). Upon recognition of its ligand GITRL (TNFSF18), predominantly expressed by activated APCs, or with agonist antibodies, GITR signaling enhances T cell activation (50). Mechanisms associated with T cell activation by GITR include upregulation of CD25 and secretion of IL-12 and INF-γ (50). Moreover, GITR can enhance cancer vaccine activity by providing costimulatory signaling for T cell activation (51–54). Specifically, data suggest that GITR signaling shortens the threshold for CD28 signaling on $CD8^+$ T cells and induces 4-1BB expression on $CD8^+$ Tm (50). GITR high expression on Tregs represents a more complex mechanism, because while GITR modulation triggers Tregs expansion (50, 55), it also inhibits Tregs immune suppressive mechanisms (50, 56, 57). Indeed, growing evidence suggests that the use of anti-GITR as an agonist increases Teff/Treg ratio by increasing $CD8^+$ T cell population and depleting Tregs (50, 58–60). As an example, a study using a melanoma mouse model demonstrated that costimulation of GITR with an agonist mAb achieved a loss on FoxP3 expression within the intratumoral Treg compartment (50, 60).

The therapeutic benefit of agonistic 4-1BB, OX40, and GITR costimulation has been demonstrated in several preclinical murine models of breast, colon, lymphoma, and melanoma cancers. In melanoma, 4-1BB signaling was shown to rescue chronic activated/exhausted $CD8^+$ T cells (61). Importantly, when 4-1BB and OX40 agonists are used in combination with ICIs, vaccines or cytokines, a synergistic immune boost protects against poorly immunogenic cancer types. For example, a combination of costimulatory agonists anti-OX40 and anti-4-1BB mAbs with vaccine, in a breast Her-2/neu transgenic mouse model, enhanced both $CD4^+$ and $CD8^+$ T cell activity and proliferation associated with the retardation of tumor growth (62, 63). Combination therapy of anti-OX40, anti-4-1BB, anti-PD-L1, docetaxel, and adenovirus-based tumor antigen vaccine was shown to induce $CD4^+$/$CD8^+$ T cell proliferation and activity, overcome $CD4^+$ and $CD8^+$ T cell exhaustion, and delay tumor growth in both T cell–inflamed and non-T cell–inflamed murine tumor models (64). In terms of GITR costimulation in preclinical models, there is seminal work using agonist antibodies DTA-1 or GITRL-Fc demonstrating $CD8^+$ T cell expansion and cytokine production (50). For example, a study showed tumor regression after costimulation with DTA-1 in a CT26 murine model (65). Additionally, another study showed tumor control associated with the increase in TILs and granzyme B in a Colon26 murine model [for an in-depth review, see (50)].

The clinical efficacy of several agonists for 4-1BB and OX40 in combination with ICIs is currently under investigation. Recently published results from a clinical trial (NCT02315066) of OX40 agonist, alone or in combination with a 4-1BB agonist, have shown disease control in 56% of patients associated with an increase in $CD4^+$ memory T cell proliferation and activation without dose-limiting toxicities (66). In a phase I study (NCT02554812), 26.1% of the patients who received combination treatment with the 4-1BB agonist utomilumab and pembrolizumab had complete or partial responses. Furthermore, the responders had high levels of activated memory/effector peripheral blood $CD8^+$ T cells (67). In an ongoing clinical trial (INTRUST), the 4-1BB agonist urelumab is being studied in advanced solid tumors including NSCLC alone or in combination with nivolumab (NCT03792724); at the time of this review, however, no results have been posted.

Recently, results were published for the first-in-human phase I clinical trial (NCT01239134) using the anti-GITR antibody, TRX518, a fully humanized Fc-dysfunctional aglycosylated IgG1K (68). During the trial, 43 patients with refractory solid tumors were treated with TRX518 monotherapy and a reduction in circulating and intratumoral Tregs was observed (68). Despite the increase in Teff/Treg ratio, however, no substantial clinical responses were observed (68). Because TRX518 monotherapy was not sufficient to activate cytolytic $CD8^+$ T cells due to persistent exhaustion, the group is now evaluating TRX518 in combination with PD-1 blockade in a new clinical trial (NCT02628574) (68). A separate clinical trial (NCT02132754) is evaluating the GITR agonist MK-4166, alone or in combination with pembrolizumab in patients with advanced solid tumors (69). The combination was well-tolerated and the highest overall objective responses (ORR, 69%) were observed in ICI-naïve melanoma patients (69).

In addition to checkpoint inhibitors, tumors also produce immunosuppressive cytokines such as TGF-β and IL-8 (2). TGF-β is a pleiotropic cytokine that under physiological conditions maintains immune homeostasis and even suppresses tumor initiation (70). However, TGF-β signaling can also drive tumor progression by suppressing $CD8^+$ T cells tumor infiltration (71), supporting angiogenesis (72), upregulating PD-L1 expression (73), and promoting epithelial-to-mesenchymal transition (EMT) (74). Several therapeutic agents targeting this cytokine are currently under development for the treatment of cancer.

Bintrafusp alfa, previously known as M7824, is a first-in-class bifunctional fusion protein that consists of an anti-PD-L1 antibody covalently linked to the extracellular domain of two TGF-βRII molecules that is designed to block the PD-1/PD-L1 axis while also sequestering TGF-β molecules (75, 76). Several preclinical studies have confirmed the antitumor efficacy of bintrafusp alfa and its ability to increase the immune response in triple negative breast, bladder, and HPV^+ cervical cancer models (77, 78). In the EMT6 syngeneic breast cancer model, bintrafusp alfa resulted in an antitumor response that was associated with increased $CD8^+$ T cell and NK cell activation (77). Likewise, in HTB-1 bladder, HPV^+ SiHa cervical, and MDA-MB-231 triple negative breast cancer models in PBMC-humanized NSG mice, bintrafusp alfa achieved significant tumor growth control linked with increased tumor infiltration IFN-γ producing $CD4^+$ and $CD8^+$ T cells (78).

TGF-β is considered a master regulator of the EMT, and *in vitro* and *in vivo* studies have shown that bintrafusp alfa can suppress TGF-β–induced EMT in NSCLC (73). NSCLC cells treated with bintrafusp alfa showed decreased expression of the mesenchymal markers, vimentin and fibronectin, while maintaining expression of the epithelial marker E-cadherin. Likewise, a xenograft NSCLC model showed a significant reduction in vimentin expression in bintrafusp alfa-treated mice compared to untreated and anti-PD-L1-treated mice (73).

In addition to blocking PD-1/PD-L1 interaction, bintrafusp alfa can also target PD-L1 through other mechanisms. Like avelumab, the anti-PD-L1 moiety of bintrafusp alfa allows for ADCC-mediated lysis of tumor cells (39, 73). Lung, urothelial, cervical, breast and prostate cancer cells pre-treated with bintrafusp alfa showed an enhanced susceptibility to ADCC-mediated lysis by donor-derived NK cells as compared to avelumab-treated cells (73, 79, 80). Furthermore, TGF-β contributes to the upregulation of PD-L1 expression on tumor cells and TGF-β sequestration by bintrafusp alfa could subsequently result in reduced PD-L1 expression (73).

Bintrafusp alfa monotherapy, or in combination with other IO agents, is the subject of investigation in ongoing clinical trials in metastatic prostate cancer (NCT03493945), urothelial cancer (NCT04501094), colorectal cancer (NCT03436563), and HPV-associated malignancies (NCT03427411), among other cancers. A previous phase I study (NCT02517398) in advanced solid tumors showed a complete response (CR) in a patient with cervical cancer and partial responses (PR) in some patients with pancreatic and anal cancer (81). Treatment-related adverse events were observed in 4 out of 19 patients and the maximum tolerated dose (MTD) was not determined. Previous clinical trial findings using bintrafusp alfa have been well-described in other publications (75, 76).

In addition to being a physical barrier that impedes the immune cell infiltration, the tumor extracellular matrix (ECM) also regulates the activation of effectors cells (82). Collagen, which is a component of the ECM released by cancer-associated fibroblasts (CAFs), tumor cells and macrophages, has been demonstrated to impair the immune response by acting as an immune checkpoint when interacting with leukocyte-associated immunoglobulin-like receptor-1 (LAIR-1, CD305) on immune cells (83). LAIR-1 activation and signaling inhibit the function of T cells, NK cells, monocytes, and DCs (83–85). Meta-analysis of human datasets showed an association between high collagen and LAIR-1 expression with low overall survival in glioblastoma multiforme and mesothelioma and other advanced cancer types (86).

Recently, a novel fusion protein consisting of two LAIR-2 molecules—a soluble receptor that competes with LAIR-1 for binding of collagen-like domains (87)—fused to the functional IgG1 Fc tail was developed to block LAIR-1 signaling (83, 86). This molecule, called NC410, reduced human HT-29 colorectal tumor growth and promoted T cell anti-tumor activity in humanized NSG mice (86). NC410 bound to collagen-rich areas where LAIR-1$^+$ immune cells were localized in the tumor (86). In the murine EMT6 breast and MC38 colon cancer models, NC410 in combination with bintrafusp alfa remodeled the tumor collagen matrix, enhanced T cell tumor infiltration and antitumor activity, and repolarized the suppressive M2 macrophages population (83). An ongoing clinical trial is evaluating the safety of NC410 in patients with advanced and metastatic solid tumors, such as ovarian, gastric, and colorectal cancer (NCT04408599). At the time of this review, no results have been posted.

Specific targeting of immune suppressive population of the TME

Targeting MDSCs population

Immune suppressive cells, such as MDSCs and Tregs, play a key role in promoting tumor growth by inhibiting the proliferation and cytotoxic activity of NK and T cells (2, 88). MDSCs are a heterogeneous group of immature and dysfunctional myeloid cells classified in two major subsets based on their phenotypic and morphological features: monocytic-MDSCs (M-MDSCs) and granulocytic-MDSCs (G-MDSCs) (89). MDSCs are recruited to the tumor site through signaling molecules secreted by tumor cells and tumor stroma (88, 89). Factors such as stem cell factor (SCF), GM-CSF, granulocyte colony stimulating factor (G-CSF), vascular endothelial growth factor (VEGF), and macrophage colony-stimulating factor (M-CSF) are released by tumor cells to promote the expansion of MDSC populations in the TME (89). Furthermore, the tumor induces immune suppressive functions of MDSCs by secreting inflammatory cytokines and chemokines, such as IFN-γ, IL-4, IL-6, IL-1β, and C-X-C motif chemokine ligand 1 (CXCL1) (88, 89). The main mechanisms associated with MDSC immune suppression include depriving T cells of essential amino acids and adhesion molecules (90, 91), inducing oxidative stress (90), and increasing Tregs and M2 macrophage population (90). Specifically, G-MDSCs can suppress T cell response in an antigen-specific manner, while M-MDSCs can do it using both antigen-specific and non-specific mechanisms (89, 92).

In cancer patients, tumor progression and resistance to immunotherapy are correlated with MDSC-mediated immune suppression (88, 89, 93). Indeed, MDSCs in peripheral blood of breast cancer patients are associated with advance cancer stage and metastasis (89). For example, in CRC patients, both circulating and tumor infiltrating percentages of MDSCs have shown to increase proportionally to tumor stage (89). Therefore, during the past years, preclinical and clinical studies have been focused on suppressing the MDSC population. Therapeutic agents designed to deplete the MDSC population (i.e., gemcitabine and peptibodies), block their recruitment to the tumor site (i.e., anti-CCL2 and anti-CCR5), promote their differentiation (i.e., ATRA and vitamin D3) or inhibit MDSC-mediated immunosuppression (i.e., anti-CCL2 and anti-CCR5) have been extensively reviewed in the literature (88, 89, 93). Furthermore, conventional therapies have also been reported to affect MDSC populations. For instance, clinical data have also shown a decrease of G-MDSCs population in peripheral blood of pancreatic cancer patients receiving therapy with the chemotherapeutic agent gemcitabine (94), which is the standard first-line treatment for patients with unresectable locally advanced or metastatic pancreatic cancer (95). Although several agents to deplete MDSCs are under investigation, to date no agent has been FDA approved.

Recently, a study showed that the engineered PD-L1 targeting high-affinity NK (PD-L1 t-haNK) cells may be a novel treatment that can target MDSCs (96). PD-L1 t-haNK cells were designed to express high-affinity CD16/FcγRIIIa (158V) allele, promote ADCC-mediated lysis, possess an ER-retained IL-2; circumvent the need for exogenous IL-2 in culture, and express a chimeric antigen receptor (CAR) against PD-L1 to target PD-L1 expressing cells (80, 96, 97). PD-L1 t-haNK cells were developed to target PD-L1-expressing tumor cells and were also shown to directly lyse MDSCs (96). Among the immune cells, MDSCs express high surface levels of PD-L1; however, they are not significantly targeted by NK cells in the presence of avelumab (98). *In vitro*, coincubation of PD-L1 t-haNK cells with human PBMCs from healthy donors and patients with prostate and HNSCC cancer showed a 60% reduction in peripheral MDSCs while other immune populations remained unaffected (96). *In vivo*, PD-L1 t-haNK cells trafficked in PD-L1$^+$ tumors and delayed tumor growth in breast and lung cancer models in PBMC-humanized NSG mice (96).

Targeting Tregs population

In addition to MDSCs, Tregs cells also represent a target because tumor infiltrating FoxP3$^+$ CD25$^+$ CD4$^+$ Tregs cells are highly proliferative and suppressive (99). Tumor infiltrating Tregs express higher levels of surface molecules associated with T cell activation, such as 4-1BB, OX40, GITR, LAG-3, TIGIT, CD25, and CTLA-4 (100). Some of these molecules possess a dual role supporting Treg immune suppressive machinery. For example, Tregs use CD25 high affinity receptor to acquire endogenous IL-2 for survival while also limiting IL-2

in the TME necessary for Teff cell activation and proliferation (100, 101). CTLA-4 on Tregs interacts with CD80/86 ligands downregulating its expression in APC, resulting in inhibition of T cell activation (33, 100). Additionally, Treg cells secrete suppressive cytokine IL-10, which inhibits NK and T cells functions (102) and secrete the inhibitory molecule adenosine that suppresses Teff cell activity while maintaining a positive feedback loop for Tregs proliferation (103).

Based on the suppressive role of Tregs, many studies have been focused on the depletion or functional modulation of Tregs in the tumor milieu. Since Tregs and Teff cells share receptors, one of the main challenges of immunotherapy is depleting Tregs without depleting Teff cells. Treg-specific depleting antibody is one of the approaches used to abrogate Treg-mediated immunosuppression (100). For this purpose, surface molecules expressed at much higher levels on Tregs than T cells are used as targets, such as CD25, CTLA-4, GITR, 4-1BB, OX-40, LAG3, TIGIT, CCR4, and CCR8; tumor burden control has also been observed (58, 100, 104, 105). For instance, in a murine pancreatic tumor model, when an anti-CD25 antibody to deplete Tregs was combined with vaccine, mice showed smaller tumors, longer survival, and a tumor-specific immune response (106). In addition to the commonly used systemic administration of Treg-specific antibodies, local delivery to the tumor site can be performed. A recent study conjugated anti-CD25 mAb with photoactivatable dye to selectively damage the cell membrane of Tregs upon near-infrared (NIR) light exposure, resulting in the tumor regression of the Lewis lung carcinoma model (100, 107). The efficacy of CD25-depleting antibodies to promote antitumor immunity is still unclear. While anti-CD25 depleting antibodies can decrease Treg populations, they can also target activated Teff cells that also express CD25 (108).

Further studies have interrogated Treg depletion in cancer immunotherapy using the agonistic anti-GITR or small molecule drugs in low doses, such as the alkylating agent cyclophosphamide (99). Tyrosine kinase inhibitors (TKIs) are also used to achieve Treg depletion and augment antitumor immunity (109). For example, a study using the TKI, imatinib, to treat chronic myelogenous leukemia (CML) patients, observed a depletion of Tregs and a significant increase in effector/memory $CD8^+$ T cells in CML patients in complete molecular remission (CMR) compared to non-CMR patients (109).

CCR4, a chemokine receptor predominantly expressed on Tregs (110), has been investigated as a target for Treg depletion and several clinical trials using a humanized anti-CCR4 IgG1 mAb with a defucosylated Fc region, known as mogamulizumab (KW-0761), are underway. In a phase Ia study, KW-0761 was shown to efficiently deplete $FoxP3^+$ Tregs cells with no toxicity in lung and esophageal cancer patients (111). However, the treatment also showed a limited reduction in Th1 CD4 T cells and CD8 T cells and a significant reduction in Th2 and Th17 CD4 T cell populations (111). Currently, KW-0761 in combination with chemotherapy agents or with ICIs continue under evaluation for several advanced solid tumors.

Overwhelming immune suppression

Shifting Teff/Treg ratio through chemotherapy

As mentioned earlier, Tregs in the TME can decrease the number of cytotoxic Teff cells, block Teff cell activation, and maintain a positive feedback loop for Treg accumulation. In fact, a high Teff to Treg (Teff/Treg) ratio in murine models is associated with response to ICIs, while a low Teff/Treg ratio is associated with ICI treatment resistance (16). In the clinic, a low Teff/Treg ratio also correlated with poor prognosis in patients with melanoma (112), breast (113), ovarian (114), and gastric cancers (115). Conversely, a high $CD8^+$ TILs/Treg ratio in patients with epithelial ovarian cancer was associated with better prognosis (114). Therefore, efforts in improving immunotherapy outcomes have been focused on increasing the Teff/Treg ratio in the TME.

Clinical and preclinical data using taxanes, antimetabolites, and DNA-alkylating drugs as monotherapies or in combination with IO agents have shown to increase Teff cells and decrease Tregs in several cancer models (21, 116–118). For example, a study using cisplatin, a platinum-based chemotherapy, in combination with vinorelbine, a tubulin inhibitor-based chemotherapy, showed a sustained depletion in the number of Tregs with an increase in $CD4^+$ Teff cells in a murine lung adenocarcinoma model (117). Here, a 1.5 and 2-fold increase in $CD4^+$ Teff/Treg ratio, 4 and 7 days after a cisplatin/vinorelbine chemotherapy regimen, respectively, was observed (117).

In another study, clinical data have shown that patients sensitive to cisplatin-based neoadjuvant chemotherapy (119) exhibit a 5-year survival rate of 80-90%, while patients resistant to the therapy exhibit a 5-year survival rate of 30-40% (118). To interrogate the difference between responders and non-responders to NAC therapy, a study analyzed tumor biopsies from a cohort of muscle invasive bladder cancer patients and found that, individually, neither $CD8^+$ T cell nor Treg density was associated with NAC response but NAC response was strongly associated with $CD8^+$ T cell/Treg ratio (118). However, these findings are not representative of all cancers, as indicated in another study that showed no correlation between the $CD8^+$ T cells/$FoxP3^+$Treg ratio and response to therapy in HNSCC patients treated with a chemotherapy regimen (116). These contradicting observations raise the question whether Teff/Treg ratio is a good indicator of the immune response to chemotherapy.

A body of data has set the rationale for the development of clinical trials testing ICIs in combination with chemotherapy agents in cancers such as NSCLC (21, 120). For example, although nivolumab outperformed platinum-based chemotherapy for the

treatment of NSCLC patients, chemotherapy may synergize with nivolumab through immunogenic modulation and abrogation of immunosuppressive cell populations (120, 121). An ongoing phase 1/2 clinical trial is evaluating the safety and efficacy of nivolumab and ipilimumab in combination with immunogenic chemotherapy for patients with advanced NSCLC (NCT04043195). Additionally, a phase 3 clinical trial (IMpower130) showed a significant improvement in OS and progression-free survival in stage IV NSCLC patients who received atezolizumab (anti-PD-L1 mAb), in combination with chemotherapy (carboplatin plus Nab-paclitaxel) compared to patients receiving standard-of-care chemotherapy alone (21).

Shifting Teff/Treg ratio through vaccines and immunocytokines

Cancer vaccines engage the antitumor immune response to generate tumor-specific effector cells (122). A cancer vaccine has four key components, the transgene of a tumor-specific antigen (TSA) or a tumor-associated antigen (TAA), the formulation, an immune adjuvant, and the delivery vehicle (123). After vaccine administration, the professional APC (i.e., DCs) processes the antigen, presents it on its surface *via* MHC molecules, and induces a polyclonal $CD4^+$ and $CD8^+$ T cell response (124–126). In preclinical studies, cancer vaccines have been shown to inhibit tumor growth and promote TILs while decreasing $FoxP3^+$ Tregs, thereby improving the Teff/Treg ratio (119, 126–128). In the clinic, cancer vaccines have been proven safe; however, they lack clinical efficacy as monotherapy (122). This treatment modality, nevertheless, represents a feasible backbone for combination therapy, wherein other immune-oncology agents can capitalize on the tumor antigen-specific immune cells elicited by the vaccine.

Studies to test the efficacy of vaccines in combination with immunocytokines, which are antibody-cytokine fusion proteins (129), to treat tumors and to circumvent immunosuppressive mechanisms are underway. For instance, a preclinical study using the adenovirus-based vaccine targeting the carcinoembryonic antigen Ad-CEA, which is an oncofetal tumor antigen, in combination with N-803, an IL-15 superagonist complex consisting of an IL-15 mutant (IL-15N72D) bound to an IL-15 receptor α/IgG1 Fc fusion protein (130–132), showed improved immune response and antitumor activity in a CEA-expressing MC38 murine colon carcinoma model (51). Ad-CEA + N-803 combination therapy resulted in increased CEA-specific $CD8^+$ T cells in the periphery compared to treatment with Ad-CEA or N-803 alone. This suggests that the expansion of CEA-specific T cells may be due to the inflammatory stimulus of N-803 (51, 131), in concordance with an earlier study showing the positive effect of N803 on NK and CD8+ T cell populations (133). Similarly, the Ad-CEA + N-803 combination also resulted in decreased $CD4^+CD25^+FoxP3^+$ Treg population, effectively increasing the Teff/Treg ratio when compared to Ad-CEA or N-803 monotherapies (51). Currently, there are several clinical trials evaluating the safety and efficacy of Ad-CEA + N803 in combination with standard of care and other immune-oncology agents (NCT04247282, NCT03387085, NCT03387111, and NCT03563157); results have yet to be posted.

Another immunocytokine that is currently being studied in combination with cancer vaccines is NHS-IL12, an engineered immunocytokine composed of two molecules of IL-12 fused to a tumor necrosis-targeting human IgG (NHS76) (134). The combination of MUC1-targeting vaccine and NHS-IL12 delayed the growth of MUC1-expressing tumors and promoted a robust peptide-specific CD4+ T cell proliferation (135). NHS-IL12 has also been shown to cause a shift from an immunosuppressive to inflammatory TME by promoting the activation of $CD4^+$ and $CD8^+$ T cells, increasing the $CD4^+/CD8^+$ T cells to MDSC ratio, and reducing intratumoral TGF-β (136). In another preclinical study, a human papillomavirus (HPV) therapeutic vaccine in combination with NHS-IL12 controlled the tumor growth of an HPV^+ murine tumor, which was associated with the expansion of activated CD8+ T cell population in the TME (137). Treatment efficacy was further enhanced when HPV vaccine + NHS-IL12 was combined with bintrafusp alfa. A phase I/II trial evaluating the safety, overall response rate, and survival with the HPV vaccine + NHS-IL12 + bintrafusp alfa combination in patients with advanced HPV-associated malignancies is currently underway (NCT04287868).

The outbreak of COVID-19 in 2020 not only boosted the messenger RNA (mRNA) technologies for the development of SARS-CoV-2 vaccine but also renewed interest in mRNA vaccines as an alternative treatment strategy for cancer (124). In fact, over twenty mRNA-based immunotherapies have entered clinical trials for the treatment of solid tumors, including NSCLC, advanced melanoma, CRC, pancreatic and bladder cancers, and metastatic CEA-expressing solid tumors (126). Currently, several RNA types are under investigation for cancer vaccines, including virus-derived self-amplifying (49) RNA, non-replicating unmodified mRNA and modified mRNA (126). SAM-RNA vaccines, which encode for tumor antigen(s) as well as genes for viral RNA replication machinery, have been shown to induce higher antigen expression and elicit a stronger immune response compared to other mRNA type vaccines (138, 139). SAM-RNA vaccines can be delivered in the form of plasmid DNA, *in vitro* transcribed (IVT) RNA, and virus-like RNA particles (138).

An alphavirus SAM-RNA vaccine, known as virus-like replicon particle (VRP)-CEA (6D) vaccine or AVX701, has been investigated in two clinical trials for the treatment of stage III CRC and advanced or metastatic CEA-expressing tumors (NCT00529984, NCT01890213) (126, 140). The components of this platform have been designed to improve vaccine efficacy – the VRP promotes tropism towards DCs while

CEA (6D), which has an Asn to Asp substitution in position 6, enhances recognition by cognate $CD8^+$ T cell receptor (140). Crosby et al. reported that among the stage IV cancer patients treated with VRP-CEA (6D) vaccine, the median follow-up was 10.9 years and the 5-year relapse-free survival (RFS) was 17% (140). Among the stage III cancer patients, the survival at a median follow-up of 5.8 years was 100% and the 5-year RFS was 75%. Patients in the stage III cancer cohort were shown to have increased CEA-specific $CD8^+$ Teff cells and decreased $FoxP3^+$ Tregs (140). The shift in the Teff/Treg ratio after VRP-CEA (6D) vaccination suggests an effective immune modulation and provides a rationale for the combination of this virus-like SAM-RNA vaccine with ICB (140). Other mRNA vaccines using different formulations as delivery systems and for the treatment of other malignancies are currently under study; they are well described by others (125, 126, 141, 142) and beyond the scope of this review.

Shifting Teff/Treg ratio through inhibition of immunosuppressive pathways

Another approach to promote immune response is to inhibit the immunosuppressive molecule indoleamine 2,3-dioxygenase (143) (51, 64, 144). IDO secretion promotes apoptosis of Teff and the activation of Tregs mainly by reducing the availability of the amino acid tryptophan and increasing its metabolite, kynurenine, in the TME (23, 145). The immunosuppressive effect fostered by IDO is also magnified in the TME, since IDO is induced by several pro-inflammatory signals (IFN-γ, TNF-α, TGF-β), resulting in its expression by tumor, immune, and stromal cells (23, 145). A preclinical study investigating the effect of the IDO inhibitor (IDOi) epacadostat in combination with Ad-CEA, N-803, OX40 agonist, and GITR agonist demonstrated antitumor efficacy in a MC38-CEA murine tumor model that was associated with an expansion of splenic and tumor infiltrating $CD8^+$ T cells (51). Furthermore, not only did the combination promote the expansion of Teff cells over Tregs, but it also dampened the suppressive activity of Tregs (51). Additionally, analysis of serum from mice treated with the combination therapy showed significant reduction in kynurenine levels compared to control.

IDO inhibitors are currently being evaluated in combination with checkpoint inhibitors (22). Several clinical trials are evaluating how blocking the enzymatic activity of IDO inhibits the suppressive mechanisms fostered by IDO in the TME (146). However, a recently concluded phase 3 clinical trial, ECHO-301, evaluating epacadostat in combination with pembrolizumab, failed to show any clinical benefit in unresectable or metastatic melanoma patients (143). Despite these findings, rather than discard the idea that blocking IDO pathway will improve the immune response, researchers should rethink which IO agents should be combined with IDOi as well as optimal dosages. As described by Fabian et al., the combination of a specific antigen vaccine and costimulating agents with the IDOi epacadostat showed a robust antitumor activity and an immune response (51). Other clinical trials are also evaluating costimulation through anti-GITR agonist alone in solid tumors (NCT 01239134), or in combination with an IDOi and checkpoint inhibitors in patients with glioblastoma (NCT03707457).

Future perspectives

Immunosuppression is a hurdle to overcome for the success of immunotherapeutic strategies in cancer treatment (147). However, not only should immunosuppressive mechanisms be addressed, but immunomodulatory mechanisms promoting T cell priming and activation should also be met. This often requires a treatment strategy that combines different agents to target different facets of the tumor-immunity interactions. Combination therapies, however, also come with their own challenges. For such strategies, it is crucial to interrogate not only their antitumor efficacy, but also the safest doses that maintain effectiveness, as well as the schedules for the agent's administration. Moreover, a deeper understanding of the known immunosuppressive pathways, as well as identifying new ones, could enable the development of immunotherapies relevant to many cancers.

Author contributions

All authors listed have made a substantial, direct, and intellectual contribution to the work, and approved it for publication.

Funding

This research was supported by the Intramural Research Program of the Center for Cancer Research, National Cancer Institute, National Institutes of Health (NIH).

Acknowledgments

The authors thank Debra Weingarten for her editorial assistance in the preparation of this manuscript.

Conflict of interest

The authors declare that the research was conducted in the absence of any commercial or financial relationships that could be construed as a potential conflict of interest.

Publisher's note

References

1. Mittal D, Gubin MM, Schreiber RD, Smyth MJ. New insights into cancer immunoediting and its three component phases–elimination, equilibrium and escape. *Curr Opin Immunol* (2014) 27:16–25. doi: 10.1016/j.coi.2014.01.004

2. O'Donnell JS, Teng MWL, Smyth MJ. Cancer immunoediting and resistance to T cell-based immunotherapy. *Nat Rev Clin Oncol* (2019) 16(3):151–67. doi: 10.1038/s41571-018-0142-8

3. Dine J, Gordon R, Shames Y, Kasler MK, Barton-Burke M. Immune checkpoint inhibitors: An innovation in immunotherapy for the treatment and management of patients with cancer. *Asia Pac J Oncol Nurs* (2017) 4(2):127–35. doi: 10.4103/apjon.apjon_4_17

4. Haslam A, Prasad V. Estimation of the percentage of US patients with cancer who are eligible for and respond to checkpoint inhibitor immunotherapy drugs. *JAMA Netw Open* (2019) 2(5):e192535. doi: 10.1001/jamanetworkopen.2019.2535

5. O'Connor JM, Fessele KL, Steiner J, Seidl-Rathkopf K, Carson KR, Nussbaum NC, et al. Speed of adoption of immune checkpoint inhibitors of programmed cell death 1 protein and comparison of patient ages in clinical practice vs pivotal clinical trials. *JAMA Oncol* (2018) 4(8):e180798. doi: 10.1001/jamaoncol.2018.0798

6. Hodi FS, O'Day SJ, McDermott DF, Weber RW, Sosman JA, Haanen JB, et al. Improved survival with ipilimumab in patients with metastatic melanoma. *N Engl J Med* (2010) 363(8):711–23. doi: 10.1056/NEJMoa1003466

7. Twomey JD, Zhang B. Cancer immunotherapy update: FDA-approved checkpoint inhibitors and companion diagnostics. *AAPS J* (2021) 23(2):39. doi: 10.1208/s12248-021-00574-0

8. Byun HK, Chang JS, Jung M, Koom WS, Chung KY, Oh BH, et al. Prediction of immune-checkpoint blockade monotherapy response in patients with melanoma based on easily accessible clinical indicators. *Front Oncol* (2021) 11:659754. doi: 10.3389/fonc.2021.659754

9. Howlader N NA, Krapcho M, Miller D, Brest A, Yu M, Ruhl J, et al. *EER cancer statistics review*. (Bethesda, MD: National Cancer Institute) (2020) p. 1975–2017.

10. Lumish MA, Cercek A. Immunotherapy for the treatment of colorectal cancer. *J Surg Oncol* (2021) 123(3):760–74. doi: 10.1002/jso.26357

11. Weng J, Li S, Zhu Z, Liu Q, Zhang R, Yang Y, et al. Exploring immunotherapy in colorectal cancer. *J Hematol Oncol* (2022) 15(1):95. doi: 10.1186/s13045-022-01294-4

12. Ferris RL, Blumenschein GJr., Fayette J, Guigay J, Colevas AD, Licitra L, et al. Nivolumab for recurrent squamous-cell carcinoma of the head and neck. *N Engl J Med* (2016) 375(19):1856–67. doi: 10.1056/NEJMoa1602252

13. Zhou L, Zeng Z, Egloff AM, Zhang F, Guo F, Campbell KM, et al. Checkpoint blockade-induced CD8+ T cell differentiation in head and neck cancer responders. *J Immunother Cancer* (2022) 10(1):e004034. doi: 10.1136/jitc-2021-004034

14. Robert C, Schachter J, Long GV, Arance A, Grob JJ, Mortier L, et al. Pembrolizumab versus ipilimumab in advanced melanoma. *N Engl J Med* (2015) 372(26):2521–32. doi: 10.1056/NEJMoa1503093

15. Wolchok JD, Chiarion-Sileni V, Gonzalez R, Rutkowski P, Grob JJ, Cowey CL, et al. Overall survival with combined nivolumab and ipilimumab in advanced melanoma. *N Engl J Med* (2017) 377(14):1345–56. doi: 10.1056/NEJMoa1709684

16. Sharma P, Hu-Lieskovan S, Wargo JA, Ribas A. Primary, adaptive, and acquired resistance to cancer immunotherapy. *Cell.* (2017) 168(4):707–23. doi: 10.1016/j.cell.2017.01.017

17. Zhou B, Gao Y, Zhang P, Chu Q. Acquired resistance to immune checkpoint blockades: The underlying mechanisms and potential strategies. *Front Immunol* (2021) 12:693609. doi: 10.3389/fimmu.2021.693609

18. Schoenfeld AJ, Hellmann MD. Acquired resistance to immune checkpoint inhibitors. *Cancer Cell* (2020) 37(4):443–55. doi: 10.1016/j.ccell.2020.03.017

19. Schachter J, Rivas A, Long GV, Arance A, Grob JJ, Mortier L, et al. Pembrolizumab versus ipilimumab for advanced melanoma: final overall survival results of a multicentre, randomised, open-label phase 3 study (KEYNOTE-006). *Lancet* (2017) 390(10105):1853–62. doi: 10.1200/JCO.2016.34.15_suppl.9504

20. Pruneri G, Vingiani A, Denkert C. Tumor infiltrating lymphocytes in early breast cancer. *Breast.* (2018) 37:207–14. doi: 10.1016/j.breast.2017.03.010

21. West H, McCleod M, Hussein M, Morabito A, Rittmeyer A, Conter HJ, et al. Atezolizumab in combination with carboplatin plus nab-paclitaxel chemotherapy compared with chemotherapy alone as first-line treatment for metastatic non-squamous non-small-cell lung cancer (IMpower130): a multicentre, randomised, open-label, phase 3 trial. *Lancet Oncol* (2019) 20(7):924–37. doi: 10.1016/S1470-2045(19)30167-6

22. Muller AJ, Manfredi MG, Zakharia Y, Prendergast GC. Inhibiting IDO pathways to treat cancer: lessons from the ECHO-301 trial and beyond. *Semin Immunopathol* (2019) 41(1):41–8. doi: 10.1007/s00281-018-0702-0

23. De Giglio A, Di Federico A, Nuvola G, Deiana C, Gelsomino F. The landscape of immunotherapy in advanced NSCLC: Driving beyond PD-1/PD-L1 inhibitors (CTLA-4, LAG3, IDO, OX40, TIGIT, vaccines). *Curr Oncol Rep* (2021) 23(11):126. doi: 10.1007/s11912-021-01124-9

24. Zappasodi R, Merghoub T, Wolchok JD. Emerging concepts for immune checkpoint blockade-based combination therapies. *Cancer Cell* (2018) 33(4):581–98. doi: 10.1016/j.ccell.2018.03.005

25. Brahmer JR, Tykodi SS, Chow LQ, Hwu WJ, Topalian SL, Hwu P, et al. Safety and activity of anti-PD-L1 antibody in patients with advanced cancer. *N Engl J Med* (2012) 366(26):2455–65. doi: 10.1056/NEJMoa1200694

26. Garon EB, Rizvi NA, Hui R, Leighl N, Balmanoukian AS, Eder JP, et al. Pembrolizumab for the treatment of non-small-cell lung cancer. *N Engl J Med* (2015) 372(21):2018–28. doi: 10.1056/NEJMoa1501824

27. Topalian SL, Hodi FS, Brahmer JR, Gettinger SN, Smith DC, McDermott DF, et al. Safety, activity, and immune correlates of anti-PD-1 antibody in cancer. *N Engl J Med* (2012) 366(26):2443–54. doi: 10.1056/NEJMoa1200690

28. Bouchereau S, Chaplain L, Fort M, Beauchet A, Sidibe T, Chapalain M, et al. Impact of prior treatment with immune checkpoint inhibitors on dacarbazine efficacy in metastatic melanoma. *Br J Cancer* (2021) 125(7):948–54. doi: 10.1038/s41416-021-01486-8

29. Linsley PS, Greene JL, Brady W, Bajorath J, Ledbetter JA, Peach R. Human B7-1 (CD80) and B7-2 (CD86) bind with similar avidities but distinct kinetics to CD28 and CTLA-4 receptors. *Immunity.* (1994) 1(9):793–801. doi: 10.1016/S1074-7613(94)80021-9

30. Zhao Y, Yang W, Huang Y, Cui R, Li X, Li B. Evolving roles for targeting CTLA-4 in cancer immunotherapy. *Cell Physiol Biochem* (2018) 47(2):721–34. doi: 10.1159/000490025

31. Quezada SA, Peggs KS, Curran MA, Allison JP. CTLA4 blockade and GM-CSF combination immunotherapy alters the intratumor balance of effector and regulatory T cells. *J Clin Invest* (2006) 116(7):1935–45. doi: 10.1172/JCI27745

32. Simpson TR, Li F, Montalvo-Ortiz W, Sepulveda MA, Bergerhoff K, Arce F, et al. Fc-dependent depletion of tumor-infiltrating regulatory T cells co-defines the efficacy of anti-CTLA-4 therapy against melanoma. *J Exp Med* (2013) 210(9):1695–710. doi: 10.1084/jem.20130579

33. Wing K, Onishi Y, Prieto-Martin P, Yamaguchi T, Miyara M, Fehervari Z, et al. CTLA-4 control over Foxp3+ regulatory T cell function. *Science.* (2008) 322 (5899):271–5. doi: 10.1126/science.1160062

34. Vaddepally RK, Kharel P, Pandey R, Garje R, Chandra AB. Review of indications of FDA-approved immune checkpoint inhibitors per NCCN guidelines with the level of evidence. *Cancers (Basel)* (2020) 12(3):738. doi: 10.3390/cancers12030738

35. Amarnath S, Mangus CW, Wang JC, Wei F, He A, Kapoor V, et al. The PDL1-PD1 axis converts human TH1 cells into regulatory T cells. *Sci Transl Med* (2011) 3(111):111ra20. doi: 10.1126/scitranslmed.3003130

36. Francisco LM, Salinas VH, Brown KE, Vanguri VK, Freeman GJ, Kuchroo VK, et al. PD-L1 regulates the development, maintenance, and function of induced regulatory T cells. *J Exp Med* (2009) 206(13):3015–29. doi: 10.1084/jem.20090847

37. Shevyrev D, Tereshchenko V. Treg heterogeneity, function, and homeostasis. *Front Immunol* (2019) 10:3100. doi: 10.3389/fimmu.2019.03100

38. Boyerinas B, Jochems C, Fantini M, Heery CR, Gulley JL, Tsang KY, et al. Antibody-dependent cellular cytotoxicity activity of a novel anti-PD-L1 antibody avelumab (MSB0010718C) on human tumor cells. *Cancer Immunol Res* (2015) 3 (10):1148–57. doi: 10.1158/2326-6066.CIR-15-0059

39. Fujii R, Friedman ER, Richards J, Tsang KY, Heery CR, Schlom J, et al. Enhanced killing of chordoma cells by antibody-dependent cell-mediated cytotoxicity employing the novel anti-PD-L1 antibody avelumab. *Oncotarget.* (2016) 7(23):33498–511. doi: 10.18632/oncotarget.9256

40. Mascarelli DE, Rosa RSM, Toscaro JM, Semionatto IF, Ruas LP, Fogagnolo CT, et al. Boosting antitumor response by costimulatory strategies driven to 4-1BB and OX40 T-cell receptors. *Front Cell Dev Biol* (2021) 9:692982. doi: 10.3389/fcell.2021.692982

41. Melero I, Hirschhorn-Cymerman D, Morales-Kastresana A, Sanmamed MF, Wolchok JD. Agonist antibodies to TNFR molecules that costimulate T and NK cells. *Clin Cancer Res* (2013) 19(5):1044–53. doi: 10.1158/1078-0432.CCR-12-2065

42. Vinay DS, Kwon BS. Immunotherapy of cancer with 4-1BB. *Mol Cancer Ther* (2012) 11(5):1062–70. doi: 10.1158/1535-7163.MCT-11-0677

43. Sabbagh L, Pulle G, Liu Y, Tsitsikov EN, Watts TH. ERK-dependent bim modulation downstream of the 4-1BB-TRAF1 signaling axis is a critical mediator of CD8 T cell survival in vivo. *J Immunol* (2008) 180(12):8093–101. doi: 10.4049/jimmunol.180.12.8093

44. Kim YJ, Kim SH, Mantel P, Kwon BS. Human 4-1BB regulates CD28 co-stimulation to promote Th1 cell responses. *Eur J Immunol* (1998) 28(3):881–90. doi: 10.1002/(SICI)1521-4141(199803)28:03<881::AID-IMMU881>3.0.CO;2-0

45. He Y, Vlaming M, van Meerten T, Bremer E. The implementation of TNFRSF co-stimulatory domains in CAR-T cells for optimal functional activity. *Cancers (Basel)* (2022) 14(2):299. doi: 10.3390/cancers14020299

46. Song J, Salek-Ardakani S, Rogers PR, Cheng M, Van Parijs L, Croft M. The costimulation-regulated duration of PKB activation controls T cell longevity. *Nat Immunol* (2004) 5(2):150–8. doi: 10.1038/ni1030

47. Popovic A, Jaffee EM, Zaidi N. Emerging strategies for combination checkpoint modulators in cancer immunotherapy. *J Clin Invest* (2018) 128 (8):3209–18. doi: 10.1172/JCI120775

48. Gramaglia I, Jember A, Pippig SD, Weinberg AD, Killeen N, Croft M. The OX40 costimulatory receptor determines the development of CD4 memory by regulating primary clonal expansion. *J Immunol* (2000) 165(6):3043–50. doi: 10.4049/jimmunol.165.6.3043

49. Poropatich K, Dominguez D, Chan WC, Andrade J, Zha Y, Wray B, et al. OX40+ plasmacytoid dendritic cells in the tumor microenvironment promote antitumor immunity. *J Clin Invest* (2020) 130(7):3528–42. doi: 10.1172/JCI131992

50. Knee DA, Hewes B, Brogdon JL. Rationale for anti-GITR cancer immunotherapy. *Eur J Cancer* (2016) 67:1–10. doi: 10.1016/j.ejca.2016.06.028

51. Fabian KP, Malamas AS, Padget MR, Solocinski K, Wolfson B, Fujii R, et al. Therapy of established tumors with rationally designed multiple agents targeting diverse immune-tumor interactions: Engage, expand, enable. *Cancer Immunol Res* (2021) 9(2):239–52. doi: 10.1158/2326-6066.CIR-20-0638

52. Hollingsworth RE, Jansen K. Turning the corner on therapeutic cancer vaccines. *NPJ Vaccines* (2019) 4:7. doi: 10.1038/s41541-019-0103-y

53. Marin-Acevedo JA, Dholaria B, Soyano AE, Knutson KL, Chumsri S, Lou Y. Next generation of immune checkpoint therapy in cancer: New developments and challenges. *J Hematol Oncol* (2018) 11(1):39. doi: 10.1186/s13045-018-0582-8

54. Sanmamed MF, Pastor F, Rodriguez A, Perez-Gracia JL, Rodriguez-Ruiz ME, Jure-Kunkel M, et al. Agonists of Co-stimulation in cancer immunotherapy directed against CD137, OX40, GITR, CD27, CD28, and ICOS. *Semin Oncol* (2015) 42(4):640–55. doi: 10.1053/j.seminoncol.2015.05.014

55. van Olffen RW, Koning N, van Gisbergen KP, Wensveen FM, Hoek RM, Boon L, et al. GITR triggering induces expansion of both effector and regulatory CD4+ T cells in vivo. *J Immunol* (2009) 182(12):7490–500. doi: 10.4049/jimmunol.0802751

56. Ko K, Yamazaki S, Nakamura K, Nishioka T, Hirota K, Yamaguchi T, et al. Treatment of advanced tumors with agonistic anti-GITR mAb and its effects on tumor-infiltrating Foxp3+CD25+CD4+ regulatory T cells. *J Exp Med* (2005) 202 (7):885–91. doi: 10.1084/jem.20050940

57. Stephens GL, McHugh RS, Whitters MJ, Young DA, Luxenberg D, Carreno BM, et al. Engagement of glucocorticoid-induced TNFR family-related receptor on effector T cells by its ligand mediates resistance to suppression by CD4+CD25+ T cells. *J Immunol* (2004) 173(8):5008–20. doi: 10.4049/jimmunol.173.8.5008

58. Bulliard Y, Jolicoeur R, Windman M, Rue SM, Ettenberg S, Knee DA, et al. Activating fc gamma receptors contribute to the antitumor activities of immunoregulatory receptor-targeting antibodies. *J Exp Med* (2013) 210(9):1685–93. doi: 10.1084/jem.20130573

59. Coe D, Begom S, Addey C, White M, Dyson J, Chai JG. Depletion of regulatory T cells by anti-GITR mAb as a novel mechanism for cancer immunotherapy. *Cancer Immunol Immunother* (2010) 59(9):1367–77. doi: 10.1007/s00262-010-0866-5

60. Cohen AD, Schaer DA, Liu C, Li Y, Hirschhorn-Cymmerman D, Kim SC, et al. Agonist anti-GITR monoclonal antibody induces melanoma tumor immunity in mice by altering regulatory T cell stability and intra-tumor accumulation. *PloS One* (2010) 5(5):e10436. doi: 10.1371/journal.pone.0010436

61. Williams JB, Horton BL, Zheng Y, Duan Y, Powell JD, Gajewski TF. The EGR2 targets LAG-3 and 4-1BB describe and regulate dysfunctional antigen-specific CD8+ T cells in the tumor microenvironment. *J Exp Med* (2017) 214 (2):381–400. doi: 10.1084/jem.20160485

62. Cuadros C, Dominguez AL, Lollini PL, Croft M, Mittler RS, Borgstrom P, et al. Vaccination with dendritic cells pulsed with apoptotic tumors in combination with anti-OX40 and anti-4-1BB monoclonal antibodies induces T cell-mediated protective immunity in her-2/neu transgenic mice. *Int J Cancer* (2005) 116(6):934–43. doi: 10.1002/ijc.21098

63. Fu Y, Lin Q, Zhang Z, Zhang L. Therapeutic strategies for the costimulatory molecule OX40 in T-cell-mediated immunity. *Acta Pharm Sin B* (2020) 10(3):414–33. doi: 10.1016/j.apsb.2019.08.010

64. Fabian KP, Padget MR, Fujii R, Schlom J, Hodge JW. Differential combination immunotherapy requirements for inflamed (warm) tumors versus T cell excluded (cool) tumors: Engage, expand, enable, and evolve. *J Immunother Cancer* (2021) 9(2):e001691. doi: 10.1136/jitc-2020-001691

65. Kim IK, Kim BS, Koh CH, Seok JW, Park JS, Shin KS, et al. Glucocorticoid-induced tumor necrosis factor receptor-related protein co-stimulation facilitates tumor regression by inducing IL-9-producing helper T cells. *Nat Med* (2015) 21 (9):1010–7. doi: 10.1038/nm.3922

66. Diab A, Hamid O, Thompson JA, Ros W, Eskens F, Doi T, et al. Open-label, dose-escalation study of the OX40 agonist ivuxolimab in patients with locally advanced or metastatic cancers. *Clin Cancer Res* (2022) 28(1):71–83. doi: 10.1158/1078-0432.CCR-21-0845

67. Tolcher AW, Sznol M, Hu-Lieskovan S, Papadopoulos KP, Patnaik A, Rasco DW, et al. Phase ib study of utomilumab (PF-05082566), a 4-1BB/CD137 agonist, in combination with pembrolizumab (MK-3475) in patients with advanced solid tumors. *Clin Cancer Res* (2017) 23(18):5349–57. doi: 10.1158/1078-0432.CCR-17-1243

68. Zappasodi R, Sirard C, Li Y, Budhu S, Abu-Akeel M, Liu C, et al. Rational design of anti-GITR-based combination immunotherapy. *Nat Med* (2019) 25 (5):759–66. doi: 10.1038/s41591-019-0420-8

69. Papadopoulos KP, Autio K, Golan T, Dobrenkov K, Chartash E, Chen Q, et al. Phase I study of MK-4166, an anti-human glucocorticoid-induced TNF receptor antibody, alone or with pembrolizumab in advanced solid tumors. *Clin Cancer Res* (2021) 27(7):1904–11. doi: 10.1158/1078-0432.CCR-20-2886

70. Guerrouahen BS, Maccalli C, Cugno C, Rutella S, Akporiaye ET. Reverting immune suppression to enhance cancer immunotherapy. *Front Oncol* (2019) 9:1554. doi: 10.3389/fonc.2019.01554

71. Ahmadzadeh M, Rosenberg SA. TGF-beta 1 attenuates the acquisition and expression of effector function by tumor antigen-specific human memory CD8 T cells. *J Immunol* (2005) 174(9):5215–23. doi: 10.4049/jimmunol.174.9.5215

72. Goumans MJ, Liu Z, ten Dijke P. TGF-beta signaling in vascular biology and dysfunction. *Cell Res* (2009) 19(1):116–27. doi: 10.1038/cr.2008.326

73. David JM, Dominguez C, McCampbell KK, Gulley JL, Schlom J, Palena C. A novel bifunctional anti-PD-L1/TGF-beta trap fusion protein (M7824) efficiently reverts mesenchymalization of human lung cancer cells. *Oncoimmunology.* (2017) 6(10):e1349589. doi: 10.1080/2162402X.2017.1349589

74. Batlle E, Massague J. Transforming growth factor-beta signaling in immunity and cancer. *Immunity.* (2019) 50(4):924–40. doi: 10.1016/j.immuni.2019.03.024

75. Gameiro SR, Strauss J, Gulley JL, Schlom J. Preclinical and clinical studies of bintrafusp alfa, a novel bifunctional anti-PD-L1/TGFbetaRII agent: Current status. *Exp Biol Med (Maywood)* (2022) 247(13):1124–34. doi: 10.1177/15353702221089910

76. Lind H, Gameiro SR, Jochems C, Donahue RN, Strauss J, Gulley JM, et al. Dual targeting of TGF-beta and PD-L1 via a bifunctional anti-PD-L1/TGF-betaRII agent: status of preclinical and clinical advances. *J Immunother Cancer* (2020) 8(1): e000433. doi: 10.1136/jitc-2019-000433

77. Knudson KM, Hicks KC, Luo X, Chen JQ, Schlom J, Gameiro SR. M7824, a novel bifunctional anti-PD-L1/TGFbeta trap fusion protein, promotes anti-tumor efficacy as monotherapy and in combination with vaccine. *Oncoimmunology.* (2018) 7(5):e1426519. doi: 10.1080/2162402X.2018.1426519

78. Morillon YMI, Smalley Rumfield C, Pellom ST, Sabzevari A, Roller NT, Horn LA, et al. The use of a humanized NSG-beta2m(-/-) model for investigation of immune and anti-tumor effects mediated by the bifunctional immunotherapeutic bintrafusp Alfa. *Front Oncol* (2020) 10:549. doi: 10.3389/fonc.2020.00549

79. Grenga I, Donahue RN, Gargulak ML, Lepone LM, Roselli M, Bilusic M, et al. Anti-PD-L1/TGFbetaR2 (M7824) fusion protein induces immunogenic modulation of human urothelial carcinoma cell lines, rendering them more susceptible to immune-mediated recognition and lysis. *Urol Oncol* (2018) 36 (3):93 e1–e11. doi: 10.1016/j.urolonc.2017.09.027

80. Jochems C, Tritsch SR, Pellom ST, Su Z, Soon-Shiong P, Wong HC, et al. Analyses of functions of an anti-PD-L1/TGFbetaR2 bispecific fusion protein (M7824). *Oncotarget.* (2017) 8(43):75217–31. doi: 10.18632/oncotarget.20680

81. Strauss J, Heery CR, Schlom J, Madan RA, Cao L, Kang Z, et al. Phase I trial of M7824 (MSB0011359C), a bifunctional fusion protein targeting PD-L1 and TGFbeta, in advanced solid tumors. *Clin Cancer Res* (2018) 24(6):1287–95. doi: 10.1158/1078-0432.CCR-17-2653

82. Mushtaq MU, Papadas A, Pagenkopf A, Flietner E, Morrow Z, Chaudhary SG, et al. Tumor matrix remodeling and novel immunotherapies: the promise of matrix-derived immune biomarkers. *J ImmunoTher Cancer* (2018) 6(1):65. doi: 10.1186/s40425-018-0376-0

83. Horn LA, Chariou PL, Gameiro SR, Qin H, Iida M, Fousek K, et al. Remodeling the tumor microenvironment via blockade of LAIR-1 and TGF-beta signaling enables PD-L1-mediated tumor eradication. *J Clin Invest* (2022) 132(8): e155148. doi: 10.1172/JCI155148

84. Carvalheiro T, Garcia S, Pascoal Ramos MI, Giovannone B, Radstake T, Marut W, et al. Leukocyte associated immunoglobulin like receptor 1 regulation and function on monocytes and dendritic cells during inflammation. *Front Immunol* (2020) 11:1793. doi: 10.3389/fimmu.2020.01793

85. Rygiel TP, Stolte EH, de Ruiter T, van de Weijer ML, Meyaard L. Tumor-expressed collagens can modulate immune cell function through the inhibitory collagen receptor LAIR-1. *Mol Immunol* (2011) 49(1-2):402–6. doi: 10.1016/j.molimm.2011.09.006

86. Ramos MIP, Tian L, de Ruiter EJ, Song C, Paucarmayta A, Singh A, et al. Cancer immunotherapy by NC410, a LAIR-2 fc protein blocking human LAIR-collagen interaction. *Elife* (2021) 10:e62927. doi: 10.7554/eLife.62927.sa2

87. Lebbink RJ, van den Berg MC, de Ruiter T, Raynal N, van Roon JA, Lenting PJ, et al. The soluble leukocyte-associated ig-like receptor (LAIR)-2 antagonizes the collagen/LAIR-1 inhibitory immune interaction. *J Immunol* (2008) 180(3):1662–9. doi: 10.4049/jimmunol.180.3.1662

88. Law AMK, Valdes-Mora F, Gallego-Ortega D. Myeloid-derived suppressor cells as a therapeutic target for cancer. *Cells.* (2020) 9(3):561. doi: 10.3390/cells9030561

89. De Cicco P, Ercolano G, Ianaro A. The new era of cancer immunotherapy: Targeting myeloid-derived suppressor cells to overcome immune evasion. *Front Immunol* (2020) 11:1680. doi: 10.3389/fimmu.2020.01680

90. Groth C, Hu X, Weber R, Fleming V, Altevogt P, Utikal J, et al. Immunosuppression mediated by myeloid-derived suppressor cells (MDSCs) during tumour progression. *Br J Cancer* (2019) 120(1):16–25. doi: 10.1038/s41416-018-0333-1

91. Ivetic A, Hoskins Green HL, Hart SJ. L-selectin: A major regulator of leukocyte adhesion, migration and signaling. *Front Immunol* (2019) 10:1068. doi: 10.3389/fimmu.2019.01068

92. Youn JI, Gabrilovich DI. The biology of myeloid-derived suppressor cells: The blessing and the curse of morphological and functional heterogeneity. *Eur J Immunol* (2010) 40(11):2969–75. doi: 10.1002/eji.201040895

93. Weber R, Fleming V, Hu X, Nagibin V, Groth C, Altevogt P, et al. Myeloid-derived suppressor cells hinder the anti-cancer activity of immune checkpoint inhibitors. *Front Immunol* (2018) 9:1310. doi: 10.3389/fimmu.2018.01310

94. Eriksson E, Wenthe J, Irenaeus S, Loskog A, Ullenhag G. Gemcitabine reduces MDSCs, tregs and TGFbeta-1 while restoring the teff/treg ratio in patients with pancreatic cancer. *J Transl Med* (2016) 14(1):282. doi: 10.1186/s12967-016-1037-z

95. Von Hoff DD, Ervin T, Arena FP, Chiorean EG, Infante J, Moore M, et al. Increased survival in pancreatic cancer with nab-paclitaxel plus gemcitabine. *N Engl J Med* (2013) 369(18):1691–703. doi: 10.1056/NEJMoa1304369

96. Fabian KP, Padget MR, Donahue RN, Solocinski K, Robbins Y, Allen CT, et al. PD-L1 targeting high-affinity NK (t-haNK) cells induce direct antitumor effects and target suppressive MDSC populations. *J Immunother Cancer* (2020) 8 (1):e000450. doi: 10.1136/jitc-2019-000450

97. Jochems C, Hodge JW, Fantini M, Fujii R, Morillon YM2nd, Greiner JW, et al. An NK cell line (haNK) expressing high levels of granzyme and engineered to express the high affinity CD16 allele. *Oncotarget.* (2016) 7(52):86359–73. doi: 10.18632/oncotarget.13411

98. Donahue RN, Lepone LM, Grenga I, Jochems C, Fantini M, Madan RA, et al. Analyses of the peripheral immunome following multiple administrations of avelumab, a human IgG1 anti-PD-L1 monoclonal antibody. *J Immunother Cancer* (2017) 5:20. doi: 10.1186/s40425-017-0220-y

99. Tanaka A, Sakaguchi S. Regulatory T cells in cancer immunotherapy. *Cell Res* (2017) 27(1):109–18. doi: 10.1038/cr.2016.151

100. Tanaka A, Sakaguchi S. Targeting treg cells in cancer immunotherapy. *Eur J Immunol* (2019) 49(8):1140–6. doi: 10.1002/eji.201847659

101. Sakaguchi S, Yamaguchi T, Nomura T, Ono M. Regulatory T cells and immune tolerance. *Cell.* (2008) 133(5):775–87. doi: 10.1016/j.cell.2008.05.009

102. Trinchieri G. Interleukin-10 production by effector T cells: Th1 cells show self control. *J Exp Med* (2007) 204(2):239–43. doi: 10.1084/jem.20070104

103. Ohta A, Sitkovsky M. Extracellular adenosine-mediated modulation of regulatory T cells. *Front Immunol* (2014) 5:304. doi: 10.3389/fimmu.2014.00304

104. Arce Vargas F, Furness AJS, Solomon I, Joshi K, Mekkaoui L, Lesko MH, et al. Fc-optimized anti-CD25 depletes tumor-infiltrating regulatory T cells and synergizes with PD-1 blockade to eradicate established tumors. *Immunity.* (2017) 46(4):577–86. doi: 10.1016/j.immuni.2017.03.013

105. Bulliard Y, Jolicoeur R, Zhang J, Dranoff G, Wilson NS, Brogdon JL. OX40 engagement depletes intratumoral tregs *via* activating FcgammaRs, leading to antitumor efficacy. *Immunol Cell Biol* (2014) 92(6):475–80. doi: 10.1038/icb.2014.26

106. Viehl CT, Moore TT, Liyanage UK, Frey DM, Ehlers JP, Eberlein TJ, et al. Depletion of CD4+CD25+ regulatory T cells promotes a tumor-specific immune response in pancreas cancer-bearing mice. *Ann Surg Oncol* (2006) 13(9):1252–8. doi: 10.1245/s10434-006-9015-y

107. Sato K, Sato N, Xu B, Nakamura Y, Nagaya T, Choyke PL, et al. Spatially selective depletion of tumor-associated regulatory T cells with near-infrared photoimmunotherapy. *Sci Transl Med* (2016) 8(352):352ra110. doi: 10.1126/scitranslmed.aaf6843

108. Sugiyama D, Nishikawa H, Maeda Y, Nishioka M, Tanemura A, Katayama I, et al. Anti-CCR4 mAb selectively depletes effector-type FoxP3+CD4+ regulatory T cells, evoking antitumor immune responses in humans. *Proc Natl Acad Sci* (2013) 110(44):17945–50. doi: 10.1073/pnas.1316796110

109. Tanaka A, Nishikawa H, Noguchi S, Sugiyama D, Morikawa H, Takeuchi Y, et al. Tyrosine kinase inhibitor imatinib augments tumor immunity by depleting effector regulatory T cells. *J Exp Med* (2020) 217(2):e20191009. doi: 10.1084/jem.20191009

110. Yoshie O, Matsushima K. CCR4 and its ligands: From bench to bedside. *Int Immunol* (2014) 27(1):11–20. doi: 10.1093/intimm/dxu079

111. Kurose K, Ohue Y, Wada H, Iida S, Ishida T, Kojima T, et al. Phase ia study of FoxP3+ CD4 treg depletion by infusion of a humanized anti-CCR4 antibody, KW-0761, in cancer patients. *Clin Cancer Res* (2015) 21(19):4327–36. doi: 10.1158/1078-0432.CCR-15-0357

112. Saleh R, Elkord E. Treg-mediated acquired resistance to immune checkpoint inhibitors. *Cancer Lett* (2019) 457:168–79. doi: 10.1016/j.canlet.2019.05.003

113. Bates GJ, Fox SB, Han C, Leek RD, Garcia JF, Harris AL, et al. Quantification of regulatory T cells enables the identification of high-risk breast cancer patients and those at risk of late relapse. *J Clin Oncol* (2006) 24(34):5373–80. doi: 10.1200/JCO.2006.05.9584

114. Sato E, Olson SH, Ahn J, Bundy B, Nishikawa H, Qian F, et al. Intraepithelial CD8+ tumor-infiltrating lymphocytes and a high CD8+/regulatory T cell ratio are associated with favorable prognosis in ovarian cancer. *Proc Natl Acad Sci U S A.* (2005) 102(51):18538–43. doi: 10.1073/pnas.0509182102

115. Sasidharan Nair V, Elkord E. Immune checkpoint inhibitors in cancer therapy: a focus on T-regulatory cells. *Immunol Cell Biol* (2018) 96(1):21–33. doi: 10.1111/imcb.1003

116. Leduc C, Adam J, Louvet E, Sourisseau T, Dorvault N, Bernard M, et al. TPF induction chemotherapy increases PD-L1 expression in tumour cells and immune cells in head and neck squamous cell carcinoma. *ESMO Open* (2018) 3(1): e000257. doi: 10.1136/esmoopen-2017-000257

117. Gameiro SR, Caballero JA, Higgins JP, Apelian D, Hodge JW. Exploitation of differential homeostatic proliferation of T-cell subsets following chemotherapy to enhance the efficacy of vaccine-mediated antitumor responses. *Cancer Immunol Immunother* (2011) 60(9):1227–42. doi: 10.1007/s00262-011-1020-8

118. Baras AS, Drake C, Liu JJ, Gandhi N, Kates M, Hoque MO, et al. The ratio of CD8 to treg tumor-infiltrating lymphocytes is associated with response to cisplatin-based neoadjuvant chemotherapy in patients with muscle invasive urothelial carcinoma of the bladder. *Oncoimmunology.* (2016) 5(5):e1134412. doi: 10.1080/2162402X.2015.1134412

119. Nair S, Boczkowski D, Fassnacht M, Pisetsky D, Gilboa E. Vaccination against the forkhead family transcription factor Foxp3 enhances tumor immunity. *Cancer Res* (2007) 67(1):371–80. doi: 10.1158/0008-5472.CAN-06-2903

120. Shafique M, Tanvetyanon T. Immunotherapy alone or chemo-immunotherapy as front-line treatment for advanced non-small cell lung cancer. *Expert Opin Biol Ther* (2019) 19(3):225–32. doi: 10.1080/14712598.2019.1571036

121. Fabian KP, Wolfson B, Hodge JW. From immunogenic cell death to immunogenic modulation: Select chemotherapy regimens induce a spectrum of immune-enhancing activities in the tumor microenvironment. *Front Oncol* (2021) 11:728018. doi: 10.3389/fonc.2021.728018

122. Wolfson B, Franks SE, Hodge JW. Stay on target: Reengaging cancer vaccines in combination immunotherapy. *Vaccines (Basel)* (2021) 9(5):509. doi: 10.3390/vaccines9050509

123. Hu Z, Ott PA, Wu CJ. Towards personalized, tumour-specific, therapeutic vaccines for cancer. *Nat Rev Immunol* (2018) 18(3):168–82. doi: 10.1038/nri.2017.131

124. Deng Z, Tian Y, Song J, An G, Yang P. mRNA vaccines: The dawn of a new era of cancer immunotherapy. *Front Immunol* (2022) 13:887125. doi: 10.3389/fimmu.2022.887125

125. Guo Y, Lei K, Tang L. Neoantigen vaccine delivery for personalized anticancer immunotherapy. *Front Immunol* (2018) 9:1499. doi: 10.3389/fimmu.2018.01499

126. Miao L, Zhang Y, Huang L. mRNA vaccine for cancer immunotherapy. *Mol Cancer* (2021) 20(1):41. doi: 10.1186/s12943-021-01335-5

127. Liu J, Fu M, Wang M, Wan D, Wei Y, Wei X. Cancer vaccines as promising immuno-therapeutics: platforms and current progress. *J Hematol Oncol* (2022) 15 (1):28. doi: 10.1186/s13045-022-01247-x

128. Huang L, Guo Y, Liu S, Wang H, Zhu J, Ou L, et al. Targeting regulatory T cells for immunotherapy in melanoma. *Mol Biomed* (2021) 2(1):11. doi: 10.1186/s43556-021-00038-z

129. Runbeck E, Crescioli S, Karagiannis SN, Papa S. Utilizing immunocytokines for cancer therapy. *Antibodies (Basel)* (2021) 10(1):10. doi: 10.3390/antib10010010

130. Han KP, Zhu X, Liu B, Jeng E, Kong L, Yovandich JL, et al. IL-15:IL-15 receptor alpha superagonist complex: high-level co-expression in recombinant mammalian cells, purification and characterization. *Cytokine.* (2011) 56(3):804–10. doi: 10.1016/j.cyto.2011.09.028

131. Xu W, Jones M, Liu B, Zhu X, Johnson CB, Edwards AC, et al. Efficacy and mechanism-of-action of a novel superagonist interleukin-15: Interleukin-15 receptor alphaSu/Fc fusion complex in syngeneic murine models of multiple myeloma. *Cancer Res* (2013) 73(10):3075–86. doi: 10.1158/0008-5472.CAN-12-2357

132. Zhu X, Marcus WD, Xu W, Lee HI, Han K, Egan JO, et al. Novel human interleukin-15 agonists. *J Immunol* (2009) 183(6):3598–607. doi: 10.4049/jimmunol.0901244

133. Knudson KM, Hicks KC, Alter S, Schlom J, Gameiro SR. Mechanisms involved in IL-15 superagonist enhancement of anti-PD-L1 therapy. *J Immunother Cancer* (2019) 7(1):82. doi: 10.1186/s40425-019-0551-y

134. Greiner JW, Morillon YM2nd, Schlom J. NHS-IL12, a tumor-targeting immunocytokine. *Immunotargets Ther* (2021) 10:155–69. doi: 10.2147/ITT.S306150

135. Fallon J, Tighe R, Kradjian G, Guzman W, Bernhardt A, Neuteboom B, et al. The immunocytokine NHS-IL12 as a potential cancer therapeutic. *Oncotarget.* (2014) 5(7):1869–84. doi: 10.18632/oncotarget.1853

136. Morillon II YM, Su Z, Schlom J, Greiner JW. Temporal changes within the (bladder) tumor microenvironment that accompany the therapeutic effects of the immunocytokine NHS-IL12. *J Immunother Cancer* (2019) 7(1):150. doi: 10.1186/s40425-019-0620-2

137. Smalley Rumfield C, Pellom ST, Morillon II YM, Schlom J, Jochems C. Immunomodulation to enhance the efficacy of an HPV therapeutic vaccine. *J Immunother Cancer* (2020) 8(1):e000612. doi: 10.1136/jitc-2020-000612

138. Fuller DH, Berglund P. Amplifying RNA vaccine development. *N Engl J Med* (2020) 382(25):2469–71. doi: 10.1056/NEJMcibr2009737

139. Vogel AB, Lambert L, Kinnear E, Busse D, Erbar S, Reuter KC, et al. Self-amplifying RNA vaccines give equivalent protection against influenza to mRNA vaccines but at much lower doses. *Mol Ther* (2018) 26(2):446–55. doi: 10.1016/j.ymthe.2017.11.017

140. Crosby EJ, Hobeika AC, Niedzwiecki D, Rushing C, Hsu D, Berglund P, et al. Long-term survival of patients with stage III colon cancer treated with VRP-CEA(6D), an alphavirus vector that increases the CD8+ effector memory T cell to Treg ratio. *J Immunother Cancer* (2020) 8(2):e001662. doi: 10.1136/jitc-2020-001662

141. Huff AL, Jaffee EM, Zaidi N. Messenger RNA vaccines for cancer immunotherapy: progress promotes promise. *J Clin Invest* (2022) 132(6): e156211. doi: 10.1172/JCI156211

142. McNamara MA, Nair SK, Holl EK. RNA-Based vaccines in cancer immunotherapy. *J Immunol Res* (2015) 2015:794528. doi: 10.1155/2015/794528

143. Long GV, Dummer R, Hamid O, Gajewski TF, Caglevic C, Dalle S, et al. Epacadostat plus pembrolizumab versus placebo plus pembrolizumab in patients with unresectable or metastatic melanoma (ECHO-301/KEYNOTE-252): A phase 3, randomised, double-blind study. *Lancet Oncol* (2019) 20(8):1083–97. doi: 10.1016/S1470-2045(19)30274-8

144. Le Naour J, Galluzzi L, Zitvogel L, Kroemer G, Vacchelli E. Trial watch: IDO inhibitors in cancer therapy. *Oncoimmunology.* (2020) 9(1):1777625. doi: 10.1080/2162402X.2020.1777625

145. Munn DH, Mellor AL. Indoleamine 2,3-dioxygenase and tumor-induced tolerance. *J Clin Invest* (2007) 117(5):1147–54. doi: 10.1172/JCI31178

146. Tang K, Wu YH, Song Y, Yu B. Indoleamine 2,3-dioxygenase 1 (IDO1) inhibitors in clinical trials for cancer immunotherapy. *J Hematol Oncol* (2021) 14 (1):68. doi: 10.1186/s13045-021-01080-8

147. Wei F, Wang D, Wei J, Tang N, Tang L, Xiong F, et al. Metabolic crosstalk in the tumor microenvironment regulates antitumor immunosuppression and immunotherapy resisitance. *Cell Mol Life Sci* (2021) 78(1):173–93. doi: 10.1007/s00018-020-03581-0

frontiers | Frontiers in Immunology

TYPE Original Research
PUBLISHED 09 September 2022
DOI 10.3389/fimmu.2022.975787

OPEN ACCESS

EDITED BY
Liusheng Peng,
Third Military Medical University, China

REVIEWED BY
Huimin Cui,
Yantaishan Hospital, China
Takashi Tanikawa,
Josai University, Japan
Hongbo Xu,
Wenzhou Medical University, China

*CORRESPONDENCE
Xiaodong He
hxd@lzu.edu.cn
Xiabin Lan
lanxia99@sina.com

SPECIALTY SECTION
This article was submitted to Cancer Immunity and Immunotherapy, a section of the journal Frontiers in Immunology

RECEIVED 22 June 2022
ACCEPTED 17 August 2022
PUBLISHED 09 September 2022

CITATION
Hou X, Chen C, Lan X and He X (2022) Unveiling the molecular features, relevant immune and clinical characteristics of *SIGLEC15* in thyroid cancer.
Front. Immunol. 13:975787.
doi: 10.3389/fimmu.2022.975787

Unveiling the molecular features, relevant immune and clinical characteristics of *SIGLEC15* in thyroid cancer

Xiaofeng Hou[1,2,3], Chao Chen[2,3], Xiabin Lan[2,3]* and Xiaodong He[1]*

[1]The Second Clinical Medical College, Lanzhou University, Lanzhou, China, [2]Department of Head & Neck Oncology Surgery, the Cancer Hospital of the University of Chinese Academy of Sciences (Zhejiang Cancer Hospital), Hangzhou, China, [3]Key Laboratory of Head & Neck Cancer Translational Research of Zhejiang Province, Hangzhou, China

The groundbreaking research work about *SIGLEC15* has raised it as a potential promising target in cancer immunotherapy. Unfortunately, the role of *SIGLEC15* in thyroid carcinoma (THCA) remains obscure. Public and home multi-omics data were collected to investigate the role of *SIGLEC15* in THCA in our study. *SIGLEC15* was upregulated in THCA tumor tissue compared to nontumor tissue in both mRNA and protein levels; gene set enrichment analysis (GSEA) results showed that high *SIGLEC15* mRNA expression was positively correlated to many immune pathways. Results of the examination of immunological landscape characteristics displayed high *SIGLEC15* mRNA expression that mainly positively correlated with a large number of cancer immunity immunomodulators and pathways. In addition, upregulation of *SIGLEC15* was positively correlated with an enhanced immune score, stromal score, and estimate score. However, higher *SIGLEC15* mRNA also met high immune exhausted status. The majority of CpG methylation sites negatively correlated with *SIGLEC15* mRNA expression. Analysis of clinical characteristics supported increased *SIGLEC15* expression that was positively correlated with more extrathyroid extension and lymph node metastasis. We observed different single nucleotide variant (SNV) and copy number variation (CNV) patterns in high and low *SIGLEC15* mRNA expression subgroups; some vital DNA damage repair deficiency scores addressed a negative correlation with *SIGLEC15* mRNA expression. We also found that some commonly used chemotherapy drugs might be suitable for different *SIGLEC15* mRNA expression subgroups. This study highlighted the vital role of *SIGLEC15* in THCA. Targeting *SIGLEC15* may offer a potential novel therapeutic opportunity for THCA patients. However, the detailed exact cellular mechanisms of *SIGLEC15* in THCA still needed to be elucidated by further studies.

KEYWORDS

thyroid cancer, *SIGLEC15*, mRNA expression, clinical characteristics, immune dysfunction

Introduction

Thyroid cancer is a common endocrine system tumor, and its incidence rate has been increasing steadily in recent years (1–3). What was worse is that it was reported that thyroid cancer is the fifth most common cancer in women (4). Although the increase in incidence rate could be largely attributed to the improvement in the detection and diagnosis technology of papillary thyroid cancer (PTC) (diameter <2 cm), the ratio of more invasive PTC (diameter 2.1–4.0 cm and >4 cm) increased by 1.5–5 times in the past 30 years (5), even if the majority of them had excellent long-term prognoses. However, some kind of thyroid cancer may also exhibit very aggressive behavior, and the mortality rate remains stubbornly high (6). There are still a small number of patients with advanced differentiated, poorly differentiated, and undifferentiated thyroid cancer with high mortality. To date, the most efficacious approach is targeted therapy with or without surgical resection, but the curative effect is still poor. Therefore, there is an urgent need for newer therapies.

More and more studies believed that the tumor microenvironment (TME) was an essential factor that affected tumor formation, development, and prognosis (7–10). Therefore, a lot of effort has been stimulated to identify immune factors that contribute to the prognosis of cancer patients. Checkpoint inhibitors, chemotherapy drugs, radiotherapy, and antiangiogenic drugs all enhanced T-cell infiltration in the tumor microenvironment (11). Immunotherapy has become the fourth primary treatment of tumors following surgery, radiotherapy, and chemotherapy. Immune checkpoint inhibitors, especially, have accomplished unprecedented success in the clinical treatment of multiple cancer types. There was also a growing body of cancer clinical trials that were approved by the US Food and Drug Administration (FDA) in which a single-agent checkpoint inhibitor or a kind of combination of checkpoint blockades was a treatment (12–14), demonstrating the breadth of interest from scientists and pharmaceutical factories in immuno-oncology and the great potential for additional immunotherapeutics.

Immune checkpoint-blocking therapy such as cytotoxic T lymphocyte-associated antigen 4 (*CTLA4*) (15, 16), programmed cell death protein 1 ligand 1 *(PD-L1)*, and programmed cell death 1 *(PD-1)* have been widely used in many types of solid tumors (17, 18). Although anti-*PD-1*/*PD-L1* therapy was the most famous and clinically effective immunotherapy, its effectiveness in human solid tumors remains only 20%–30% (19). In recent years, immunotherapy has been successfully applied to the treatment of advanced differentiated thyroid cancer and anaplastic thyroid cancer and changed the treatment paradigm (20, 21).

SIGLEC15, an alias of *CD33L3* and *HsT1361*, belonged to the sialic acid-binding immunoglobulin-like lectin family. Angata et al. (22) first identified *SIGLEC15* in 2007 and inferred that it probably played a conserved regulatory role in the immune system of vertebrates. The following studies demonstrated that *SIGLEC15* played an important role in the development and differentiation of osteoclastogenesis, and it could also act as a potential therapeutic target with its versatile role of suppressed bone resorption but also facilitated bone remodeling (23–25). Jaeger et al. (26) identified *SIGLEC15* as a susceptibility factor in recurrent vulvovaginal candidiasis. Wang et al. (27) first supported that *SIGLEC15* could be an immune suppressor and potential target for normalization cancer immunotherapy by using a genome-scale T-cell activity array in 2019, and they also revealed upregulation of *SIGLEC15* on various cancer types. Moreover, *SIGLEC15* had unique molecular features when compared with the majority of known checkpoint inhibitory ligands and a mutually exclusive expression with *PDL1*, proposing that it could be a critical immune evasion mechanism in PD-L1-negative patients (27). *SIGLEC15* was proven to be an immune suppressor in the premetastatic lymph node of colorectal cancer (28). Several studies displayed the complicated function of *SIGLEC15* and validated that *SIGLEC15* could act as a potential immunotherapeutic target for pancreatic ductal adenocarcinoma (29, 30). *SIGLEC15* shaped a non-inflamed TME and predicted the molecular subtypes in bladder cancer (31). Furthermore, *SIGLEC15* acted as a mediator of *LINC00973*t to suppress immune in clear-cell renal cell carcinoma (32). Most importantly, in a phase I clinical trial of *SIGLEC15*-positive patients who were diagnosed with advanced/metastatic solid tumors refractory or resistant to currently available therapies with a tumor proportion score Tumor Proportion Score (TPS) PDL1 score <50% could benefit from NC318 (anti-*SIGLEC15* antibody) (33).

In the present study, we aimed to decipher the comprehensive picture of the role of *SIGLEC15* in thyroid carcinoma (THCA) by

Abbreviations: Abbreviations: ACC, Adrenocortical carcinoma; BLCA, Bladder Urothelial Carcinoma; BRCA, Breast invasive carcinoma; CESC, Cervical squamous cell carcinoma and endocervical adenocarcinoma; CHOL, Cholangiocarcinoma; COAD, Colon adenocarcinoma; COADREAD, Colon adenocarcinoma/Rectum adenocarcinoma Esophageal carcinoma; ESCA, Esophageal carcinoma; GBM, Glioblastoma multiforme; GBMLGG, Glioma; HNSC, Head and Neck squamous cell carcinoma; KICH, Kidney Chromophobe; KIPAN, Pan-kidney cohort (KICH+KIRC+KIRP); KIRC, Kidney renal clear cell carcinoma; KIRP, Kidney renal papillary cell carcinoma; LAML, Acute Myeloid Leukemia; LGG, Brain Lower Grade Glioma; LIHC, Liver hepatocellular carcinoma; LUAD, Lung adenocarcinoma; LUSC, Lung squamous cell carcinoma; OV, Ovarian serous cystadenocarcinoma; PAAD, Pancreatic adenocarcinoma; PCPG, Pheochromocytoma and Paraganglioma; PRAD, Prostate adenocarcinoma; READ, Rectum adenocarcinoma; STAD, Stomach adenocarcinoma; SKCM, Skin Cutaneous Melanoma; STES, Stomach and Esophageal carcinoma; TGCT, Testicular Germ Cell Tumors; THCA, Thyroid carcinoma; UCEC, Uterine Corpus Endometrial Carcinoma; UCS, Uterine Carcinosarcoma; ALL, Acute Lymphoblastic Leukemia; WT, High-Risk Wilms Tumor.

datamining the well-known multi-omics databases, such as The Cancer Genome Atlas (TCGA) and Gene Expression Omnibus (GEO), and validated it in our own dataset by experiments.

Materials and methods

Data acquisition

We obtained TCGA and Genotype-Tissue Expression (GTEX) RNA sequencing data (FPKM), clinical data, and DNA methylation data from xenabrowser (https://xenabrowser.net/datapages/) (34, 35), and FPKM values were transformed to log2(TPM + 1) values. *SIGLEC15* mRNA differential expression from the Pan-Cancer Analysis of Whole Genomes (PCAWG) was completed by R package UCSCXenaShiny (36). GEO datasets (GSE3467, GSE3678, GSE29265, GSE33630, GSE60542, GSE65144, GSE97001) were downloaded from GEO database (https://www.ncbi.nlm.nih.gov/geo/) (37). R package limma was used to get the mean value of repeated probes in GEO datasets (38). Wilcoxon rank-sum test was used to compare the differential expression of *SIGLEC15* between tumor and normal samples in both The Cancer Genome Atlas, and GEO is Gene Expression Omnibus and GEO datasets; R package ggpubr and ggplot2 were used to visualize the difference (38). R package survival was used to explore the relationship between *SIGLEC15* expression and overall survival. Somatic mutation MAF (Varscan2 version) file was downloaded from the GDC data portal (https://portal.gdc.cancer.gov/) and presented gene mutation between high and low *SIGLEC15* (cut by median value of *SIGLEC15*) (39). Copy number information was harvested from Masked Copy Number Segment by R package TCGAbiolinks (40), then separated into two files by high and low *SIGLEC15* (cut by median value of *SIGLEC15*); these two files were used as input for the online tools GenePattern module GISTIC_2.0 (version 6.15.28) (https://www.genepattern.org/#) to visualize the copy number variation (CNV) difference (41). We downloaded the genomic and molecular landscape of DNA damage repair deficiency scores file (42) and explored the correlation with *SIGLEC15* mRNA expression. Online database Tumor Immune Single-cell Hub (TISCH) was conducted to explore the expression cell type of *SIGLEC15* (43).

SIGLEC15 mRNA expression correlation with DNA methylation and N6-Methyladenosine regulator mRNA expression

We extracted DNA methylation site beta values 2 kb upstream to 0.5 kb downstream of the transcription start site (TSS) of gene *SIGLEC15*, then conducted a Spearman correlation analysis between *SIGLEC15* DNA methylation and mRNA expression (including gene level and site level; gene level is the mean value of all site values). We also explored the correlation between *SIGLEC15* mRNA expression and N6-methyladenosine (m6A) genes (including 13 readers, eight writers, and two erasers) (44).

Functional enrichment analysis

We used Wilcoxon rank-sum test to find the differentially expressed genes between high and low *SIGLEC15* (cut by median value of *SIGLEC15*) groups and visualized by R package pheatmap. Gene set enrichment analysis (GSEA) software (GSEA v4.2.3) (45, 46), h.all.v7.5.1.symbols.gmt, and c5.go.v7.5.1.symbols.gmt were harvested from msigdb (http://www.gsea-msigdb.org/gsea/downloads.jsp) and then for GSEA with the high and low *SIGLEC15* mRNA expression groups. Significant signaling pathways were selected by criteria false discovery rate (FDA) <0.25 and p-value <0.05.

Protein–protein interaction (PPI) network and hub genes

Significant differentially expressed genes between high and low *SIGLEC15* (cut by median value of *SIGLEC15*) groups were based on the criteria of false discovery rate <0.05 and absolute value log2 fold change >1, then the selected genes were input into SRTING (v11.5, http://string-db.org/) for the retrieval of protein–protein interaction network information (47). A cutoff of 0.4 for minimum interaction score was set to get the biological functions with disconnected nodes hidden from the network, and the interaction file acted as input for Cytoscape3.9.1 to visualize the interaction network of these proteins (48); plug-in CytoHubba was applied to get hub genes with default parameters (49).

Evaluation of the immunological landscape characteristics with *SIGLEC15* of the thyroid carcinoma

To decipher the immunological landscape characteristics of the TME in THCA, we firstly gained 122 immunomodulator genes [major histocompatibility complex (MHC), receptors, chemokines, and immune stimulators] (50), 47 immune checkpoint (ICP) genes, and 25 immunogenic cell death (ICD) genes (51). We displayed the different expressions between high and low *SIGLEC15* (cut by median value of *SIGLEC15*) groups or correlation with gene *SIGLEC15*. The activity of the cancer immunity cycle data was obtained from online website TIP (http://biocc.hrbmu.edu.cn/TIP/index.jsp) (52) and immune

features from the online website iAtlas Explorer (https://isb-cgc.shinyapps.io/iatlas/) were downloaded (53) and then were visualized by R package ggpurb between high and low *SIGLEC15* (cut by median value of *SIGLEC15*) groups. R package estimate was used to output the estimated levels of infiltrating stromal and immune cells and calculated stromal score, immune score, and estimate score (54). The TIMER website (https://cistrome.shinyapps.io/timer/) was utilized to validate the influence of *SIGLEC15* expression on immune cell infiltration in THCA (55). We also used single-sample gene set enrichment analysis (ssGSEA) to compare the immune infiltration scores between high and low *SIGLEC15* (cut by median value of *SIGLEC15*) groups (56). The Tumor Immune Dysfunction and Exclusion (TIDE) score and exclusion score were evaluated using an online database (http://tide.dfci.harvard.edu/) (57).

Tissue microarray analysis

This study was approved by the institutional review board of Zhejiang Cancer Hospital. The informed consents were signed from all subjects in the study. The tissue microarray (TMA) chips were obtained from Wuhan Xavier Biotechnology Co., Ltd. A total of 110 thyroid cancer tissue specimens and 54 adjacent tissue specimens were obtained; each formalin-fixed paraffin-embedded block was cut into 4-μm-thick sections for arraying. *SIGLEC15* antibody (GTX32061, GeneTex, CA, USA) was used for immunohistochemistry (IHC); representative cancer tissue areas were marked on hematoxylin–eosin-stained slides, and TMA construction sampling was performed using tissue chip scanner (3DHistech®, Pannoramic MIDI, Hungary). The Densito Quant software in Quant Center was used to automatically identify and set all dark brown on the tissue section as strong positive, brown yellow as medium positive, light yellow as weak positive, and blue nucleus as negative. Then, each tissue point was identified; the strong positive, medium positive, weak positive, and negative areas (unit: pixel) were analyzed; and the positivity percentage and histochemistry score (H-score) were calculated.

Evaluation of potential chemotherapy drugs to *SIGLEC15* mRNA expression

Cellminer™ database [Version: 2022.1 (database: 2.8.1)] was used for the research of pharmacological data of the NCI-60 cancerous cell lines (58).

Statistical analysis

Statistical analysis was finished with R software (v4.1.1, https://www.r-project.org/) and its corresponding packages. Comparison between two groups was conducted utilizing Wilcoxon rank-sum test, and Kruskal–Wallis test was carried out for normal multiple groups. Spearman correlation test was adopted to determine the correlation between variables. Fisher exact test was performed to analyze the correlation between *SIGLEC15* and clinicopathologic characteristics. p-value <0.05 was set as the threshold; if not specially noted, ns, *, **, ***, and **** stand for p-value >0.05, p-value <=0.05, pvalue <=0.01, pvalue <=0.001 and pvalue <=0.0001, respectively.

Results

Analysis of expression of *SIGLEC15* in thyroid carcinoma samples

Figure 1 showed the workflow of this study, which was presented for *SIGLEC15* differential expression, immune genes, cells, pathways, immune infiltration scores, clinical features, mutations, CNV, DNA methylation, and m6A genes with *SIGLEC15*. After a comprehensive analysis of the expression data from The Cancer Genome Atlas, and GEO is Gene Expression Omnibus, Genotype-Tissue Expression, and PCAWG database, we found that *SIGLEC15* was highly expressed in THCA compared with normal tissues in all databases (Figure 2A; Supplementary Figure S1A). In

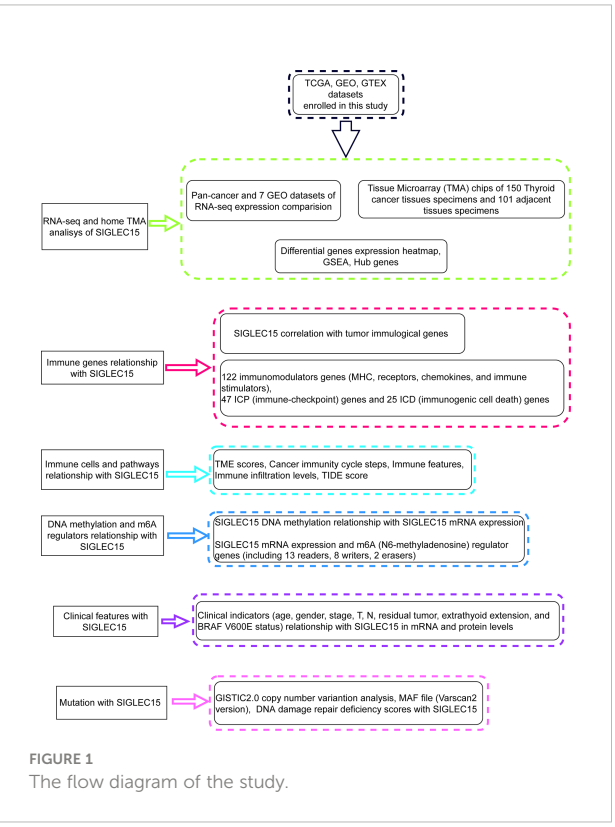

FIGURE 1
The flow diagram of the study.

10.3389/fimmu.2022.975787

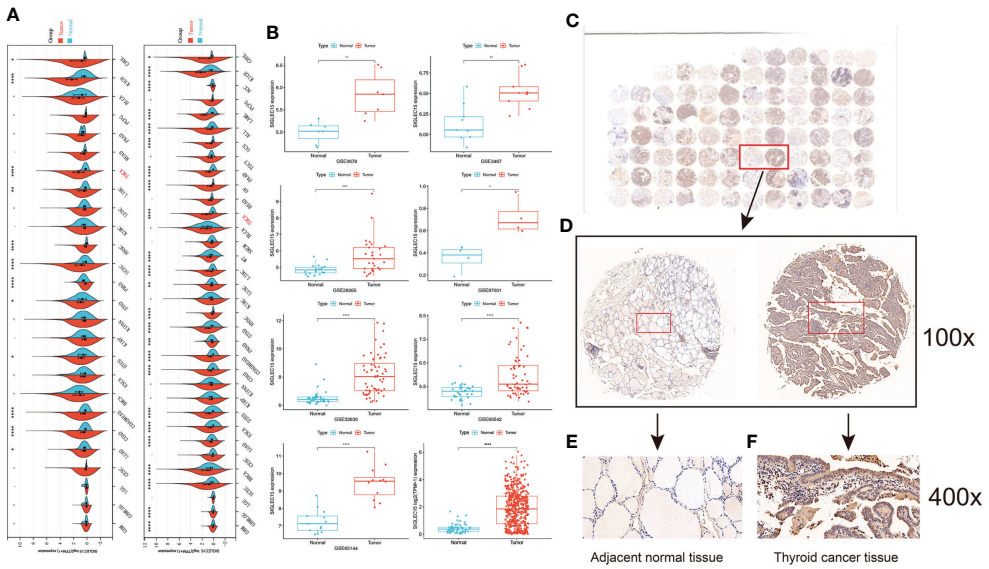

FIGURE 2
Analysis of the expression of *SIGLEC15*. **(A)** Pan-cancer mRNA expression of *SIGLEC15* between tumor and normal tissues from The Cancer Genome Atlas, and GEO is Gene Expression Omnibus and Genotype-Tissue Expression database. **(B)** mRNA expression of *SIGLEC15* between tumor and normal tissues from GEO and The Cancer Genome Atlas, and GEO is Gene Expression Omnibus database. **(C)** A classic pair of samples. **(D–F)** Left sample was adjacent normal tissue. Right sample was thyroid carcinoma tissue. Thyroid carcinoma tissue has higher *SIGLEC15*-positive staining than the adjacent normal tissue. ns, *, **, ***, and **** stand for p-value >0.05, p-value <=0.05, p-value <=0.01, pvalue <=0.001 and pvalue <=0.0001, respectively.

addition, *SIGLEC15* mRNA expression from database The Cancer Genome Atlas, and GEO is Gene Expression Omnibus of THCA in tumor and normal samples was shown in Figure 2B. Paired tumor and normal samples in Supplementary Figure S1B, *SIGLEC15* was also found to be highly expressed in tumor samples in gene expression profiles (GSE3467, GSE3678, GSE29265, GSE33630, GSE60542, GSE65144, GSE97001) from the GEO database in Figure 2B. The expression level and the positive rates of *SIGLEC15* were compared between thyroid cancer tissue and adjacent normal tissue samples by immunohistochemistry on microarray. Figures 2C, D were a representative area of TMA, a classic pair of samples. Adjacent tissue had lower positive staining (Figure 2E) than thyroid cancer tissue (Figure 2F); the concrete H-score was in Table 1.

TABLE 1 *SIGLEC15* expression levels in different pathological tissues.

	N	H-Score ($\bar{X} \pm S$)	t-value	p-value
Tumor tissue	110	95.18 ± 29.10	6.124	0.001
Paratumor tissue	54	64.92 ± 31.0		

H-Score, histochemistry score.

Differential genes, signaling pathways, and hub genes associated with *SIGLEC15* mRNA expression groups

We obtained significant differentially expressed genes between high and low *SIGLEC15* groups. The 20 most highly and lowly expressed genes were presented, and we noted that the SIGLEC family genes *SIGLEC15* and *SIGLEC6* were in the 20 most highly expressed genes in tumor samples (Figure 3A). We further analyzed the signaling pathways involving *SIGLEC15 via* GSEA; high *SIGLEC15* mRNA expression was positively correlated with pathways such as the regulation of adaptive immune response, positive regulation of cytokine production, T cell-mediated immunity (Figure 3B), inflammatory response, interferon alpha response, and interferon gamma response (Figure 3C). Thereafter, we used the methods mentioned above to identify hub genes; 10 hub genes were harvested, as Figure 3D presented; several CXC family genes were in the hub gene list, such as genes *CXCL1*, *CXCL2*, and *CXCL8* (Figure 3D).

Immunological and biological significance of *SIGLEC15* in thyroid carcinoma

The majority of 122 highly expressed immunomodulators were found in the high *SIGLEC15* mRNA expression group, such

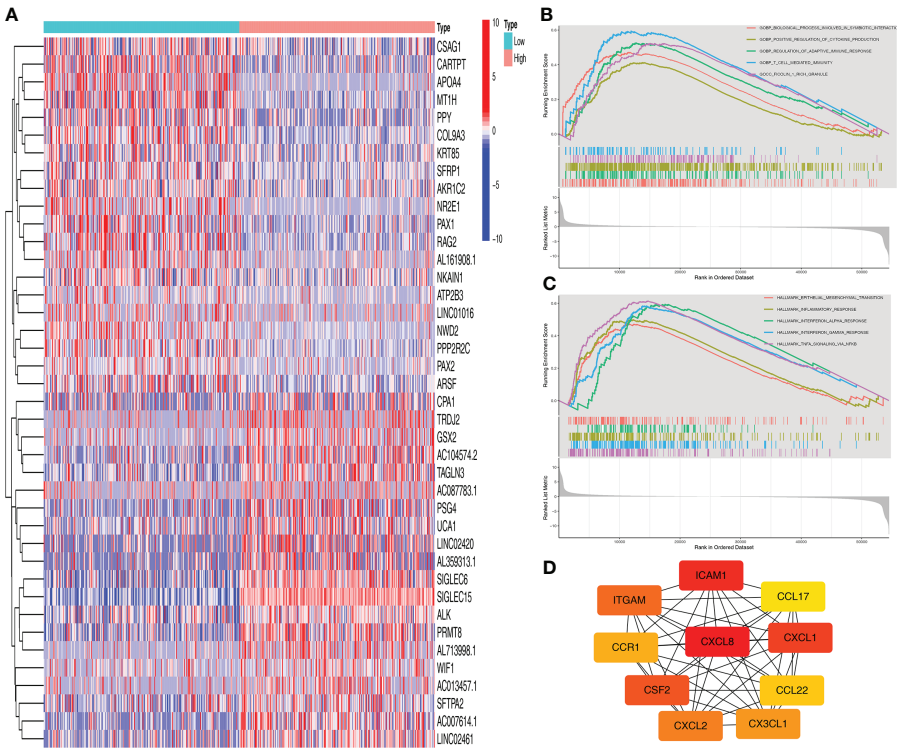

FIGURE 3
Functional enrichment analysis of *SIGLEC15*. **(A)** Top 20 differentially expressed genes between high and low *SIGLEC15* groups. **(B, C)** GSEA for the signaling pathways activated in the high *SIGLEC15* mRNA expression group with **(B)** GO pathways and **(C)** HALLMARK pathways. **(D)** Hub genes related to *SIGLEC15*.

as MHC family member genes, CXC family member genes, CXC chemokine receptors that played important roles in cancer immunity (Figure 4A), and ICPs and ICD genes, which played critical roles in modulating the host antitumor immunity. *SIGLEC15* had a positive correlation with most of the ICPs, and some had a significant positive correlation (e.g., *CD200*, *CD276*, *CD40*) but had no significant correlation with *PDCD1 (PD-1)* (Figure 4B). *SIGLEC15* also had a significant positive correlation with some ICDs (e.g., *ANXA1*, *MET*) and significant negative correlation with *CALR* (Figure 4C). We also found a significant positive correlation between *SIGLEC15* and *CD44* (Supplementary Figure S1C; Supplementary Table S1). Systematically tracking the activity of anticancer immunity and the extent of tumor-infiltrating immune cells were important for cancer immunotherapy. The majority of the steps of the cancer immunity cycle were found to be significantly upregulated, including step 3 (priming and activation), step 5 (infiltration of immune cells into tumors), and most parts of step 4 (trafficking of immune cells to tumors) (Figure 5A). Furthermore, we also assessed the correlation between *SIGLEC15* mRNA expression and 56 previously defined immune-related molecular features; the expressions of 11 molecular features were significantly higher in the high *SIGLEC15* group, including Dendritic Activated, IFN gamma Response, and Leukocyte Fraction (Supplementary Figures S2A–K). We further evaluated the correlation between *SIGLEC15* expression and immunocyte infiltration and observed that *SIGLEC15* significantly positively correlated with the infiltration of B cells, CD4 T cells, macrophages, neutrophils, and dendritic cells (Figure 5B). Moreover, the high *SIGLEC15* group employed a higher stromal score, immune score, and estimate score (Figure 5C). We also used the ssGSEA algorithm to calculate immunocyte infiltration; it was easy to see that all of the 16 immune cells and 13 immune-related pathway scores were significantly upregulated in the high *SIGLEC15* group (Figures 5E, F). Although the high *SIGLEC15* group had a higher proportion of immunocytes and an elevated level of immune checkpoints, we also observed that the high *SIGLEC15* group linked with an increased score of TIDE, immune exclusion by TIDE database (Figure 5D). Moreover, by integrating some known gene sets correlated with exhausted immunity, we found that although patients with high *SIGLEC15* had a high proportion of immunocytes, they also had higher scores of immune checkpoint blockade (ICB) resistance, exhausted CD8, T-cell exhaustion, immune checkpoint, and T-cell regulatory, which would lead to immune exhaustion. So,

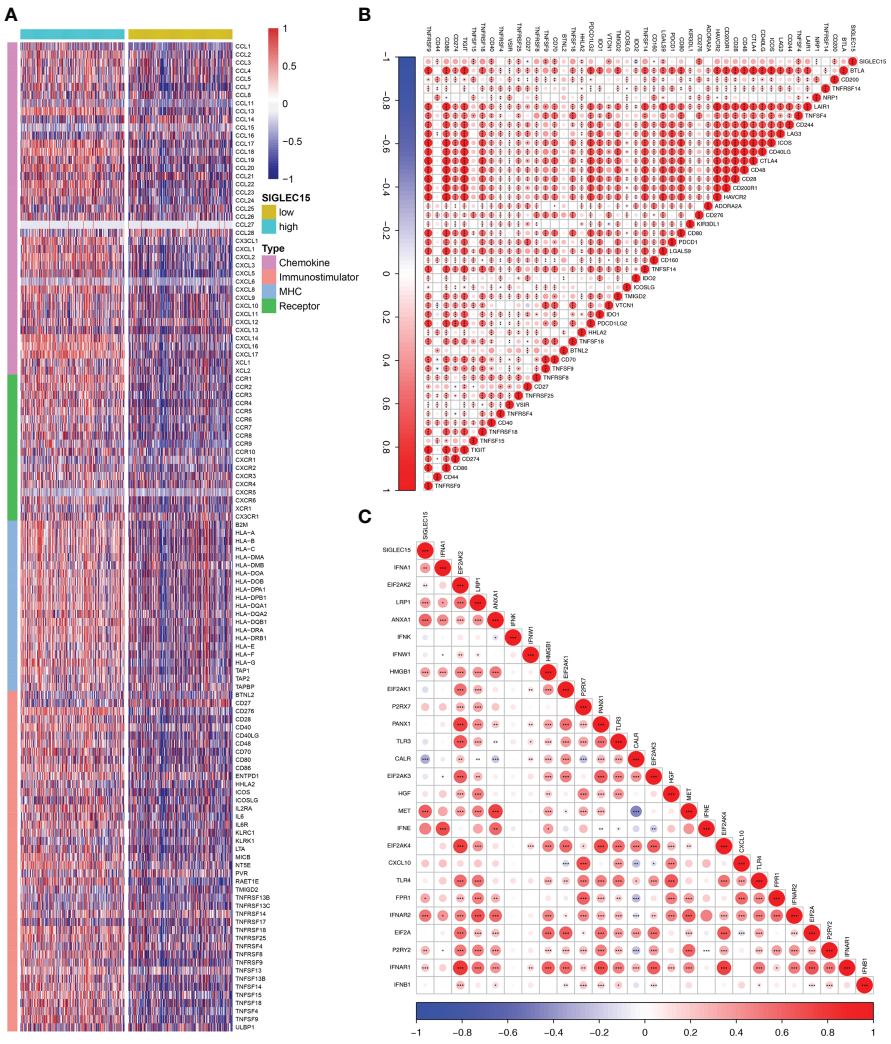

FIGURE 4
Immunological gene patterns related to *SIGLEC15*. **(A)** Differential expression of 122 immunomodulators (chemokines, receptors, MHC, and immunostimulators) between the high and low *SIGLEC15* groups. **(B)** ICP modulator relationship with *SIGLEC15*. **(C)** ICD modulator relationship with *SIGLEC15*. ns, *, **, and *** stand for p-value ≤0.05, p-value ≤0.01, pvalue ≤0.001.

high *SIGLEC15* subgroup patients met immune exhaustion, which indicated that patients with a low *SIGLEC15* expression could benefit more from Immune checkpoint inhibitor (ICI) therapy than patients with a high *SIGLEC15* expression (Supplementary Figure S2L). We also figured out that mainly immune cells express *SIGLEC15*, especially on Monocytes and Macrophages (Supplementary Figure S3A).

SIGLEC15 mRNA expression correlates with methylation

m6A RNA methylation was a kind of epigenetic modification measured by methyltransferases, demethylases, and binding proteins, which were also called "writers," "erasers," and "readers." We conducted the relationship analysis of these regulated genes with *SIGLEC15* mRNA expression levels; it could be easily seen that the majority of reader genes had a significant positive correlation with *SIGLEC15* (Figure 6A), and all of the writer genes except RBM15 had a significant positive correlation with *SIGLEC15* (Figure 6B). However, eraser genes had no significant correlation with *SIGLEC15* (Figure 6C). We also analyzed the extent to which *SIGLEC15* mRNA expression correlated with CpG methylation and the whole CpG methylation site levels of *SIGLEC15*, which varied from a broad scope (Figure 6D). Interestingly, the averaged *SIGLEC15* promoter and body hypermethylation were associated with decreased *SIGLEC15* mRNA expression, indicated by a strong negative correlation coefficient (Figure 6E). Moreover, we measured each CpG

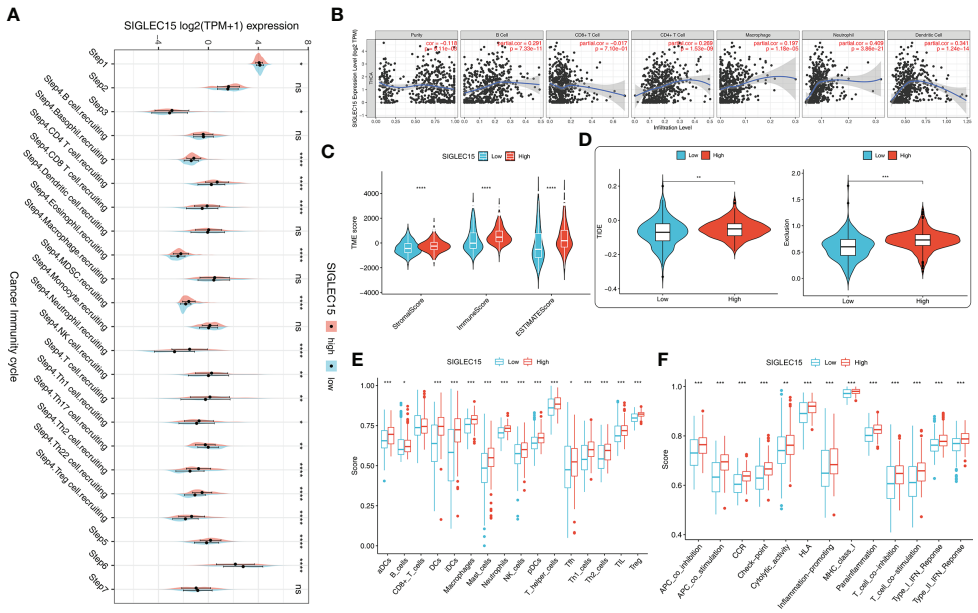

FIGURE 5
Immunological cell patterns related to *SIGLEC15*. **(A)** Differences in the seven steps of the cancer immunity cycle between the high and low *SIGLEC15* groups. **(B)** *SIGLEC15* was associated with immune cell infiltration in THCA obtained from the TIMER database. **(C)** TME scores were compared between the high and low *SIGLEC15* groups. **(D)** Scores were compared between the low and high *SIGLEC15* groups in TIDE score and Exclusion score. **(E)** Enrichment scores for 16 immunocytes were compared between the low and high *SIGLEC15* groups. **(F)** Enrichment scores for 13 immune-related pathways were compared between the low and high *SIGLEC15* groups. ns, *, **, ***, and **** stand for p-value >0.05, p-value <=0.05, p-value <=0.01, pvalue <=0.001 and pvalue <=0.0001, respectively.

methylation site level with *SIGLEC15* mRNA expression levels; we found that six out of nine sites had a negative correlation with *SIGLEC15*, and CpG methylation site cg05752393 had a positive correlation with *SIGLEC15* (Figures 6F–L). However, the CpG methylation site cg13741394 and cg00425636 had no significant correlation with *SIGLEC15* (Figures 6M, N).

Clinical significance of *SIGLEC15*

We quantified vital clinical feature associations with *SIGLEC15* mRNA expression in THCA, and stage, lymph node metastasis (N stage), extrathyroid extension, and *BRAF* V600E status were found to be positively correlated with *SIGLEC15* mRNA expression levels; other clinical factors (e.g., age, gender, residual tumor) indicated no significant relationship with *SIGLEC15* mRNA expression (Figures 7A–I). Furthermore, we analyzed the clinical feature associations with *SIGLEC15* IHC level, and we revealed that N stage and extrathyroid extension were positively related to *SIGLEC15* in Table 2. However, there was no significant relationship between *SIGLEC15* expression and overall survival (Supplementary Figure S4A).

Mutational analyses of *SIGLEC15* in thyroid carcinoma

No mutations were found in the MAF file of the gene *SIGLEC15* of THCA patients produced by varscan2 software obtained from The Cancer Genome Atlas, and GEO is Gene Expression Omnibus. We also investigated mutational profiles of low and high *SIGLEC15* groups; it could be clearly seen that more patient samples in the high *SIGLEC15* group had gene *BRAF* mutations. Moreover, the majority of mutations in patient samples of the high *SIGLEC15* group were located in gene *BRAF* (Figure 8A); patient samples in the low *SIGLEC15* group had mutations in genes *BRAF*, *NRAS*, and *HRAS* (Figure 8B), not focused as that in the high *SIGLEC15* group. The GISTIC2.0 results indicated that amplification displayed a lower frequency in the high *SIGLEC15* mRNA expression group compared to the low *SIGLEC15* expression group (Figures 8C, D) and similar frequency of deletion in the two groups (Figures 8C, D). Furthermore, we calculated the G-score, which also showed more amplification events in the low *SIGLEC15* expression group (Supplementary Figures S5A, S5B).

10.3389/fimmu.2022.975787

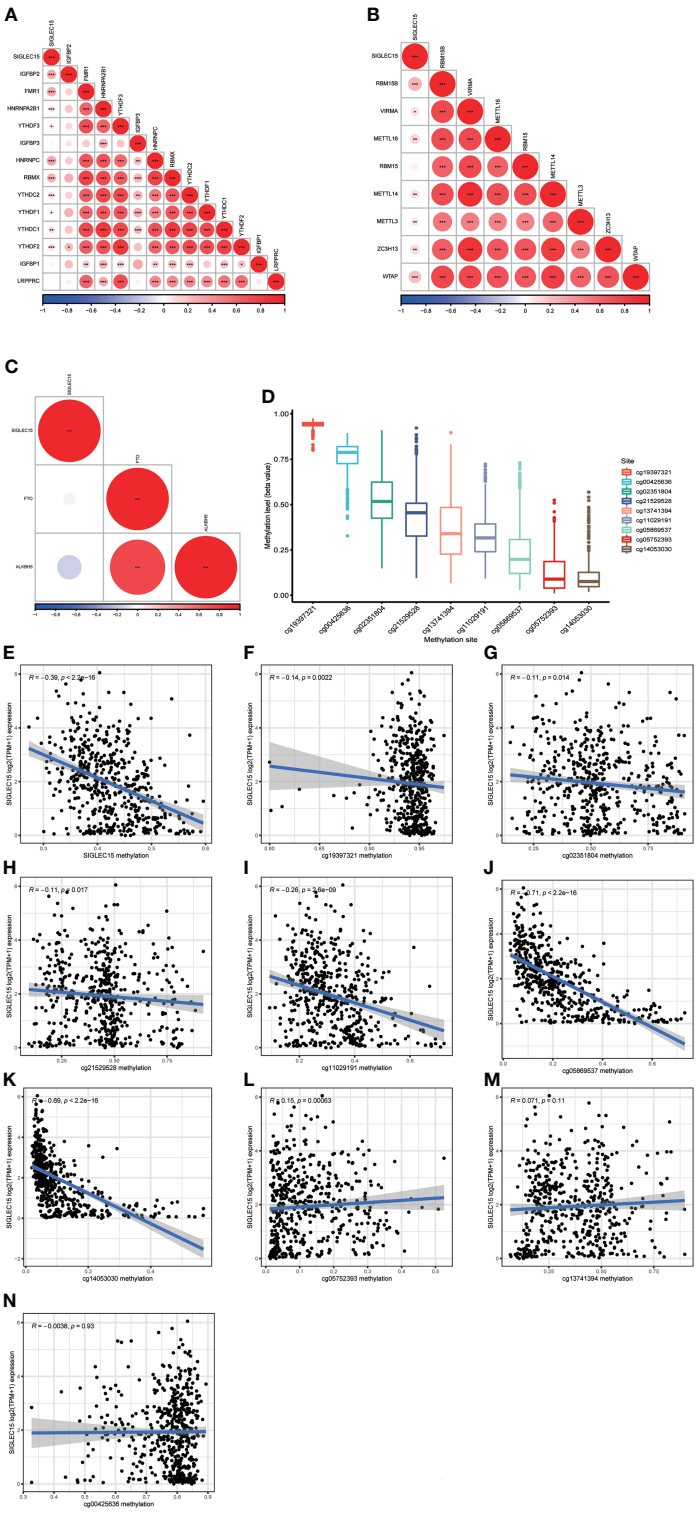

FIGURE 6
SIGLEC15 mRNA expression correlation with DNA methylation and m6A regulator mRNA expression. **(A–C)** *SIGLEC15* mRNA expression correlation with **(A)** m6A readers, **(B)** writers, and **(C)** erasers. **(D)** Each CpG methylation site level of *SIGLEC15*. **(E)** *SIGLEC15* mRNA expression correlation with averaged CpG methylation site. **(F–N)** *SIGLEC15* mRNA expression correlation with DNA methylation of each CpG methylation site.

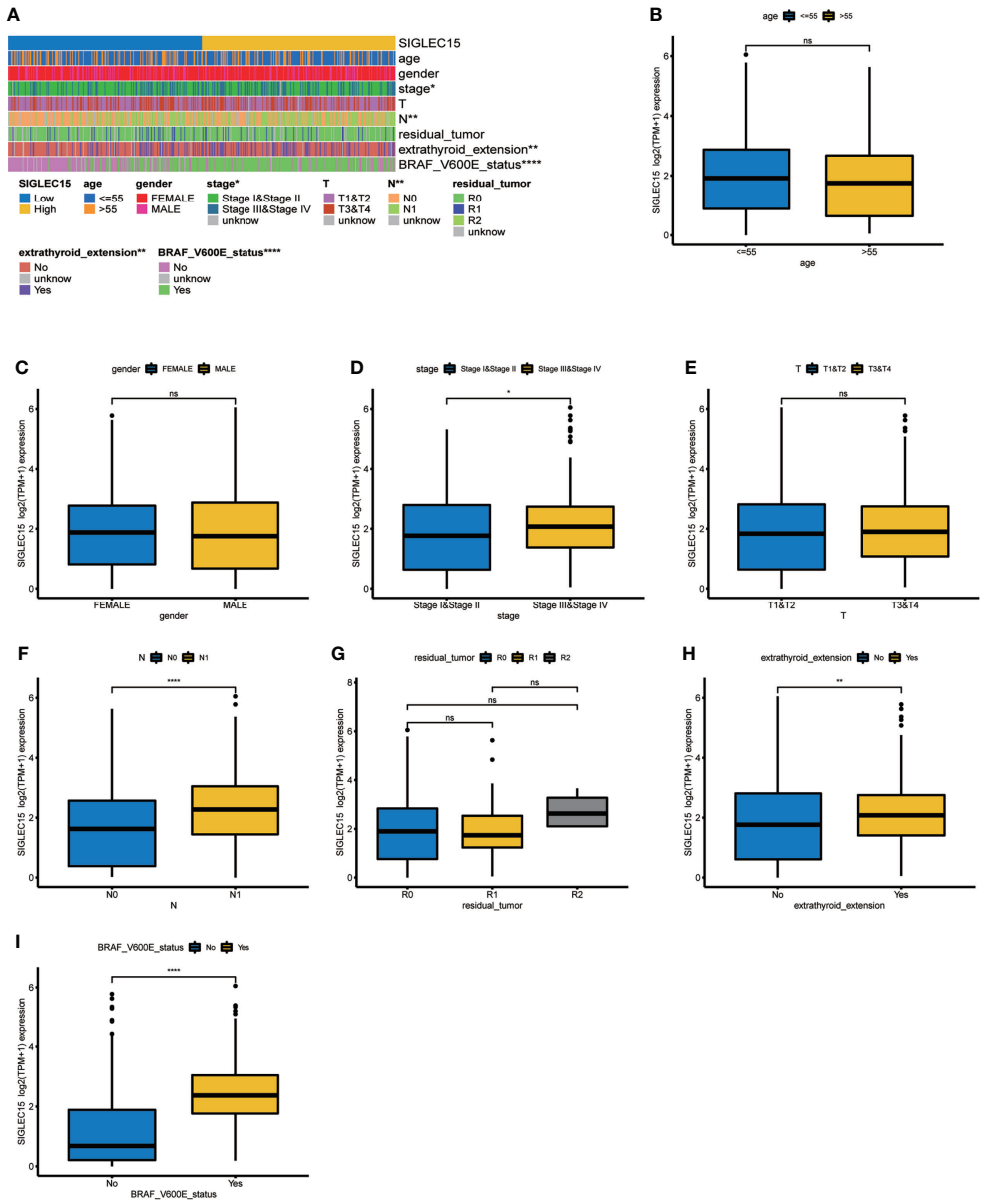

FIGURE 7
Clinical significance of *SIGLEC15*. **(A)** Heatmap of clinical feature correlation with *SIGLEC15*. **(B–I)** High and low *SIGLEC15* mRNA expression group difference in **(B)** Age, **(C)** Gender, **(D)** Stage, **(E)** T stage, **(F)** N stage, **(G)** Tumor residual size, **(H)** Extrathyroid extension, and **(I)** *BRAF* V600E status. ns, *, **, ***, and **** stand for p-value >0.05, p-value <=0.05, p-value <=0.01, pvalue <=0.001 and pvalue <=0.0001, respectively.

DDR deficiency association with *SIGLEC15*

DDR genes played vital roles in maintaining genomic stability, so the relationship between DDR deficiency scores and *SIGLEC15* was evaluated. We observed that many scores had a negative correlation with *SIGLEC15*, aneuploidy score prime (correlation coefficient = -0.23) (Figure 9A), aneuploidy score (correlation coefficient = -0.18) (Figure 9B), CNA frac altered (correlation coefficient = -0.19) (Figure 9C), LOH frac altered (correlation coefficient = -0.15) (Figure 9D), expression CDF trAnsform of Rank Distribution (eCARD) (correlation coefficient = -0.22) (Figure 9E), and repair proficiency scoring (RPS) (correlation coefficient = -0.24) (Figure 9F); nevertheless, PARPi7 (7-gene DNA repair deficiency expression signature) had a positive correlation with *SIGLEC15* mRNA expression (correlation coefficient = 0.34) (Figure 9G).

10.3389/fimmu.2022.975787

TABLE 2 Relationship between clinicopathological characteristics and expression of *SIGLEC15*.

Parameter	N	H-Score ($\bar{X}$ ± S)	t-value	p-value
Gender				
Men	29	92.63 ± 30.19	0.525	0.601
Women	81	95.95 ± 29.02		
Age, years				
≤55	84	95.62 ± 27.23	0.355	0.723
>55	26	93.28 ± 35.49		
Extrathyroid extension				
No	67	88.13 ± 31.59	3.184	0.002
yes	43	105.72 ± 21.94		
Tumor focality				
Unifocal	76	94.30 ± 30.0	0.134	0.894
Multifocal	34	93.45 ± 31.98		
Lesion side				
Ipsilateral	77	92.81 ± 27.27	1.24	0.21
Bilateral	33	100.34 ± 33.21		
Lymph node metastasis				
N0	44	87.91 ± 28.68	2.31	0.035
N1a+N1b	66	99.84 ± 28.82		

H-Score, histochemistry score; N0, no lymph node metastasis; N1a, central lymph node metastasis; N1b, lateral cervical lymph node metastasis.

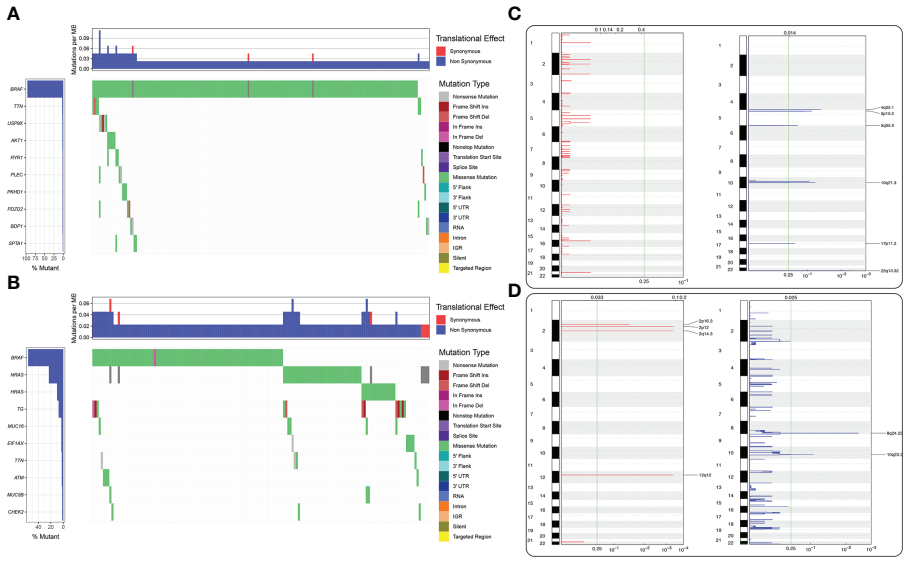

FIGURE 8
Differential mutational landscape in the high and low SIGLEC15 mRNA expression groups. **(A)** Genes were ranked according to the mutational frequency. SNV and Indel mutations in the high SIGLEC15 mRNA expression group. **(B)** Genes were ranked according to the mutational frequency. SNV and Indel mutations in the low SIGLEC15 mRNA expression group. **(C, D)** CNV landscape of **(C)** amplification and **(D)** deletion in the high and low SIGLEC15 mRNA expression groups; the chromosome was oriented vertically from top to bottom and GenePattern GISTIC2.0 q-value at each locus was placed from left to right. The green line displayed the cutoff value of q-value = 0.25.

10.3389/fimmu.2022.975787

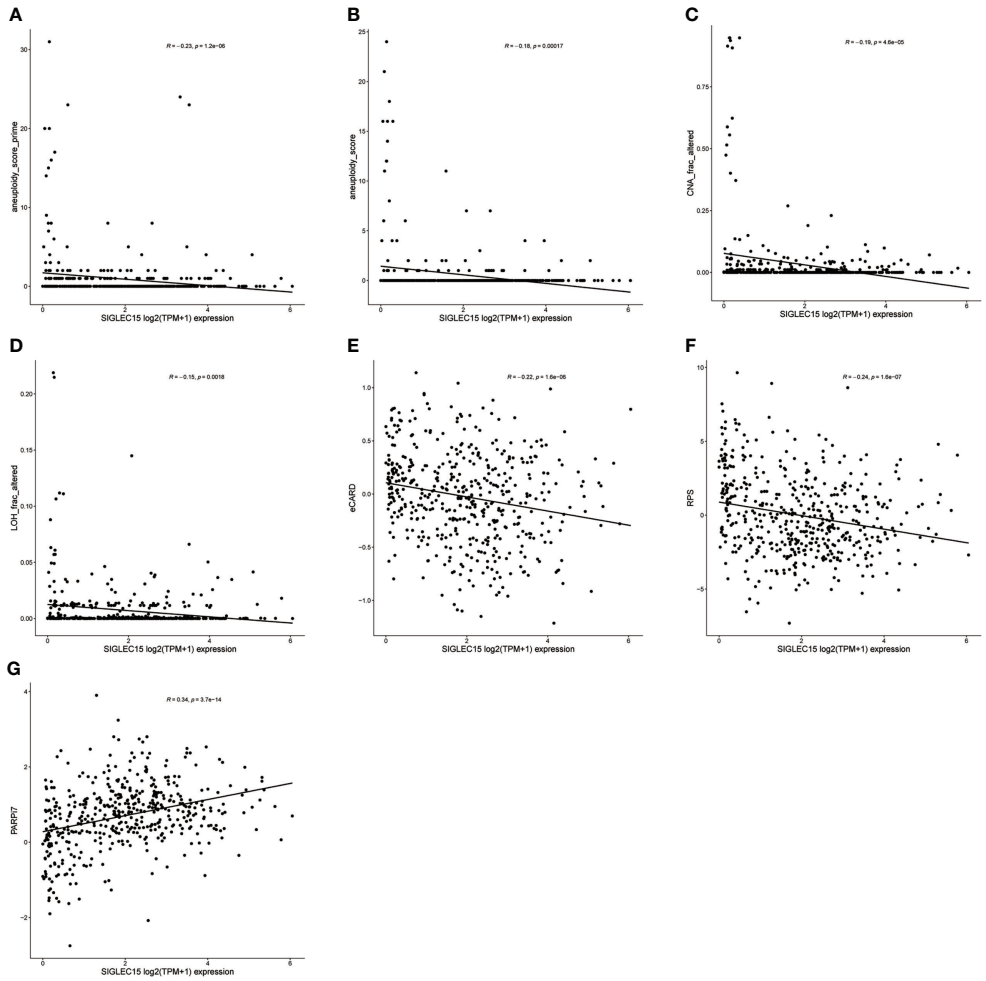

FIGURE 9
DDR deficiency score correlation with *SIGLEC15* mRNA expression. **(A–G)** *SIGLEC15* mRNA expression with score of **(A)** aneuploidy score prime, **(B)** aneuploidy score, **(C)** CNA frac altered, **(D)** LOH frac altered, **(E)** eCARD, **(F)** RPS, and **(G)** PARPi7.

Potential chemotherapy drugs for *SIGLEC15* determined thyroid carcinoma progress

Combining chemotherapy drugs with a single-agent immune checkpoint therapeutic approach may enhance antitumor immune response and overcome primary resistance. We revealed that *SIGLEC15* mRNA expression was negatively associated with the IC50 of tyrothricin, estramustine, pipamperone, fulvestrant, and salinomycin and implied that these selected chemotherapeutic drugs may be suitable for the treatment of those with a high expression level of *SIGLEC15*, while selected chemotherapeutic drugs like pelitrexol, triciribine phosphate, staurosporine, dasatinib, amonafide, and midostaurin might exert an opposite effect for the treatment of those with a high expression level of *SIGLEC15* (Figures 10A–K).

Discussion

Thyroid cancer was one of the most prevalent endocrine cancers with an elevated incidence rate over the past decades, and it was the fifth leading incidence of cancer in women (4). Although the low mortality and moderate prognosis were frequently mentioned, the recurrence and the complications were still obscure. In these years, immunotherapy was applied to the treatment of advanced differentiated thyroid cancer and anaplastic thyroid cancer, with some success (20). Despite the immense success of multiple antibody-based immune therapies targeting *PD-1*/*PD-L1* in common clinical regimens, there were still many non-responding patients (59). Since *PD-1*/*PD-L1* represented only one of many inhibitory immune checkpoints, exploration of other potential new immune modulators that could be blocked to expand the success of cancer immunotherapy and promote the anticancer immune response is urgently needed.

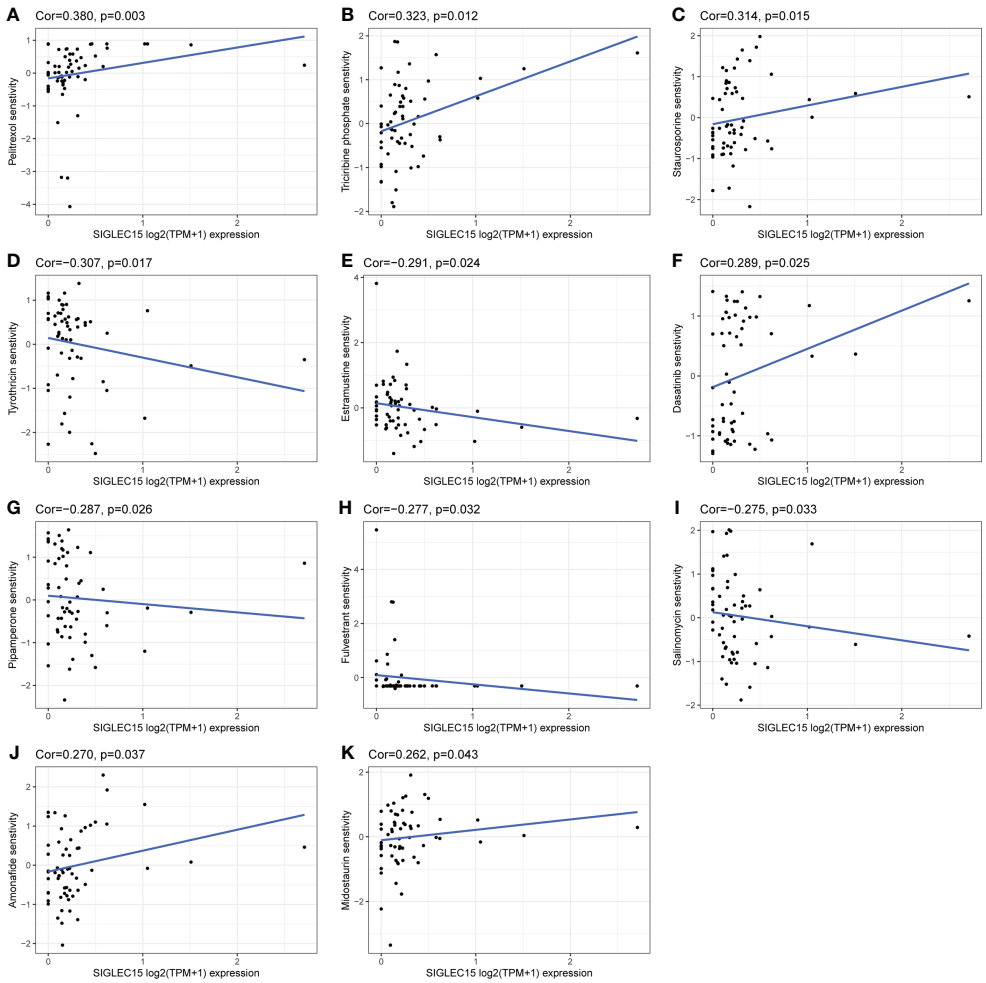

FIGURE 10
Potential effective chemotherapy drugs with *SIGLEC15*. **(A–K)** Correlation of *SIGLEC15* mRNA expression level and IC50 of different drugs based on the CellMiner database.

In this study, the features of *SIGLEC15* in multi-omics data in THCA cases were comprehensively characterized for the first time. We revealed that *SIGLEC15* was overexpressed in THCA. Consistent with our result, previous studies through integrative data mining of *SIGLEC15* mRNA expression in human tumors showed that higher *SIGLEC15* levels were observed in colon adenocarcinoma and thyroid carcinoma (60), colon adenocarcinoma, esophageal carcinoma and thyroid carcinoma (61). Chen et al. found that *SIGLEC15*-knockout mice exhibited retarded tumor growth and prolonged survival compared to wild-type mice. Hao et al. (62) showed that *SIGLEC15* mRNA expression was not associated with the prognosis of early non-small cell lung cancer. Liang et al. (63) proved that high *SIGLEC15* mRNA expression was not related to either overall survival or disease-free survival in patients with non-small cell lung cancer. Quirino et al. (64) found that *SIGLEC15* was also not correlated with either overall survival or relapse-free survival in gastric adenocarcinoma. In contrast, *SIGLEC15* positivity had better disease-specific survival and progression-free survival compared to *SIGLEC15* negativity in pancreatic ductal adenocarcinoma (30). Nevertheless, Li et al. (65) demonstrated that patients with a high *SIGLEC15* mRNA expression had worse overall survival and disease-free survival than patients with low *SIGLEC15* in the PACA-AU database, but no association was observed between *SIGLEC15* and prognosis in their own microarray cohort. Thus, it remained to be determined which biomarkers (*SIGLEC15* IHC or mRNA) could better guide patient selection for treatment response to *SIGLEC15*-associated therapy, and there has exited a companion diagnostic assay of SIGLEC5 by immunohistochemical was conducted by Shafi et al. (66). In addition, the pan-cancer analysis and our result showed that the expression of *SIGLEC15* may play distinctive roles in

different human cancers, such as acting as an immunosuppressor in "hot tumor" non-small cell lung cancer, so anti-*SIGLEC15* therapy was suitable for such tumor. Meanwhile, in our study, we proved that increased *SIGLEC15* expression positively correlated with more extrathyroid extension and lymph node metastasis, indicating the vital role of *SIGLEC15* in the malignant progression of THCA; thus, THCA patients may benefit from the block antibodies for *SIGLEC15*.

Hu et al. (31) indicated that anti-*SIGLEC15* therapy could be feasible for bladder cancer treatment as *SIGLEC15* related to a non-inflamed TME in bladder cancer. Chen et al. (30) revealed that *SIGLEC15* was related to a low density of Regulatory T cells (Tregs) and CD45RO T cells, and Wang et al. (27) also showed that *SIGLEC15* suppressed antigen-specific T-cell responses. Liu et al. (67) demonstrated that *SIGLEC15* promoted the migration of hepatoma cells through regulating the *CD44* protein stability in liver cancer. Li et al. showed that *SIGLEC15* performed immunosuppressive functions by directly inducing immunosuppressive tumor-associated macrophages (TAMs) *via* binding to α-2,3 sialic acid. Liu et al. (32) clarified the importance of LINC00973-*miR-7109- SIGLEC15* regulation axis in immune evasion of clear-cell renal cell carcinoma. Our results showed that immunomodulators such as HLA class I and II and chemokines were upregulated in the higher *SIGLEC15* group, which were vital molecules that induced adaptive immune responses (68); our results also showed a significant positive correlation between *SIGLEC15* and *CD44*. In the cancer immunity cycle process, there existed seemingly contradictory results, step 1 (release of cancer cell antigens), step 6 (recognition of cancer cells by T cells), and step 4 (Th17 cell recruiting) were downregulated in the higher *SIGLEC15* group; nevertheless, the higher *SIGLEC15* group also met immune exhaustion and thus may induce an immune escape environment for patients and finally responded less to ICB therapy. In addition, patients who were in the higher *SIGLEC15* group had more *BRAF* V600E mutation, which was a poor prognosis factor in THCA. Previous studies evidenced that treatment with inhibitors that target the *BRAF* kinase combined with anti-*PD-1* therapy improved antitumor immunity in *BRAF*-mutant melanoma (69, 70). Clinical trial NCT02130466 showed that combined dabrafenib (a *BRAF* inhibitor) plus trametinib (a *MEK1* and *MEK2 (MEK1/2)* inhibitor) plus pembrolizumab (an anti-*PD-1* antibody) had more antitumor activity than dabrafenib plus trametinib plus placebo (71, 72). Our result also found some potent chemotherapy drugs for the high and low *SIGLEC15* groups, so this may provide a rationale for using immuno-oncology agent combinations for THCA patients. The mentioned above result also signified the complex TME in THCA.

DNA methylation and m6A methylation were two epigenetic mechanisms for the regulation of gene expression in eukaryotes and acted as vital regulators in cancer (73–75). We firstly fully described the negative correlation of DNA methylation and expression of *SIGLEC15* and prognosis in THCA in detail. Another pan-cancer also revealed the negative correlation in bladder cancer, uterine corpus endometrial carcinoma, breast invasive carcinoma, pancreatic ductal adenocarcinoma, etc. (61). We also firstly revealed the m6A methylation regulator relationship with *SIGLEC15*; regulating the expression of *SIGLEC15 via* methylation in cancer may be another road.

In addition to its function in immune regulation, Chen et al. (30) demonstrated that *SIGLEC15* mRNA expression had a positive correlation with high *BRCA1* status by IHC, and combining *SIGLEC15* with different DDR molecular statuses may be a potential prognosis predictor. Read et al. (76) revealed that elevated pituitary tumor transform gene (PTTG) and pituitary tumor transforming gene binding factor (PBF) modulate DNA damage response genes in thyroid cancer. We found that *SIGLEC15* was negatively related to *BRCA1* in the mRNA level but no correlation with *BRCA2*. We also found that high *SIGLEC15* had a negative correlation with DDR deficiency scores, such as aneuploidy score, CNA frac altered, and LOH frac altered, and these results implied that *SIGLEC15* may affect thyroid cancer progression through interacting with DDR genes.

There were some limitations in the current work. Firstly, more experiments need to be done to figure out the cellular mechanism of *SIGLEC15* in THCA. Secondly, there was no animal model experiment, so mouse models and either humanized or spontaneous but containing genomic features relevant to THCA animal models were needed to prove the results. Therefore, animal models, clinical verification data from multiple centers, and prospective studies were required to confirm our findings.

Conclusion

In conclusion, we found that *SIGLEC15* mRNA expression was upregulated in tumor tissue and validated that by TMA. Clinical feature integration supported that increased *SIGLEC15* mRNA expression promoted extrathyroid extension and lymph node metastasis, and elevated *SIGLEC15* group patients met immune exhaustion. Specifying the role of *SIGLEC15* in THCA could represent a potential next-generation cancer immunotherapy option for patients.

Data availability statement

The original contributions presented in the study are included in the article/Supplementary Material. Further inquiries can be directed to the corresponding authors.

Ethics statement

The studies involving human participants were reviewed and approved by Ethics Committee of Zhejiang Cancer Hospital. The patients/participants provided their written informed consent to participate in this study.

Author contributions

XFH, CC, XBL, and XDH have contributed equally to this work. XDH, XBL conceptualized and designed this study. CC, XFH Provision and collection of study materials, XFH, XBL, and XDH wrote the first draft of the manuscript. All authors contributed to the article and approved the submitted version.

Funding

This study was funded by the Medical and Health Research Program of Zhejiang Province 2022 Grant/Award Number: 2022PY005.

Conflict of interest

The authors declare that the research was conducted in the absence of any commercial or financial relationships that could be construed as a potential conflict of interest.

Publisher's note

Supplementary material

The Supplementary Material for this article can be found online at: https://www.frontiersin.org/articles/10.3389/fimmu.2022.975787/full#supplementary-material

SUPPLEMENTARY FIGURE 1
Analysis of expression of *SIGLEC15*. **(A)** pan-cancer mRNA expression of *SIGLEC15* between tumor and normal tissues from PCAWG database. **(B)** mRNA expression of *SIGLEC15* between paired tumor and normal tissues from THCA (Thyroid carcinoma). **(C)** Correlation between mRNA expression of *SIGLEC15* and *CD44*.

SUPPLEMENTARY FIGURE 2
(A-K) Differential enrichment scores of immune signatures between high and low *SIGLEC15* groups. **(L)** Enrichment scores of immune exhausted scores in low and high *SIGLEC15* groups.

SUPPLEMENTARY FIGURE 3
Single-cell analysis exploration of the expression cell type of *SIGLEC15*.

SUPPLEMENTARY FIGURE 4
Kaplan-Meier survival curves between *SIGLEC15* expression and survival.

SUPPLEMENTARY FIGURE 5
(A, B) Comparison of amplification and deletion of CNV in high and low *SIGLEC15* mRNA expression groups.

SUPPLEMENTARY TABLE 1
Correlation details in expression of *SIGLEC15* and *CD44*.

References

1. Lim H, Devesa SS, Sosa JA, Check D, Kitahara CM. Trends in Thyroid Cancer Incidence and Mortality in the United States, 1974–2013. *JAMA* (2017) 317 (13):1338–48. doi: 10.1001/jama.2017.2719

2. Ancker OV, Wehland M, Bauer J, Infanger M, Grimm D. Adverse Effect of Hypertension in the Treatment of Thyroid Cancer with Multi-Kinase Inhibitors. *Int J Mol Sci* (2017) 18(3):625. doi: 10.3390/ijms18030625

3. Siegel RL, Miller KD, Jemal A. Cancer statistics, 2015. *CA Cancer J Clin* (2015) 65(1):5–29. doi: 10.3322/caac.21254

4. Bray F, Ferlay J, Soerjomataram I, Siegel RL, Torre LA, Jemal A. Global cancer statistics 2018: GLOBOCAN estimates of incidence and mortality worldwide for 36 cancers in 185 countries. *CA Cancer J Clin* (2018) 68(6):394–424. doi: 10.3322/caac.21492

5. Mazzaferri EL, Kloos RT. Current approaches to primary therapy for papillary and follicular thyroid cancer. *J Clin Endocrinol Metab* (2001) 86 (4):1447–63. doi: 10.1210/jcem.86.4.7407

6. Cabanillas ME, McFadden DG, Durante C. Thyroid cancer. *Lancet* (2016) 388(10061):2783–95. doi: 10.1016/S0140-6736(16)30172-6

7. Fridman WH, Sautès-Fridman C, Galon J. The immune contexture in human tumours: Impact on clinical outcome. *Nat Rev Cancer* (2012) 12(4):298–306. doi: 10.1038/nrc3245

8. Giraldo NA, Sanchez-Salas R, Peske JD, Vano Y, Becht E, Petitprez F, et al. The clinical role of the tme in solid cancer. *Br J Cancer* (2019) 120(1):45–53. doi: 10.1038/s41416-018-0327-z

9. Maman S, Witz IP. A history of exploring cancer in context. *Nat Rev Cancer* (2018) 18(6):359–76. doi: 10.1038/s41568-018-0006-7

10. Klemm F, Joyce JA. Microenvironmental regulation of therapeutic response in cancer. *Trends Cell Biol* (2015) 25(4):198–213. doi: 10.1016/j.tcb.2014.11.006

11. Kubli SP, Berger T, Araujo DV, Siu LL, Mak TW. Beyond immune checkpoint blockade: Emerging immunological strategies. *Nat Rev Drug Discov* (2021) 20(12):899–919. doi: 10.1038/s41573-021-00155-y

12. Vaddepally RK, Kharel P, Pandey R, Garje R, Chandra AB. Review of Indications of FDA-Approved Immune Checkpoint Inhibitors per NCCN Guidelines with the Level of Evidence. *Cancers (Basel)* (2020) 12(3):738. doi: 10.3390/cancers12030738

13. Twomey JD, Zhang B. Cancer Immunotherapy Update: FDA-Approved Checkpoint Inhibitors and Companion Diagnostics. *AAPS J* (2021) 23(2):39. doi: 10.1208/s12248-021-00574-0

14. Hargadon KM, Johnson CE, Williams CJ. Immune checkpoint blockade therapy for cancer: An overview of FDA-approved immune checkpoint

inhibitors. *Int Immunopharmacol* (2018) 62:29–39. doi: 10.1016/j.intimp.2018.06.001

15. Rowshanravan B, Halliday N, Sansom DM. Ctla-4: A moving target in immunotherapy - sciencedirect. *Blood* (2018) 131(1):58–67. doi: 10.1182/blood-2017-06-741033

16. Wright JJ, Powers AC, Johnson D. Endocrine toxicities of immune checkpoint inhibitors. *Nat Rev Endocrinol* (2021) 17(7):389–99. doi: 10.1038/s41574-021-00484-3

17. Doroshow DB, Bhalla S, Beasley MB, Sholl LM, Kerr KM, Gnjatic S, et al. *Pd-L1* as a biomarker of response to immune-checkpoint inhibitors. *Nat Rev Clin Oncol* (2021) 18(6):345–62. doi: 10.1038/s41571-021-00473-5

18. Sharpe AH, Pauken KE. The diverse functions of the Pd1 inhibitory pathway. *Nat Rev Immunol* (2018) 18(3):153–67. doi: 10.1038/nri.2017.108

19. Jiang Y, Zhao X, Fu J, Wang H. Progress and challenges in precise treatment of tumors with *pd-1*/*Pd-L1* blockade. *Front Immunol* (2020) 11:339. doi: 10.3389/fimmu.2020.00339

20. Capdevila J, Wirth LJ, Ernst T, Aix SP, Taylor M. *Pd-1* blockade in anaplastic thyroid carcinoma. *J Clin Oncol* (2020) 38(23):2620–7. doi: 10.1200/JCO.19.02727

21. Ahn S, Kim TH, Kim SW, Ki CS, Jang HW, Kim JS, et al. Comprehensive screening for *pd-L1* expression in thyroid cancer. *Endocrine-related Cancer* (2017) 24(2):97. doi: 10.1530/ERC-16-0421

22. Angata T, Tabuchi Y, Nakamura K, Nakamura M. Siglec-15: An immune system siglec conserved throughout vertebrate evolution. *Glycobiology* (2007) 17(8):838–46. doi: 10.1093/glycob/cwm049

23. Shimizu T, Takahata M, Kameda Y, Endo T, Hamano H, Hiratsuka S, et alSialic acid-binding immunoglobulin-like lectin 15 (Siglec-15) mediates periarticular bone loss, but not joint destruction, in murine antigen-induced arthritis. *Bone* (2015) 79:65–70. doi: 10.1016/j.bone.2015.05.029

24. YK A, MT A, SM B, TS A, HH A, TA D, et al. Siglec-15 is a potential therapeutic target for postmenopausal osteoporosis. *Bone* (2015) 71:217–26. doi: 10.1016/j.bone.2014.10.027

25. Sato D, Takahata M, Ota M, Fukuda C, Tsuda E, Shimizu T, et al . Siglec-15-Targeting therapy increases bone mass in rats without impairing skeletal growth. *Bone* (2018) 116:172–80. doi: 10.1016/j.bone.2018.07.026

26. Jaeger M, Pinelli M, Borghi M, Constantini C, Dindo M, van Emst L, et al. A systems genomics approach identifies *SIGLEC15* as a susceptibility factor in recurrent vulvovaginal candidiasis. *Sci Transl Med* (2019) 11(496):eaar3558. doi: 10.1126/scitranslmed.aar3558

27. Wang J, Sun J, Liu LN, Flies DB, Nie X, Toki M, et al. Siglec-15 as an immune suppressor and potential target for normalization cancer immunotherapy. *Nat Med* (2019) 25(4):656–66. doi: 10.1038/s41591-019-0374-x

28. Du H, Tang J, Li X, Wang X, Wu L, Zhang R, et al. Siglec-15 is an immune suppressor and potential target for immunotherapy in the pre-metastatic lymph node of colorectal cancer. *Front Cell Dev Biol* (2021) 9:691937. doi: 10.3389/fcell.2021.691937

29. Li TJ, Jin KZ, Li H, Ye LY, Li PC, Jiang B, et al. *SIGLEC15* amplifies immunosuppressive properties of tumor-associated macrophages in pancreatic cancer. *Cancer Lett* (2022) 530:142–55. doi: 10.1016/j.canlet.2022.01.026

30. Chen X, Mo S, Zhang Y, Ma H, Lu Z, Yu S, et al. Analysis of a novel immune checkpoint, siglec-15, in pancreatic ductal adenocarcinoma. *J Pathol Clin Res* (2022) 8(3):268–78. doi: 10.1002/cjp2.260

31. Hu J, Yu A, Othmane B, Qiu D, Li H, Li C, et al. *SIGLEC15* shapes a non-inflamed tumor microenvironment and predicts the molecular subtype in bladder cancer. *Theranostics* (2021) 11(7):3089–108. doi: 10.7150/thno.53649

32. Liu Y, Li X, Zhang C, Zhang H, Huang Y. *Linc00973* is involved in cancer immune suppression through positive regulation of siglec-15 in clear-cell renal cell carcinoma. *Cancer Sci* (2020) 111(10):3693–704. doi: 10.1111/cas.14611

33. Shum E, Myint H, Shaik J, Zhou Q, Barbu E, Morawski A, et al. 490 clinical benefit through siglec-15 targeting with Nc318 antibody in subjects with siglec-15 positive advanced solid tumors. *Journal for ImmunoTherapy of Cancer* (2021) 9:A520–1. doi: 10.1136/jitc-2021-SITC2021.490

34. Goldman MJ, Craft B, Hastie M, Repečka K, McDade F, Kamath A, et al. Visualizing and interpreting cancer genomics data *Via* the xena platform. *Nat Biotechnol* (2020) 38(6):675–8. doi: 10.1038/s41587-020-0546-8

35. Izzi V, Davis MN, Naba A. A. Pan-Cancer Analysis of the Genomic Alterations and Mutations of the Matrisome. *Cancers (Basel)* 12(8):2046. doi: 10.3390/cancers12082046

36. Wang S, Xiong Y, Zhao L, Gu K, Li Y, Zhao F, et al. Ucscxenashiny: An R/Cran package for interactive analysis of ucsc xena data. *Bioinformatics* (2021) 2):2. doi: 10.1093/bioinformatics/btab561

37. Edgar R, Domrachev M, Lash AE. Gene expression omnibus: Ncbi gene expression and hybridization array data repository. *Nucleic Acids Res* (2002) 30(1):207–10. doi: 10.1093/nar/30.1.207

38. Ritchie ME, Phipson B, Wu D, Hu Y, Law CW, Shi W, et al. Limma powers differential expression analyses for rna-sequencing and microarray studies. *Nucleic Acids Res* (2015) 43(7):e47–e. doi: 10.1093/nar/gkv007

39. Grossman RL, Heath AP, Ferretti V, Varmus HE, Lowy DR, Kibbe WA, et al. Toward a shared vision for cancer genomic data. *N Engl J Med* (2016) 375(12):1109–12. doi: 10.1056/NEJMp1607591

40. Colaprico A, Silva TC, Olsen C, Garofano L, Cava C, Garolini D, et al. Tcgabiolinks: An R/Bioconductor package for integrative analysis of tcga data. *Nucleic Acids Res* (2015) 44(8):e71. doi: 10.1093/nar/gkv1507

41. Reich M, Liefeld T, Gould J, Lerner J, Tamayo P, Mesirov JP. Genepattern 2.0. *Nat Genet* (2006) 38(5):500–1. doi: 10.1038/ng0506-500

42. Knijnenburg TA, Wang L, Zimmermann MT, Chambwe N, Gao GF, Cherniack AD, et al. Genomic and molecular landscape of DNA damage repair deficiency across the cancer genome atlas. *Cell Rep* (2018) 23(1):239–54.e6. doi: 10.1016/j.celrep.2018.03.076

43. Sun D, Wang J, Han Y, Dong X, Ge J, Zheng R, et al. Tisch: A comprehensive web resource enabling interactive single-cell transcriptome visualization of tumor microenvironment. *Nucleic Acids Res* (2020) 49(D1):D1420–D30. doi: 10.1093/nar/gkaa1020

44. Zhang C, Fu J, Zhou Y. A review in research progress concerning M6a methylation and immunoregulation. *Front Immunol* (2019) 10:922. doi: 10.3389/fimmu.2019.00922

45. Subramanian A, Tamayo P, Mootha VK, Mukherjee S, Ebert BL, Gillette MA, et al. Gene set enrichment analysis: A knowledge-based approach for interpreting genome-wide expression profiles. *Proc Natl Acad Sci USA* (2005) 102(43):15545–50. doi: 10.1073/pnas.0506580102

46. Mootha VK, Lindgren CM, Eriksson KF, Subramanian A, Sihag S, Lehar J, et al. PGC-1α-Responsive genes involved in oxidative phosphorylation are coordinately downregulated in human diabetes. *Nat Genet* (2003) 34(3):267–73. doi: 10.1038/ng1180

47. Szklarczyk D, Gable AL, Lyon D, Junge A, Wyder S, Huerta-Cepas J, et al. String V11: Protein–protein association networks with increased coverage, supporting functional discovery in genome-wide experimental datasets. *Nucleic Acids Res* (2018) 47(D1):D607–13. doi: 10.1093/nar/gky1131

48. Shannon P. Cytoscape: A software environment for integrated models of biomolecular interaction networks. *Genome Res* (2003) 13(11):2498–504. doi: 10.1101/gr.1239303

49. Chin C-H, Chen S-H, Wu H-H, Ho C-W, Ko M-T, Lin C-Y. Cytohubba: Identifying hub objects and Sub-networks from complex interactome. *BMC Syst Biol* (2014) 8(4):S11. doi: 10.1186/1752-0509-8-S4-S11

50. Charoentong P, Finotello F, Angelova M, Mayer C, Efremova M, Rieder D, et al. Pan-cancer immunogenomic analyses reveal genotype-immunophenotype relationships and predictors of response to checkpoint blockade. *Cell Rep* (2017) 18(1):248–62. doi: 10.1016/j.celrep.2016.12.019

51. Huang X, Zhang G, Tang T, Liang T. Identification of tumor antigens and immune subtypes of pancreatic adenocarcinoma for mrna vaccine development. *Mol Cancer* (2021) 20(1):44. doi: 10.1186/s12943-021-01310-0

52. Xu L, Deng C, Pang B, Zhang X, Liu W, Liao G, et al. Tip: A web server for resolving tumor immunophenotype profiling. *Cancer Res* (2018) 78(23):6575–80. doi: 10.1158/0008-5472.Can-18-0689

53. Eddy JA, Thorsson V, Lamb AE, Gibbs DL, Heimann C, Yu JX, et al. Cri iatlas: An interactive portal for immuno-oncology research. *F1000Res* (2020) 9:1028. doi: 10.12688/f1000research.25141.1

54. Yoshihara K, Shahmoradgoli M, Martínez E, Vegesna R, Kim H, Torres-Garcia W, et al. Inferring tumour purity and stromal and immune cell admixture from expression data. *Nat Commun* (2013) 4:2612. doi: 10.1038/ncomms3612

55. Li T, Fan J, Wang B, Traugh N, Chen Q, Liu JS, et al. Timer: A web server for comprehensive analysis of tumor-infiltrating immune cells. *Cancer Res* (2017) 77(21):e108–10. doi: 10.1158/0008-5472.Can-17-0307

56. Hänzelmann S, Castelo R, Guinney J. GSVA: gene set variation analysis for microarray and RNA-seq data. *BMC Bioinformatics* (2013) 14:7–21. doi: 10.1186/1471-2105-14-7

57. Jiang P, Gu S, Deng P, Fu J, Sahu A, Hu X, et al. Signatures of T cell dysfunction and exclusion predict cancer immunotherapy response. *Nat Med* (2018) 24(10):1550–58. doi: 10.1038/s41591-018-0136-1

58. Luna A, Elloumi F, Varma S, Wang Y, Rajapakse VN, Aladjem MI, et al. CellMiner Cross-Database (CellMinerCDB) version 1.2: Exploration of patient-derived cancer cell line pharmacogenomics. *Nucleic Acids Res* (2021) 49(D1):D1083–93. doi: 10.1093/nar/gkaa968

59. O'Donnell J, Long GV, Scolyer RA, Teng MW, Smyth MJ. Resistance to Pd1/Pdl1 checkpoint inhibition. *Cancer Treat Rev* (2017) 52:71–81. doi: 10.1016/j.ctrv.2016.11.007

60. Li QT, Huang ZZ, Chen YB, Yao HY, Ke ZH, He XX, et al. Integrative analysis of siglec-15 mrna in human cancers based on data mining. *J Cancer* (2020) 11(9):2453–64. doi: 10.7150/jca.38747

61. Li B, Zhang B, Wang X, Zeng Z, Huang Z, Zhang L, et al. Expression signature, prognosis value, and immune characteristics of siglec-15 identified by pan-cancer analysis. *Oncoimmunology* (2020) 9(1):1807291. doi: 10.1080/2162402x.2020.1807291

62. Hao JQ, Nong JY, Zhao D, Li HY, Wang JH. The significance of siglec-15 expression in resectable non-small cell lung cancer. *Neoplasma* (2020) 67(6):1214–22. doi: 10.4149/neo_2020_200220N161

63. Liang H, Chen Q, Hu Z, Zhou L, Meng Q, Zhang T, et al. *SIGLEC15* facilitates the progression of non-small cell lung cancer and is correlated with spinal metastasis. *Ann Transl Med* (2022) 10(6):281. doi: 10.21037/atm-22-764

64. Quirino MWL, Pereira MC, Deodato de Souza MF, Pitta IDR, Da Silva Filho AF, Albuquerque MSS, et al. Immunopositivity for siglec-15 in gastric cancer and its association with clinical and pathological parameters. *Eur J Histochem* (2021) 65(1). doi: 10.4081/ejh.2021.3174

65. Li TJ, Jin KZ, Li H, Ye LY, Li PC, Jiang B, et al. *SIGLEC15* amplifies immunosuppressive properties of tumor-associated macrophages in pancreatic cancer. *Cancer Lett* (2022) 530:142–55. doi: 10.1016/j.canlet.2022.01.026

66. Shafi S, Aung TN, Robbins C, Zugazagoitia J, Vathiotis I, Gavrielatou N, et al. Development of an immunohistochemical assay for siglec-15. *Lab Invest* (2022) 102(7):771–8. doi: 10.1038/s41374-022-00785-9

67. Liu W, Ji Z, Wu B, Huang S, Chen Q, Chen X, et al. Siglec-15 promotes the migration of liver cancer cells by repressing lysosomal degradation of *Cd44*. *FEBS Lett* (2021) 595(17):2290–302. doi: 10.1002/1873-3468.14169

68. Wang C, Xiong C, Hsu Y-C, Wang X, Chen L. Human leukocyte antigen (Hla) and cancer immunotherapy: Hla-dependent and-independent adoptive immunotherapies. (2020) 5(14):14–26. doi: 10.21037/aob-20-27

69. Salmon H, Idoyaga J, Rahman A, Leboeuf M, Remark R, Jordan S, et al. Expansion and activation of Cd103(+) dendritic cell progenitors at the tumor site enhances tumor responses to therapeutic *pd-L1* and *braf* inhibition. *Immunity* (2016) 44(4):924–38. doi: 10.1016/j.immuni.2016.03.012

70. Cooper ZA, Frederick DT, Ahmed Z, Wargo JA. Combining checkpoint inhibitors and *braf*-targeted agents against metastatic melanoma. *Oncoimmunology* (2013) 2(5):e24320. doi: 10.4161/onci.24320

71. Ascierto P, Ferrucci P, Stephens R, Del Vecchio M, Atkinson V, Schmidt H, et al. Keynote-022 part 3: Phase ii randomized study of 1l dabrafenib (D) and trametinib (T) plus pembrolizumab (Pembro) or placebo (Pbo) for *braf*-mutant advanced melanoma. *Ann Oncol* (2018) 29:viii442. doi: 10.1093/annonc/mdy289

72. Ascierto PA, Ferrucci PF, Fisher R, Del Vecchio M, Atkinson V, Schmidt H, et al. Dabrafenib, trametinib and pembrolizumab or placebo in *braf*-mutant melanoma. *Nat Med* (2019) 25(6):941–6. doi: 10.1038/s41591-019-0448-9

73. Fu Y, Dominissini D, Rechavi G, He C. Gene expression regulation mediated through reversible M6a rna methylation. *Nat Rev Genet* (2014) 15(5):293–306. doi: 10.1038/nrg3724

74. Bradner JE, Hnisz D, Young RA. Transcriptional addiction in cancer. *Cell* (2017) 168(4):629–43. doi: 10.1016/j.cell.2016.12.013

75. Chen XY, Zhang J, Zhu JS. The role of M(6)a rna methylation in human cancer. *Mol Cancer* (2019) 18(1):103. doi: 10.1186/s12943-019-1033-z

76. Read ML, Fong JC, Modasia B, Fletcher A, Imruetaicharoenchoke W, Thompson RJ, et al. Elevated *PTTG* and *PBF* predicts poor patient outcome and modulates DNA damage response genes in thyroid cancer. *Oncogene* (2017) 36(37):5296–308. doi: 10.1038/onc.2017.154

frontiers | Frontiers in Immunology

TYPE Systematic Review
PUBLISHED 21 September 2022
DOI 10.3389/fimmu.2022.977016

OPEN ACCESS

EDITED BY
Faris Alenzi,
Prince Sattam Bin Abdulaziz University, Saudi Arabia

REVIEWED BY
Stephen Blake,
South Australian Health and Medical Research Institute (SAHMRI), Australia
Fan Yun,
Zhejiang Cancer Hospital, China

*CORRESPONDENCE
Yongdong Jin
cccjin@163.com

†These authors have contributed equally to this work

SPECIALTY SECTION
This article was submitted to Cancer Immunity and Immunotherapy, a section of the journal Frontiers in Immunology

RECEIVED 24 June 2022
ACCEPTED 26 August 2022
PUBLISHED 21 September 2022

CITATION
Li S, Li L, Pan T, Li X, Tong Y and Jin Y (2022) Prognostic value of TIGIT in East Asian patients with solid cancers: A systematic review, meta-analysis and pancancer analysis.
Front. Immunol. 13:977016.
doi: 10.3389/fimmu.2022.977016

Prognostic value of TIGIT in East Asian patients with solid cancers: A systematic review, meta-analysis and pancancer analysis

Sicong Li[1†], Lanxing Li[2†], Tianyan Pan[2], Xiaoqun Li[3], Yujia Tong[4] and Yongdong Jin[5*]

[1]School of Pharmacy, Peking University Health Science Centre, Beijing, China, [2]School of Medicine, University of Electronic Science and Technology of China, Chengdu, China, [3]Center of Disease Prevention Treatment, The Third Affiliated Hospital of Beijing University of Chinese Medicine, Beijing, China, [4]Institute of Medical Information, Chinese Academy of Medical Sciences/Peking Union Medical College, Beijing, China, [5]Department of Medical Oncology, Sichuan Cancer Hospital and Institute, Sichuan Cancer Center, School of Medicine, University of Electronic Science and Technology of China, Chengdu, China

Background: T-cell immunoreceptor with Ig and ITIM domains (TIGIT) participates in tumor immune escape by delivering inhibitory signals to T cells. The purpose of this article was to assess the prognostic value of TIGIT and its immunological function in solid cancers.

Methods: Three databases were searched for relevant articles. The main endpoints were overall survival (OS), progression-free survival (PFS), recurrence-free survival (RFS), and disease-free survival (DFS). Hazard ratios (HR) were pooled by using fixed-effects or random-effects models. Pancancer analysis of TIGIT was performed based on public online databases, mainly The Cancer Genome Atlas (TCGA), Genotype-Tissue Expression (GTEx), and UCSC Xena. The possible relationships between TIGIT expression and the tumor microenvironment (TME), infiltration of immune cells, immune-related genes, tumor mutation burden (TMB), and microsatellite instability (MSI) were revealed in this article.

Results: Sixteen studies met the inclusion criteria. High expression of TIGIT was associated with worse OS [HR= 1.73, 95% confidence interval (CI) 1.50, 1.99], PFS (HR = 1.53, 95% CI [1.25, 1.88]), RFS (HR = 2.40, 95% CI [1.97, 2.93]), and DFS (HR= 6.57, 95% CI [0.73, 59.16]) in East Asian patients with solid cancers. TIGIT expression was positively correlated with immune infiltration scores and infiltration of CD8 T lymphocytes in all of the cancers included. TIGIT was found to be coexpressed with the genes encoding immunostimulators, immunoinhibitors, chemokines, chemokine receptors, and major histocompatibility complex (MHC), especially in gastroesophageal cancer. TMB and MSI were also associated with TIGIT upregulation in diverse kinds of cancers.

Conclusion: High expression of TIGIT is associated with poorer prognosis in East Asian patients with solid cancers. TIGIT is a novel prognostic biomarker and immunotherapeutic target for various solid cancers because of its activity in cancer immunity and tumorigenesis.

KEYWORDS

TIGIT, solid cancer, prognosis, meta-analysis, systematic review

1 Introduction

In the tumor microenvironment (TME), T cells are the second most abundant cell type after tumor-associated macrophages (TAMs) (1–3). Several immune inhibitor receptors (IRs), such as TIGIT, are upregulated in solid cancers and take part in tumor immune escape (4–6). As an important T-cell receptor in the TME, TIGIT competes with the costimulatory receptor cluster of differentiation 226 (CD226) for its interaction with the cluster of differentiation 155 (CD155) (7, 8) and participates in inhibiting adaptive and innate immunity. Highly expressed on active Regulatory T cells(Tregs), memory cluster of differentiation8(CD8) and memory cluster of differentiation (CD4) T-cell (9, 10), TIGIT can inhibit the cytotoxicity mediated by natural killer (NK) cells (1), the maturation and proinflammatory response of dendritic cells (DCs) (11), the effector functions of T helper cell 17(Th17) and T helper cell 1(Th1) cells (12), and enhance the immunosuppressive functions of Tregs by promoting the production of interleukin-10(IL-10) and fibrinogen-like protein 2 (Fgl2) (13).

The prognostic value of TIGIT has become a research hotspot in recent years, but the results remain controversial. Therefore, we conducted a meta- and bioinformatic analysis in this article for the following purposes: ①to evaluate the prognostic value of TIGIT in OS, DFS, PFS, and RFS and ② to determine the relationship between TIGIT expression and the tumor microenvironment and immune microenvironment.

2 Methods

2.1 Meta-analysis

2.1.1 Data sources and search strategy

This systematic review and meta-analysis were performed according to the Preferred Reporting Items for Systematic Reviews and Meta-Analysis (PRISMA) guidelines (14). Embase (https://www.embase.com/), PubMed (https://pubmed.ncbi.nlm.nih.gov/), and the Cochrane Library (https://www.cochranelibrary.com/) were searched for articles. The retrieval time was from inception to May 28, 2022. This review was registered on the PROSPERO platform (CRD42022324498). The search strategy is described in Supplementary Materials Tables 1–3.

2.1.2 Inclusion and exclusion criteria

Inclusion criteria included ① East Asian patients diagnosed with solid cancer before enrollment, ② randomized controlled trials (RCTs) or observational studies, ③ sufficient data about TIGIT expression and clinical outcome for meta-analysis, and ④ TIGIT expression was determined by using immunohistochemistry.

The exclusion criteria included ① case reports, single-cell sequencing data, animal experiments, meta-analyses, network meta-analyses, conference presentations, or study protocols.

2.1.3 Outcomes

Outcomes included ①overall survival (OS), ② progression-free survival (PFS), ③ recurrence-free survival (RFS), and ④ disease-free survival (DFS).

2.1.4 Study selection and data extraction

Two review authors (Sicong Li and Lanxing Li) independently reviewed the titles and abstracts of trials with potential eligibility. After that, we downloaded the full texts of trials eligible for inclusion. Two authors (Xiaoqun Li and Tianyan Pan) independently extracted the following data: ① basic information, including first author, publication year, sample size, country, and study design; ② characteristics of patients, including sex, age, type, and stage of cancer; ③ details about TIGIT, including expression location and cutoff value to judge high expression; ④ details about clinical outcomes; ⑤ information of cancer treatment; ⑥ information of quality assessment. Any disagreement was resolved by group discussion and consensus. We excluded results reported in

only one study. In the studies that did not report HR values, we obtained the required data related to survival analysis from the survival curve by using GetData Graph Digitizer software.

2.1.5 Strategy for meta-analysis

This meta-analysis was performed by using R (version 4.0.3). The chi-square test and χ^2 value were used to measure statistical heterogeneity. I2<50% and P value>0.05 indicated no substantial heterogeneity, and a fixed-effects model was used to pool the value of HR and 95% confidence interval. Otherwise, the random-effects model was used because of significant heterogeneity. Subgroup analysis was conducted to analyze sources of heterogeneity, while sensitivity analysis was conducted by excluding one study each time. Begg's and Egger's tests were used to assess publication bias. Statistical significance was set as α=0.05 in this study.

2.1.6 Quality assessment

Two reviewers (Yongdong Jin, Yujia Tong) assessed the quality of eligible studies independently by using the Newcastle–Ottawa Quality Assessment Scale (NOS) (15). The NOS assessed the quality of studies from the aspects of selection, comparability, and exposure, with a total score ranging from 0 to 9 points. More than 6 points was defined as high-quality.

2.2 Pan-cancer analysis

2.2.1 Data extraction and preprocessing

We downloaded the standardized pancancer data set from the UCSC (https://xenabrowser.net/) database: TCGA TARGET GTEx (PANCAN, N=19131, G=60499). Then, we extracted the expression data of the ENSG00000181847 (TIGIT) gene and 150 immune-related genes, including chemokines (n = 41), receptors (n = 18), major histocompatibility complexes (n = 21), immunoinhibitors (n = 24) and immunostimulators (n = 46), in normal solid tissues, primary solid tumors, normal tissues, primary blood-derived cancer-bone marrow, and peripheral blood. After excluding the cancer species with less than 3 samples in a single cancer species, the expression data of cancer species mentioned in the meta-analysis were finally obtained, including bladder urothelial carcinoma (BLCA), colon adenocarcinoma (COAD), colon adenocarcinoma/Rectum adenocarcinoma esophageal carcinoma (COADREAD), esophageal carcinoma (ESCA), liver hepatocellular carcinoma (LIHC), lung adenocarcinoma(LUAD), lung squamous cell carcinoma (LUSC), rectum adenocarcinoma (READ), stomach adenocarcinoma (STAD), skin cutaneous melanoma (SKCM), stomach and esophageal carcinoma(STES), thyroid carcinoma (THCA). We also extracted the gene expression profile of each tumor and converted the Tag names into gene symbols.

2.2.2 Differential expression of TIGIT among tumor and normal samples

We used the unpaired Wilcoxon-rank sum and signed-rank tests to compare the difference in TIGIT expression between normal samples and tumor samples in each tumor. A violin plot was used to visualize the results.

2.2.3 Differential expression of TIGIT among simple nucleotide variation (SNV) and copy number variation (CNV) data

From the GDC (https://portal.gdc.cancer.gov/) database, we downloaded the simple nucleoside variation (SNV) data set (level 4) and the copy number variation (CNV) data set (level 4) of all TCGA samples processed by MuTect2 (16) and GISTIC software (17), respectively. After removing samples of synonymous mutations, we obtained the expression data of 9 and 6 cancer species for CNV and SNV, respectively. Moreover, the domain information of TIGIT was obtained from the maftools package (version 2.2.10) of R software. A lollipop plot was used to depict the protein mutational distribution and domains.

2.2.4 Relevance between TIGIT expression and the tumor microenvironment

We used the ESTIMATE package (version 1.0.13, https://bioinformatics.mdanderson.org/public software/estimate/) (18) to calculate the stromal, immune, and estimate scores for the cancers included in this article. The increased stromal and immune scores indicated an increased proportion of immune cells or stromal cells in the TME. Furthermore, the corr.test function of the psych package in R software (version 2.1.6) was used to conduct Pearson's correlation test.

2.2.5 Correlation between TIGIT expression and immune cell infiltration

We used the deconvo_CIBERSOR (19) and TIMER methods (20) in IOBR (version 0.99.9) (21) of R software to calculate the infiltration score of the 22 tumor-infiltrating immune cells, including naive B cells, memory B cells, plasma cells, CD8 T cells, naive CD4 T cells, resting and activated memory T cells, follicular helper T cells (Tfhs), regulatory T cells (Tregs), gamma delta T cells, resting and activated NK cells, monocytes, resting M0, M1 and M2 macrophages, resting and activated dendritic cells (DCs), resting and activated mast cells, eosinophils, and neutrophils. The results are displayed in the form of heatmap plots.

2.2.6 Associations of TIGIT expression with immune-related genes, tumor mutation burden (TMB) level and microsatellite instability (MSI) status

First, we calculated the Spearman correlation between TIGIT and the 150 immunomodulators. The results were

visualized in heatmap plots. Then, we used the TMB function of the maftools package (version 2.8.05) in R software to calculate the TMB score for each tumor and obtained the MSI score of each tumor from a previous study reported by Russell Bonneville (22). We integrated the MSI and gene expression data of the samples and further performed log2 (x+0.001) transformation on each expression value. The correlation between TIGIT expression and TMB or MSI was analyzed by means of the Spearman correlation coefficient, and the results are displayed in the form of lollipop plots (23).

2.2.7 Protein–protein interaction network construction

GeneMANIA (http://www.genemania.org) was used to build a protein–protein interaction (PPI) network. Physical interaction, coexpression, and gene enrichment analyses were performed by using the network integration algorithm. The results were visualized by using the bioinformatic website (http://www.bioinformatics.com.cn/).

2.2.8 Construction of competing endogenous RNA (ceRNA) networks

First, we used miRwalk (http://mirwalk.umm.uni-heidelberg.de/ accessed on 30 May 2022) to predict target miRNAs of TIGIT that can bind to the TIGIT 3′-UTR. Next, miRNA–lncRNA interactions were obtained from RNAInter v4.0 (http://www.rnainter.org/search/) with the species set as Homo sapiens. Finally, the ceRNA network was visualized by using Cytoscape 3.8.2 (24) software.

2.2.9 Statistical analysis

Statistical data analysis was conducted by using R software (version 4.0.3) (https://www.r-project.org/). The unpaired Wilcoxon-rank sum and signed-rank tests were used to analyze the significance of the difference between two groups, and the Kruskal test was used to test the difference among multiple groups of samples. The correlation between TIGIT expression and the other variable was assessed utilizing the Spearman correlation coefficient. P values of less than 0.05, 0.01 and 0.001 are presented as "*", "**", and "***", respectively.

3 Results

3.1 Results of the meta-analysis

3.1.1 Search results

In total, 16 studies involving 2488 patients with solid cancers were found to meet the inclusion criteria. All of them were retrospective cohort studies. Although Pooja Ghatalia (25) and Pankaj Ahluwalia (26) reported the prognostic value of TIGIT in cancer patients, they did not report the hazard ratio or odds ratio value of TIGIT. Therefore, the patients included were from the East Asian population. The flow chart of the study selection process is presented in Figure 1.

3.1.2 Study characteristics

The basic characteristics of the included studies are shown in Table 1. Studies were published between 2018 and 2022. Zhao JJ (27), Peipei Wang (28) and Zhao K (29) reported survival outcomes of esophageal squamous cell carcinoma (ESCC) or primary small cell carcinoma of esophagus (PSCCE), Tang W (30) and Liu HF (31) reported gastric cancer (GC), Xu Y (32) reported small cell lung cancer (SCLC), Sun Y (33) and Jiang C (34) reported non-small cell

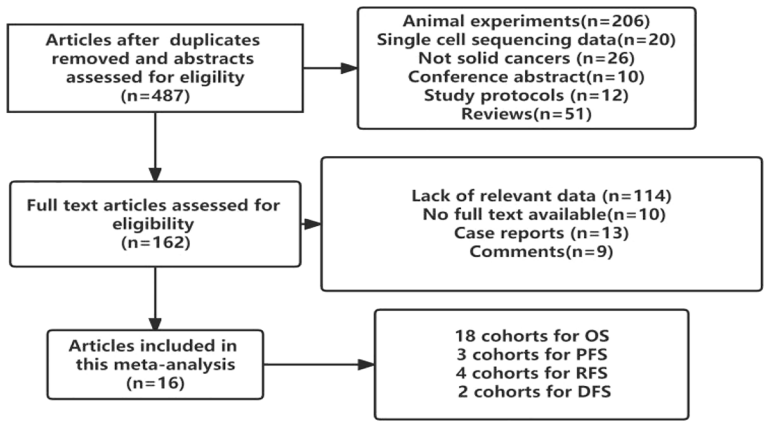

FIGURE 1
Study selection flowchart.

10.3389/fimmu.2022.977016

TABLE 1 Basic characteristics.

Author	Sample size	Country	Age	male/ female	Cancer	Treatment other than surgery	TIGIT+ expression	Expression location	Cutoff value of TIGIT	Outcome	Method to estimate HR
Zhao JJ (2018)	154	China	55 (37–48)	(124/30)	ESCC	Not available	76 (49.4%)	TIL	Median level	OS	Multivariate
Tang W (2019)	441	China	(<62:159, ≥62:282)	(245/196)	GC	Adjuvant chemotherapy	343 (77.8%)	Tumor cell	≥5% positivity cell	OS	Multivariate
Xu Y (2019)	60	China	(≤60:34, >60:26)	(43/17)	SCLC	Adjuvant chemotherapy	21 (35%)	Tumor cell	Median level	OS	Univariate
Lee WJ (2020)	124	Korea	61.8(25-89)	(68/56)	Melanoma	Not available	52 (41.9%)	Tumor cell	≥20% positivity cell	OS/PFS	Univariate
Sun Y (2020)	334	China	56(28-81)	(182/152)	NSCLC	Not available	204 (61.1%)	TIL	≥5% positivity cell	OS/PFS	Multivariate
Zhao K (2020)	114	China	≤60 76, >60 38	(84/30)	PSCCE	Adjuvant chemotherapy/ chemoradiotherapy.	74 (64.9%)	Tumor cell	≥5% positivity cell	OS/PFS	Multivariate
Zhou X (2020)	60	China	≤60 34, >60 26	(35/25)	CRC	Not available	21 (35%)	Tumor cell	CPS≥1	OS/DFS	Multivariate
Liang R (2021)	139	China	≤45:25, >45 114	(82/57)	CRC	Not available	40 (28.8%)	Tumor cell	Median level	OS/RFS	Univariate
Liu HF (2022)	194	China	56 ± 12.66	(135/59)	GC	Adjuvant chemotherapy	97(50%)	TIL	Median level	OS	Multivariate
Peipei Wang (2021)	95	China	58 ± 10	(81/14)	ESCC	Not available	68(72%)	Tumor cell	Median level	OS	Multivariate
Daisuke Murakami (2022)	100	Japan	> 70 53 (53%); < 70 years 47 (47%)	(55/45)	CRC	Not available	79(79%)	TIL	≥10% positivity cell	OS	Multivariate
Jiang C (2022)	81	China	63(29–81)	(68/13)	NSCLC	Not available	33 (40.7%)	TIL	CPS≥1	OS	Multivariate
Yu LH (2021)	133	China	58.3 ± 11.4	(103/30)	HBV-HCC	Adjuvant immunotherapy ± adjuvant chemotherapy	65(48.87%)	TIL	Median level	PFS	Multivariate
Shi X (2021)	200	China	49 (12–80)	(105/95)	MTC	Not available	6 (3.0%)	Tumor cell	CPS≥1	OS/RFS	Univariate
Liu ZP (2020)	141	China	ZSHC cohort 62 (56-71); FUSCC cohort 62 (56-68)	ZSHC cohort (117/24); FUSCC cohort (102/16)	MIBC	Adjuvant chemotherapy	ZSHC cohort46 (32.62%); FUSCC cohort 68 (57.63%)	TIL	Median level	OS/RFS	Multivariate
Luo Y (2022)	234	China	55.50 (41.25, 66.50)	112 (47.86%)	TC	Not available	37(15.81%)	Tumor cell and TIL	CPS≥1	OS/DFS	Multivariate

lung cancer (NSCLC), Zhou X (35), Liang R (36) and Daisuke Murakami (37) reported colorectal cancer (CRC), Lee WJ (38) reported melanoma, Yu LH (39) reported hepatitis B virus hepatocellular carcinoma (HBV-HCC), and Liu ZP et al. reported the ZSHS cohort and the FUSCC cohort that reported survival outcomes of patients with muscle-invasive bladder cancer (MIBC) (40). Luo Y [reported] (41) 3 cohorts of patients with advanced thyroid carcinoma (ATC), including anaplastic thyroid carcinoma (ATC), poorly differentiated thyroid carcinoma (PDTC), and locally advanced papillary thyroid carcinoma (PTC). HR values in the studies reported by Xu Y (2019), Liang R (2021), Lee WJ (2020), Sun Y (2020),

A Overall survival

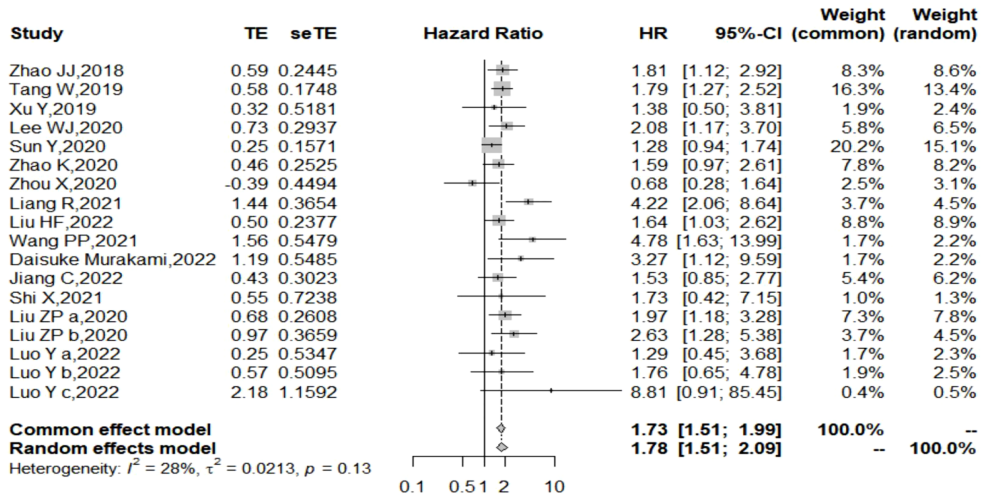

B Progression free survival

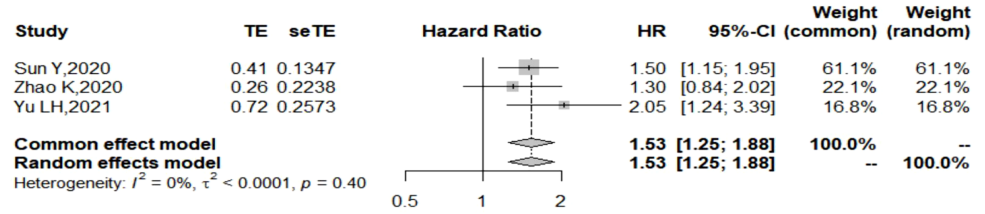

C Recurrence free survival

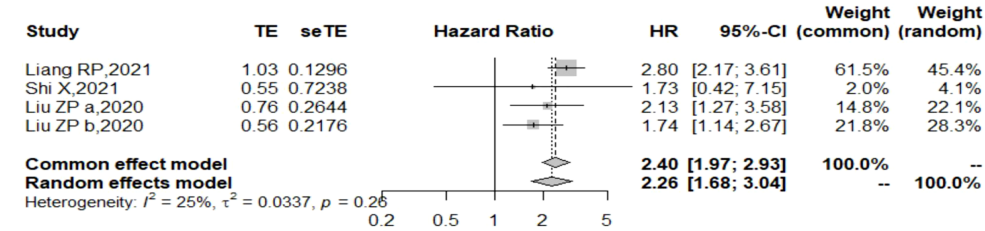

D Disease free survival

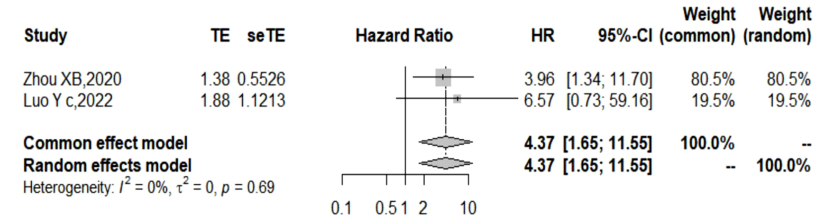

FIGURE 2
Forest plot for all outcomes. (**A**. Overall survival **B**. Progression free survival **C**. Recurrence free survival **D**. Disease free survival).

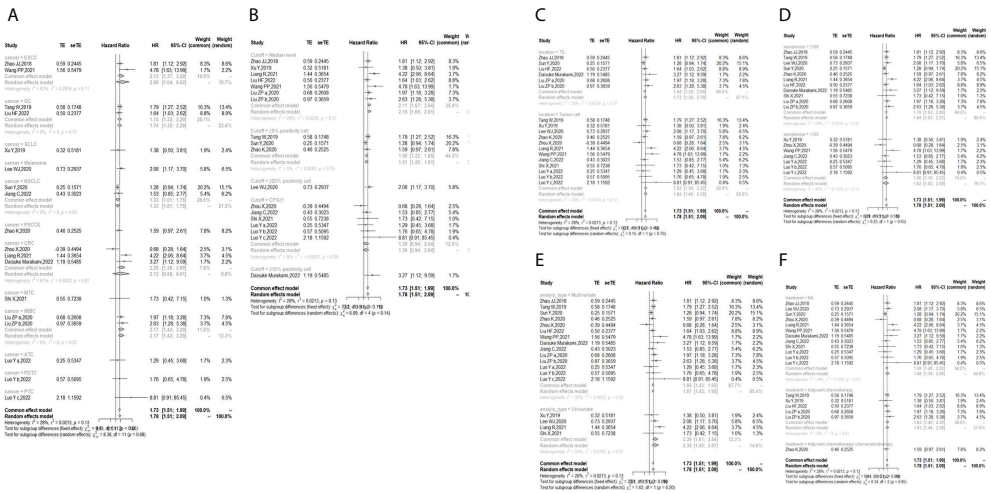

FIGURE 3
Subgroup analysis for the relationship between TIGIT and overall survival **(A)** Grouped by different cancers **(B)** Grouped by different cutoff values of TIGIT expression **(C)** Grouped by location of TIGIT expression **(D)** Grouped by sample size **(E)** Grouped by different methods to estimate HR **(F)** Grouped by different postoperative treatments).

and Zhao K (2020) were obtained by calculating the data extracted from the survival curve.

The HR values in the studies reported by Xu Y (2019), Liang R (2021), Lee WJ (2020), and Shi X (2021) were estimated by only univariate analysis, while the others were estimated by both multivariate analyses. Regarding the quality of the included studies, NOS scores ranged from 6 to 8.

3.1.3 Results of OS, PFS, RFS, and DFS

The I (2) value was less than 50%, and the p value was above 0.05, so the fixed-effect model was used in the comparison of OS, PFS, RFS, and DFS. The pooled results of the meta-analysis showed that high expression of TIGIT was associated with shorter OS (HR = 1.73, 95% CI [1.50, 1.99]), PFS (HR =1.53, 95% CI[1.25,1.88]), RFS (HR = 2.40, 95% CI [1.97, 2.93] and

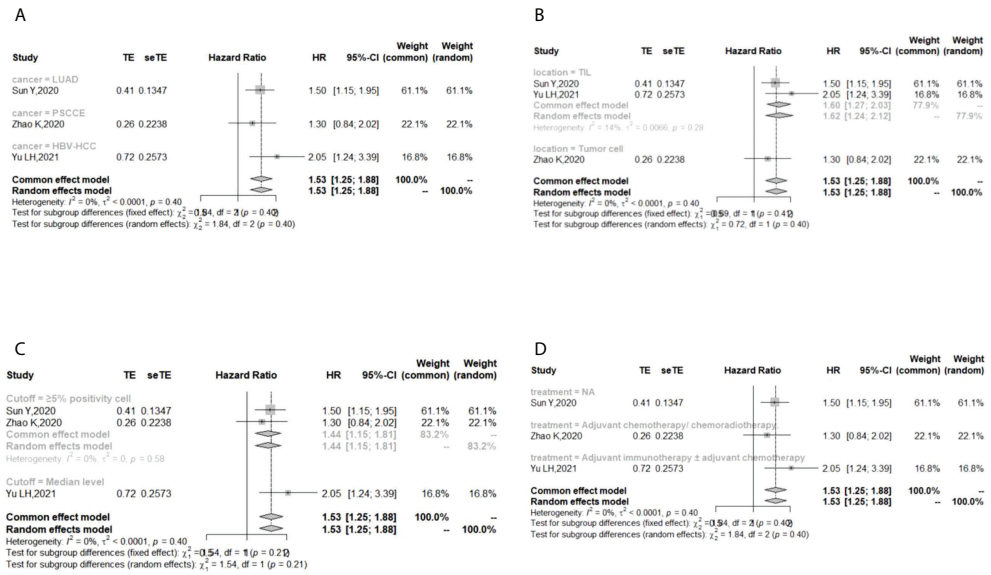

FIGURE 4
Subgroup analysis for the relationship between TIGIT and progression-free survival **(A)** Grouped by different cancers **(B)** Grouped by location of TIGIT expression **(C)** Grouped by different cutoff values of TIGIT expression **(D)** Grouped by different postoperative treatments).

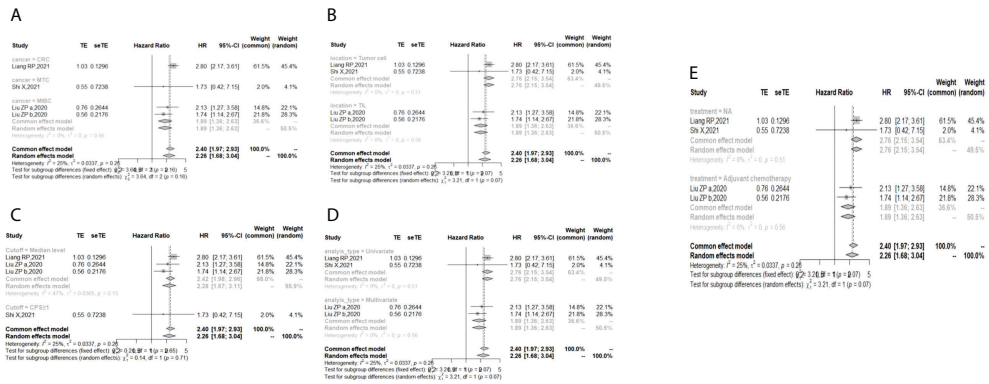

FIGURE 5
Subgroup analysis for the relationship between TIGIT and recurrence-free survival **(A)** Grouped by different cancers **(B)** Grouped by location of TIGIT expression **(C)** Grouped by different cutoff values of TIGIT expression **(D)** Grouped method to estimate HR **(E)** Grouped by different postoperative treatments).

DFS (HR = 4.37, 95% CI [1.65, 11.55]) in patients with solid cancers than low expression of TIGIT (see Figure 2).

In the 2 studies about DFS, TIGIT was expressed on tumor cells, and CPS≥1 was set as the cutoff value of TIGIT expression. Moreover, multivariate analysis was used to estimate the HR value in the comparison of DFS and PFS, so we did not conduct subgroup analysis in these aspects. No significant prognostic value of TIGIT was found in the OS of cancers, including SCLC, CRC, MTC, ATC, PDTC and PTC. Studies with sample sizes <100 did not support the prognostic value of TIGIT and OS (HR = 1.55, 95% CI [0.76, 3.19]). PSCCE and TIGIT expressed on tumor cells did not support the prognostic value of TIGIT in PFS, while medullary thyroid carcinoma and papillary thyroid carcinoma did not support the prognostic value of TIGIT in RFS and DFS, respectively. Postoperative treatments were not found to be a source of heterogeneity in OS and RFS, probably because nearly half of the studies did not describe them. In terms of PFS, adjuvant chemotherapy/chemoradiotherapy did not support the prognostic value of TIGIT, and this result should be discussed with care because of limited study numbers and sample sizes (see Figures 3–6).

The p values of Begg's test and Egger's test for OS and RFS were above 0.05, which indicated no significant publication bias. In the sensitivity analysis, the DFS results would change if Zhou XB (2020) was omitted. (Liang R, 2021), (Yu LH,2021), (Liu ZP, 2020), and (Luo YC,2022) contributed the most to the overall heterogeneity in OS, PFS, RFS, and DFS, respectively.

3.2 Pancancer analysis

The design flow and implementation approaches of this study are illustrated in Figure 7. This study integrally revealed the role of TIGIT in the tumor immune microenvironment.

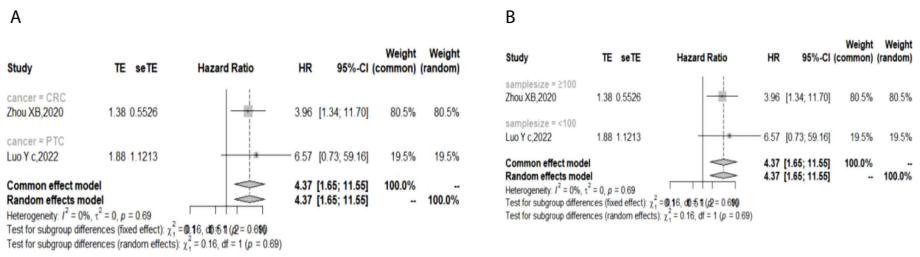

FIGURE 6
Subgroup analysis for the relationship between TIGIT and disease-free survival **(A)** Grouped by different cancers **(B)** Grouped by different sample sizes).

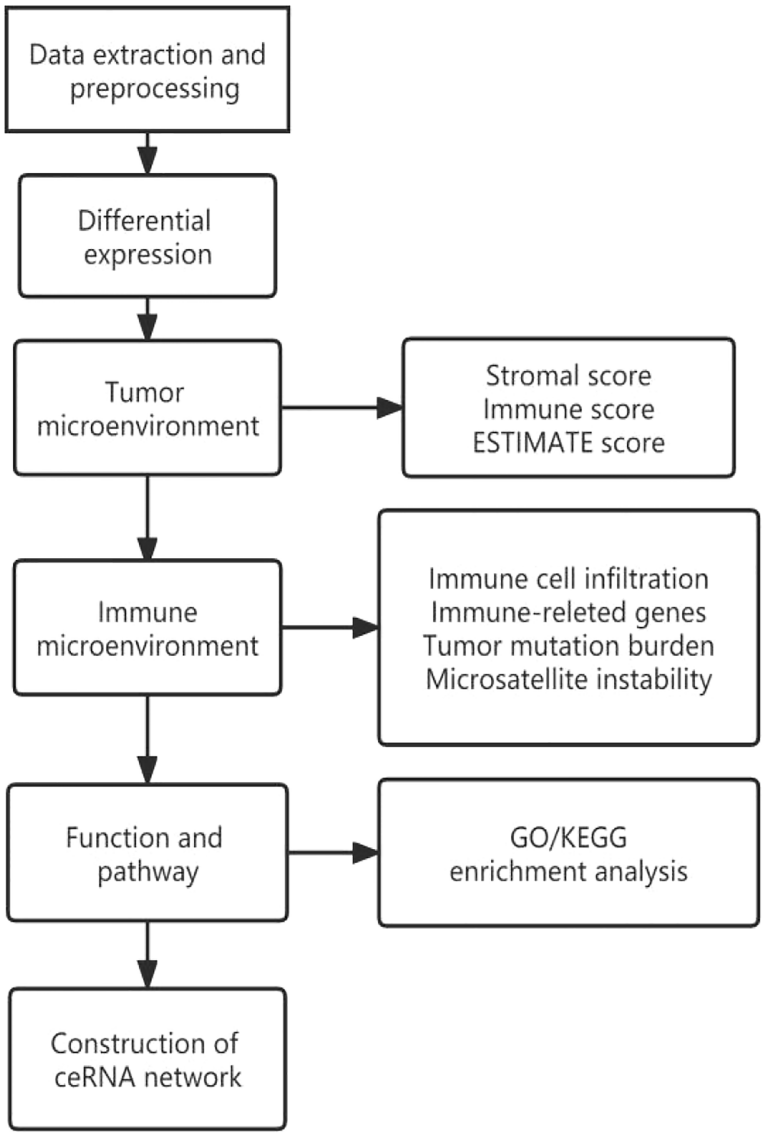

FIGURE 7
Flow chart of pancancer analysis.

3.2.1 Differential expression of TIGIT among cancer and normal samples

The expression of TIGIT was significantly upregulated in the 9 cancers involved in this study, including LUAD (tumor:1.44 ± 1.33, normal:0.49 ± 0.99, $P=2.6e^{-32}<0.05$), ESCA (tumor: 0.29 ± 1.59, normal:-2.58 ± 1.72,$P=2.5e^{-57}<0.05$), STES (tumor: 0.71 ± 1.57, normal: -2.35 ± 1.73, $P=1.3e^{-151}<0.05$), COAD (tumor:0.01 ± 1.62,normal:-1.81 ± 2.07, $P=1.4e^{-26}<0.05$), COADREAD (tumor:-0.03 ± 1.60,normal:-1.75 ± 2.08,$P=1.9e^{-27}<0.05$), STAD (tumor:0.89 ± 1.53,normal:-1.66± 1.58,$P=7.8e^{-54}<0.05$),LUSC (tumor:1.25 ± 1.36,normal:0.49 ± 0.99,$P=1.8e^{-22}<0.05$), LIHC (tumor:-1.18 ± 1.86,normal:-1.71 ± 1.23,$P=3.4e^{-3}<0.05$), SKCM (tumor:-0.10 ± 2.07,normal:-2.40 ± 1.31,$P=1.6e^{-26}<0.05$), THCA (tumor:-0.51 ± 2.01,normal:-0.89 ± 1.92,$P=1.6e^{-4}<0.05$). However, no significant difference was observed between cancer and normal samples in BLCA ($P=0.09>0.05$) and READ ($P=0.11>0.05$) (Figure 8). The TIGIT expression values in different cancers are shown in Supplementary Table 5.

3.2.2 Impact of CNV and SNV on TIGIT expression

TIGIT expression was higher in CNV neutrals than in CNV gains in STAD and LUSC. Moreover, TIGIT expression was

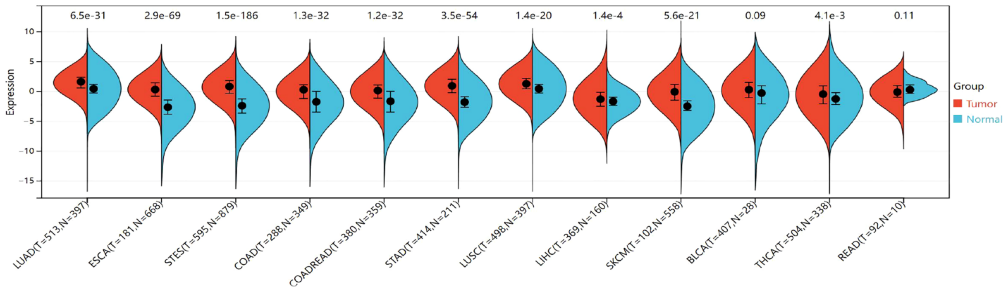

FIGURE 8
Differential TIGIT mRNA expression in 12 kinds of cancers and normal tissues by using the combination of box diagram and violin diagram. P values were presented by using scientific notation. LUAD, lung adenocarcinoma; ESCA, esophageal carcinoma; STES, Stomach and Esophageal carcinoma; COAD, colon adenocarcinoma; COADREAD, colon adenocarcinoma/Rectum adenocarcinoma esophageal carcinoma; STAD stomach adenocarcinoma; LUSC, Lung squamous cell carcinoma; LIHC, liver hepatocellular carcinoma; SKCM, skin cutaneous melanoma; THCA, hyroid carcinoma; READ, rectum adenocarcinoma.

higher in CNV neutral samples than in samples with CNV losses in LIHC and SKCM. This result indicated that CNV influenced TIGIT expression. No significant difference was found in TIGIT expression among patients with wild type and TIGIT mutation in terms of SNV.

Missense mutation was the most common type of mutation in the cancers included. Missense mutations in V-seIg were found in STES, COAD, COADREAD, LUAD, STAD, SKCM and READ. Among them, LUAD was found to have the most missense mutations. In-frame deletion occurred in COAD and COADREAD. A splice site was found in STAD and STES (see Figure 9). READ presented a relatively high mutation frequency (2.2%). TIGIT expression values in patients with wild-type, SNV or CNV are presented in Supplementary Tables 6, 7.

3.2.3 Correlation between TIGIT expression and the tumor microenvironment

Stromal and immune cells are two main types of nontumor components in the TME. The ESTIMATE algorithm can help to predict the tumor purity in tumor samples. We calculated the Spearman correlation coefficient between TIGIT expression and immune infiltration scores by using corr.test psych (version 2.1.6) in R software. Finally, a significant positive correlation was observed between TIGIT expression and immune infiltration scores (Stromals score, Immunes score and ESTIMATE score) in 12 kinds of cancers involved in these studies (see Supplementary Figures 5–7).

3.2.4 Correlation between TIGIT expression and the infiltration score of immune cells (CIBERSORT AND TIMER)

Tumor-infiltrating immunocytes could affect the survival prognosis of patients. TIGIT expression showed a positive correlation with the infiltration scores of CD8 T cells (especially in SKCM), M1 macrophages in 12 kinds of cancers, naive B cells in 10 kinds of cancers, activated memory CD4 T cells, Tregs in LUAD, LUSC, LIHC, SKCM, THCA, COADREAD and activated NK cells in LUAD, LUSC, SKCM, STES, BLCA. TIGIT expression was also negatively correlated with activated dendritic cells and mast cells in most of the cancers included. The correlation coefficient between TIGIT expression and immune cell infiltration (CIBERSORT) is presented in Supplementary Table 8. Moreover, TIGIT expression was found to be positively related to B cell, CD4, CD8 T cell, neutrophil, macrophage and DC infiltration in most cancers based upon the TIMER algorithm (Figure 10).

3.2.5 Correlation between TIGIT expression and 150 immune-related genes

The results showed that TIGIT exhibited a significant coexpression relationship with most chemokines, receptors, major histocompatibility complex (MHC), immunoinhibitors and immunostimulators. Notably, TIGIT expression was positively correlated with the expression of programmed cell death 1 (PDCD1), programmed cell death 1 ligand 2 (PDCD1LG2), cytotoxic T-lymphocyte associated protein 4 (CTLA4), lymphocyte activating 3 (LAG3), indoleamine 2,3-dioxygenase 1 (IDO1), interleukin 10 (IL-10), and transforming growth factor beta 1 (TGFB1), especially in gastroesophageal tumors and melanoma (Figure 11).

The correlation coefficients are presented in detail in Supplementary Table 9.

3.2.6 Associations of TIGIT expression with tumor mutational burden (TMB) and microsatellite instability (MSI)

Because of the essential roles of TMB and MSI in the prediction of the response to immune therapy, Spearman

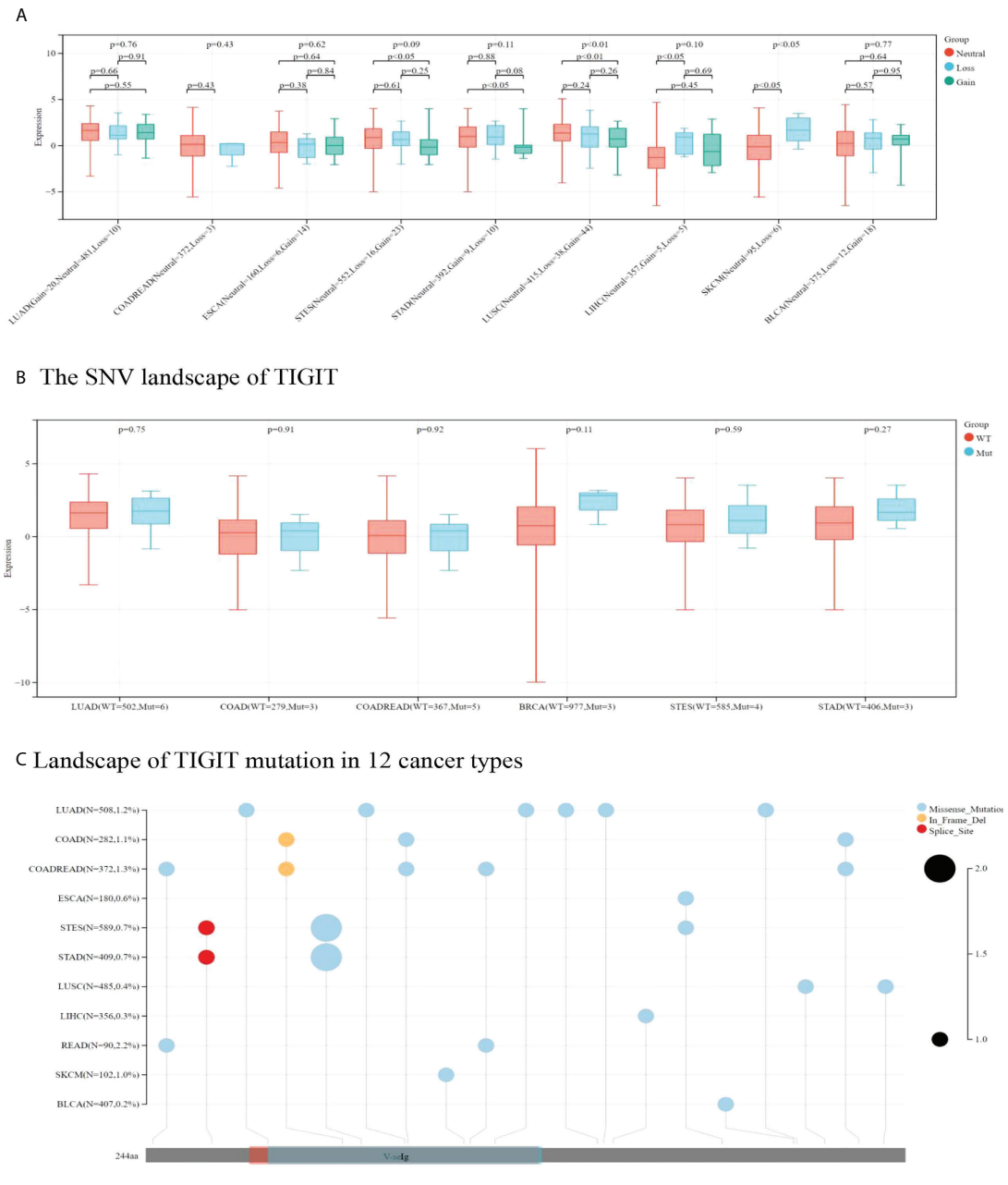

FIGURE 9
In **A** and **B** correlation between TIGIT expression and CNV and SNV were presented in boxplot. P values were presented by using scientific notation. In **C**, different color patches represent different domains of TIGIT. The sites marked with lollipops are mutation sites. Circular size represents mutation frequency.

correlation analysis was conducted to assess the relationship between TIGIT expression, TMB and MSI. The results showed that TIGIT expression was positively related to TMB in BLCA, COADREAD, COAD, and SKCM but negatively related to TMB in THCA. Moreover, TIGIT expression was positively correlated with MSI in COAD, COADREAD, and LUAD, while it was negatively correlated with MSI in ESCA and STES (see Figure 12). The correlation coefficients and P values are presented in Supplementary Tables 10, 11.

The results strongly indicated that TIGIT was well associated with tumor immunity. Therefore, TIGIT might be considered a promising biomarker for predicting the immunotherapy response.

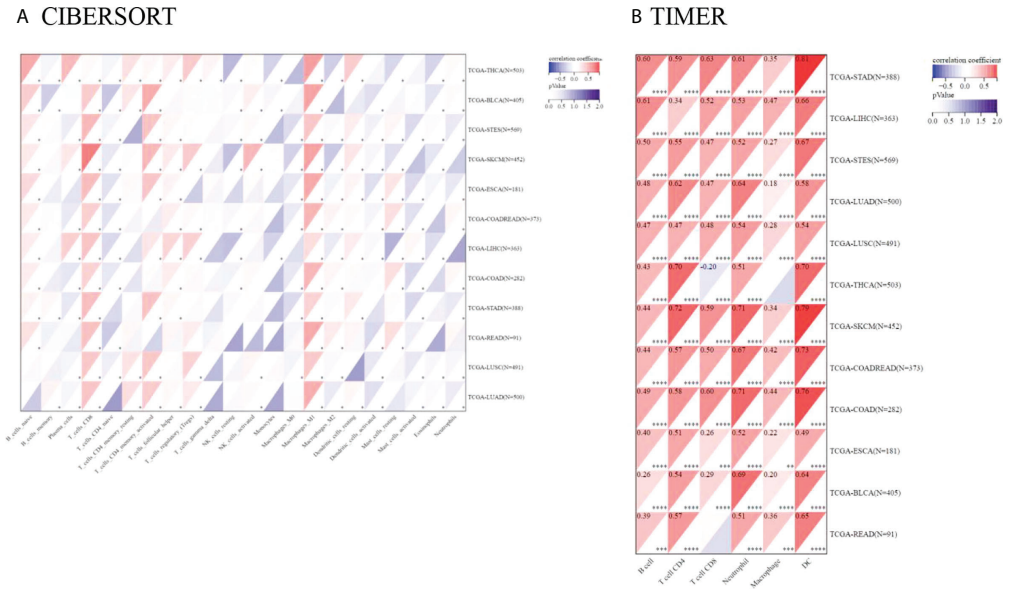

FIGURE 10
Pancancer analysis of the Spearman correlation between TIGIT expression and immune cell infiltration. CIBERSORT in **(A)**, TIMER in **(B)**. Red represents a positive correlation, and blue represents a negative correlation. The darker the color is, the greater the correlation coefficient. *P< 0.05, **P< 0.01, ***P< 0.001 and ****p< 0.0001.

3.2.7 Construction of the protein protein interaction (PPI) network, gene ontology (GO) and Kyoto encyclopedia of gene and genomes (KEGG) enrichment analysis

As presented in Figure 13A, we utilized the GeneMANIA online program to create a PPI network for 21 genes that interacted with TIGIT. TIGIT was found to interact with PDCD1, which indicated that patients with resistance to PD-1 inhibitors might benefit from the combination of TIGIT inhibitors. The biological processes (BP) enriched in this gene set were primarily those related to cell adhesion, heterophilic cell–cell adhesion *via* plasma membrane cell adhesion molecules and homophilic cell adhesion *via* plasma membrane adhesion molecules, while the cellular components (CC) enriched were plasma membrane AND integral component of membrane. The enriched molecular functions (MF) were linked to identical protein binding and receptor binding. The KEGG results showed that they were mainly enriched in the cell adhesion molecules, adherens junction and T-cell receptor signaling pathways (Figures 13B, C).

3.2.8 Construction of the ceRNA regulatory network

As shown in Figure 14, a ceRNA coexpression network consisting of 70 lncRNAs, 34 miRNAs, and 1 mRNA was visualized by Cytoscape after merging these predicted results. By using the CytoHubba plug-in in Cytoscape, we screened out the top 10 node degrees to represent the central genes of the PPI network, including TIGIT, hsa-miR-4516, hsa-miR-1255a, hsa-miR-1255b-5p, hsa-miR-1306-5p, hsa-miR-514a-3p, hsa-miR-6849-3p, hsa-miR-514b-3p, SNHG16, and hsa-miR-4534.

4 Discussion

The results of the meta-analysis showed that high expression of TIGIT was associated with poorer OS, PFS, RFS and DFS in East Asian patients with solid cancers. In contrast to the study reported by Kunmin Xiao et al (42), we also discussed the relationship between TIGIT and DFS and RFS. DFS and RFS are important clinical outcomes for cancers with relatively good clinical prognosis. Most importantly, we discussed the heterogeneity caused by postoperative treatments, which might have a very important impact on the prognosis of cancer patients. It was found in our study that the cancer type, sample sizes, and different cutoff values might be the source of heterogeneity. The high expression of TIGIT was not significantly correlated with poor PFS of PSCCE, RFS of MTC, DFS of PTC or OS of SCLC, CRC, MTC, ATC, PDTC and PTC. Studies with sample sizes <100 did not support the relationship between high expression of TIGIT and OS or DFS, while studies taking CPS≥1 as the cutoff value did not support the relationship

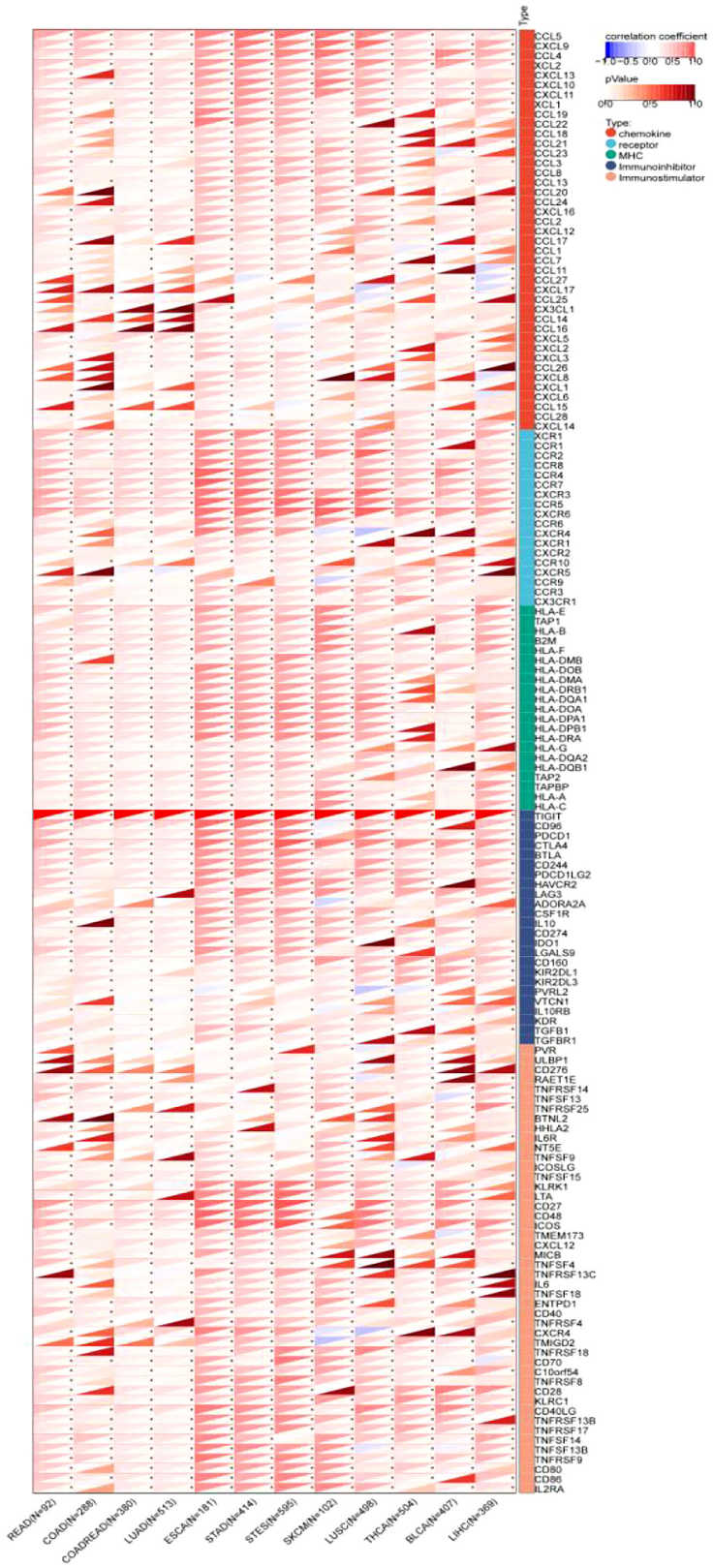

FIGURE 11 (Continued)

FIGURE 11 (Continued)
Pancancer analysis of the Spearman correlation betweenTIGIT expression and 150 immune-related genes, including 41 chemokines, 24 immunoinhibitors, 46 immunostulators, 21 MHCs and 18 receptors. Red represents a positive correlation, and blue represents a negative correlation. The darker the color is, the greater the correlation coefficient. *P< 0.05, **P< 0.01, and ***P< 0.001. CCL5, C-C Motif Chemokine Ligand 5; CXCL9, C-X-C Motif Chemokine Ligand 9; CCL4, C-C Motif Chemokine Ligand 4;XCL2, X-C Motif Chemokine Ligand 2; CXCL13, C-X-C Motif Chemokine Ligand 13; CXCL10, C-X-C Motif Chemokine Ligand 10; CXCL11, C-X-C Motif Chemokine Ligand 11; XCL1, X-C Motif Chemokine Ligand 1; CCL19, C-C Motif Chemokine Ligand 19; CCL22, C-C Motif Chemokine Ligand 22; CCL18, C-C Motif Chemokine Ligand 18; CCL21, C-C Motif Chemokine Ligand 21; CCL23, C-C Motif Chemokine Ligand 23; CCL3, C-C Motif Chemokine Ligand 3; CCL8, CC Motif Chemokine Ligand 8; CCL13, C-C Motif Chemokine Ligand 13; CCL20, C-C Motif Chemokine Ligand 20; CCL24, C-C Motif Chemokine Ligand 24; CXCL16, C-X-C Motif Chemokine Ligand 16; CCL2, C-C Motif Chemokine Ligand 2; CXCL12, C-X-C Motif Chemokine Ligand 12; CCL17, C-C Motif Chemokine Ligand 17; CCL1, C-C Motif Chemokine Ligand 1; CCL7, C-C Motif Chemokine Ligand 7; CCL11, C-C Motif Chemokine Ligand 11; CCL27, C-C Motif Chemokine Ligand 27; CXCL17, C-X-C Motif Chemokine Ligand 17; CCL25, C-C Motif Chemokine Ligand 25; CX3CL1, C-X3-C Motif Chemokine Ligand 1; CCL14, C-C Motif Chemokine Ligand 14; CCL16, C-C Motif Chemokine Ligand 16; CXCL5, C-X-C Motif Chemokine Ligand 5; CXCL2, C-X-C Motif Chemokine Ligand 2; CXCL3, C-X-C Motif Chemokine Ligand 3; CCL26, C-C Motif Chemokine Ligand 26; CXCL8, C-X-C Motif Chemokine Ligand 8; CXCL1, C-X-C Motif Chemokine Ligand 1; CXCL6, C-X-C Motif Chemokine Ligand 6; CCL15, C-C Motif Chemokine Ligand 15; CCL28, C-C Motif Chemokine Ligand 28; CXCL14, C-X-C Motif Chemokine Ligand 14; XCR1, X-C Motif Chemokine Receptor 1; CCR1, C-C Motif Chemokine Receptor 1; CCR2, C-C Motif Chemokine Receptor 2; CCR8, C-C Motif Chemokine Receptor 8; CCR4, C-C Motif Chemokine Receptor 4; CCR7, C-C Motif Chemokine Receptor 7; CXCR3, C-X-C Motif Chemokine Receptor 3; CCR5, C-C Motif Chemokine Receptor 5; CXCR6, C-X-C Motif Chemokine Receptor 6; CCR6, C-C Motif Chemokine Receptor 6; CXCR4, C-X-C Motif Chemokine Receptor 4; CXCR1, C-X-C Motif Chemokine Receptor 1; CXCR2, C-X-C Motif Chemokine Receptor 2; CCR10, C-C Motif Chemokine Receptor 10; CXCR5, C-X-C Motif Chemokine Receptor 5; CCR9, C-C Motif Chemokine Receptor 9; CCR3, C-C Motif Chemokine Receptor 3; CX3CR1, C-X3-C Motif Chemokine Receptor 1; HLA-E, Major Histocompatibility Complex, Class I, E; TAP1, Transporter 1, ATP Binding Cassette Subfamily B Member; HLA-B, Major Histocompatibility Complex, Class I, B; B2M, Beta-2-Microglobulin; HLA-F, Major Histocompatibility Complex, Class I, F; HLA-DMB, Major Histocompatibility Complex, Class II, DM Beta; HLA-DOB, Major Histocompatibility Complex, Class II, DO Beta; HLA-DMA, Major Histocompatibility Complex, Class II, DM Alpha; HLA-DRB1, Major Histocompatibility Complex, Class II, DR Beta 1; HLA-DQA1, Major Histocompatibility Complex, Class II, DQ Alpha 1; HLA-DOA, Major Histocompatibility Complex, Class II, DO Alpha; HLA-DPA1, Major Histocompatibility Complex, Class II, DP Alpha 1; HLA-DPB1, Major Histocompatibility Complex, Class II, DP Beta 1; HLA-DRA, Major Histocompatibility Complex, Class II, DR Alpha; HLA-G, Major Histocompatibility Complex, Class I, G; HLA-DQA2, Major Histocompatibility Complex, Class II, DQ Alpha 2; HLA-DQB1, Major Histocompatibility Complex, Class II, DQ Beta 1; TAP2, Transporter 2, ATP Binding Cassette Subfamily B Member; TAPBP, TAP Binding Protein; HLA-A, Major Histocompatibility Complex, Class I, A; HLA-C, Major Histocompatibility Complex, Class I, C; TIGIT, T-Cell Immunoreceptor With Ig And ITIM Domains; CD96, CD96 Molecule; PDCD1, Programmed Cell Death 1; CTLA4, Cytotoxic T-Lymphocyte Associated Protein 4; BTLA, B And T Lymphocyte Associated; CD244, CD244 Molecule; PDCD1LG2, Programmed Cell Death 1 Ligand 2; HAVCR2, Hepatitis A Virus Cellular Receptor 2; LAG3, Lymphocyte Activating 3; ADORA2A, Adenosine A2a Receptor; CSF1R, Colony Stimulating Factor 1 Receptor; IL10, Interleukin 10; CD274, CD274 Molecule; IDO1, Indoleamine 2,3-Dioxygenase 1; LGALS9, Galectin 9; CD160, CD160 Molecule; KIR2DL1, Killer Cell Immunoglobulin Like Receptor, Two Ig Domains And Long Cytoplasmic Tail 1; KIR2DL3, Killer Cell Immunoglobulin Like Receptor, Two Ig Domains And Long Cytoplasmic Tail 3; NECTIN2, Nectin Cell Adhesion Molecule 2; VTCN1, V-Set Domain Containing T-Cell Activation Inhibitor 1; IL10RB, Interleukin 10 Receptor Subunit Beta; KDR, Kinase Insert Domain Receptor; TGFBR1, Transforming Growth Factor Beta 1 Transforming Growth Factor Beta Receptor 1; PVR, PVR Cell Adhesion Molecule; ULBP1, UL16 Binding Protein 1; CD276, CD276 Molecule; RAET1E, Retinoic Acid Early Transcript 1E; TNFRSF14, TNF Receptor Superfamily Member 14; TNFSF13, TNF Superfamily Member 13; TNFRSF25, TNF Receptor Superfamily Member 25; BTNL2, Butyrophilin Like 2; HHLA2, HERV-H LTR-Associating 2; IL6R, Interleukin 6 Receptor; NT5E, 5'- Nucleotidase Ecto; TNFSF9, TNF Superfamily Member 9; ICOSLG, Inducible T-Cell Costimulator Ligand; TNFSF15, TNF Superfamily Member 15; KLRK1, Killer Cell Lectin Like Receptor K1; LTA, Lymphotoxin Alpha; CD27, CD27 Molecule; CD48, CD48 Molecule; ICOS, Inducible T-Cell Costimulator; STING1, Stimulator Of Interferon Response CGAMP Interactor 1; CXCL12, C-X-C Motif Chemokine Ligand 12; MICB, MHC Class I Polypeptide-Related Sequence B; TNFSF4, TNF Superfamily Member 4; TNFRSF13C, TNF Receptor Superfamily Member 13C; IL6, Interleukin 6; TNFSF18, TNF Superfamily Member 18; ENTPD1, Ectonucleoside Triphosphate Diphosphohydrolase 1; CD40, CD40 Molecule; TNFRSF4, TNF Receptor Superfamily Member 4; CXCR4, C-X-C Motif Chemokine Receptor 4; TMIGD2, Transmembrane And Immunoglobulin Domain Containing 2; TNFRSF18, TNF Receptor Superfamily Member 18; CD70, CD70 Molecule; VSIR, V-Set Immunoregulatory Receptor; TNFRSF8, TNF Receptor Superfamily Member 8; CD28, CD28 Molecule; KLRC1, Killer Cell Lectin Like Receptor C1; CD40LG, CD40 Ligand; TNFRSF13B, TNF Receptor Superfamily Member 13B; TNFRSF17, TNF Receptor Superfamily Member 17; TNFSF14, TNF Superfamily Member 14; TNFSF13B, TNF Superfamily Member 13b; TNFRSF9, TNF Receptor Superfamily Member 9; CD80, CD80 Molecule; CD86, CD86 Molecule; IL2RA, Interleukin 2 Receptor Subunit Alpha.CCL5, C-C Motif Chemokine Ligand 5; CXCL9, C-X-C Motif Chemokine Ligand 9; CCL4, C-C Motif Chemokine Ligand 4;XCL2, X-C Motif Chemokine Ligand 2; CXCL13, C-X-C Motif Chemokine Ligand 13; CXCL10, C-X-C Motif Chemokine Ligand 10; CXCL11, C-X-C Motif Chemokine Ligand 11; XCL1, X-C Motif Chemokine Ligand 1; CCL19, C-C Motif Chemokine Ligand 19; CCL22, C-C Motif Chemokine Ligand 22; CCL18, C-C Motif Chemokine Ligand 18; CCL21, C-C Motif Chemokine Ligand 21; CCL23, C-C Motif Chemokine Ligand 23; CCL3, C-C Motif Chemokine Ligand 3; CCL8, CC Motif Chemokine Ligand 8; CCL13, C-C Motif Chemokine Ligand 13; CCL20, C-C Motif Chemokine Ligand 20; CCL24, C-C Motif Chemokine Ligand 24; CXCL16, C-X-C Motif Chemokine Ligand 16; CCL2, C-C Motif Chemokine Ligand 2; CXCL12, C-X-C Motif Chemokine Ligand 12; CCL17, C-C Motif Chemokine Ligand 17; CCL1, C-C Motif Chemokine Ligand 1; CCL7, C-C Motif Chemokine Ligand 7; CCL11, C-C Motif Chemokine Ligand 11; CCL27, C-C Motif Chemokine Ligand 27; CXCL17, C-X-C Motif Chemokine Ligand 17; CCL25, C-C Motif Chemokine Ligand 25; CX3CL1, C-X3-C Motif Chemokine Ligand 1; CCL14, C-C Motif Chemokine Ligand 14; CCL16, C-C Motif Chemokine Ligand 16; CXCL5, C-X-C Motif Chemokine Ligand 5; CXCL2, C-X-C Motif Chemokine Ligand 2; CXCL3, C-X-C Motif Chemokine Ligand 3; CCL26, C-C Motif Chemokine Ligand 26; CXCL8, C-X-C Motif Chemokine Ligand 8; CXCL1, C-X-C Motif Chemokine Ligand 1; CXCL6, C-X-C Motif Chemokine Ligand 6; CCL15, C-C Motif Chemokine Ligand 15; CCL28, C-C Motif Chemokine Ligand 28; CXCL14, C-X-C Motif Chemokine Ligand 14; XCR1, X-C Motif Chemokine Receptor 1; CCR1, C-C Motif Chemokine Receptor 1; CCR2, C-C Motif Chemokine Receptor 2; CCR8, C-C Motif Chemokine Receptor 8; CCR4, C-C Motif Chemokine Receptor 4; CCR7, C-C Motif Chemokine Receptor 7; CXCR3, C-X-C Motif Chemokine Receptor 3; CCR5, C-C Motif Chemokine Receptor 5; CXCR6, C-X-C Motif Chemokine Receptor 6; CCR6, C-C Motif Chemokine Receptor 6; CXCR4, C-X-C Motif Chemokine Receptor 4; CXCR1, C-X-C Motif Chemokine Receptor 1; CXCR2, C-X-C Motif Chemokine Receptor 2; CCR10, C-C Motif Chemokine Receptor 10; CXCR5, C-X-C Motif Chemokine Receptor 5; CCR9, C-C Motif Chemokine Receptor 9; CCR3, C-C Motif Chemokine Receptor 3; CX3CR1, C-X3-C Motif Chemokine Receptor 1; HLA-E, Major Histocompatibility Complex, Class I, E; TAP1, Transporter 1, ATP Binding Cassette Subfamily B Member; HLA-B, Major Histocompatibility Complex, Class I, B; B2M, Beta-2-Microglobulin; HLA-F, Major Histocompatibility Complex, Class I, F; HLA-DMB, Major Histocompatibility Complex, Class II, DM Beta; HLA-DOB, Major Histocompatibility Complex, Class II, DO Beta; HLA-DMA, Major Histocompatibility

Complex, Class II, DM Alpha; HLA-DRB1, Major Histocompatibility Complex, Class II, DR Beta 1; HLA-DQA1, Major Histocompatibility Complex, Class II, DQ Alpha 1; HLA-DOA, Major Histocompatibility Complex, Class II, DO Alpha; HLA-DPA1, Major Histocompatibility Complex, Class II, DP Alpha 1; HLA-DPB1, Major Histocompatibility Complex, Class II, DP Beta 1; HLA-DRA, Major Histocompatibility Complex, Class II, DR Alpha; HLA-G, Major Histocompatibility Complex, Class I, G; HLA-DQA2, Major Histocompatibility Complex, Class II, DQ Alpha 2; HLA-DQB1, Major Histocompatibility Complex, Class II, DQ Beta 1; TAP2, Transporter 2, ATP Binding Cassette Subfamily B Member; TAPBP, TAP Binding Protein; HLA-A, Major Histocompatibility Complex, Class I, A; HLA-C, Major Histocompatibility Complex, Class I, C; TIGIT, T-Cell Immunoreceptor With Ig And ITIM Domains; CD96, CD96 Molecule; PDCD1, Programmed Cell Death 1; CTLA4, Cytotoxic T-Lymphocyte Associated Protein 4; BTLA, B And T Lymphocyte Associated; CD244, CD244 Molecule; PDCD1LG2, Programmed Cell Death 1 Ligand 2; HAVCR2, Hepatitis A Virus Cellular Receptor 2; LAG3, Lymphocyte Activating 3; ADORA2A, Adenosine A2a Receptor; CSF1R, Colony Stimulating Factor 1 Receptor; IL10, Interleukin 10; CD274, CD274 Molecule; IDO1, Indoleamine 2,3-Dioxygenase 1; LGALS9, Galectin 9; CD160, CD160 Molecule; KIR2DL1, Killer Cell Immunoglobulin Like Receptor, Two Ig Domains And Long Cytoplasmic Tail 1; KIR2DL3, Killer Cell Immunoglobulin Like Receptor, Two Ig Domains And Long Cytoplasmic Tail 3; NECTIN2, Nectin Cell Adhesion Molecule 2; VTCN1, V-Set Domain Containing T-Cell Activation Inhibitor 1; IL10RB, Interleukin 10 Receptor Subunit Beta; KDR, Kinase Insert Domain Receptor; TGFBR1, Transforming Growth Factor Beta 1 Transforming Growth Factor Beta Receptor 1; PVR, PVR Cell Adhesion Molecule; ULBP1, UL16 Binding Protein 1; CD276, CD276 Molecule; RAET1E, Retinoic Acid Early Transcript 1E; TNFRSF14, TNF Receptor Superfamily Member 14; TNFSF13, TNF Superfamily Member 13; TNFRSF25, TNF Receptor Superfamily Member 25; BTNL2, Butyrophilin Like 2; HHLA2, HERV-H LTR-Associating 2; IL6R, Interleukin 6 Receptor; NT5E, 5'- Nucleotidase Ecto; TNFSF9, TNF Superfamily Member 9; ICOSLG, Inducible T-Cell Costimulator Ligand; TNFSF15, TNF Superfamily Member 15; KLRK1, Killer Cell Lectin Like Receptor K1; LTA, Lymphotoxin Alpha; CD27, CD27 Molecule; CD48, CD48 Molecule; ICOS, Inducible T-Cell Costimulator; STING1, Stimulator Of Interferon Response CGAMP Interactor 1; CXCL12, C-X-C Motif Chemokine Ligand 12; MICB, MHC Class I Polypeptide-Related Sequence B; TNFSF4, TNF Superfamily Member 4; TNFRSF13C, TNF Receptor Superfamily Member 13C; IL6, Interleukin 6; TNFSF18, TNF Superfamily Member 18; ENTPD1, Ectonucleoside Triphosphate Diphosphohydrolase 1; CD40, CD40 Molecule; TNFRSF4, TNF Receptor Superfamily Member 4; CXCR4, C-X-C Motif Chemokine Receptor 4; TMIGD2, Transmembrane And Immunoglobulin Domain Containing 2; TNFRSF18, TNF Receptor Superfamily Member 18; CD70, CD70 Molecule; VSIR, V-Set Immunoregulatory Receptor; TNFRSF8, TNF Receptor Superfamily Member 8; CD28, CD28 Molecule; KLRC1, Killer Cell Lectin Like Receptor C1; CD40LG, CD40 Ligand; TNFRSF13B, TNF Receptor Superfamily Member 13B; TNFRSF17, TNF Receptor Superfamily Member 17; TNFSF14, TNF Superfamily Member 14; TNFSF13B, TNF Superfamily Member 13b; TNFRSF9, TNF Receptor Superfamily Member 9; CD80, CD80 Molecule; CD86, CD86 Molecule; IL2RA, Interleukin 2 Receptor Subunit Alpha.

between high expression of TIGIT and OS or RFS. Whether postoperative treatments result in heterogeneity still needs further study.

SCLC is a classical neuroendocrine tumor with low immunogenicity and low MHC I expression levels, which makes it difficult to recognize by CD8 T-cell receptors. Its immune regulation is more complex than that of other solid tumors due to the existence of autocrine or paracrine molecules. In ATC, TIGIT expression is not found to have prognostic value (38). The reason may be that ATC patients suffer from extremely short survival, and the sample size may be too small to distinguish the prognosis.

In our meta-analysis, a relationship between high expression of TIGIT and poorer OS was not found in the studies taking CPS≥1 as the cutoff value. The tumor proportion score (TPS) and the combined positive score (CPS) have been widely used in clinical research. TPS calculates the ratio of TIGIT-stained tumor cells to the total number of viable tumor cells, while CPS calculates the ratio of potential TIGIT expression, including tumor cells and immune cells, to the

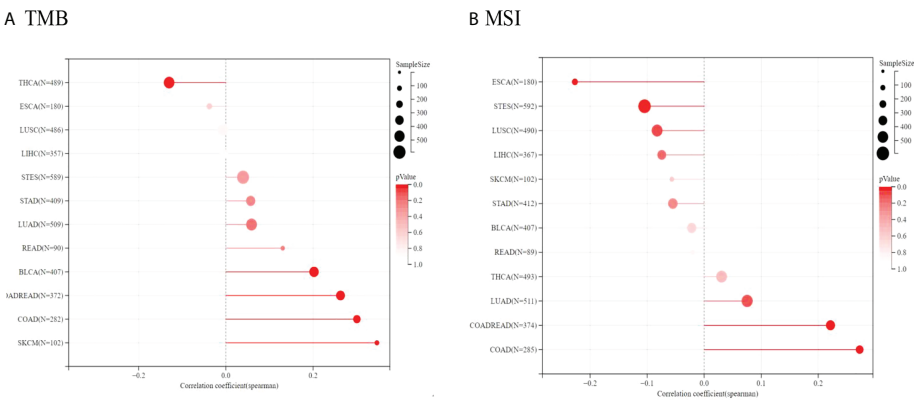

FIGURE 12
Spearman correlation between TMB, MSI and TIGIT gene expression were presented in **(A, B)** respectively. The correlation coefficient is presented by using the length of the lollipop. The redder the color, the more statistically significant it is.

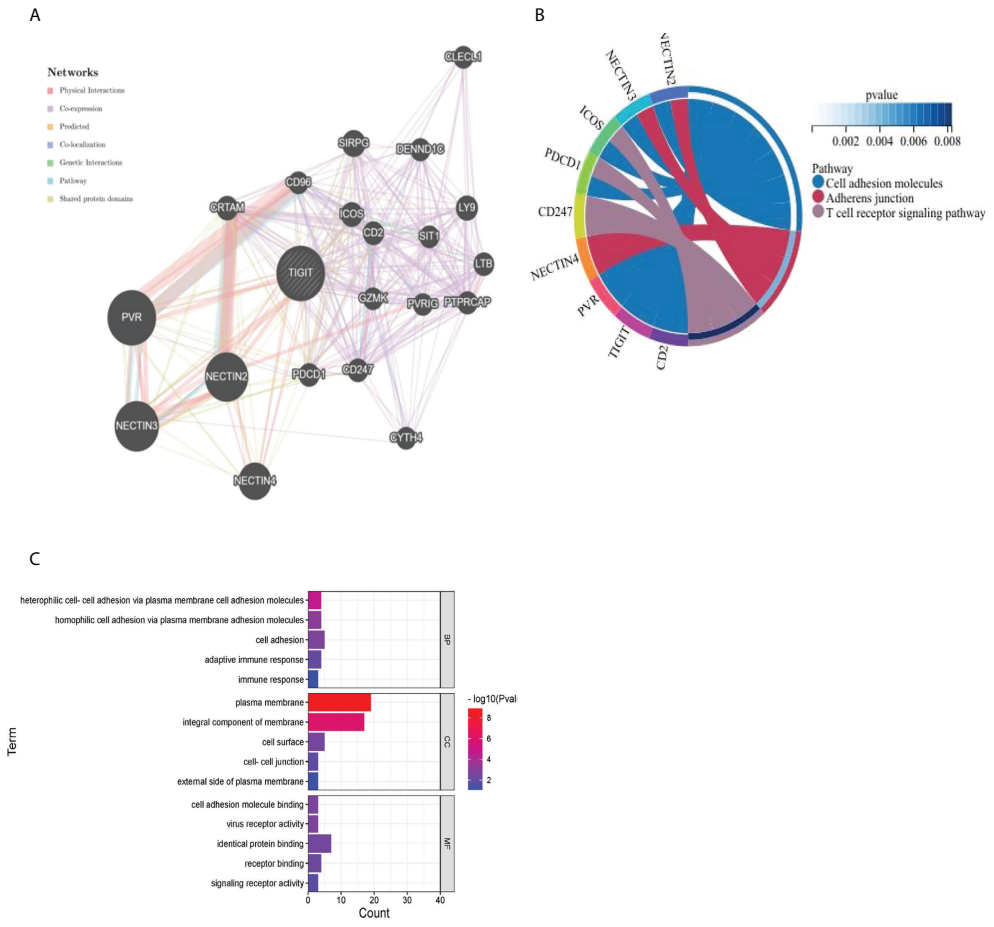

FIGURE 13
Visualization and enrichment analysis for genes that interacted with TIGIT **(A)** PPI network **(B)** Chord diagram for KEGG analysis **(C)** Bar graph for GO analysis).

total number of viable tumor cells. However, it remains unclear which is more suitable for assessing TIGIT expression as a prognostic biomarker (43).

Vascular endothelial cells, nonmalignant cells, immunocytes, tumor-associated macrophages (TAMs), cancer-associated fibroblasts (CAFs), myeloid-derived suppressor cells (MDSCs), natural killer (NK) cells, dendritic cells (DCs) and tumor-associated neutrophils (TANs) make up the tumor microenvironment (TME) (44, 45). TIGIT was highly positively correlated with the ESTIMATE score in all of the cancers included, which indicated an advanced cancer stage with a poor prognosis.

Tumor-infiltrating immunocytes can promote or antagonize tumorigenesis and progression (46). TIGIT expressed on TILs responded to the TME. TIGIT marks the most dysfunctional subset of CD8+ T cells and Tregs with a highly suppressive function (47). In this study, high TIGIT expression promoted the infiltration levels of CD8 T cells, M1 macrophages, naive B cells, activated memory CD4 T cells, Tregs and activated NK cells while inhibiting the infiltration levels of activated dendritic cells and mast cells in most of the cancers included. Among them, M1 macrophages, activated memory CD4 T cells, activated dendritic cells, mast cells and activated NK cells play antitumor roles in the TME and are related to better outcomes, while Tregs play immune suppression roles and are related to worse survival prognosis (48). A positive correlation was discovered between the expression of TIGIT and most of the other immune checkpoints, especially in ESCA, STAD, STES and SKCM (12, 47, 49, 50). This result suggested that TIGIT might be involved in different immune responses and immunocyte infiltration. The combined blockade of TIGIT and other new immune checkpoints may be a possible option for immunotherapy, especially in patients with gastroesophageal tumors and melanoma.

MSI and TMB are two valuable indexes suggesting the sensitivity of immune checkpoint inhibitors. TMB can induce

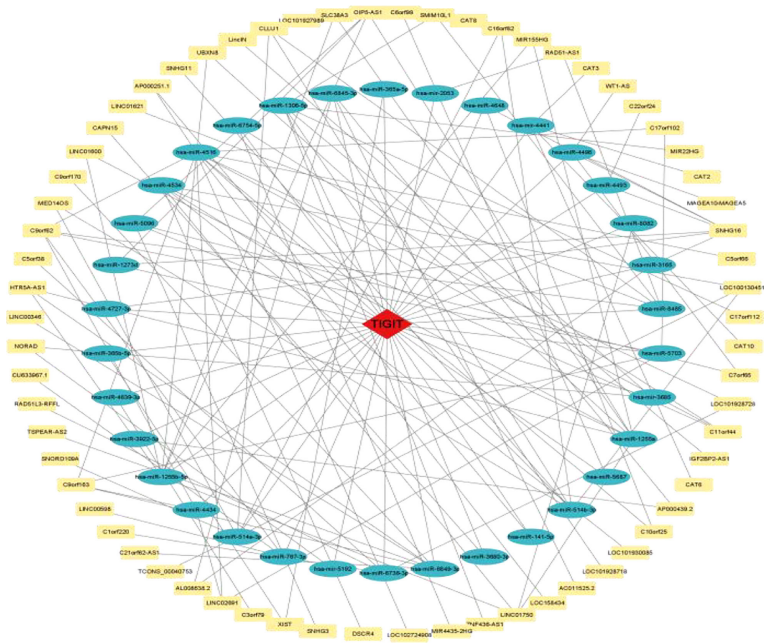

FIGURE 14
TIGIT-miRNA–lncRNA network.

new antigens to facilitate immune recognition. MSI caused by hypermutability (gain or loss) of nucleotides from DNA elements is associated with increased expression of neoantigens, higher PD-L1 expression and TMB-H (51). In this study, TIGIT expression was positively related to TMB and MSI in COAD and COADREAD, which indicated that patients with COAD or COADREAD might benefit from TIGIT inhibitors.

Regarding the possible regulatory mechanisms, the results of the GO and KEGG enrichment analyses indicated that TIGIT was closely related to the functions of cell adhesion, adherens junction and the T-cell receptor signaling pathway, which supported the oncogenic role and immunological function of TIGIT in the tumor immune microenvironment.

Currently, it is urgent to find new immune checkpoints to compensate for drug resistance and severe adverse reactions caused by PD-1/PD-L1 and CTLA4 inhibitors. Studies on TIGIT expression provided more encouraging results than those on LAG-3 and TIM-3 (52). TIGIT inhibitors, such as tibolumab, vibostolimab, ocperlimab, M-6223, ASP-8374, COM-902 and IBI-939, have been under clinical trials in patients with non-small cell lung cancer (NSCLC), esophageal squamous cell carcinoma (ESCC) and gastric adenocarcinoma (GAC). TIGIT expression paralleled that of PD-1 (2). Most TIGIT inhibitors are used in combination with PD-L1/PD-1 inhibitors, such as zimberelimab and atezolizumab (53, 54). We will continue to follow up the results of relevant clinical reports.

There were some limitations in our meta-analysis. Over half of the studies did not report postoperative therapy, which led to some bias in our analysis. Second, all of the subjects were Asian, and whether the conclusion could be applied to other populations remained uncertain. Third, the scale of the included studies was limited. Some parts of the subgroup analysis only included one kind of cancer. Large sample size studies are still needed to determine the relationship between TIGIT expression and survival prognosis, especially PFS, RFS and DFS.

5 Conclusion

TIGIT is valuable in predicting the survival prognosis of patients with solid cancers. TIGIT is correlated with the TME, infiltration of immune cells, immune-related genes, MSI and TMB. The results indicate the role of TIGIT in tumoriFabbrevgenesis and progression. TIGIT inhibitors may be promising choices for solid cancers in the future.

Data availability statement

The original contributions presented in the study are included in the article/Supplementary Material. Further inquiries can be directed to the corresponding author.

Author contributions

SL and LL contributed equally to article review, manuscript writing and revisions for intellectual content. TP and XL were responsible for data extraction and English translation. YT was responsible for data extraction, English translation and quality assessment. YJ was the corresponding author and was responsible for quality assessment and revisions for intellectual content. All authors contributed to the article and approved the submitted version.

Acknowledgments

The authors would like to thank all the scholars who made constant efforts for cancer research.

Conflict of interest

The authors declare that the research was conducted in the absence of any commercial or financial relationships that could be construed as a potential conflict of interest.

Publisher's note

Supplementary material

The Supplementary Material for this article can be found online at: https://www.frontiersin.org/articles/10.3389/fimmu.2022.977016/full#supplementary-material

References

1. Noguchi Y, Maeda A, Lo PC, Takakura C, Haneda T, Kodama T, et al. Human TIGIT on porcine aortic endothelial cells suppresses xenogeneic macrophage-mediated cytotoxicity. *Immunobiology* (2019) 224(5):605–13. doi: 10.1016/j.imbio.2019.07.008

2. Alenzi FQ, Lotfy M, Wyse R. Swords of cell death: Caspase activation and regulation. *Asian Pac J Cancer Prev* (2010) 11(2):271–80.

3. Alenzi FQ. The significance and occurrence of TNF receptor polymorphisms in the Saudi population. *Saudi J Biol Sci* (2016) 23(6):767–72. doi: 10.1016/j.sjbs.2016.04.015

4. Blackburn SD, Shin H, Haining WN, Zou T, Workman CJ, Polley A, et al. Coregulation of CD8+ T-cell exhaustion by multiple inhibitory receptors during chronic viral infection. *Nat Immunol* (2009) 10(1):29–37. doi: 10.1038/ni.1679

5. Zarour HM. Reversing T-cell dysfunction and exhaustion in cancer. *Clin Cancer Res* (2016) 22(8):1856–64. doi: 10.1158/1078-0432.CCR-15-1849

6. Alenzi FQ, Alenazi FA, Al-Kaabi Y, Salem ML. The use of growth factors to modulate the activities of antigen-specific CD8+ T cells *in vitro*. *J Med Life* (2011) 4 (4):399–406.

7. Stengel KF, Harden-Bowles K, Yu X, Rouge L, Yin J, Comps-Agrar L, et al. Structure of TIGIT immunoreceptor bound to poliovirus receptor reveals a cell–cell adhesion and signaling mechanism that requires cis-trans receptor clustering. *Proc Natl Acad Sci USA* (2012) 109(14):5399–404. doi: 10.1073/pnas.1120606109

8. Yu X, Harden K, Gonzalez LC, Francesco M, Chiang E, Irving B, et al. The surface protein TIGIT suppresses T-cell activation by promoting the generation of mature immunoregulatory dendritic cells. *Nat Immunol* (2009) 10(1):48–57. doi: 10.1038/ni.1674

9. Uhlén M, Fagerberg L, Hallström BM, Lindskog C, Oksvold P, Mardinoglu A, et al. Proteomics. tissue-based map of the human proteome. *Science* (2015) 347 (6220):1260419. doi: 10.1126/science.1260419

10. Wang F, Hou H, Wu S, Tang Q, Liu W, Huang M, et al. TIGIT expression levels on human NK cells correlate with functional heterogeneity among healthy individuals. *Eur J Immunol* (2015) 45(10):2886–97. doi: 10.1002/eji.201545480

11. Hasan MM, Nair SS, O'Leary JG, Thompson-Snipes L, Nyarige V, Wang J, et al. Implication of TIGIT+ human memory b cells in immune regulation. *Nat Commun* (2021) 12(1):1534. doi: 10.1038/s41467-021-21413-y

12. Joller N, Lozano E, Burkett PR, Patel B, Xiao S, Zhu C, et al. Treg cells expressing the coinhibitory molecule TIGIT selectively inhibit proinflammatory Th1 and Th17-cell responses. *Immunity* (2014) 40(4):569–81. doi: 10.1016/j.immuni.2014.02.012

13. Rabea MA, Nafea MA, Tamimi W, Alenzi FQ. Role of T lymphocytes in chronic leukemia. *Bangladesh J Med Sci* (2017) 16(2):207–11. doi: 10.3329/bjms.v16i2.31939

14. Page MJ, McKenzie JE, Bossuyt PM, Boutron I, Hoffmann TC, Mulrow CD, et al. The PRISMA 2020 statement: An updated guideline for reporting systematic reviews. *Syst Rev* (2021) 10(1):89. doi: 10.1186/s13643-021-01626-4

15. Stang A. Critical evaluation of the Newcastle–Ottawa scale for the assessment of the quality of nonrandomized studies in meta-analyses. *Eur J Epidemiol* (2010) 25(9):603–5. doi: 10.1007/s10654-010-9491-z

16. Beroukhim R, Mermel CH, Porter D, Wei G, Raychaudhuri S, Donovan J, et al. The landscape of somatic copy-number alteration across human cancers. *Nature* (2010) 463(7283):899–905. doi: 10.1038/nature08822

17. Mermel CH, Schumacher SE, Hill B, Meyerson ML, Beroukhim R, Getz G, et al. GISTIC2.0 facilitates sensitive and confident localization of the targets of focal somatic copy-number alteration in human cancers. *Genome Biol* (2011) 12(4):R41. doi: 10.1186/gb-2011-12-4-r41

18. Yoshihara K, Shahmoradgoli M, Martínez E, Vegesna R, Kim H, Torres-Garcia W, et al. Inferring tumor purity and stromal and immune cell admixture from expression data. *Nat Commun* (2013) 4:2612. doi: 10.1038/ncomms3612

19. Newman AM, Liu CL, Green MR, Gentles AJ, Feng W, Xu Y, et al. Robust enumeration of cell subsets from tissue expression profiles. *Nat Methods* (2015) 12 (5):453–7. doi: 10.1038/nmeth.3337

20. Li T, Fan J, Wang B, Traugh N, Chen Q, Liu JS, et al. TIMER: A web server for comprehensive analysis of tumor-infiltrating immune cells. *Cancer Res* (2017) 77(21):e108–10. doi: 10.1158/0008-5472.CAN-17-0307

21. Zeng D, Ye Z, Shen R, Yu G, Wu J, Xiong Y, et al. IOBR: Multi-omics immuno-oncology biological research to decode tumor microenvironment and signatures. *Front Immunol* (2021) 12 doi: 10.3389/fimmu

22. Bonneville R, Krook MA, Kautto EA, Miya J, Wing MR, Chen HZ, et al. Landscape of microsatellite instability across 39 cancer types. *JCO Precis Oncol* (2017) 2017:23–31. doi: 10.1200/PO.17.00073

23. Shen W, Song Z, Zhong X, Huang M, Shen D, Gao P, et al. Sangerbox: A comprehensive, interaction-friendly clinical bioinformatics analysis platform. *iMeta* (2022) 1:e36. doi: 10.1002/imt2.36

24. Ragueneau E, Shrivastava A, Morris JH, Del-Toro N, Hermjakob H, Porras P., et al. IntAct app: a cytoscape application for molecular interaction network visualization and analysis. *Bioinformatics* (2021) 37(20):3684–5. doi: 10.1093/bioinformatics/btab319

25. Ghatalia P, Gordetsky J, Kuo F, Dulaimi E, Cai KQ, Devarajan K, et al. Prognostic impact of immune gene expression signature and tumor infiltrating immune cells in localized clear cell renal cell carcinoma. *J Immunother Cancer* (2019) 7(1):273. doi: 10.1186/s40425-019-0621-1

26. Ahluwalia P, Ahluwalia M, Mondal AK, Sahajpal N, Kota V, Rojiani MV, et al. Immunogenomic gene signature of cell-death associated genes with prognostic implications in lung cancer. *Cancers (Basel)* (2021) 13(1):155. doi: 10.3390/cancers13010155

27. Zhao JJ, Zhou ZQ, Wang P, Chen CL, Liu Y, Pan QZ, et al. Orchestration of immune checkpoints in tumor immune contexture and their prognostic significance in esophageal squamous cell carcinoma. *Cancer Manag Res* (2018) 10:6457–68. doi: 10.2147/CMAR.S181949

28. Wang P, Chen Y, Long Q, Li Q, Tian J, Liu T, et al. Increased coexpression of PD-L1 and TIM3/TIGIT is associated with poor overall survival of patients with esophageal squamous cell carcinoma. *J Immunother Cancer* (2021) 9(10):e002836. doi: 10.1136/jitc-2021-002836

29. Zhao K, Ma L, Feng L, Huang Z, Meng X, Yu J, et al. CD155 overexpression correlates with poor prognosis in primary small cell carcinoma of the esophagus. *Front Mol Biosci* (2021) 7:608404. doi: 10.3389/fmolb.2020.608404

30. Tang W, Pan X, Han D, Rong D, Zhang M, Yang L, et al. Clinical significance of CD8+ T-cell immunoreceptor with ig and ITIM domains+ in locally advanced gastric cancer treated with SOX regimen after D2 gastrectomy. *Oncoimmunology* (2019) 8(6):e1593807. doi: 10.1080/2162402X.2019.1593807

31. Liu H, Wu J, Xu X, Wang H, Zhang C, Yin S, et al. Peritumoral TIGIT +CD20+ b-cell infiltration indicates poor prognosis but favorable adjuvant chemotherapeutic response in gastric cancer. *Int Immunopharmacol* (2022) 108:108735. doi: 10.1016/j.intimp.2022.108735

32. Xu Y, Cui G, Jiang Z, Li N, Zhang X. Survival analysis with regard to PD-L1 and CD155 expression in human small cell lung cancer and a comparison with associated receptors. *Oncol Lett* (2019) 17(3):2960–8. doi: 10.3892/ol.2019.9910

33. Sun Y, Luo J, Chen Y, Cui J, Lei Y, Cui Y, et al. Combined evaluation of the expression status of CD155 and TIGIT plays an important role in the prognosis of LUAD (lung adenocarcinoma). *Int Immunopharmacol* (2020) 80:106198. doi: 10.1016/j.intimp.2020.106198

34. Jiang C, Qu X, Ma L, Cheng X, Gao X. CD155 expression impairs anti-PD1 therapy response in non-small cell lung cancer. *Clin Exp Immunol* (2022) 208 (2):220–32. doi: 10.1093/cei/uxac020

35. Zhou X, Ding X, Li H, Yang C, Ma Z, Xu G, et al. Upregulation of TIGIT and PD-1 in colorectal cancer with mismatch-repair deficiency. *Immunol Invest* (2021) 50(4):338–55. doi: 10.1080/08820139.2020.1758130

36. Liang R, Zhu X, Lan T, Ding D, Zheng Z, Chen T, et al. TIGIT promotes CD8+T cells exhaustion and predicts poor prognosis of colorectal cancer. *Cancer Immunol Immunother* (2021) 70(10):2781–93. doi: 10.1007/s00262-021-02886-8

37. Murakami D, Matsuda K, Iwamoto H, Mitani Y, Mizumoto Y, Nakamura Y, et al. Prognostic value of CD155/TIGIT expression in patients with colorectal cancer. *PLoS One* (2022) 17(3):e0265908. doi: 10.1371/journal.pone.0265908

38. Lee WJ, Lee YJ, Choi ME, Yun KA, Won CH, Lee MW, et al. Expression of lymphocyte-activating gene 3 and T-cell immunoreceptor with immunoglobulin and ITIM domains in cutaneous melanoma and their correlation with programmed cell death 1 expression in tumor-infiltrating lymphocytes. *J Am Acad Dermatol* (2019) 81(1):219–27. doi: 10.1016/j.jaad.2019.03.012

39. Yu L, Liu X, Wang X, Yan F, Wang P, Jiang Y, et al. TIGIT+ TIM-3+ NK cells are correlated with NK-cell exhaustion and disease progression in patients with hepatitis b virus–related hepatocellular carcinoma. *Oncoimmunology* (2021) 10(1):1942673. doi: 10.1080/2162402X.2021.1942673

40. Liu Z, Zhou Q, Wang Z, Zhang H, Zeng H, Huang Q, et al. Intratumoral TIGIT+ CD8+ T-cell infiltration determines poor prognosis and immune evasion in patients with muscle-invasive bladder cancer. *J Immunother Cancer* (2020) 8(2): e000978. doi: 10.1136/jitc-2020-000978

41. Luo Y, Yang YC, Shen CK, Ma B, Xu WB, Wang QF, et al. Immune checkpoint protein expression defines the prognosis of advanced thyroid carcinoma. *Front Endocrinol (Lausanne)* (2022) 13:859013. doi: 10.3389/ fendo.2022.859013

42. Xiao K, Xiao K, Li K, Xue P, Zhu S. Prognostic role of TIGIT expression in patients with solid tumors: A meta-analysis. *J Immunol Res* (2021) 2021:5440572. doi: 10.1155/2021/5440572

43. Yamashita K, Iwatsuki M, Harada K, Eto K, Hiyoshi Y, Ishimoto T, et al. Prognostic impacts of the combined positive score and the tumor proportion score for programmed death ligand-1 expression by double immunohistochemical staining in patients with advanced gastric cancer. *Gastric Cancer* (2020) 23 (1):95–104. doi: 10.1007/s10120-019-00999-9

44. Fathi M, Pustokhina I, Kuznetsov SV, Khayrullin M, Hojjat-Farsangi M, Karpisheh V, et al. T-Cell immunoglobulin and ITIM domain, as a potential immune checkpoint target for immunotherapy of colorectal cancer. *IUBMB Life* (2021) 73(5):726–38. doi: 10.1002/iub.2461

45. Lei X, Lei Y, Li JK, Du WX, Li RG, Yang J, et al. Immune cells within the tumor microenvironment: Biological functions and roles in cancer immunotherapy. *Cancer Lett* (2020) 470:126–33. doi: 10.1016/j.canlet.2019.11.009

46. Kondělková K, Vokurková D, Krejsek J, Borská L, Fiala Z, Ctirad A. Regulatory T cells (TREG) and their roles in immune system with respect to immunopathological disorders. *Acta Med (Hradec Kralove)* (2010) 53(2):73–7. doi: 10.14712/18059694.2016.63

47. Kurtulus S, Sakuishi K, Ngiow SF, Joller N, Tan DJ, Teng MW, et al. TIGIT predominantly regulates the immune response *via* regulatory T cells. *J Clin Invest* (2015) 125(11):4053–62. doi: 10.1172/JCI81187

48. Melo V, Bremer E, Martin JD. Toward immunotherapy-induced normalization of the tumor microenvironment. *Front Cell Dev Biol* (2022) 10:908389. doi: 10.3389/fcell.2022.908389

49. Chauvin JM, Pagliano O, Fourcade J, Sun Z, Wang H, Sander C, et al. TIGIT and PD-1 impair tumor antigen-specific $CD8^+$ T cells in melanoma patients. *J Clin Invest* (2015) 125(5):2046–58. doi: 10.1172/JCI80445

50. Josefsson SE, Huse K, Kolstad A, Beiske K, Pende D, Steen CB, et al. T Cells expressing checkpoint receptor TIGIT are enriched in follicular lymphoma tumors and characterized by reversible suppression of T-cell receptor signaling. *Clin Cancer Res* (2018) 24(4):870–81. doi: 10.1158/1078-0432.CCR-17-2337

51. Dudley JC, Lin MT, Le DT, Sun Z, Wang H, Sander C, et al. Microsatellite instability as a biomarker for PD-1 blockade. *Clin Cancer Res* (2016) 22(4):813–20. doi: 10.1158/1078-0432.CCR-15-1678

52. Ge Z, Peppelenbosch MP, Sprengers D, Beiske K, Pende D, Steen CB, et al. TIGIT, the next step toward successful combination immune checkpoint therapy in cancer. *Front Immunol* (2021) 12:699895. doi: 10.3389/ fimmu.2021.699895

53. Tian X, Ning Q, Yu J, Dudley JC, Lin MT, Le DT, et al. T-Cell immunoglobulin and ITIM domain in cancer immunotherapy: A focus on tumor-infiltrating regulatory T cells. *Mol Immunol* (2022) 147:62–70. doi: 10.1016/j.molimm.2022.04.014

54. Blessin NC, Simon R, Kluth M, Fischer K, Hube-Magg C, Li W, et al. Patterns of TIGIT expression in lymphatic tissue, inflammation, and cancer. *Dis Markers* (2019) 2019:5160565. doi: 10.1155/2019/5160565

Glossary

Bladder Urothelial Carcinoma	BLCA
Colon adenocarcinoma	COAD
Colon adenocarcinoma/Rectum adenocarcinoma Esophageal carcinoma	COADREAD
Esophageal carcinoma	ESCA
Liver hepatocellular carcinoma	LIHC
Lung squamous cell carcinoma	LUSC
Rectum adenocarcinoma	READ
Skin Cutaneous Melanoma	SKCM
Stomach adenocarcinoma	STAD
Stomach and Esophageal carcinoma	STES
activated dendritic cells	DCs
advanced thyroid carcinoma	ATC
anaplastic thyroid carcinoma	ATC
bladder urothelial carcinoma	BLCA
cancer-associated fibroblasts	CAFs
cancer-associated fibroblasts	CAFs
China national knowledge infrastructure	CNKI
colon adenocarcinoma	COAD
colon adenocarcinoma/Rectum adenocarcinoma esophageal carcinoma	COADREAD
colorectal cancer	CRC
combined positive score	CPS
cytotoxic T-lymphocyte associated protein 4	CTLA4
defective DNA mismatch repair	dMMR
dendritic cells	DCs
disease free survival	DFS
disease-free survival	DFS
esophageal carcinoma	ESCA
esophageal squamous cell carcinoma	ESCC
follicular helper T cells	Tfh
gastric adenocarcinoma	GAC
gastric cancer	GC
Hepatitis B virus hepatocellular carcinoma	HBV-HCC
indoleamine 2 3-dioxygenase 1	IDO1
Interleukin 10	IL-10
liver hepatocellular carcinoma	LIHC
locally advanced papillary thyroid carcinoma	PTC
lung adenocarcinoma	LUAD
lung squamous cell carcinoma	LUSC
lymphocyte activating 3	LAG3
Microsatellite instability	MSI
muscle-invasive bladder cancer	MIBC
muscle-invasive bladder cancer	MIBC
myeloid-derived suppressor cells	MDSCs
myeloid-derived suppressor cells	MDSCs
natural killer	NK
Newcastle–Ottawa Quality Assessment Scale	NOS
non-small cell lung cancer	NSCLC
overall survival	OS
poorly differentiated thyroid carcinoma	PDTC
Preferred Reporting Items for Systematic Reviews and Meta-Analyses	PRISMA
primary small cell carcinoma of esophagus	PSCCE
programmed cell death 1 ligand 2	PDCD1LG2
programmed cell death 1	PDCD1
progression-free survival	PFS
Randomized controlled Trial	RCT
Rectum adenocarcinoma	READ
recurrence free survival	RFS
regulatory T cells	Tregs
skin cutaneous melanoma	SKCM
small cell lung cancer	SCLC
stomach adenocarcinoma	STAD
stomach and esophageal carcinoma	STES
structural recurrence free survival	SRFS
Thyroid carcinoma	THCA
transforming Growth Factor Beta 1	TGFB1
tumor infiltrating lymphocytes	TILs
tumor microenvironment	TME
tumor proportion score	TPS
tumor-associated macrophages	TAMs
tumor-associated neutrophils	TANs
tumor-associated neutrophils	TANs
V-set and immunoglobulin domain-containing protein 9	VSIG9
V-set and transmembrane do-main-containing protein 3	VSTM3
Washington University cell adhesion molecule	WUCAM
C-C Motif Chemokine Ligand 5	CCL5
C-X-C Motif Chemokine Ligand 9	CXCL9
C-C Motif Chemokine Ligand 4	CCL4
X-C Motif Chemokine Ligand 2	XCL2
C-X-C Motif Chemokine Ligand 13	CXCL13
C-X-C Motif Chemokine Ligand 10	CXCL10
C-X-C Motif Chemokine Ligand 11	CXCL11
X-C Motif Chemokine Ligand 1	XCL1
C-C Motif Chemokine Ligand 19	CCL19
CC Motif Chemokine Ligand 22	CCL22
C-C Motif Chemokine Ligand 18	CCL18
C-C Motif Chemokine Ligand 21	CCL21
C-C Motif Chemokine Ligand 23	CCL23
C-C Motif Chemokine Ligand 3	CCL3
C-C Motif Chemokine Ligand 8	CCL8
C-C Motif Chemokine Ligand 13	CCL13
CC Motif Chemokine Ligand 20	CCL20
C-C Motif Chemokine Ligand 24	CCL24

(Continued)

Continued

(Continued)

Continued

C-X-C Motif Chemokine Ligand 16	CXCL16
C-C Motif Chemokine Ligand 2	CCL2
C-X-C Motif Chemokine Ligand 12	CXCL12
C-C Motif Chemokine Ligand 17	CCL17
C-C Motif Chemokine Ligand 1	CCL1
C-C Motif Chemokine Ligand 7	CCL7
C-C Motif Chemokine Ligand 11	CCL11
C-C Motif Chemokine Ligand 27	CCL27
C-X-C Motif Chemokine Ligand 17	CXCL17
C-C Motif Chemokine Ligand 25	CCL25
C-X3-C Motif Chemokine Ligand 1	CX3CL1
C-C Motif Chemokine Ligand 14	CCL14
C-C Motif Chemokine Ligand 16	CCL16
C-X-C Motif Chemokine Ligand 5	CXCL5
C-X-C Motif Chemokine Ligand 2	CXCL2
C-X-C Motif Chemokine Ligand 3	CXCL3
C-C Motif Chemokine Ligand 26	CCL26
C-X-C Motif Chemokine Ligand 8	CXCL8
C-X-C Motif Chemokine Ligand1	CXCL1
C-X-C Motif Chemokine Ligand 6	CXCL6
C-C Motif Chemokine Ligand 15	CCL15
C-C Motif Chemokine Ligand 28	CCL28
C-X-C Motif Chemokine Ligand 14	CXCL14
X-C Motif Chemokine Receptor 1	XCR1
C-C Motif Chemokine Receptor 1	CCR1
C-C Motif Chemokine Receptor 2	CCR2
C-C Motif Chemokine Receptor 8	CCR8
CCMotif Chemokine Receptor 4	CCR4
C-C Motif Chemokine Receptor 7	CCR7
C-X-C Motif Chemokine Receptor 3	CXCR3
C-C Motif Chemokine Receptor 5	CCR5
C-X-C Motif Chemokine Receptor 6	CXCR6
C-C Motif Chemokine Receptor 6	CCR6
C-X-C MotifChemokine Receptor 4	CXCR4
C-X-C Motif Chemokine Receptor 1	CXCR1
C-X-C Motif Chemokine Receptor 2	CXCR2
C-C Motif Chemokine Receptor 10	CCR10
C-X-C Motif Chemokine Receptor 5	CXCR5
C-C Motif Chemokine Receptor 9	CCR9
C-C Motif Chemokine Receptor 3	CCR3
C-X3-C Motif Chemokine Receptor 1	CX3CR1
Major Histocompatibility Complex Class I E	HLA-E
Transporter 1 ATP Binding Cassette Subfamily B Member	TAP1
Major Histocompatibility Complex Class I B	HLA-B
Beta-2-Microglobulin	B2 M
Major Histocompatibility Complex Class I F	HLA-F
Major Histocompatibility Complex Class II DM Beta	HLA-DMB
Major Histocompatibility Complex Class II DO Beta	HLA-DOB
Major Histocompatibility Complex Class II DM Alpha	HLA-DMA

(Continued)

Continued

Major Histocompatibility Complex Class II DR Beta 1	HLA-DRB1
Major Histocompatibility Complex Class II DQ Alpha 1	HLA-DQA1
Major Histocompatibility Complex Class II DO Alpha	HLA-DOA
Major Histocompatibility Complex Class II DP Alpha 1	HLA-DPA1
Major Histocompatibility Complex Class II DP Beta 1	HLA-DPB1
Major Histocompatibility Complex Class II DR Alpha	HLA-DRA
Major Histocompatibility Complex Class I G	HLA-G
Major Histocompatibility Complex Class II DQ Alpha 2	HLA-DQA2
Major Histocompatibility Complex Class II DQ Beta 1	HLA-DQB1
Transporter 2 ATP Binding Cassette Subfamily B Member	TAP2
TAP Binding Protein	TAPBP
Major Histocompatibility Complex Class I A	HLA-A
Major Histocompatibility Complex Class I C	HLA-C
T-Cell Immunoreceptor With Ig And ITIM Domains	TIGIT
CD96 Molecule	CD96
Programmed Cell Death 1	PDCD1
Cytotoxic T-Lymphocyte Associated Protein 4	CTLA4
B And T Lymphocyte Associated	BTLA
CD244 Molecule	CD244
Programmed Cell Death 1 Ligand 2	PDCD1LG2
Hepatitis A Virus Cellular Receptor 2	HAVCR2
Lymphocyte Activating 3	LAG3
Adenosine A2a Receptor	ADORA2A
Colony Stimulating Factor 1 Receptor	CSF1R
Interleukin 10	IL10
CD274 Molecule	CD274
Indoleamine 2, 3-Dioxygenase 1	IDO1
Galectin 9	LGALS9
CD160 Molecule	CD160
Killer Cell Immunoglobulin	

frontiers | Frontiers in Immunology

TYPE Original Research
PUBLISHED 01 November 2022
DOI 10.3389/fimmu.2022.974916

OPEN ACCESS

EDITED BY
Liusheng Peng,
Third Military Medical University, China

REVIEWED BY
Jiandong Guo,
Hangzhou Ninth People's Hospital, China
Wenjian Hu,
Southwest Medical University, China

*CORRESPONDENCE
Hong Wang
wanghong@dmu.edu.cn

†These authors have contributed equally to this work

SPECIALTY SECTION
This article was submitted to Cancer Immunity and Immunotherapy, a section of the journal Frontiers in Immunology

RECEIVED 21 June 2022
ACCEPTED 23 September 2022
PUBLISHED 01 November 2022

CITATION
Han J, Hu Y, Ding S, Liu S and Wang H (2022) The analysis of the pyroptosis-related genes and hub gene TP63 ceRNA axis in osteosarcoma. *Front. Immunol.* 13:974916. doi: 10.3389/fimmu.2022.974916

The analysis of the pyroptosis-related genes and hub gene TP63 ceRNA axis in osteosarcoma

Jun Han[1,2†], Yunxiang Hu[1,2†], Shengqiang Ding[3†], Sanmao Liu[1,2] and Hong Wang[2*]

[1]School of Graduates, Dalian Medical University, Dalian, China, [2]Department of Orthopedics, Dalian Municipal Central Hospital, Dalian City, China, [3]Department of Spine Surgery, The People's Hospital of Liuyang City, Changsha, China

Pyroptosis is a type of programmed cell death that is associated with tumor development, prognosis, and therapeutic response. The significance of pyroptosis-related genes (PRGs) in the tumor microenvironment (TME) remains unclear. We examined the expression patterns of PRGs in 141 OS samples from two different datasets and characterized the genetic and transcriptional changes in PRGs. Based on these PRGs, all OS samples could be classified into two clusters. We discovered that multilayer PRG changes were linked to clinicopathological traits, prognosis, and TME characteristics in two separate genetic subtypes. The PRG score was then developed for predicting overall survival, and its predictive efficacy in OS patients was tested. As a result, we developed a very precise nomogram to improve the PRG-predictive model in clinical application. Furthermore, a competing endogenous RNA (ceRNA) network was built to find a LAMTOR5-AS1/hsa-miR-23a-3p/TP63 regulatory axis. Through experimental verification, it was found that the pyroptosis gene TP63 plays an important role in the regulation of osteosarcoma pyroptosis. The possible functions of PRGs in the TME, clinicopathological characteristics, and prognosis were established in our investigation of PRGs in OS. These findings may aid in our understanding of PRGs in OS as well as provide a novel way for prognostic evaluation and the creation of more effective immunotherapy treatments.

KEYWORDS

pyroptosis, osteosarcoma, TP63, ceRNA, immunotherapy, tumor microenvironment

Introduction

Osteosarcoma (OS) is the most common primary malignant bone tumor in children and young adults, usually occurring in the metaphysis of long bones (1). Patients with localized tumor present a 5-year survival rate of 60%, while those with metastatic tumor have a 5-year survival rate of only 20% (2). Despite the current standard treatment for primary bone osteosarcoma, which consists of neoadjuvant chemotherapy and surgery, the survival rate has significantly improved, and its treatment outcomes are unfavorable owing to tumor invasion and metastasis (3). Therefore, defining a novel prognostic gene markers model of OS is imperative for improving the overall survival of OS patients.

Pyroptosis is a type of programmed cell death caused by inflammation, which is unusual compared to other kinds of programmed cell death (4). The cleavage of the gasdermin family characterizes pyroptotic cells through classical pathways, non-classical pathways, the caspase-3/8-mediated pathway, and the granzyme-mediated pathway, followed by the cell membrane ruptures and the release of the cell contents (5). Many studies indicated that pyroptosis plays a pivotal role in the pathogenesis and progression of multiple cancers. However, pyroptosis is complicated in cancers and exhibit cancer-inhibiting or cancer-promoting activities in different cancers (6, 7). Previous studies also indicate that there are associations between pyroptosis and the tumor microenvironment (TME) (8, 9). Especially, a wide variety of immune cell types are involved in the TME, primarily lymphocytes, dendritic cells, macrophages, mast cells, neutrophils, and myeloid-derived suppressor cells (10, 11). These cells can inhibit tumor progression by recognizing and killing tumor cells. Thus, immunotherapy has emerged as an effective therapeutic approach to killing tumor cells by activating immune responses (12, 13). However, as compared to other cancers, there have been fewer investigations into immunotherapy for OS. Hence, a comprehensive analysis of the TME mediated by pyroptosis-related genes (PRGs) may be more helpful to understand the underlying mechanism of OS tumorigenesis and guide clinical therapy.

We used the RNA sequencing data of OS patients and normal muscle-skeletal tissues downloaded from the Therapeutically Applicable Research to Generate Effective Treatments (TARGET) and Genotype-Tissue Expression (GTEx) databases to construct a tumor vs. normal datasets for identifying differentially expressed PRGs (DEPRGs). We identified two pyroptosis-related subtypes of OS according to DEPRGs. In addition, two advanced computational algorithms gave us a comprehensive view of the immune cell infiltration landscape of OS: the Cell-type Identification By Estimating Relative Subsets Of RNA Transcripts (CIBERSORT) and Estimation of Stromal and Immune cells in Malignant Tumor tissues using Expression data (ESTIMATE). Furthermore, we constructed a five-gene signature (PRG_score) by using the LASSO–Cox method to predict prognosis, immune infiltration, and chemotherapy drugs. Lastly, we constructed a PRG competing endogenous RNA (ceRNA) network and found one hub gene in the pyroptosis regulation of OS cells.

Materials and methods

OS data source and preprocessing

The RNA sequencing data, clinical information, and copy number variation (CNV) data of osteosarcoma patients were downloaded from the TARGET-OS database (https://xenabrowser.net/datapages/), and the RNA sequencing data of 396 normal human muscle-skeletal tissue samples were downloaded from the GTEx database (https://xenabrowser.net/datapages/). Two datasets are fragments per kilobase million (FPKM) value, and the expression data were normalized to log2 (FPKM + 1) before merging the two datasets. The microarray datasets of GSE21257 (53 OS patients) were downloaded from the Gene Expression Omnibus (GEO) database (https://www.ncbi.nlm.nih.gov/geo/). Because the expression profile data of the TARGET dataset (FPKM value) were significantly different from the microarray data (transcripts per kilobase million, TPM), we transformed the TARGET data into TPMs by the "limma" R package. Then, we merged TARGET and GEO into a dataset including 141 OS patients. The "combat" algorithm of the "sva" package was applied to address the batch effects caused by non-biological technical biases. Further analysis was not conducted on patients without survival information.

Identification of DEPRGs and consensus clustering analysis

A total of 52 PRGs were retrieved from the MSigDB Team (REACTOME_PYROPTOSIS) (http://www.broad.mit.edu/gsea/msigdb/) and prior reviews, which are shown in Table S1 (6, 14–17). The "limma" package was used to determined DEPRGs by setting the cutoff criteria as p-value <0.05. After merging the RNA expression of the TARGET cohort and GEO cohort into a dataset with 141 OS patients, consensus clustering analysis was performed to identify distinct pyroptosis patterns based on the expression of PRGs and cluster the 141 OS patients for further analysis. The number of PRGclusters and their stability were determined by increasing the "k" index from 2 to 9 using the R package "ConsensuClusterPlus."

Functional enrichment analyses

To study the differences in PRGcluster in biological processes, the "GSVA," "limma," and "pheatmap" R packages were used to perform enrichment analysis in a heatmap with the hallmark gene

set (c2.cp.kegg.v7.2) downloaded from the MSigDB database (https://www.gsea-msigdb.org). The single-sample gene set enrichment analysis (ssGSEA) has been conducted using the R package "GSVA" to calculate the scores of infiltrating immune cells. We identified DEGs between PRGclusters using the "limma" package. The Gene Ontology (GO) and Kyoto Encyclopedia of Genes and Genomes (KEGG) analyses were performed by applying the "clusterProfiler" package based on the DEGs between PRGclusters, with p-value <0.05.

Immune infiltration analysis

CIBERSORT was applied to estimate the relative abundance of 22 tumor-infiltrating immune cell subtypes in each sample of the TARGET and GEO cohorts using the R package. The ESTIMATE algorithm was exploited to determine the fractions of stromal and immune cells in tumor samples of the TARGET and GEO cohorts using the "estimate" R package.

The establishment of the pyroptosis score model and prognostic analysis

The pyroptosis score system was established to quantify the pyroptosis patterns of the OS patients. The method of constructing the pyroptosis score system is as follows: the DEGs of different PRGclusters were subjected to univariate Cox regression analysis where p-value <0.05 was considered statistically significant. The TARGET and GEO cohorts were randomly divided into training set and testing set with a proportion of 1:1 by using the "caret" package. After that, by using Least Absolute Shrinkage and Selection Operator (LASSO) regression, we were able to further compress the screened genes and eventually identified a novel gene signature. Using the LASSO regression results, we developed a prognostic risk score formula, which was calculated as follows: Risk score = patient × i Coefficient (mRNAi) × Expression (mRNAi). The training set, testing set, and all sets were classified into low and high PRG-score groups. The efficiency of the model was determined by the Kaplan–Meier method and time-dependent receiver operating characteristic (ROC) curve constructed with the "SurvivalROC" package. The clinical characteristics (gender, age, and metastasis) of patients were extracted from the TARGET cohort and the GEO cohort to construct a nomogram to predict the overall survival of OS patients after 1, 3, and 5 years.

PRG competing endogenous RNA network construction

Different-expression pyroptosis-related mRNAs (DEPRMs), different-expression miRNAs (DEMis), and different-expression lncRNAs (DELs) between the TARGET samples and matching GTEx normal samples were identified using the limma package. The adjusted p-value of DEMs, DEMis, and DELs was defined as <0.05, and the log2 fold changes (|log2FC|) of DEMs and DELs were defined as >1 and 2, respectively. The weighted gene co-expression network analysis (WGCNA) package in R software was used to create gene co-expression networks based on DEMs, DEMis, and DELs. First, outliers in samples with low expression data were identified and eliminated. Following that, the mean connectivity and scale-free fit index for numbers 1–30 [as soft-threshold power (β)] were determined individually, with the best result determining the adjacency matrix's co-expression similarity. The estimated correlation matrix (based on Pearson's correlation) was then transformed to an adjacency matrix, and a topological overlap matrix (TOM) was constructed, which takes into account indirect gene interactions. The negative interactions of miRNA–mRNA and miRNA–lncRNA were used to make the lncRNA–miRNA–mRNA network, which was constructed by using Cytoscape 3.5.1 (www.cytoscape.org/) based on co-expression WGCNA data. The Cytoscape "plugin molecular complex detection" (MCODE) was used to find the most relevant subnetworks, using the following cutoff value: node score cutoff = 0.2, degree cutoff = 2, max depth = 100, and k-core = 2. To construct a PRG ceRNA network, the starBase database (starBase, v2.0, http://starbase.sysu.edu.cn/) was further applied to identify the potential relationship of lncRNA–miRNA–mRNA.

Cell culture and transfection

The ScienCell Research Laboratories (USA) provided two OS cell lines (143B and U2OS). Cell lines were cultured at 37°C in Dulbecco's modified Eagle's medium (Gibco, USA) supplemented with 10% (v/v) fetal bovine serum (Invitrogen, USA) in a 5% CO_2 atmosphere. The four types of pGPU6/GFP/Neo vector shRNA targeting TP63 and the three types of Lamtor-AS1 siRNA (GenePharma, Shanghai, China) were transfected by Lipo3000 (Invitrogen, USA) according to the manufacturer's protocol. Sequences of siRNA and shRNA are shown in Table S2. The experiments were implemented in three groups as follows: the knockdown group (cells transfected with siRNA or shRNA), the NC group (cells transfected with NC), and the control group (untransfected cells).

Quantitative real-time PCR

Quantitative real-time PCR (qRT-PCR) was used to determine the relatively higher knockdown efficiency of shRNA and siRNA for further experiments. Total RNA was extracted from OS cells using TRIpure Reagent (Bioteke, Beijing, China). The BeyoRT II M-MLV Reverse Transcriptase

(Beyotime Biotechnology, Shanghai, China) and RNase inhibitor (Bioteke, Beijing, China) were used for reverse transcription. The 2×Taq PCR MasterMix and SYBR Green (Solarbio, Beijing, China) were employed to carry out the qRT-PCR assay. In order to normalize lncRNA and mRNA expression, β-actin was used as an endogenous control. $2^{-\Delta\Delta Ct}$ was used to calculate the relative expression level of the target RNA. Table S3 lists the primers used for target RNA amplification.

Western blotting

The cells were harvested in RIPA Lysis Buffer and lysed using ultrasound (Wanleibio, Shenyang, China). BCA Reagent was used to determine total protein content (Wanleibio, Shenyang, China). SDS-PAGE (Wanleibio, Shenyang, China) was used to separate equivalent quantities of protein extract, which was then deposited onto PVDF membranes (Millipore, USA). Cleaved-Caspase-1 (Wanleibio, Shenyang, China), cleaved-Caspase-3 (Wanleibio, Shenyang, China), cleaved-Caspase-4 (Affinity Biosciences, Suzhou, China), cleaved-Caspase-8 (Affinity Biosciences, Suzhou, China), GSDMD (Affinity Biosciences, Suzhou, China), GSDME (ABclonal, Wuhan, China), and GSDMD-N (Affinity Biosciences, Suzhou, China) were the primary antibodies employed in this test. After blocking with 5% skim milk for an hour, the membranes were incubated overnight with primary antibodies at 4°C. The membranes were then incubated with HRP-conjugated secondary antibodies (Wanleibio, Shenyang, China) and detected using an enhanced chemiluminescence substrate kit (Wanleibio, Shenyang, China) after washing.

Statistical analysis

Statistical comparisons between groups were made using the Student's *t*-test. Data were provided as mean and standard deviation. Statistical significance was defined as a p value of less than 0.05. SPSS V. 26.0 (IBM, NY, USA) was used to conduct all statistical tests.

Results

Genetic variation and expression of PRGs in OS

We compared the 52 PRG expression levels between human OS samples (TARGET) and normal muscle-skeletal tissues (GTEx) and found that 46 PRGs expressed differently (p-value < 0.05) (Figure 1A). To evaluate the levels of CNV among OS patients, we analyzed the CNV data from TARGET. Figure 1B shows that CHMP4A, GSDMD, GZMB, and GSDMC represented the highest frequency of CNV gain and TP53, CHMP2B, CASP3, and IRF2 represented the highest frequency of CNV loss. Also, we located the 12 PRGs with CNVs on their respective chromosomes (Figure 1C). In the correlation analysis between PRG CNV and PRG RNA sequence expression, CHMP7, CHMP2B, TIRAP, and CHMP3 had the strongest correlation with their CNV (Figure 1D). After integrating the data of survival time and gene expression of the TARGET cohort and GEO cohort, the expressions of 28 PRGs were obtained from 141 patients (Table S4). We performed Kaplan–Meier (K–M) survival curve analysis on the PRGs, and the results indicated that the most abnormal expression of PRGs was significantly related to the prognosis of OS patients. The high expression of CASP5, CHMP4A, CHMP4C, and HMGB1 correlated with patients' poor prognosis. The high expression of AIM2, BAK1, CASP1, CASP6, CHMP2A, CHMP4B, CHMP6, CHMP7, GPX4, GZMA, GZMB, and IL1B correlated with patients' better prognosis (Figure 1E). The comprehensive landscape of PRG correlation and prognostic value in patients with OS was demonstrated in a prognosis network by a univariate Cox regression analysis and co-expression analysis (Figure 1F). The results were consistent with the K–M survival analysis showing that CASP4, CASP5, CHMP4A, CHMP4C, HMGB1, and IRF2 were risk factors for OS patients.

Identification of pyroptosis clusters mediated by 28 pyroptosis-related regulators

We obtained 28 PRG expression levels of the cohort consisting of two OS datasets (TARGET, GEO). Based on the 28 PRG expression levels, two different OS patterns were determined by using the unsupervised clustering method (k = 2), including 76 cases in PRGcluster A and 65 cases in PRGcluster B (Figure 2A). The two-dimensional principal component analysis (PCA) biplots showed significant differences between the pyroptosis transcription profiles of the two subtypes (Figure 2B). The K–M curve revealed that the overall survival rate of PRGcluster A is better than that of PRGcluster B (p-value < 0.05) (Figure 2C). There is no significant difference in the clinicopathological features of these two different clusters (Figure 2D). The ssGSEA algorithm was employed to estimate the relative infiltration of 24 intratumoral immune cell types for 141 OS samples. We found that PRGcluster A was remarkably richer in the infiltration of most immune cells than PRGcluster B. The infiltration levels of B cell, CD8 T cell, dendritic cell, MDSC, macrophage, mast cell, killer T cell, natural killer cell, plasmacytoid dendritic cell, regulatory T cell, T follicular helper cell, and type 1 T helper cell were higher in PRGcluster A than those in PRGcluster B, while that of CD56dim natural killer cell in PRGcluster A was lower than in PRGcluster B (Figure 2E). We performed GSVA enrichment analysis to reveal the regulation pathways in which PRGcluster A was significantly enriched in immune response-related pathways, including NOD-like receptor signaling pathway, B-cell receptor signaling pathway, T-cell

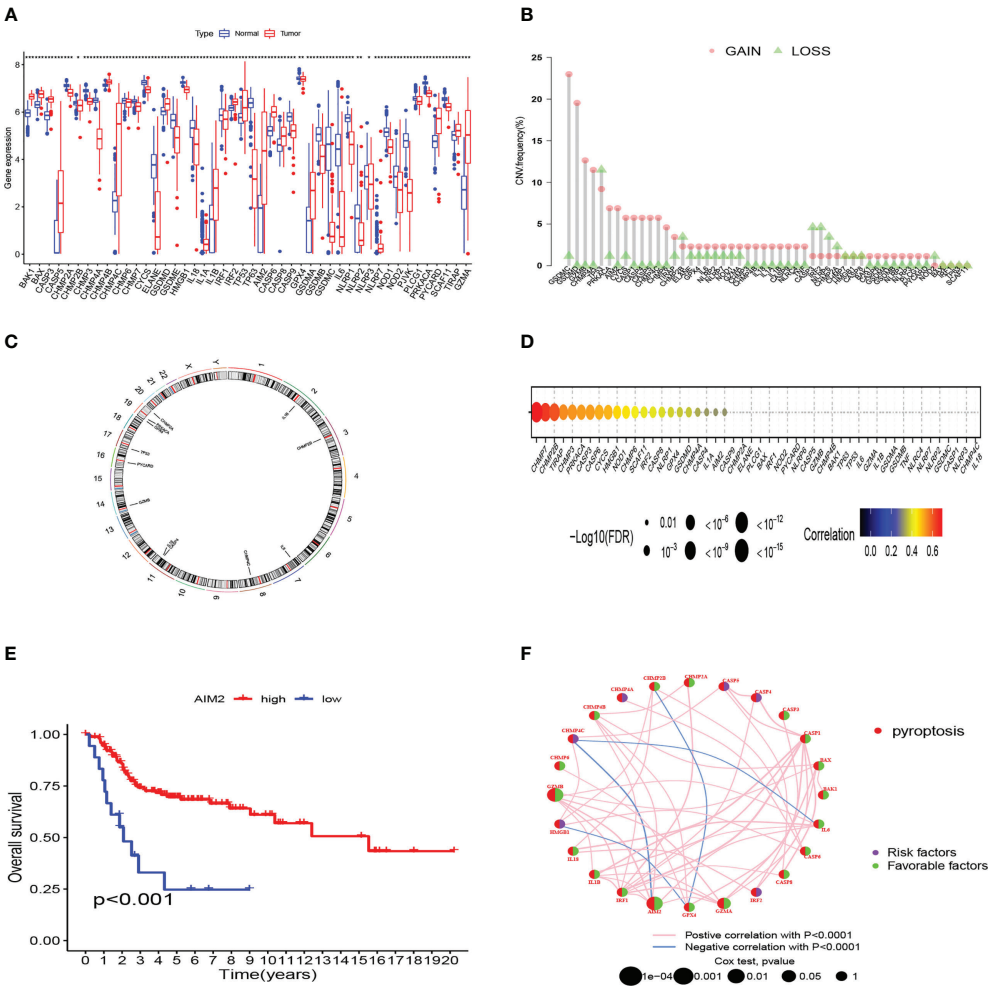

FIGURE 1
Genetic and transcriptional characteristics of PRGs in OS. **(A)** The differential expression of 46 PRGs between normal and OS tissues. (***:p value <0.001, **:p value <0.01, *:p value <0.05) **(B)** CNV frequency of PRGs in the TARGET cohort. **(C)** Locations of CNV alterations of PRGs on 23 chromosomes by the TARGET cohort. **(D)** The correlation analysis between CNV of PRGs and RNA sequence expression of PRGs in the TARGET cohort. **(E)** The K-M curves of AIM2 gene in OS. **(F)** Prognosis value and correlations between PRGs in OS. The line linking the PRGs is their correlation. PRGs, pyroptosis-related genes; OS, osteosarcoma; CNV, copy number variations.

receptor signaling pathway, natural killer cell-mediated cytotoxicity, chemokine signaling pathway, primary immunodeficiency, and cytokine receptor interaction (Figure 2F). On the basis of the above analysis, PRGcluster A was classified as an immunoinflammatory phenotype, characterized by adaptive immune cell infiltration and immune activation, whereas PRGcluster B was classified as immune-excluded phenotype.

Generation of gene subtypes based on PRG clusters

To further define the potential biological function of different pyroptosis clusters, 453 PRGcluster-related DEGs were identified between PRGcluster A and PRGcluster B (Table S5). The functional enrichment analysis were performed to indicate that these DEGs were enriched in biological processes of GO and cytokine receptor interaction, cell adhesion molecules, and chemokine signaling pathway of KEGG, which were correlated with immune response regulation (Figures 3A, B). After that, to identify the prognostic value of 453 DEGs, a univariate Cox regression analysis was conducted, and 189 prognostic genes were screened out (Table S6). Based on 189 prognostic genes, 141 patients with OS were classified into three genomic subtypes using a consensus clustering algorithm to understand the intrinsic regulation mechanism: geneClusters A, B, and C (Figure S1). The expressions of PRGs in the three gene clusters were significantly different (Figure 3C). The differences were significant in survival time among the three gene clusters ($p < 0.001$), and the results of the K–M survival curves showed that geneCluster A had the best survival, and geneCluster B

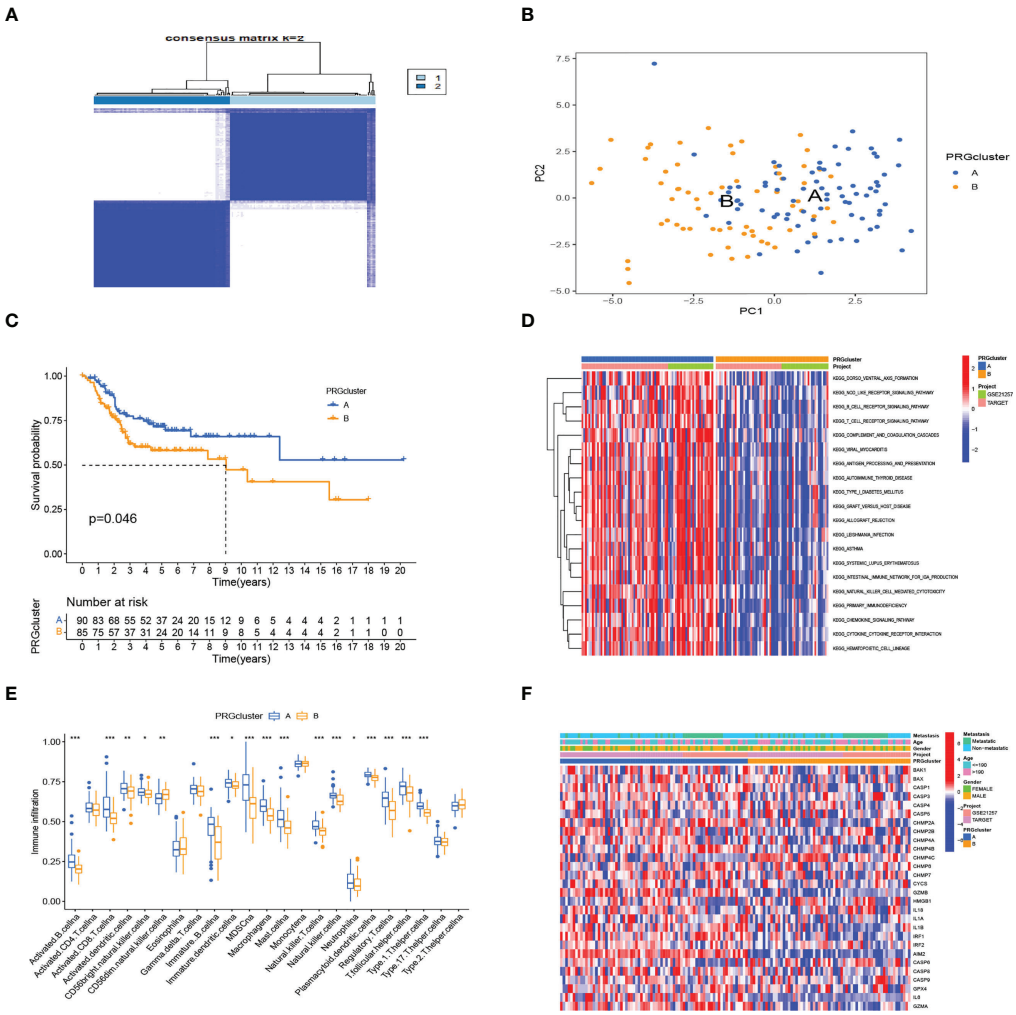

FIGURE 2
Subtypes of OS divided by pyroptosis-related regulators. **(A)** Consensus matrix heatmap defining two clusters (k = 2) in the TARGET and GSE21257 cohorts. **(B)** PCA of the expression of PRGs indicating a significant difference between the two clusters. **(C)** Kaplan–Meier analysis showing the survival of the two clusters. **(D)** Differences in characteristics of clinicopathology and PRG expression levels among two clusters. **(E)** In the two subtypes, the tumor infiltration of 24 immune cell types. (***:p value <0.001, **:p value <0.01, *:p value <0.05) **(F)** The heatmap was used to depict the active biological pathways in different pyroptosis-related clusters, which were examined by GSVA. OS, osteosarcoma; PRGs, pyroptosis-related genes.

was significantly related to poor prognosis (Figure 3D). The heatmap shows the correlation of clinical characteristics, pyroptosis clusters, and gene clusters. The different gene expression profiles were observed between geneCluster A, geneCluster B, and geneCluster C (Figure 3E).

Construction and validation of the prognostic PRG_score

The alluvial diagram illustrates the changes in the attributes of patients in the two pyroptosis clusters, three gene clusters, and two PRG_score groups (Figure 4A). We established a pyroptosis-related signature score to quantify each patient based on the 189 prognostic genes, which was named as PRG_score. The patients were randomly divided into training (n = 69) and testing (n = 69) groups using the "caret" package. Next, a signature with seven of the 189 prognosis genes was obtained by application of LASSO–Cox regression with a minimum of lambda value (Figure 4B). A stepwise multivariate Cox regression was then performed to analyze seven prognosis genes, finally obtaining five genes (CORT, CPB1, ARMC4, CATSPER1, CD79A; Table S7). The outcomes of the multivariate Cox regression analysis showed that PRG_score was constructed as follows: Risk score = (0.601670827227929*expression of CORT) + (-1.39124104164683 *expression of CPB1) + (0.470462955630426*expression of

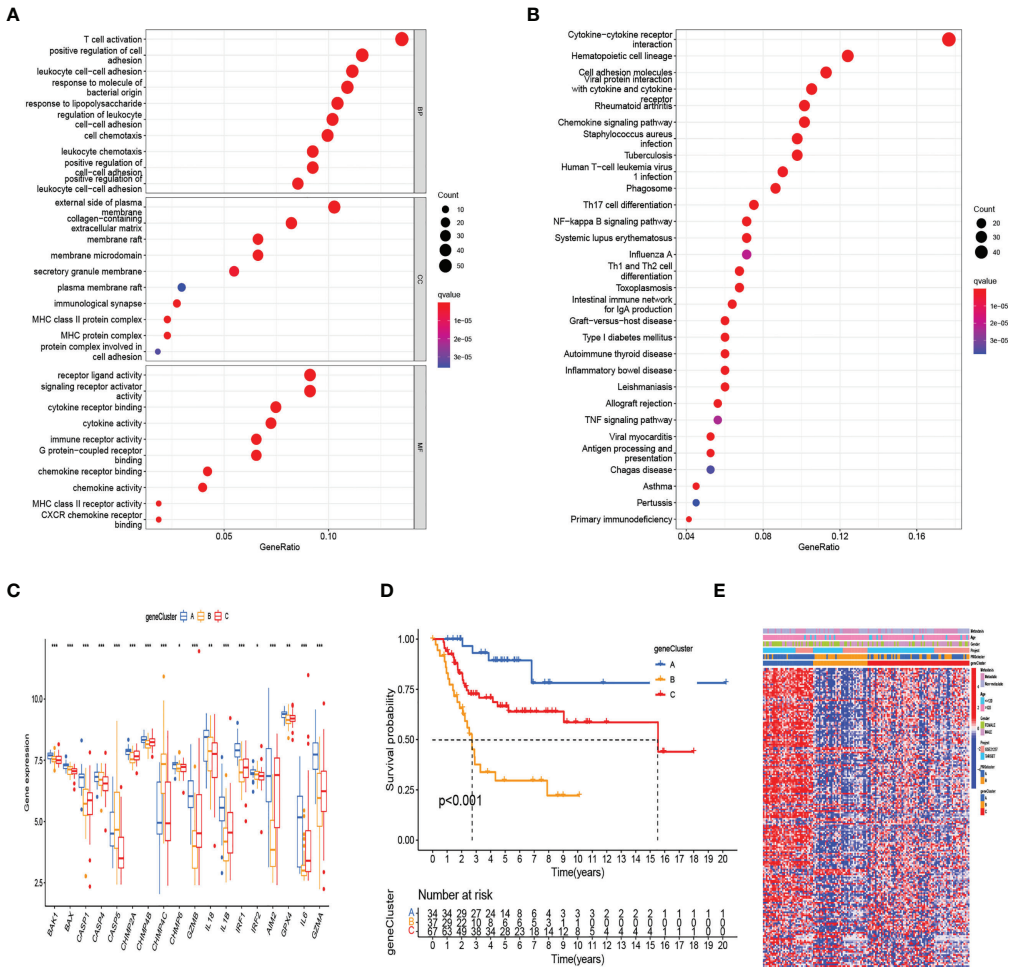

FIGURE 3
Identification of gene subtypes based on DEGs between two RRG clusters. **(A, B)** The functional enrichment analysis of DEGs among two PRGclusters. **(C)** The differential expressions of 18 PRGs among the three gene subtypes. (***:p value <0.001, **:p value <0.01, *:p value <0.05) **(D)** Kaplan–Meier analysis for overall survival of the three gene subtypes. **(E)** Relationships between clinicopathologic features and the two gene subtypes. DEGs, differentially expressed genes; PRGs, pyroptosis-related genes.

ARMC4) + (-0.762527227347988*expression of CATSPER1) + (-1.10584366215719 *expression of CD79A). PRGcluster A had a lower PRG_score than PRGcluster B, which indicated that a lower PRG_score might be associated with immune inducing function (Figure 4C). In addition, a significant difference was represented in PRG_scores among geneClusters. PRG_score was the lowest in geneCluster A (Figure 4D). Through the "survminer" program to find the median risk score based on the training group, the patients with PRG_score higher than the median risk score were classified into the low-risk group, whereas those with PRG_score lower than the median risk score were identified into the high-risk group. The survival status plot of the training group revealed that survival times decreased with an increase in PRG_scores (Figures 4E, F). The Kaplan–Meier plots show that the overall survival of the high-risk group is significantly shorter than the low-risk group ($p = 0.019$) (Figure 4G). The ROC curves of PRG_score showed that the 1-, 3-, and 5-year survival rates were represented by AUC values of 0.730, 0.878, and 0.867, respectively (Figure 4H). For the purpose of validating PRG_score's stability, the testing group and the all-patient group were used as validation groups. Based on the median risk score in the training cohort, the patients in the testing group and all-patient group were also classified into low- and high-risk groups, respectively. It was shown that the low-risk subgroup represents lower death rates and longer survival times than those in the high-risk subgroup. Kaplan–Meier curve analysis also revealed a significantly better survival in the low-risk group compared to that in the high-risk group. ROC curve analysis showed that PRG_score had relatively high AUC values and predicted the survival of OS patients excellently (Figure S2). We also evaluated the correlation between PRGs and our risk model. Fourteen pyroptosis genes were differentially expressed in the high-risk and low-risk groups (Figure 4I).

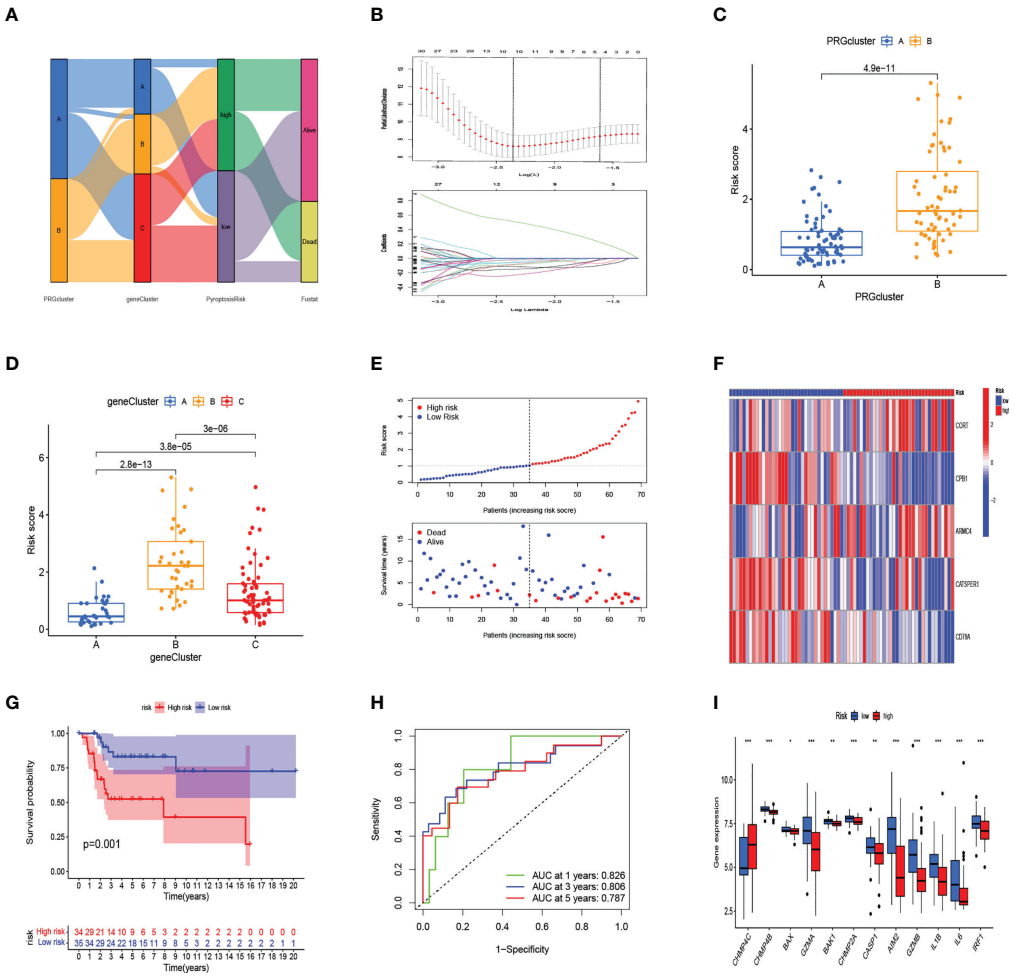

FIGURE 4
In the training set, generation of PRG_score to predict patient survival. **(A)** Alluvial diagram of pyroptosis-related clusters in groups with different geneClusters, PRG_score, and overall survival. **(B)** The minimal standard was used in the LASSO−Cox model to obtain the value of the super parameter *via* 10-fold cross-validation. **(C)** The differences in PRG_score between PRGclusters. **(D)** The differences in PRG_score between geneClusters. **(E)** Ranked dot and scatter plots showing PRG score distribution and survival status. **(F)** The expression heatmap of the five-gene signature in the training group. **(G)** Kaplan−Meier analysis of the survival between the high- and low-risk groups. **(H)** The prognostic accuracy of the risk scores in the training group was verified by the ROC curve. **(I)** Expression of PRGs in the high- and low-risk groups. (***:p value <0.001, **:p value <0.01,*:p value <0.05) PRG, pyroptosis-related gene; ROC, receiver operating characteristic.

The clinical prediction and immune infiltration of PRG_score

Considering that PRG_score was important in predicting the prognosis of OS patients, a nomogram incorporating the clinicopathological features and PRG_score was constructed to predict the survival rates of OS patients at 1, 3, and 5 years (Figure 5A). The predictive nomogram included PRG_score, age, gender, and metastasis. The calibration curves suggested that the predictors had a good predictive value (Figure 5B). Next, we investigated whether PRG_score has an instructive significance for immunotherapy. We used the CIBERSORT algorithm to assess the correlation of PRG_score and immune cell infiltration. The scatter diagrams showed that PRG_score was negatively correlated with CD8 + T cells, activated memory CD4 + T cells, monocytes, neutrophils, M2 macrophages, and memory B cells and positively correlated with M0 macrophages and naive B cells (Figure S3). We also examined the correlation between the five genes in the proposed model and the proportion of immune cells. We discovered that CD8 + T cells, monocytes, M2 macrophages, memory B cells, M0 macrophages, and naive B cells were mainly correlated with the five genes (Figure 5C). The ImmuneScore, StromalScore, and ESTIMATEScore of each of the OS samples were determined using the ESTIMATE

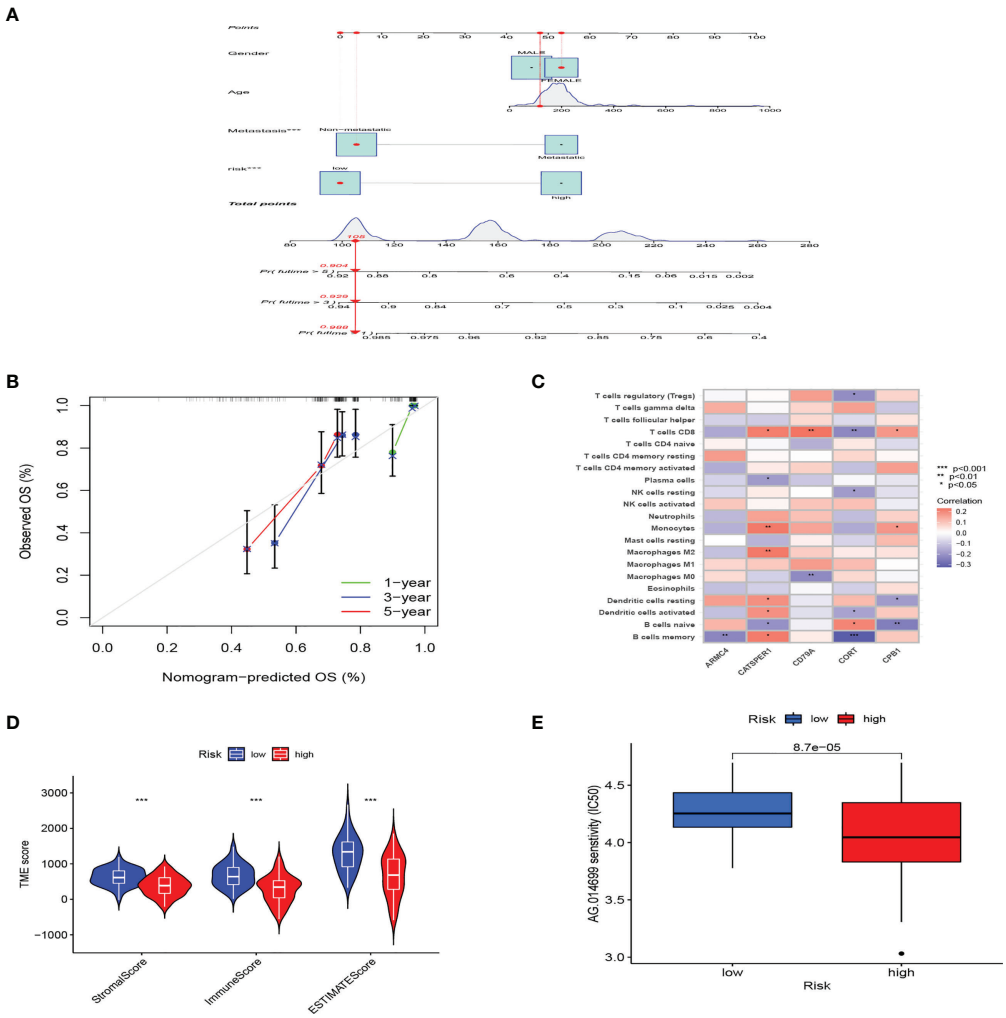

FIGURE 5
The clinical application value of PRG_score and evaluation of the TME of different subgroups. **(A)** In the training group, nomogram for predicting the 1-, 3-, and 5-year survival of OS patients. **(B)** In the training group, calibration curves of the nomogram for predicting of 1-, 3-, and 5-year overall survival. **(C)** Correlation analysis among the tumor infiltrations of immune cells and five genes in the risk model. **(D)** Correlations between PRG_score and TME scores. (***:p value <0.001). **(E)** PRG score and chemotherapeutic sensitivity relationships. PRG, pyroptosis-related gene; TME, tumor microenvironment; OS, osteosarcoma.

algorithm. Figure 5D represents that PRG_scores were negatively correlated with the ImmuneScore, StromalScore, and ESTIMATEScore, which indicated that the survival of OS patients is influenced by immune cells and stromal cells. Lastly, we looked at the sensitivity of patients in the low- and high-risk groups to a variety of chemotherapeutic agents presently used to treat OS. Patients with low PRG scores had lower IC50 values for chemotherapeutics such as roscovitine, RDEA119, rapamycin, and shikonin, while patients with high PRG scores had considerably lower IC50 values for axitinib, elesclomol, GW.441756, and thapsigargin (Figures 5E, S4). These findings demonstrated that PRGs were linked to pharmaceutical sensitivity.

PRG competing endogenous RNA network construction

Between 88 OS samples and 396 normal samples, the expression patterns of 52 pyroptosis-related mRNAs, miRNAs, and lncRNAs were determined. A total of 18 pyroptosis-related mRNAs, 53 lncRNAs, and 234 miRNAs were found to be differentially expressed (Tables S8–S10). Overexpressed genes included nine pyroptosis-related mRNAs, six lncRNAs, and 100 miRNAs. Nine pyroptosis-related mRNAs, 47 lncRNAs, and 134 miRNAs were all found to be underexpressed. Figure 6A depicts the heatmap of clustering analysis of the analyzed RNA. A ceRNA network of the DEls, DEMis, and DEPRMs was constructed using

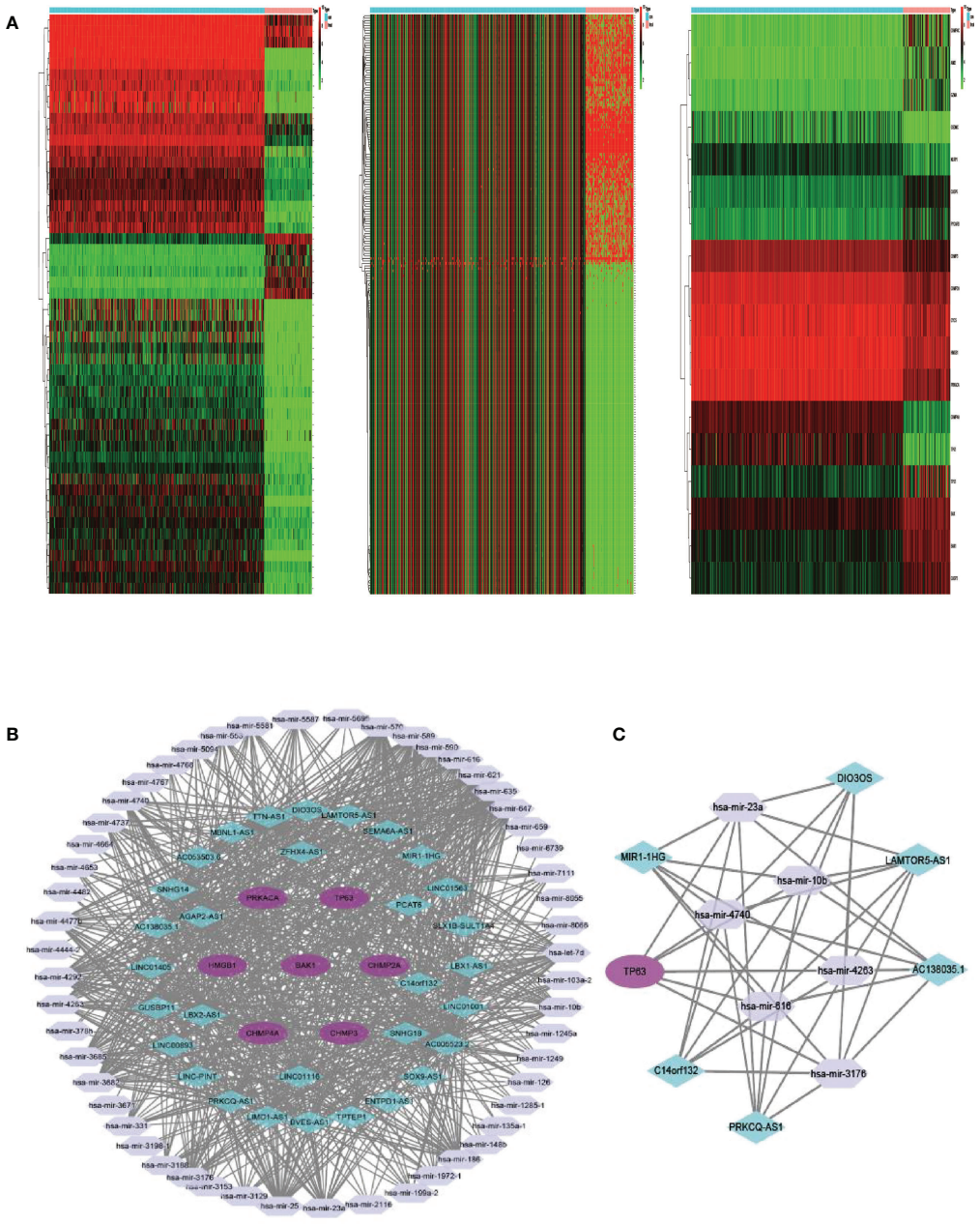

FIGURE 6
(A) Heatmap analysis for differential expressions of mRNAs, lncRNAs, and miRNAs in OS. **(B)** The ceRNA network of seven hub PRGs in OS. **(C)** The network of lncRNA–miRNA–mRNA. OS, osteosarcoma; ceRNA, competing endogenous RNA.

the WGCNA package (Figure 6B). We found 31 lncRNA nodes, 53 miRNA nodes, seven mRNA nodes, and 6,153 edges as differentially expressed profiles in the ceRNA network. Using the Cytoscape plug-in MCODE, a cluster with TP63 as the hub gene was extracted from the ceRNA network (Figure 6C). Finally, we used the starBase dataset to identify the LAMTOR5-AS1/hsa-miR-23a-3p/TP63 ceRNA regulatory axis.

Ablation of TP63 and LAMTOR5-AS1 promotes the pyroptosis of OS cells

We used shRNA and siRNA separately to silence TP63 and LAMTOR5-AS1 expression, and effective knockdown of TP63 and LAMTOR5-AS1 in both 143B and U2OS cell lines was verified by qRT-PCR (Table S2). We observed that abnormal

expressions of pyroptosis-related proteins were induced by TP63 knockdown (Figure 7A). Cleaved-Caspase-1, which mediates the canonical pathway, and cleaved-Caspase-4, which mediates the non-canonical pathway, both had their expression levels reduced. Caspase-3 and Caspase-8 were previously considered to be marker proteins related to apoptosis, and they can also activate gasdermin proteins under specific induction conditions to regulate the occurrence of pyroptosis (18, 19). When TP63 was knocked down, cleaved-Caspase-3 and cleaved-Caspase-8 also showed decreased expressions. The expressions of GSDMD-N and GSDME, as gasdermin family proteins, were decreased when TP63 was silenced. However, GSDMD was shown to have a negative relationship with TP63. Like the results of TP63 knockdown, the expressions of cleaved-Caspase-1, cleaved-Caspase-3, cleaved-Caspase-4, cleaved-Caspase-8, GSDMD, GSDME, and GSDMD-N showed a significant decrease after LAMTOR5-AS1 knockdown (Figure 7B). To summarize, TP63 should be modulated by the LAMTOR5-AS1/hsa-miR-23a-3p ceRNA regulatory network to induce the pyroptosis process of OS cells.

Discussion

OS is a malignant bone tumor most commonly found in children and adolescents who have a high mortality rate and high morbidity rate. Although chemotherapy and surgery treatments have improved the survival of OS patients, patients with metastases or those who are resistant to chemotherapy necessitate the development of new customized treatment strategies to enhance their prognosis (20). Pyroptosis as an embodiment of programmed cell death is implicated in the

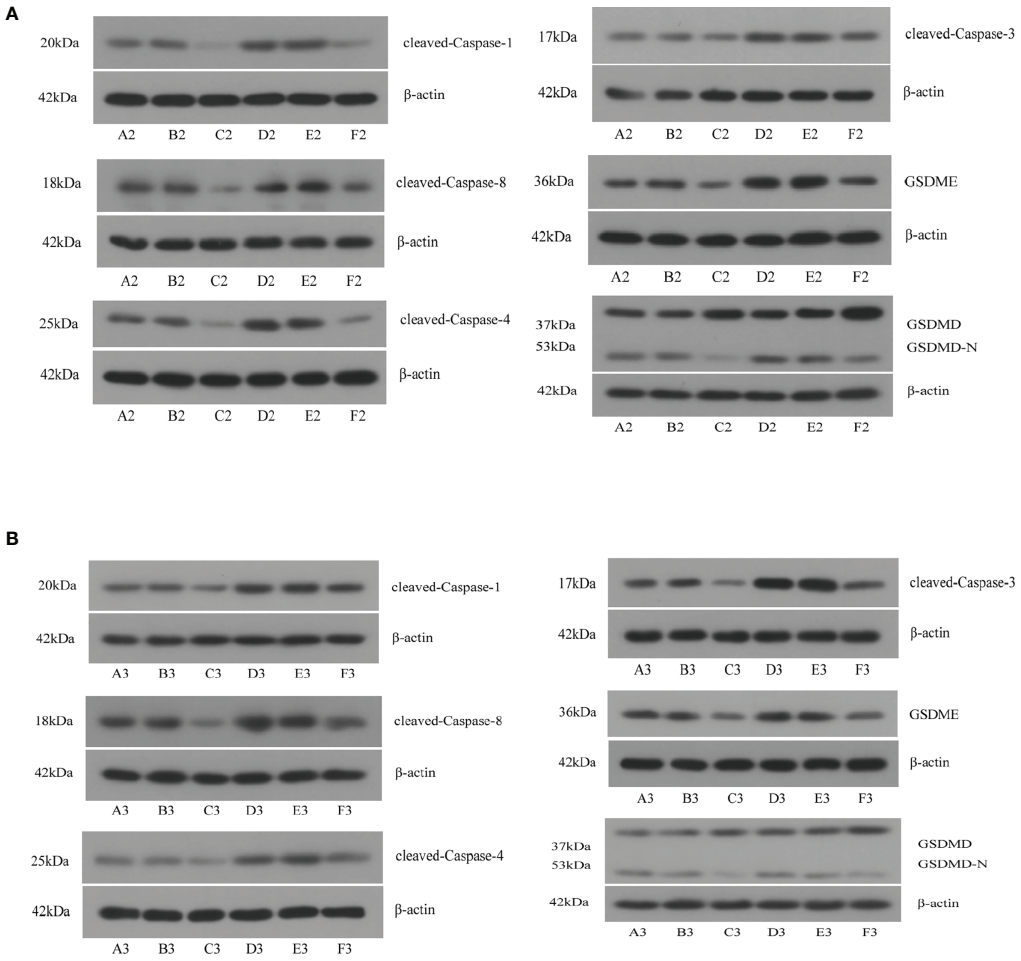

FIGURE 7
(A) After knockdown of TP63, significant decreases were observed on cleaved-Caspase-1, cleaved-Caspase-3, cleaved-Caspase-4, cleaved-Caspase-8, GSDMD, GSDME, and GSDMD-N. A2, B2, C2: 143B cell; D2, E2, F2: U2OS cell. **(B)** After knockdown of LAMTOR5-AS1, significant decreases were observed on cleaved-Caspase-1, cleaved-Caspase-3, cleaved-Caspase-4, cleaved-Caspase-8, GSDMD, GSDME, and GSDMD-N. A2, B2, C2: 143B cell; D2, E2, F2: U2OS cell.

potential molecular mechanism of tumors. Numerous studies have indicated that pyroptosis plays a crucial role in various tumors' growth and metastasis by modulating the TME (21, 22). Therefore, studying the therapeutic benefit and possible molecular mechanism of pyroptosis genes in osteosarcoma is critical. Despite that recent advances had demonstrated the regulatory effect of PRGs on a genetic and transcriptional level for OS, the global alterations in PRGs have not been characterized at CNV and ceRNA in OS.

In this study, using public databases, we determined the expression of 52 pyroptosis-related mRNAs in OS and normal tissues and discovered that most of these mRNAs were expressed differently. Although PRGs had a modest mutation frequency, the bulk of them were disordered in OS patients and were linked to prognosis. The expressions of pyroptosis-related genes were then used to classify individuals with OS. Two distinct pyroptosis patterns of OS patients were identified by the expression of pyroptosis-related genes, which showed that PRGcluster A patients had more advanced survival than PRGcluster B patients. The immune cell infiltration also differed significantly between the two clusters. PRGcluster A was characterized as an immunoinflammatory phenotype, as B cells, CD8+ T cells, immature B cells, macrophages, mast cells, MDSCs, natural killer T cells, and natural killer cells were notably rich in innate immune cell infiltration in PRGcluster A. Moreover, the T-cell receptor signaling pathway, B-cell receptor signaling pathway, NOD-like receptor signaling pathway, and chemokine signaling pathway were all found to be significantly related to immune activation in cluster A. Using the DEGs between the two subtypes of pyroptosis, three gene clusters were identified and proved to be significant in PRGs. As a result, PRGs might be used to predict the clinical prognosis and chemical therapeutic response of OS patients. We developed PRG_score, a reliable and useful prognostic tool, and proved its predictive power. The CNV, TME, prognosis, and drug susceptibility of patients with high-risk and low-risk PRG_scores were significantly different. Then, we created a quantitative nomogram by combining the PRG_score and gender, which improved PRG_score to be better utilized clinically. The predictive model could be used to stratify the OS patients' prognosis as well as help researchers better understand the disease's underlying process and provide novel treatment options.

According to various studies, the immune cells and stromal cells in the TME play critical regulatory roles in the OS patients' prognosis (23, 24). The findings of our study was consistent with the results abovementioned. The stromal score, immune score, and estimate score in the lower PRG_score group were all higher than in the higher PRG_score group, which indicated the TME as an independent risk factor influencing the prognosis of OS. Moreover, the immune microenvironment in the TME could play an important role for OS. For the present study, the relative numbers of immune cells infiltrating tumors varied considerably in two different pyroptosis clusters and two different PRG_score groups. Consequently, this finding suggested that PRGs play an important role in OS immunity regulation. PRGcluster B, which exhibited immune inhibition, had a higher PRG_score, while PRGcluster A, which exhibited immune activation, had a lower PRG_score. geneCluster A was mainly from PRGcluster A, geneCluster B from PRGcluster B, and geneCluster C from PRGcluster A and PRGcluster B, and their PRG_scores were in the following arrangement: geneCluster B > geneCluster C > geneCluster A. This suggested that immunomodulation plays an important role in OS patients' prognosis.

According to growing evidence, macrophages and CD8+ T lymphocytes play a critical role in OS immune response (25, 26). A lower CD4+/CD8+ ratio in the peripheral blood of OS patients was associated with a greater risk of mortality (27). Anne et al. suggested that CD8+ T lymphocytes were related to a lower risk of OS metastases at the time of diagnosis (25). With a better prognosis, PRGcluster A and low PRG score exhibited increased infiltration of CD8 + T cells, suggesting that they play an antitumor immunology role in OS progression. Increasing data suggest that the immunological context of the osteosarcoma microenvironment is mostly made up of tumor-associated macrophages, with a high ratio of M0 and M2 macrophages (28–30). Unlike macrophages' tumor-supportive role in many other tumor types, macrophage infiltration was associated with improved survival in OS (31, 32). In high-grade osteosarcoma patients, Buddin et al. showed that CD14-expressed macrophages were related to metastasis suppression and enhanced overall survival (33). However, several studies have shown conflicting results when it comes to the correlation between macrophage phenotypes and clinical prognosis in OS (34, 35). The results of this study indicated that the M1 and M2 macrophage infiltrations in the low PRG score group were significantly higher than those in the high PRG score group. Moreover, the patients with higher M0 and M2 macrophage infiltration had a favorable survival rate. Lastly, we investigated the sensitivity of patients in the low- and high-risk groups to a variety of chemotherapeutic agents presently used to treat OS. It was shown that patients with low PRG scores had lower IC50 values for chemotherapeutics such as roscovitine, RDEA119, rapamycin, and shikonin, while patients with high PRG scores had considerably lower IC50 values for axitinib, elesclomol, GW.441756, and thapsigargin. Using these findings, we would be able to provide our patients with a more accurate targeted therapy.

To find the hub PRG for OS regulation, a ceRNA network was constructed and a potential LAMTOR5-AS1/hsa-miR-23a-3p/TP63 regulatory axis was proposed. The TP63 gene belongs to the tumor-suppressor gene TP53 family, located on chromosome 3q28; it has a high degree of homology with TP53 in sequence and structure, so some of its biological functions are similar to TP53 (36). Sayles et al. demonstrated that TP53 alterations including structural variation (SV) and

somatic nucleotide variants (SNVs) are detected in 74% of human osteosarcoma (37). Ito et al. found that 35% of osteosarcoma cases have over three-fold MDM2 amplification (38). Another major inhibitor of TP53 is MDM4. Although it is a homolog of MDM2, MDM4 does not have ubiquitin ligase activity like MDM2. However, MDM4 still binds with TP53 and inhibits TP53 activity (PMID: 30689920, PMCID: PMC6478121, DOI: 10.1093/jmcb/mjz007). Unfortunately, to our understanding, there were no studies discussing about the correlations between TP53 and MDM2 together with MDM4; therefore, the mechanisms and axis between them need to be further investigated. As a pyroptosis hub gene, TP63 may be involved in various aspects in the modulation of pyroptosis in tumors. Celardo et al. (39) overexpressed TP63 in the OS Saos-2 cell line, and the results showed that Caspase-1 expression increased with time in a time-dependent way. Further verification showed that TP63, as a transcription factor, can bind to the promoter of the Caspase-1 gene and promote the transcription of the Caspase-1 gene. Caspase-1 is an important node in the activation of the classical pathway of pyroptosis, and TP63 may promote osteosarcoma pyroptosis by increasing the expression of Caspase-1 (40). In breast cancer, TP63 induced the expression of GSDME *via* binding a specific site in GSDME (41). The findings of this study are consistent with the above conclusions. After silencing of the gene TP63 by siRNA transfection in OS cells, the protein levels of cleaved-Caspase-1 and GSDME were downregulated when measured by WB, and other pyroptosis marker proteins including cleaved-Caspase-3, cleaved-Caspase-4, cleaved-Caspase-8, and GSDMD-N were also downregulated. This indicated that TP63 could activate cell pyroptosis in OS through multiple pathways including canonical (Caspase-1 mediated) and non-canonical (Caspase-4 mediated) pathways. Moreover, we used the starBase v2.0 database to predict that LAMTOR5-AS1 regulates the expression of TP63 in OS through the ceRNA mechanism in combination with hsa-miR-23a-3p. Pu et al. (42) demonstrated that LAMTOR5-AS1 reduces OS cell growth and multidrug resistance in a considerable way. In this study, LAMTOR5-AS1 knockdown decreased the expression of cleaved-Caspase-1, cleaved-Caspase-3, cleaved-Caspase-4, cleaved-Caspase-8, GSDME, and GSDMD-N in OS cells, which demonstrated that the type and expression trend of pyroptosis marker proteins regulated by LAMTOR5-AS1 was consistent with those regulated by TP63. This could prove that TP63 as hub pyroptosis gene could be modulated by the LAMTOR5-AS1/hsa-miR-23a-3p ceRNA regulatory network.

There were various flaws in this research. To begin, all studies were based exclusively on data from public sources, and clinical samples were not collected. As a consequence, there may have been an inherent bias in selection of cases that affected the study findings. To corroborate our results, large-scale prospective investigations as well as more *in vivo* and *in vitro* experimental research are required. Furthermore, the LAMTOR5-AS1/hsa-miR-23a-3p/TP63 ceRNA network lacked validation by using the luciferase reporter system to confirm that hsa-miR-23a-3p was the miRNA sponged by LAMTOR5-AS1.

Conclusions

Based on our thorough investigation of PRGs, we found a complex regulatory system through which they influence the tumor-immune-stroma environment, clinicopathological characteristics, and prognosis. Meanwhile, a ceRNA network was built to find a LAMTOR5-AS1/hsa-miR-23a-3p/TP63 regulatory axis. We also further looked at PRGs' therapeutic potential in targeted therapy and immunotherapy. These results emphasized PRGs' critical clinical significance and provide fresh ideas for directing individualized chemotherapy and immunotherapy for OS patients.

Data availability statement

The original contributions presented in the study are included in the article/Supplementary Material. Further inquiries can be directed to the corresponding author.

Author contributions

The study was designed and conceptualized by JH, YH, SD, and HW. JH, YH, SD, and SL curated the data. The statistical analysis was carried out by JH, and YH. The manuscript was written by JH and YH. The study was overseen by HW. We all revised the manuscript, read the submitted version, and agreed with it.

Funding

This work was funded by the National Natural Science Foundation of China (grant number: 31971275).

Conflict of interest

The authors declare that the research was conducted in the absence of any commercial or financial relationships that could be construed as a potential conflict of interest.

Publisher's note

All claims expressed in this article are solely those of the authors and do not necessarily represent those of their affiliated

organizations, or those of the publisher, the editors and the reviewers. Any product that may be evaluated in this article, or claim that may be made by its manufacturer, is not guaranteed or endorsed by the publisher.

Supplementary material

The Supplementary Material for this article can be found online at: https://www.frontiersin.org/articles/10.3389/fimmu.2022.974916/full#supplementary-material

SUPPLEMENTARY FIGURE 1
Consensus matrix heatmap defining two clusters (k = 3) in TARGET and GSE21257 cohort based on DEGs expression.

SUPPLEMENTARY FIGURE 2
(A) PRG score distribution and survival status in ranked dot and scatter plots in the testing group. **(B)** The expression heatmap of 5 gene signature in the testing group. **(C)** Kaplan–Meier analysis of the survival between the high- and low-risk groups in the testing group. **(D)** The prognostic accuracy of the risk scores in the testing group was verified by ROC curve. **(E)** PRG score distribution and survival status in ranked dot and scatter plots in the all group. **(F)** The expression heatmap of 5 gene signature in the all group. **(G)** Kaplan–Meier analysis of the survival between the high- and low-risk groups in the all group. **(H)** The prognostic accuracy of the risk scores in the all group was verified by ROC curve.

SUPPLEMENTARY FIGURE 3
(A–H) Correlations between PRG_score and immune cell types.

SUPPLEMENTARY FIGURE 4
Relationships between PRG_score and chemotherapeutic sensitivity.

References

1. Harrison DJ, Schwartz CL. Osteogenic sarcoma: Systemic chemotherapy options for localized disease. *Curr Treat Options Oncol* (2017) 18(4):24. doi: 10.1007/s11864-017-0464-2

2. Meltzer PS, Helman LJ. New horizons in the treatment of osteosarcoma. *N Engl J Med* (2021) 385(22):2066–76. doi: 10.1056/NEJMra2103423

3. Misaghi A, Goldin A, Awad M, Kulidjian AA. Osteosarcoma: A comprehensive review. *SICOT J* (2018) 4:12. doi: 10.1051/sicotj/2017028

4. Fang Y, Tian S, Pan Y, Li W, Wang Q, Tang Y, et al. Pyroptosis: A new frontier in cancer. *BioMed Pharmacother.* (2020) 121:109595. doi: 10.1016/j.biopha.2019.109595

5. Broz P, Pelegrin P, Shao F. The gasdermins, a protein family executing cell death and inflammation. *Nat Rev Immunol* (2020) 20(3):143–57. doi: 10.1038/s41577-019-0228-2

6. Xia X, Wang X, Cheng Z, Qin W, Lei L, Jiang J, et al. The role of pyroptosis in cancer: pro-cancer or pro-"host"? *Cell Death Dis* (2019) 10(9):650. doi: 10.1038/s41419-019-1883-8

7. Ruan J, Wang S, Wang J. Mechanism and regulation of pyroptosis-mediated in cancer cell death. *Chem Biol Interact* (2020) 323:109052. doi: 10.1016/j.cbi.2020.109052

8. Orning P, Lien E, Fitzgerald KA. Gasdermins and their role in immunity and inflammation. *J Exp Med* (2019) 216(11):2453–65. doi: 10.1084/jem.20190545

9. Erkes DA, Cai W, Sanchez IM, Purwin TJ, Rogers C, Field CO, et al. Mutant BRAF and MEK inhibitors regulate the tumor immune microenvironment *via* pyroptosis. *Cancer Discovery* (2020) 10(2):254–69. doi: 10.1158/2159-8290.CD-19-0672

10. Lambrechts D, Wauters E, Boeckx B, Aibar S, Nittner D, Burton O, et al. Phenotype molding of stromal cells in the lung tumor microenvironment. *Nat Med* (2018) 24(8):1277–89. doi: 10.1038/s41591-018-0096-5

11. Zhao W, Wang P, Jia H, Chen M, Gu X, Liu M, et al. Lymphocyte count or percentage: Which can better predict the prognosis of advanced cancer patients following palliative care? *BMC Cancer* (2017) 17(1):514. doi: 10.1186/s12885-017-3498-8

12. Constantinidou A, Alifieris C, Trafalis DT. Targeting programmed cell death -1 (PD-1) and ligand (PD-L1): A new era in cancer active immunotherapy. *Pharmacol Ther* (2019) 194:84–106. doi: 10.1016/j.pharmthera.2018.09.008

13. Cook KW, Xue W, Symonds P, Daniels I, Gijon M, Boocock D, et al. Homocitrullination of lysine residues mediated by myeloid-derived suppressor cells in the tumor environment is a target for cancer immunotherapy. *J Immunother Cancer* (2021) 9(7). doi: 10.1136/jitc-2020-001910

14. Xing X, Gu F, Hua L, Cui X, Li D, Wu Z, et al. TIMELESS promotes tumor progression by enhancing macrophages recruitment in ovarian cancer. *Front Oncol* (2021) 11:732058. doi: 10.3389/fonc.2021.732058

15. Yao Q, Chen T. LINC01128 regulates the development of osteosarcoma by sponging miR-299-3p to mediate MMP2 expression and activating wnt/beta-catenin signalling pathway. *J Cell Mol Med* (2020) 24(24):14293–305. doi: 10.1111/jcmm.16046

16. Zhang B, Mao S, Liu X, Li S, Zhou H, Gu Y, et al. MiR-125b inhibits cardiomyocyte apoptosis by targeting BAK1 in heart failure. *Mol Med* (2021) 27(1):72. doi: 10.1186/s10020-021-00328-w

17. Zheng M, Kanneganti TD. The regulation of the ZBP1-NLRP3 inflammasome and its implications in pyroptosis, apoptosis, and necroptosis (PANoptosis). *Immunol Rev* (2020) 297(1):26–38. doi: 10.1111/imr.12909

18. Shi J, Zhao Y, Wang Y, Gao W, Ding J, Li P, et al. Inflammatory caspases are innate immune receptors for intracellular LPS. *Nature.* (2014) 514(7521):187–92. doi: 10.1038/nature13683

19. Frank D, Vince JE. Pyroptosis versus necroptosis: similarities, differences, and crosstalk. *Cell Death Differ* (2019) 26(1):99–114. doi: 10.1038/s41418-018-0212-6

20. Yang Y, Han L, He Z, Li X, Yang S, Yang J, et al. Advances in limb salvage treatment of osteosarcoma. *J Bone Oncol* (2018) 10:36–40. doi: 10.1016/j.jbo.2017.11.005

21. Wang Q, Wang Y, Ding J, Wang C, Zhou X, Gao W, et al. A bioorthogonal system reveals antitumour immune function of pyroptosis. *Nature.* (2020) 579(7799):421–6. doi: 10.1038/s41586-020-2079-1

22. Tsuchiya K. Switching from apoptosis to pyroptosis: Gasdermin-elicited inflammation and antitumor immunity. *Int J Mol Sci* (2021) 22(1). doi: 10.3390/ijms22010426

23. Zhang C, Zheng JH, Lin ZH, Lv HY, Ye ZM, Chen YP, et al. Profiles of immune cell infiltration and immune-related genes in the tumor microenvironment of osteosarcoma. *Aging (Albany NY).* (2020) 12(4):3486–501. doi: 10.18632/aging.102824

24. Li B, Wang Z, Wu H, Xue M, Lin P, Wang S, et al. Epigenetic regulation of CXCL12 plays a critical role in mediating tumor progression and the immune response in osteosarcoma. *Cancer Res* (2018) 78(14):3938–53. doi: 10.1158/0008-5472.CAN-17-3801

25. Gomez-Brouchet A, Illac C, Gilhodes J, Bouvier C, Aubert S, Guinebretiere JM, et al. CD163-positive tumor-associated macrophages and CD8-positive cytotoxic lymphocytes are powerful diagnostic markers for the therapeutic stratification of osteosarcoma patients: An immunohistochemical analysis of the biopsies fromthe French OS2006 phase 3 trial. *Oncoimmunology.* (2017) 6(9):e1331193. doi: 10.1080/2162402X.2017.1331193

26. Fritzsching B, Fellenberg J, Moskovszky L, Sapi Z, Krenacs T, Machado I, et al. CD8(+)/FOXP3(+)-ratio in osteosarcoma microenvironment separates survivors from non-survivors: a multicenter validated retrospective study. *Oncoimmunology.* (2015) 4(3):e990800. doi: 10.4161/2162402X.2014.990800

27. Yang QK, Su YN, Wang W, Wang N, Yao ZX, Zhang XJ. CONUT score or/and peripheral blood CD4+/CD8+ ratio-based web dynamic nomograms to predict the individualized survival of patients with advanced osteosarcoma. *Cancer Manag Res* (2020) 12:4193–208. doi: 10.2147/CMAR.S251814

28. Inagaki Y, Hookway E, Williams KA, Hassan AB, Oppermann U, Tanaka Y, et al. Dendritic and mast cell involvement in the inflammatory response to primary malignant bone tumours. *Clin Sarcoma Res* (2016) 6:13. doi: 10.1186/s13569-016-0053-3

29. Deng C, Xu Y, Fu J, Zhu X, Chen H, Xu H, et al. Reprograming the tumor immunologic microenvironment using neoadjuvant chemotherapy in osteosarcoma. *Cancer Sci* (2020) 111(6):1899–909. doi: 10.1111/cas.14398

30. Shao XJ, Xiang SF, Chen YQ, Zhang N, Cao J, Zhu H, et al. Inhibition of M2-like macrophages by all-trans retinoic acid prevents cancer initiation and stemness in osteosarcoma cells. *Acta Pharmacol Sin* (2019) 40(10):1343–50. doi: 10.1038/s41401-019-0262-4

31. Noy R, Pollard JW. Tumor-associated macrophages: from mechanisms to therapy. *Immunity*. (2014) 41(1):49–61. doi: 10.1016/j.immuni.2014.06.010

32. Halbrook CJ, Pontious C, Kovalenko I, Lapienyte L, Dreyer S, Lee HJ, et al. Macrophage-released pyrimidines inhibit gemcitabine therapy in pancreatic cancer. *Cell Metab* (2019) 29(6):1390–9.e6. doi: 10.1016/j.cmet.2019.02.001

33. Buddingh EP, Kuijjer ML, Duim RA, Burger H, Agelopoulos K, Myklebost O, et al. Tumor-infiltrating macrophages are associated with metastasis suppression in high-grade osteosarcoma: A rationale for treatment with macrophage activating agents. *Clin Cancer Res* (2011) 17(8):2110–9. doi: 10.1158/1078-0432.CCR-10-2047

34. Koirala P, Roth ME, Gill J, Piperdi S, Chinai JM, Geller DS, et al. Immune infiltration and PD-L1 expression in the tumor microenvironment are prognostic in osteosarcoma. *Sci Rep* (2016) 6:30093. doi: 10.1038/srep30093

35. Su Y, Zhou Y, Sun YJ, Wang YL, Yin JY, Huang YJ, et al. Macrophage-derived CCL18 promotes osteosarcoma proliferation and migration by upregulating the expression of UCA1. *J Mol Med (Berl)*. (2019) 97(1):49–61. doi: 10.1007/s00109-018-1711-0

36. Yang A, Kaghad M, Wang Y, Gillett E, Fleming MD, Dotsch V, et al. p63, a p53 homolog at 3q27-29, encodes multiple products with transactivating, death-inducing, and dominant-negative activities. *Mol Cell* (1998) 2(3):305–16. doi: 10.1016/S1097-2765(00)80275-0

37. Sayles LC, Breese MR, Koehne AL, Leung SG, Lee AG, Liu HY, et al. Genome-Informed Targeted Therapy for Osteosarcoma. *Cancer Discov*. (2019) 9(1):46–63.

38. Ito M, Barys L, O'Reilly T, Young S, Gorbatcheva B, Monahan J, et al. Comprehensive mapping of p53 pathway alterations reveals an apparent role for both SNP309 and MDM2 amplification in sarcomagenesis. *CClin Cancer Res*. (2011) 17(3):416–26.

39. Celardo I, Grespi F, Antonov A, Bernassola F, Garabadgiu AV, Melino G, et al. Caspase-1 is a novel target of p63 in tumor suppression. *Cell Death Dis* (2013) 4:e645. doi: 10.1038/cddis.2013.175

40. Man SM, Karki R, Kanneganti TD. Molecular mechanisms and functions of pyroptosis, inflammatory caspases and inflammasomes in infectious diseases. *Immunol Rev* (2017) 277(1):61–75. doi: 10.1111/imr.12534

41. Fujikane T, Nishikawa N, Toyota M, Suzuki H, Nojima M, Maruyama R, et al. Genomic screening for genes upregulated by demethylation revealed novel targets of epigenetic silencing in breast cancer. *Breast Cancer Res Treat* (2010) 122 (3):699–710. doi: 10.1007/s10549-009-0600-1

42. Pu Y, Tan Y, Zang C, Zhao F, Cai C, Kong L, et al. LAMTOR5-AS1 regulates chemotherapy-induced oxidative stress by controlling the expression level and transcriptional activity of NRF2 in osteosarcoma cells. *Cell Death Dis* (2021) 12 (12):1125. doi: 10.1038/s41419-021-04413-0

Frontiers in Immunology

Explores novel approaches and diagnoses to treat immune disorders.

The official journal of the International Union of Immunological Societies (IUIS) and the most cited in its field, leading the way for research across basic, translational and clinical immunology.

Discover the latest Research Topics

See more →

Frontiers

Avenue du Tribunal-Fédéral 34
1005 Lausanne, Switzerland
frontiersin.org

Contact us

+41 (0)21 510 17 00
frontiersin.org/about/contact